Habilitationsschrift

vorgelegt von

Dr. Birger Horstmann

zur Erlangung der Lehrbefugnis im

Fachgebiet Physikalische Chemie

an der Fakultät für Naturwissenschaften
der Universität Ulm

HIU & DLR

April 2018

Electrochemical theory of reaction, transport, nucleation and growth in batteries

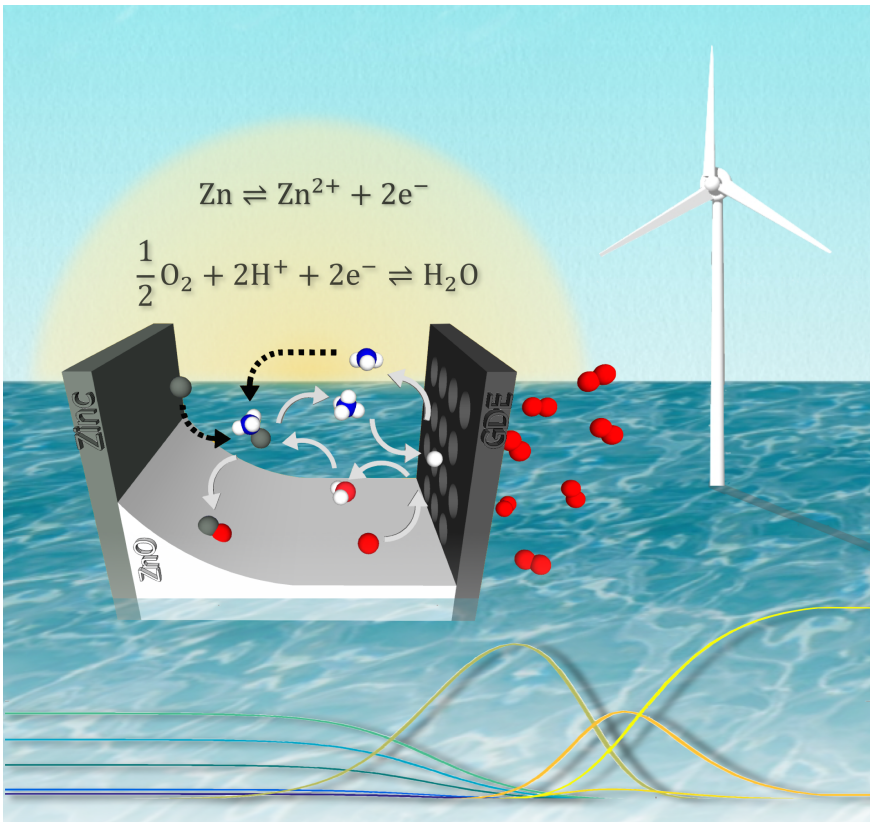

This thesis is dedicated to my sympathetically loving wife.

Front picture reprinted from Clark et al. [13] with permission from Wiley.

Acknowledgements

The acknowledgements have been removed for privacy reasons.

The acknowledgements have been removed for privacy reasons.

The acknowledgements have been removed for privacy reasons.

Abstract

Electrochemical energy storage systems become increasingly important due to the advent of large-scale renewable energy generation and electric mobility. Commercial lithium-ion batteries achieve an acceptable performance, but cannot fulfill the expectations of society. Metal-air batteries offer high theoretical energy densities and are a major candidate for next-generation energy storage. Theory-based models improve researchers' understanding of complex electrochemical systems and guide development. Along this line, we validate our models with experiments and suggest battery design optimizations throughout this work.

In this thesis, we discuss the development of consistent modeling methods and their implementation to advance metal-air and lithium-ion batteries. Non-equilibrium thermodynamics is the point of origin for deriving consistent equations for reaction and transport in electrochemical systems based on various electrolytes. Structural changes due to dissolution and crystallization reactions determine the behavior of metal-air batteries. With analogous modeling methodologies, we study the morphologic evolution of the solid electrolyte interphase in lithium-ion batteries. Our electrochemical continuum theories describe mesoscopic processes at the interfaces of battery electrodes as well as macroscopic processes governing battery cell performance.

Contents

Chapter 1

Introduction

1.1 History and motivation

The history of battery research is tightly linked to the development of electric devices [14]. The first electrochemical cell was developed by Alessandro Volta following a dispute with Luigi Galvani in the late 1700s [15]. The Voltaic pile, combining zinc and copper electrodes facilitated research on electromagnetism and electrochemistry in the following decades. The improvements of the Voltaic pile culminated in the invention of Georges-Lionel Leclanché in 1866. His battery consisted of a zinc anode and a manganese oxide-carbon cathode, the prototype of today's primary alkaline-manganese batteries. This zinc-manganese battery soon spread out to power the telegraphic revolution.

In contrast to primary batteries, secondary batteries are electrically rechargeable. Gaston Planté in 1859 and Waldmar Jungner in 1901 demonstrated the rechargeable lead-acid and nickel-cadmium batteries. These batteries served their purpose for many applications from lighting to transportation. Between the late 1960s and early 1990s new portable applications emerged and demanded for secondary batteries with higher energy densities. These applications comprise the portable consumer electronic market and implantable medical devices [15]. The nickel-metalhydrate battery is a successful advancement of the nickel-cadmium battery and applied in electric mobility. The zinc-air battery can be viewed as an advancement of the zinc-manganese battery, but it has only reached widespread commercial success as primary battery despite many demonstrator projects [16, 17]. At the moment, the lightweight metal lithium is the clear frontrunner [15]. The lithium-ion battery is entering almost all possible markets in portable, mobile, and stationary applications.

In the last decade, research on energy storage technologies accelerated again because they are indispensable for reaching a carbon neutral society. Especially batteries store high grade electric energy with very high efficiencies and can easily be integrated into the existing electricity infrastructure [18]. They attempt to take over the traffic sector and contribute to leveling intermittent renewable energy production. Lithium-ion batteries stand out because they offer high energy and power densities at very low costs [19]. Despite steady improvements in terms of energy density and cost, it is believed that new cell architectures are necessary to achieve the same comfort as oil-powered devices. Prospective candidates to outperform lithium-ion batteries include metal batteries, e.g., lithium metal [20], and conversion batteries, e.g., magnesium-sulfur and zinc-air [21].

In this habilitation, we study processes and structures on multiple length scales in multiple battery architectures with a multi-disciplinary approach. Based on our theoretical understanding, we propose design improvements for lithium-air batteries, zinc-air batteries, and lithium-ion batteries. We start from non-equilibrium thermodynamics, which is known from (statistical) physics, derive continuum models, which are frequently used in (chemical) engineering, and describe reaction and transport in (physical) chemistry [22]. Because electrochemical devices rely on the interplay of multiple length scales, our models are applied to processes from the molecular scale to the cell scale.

Let us illustrate this interconnectedness: The discharge products in lithium-air batteries must be accommodated inside the battery cell. In the case of aqueous lithium-air batteries, our cell simulations show that lithium hydroxide precipitates on the negative electrode [2]. For aprotic electrolytes, instead, precipitation happens inside the positive electrode [1]. A microscopic surface model shows how the morphology of precipitated lithium oxide depends on the applied current density [8]. The same modeling methodology predicts the morphology of the solid electrolyte interphase (SEI) that grows on the standard negative electrode of lithium ion batteries [10–12]. In zinc-air batteries, an interphase of zinc oxide forms near the surface of zinc metal and determines the cell performance [4]. The chemical composition and morphology of this interphase of precipitants must be taken into account when designing new zinc-air battery electrolytes [5].

In the remaining of this chapter, we introduce the status of research on metal-air batteries (see section 1.2) and lithium ion batteries (see section 1.3).

Then in section 1.4, we briefly review theoretical methods used in battery research. Finally, an overview of this research summary is given in Sec. 1.5.

1.2 Metal-air batteries

This introduction to metal-air batteries is an edited excerpt of our recent review [6]. In the ever-growing search for safe and high-performance energy storage technology, development of metal-air batteries is taking on new importance [19]. The promise of these systems is clear: a significant increase in energy density over lithium-ion batteries, utilization of abundant materials, and improved safety [23]. While great progress has been made in their development, challenges remain before secondary metal-air batteries can become widely commercially viable.

Metal-air batteries comprise a metal electrode (e.g., Li, Na, Li, Si, Mg, Al, Fe etc.), electrolyte (aqueous or non-aqueous), and a bi-functional air electrode that is open to an oxygen reservoir. The basic operating principle is to electrochemically reduce O_2 from air and oxidize the metal electrode to reversibly form solid metal-oxides. This design achieves gravimetric energy densities two to five times that of lithium-ion batteries. Figure 1.1 compares the theoretical energy density and specific energy of metal-air systems.

Research into a variety of metal-air chemistries is ongoing. The very negative potential of Mg metal makes magnesium-air systems appealing [24], but magnesium-air batteries are severely limited by the corrosion of the Mg electrode in aqueous electrolytes [25] and by electrolyte decomposition in non-aqueous electrolytes [26]. Ionic liquid electrolytes have been proposed for magnesium-air systems, but they also suffer from electrochemical instability [27]. Another interesting contender is aluminum-air because Al is an abundant and safe material. However theses systems are susceptible to corrosion and have not demonstrated adequate cycling stability [28]. The natural abundance and safety of sodium combined with its comparable properties with lithium have driven research into sodium-air, but a fully reversible system has not been demonstrated [29–31]. Silicon-air batteries have also attracted attention [32]. Experimental studies of silicon-air systems have been performed in both ionic liquid [33] and alkaline electrolytes [34], but they still face multiple challenges.

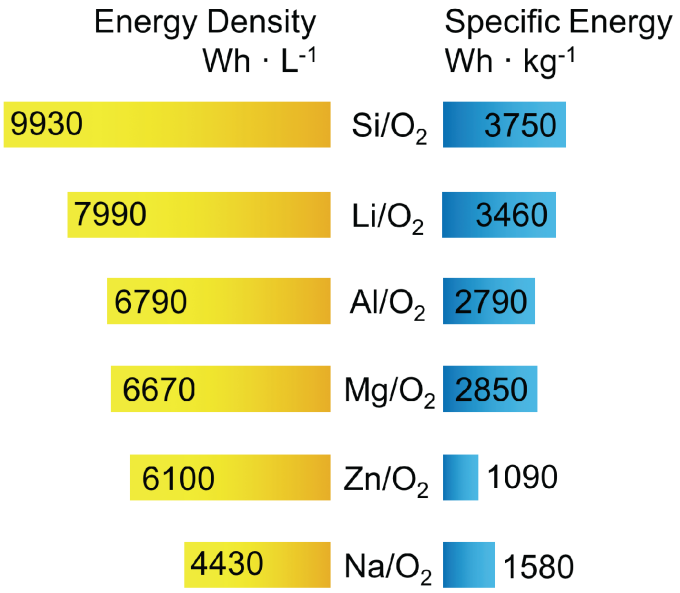

Figure 1.1 Overview of the theoretical energy density and specific energy (including oxygen) of commonly researched metal-air batteries. Values are calculated considering the specific mass and volume of the discharge product with the OCV and charge transferred in the cell reaction. Reprinted from Clark et al. [6].

Among the metal-air systems under development, lithium-air and zinc-air are the most promising [17, 23, 35].

1.2.1 Lithium-air batteries

Lithium-air batteries have been researched for decades, but have only become a widely-pursued topic since the early 2000s. The electrolyte has proved to be a limiting factor in the development of lithium-air batteries. Both non-aqueous and aqueous electrolyte configurations are common for lithium-air systems. The beginning of the lithium-air battery research wave focused on aprotic electrolytes. The first work on the aprotic lithium-air system was performed in 1996 by Abraham et al. [36], who proposed an overall reaction forming Li_2O_2 or Li_2O. Early aprotic lithium-air cells were based on a carbonate solvent, but it has since been shown that carbonate solvents are unstable, producing lithium-carbonates during discharging and evolving CO_2 during charging [37–40]. These days, carbonate electrolytes have been abandoned in favor of ether and ester solvents with lithium salts [41, 42]. A second challenge for lithium-air batteries in aprotic electrolytes relates to the precipitation of Li_2O_2.

When this solid precipitates in the cathode, it can form a dense layer over the carbon surface, inhibit the transfer of electrons, and limit the cell capacity [43]. Alternatively, lithium oxide precipitates in toroidal particles [8, 44–46]. Finally, it has been noted that oxygen transport in aprotic eletrolytes is typically a challenging factor in lithium-air battery performance, especially at higher current densities [1, 47]. This has motivated researches to learn from the success of the gas diffusion electrode in fuel cells and pursue investigations of lithium-air batterys with aqueous electrolytes.

Li metal reacts violently with water, which has until recently limited the use of aqueous electrolytes for lithium-air systems. Glass ceramic layers over the Li electrode can protect the metal electrode while still allowing the electrochemical reaction to proceed [48–50]. In alkaline aqueous electrolytes, the discharge product is $LiOH \cdot H_2O$. In these systems, $LiOH \cdot H_2O$ tends to precipitate at the separator-anode interface [2, 49], which reduces the risk of pore clogging in the cathode as observed in aprotic lithium-air batteries. However, when aqueous alkaline electrolytes are exposed to air, dissolved CO_2 reacts with OH^- to form carbonates, which slowly reduces the conductivity of the electrolyte and limits the lifetime of the cell [4, 51]. After the recent wave of interest in the development of Li-air batteries, significant challenges remain [40, 52–58].

1.2.2 Zinc-air batteries

Zn-air batteries stand alone as the only fully mature metal-air system and have been successfully commercialized as primary cells for many years. They are particularly suitable for low-current applications like hearing aids. One major advantage of Zn as an electrode material is that, unlike Li, it is stable in water. In their most common configuration, zinc-air batteries contain a metallic Zn electrode, porous separator, aqueous KOH electrolyte, and a bi-functional air electrode. While zinc-air batteries have been quite successful as primary cells, there are a number of hurdles that limit their electrical rechargeability and provide opportunities for further research [17].

The most well-known challenges relate to the aqueous KOH electrolyte. When the zinc-air battery is operated in air, CO_2 can dissolve in the electrolyte and react with OH^- to form CO_3^{2-} [51]. This parasitic reaction reduces the

conductivity of the electrolyte, slows down the cell reactions, and eventually kills the cell [4]. A second challenge for the electrolyte is the evolution of hydrogen gas. The potential of the Zn electrode reaction is below the potential for hydrogen evolution, which causes the electrolyte to be thermodynamically unstable [6]. However, H_2 evolution on the Zn surface can be kinetically suppressed with dopants, such as Hg, In, or Bi [59–61]. Metal electrodes offer the possibility of achieving very high energy density. However, the formation of mossy or dendritic metal structures during charging can cause the electrode to change shape [62]. A further challenge in Zn electrode design is the passivation of the electrode surface due to ZnO precipitation [4, 63, 64].

To address these challenges, this work contributes to the development of alternative electrolytes, e.g., alkaline with additives [4, 65, 66], near-neutral aqueous [5, 67, 68], and ionic liquid [9, 69–71]. Further research is devoted to material development to address the lifetime limitations and cell engineering to improve the performance of these systems [72]. The development of secondary zinc-air batteries has progressed to the point that they could become feasible for stationary storage applications and some Start-Ups like Eos Energy Storage [73] and Fluidic Energy [74] have begun to commercialize the technology. Zinc-air systems offer perhaps the most immediate and reliable pathway to a viable secondary metal-air battery.

1.3 Lithium-ion batteries

Lithium-ion batteries consist of two porous electrodes which are separated by an electrically insulating and porous membrane [75]. Typically, electrodes and separators are about $100\ \mu$m and $10\ \mu$m thick, respectively. These films are enclosed by metallic current collectors and folded or rolled to yield the actual battery. A liquid carbonate-based electrolyte is then filled into the pores of its constituents. The commercial materials for positive electrodes are oxides or phosphates that act as a host structure for the so-called intercalation of lithium atoms [76, 77]. Graphite can host lithium atoms in its layer structure and acts as the standard lithium negative electrode [78]. The image of lithium-ion batteries as rocking chair battery can bee drawn [79]. Lithium ions are stored in the graphite, during discharge they move through the electrolyte into the oxide cathode, during charge they move back into the graphite electrode.

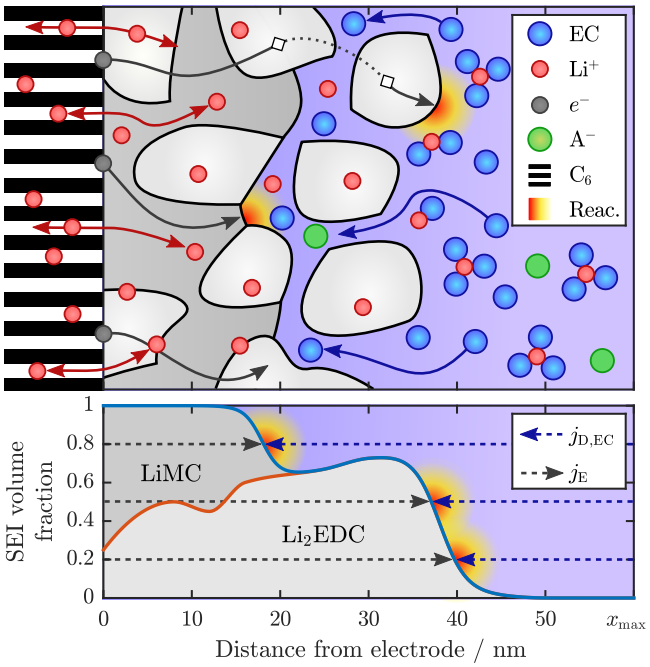

Figure 1.2 (a) Cross section through the graphite electrode (left, $x < 0$), and a SEI with dual layer structure. Solvent, Li ions and electrons are mobile species and move as indicated by the corresponding arrows. Reduction reactions (indicated red), consume these species and facility SEI growth. (b) SEI volume fraction gained by averaging the structure above in planes parallel to the electrode surface. Reprinted from Single et al. [11].

The development of graphite intercalation electrodes was the key to the success of lithium-ion batteries because the electrolytes used are unstable at the working potentials of most lithium battery electrodes. The electrolyte decomposition products form the so-called solid electrolyte interphase (SEI) that is protecting the electrolyte and slows down its decomposition (see figure 1.2) [80, 81]. Its growth, however, does never stop completely and the thickness of the SEI is found to grow with the square root of time during the lifetime of the battery [82]. The mechanism behind this continued SEI growth is still discussed among researcher. In this work, we give the first indirect experimental evidence for lithium interstitial diffusion as underlying mechanism [10–12]. Nevertheless, lithium transport through the SEI remains possible and is typically not limiting battery performance.

The SEI is in the focus of many processes that limit lifetime, performance, and safety of lithium-ion batteries. The main capacity fade during battery storage stems from the consumption of lithium due to the continued growth of

SEI [83, 84]. During battery cycling, the graphite particles undergo a notable volume change that exerts stress on the graphite material and the SEI, leading to an increased defect rate in the electrode. Furthermore, healing a broken SEI consumes further lithium and electrolyte. This volume change is even more pronounced for potential high-capacity materials for negative electrodes like lithium metal or silicon [85]. Therefore, understanding of the mechanical properties of SEI is our long-term goal. At high rates and low temperatures, it is favorable for lithium ions not to intercalate into graphite, but to plate as metallic lithium onto the graphite surface. Lithium plating is partly reversible, but irreversible loss of lithium metal contributes to capacity fade [86]. Even worse, lithium metal tends to form high surface area structures like whiskers, mossy structures, or dendrites that might penetrate the separator and short-circuit the battery [20, 87]. This is an example of a trigger event for battery overheating. If the SEI decomposes through exothermic reactions above a critical temperature, many degradation reactions are ignited. This thermal runaway is the main cause for fatal battery failure. Dependent on the cathode material, a thin cathode electrolyte interphase forms reminiscent of the SEI [88].

1.4 Theoretical methods

We review modeling methodologies for electrochemical cells in the following. Batteries like almost all modern technology products rely on the interplay of multiple length scales (see Table 1.1). On each relevant length and time scale, specifically designed models have gained maturity during the last decade. By combining several sub-models into one multi-scale model, we are able to describe the performance and degradation of batteries.

1.4.1 Atomistic quantum chemistry

Quantum physics is governing the structure and interaction of individual atoms on the nano-scale. Density functional theory (DFT) naturally predicts static atomistic properties, e.g., crystal structures, thermodynamic energies, and electronic band structures [89]. This success is transferred to dynamic situations, e.g., catalytic processes on electrode surfaces [90, 91] and electron

Name	*Length*	*Battery effect*
System	1 m	battery pack
Macro	1 mm	elementary cell
Micro	10 μm	electrode pore, electrode partice
Meso	100 nm	electrode surface, particle crack
Nano	1 nm	crystal structure, atomic defect

Table 1.1 Length scales in battery research.

transport [43, 92], for which DFT nicely explains experimental trends. Still on the nano-scale, semi-classical methods, e.g., Kinetic Monte Carlo (KMC) and molecular dynamics (MD), take the input from DFT for structure and kinetics and compute the common motion of thousands of particles, e.g., diffusion coefficients in intercalation compounds [92] and mechanical properties of SEI material [93, 94]. DFT, KMC, and MD simulation results are employed for parameter calculations within this habilitation.

1.4.2 Non-equilibrium thermodynamics

This habilitation relies on continuum models based on the fundamental works of John Newman at the University of California in Berkeley on electrolyte transport in porous electrodes from the 1970s [95]. This first approach is best suited to describe the thermal behavior of whole battery cells in engineering terms [1]. In recent years, physically more consistent approaches have been introduced to electro-chemical modeling that describe strongly interaction systems on smaller scales, such as the transport of ions in concentrated electrolytes [22, 96], rates of electrochemical reactions [97–99], dynamic phase boundaries in/on electrode particles [8, 61, 100–102], or electrochemical interfaces [9, 103–106], too. These models of non-equilibrium thermodynamics are derived from a single energy functional of the system.

Consistent non-equilibrium thermodynamics pushes the frontier of continuum models towards lower scales. Central battery mechanisms find place on the meso-scale, e.g., SEI formation, precipitation reactions. The variety of phenomena only allows to enlist examples of meso-scale models: Phase-field theories describe moving phase boundaries and predict the suppression of phase separation in lithium iron phosphate [61, 100], Nernst-Planck models

capture electrochemical double layers at electrochemical interfaces for various electrolytes [103, 105, 107], and growth models evaluate the long-term growth of SEI [11, 85, 108]. In this work, we contribute to this research endeavor by predicting nucleation, i.e., rates of the oxygen reduction reaction [7], phase separation in Li_2O_2 [8], double layers in ionic liquids [9], and long-term growth of SEI [10–12].

3D micro-structure resolved simulations of battery cells have been made possible by consistent electrolyte transport theories [22, 96] and the advance in computational power. These simulations capture the diffusion-migration of ions in the electrolyte between the electrodes from the cell level to the electrode pores and the diffusion of lithium inside the intercalation material of the electrode particles. They give insights into the effect of electrode inhomogeneity on safety, e.g., by predicting the thermodynamic onset conditions for plating [109], and allow to optimize the electrode structure, e.g., by estimating the effect of thicker electrodes [110]. In this habilitation, we show how our meso-scale models can be integrated in 3D micro-structure resolved simulations of battery cells.

On the macro-scale cell level, the electrolyte transport equations for concentrations and electric potential are often homogenized and solved in a single dimension connecting the two electrodes [1, 111, 112]. Diffusion in representative electrode particles is then taken into account in an additional artificial dimension. The resulting 1D+1D porous electrode theory was invented by Newman [95] and successfully applied to many battery types. Despite their widespread use, shortcomings of the Newman model exist. In this habilitation, we take special care and discuss that our findings do not rely on unknown empirical parameters. 3D micro-structure resolved simulations show that the Newman model faithfully simulates mean quantities, but that fluctuations are significant [22]. In the case of next-generation batteries, e.g., metal-air batteries, however, the battery design is not final, material properties, and electrochemical processes are not accurately known. Therefore, the detailed results of 3D simulations are often not needed. 1D simulations of mean quantities, instead, give the right qualitative insights to speed-up the experimental development and test novel design proposals. Therefore, we make use of 1D cell models and propose new cell designs for lithium-air [1–3] and zinc-air batteries [4–6].

1.4.3 Network models

System level battery models are typically based on electric circuits. This allows to model the thermal distribution in cylindrical batteries [113] or to analyze the state-of-charge of batteries [114]. Because these models are very empiric and rely on parameterization, they are often accompanied by measurement techniques, e.g., impedance spectroscopy [115]. Models on this length scale are not included in this work.

1.5 Overview

We will now proceed with the overview of this research summary. As stated above, the models in this habilitation can be divided into macro-scale and meso-scale models. The modeling methodology and the consistent derivation of equations from non-equilibrium thermodynamics is the unifying structure. In order to illustrate this, we introduce the reader to concepts and terminology of our modeling approach in chapter 2. Starting from the non-equilibrium free energy, we sketch the derivation of the equations for transport in electrolyte and for electrochemical reaction rates. These equations can describe the behavior of battery cells. In micro-structure resolved battery models, they are solved directly. We further describe a volume-average of these equations and obtain the equations for one-dimensional cell simulations. Unique modeling elements for metal-air batteries are briefly mentioned and discussed in detail in chapter 3, i.e., multi-phase coexistance in gas diffusion electrodes, theory of nucleation and growth, quasi-particle model for complex electrolytes. Finally, we show how meso-scale surface models are derived along the same lines and discuss similarities and differences with macro-scale models. Here we describe surface growth models and electrochemical double layers.

Our macro-scale models are summarized in chapter 3. Lithium-air batteries with aprotic electrolytes receive most attention [1], but we demonstrate the unique benefits of using aqueous electrolytes [2]. In the cathode, solid, gaseous, and liquids phases coexist and we validate our model of phase coexistence [3]. Performance of aqueous lithium-air batteries is limited by precipitation of lithium hydroxide close to the negative electrode. We study the effect of this inhomogeneous nucleation and growth process [2]. We extend

our approach to zinc-air batteries [4]. Here the sub-models take into account zinc oxide diffusion barriers, reactions of carbon dioxide to carbonate ions, and homogeneous electrolyte reactions. We show that inhomogeneous nucleation of ZnO limits the rechargeable capacity and that the lifetime of the standard alkaline electrolyte is limited by carbon dioxide absorption. Neutral aqueous electrolytes based on ammonia buffer rely on a multitude of possible zinc species complexed by chloride, ammonia, or hydroxide. We present a novel modeling concept that makes possible the dynamic simulation of battery cells with such buffered electrolytes. As a consequence, we are the first to simulate novel zinc-air battery cells with these electrolytes and propose novel electrolyte compositions for further experimental research [5].

In chapter 4, we summarize our meso-scale models. We studied the oxygen reaction process. In aqueous electrolytes, reaction intermediates and elementary reaction barriers are well-known from DFT calculations [90, 91] and we constructed a mean-field theory of the reaction process on the platinum surface that demonstrates a change in reaction mechanism as a function of applied potential [7]. In non-aqueous electrolytes, the reaction process is less clear because the electrochemical oxidation/reduction of oxygen is interwoven with the precipitation/dissolution of lithium oxide. We showed with a phase-field approach how the precipitates grow into big micro-meter sized particles [8] at small current densities. At large current densities, however, a few nano-meters thick, passivating lithium-oxide film forms. This exemplifies the strong scale-coupling in electrochemical systems.

We develop a model for the growth of SEI [10, 11]. Going beyond the standard continuum models for SEI growth, we make no prior assumption on the dominant growth limiting transport mechanism and predict the morphology of SEI. Assuming a single SEI formation reaction, we predict the growth of a porous SEI. In the presence of additional formation reactions, we study two mechanisms that lead to a dual-layer SEI with a compact, non-porous, inner layer. Finally, we compare different growth-limiting transport mechanisms and find that charge transport through the SEI is most likely limiting its growth. Then, we validate our model understanding with specific experiments. Jossen et al. show that the SEI growth rate strongly depends on the graphite potential and the graphite state-of-charge [83]. We analyze that this agrees excellently with diffusion of neutral radicals through the SEI, but not with conduction of electrons [12].

The electrochemical stability of electrolytes and the quest for battery chemistries with higher voltages motivates research on novel electrolytes, e.g., ionic liquids. As shown previously, these electrolytes show a rich quasi-crystalline behavior at electrode surfaces [103, 116]. We develop a rigorous physics-based model that captures bulk and surface properties together as well as the impact of additives. Our model predicts the appearance of a quasi-crystalline layer structure in the electrolyte near the electrode. Small amounts of charged additives have the ability to destroy this order. Again, this work aims at understanding the boundary between the meso-scale and the macro-scale world.

Chapter 2

Theory and model

In this chapter, we summarize the unifying modeling framework used in this habilitation. More detailed discussions are given in the modeling sections of the original publications on which this habilitation is based. The first section 2.1 describes the idea that the free energy functional generates the continuum model and derives the fundamental equations for ionic transport in electrolytes and electrochemical reactions at electrodes. Then, we formulate the method of volume averaged cell simulations in section 2.2 and derive surface growth models from a free-energy functional in section 2.3.

2.1 Non-equilibrium thermodynamics

2.1.1 Thermodynamics

We define the state of our models by a set of independent variables, e.g., the electrolyte potential $\phi(x, t)$ and the concentrations of ions $c_i(x, t)$ in the electrolyte. The model dynamics, i.e., the time evolution, is stated by a system of partial differential equations and algebraic conditions of this model state. It is often a difficult task to find this system of equations directly. Therefore, we do not start the modeling process from these equations, but we start from the free energy of the system. In this way, modeling affects only a single equation, the rest is a rigorous derivation based on statistical physics and mathematics. The derived models are denoted consistent because they obey the laws of physics. We use the framework of rational thermodynamics [117, 118] and its applications to electrochemical systems [22, 96, 119]. The original papers

contained in this cumulative habilitation extend the approach to multi-species, multi-phase, and incompressible systems [2, 4, 9].

The following illustration is based on the derivation of a transport theory for N arbitrarily charged species in electrolytes which is in preparation for publication, see Hoffmann et al. for reference [9]. We divide the Helmholtz free energy

$$F = \int f_{\mathrm{H}} \mathrm{d}V + F^{\mathrm{int}} \tag{2.1}$$

into a local part described by a single-particle free energy density f_{H} and a many-particle interaction energy F^{int}. The latter contains energetic contributions involving more than one particle, e.g., molecular attraction. We take into account F^{int} in section 2.3 only.

Here, we choose the single-particle free energy density for the isothermal case

$$f_{\mathrm{H}} = \frac{\vec{E}\vec{D}}{2} + \frac{\mathcal{K}}{2}\left(1 - \sum_{\alpha=1}^{\mathrm{N}} \nu_\alpha c_\alpha\right)^2 + RT \sum_{\alpha=1}^{\mathrm{N}} c_\alpha \ln\left(\frac{c_\alpha}{c}\right) + f_{\mathrm{H}}^{\mathrm{int}}(c_\beta) \tag{2.2}$$

modeling electrostatic energy, elastic energy, entropy, mean chemical interaction energy, respectively. We express $f_{\mathrm{H}}^{\mathrm{int}}$ in terms of activity coefficients f_β via $\frac{\partial f_{\mathrm{H}}^{\mathrm{int}}}{\partial c_\beta} = \mu_\beta^0 + RT\ln(f_\beta c)$. The elastic energy enforces the volumetric incompressibility constraint $\sum_{\alpha=1}^{\mathrm{N}} \nu_\alpha c_\alpha = 1$ [2, 4, 107, 119, 120] because we let the bulk modulus diverge $\mathcal{K} \to \infty$. Making use of the conservation of energy, momentum, and mass, an equation for the rate of entropy production is derived [22]

$$R = \tau : \tilde{\kappa} - \vec{j} \cdot \vec{\nabla}\varphi - \sum_{\alpha=1}^{\mathrm{N}} \vec{N}_\alpha \cdot \vec{\nabla}\mu_\alpha \geq 0, \tag{2.3}$$

where τ is the electrochemical stress tensor and $\tilde{\kappa}$ is the strain rate tensor. The semi-positiveness of the entropy production restricts the dependence of particle flux densities $\vec{N}_\alpha$ and electric current density $\vec{j}$ on concentrations c_α and electric potential φ (see section 2.1.2). For this habilitation it is most important that the derivation of the entropy production results in an expression for the chemical potential

$$\mu_\alpha = \frac{\delta F[c]}{\delta c_\alpha} = \frac{\partial f}{\partial c_\alpha} = \mu_\alpha^0 + RT\ln(f_\alpha c_\alpha). \tag{2.4}$$

Here, the second equality assumes $F^{\text{int}} = 0$ and the third equality neglects the contribution of the Maxwell pressure. These assumptions are valid in the bulk electrolyte far away from electrode surfaces.

2.1.2 Transport theory

We describe the derivation of transport equations from the free energy in Stamm et al. [4]. Here, we illustrate the equations by discussing the fundamental case of a binary salt. For simplicity, we assume constant temperature and vanishing viscosity, i.e. $\tau = 0$.

First, we note that the flux densities N_α in equation 2.3 are not independent. The velocity of the first species, typically the solvent, is determined by momentum conservation, i.e., $\sum_{\alpha=1}^{N} M_\alpha N_\alpha = 0$. In the bulk electrolyte, we use electro-neutrality which is the first order approximation of the Poisson equation, i.e., $\sum_{\alpha=1}^{N} z_\alpha c_\alpha = 0$. Thus, for a binary salt the flux density and concentration of the cation alone determines the entropy production

$$R = -\vec{j} \cdot \vec{\nabla}\varphi - \vec{N}_+ \cdot \vec{\nabla}\mu \geq 0, \tag{2.5}$$

where we introduce the salt chemical potential μ. The thermodynamical fluxes $\vec{j}$ and $\vec{N}$ fulfill the Onsager reciprocal relations, which we write compactly as

$$\begin{pmatrix} \vec{N}_+ \\ \vec{j} \end{pmatrix} = -\mathbb{O} \begin{pmatrix} \vec{\nabla}\mu \\ \vec{\nabla}\varphi \end{pmatrix} = - \begin{pmatrix} O_{11} & O_{12} \\ O_{21} & O_{22} \end{pmatrix} \begin{pmatrix} \vec{\nabla}\mu \\ \vec{\nabla}\varphi \end{pmatrix}. \tag{2.6}$$

The Onsager matrix $\mathbb{O}$ has to be positive semi-definite to ensure positive entropy production $R \geq 0$. This leads to the equations

$$\vec{N}_+ = -D \cdot \vec{\nabla} c_+ + \frac{t_+ \vec{j}}{z_+ F}, \tag{2.7}$$

$$\vec{j} = -\kappa \cdot \vec{\nabla}\phi - \kappa \frac{t_+ - 1}{z_+ F} \left(\frac{\partial \mu}{\partial c_+} \right) \vec{\nabla} c_+, \tag{2.8}$$

which depend on the electrochemical potential of the cation $z_+ F\phi = z_+ F\varphi + \mu$. This theory relies on the three parameters diffusion coefficient D, conductivity κ, and transference number t_+. In conclusion, we brought the equations into the form of Newman's concentrated solution theory [95].

In the absence of reactions, concentration and charge density are conserved. Taking the local charge neutrality of the electrolyte into account, salt concentration c and electrolyte potential ϕ satisfy

$$\frac{\partial c_+}{\partial t} = -\vec{\nabla}\vec{N}_+ + \vec{\nabla}\left(c_+\vec{v}\right), \tag{2.9}$$

$$0 = -\vec{\nabla}\vec{j}. \tag{2.10}$$

It is a small, but important finding of this work that electrolyte incompressibility in multi-species systems leads to the volumetric constraint $\sum_{\alpha=1}^{N} \nu_\alpha c_\alpha = 1$ [2]. This is utilized to determine the center-of-mass velocity v

$$\vec{\nabla}\vec{v} = \sum_{\alpha=1}^{N} \nu_\alpha \vec{\nabla}\vec{N}_\alpha, \tag{2.11}$$

which holds for non-constant partial molar volumes ν_α, too.

2.1.3 Reaction kinetics

Electrochemical reaction rates are typically modeled with Butler-Volmer expressions. Recently, thermodynamically consistent expressions have been derived [97, 98] and extensions towards Marcus-Hush-Chidsey kinetics have been discussed [99, 121]. Here, we show schematically how Butler-Volmer expressions take complex chemical potentials into account.

We want to find the reaction rate per electrode surface area I of the redox reaction

$$\mathrm{O} + z\mathrm{e}^- \leftrightharpoons \mathrm{R}. \tag{2.12}$$

The chemical potentials of the oxidized, the activated intermediate, and the reduced states are written in terms of standard and excess chemical potentials

$$\mu_\mathrm{O} = \mu_\mathrm{O}^0 + \mu_\mathrm{O}^\mathrm{ex}, \quad \mu_\mathrm{A} = \mu_\mathrm{A}^0 + \mu_\mathrm{A}^\mathrm{ex}, \quad \mu_\mathrm{R} = \mu_\mathrm{R}^0 + \mu_\mathrm{R}^\mathrm{ex}. \tag{2.13}$$

The electrochemical potentials are $\tilde{\mu}_\alpha = \mu_\alpha + z_\alpha F\varphi$. The equilibrium voltage of this reaction under standard conditions is

$$\Delta\varphi^0 = \varphi^0_\mathrm{electrode} - \varphi^0_\mathrm{electrolyte} = -\frac{\mu_\mathrm{R}^0 - \mu_\mathrm{O}^0}{zF} = -\frac{\Delta\mu^0}{zF}. \tag{2.14}$$

We model forward and backward reactions separately. In the case of rare transitions, the concentration of the activated state is determined by the Boltzmann distribution. A certain fraction of particles in the activated state is assumed to finish the half-reaction. We enforce detailed balance and get the reaction rates

$$I = \tilde{k}_0 \left[\exp\left(-(\frac{\tilde{\mu}_\mathrm{A} - \tilde{\mu}_\mathrm{O}}{RT} \right) - \exp\left(-\frac{\tilde{\mu}_\mathrm{A} - \tilde{\mu}_\mathrm{R}}{RT} \right) \right]. \tag{2.15}$$

With the symmetry factor α, we interpolate the energy of the intermediate state $\tilde{\mu}_\mathrm{A} = (1-\alpha)\tilde{\mu}_\mathrm{O} + \alpha\tilde{\mu}_\mathrm{R}$ and find

$$I = \tilde{k}_0 \left[\exp\left(-\alpha \frac{zF\eta}{RT} \right) - \exp\left((1-\alpha) \frac{zF\eta}{RT} \right) \right] \tag{2.16}$$

dependent on the true overpotential $\eta = \Delta\varphi - \Delta\varphi^0 + \Delta\mu^\mathrm{ex}$ or

$$I = k_0 \left[e^{\mu_\mathrm{O}^\mathrm{ex}/RT} \cdot \exp\left(-\alpha \frac{zF\Delta\Delta\varphi}{RT} \right) - e^{\mu_\mathrm{R}^\mathrm{ex}/RT} \cdot \exp\left((1-\alpha) \frac{zF\Delta\Delta\varphi}{RT} \right) \right] \tag{2.17}$$

dependent on the apparent overpotential $\Delta\Delta\varphi = \Delta\varphi - \Delta\varphi^0$. The last expression makes clear how the excess chemical potentials influence the reaction rates and can deal with complex chemical potentials. In the basic scenario, the excess chemical potentials are based on equation 2.4 with the activity $a_\alpha = f_\alpha c_\alpha$, yielding

$$I = k_0 \left[a_\mathrm{O} \cdot \exp\left(-\alpha \frac{zF\Delta\Delta\varphi}{RT} \right) - a_\mathrm{R} \cdot \exp\left((1-\alpha) \frac{zF\Delta\Delta\varphi}{RT} \right) \right]. \tag{2.18}$$

2.2 Volume-averaged cell models

The equations for electrolyte transport in equations 2.9 and 2.11 can be solved in the three-dimensional micro-structure of porous electrodes with the reaction rates in equation 2.18 as boundary conditions. This approach is essential for the improvement of lithium-ion batteries [22, 96]. 3D simulations are, however, numerically difficult and rely on accurate electrode tomography [110, 122] or reconstruction [109, 123]. Note that the mean of such micro-structure resolved simulations can be obtained with simpler volume-averaged one-dimensional simulations [22]. Because metal-air batteries have not yet converged into a clear structural design, we present novel insights into their behavior through careful one-dimensional volume-averaged cell simulations in this habilitation

[1–5]. This one dimension extends from the negative electrode through the separator to the positive electrode.

The method of volume-averaging is described in detail by Whitaker [111] and applied to batteries by Newman [95, 124]. In this section, we present the resulting equations for coupled electrolyte transport and electrochemical reactions [4]. We model the effects of porosity ε_e and tortuosity on the fluxes via the factor ε_e^β, with the Bruggeman coefficient β. The effective flux densities are

$$\vec{N}_+^{\text{eff}} = -\varepsilon_e^\beta D \vec{\nabla} c_+ - \varepsilon_e^\beta \frac{t_+}{z_+ F} \vec{j}, \tag{2.19}$$

$$\vec{j}^{\text{eff}} = -\varepsilon_e^\beta \kappa \vec{\nabla}\phi - \varepsilon_e^\beta \kappa \frac{t_+ - 1}{z_+ F} \left(\frac{\partial \mu}{\partial c_+} \right) \vec{\nabla} c_+ \,. \tag{2.20}$$

In our volume-averaged approach, reactions appear as species-related source terms S_i and we track the amount of lithium ion per composite volume in the transport equations. Thus, the continuity equations 2.9 become

$$\frac{\partial \varepsilon_e c_+}{\partial_t} = -\vec{\nabla} \vec{N}_+^{\text{eff}} + \vec{\nabla} \left(\varepsilon_e^\beta c_+ \vec{v} \right) + S_+, \tag{2.21}$$

$$0 = -\vec{\nabla} \vec{j}^{\text{eff}} + \sum_{\alpha=1}^{N} z_\alpha F S_\alpha \,. \tag{2.22}$$

We find the transport equations with the definition of the effective fluxes in equations 2.19 and 2.20

$$\frac{\partial \varepsilon_e c_+}{\partial_t} = \vec{\nabla} \cdot \left(\varepsilon_e^\beta D \vec{\nabla} c_+ \right) + \vec{\nabla} \cdot \left(\varepsilon_e^\beta \frac{t_+}{z_+ F} \vec{j} \right) + \vec{\nabla} \left(\varepsilon_e^\beta c_+ \vec{v} \right) + S_+ \,, \tag{2.23}$$

$$0 = \vec{\nabla} \cdot \left(\varepsilon_e^\beta \kappa \vec{\nabla}\phi \right) + \vec{\nabla} \cdot \left(\varepsilon_e^\beta \kappa \frac{t_+ - 1}{z_+ F} \left(\frac{\partial \mu}{\partial c_+} \right) \vec{\nabla} c_+ \right) + \sum_{\alpha=1}^{N} z_\alpha F S_\alpha \,. \tag{2.24}$$

The species-related source terms

$$S_\alpha = \sum_j s_j \nu_{\alpha j} \tag{2.25}$$

depend on the reaction-specific source terms s_j, where $\nu_{\alpha j}$ denotes the stoichiometric index of species α in reaction j. The reaction-specific source terms are generally given by the Butler-Volmer rate (see equation 2.18) and the

specific surface areas A_j through $s_j = A_j \cdot l_j$. The volume-average for the velocity equation 2.11 is stated in Stamm et al. [4].

We model the multi-phase coexistence in gas diffusion electrodes with a so-called Leverett approach [2, 3], which had previously been applied in models of fuel cells [125, 126]. The Leverett function, $J(s)$, uses empirical constants to approximate the saturation s of a porous structure as a function of the capillary pressure, $(p_e - p_g)$

$$p_e - p_g = J(s)\sqrt{\frac{\varepsilon_e \sigma^2}{B_e}}. \tag{2.26}$$

We use Darcy's law [127] to connect electrolyte velocity $\vec{v}_e$ and pressure p_e in porous media

$$\vec{v}_e = -\frac{B_e}{\eta_e}\vec{\nabla} p_e \,. \tag{2.27}$$

Here B_e denotes the permeability of the electrodes with respect to the electrolyte, σ the electrolyte surface tension, and η_e the dynamic viscosity of the electrolyte.

2.3 Surface models

By inserting the standard chemical potential in equation 2.4 into the transport equations 2.9 and the standard Butler-Volmer rate in equation 2.18, we accurately represent the macroscopic behavior of electrochemical cells as outlined in section 2.2 above. For the understanding of electrochemical processes at electrode surfaces, however, we have to take into account interactions among molecules and surface energies of solids. We develop our models on small mesoscopic length scales by adjusting the free energy functional F in equation 2.1.

The kinetics of multi-step and multi-electron electrochemical reactions is modeled by studying the dynamics of surface concentrations of reactants and reaction intermediates coupled by reaction rates in equation 2.18. We model the oxygen reduction reaction based on DFT energies [91, 128] and find that interactions between surface adsorbents have to be taken into account [129, 130]. We choose the most fundamental interaction model and restrict

ourselves to the pairwise interaction of adsorbents on neighboring surface sites [7]. In this case, the interaction free energy is

$$F^{\text{int}} = \frac{n}{2} \int \sum_{\alpha,\beta} E^{\text{int}}_{\alpha\beta} \frac{c_{\alpha,\text{surf}} \cdot c_{\beta,\text{surf}}}{\Gamma_{\text{surf}}} \, \mathrm{d}A, \tag{2.28}$$

where E^{int}_{jk} is the interaction energy between surface species α and β, $c_{\alpha,\text{surf}}$ is the surface concentration of species α, and Γ_{surf} is the surface site density. $n = 6$ is the coordination number on a hexagonal lattice, i.e., the number of nearest-neighbors. The chemical potential of interactions follows by differentiation

$$\mu^{\text{int}}_{\alpha} = \frac{\delta F^{\text{int}}[c_{\text{surf}}]}{\delta c_{\alpha,\text{surf}}} = n \sum_{\beta} E^{\text{int}}_{\alpha\beta} \frac{c_{\beta,\text{surf}}}{\Gamma_{\text{surf}}}. \tag{2.29}$$

This nearest-neighbor interaction could potentially include renormalized higher order interactions.

The chemical potential of solid precipitants also enters the Butler-Volmer rate equation 2.17. Typically, this contribution is neglected because the deposits are sufficiently homogeneous. We, however, show how to capture the morphology of solid precipitants in the free energy by adding its surface energies as quasi-interactions [8]. Together with an homogeneous free energy that oscillates between molecular monolayers, we simulate particle nucleation via spinodal decomposition. The surface growth theory is formulated on a one-dimensional model surface. Our continuous description of the free energy density,

$$F^{\text{int}} = \int \left\{ \frac{1}{2} \left[A \left(\sigma^{1\text{D}}_{\perp} + \sigma^{1\text{D}}_{\parallel} \right) + \sigma^{1\text{D}}_{\perp} - \sigma^{1\text{D}}_{\parallel} \right] - \sigma^{1\text{D}}_{\perp} e^{-\beta h^2/2d_{\parallel}} \right\} \mathrm{d}x \tag{2.30}$$

smooths the orientation-dependent surface energy (first term) [131] and distributes the nucleation energy $\sigma^{1\text{D}}_{\perp}$ to initiate growth over a few monolayers with $\beta = 6$ (second term). The geometrical factor A converts substrate length to normal surface length [132],

$$A = \sqrt{1 + \left(\frac{\partial h}{\partial x} \right)^2}, \tag{2.31}$$

where $h(x)$ is the heights of the Li_2O_2 deposits at position x. The interaction chemical potential then follows from

$$\mu^{\text{int}} = \frac{\delta F^{\text{int}}[c]}{\delta c} = d_{\parallel} d_{\perp} \frac{\delta F[h]}{\delta h}. \tag{2.32}$$

The inhomogeneous chemical potential reproduces the Cahn-Hilliard gradient expansion [133] for small inclinations $\left|\frac{\partial h}{\partial x}\right| \ll 1$. Inserting the chemical potential into the rate equation 2.17 results in the generalized Allen-Cahn equation for electrochemistry [98, 134].

Electrochemical double layers form at electrode surfaces because ions accumulate to shield the electric potential jump at the interface. Gouy and Chapman first modeled ion concentration and potential distribution by taking into account the Maxwell-Boltzmann distribution. In our framework, this requires to replace the charge conservation equation in equation 2.9 with the Poisson equation for the electric potential. Ionic liquids are governed by large correlations and show a clear multilayer structure at the electrode interface [103, 116]. We model this behavior by making explicit the hardcore-nature of ions in the free energy functional [9]

$$F^{\text{int}}[c] = \frac{1}{2} \sum_{\alpha,\beta} \int_{\Omega} c_{\alpha}(\vec{x}) \mathcal{F}_{\alpha\beta}(\vec{x} - \vec{y}) c_{\beta}(\vec{y}) \mathrm{d}\vec{x} \mathrm{d}\vec{y}. \tag{2.33}$$

Our choice of the repulsive interaction $\mathcal{F}_{\alpha\beta}(\vec{x} - \vec{y})$ represents impenetrable hard spheres, i.e., the repulsive interaction is non-zero in a small volume Ω determined by the particle-radii. By solving appropriate transport equation with the resulting chemical potential, we realize generalized Cahn-Hillard equations.

Chapter 3

Modeling of electrochemical cells

This chapter puts our original contributions to battery cell modeling in the context of current research. Our summary highlights two aspects, the evolution of battery design and the development of modeling methodology. We study aprotic lithium-air batteries, aqueous alkaline lithium-air batteries, aqueous alkaline zinc-air batteries, and aqueous neutral zinc-air batteries:

[1] J. P. Neidhardt, D. N. Fronczek, T. Jahnke, T. Danner, B. Horstmann and W. G. Bessler. A Flexible Framework for Modeling Multiple Solid, Liquid and Gaseous Phases in Batteries and Fuel Cells. *Journal of The Electrochemical Society* **159**, A1528–A1542 (2012).

[2] B. Horstmann, T. Danner and W. G. Bessler. Precipitation in aqueous lithium–oxygen batteries: a model-based analysis. *Energy & Environmental Science* **6**, 1299 (2013).

[3] T. Danner, B. Horstmann, D. Wittmaier, N. Wagner and W. G. Bessler. Reaction and transport in Ag/Ag2O gas diffusion electrodes of aqueous Li-O2 batteries: Experiments and modeling. *Journal of Power Sources* **264**, 320–332 (2014).

[4] J. Stamm, A. Varzi, A. Latz and B. Horstmann. Modeling nucleation and growth of zinc oxide during discharge of primary zinc-air batteries. *Journal of Power Sources* **360**, 136–149 (2017).

[5] S. Clark, A. Latz and B. Horstmann. Rational Development of Neutral Aqueous Electrolytes for Zinc-Air Batteries. *ChemSusChem* **10**, 4735–4747 (2017).

Our recent review article contains the results of these original publications. Thus, we adopt a few of its sentences in this chapter 3. Note that it presents original work on theory-based engineering of zinc-air batteries, too:

[6] S. Clark, A. Latz and B. Horstmann. A Review of Model-Based Design Tools for Metal-Air Batteries. *Batteries* **4**, 5 (2018).

3.1 Aprotic lithium-air batteries

Motivated by the experiments of Abraham et al. [36], the current research on lithium-air batteries focuses on non-aqueous electrolytes. Soon, it became clear that carbonate-based electrolytes and carbon-based electrodes tend to decompose in these systems [39–41, 135]. Lithium peroxide Li_2O_2 is the main discharge product and crystallizes in the positive electrode [136, 137]. The research is now focusing on electrolyte stability [138–142], the morphology of the discharge product [44, 46, 143], and its dependence on electrolyte properties [45, 53, 144, 145]. A couple of reviews and perspectives summarize prospects and state-of-the-art [29, 55–57, 146–148]. We contributed to this research with the first model of nucleation and growth of Li_2O_2-particles discussed in section 4.2 [8].

In 2012, we modeled the discharge behavior of aprotic Li_2O_2 batteries [1] building on a few prior models [37, 149–151] and followed by numerous continuum models [46, 143, 152–159]. Our model neglects the possible passivation of the electrochemical surface in the positive electrode due to Li_2CO_3 and Li_2O_2 films [37, 43]. We highlight a very fundamental problem of non-aqueous metal-air batteries: Cathodes are flooded and oxygen must diffuse from the oxygen inlet through the electrolyte to the active electrode surface. We model the diffusion of dissolved oxygen and the oxygen reduction reaction [1],

$$2Li^+ + O_2 + 2e^- \rightleftharpoons Li_2O_2 \tag{3.1}$$

with the equations for transport and reactions outlined in section 2.2 (see figure 3.1a). Our multi-phase management couples the Butler-Volmer rate to the change in solid volume fraction of Li_2O_2

$$\frac{\partial \varepsilon_{Li_2O_2}}{\partial_t} = \nu_{Li_2O_2} s_{Li_2O_2} \tag{3.2}$$

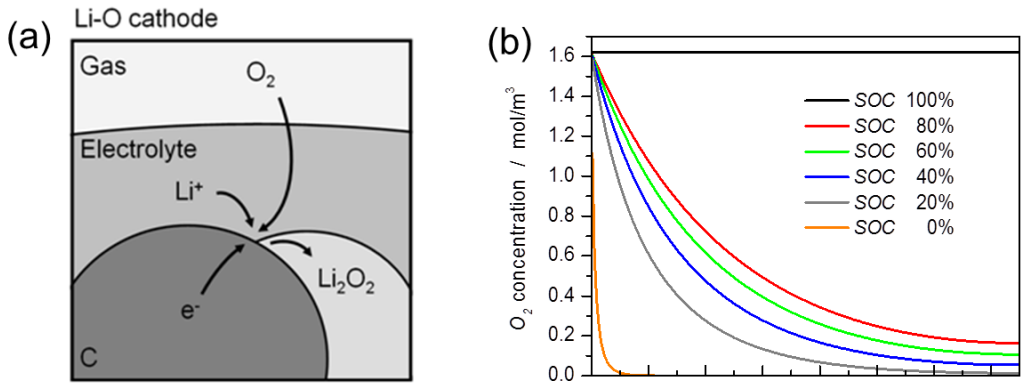

Figure 3.1 (a) Illustration of multi-phase reactions taking place on the micro-scale during the operation of Li-O_2-batteries. (b) Spatial profile of O_2 concentration inside the porous cathode at various SOC and a current density of $i = 0.5$ A/m^2. Reproduced from Neidhardt et al. [1].

with the volume fraction $\nu_{Li_2O_2}$ and the reaction source term $S_{Li_2O_2}$ (see equation 2.25). An increase in Li_2O_2 volume fraction corresponds to a decrease in porosity $\varepsilon_e = 1 - \varepsilon_{Li_2O_2}$.

Our simulations show that a steep oxygen concentration gradient builds up from the oxygen inlet towards the separator even at low current densities $i = 1$ A/m^2 (see figure 3.1b) [1]. This effect is due to the low oxygen solubility and slow oxygen diffusivity in the aprotic solvent. As a consequence, the oxygen reduction reaction is concentrated in a region close to the oxygen inlet. Therefore, Li_2O_2 predominantly forms near the oxygen inlet and blocks the electrolyte pores. This results in a further slowing down of oxygen transport and accelerates the pore blocking. When the electrolyte-filled pores are completely blocked, the cell voltage sharply decreases and the discharge ends. To summarize, oxygen transport through the electrolyte in a flooded cathode is so slow that it limits discharge capacity and discharge currents.

3.2 Aqueous alkaline lithium-air batteries

Aqueous electrolytes solve the challenges discussed above for aprotic electrolytes: the precipitation of the discharge product does not occur in the cathode and gas diffusion electrodes enable fast oxygen transport. Different designs containing aqueous electrolytes are discussed in literature [48]. The lithium metal anode is a persistent challenge for aqueous lithium-air batteries. The

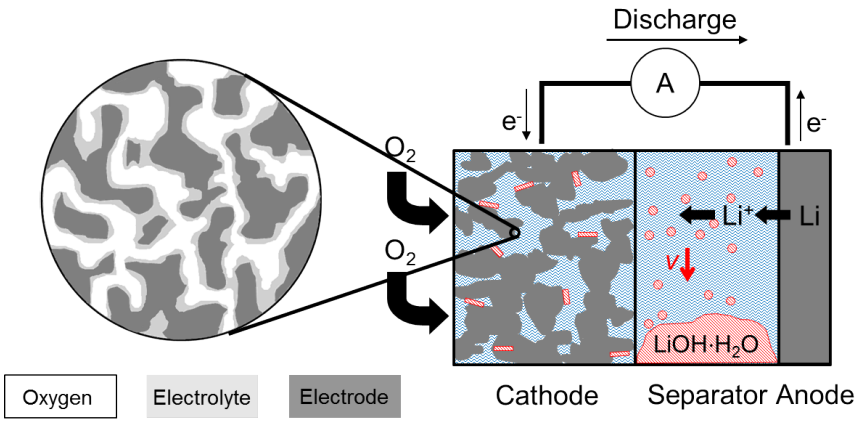

Figure 3.2 Schematic representation of Li-O_2 battery with gas diffusion electrode and precipitation of $LiOH \cdot H_2O$ on sedimenting dust particles in a bulk separator region. Reproduced from Horstmann et al. [2].

invention of suitable solid anode protection layers by Visco et al. [160], has enabled aqueous lithium-air batteries. Research on improving conductivity and stability of anode protecting layers is ongoing [161–163]. A further challenge is the absorption of CO_2 in alkaline electrolytes, which we discuss in section 3.3 [4, 51]. The unique prospects of alkaline electrolytes for lithium-air batteries, however, motivate a steady research by a couple of groups [48–50, 148, 164–167].

Prior to our model of an alkaline lithium-air battery, only a single modeling study existed [149, 168]. The existing model treated the oxygen reduction reaction and the subsequent precipitation of lithium hydroxide monohydrate within a single global reaction in a flooded cathode in analogy to the aprotic lithium-air battery [1, 47]. Our model, instead, takes into account the specifics of aqueous electrolytes and presents approaches to influence precipitation [2, 3]. We address the two most important benefits of aqueous alkaline electrolytes for lithium-air batteries, i.e., nucleation and growth of the discharge product and multi-phase oxygen transport in gas diffusion electrodes. A scheme of our 1D continuum model is shown in figure 3.2. During discharge, lithium metal dissolves at the anode

$$Li \rightleftharpoons Li^+ + e^- , \tag{3.3}$$

while dissolved oxygen is reduced in the cathode

$$O_2{}^e + 2H_2O + 4e^- \rightleftharpoons 4OH^- . \tag{3.4}$$

In this way, the salt concentration in the electrolyte raises until the solubility limit of LiOH is exceeded and solid $LiOH \cdot H_2O$ precipitates

$$Li^+ + OH^- + H_2O \rightleftharpoons LiOH \cdot H_2O\,. \tag{3.5}$$

For aqueous electrolytes, gas diffusion electrodes are available in which gas and liquid phases coexist [169]. This ensures fast oxygen transport through the gas phase and good utilization of electrode surface area in the cathode. Our macro-homogeneous model captures this behavior via a Leverett-J-function [170] and a Darcy flow [126] as outlined in section 2.2. In an effort to parameterize and validate this model of gas diffusion electrodes, we measured IV-curves and performed impedance spectroscopy in an half-cell setup [3]. Our theory compares favorably with experiments in a wide range of salt concentrations, temperatures, and overpotentials.

We make use of the classical theory of nucleation and growth to study inhomogeneous precipitation. It divides the reaction chemical potential of disc-shaped nuclei of radius r in a bulk and a surface term [171–174]

$$\Delta\mu = \Delta\mu^V + \Delta\mu^V = -\frac{4}{3}\pi\frac{r^3}{a^3}\cdot 2kT\ln S + 2\pi ra\cdot\gamma, \tag{3.6}$$

where γ is the macroscopic surface energy, a the lattice constant. The supersaturation ratio $S = c_{Li^+}/c_{Li^+}^{solubility}$ is the driving force for nucleation. Surface energy dominates in case of small nuclei, bulk energy in case of large nuclei. The maximum $\Delta\mu$ determines the critical reaction chemical potential $\Delta\mu^{crit}$ [174]

$$\Delta\mu^{crit} = \frac{\pi\gamma^2 a^4}{2kT\ln S}. \tag{3.7}$$

The nucleation rate is modeled as activation process with the critical chemical potential $\Delta\mu^{crit}$ as barrier [171]

$$\frac{\partial N}{\partial t} \propto N^0 \cdot \exp\left(-\frac{\Delta\mu^{crit}}{kT}\right). \tag{3.8}$$

We study variations in N_0, which is the number of sites on which nucleation can occur [2].

Our cell simulations explain that the discharge product of metal-air batteries in aqueous electrolytes preferentially precipitates close to the negative electrode [2, 4]. As shown in figure 3.3, the low transference number of Li^+

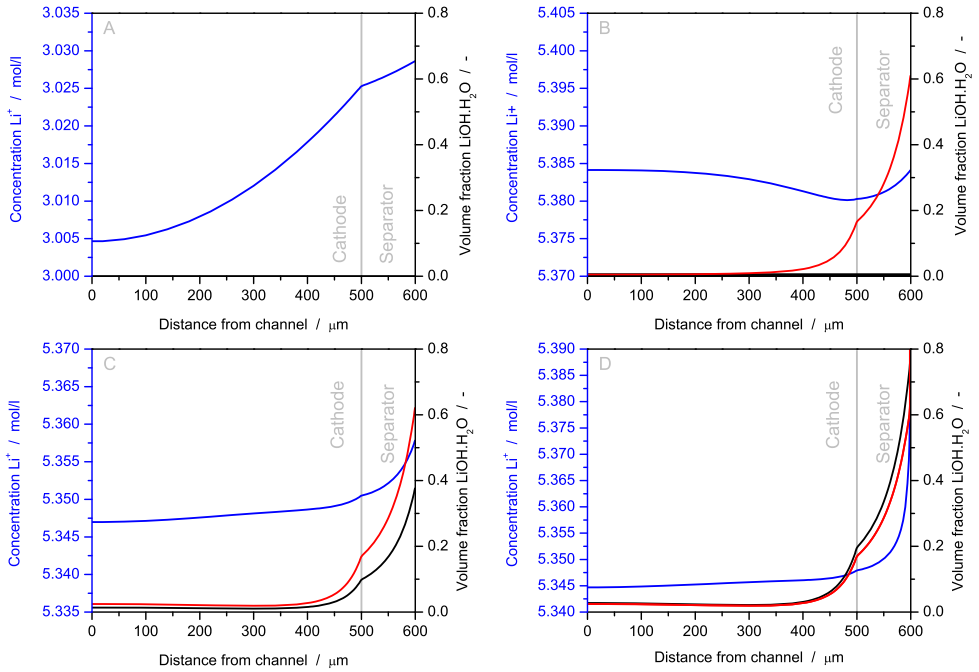

Figure 3.3 Spatial profiles of salt concentration, volume fraction of $LiOH \cdot H_2O$ crystals, and specific surface area of precipitation during galvanostatic cell discharge $i = 10$ A/m^2 at times (A) before $LiOH \cdot H_2O$ nucleation, (B) at $LiOH \cdot H_2O$ nucleation, (C) during $LiOH \cdot H_2O$ growth, and (D) at the end of discharge. Precipitation occurs mainly close to the anode due to the small transference number of Li^+. Reproduced from Horstmann et al., [2].

leads to a concentration gradient in the cell. This gradient favors nucleation of $LiOH \cdot H_2O$ on the anode protecting layer explaining earlier experimental measurements [49]. In contrast, crystallization in aprotic electrolytes mainly occurs in the positive electrode (see section 3.1). The reason behind this difference is the concentration and mobility of the reduced oxygen species. Hydroxide ions OH^- (or H_2O and H^+) efficiently transport reduced oxygen in aqueous electrolytes. This is for example represented by the low transference number of Li^+ in LiOH solutions. As a consequence, the reaction between fast reduced oxygen and slow cations takes place in the anode. In aprotic electrolytes, instead, oxygen O_2 is reduced to unstable superoxide O_2^-. Thus, reduced oxygen stays close to the surface and Li_2O_2 precipitates in the positive electrode. We emphasize that precipitation in the metal electrode is often advantageous for battery design because the dissolved metal leaves room for precipitants.

Furthermore, we evaluate two design improvements for aqueous lithium-air batteries. First, we confirm that gas diffusion electrodes sustain higher current

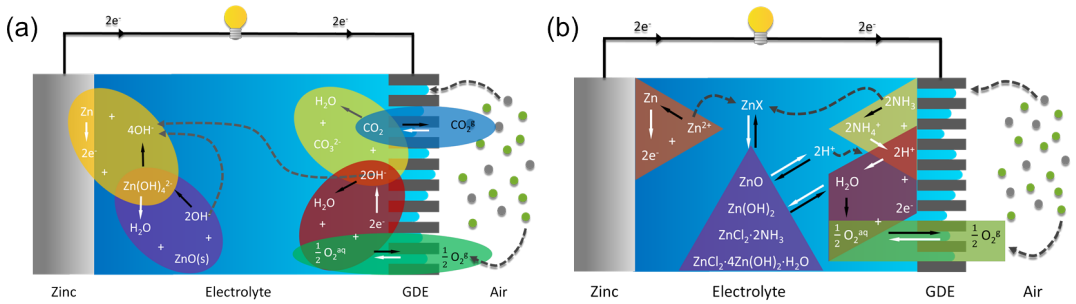

Figure 3.4 Operational schematic of (a) alkaline and (b) near-neutral zinc-air battery. The various (electro)chemical reactions are indicated by the colored ovals and triangles; white arrows indicate discharging and black arrows indicate charging. Dashed lines show important transport paths. Based on the local pH and speciation, a variety of solid discharge products may precipitate. Reprinted from Clark et al. [5, 6].

densities than flooded electrodes. Second, we propose a bulk separator region that can efficiently take up precipitants. If a $LiOH \cdot H_2O$ deposit is continuously steered, energy densities are found to remain constant up to current densities of $i = 100\ A/m^2$.

3.3 Aqueous alkaline zinc-air batteries

Our results in section 3.2 affirm the value of aqueous electrolytes for metal-air systems. Besides relatively low rates of hydrogen evolution, zinc metal is stable in water. Therefore, aqueous zinc-air batteries stand out as the single commercialized metal-air battery. As primary battery they are used in hearing aids; as rechargeable battery they have reached a mature development state [17, 62, 65, 175–178]. Most importantly, the reversible precipitation of ZnO takes place in the negative electrode and does not passivate the zinc metal surface. As a consequence, zinc-air batteries can be electrochemically cycled a few hundred times. Furthermore, their constituent materials are abundant, non-toxic, and cheap [23].

A couple of challenges remain. During repeated deposition and dissolution, metallic zinc changes its shape on various length scales, e.g., microscopic dendrites grow [179] and the electrode structure is rearranged [180]. Therefore, design improvements for zinc metal electrodes are subject of current research

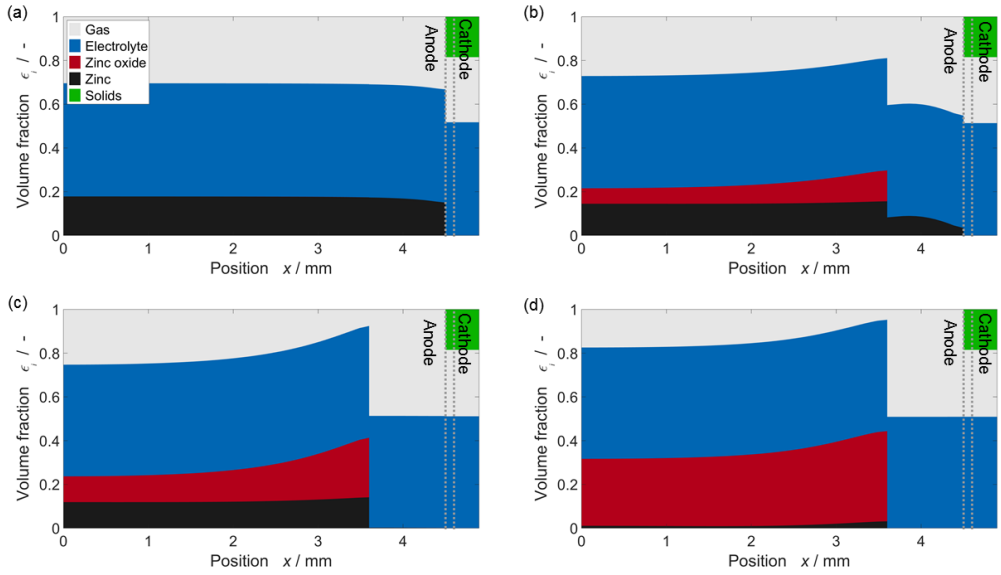

Figure 3.5 Volume fractions during galvanostatic discharge at 125 Am^{-2} at characteristic times: (a) Dip: No ZnO is precipitating. Zn dissolves slightly faster next to the separator. (b) Plateau: ZnO nucleated and precipitating in the part of the anode close to the current collector. Zn dissolution is slowed down in the presence of ZnO. (c) Step: Zn is completely dissolved in the part of the anode in which no ZnO is nucleated. (d) Drop: A thick ZnO film slows down the dissolution of the remaining Zn. Reproduced from Stamm et al. [4].

[181, 182]. Furthermore, in contact with air, atmospheric carbon dioxide enters the cell and reacts to carbonate in the electrolyte [51, 183].

Several modeling studies support the research on zinc-air batteries [183–187]. We refine these approaches and perform the first spatially resolved simulation of precipitation and carbon dioxide absorption [4]. Our model is parametrized and validated in-house with the commercial zinc-air coin cell Varta PowerOne PR44 Type p67. The operational scheme of our model is shown in figure 3.4a. During discharge, the anodic Zn is oxidized to zincate $Zn(OH)_4^{=}$, which is the only Zn-species in our model [188]

$$Zn + 4OH^- \rightleftharpoons Zn(OH)_4^{=} + 2e^- . \tag{3.9}$$

In the gas diffusion electrode, oxygen is reduced according to equation 3.4. If the zincate concentration raises above its solubility limit, precipitation of ZnO becomes possible thermodynamically

$$Zn(OH)_4^{=} \rightleftharpoons ZnO + H_2O + 2OH^- . \tag{3.10}$$

We employ the multi-phase model in the gas diffusion electrode and the classical theory of nucleation and growth introduced in section 3.2. A porous ZnO layer is assumed to form around the Zn particles, which acts as diffusion barrier [63, 184, 189]. We model carbon dioxide absorption and carbonate formation

$$CO_2 + 2OH^- \rightleftharpoons CO_3^{=} + H_2O \tag{3.11}$$

with a simplified macroscopic pseudo first-order reaction rate [190–192]. Our model for a KOH with dissolved $ZnOH_4^{=}$ and CO_3^- goes beyond the standard concentrated solution theory for binary electrolytes discussed in section 2.1.2. We derive consistent transport equations for multi-species electrolytes and replace the flux densities in equation 2.7 with

$$\vec{N}_\alpha = -D_\alpha \vec{\nabla} c_\alpha - \frac{t_\alpha}{z_\alpha F}\vec{j}\,, \tag{3.12}$$

$$\vec{j} = -\kappa\vec{\nabla}\varphi + \kappa \sum_{\alpha=1}^{N} \frac{t_\alpha}{z_\alpha F}\left(\frac{\partial \mu_\alpha}{\partial c_\alpha}\right)\vec{\nabla} c_i\,. \tag{3.13}$$

Our experimental tests of button cells show four characteristic phases in the discharge voltage [4]. Firstly, a dip signals nucleation of ZnO. Secondly, the voltage stays constant as expected for a conversion chemistry. Thirdly, a voltage step occurs that we explain below. Fourthly, the voltage decays due to the growth of the ZnO diffusion barrier. Our 1D cell model clarifies the mechanism behind this observation [4]. For high current densities, the electrolyte concentration gradients that develop in the cell are strong enough that $Zn(OH)_4^{2-}$ does not reach the critical super-saturation for nucleation in the anode-separator interface and ZnO does not nucleate. As a result, the surface concentration of OH^- in this region is much higher than in areas of the electrode covered by a ZnO film. When the uninhibited Zn near the separator is completely utilized, the overpotential of the dissolution reaction increases, causing the observed drop in cell voltage. This behavior is reflected in the time evolution of volume fractions shown in figure 3.5. We propose that Zn electrodes should contain a small amount of ZnO powder. In this way, the effects of inhomogeneous ZnO nucleation can be avoided.

Furthermore, our simulations demonstrate how carbon dioxide absorption limits battery lifetime to two months (see equation 3.11). Formation of carbonate $CO_3^{=}$ entails an irreversible reduction of hydroxide concentration, zincate solubility, and electrolyte conductivity. Therefore, without special precautions

[51], the lifetime of alkaline zinc-air batteries is limited to a few months. This is hardly tolerable for rechargeable batteries.

3.4 Aqueous neutral zinc-air batteries

Zinc-air batteries with near-neutral chloride-based electrolytes could address this electrolyte carbonation issue. In 1973, Jindra et al. first applied a $ZnCl_2$-NH_4Cl electrolyte in zinc–air batteries [193]. Recently, they have been experimentally investigated again [67, 68, 73]. The initial results are promising, but the composition and behavior of these electrolytes during cell operation is unclear. We present a continuum framework for modeling pH buffered aqueous electrolytes, and apply it to study zinc-air batteries with pH adjusted $ZnCl_2-NH_4Cl$ electrolytes [5]. The main reactions in a zinc-air battery are shown in Fig. 3.4b.

We want to study pH adjusted $ZnCl_2-NH_4Cl$ electrolytes over a wide range of conditions. Thus, it is necessary to take into account the speciation of the electrolyte, e.g., the complex formation of Zn^{2+} with Cl^-, OH^- and NH_3. Furthermore, we solve the computational challenge to follow the dynamics of solutes whose concentrations vary over orders of magnitude, e.g., the concentration of OH^- at different pH [5, 6]. In thermodynamic equilibrium, for a generic reaction, the concentrations of reactants are related by

$$\nu_A\ A + \nu_B\ B \rightleftharpoons \nu_C\ C + \nu_D\ D, \qquad \frac{(c_A)^{\nu_A} \cdot (c_B)^{\nu_B}}{(c_C)^{\nu_C} \cdot (c_D)^{\nu_D}} = \beta \tag{3.14}$$

with the thermodynamic stability constant β. Such tabulated stability constants allow to predict the thermodynamic equilibrium composition of the electrolyte. We extend this standard methodology to dynamic situations [5] by assuming that the homogeneous speciation reactions in the electrolyte are very fast and stay in equilibrium. Quasi-particles are defined as a linear superposition of their constituents

$$c_\beta = \sum_{\alpha=1}^{N} \tau_{\alpha,\beta} c_\alpha, \tag{3.15}$$

where $\tau_{\alpha,\beta}$ describes the stoichiometry of the solute in the quasi-particle. These quasi-particle represent the conserved quantities of the speciation reactions. We show that it is sufficient to simulate only the dynamics of quasi-particles [5].

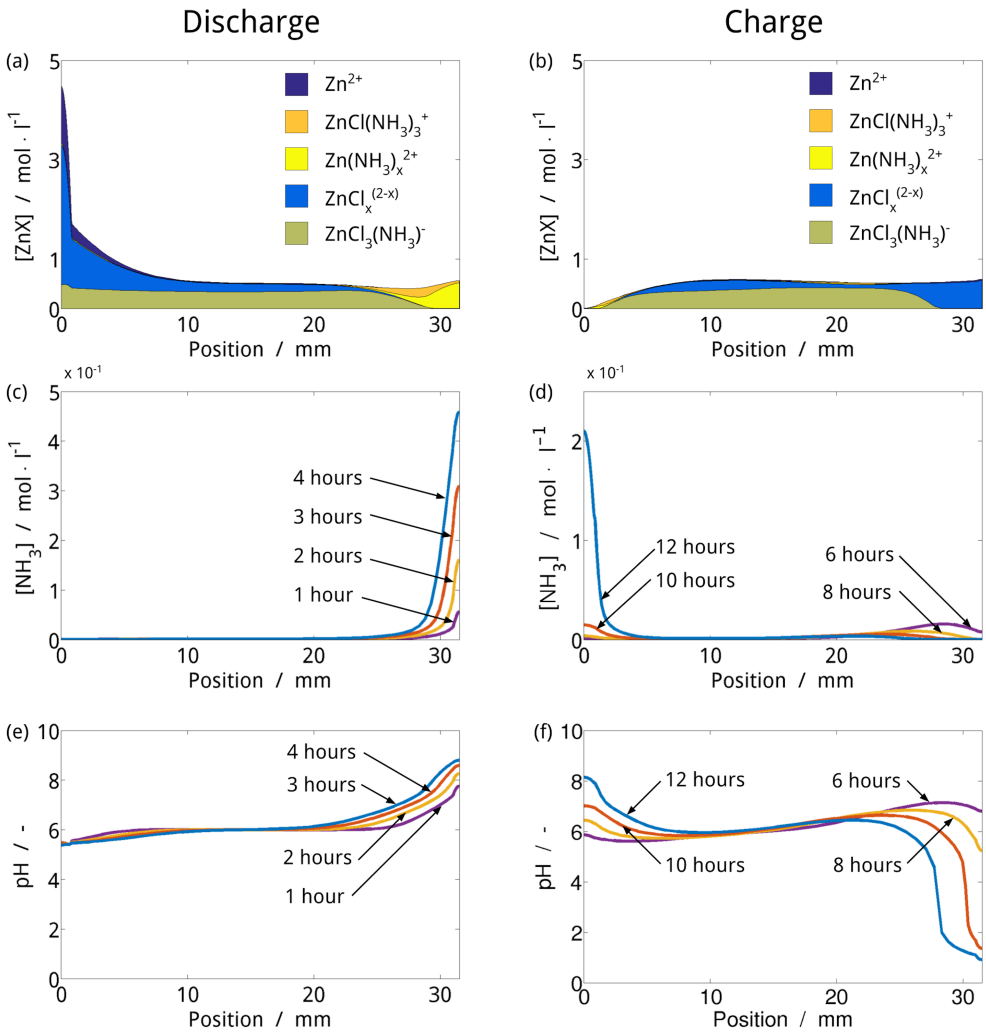

Figure 3.6 Electrolyte composition of near-neutral zinc-air battery during cycling. At the end of discharging, (a) zinc in the gas diffusion electrode (GDE) exists as $Zn(NH_3)_4$, (c) NH_3 accumulates in the GDE, and (e) the pH value in the GDE becomes slightly more alkaline. At the Zn electrode, NH_3 is consumed by dissolving zinc and the pH value becomes slightly more acidic. At the end of charging, (b) zinc in the GDE exists exclusively as zinc–chloride complexes, (d) NH_3 depletes in the GDE, and (f) the pH becomes acidic in the GDE. Zinc deposition causes the concentration of NH_3 and the pH value to increase. Reprinted from Clark et al. [5].

These quasi-particles can be chosen such that they stay in a comparable order of magnitude for any pH value. Our novel approach significantly reduces the number of independent variables and parameters in the dynamic simulations.

First, we utilize an equilibrium thermodynamic model of the electrolyte [5]. As a function of pH, it predicts speciation and zinc solubility. Possible solid

precipitants are $ZnCl_2 \cdot 2\,NH_3$, $ZnCl_2 \cdot 4\,Zn(OH)_2 \cdot H_2O$, $Zn(OH)_2$, and ZnO. Reasonable energy densities can only be obtained if the electrolyte salt is not part of the cell reaction and the discharge product is $Zn(OH)_2$ or ZnO. Our analysis, however, confirms that earlier design proposals lead to unstable electrolytes and precipitation of $ZnCl_2 \cdot 2\,NH_3$ and $ZnCl_2 \cdot 4\,Zn(OH)_2 \cdot H_2O$ [67, 68].

Integrating the thermodynamics into our dynamic quasi-particle model, we simulate experiments on near-neutral zinc-air batteries [67, 68]. Figure 3.6 shows concentration profiles of in the cell proposed by Goh et al. during cycling [67]. The Zn electrode is on the left and the gas diffusion electrode (GDE) is on the right of the domain. To maintain a neutral pH in the GDE, the buffer reaction $NH_4^+ \rightleftharpoons NH_3 + H^+$ counteracts the pH shifts inherent in the oxygen reaction. As more NH_3 is produced, it forms dominant complexes with Zn^{2+} as shown in figure 3.6a. Because there is an excess of NH_4^+ in the electrolyte, the buffer reaction is uninhibited and the pH during discharging is relatively stable (see figure 3.6e). During charging, the buffer reaction is reversed and NH_3 is converted to NH_4^+. As NH_3 is depleted, zinc-chloride complexes dominate in the GDE (see figure 3.6b). Some of the NH_3 that was produced during discharge diffuses into the bulk electrolyte and cannot be quickly recovered. When NH_3 is locally depleted, the buffer reaction becomes limited and the pH in the GDE becomes acidic (see figure 3.6f). Acidic pH values can accelerate catalyst degradation and limit the lifetime of the cell.

Finally, we employ our dynamic model to discuss how cell architecture and electrolyte composition can be adjusted to optimize for buffering capacity and discharge product [5]. To this aim, we study various electrode and separator dimensions. We propose a novel electrolyte composition with relatively high Cl^- content and near-acidic pH. Our simulations confirm a stable buffering capacity and the desired precipitation of $Zn(OH)_2$.

Chapter 4

Modeling of electrochemical surfaces

Our original contributions to the theory of electrochemical surfaces are described in this chapter. They are based on the theoretical framework of non-equilibrium thermodynamics outlined in chapter 2. We study the elementary kinetics of oxygen reduction reaction, the rate dependence of Li_2O_2 nucleation, the multilayer structure of ionic liquids at electrodes, and the growth of solid electrolyte interphase:

[7] D. Eberle and B. Horstmann. Oxygen Reduction on Pt(111) in Aqueous Electrolyte: Elementary Kinetic Modeling. *Electrochimica Acta* **137**, 714–720 (2014).

[8] B. Horstmann, B. Gallant, R. Mitchell, W. G. Bessler, Y. Shao-Horn and M. Z. Bazant. Rate-Dependent Morphology of Li2O2 Growth in Li-O2 Batteries. *The Journal of Physical Chemistry Letters* **4**, 4217–4222 (2013).

[9] V. Hoffmann, G. Pulletikurthi, T. Carstens, A. Lahiri, A. Borodin, M. Schammer, B. Horstmann, A. Latz and F. Endres. Influence of a Silver Salt on the Nanostructure of an Au(111) Ionic Liquid Interface: an Atomic Force Microscopy Study and Theoretical Concepts. *Physical Chemistry Chemical Physics* **20**, 4760–4771 (2018).

[10] F. Single, B. Horstmann and A. Latz. Dynamics and morphology of solid electrolyte interphase (SEI). *Physical Chemistry Chemical Physics* **18**, 17810–17814 (2016).

[11] F. Single, B. Horstmann and A. Latz. Revealing SEI Morphology: In-Depth Analysis of a Modeling Approach. *Journal of The Electrochemical Society* **164**, E3132–E3145 (2017).

[12] F. Single, A. Latz and B. Horstmann. Identifying the Mechanism of Continued Growth of the Solid-Electrolyte Interphase. *ChemSusChem* **11**, 1950–1955 (2018).

4.1 Elementary kinetics of oxygen reduction reaction

On the meso-scale, we contributed to understanding of the oxygen reaction process [7]. The oxygen reduction reaction (ORR) is fundamental to many technologies, e.g., oxygen sensors, fuel cells, and metal-air batteries [194]. Unfortunately, the rate of the oxygen reduction reaction is limiting the efficiency of air electrodes for energy storage and the quest for optimized catalysts is ongoing [90, 195]. Pt performs best as ORR catalyst, but the observed overpotentials are typically 0.3V [196, 197]. This lack of efficiency is traced back to the transfer of four elementary charges [90].

In aqueous electrolytes, reaction intermediates and elementary reaction barriers are well-known from DFT calculations [90, 91, 128, 129, 198–205]. Our contribution is based on detailed DFT calculations of Jacob et al. [91, 128], who study the ORR in acid aqueous electrolyte on Pt(111). Mean-field theories of surface adsorbents estimate the reaction rates under non-equilibrium conditions [206–209]. We highlight the necessity to take into account interactions between surface adsorbents in order to get reasonable predictions. Our consistent modeling method is outlined in section 2.3.

We observe a trend in reaction mechanism as a function of applied potential as shown in figure 4.1 [7]. At very high voltages, the surface is blocked by O in our simulations. At high voltages, the reaction proceeds via the direct dissociation of oxygen. At low voltages, the dominant pathway is the protonization of molecular oxygen, i.e., the formation of HO_2 or H_2O_2, and a subsequent dissociation. At very low voltages, the surface is blocked by hydrogen H. These conclusions are illustrated with the surface coverages in figure 4.1a. They correspond to a change in Tafel slope in the polarization

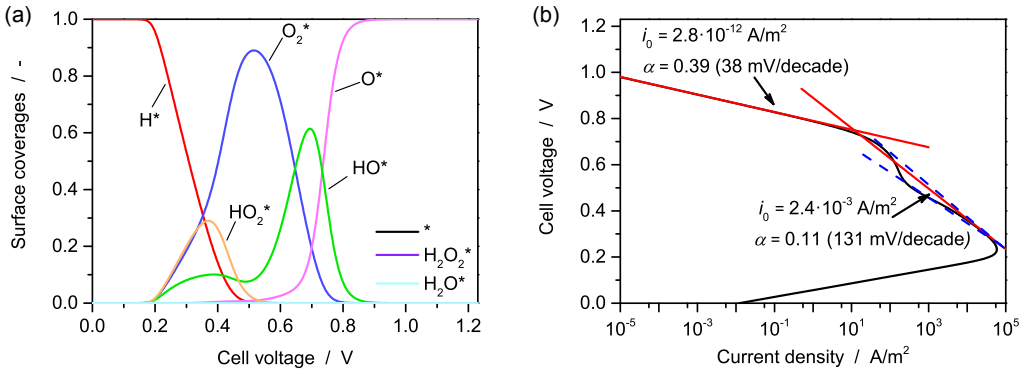

Figure 4.1 (a) Polarization curve from elementary kinetic modeling on Pt(111) in acidic electrolyte. We observe a change in Tafel slope at $U = 0.7$ V signaling a change in reaction mechanism. The red lines represent Tafel slopes at high and intermediate cell voltages fitted to the polarization curve. The blue dashed lines demonstrate the measurement uncertainty for the Tafel slope at intermediate cell voltages (see text). Below $U = 0.2$ V, the reaction rate decreases due to surface blocking by H. (b) Coverages of the surface species over the cell voltage. The surface is blocked by H at low cell voltages and by O at high cell voltages. Reproduced from Eberle et al. [7].

curve (see figure 4.1b). We confirm the change in reaction mechanism with a sensitivity analysis and analytic estimates of the Tafel slopes.

Generally, our simulations quantitatively and qualitatively agree with precision experiments [196, 197]. The simple model for adsorbent-adsorbent interactions in equation 2.29, however, leads to some deviations from experiments. At very high voltages, OH is believed to cover the Pt(111) surface [200, 210, 211], whereas our simulations result in a coverage with O. At high cell voltages, an oxygen reaction order close to unity is measured [196, 212], but our model predicts lower values.

4.2 Morphology of Li_2O_2 electrodeposition

In non-aqueous electrolytes, the reaction process is less clear because the electrochemical oxidation/reduction of oxygen is interwoven with the precipitation/dissolution of Li_2O_2. Experiments on lithium-air batteries with ether-based electrolytes revealed that the electronically insulating discharge product Li_2O_2 can deposit in micro-meter sized toroid-like morphologies [213] or in nanometer sized, passivating films [40]. Particles form at small current densities and

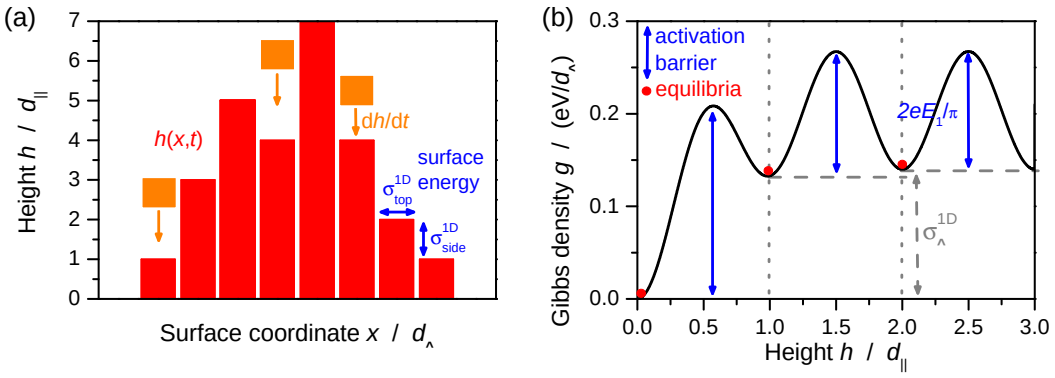

Figure 4.2 (a) Scheme of the (1+1)-D surface model. Individual Li_2O_2 molecules are added on top of a surface crystal of height $h(x,t)$ at the rate $\partial h/\partial t$. $d_{\parallel}$ and $d_{\perp}$ are the distances between molecules in the horizontal and vertical direction. (b) Homogeneous Gibbs free energy density of a Li_2O_2 deposit versus surface height h. The system is in metastable equilibrium at integer $h/d_{\parallel}$. The nucleation barrier $\sigma_{\perp}$ must be overcome during growth of the first monolayer $h \leq d_{\parallel}$. Reproduced from Horstmann et al. [8].

films at large current densities [44, 214]. We created the first meso-scale model for aprotic lithium-air batteries and explained this current dependence of the Li_2O_2 morphology through a transition in nucleation behavior [8]. Subsequent modeling studies studied the meso-scale growth process of toroid-shaped particles [45, 46, 143]. The role of electrolyte properties for the growth of Li_2O_2 particles is subject of current research [53, 144, 145].

We use the variational theory of electrochemical kinetics [98, 100, 215–218], which predicts the suppression of phase separation in $LiFePO_4$ nanoparticles, and apply it to classical surface-growth models [131, 219, 220]. Our theory is an example of thermodynamic (in)stability in driven open systems [134].

The electrodeposition oxygen reduction reaction (ORR),

$$2Li^+ + O_2 + 2e^- \rightleftharpoons Li_2O_2 \tag{4.1}$$

is modeled on a carbon surface in (1+1)-dimensional space, i.e., through the height of the crystal $h(x)$ as a function of the projected surface coordinate x (see figure 4.2a). In this way, Li_2O_2 molecules align in columns and grow at the electrochemically controlled rate

$$\frac{\partial h}{\partial t} = d_{\parallel} A_{\perp} \frac{I(\mu, \Delta\varphi)}{2e}, \tag{4.2}$$

where the two dimensional current density $I(x,t)$ is given by the Butler-Volmer equation 2.17. $d_\parallel$,$d_\perp$,$A_\parallel$, and $A_\perp$ describe the area of top facets ($\perp$) and side facets ($\parallel$) of individual molecules in one (d) and two dimensions (A). The continuous evolution of $h(x,t)$ is a standard mathematical description of surface growth [132]. We apply a galvanostatic condition and solve for the electric potential jump $\Delta\varphi$. The chemical potential is derived from the free energy functional $F[h]$ as shown in section 2.3 (see equations 2.1 and 2.29). The bulk free energy

$$\int f_\mathrm{H} \mathrm{d}V = \int \frac{2e}{d_\perp \pi} \left[-E_0 \pi \frac{h}{d_\parallel} + E_1 \sin^2(\pi \frac{h}{d_\parallel}) \right] \mathrm{d}V \tag{4.3}$$

encodes the open circuit voltage E_0 and the activation barrier between complete molecular monolayers E_1. The homogenous part of the free energy density is shown in figure 4.2b. A nucleation barrier must be overcome to deposit the first monolayer. Local energy minima correspond to the meta-stability of full molecular monolayers.

Via linear stability analysis, a transition in surface growth is identified. We calculate the exponential growth rate $s(\lambda, \bar{I})$ of fluctuations with wavelength λ in a film homogeneously growing with current density $\bar{I}$. The dynamics are unstable for all currents if $\partial\mu/\partial h < 0$. Instabilities develop into particles if they grow faster than the homogeneous film $s > A_\perp \bar{I}/2e$. We plot this condition for marginal stability in figure 4.3a. Growth is most unstable during nucleation of the first monolayer. Thus, at intermediate currents, nucleation of particles can be followed by homogeneous growth at thicker coatings. The numerical stability analysis shown in figure 4.3b confirms this picture. The growth regimes are separated by the exchange current density evaluated at the spinodal point $I_\mathrm{c} = I_0(h = d_\parallel/4)$, where instabilities emerge. At $\bar{I} \ll I_\mathrm{c}$, the growth of distinct particles is signaled by a large surface roughness; at $\bar{I} \lesssim I_\mathrm{c}$ an intermediate regime of particle coatings exists; at $\bar{I} > I_\mathrm{c}$, a passivating film grows.

By parameterizing the exchange current density I_0 with experimental Tafel analysis, we validate our simulations with experiments on high-surface area carbon nanotubes. An excellent agreement in the current dependence of growth morphologies is found between theory and experiment. Because we neglect defects, surface capacities, and transport processes, the predicted cell voltages do not quantitatively agree with the measured ones. Our model captures the nucleation of Li_2O_2 and predicts disc-shaped particles at low

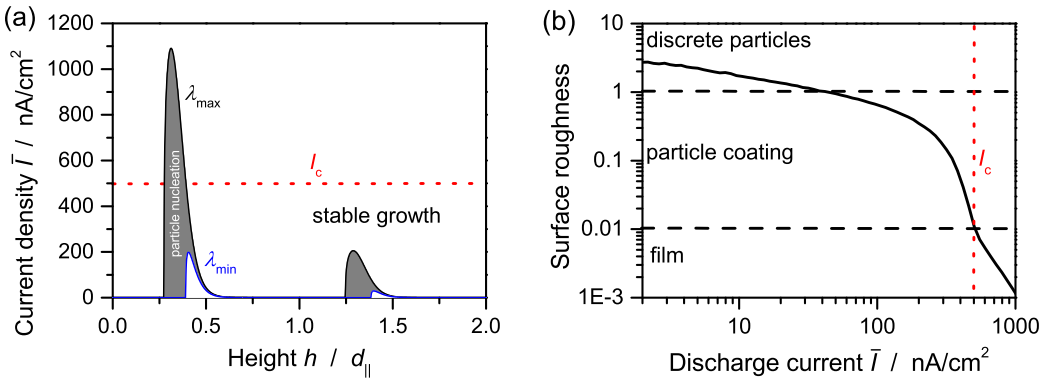

Figure 4.3 (a) Dependence of spinodal region on the applied current. The curves give the boundary between particle growth and film growth according to linear stability analysis. The black line corresponds to the most unstable wavelength $\lambda \to \infty$, the blue line to the most stable wavelength $\lambda = 3d_{\perp}$. (b) Surface roughness after numerical evolution to mean height $\overline{h} = 2d_{||}$. The standard deviation $\Delta[h]$ of $h(x)$ normalized by mean height $\overline{h}$ is depicted as a function of mean discharge rate $\bar{I}$. The dashed lines illustrate the transition from growth of discrete particles over particle coating to film growth as a function of discharge current $\bar{I}$. Reproduced from Horstmann et al. [8].

enough current densities. Indeed, disc-shaped particles are precursors of aggregated toroid-like particles as shown by electron microscopy [221]. We demonstrate that simulated aspect ratio and particle distance are consistent between theory and experiment [8].

4.3 Electrochemical double layers in ionic liquids

Electrolyte instability is often limiting performance and lifetime of batteries. In this habilitation, for example, we encounter absorbtion of carbon dioxide in alkaline electrolytes [4], precipitation of electrolyte salt [5], low tolerance to dissolved superoxide [1, 8], and growth of solid electrolyte interphase on negative electrodes [10–12]. Two types of electrolytes promise to solve these challenges, solid electrolytes [222] and room temperature ionic liquids (RTIL) [69]. RTILs are molten salts at room temperature. These liquids have wide electrochemical and thermal windows, good ionic conductivities, usually low vapor pressures at room temperature and high solubilities for a variety of compounds [223]. As a consequence, RTILs are viewed as candidates for electrolytes in next-generation batteries, e.g., metal-air batteries [69]. The

smooth electrodeposition of metals from RTILs, e.g., Al, Si, and Zn [70, 224–226], constitutes an important step towards their application [227].

The breakthrough of RTILs as electrolytes is hindered by their complex speciation in the bulk [228] and their interfacial structure formation [103]. Atomic force microscopy (AFM) is a useful tool to image the atomic structure at electrode surfaces and elucidate their quasi-crystalline structure with alternating cation and anion rich layers [229–231]. Recently, the influence of water on the Au(111)/[EMIm]TfO interface was studied [116]. The multilayer structure is predominant up to 30 vol% water, above this concentration the multilayer structure is strongly disturbed. Our collaborators performed a similar study for the influence of dissolved AgTFSA on the Au(111)/$Py_{1,4}$TFSA interface [9]. In contrast to neutral water, charged silver ions strongly disturb the multilayer structure even at very small concentrations $c_{Ag} \gtrsim 0.5 \cdot 10^{-3}$ mol/l.

The interfacial behavior of RTILs is studied with various theoretical approaches on different scales. Classical density functional theory (DFT) [232, 233] and molecular dynamics (MD) [234, 235] resolve many of the microscopic complexities of individual molecules and intermolecular interactions, but remain limited to small length and time scales. Continuum theories predict the multilayer structure of the electrochemical double layer in ionic liquids [103, 236, 237]. These models highlight the fundamental relations behind the multilayer structure by neglecting microscopic details. In this way, they connect meso-scale surface and macro-scale bulk properties of RTILs.

We derived a rigorous physics-based model from non-equilibrium thermodynamics [9]. Our model goes beyond previous continuum models as it takes into account the full hardcore interaction between molecules and describes the effect of additives, e.g., water or salt. Firstly, we derive transport equations for RTILs in the bulk as outlined in section 2.1.2. In Hoffmann et al. [9] we show the equations for ternary systems taking into account mixtures with water or silver ions. Note that a model for an unconstrained number of species with arbitrary charges is behind these presentations and will be submitted for publication soon. The development of a novel transport theory is necessary for RTILs because standard models for lithium ion batteries assume a neutral solvent [22, 95]. Secondly, we take into account hardcore interactions between ions as a strong repulsion between particles at atomistic separations as shown in equation 2.33. These microscopic details become relevant in the nano-sized electrochemical double layer.

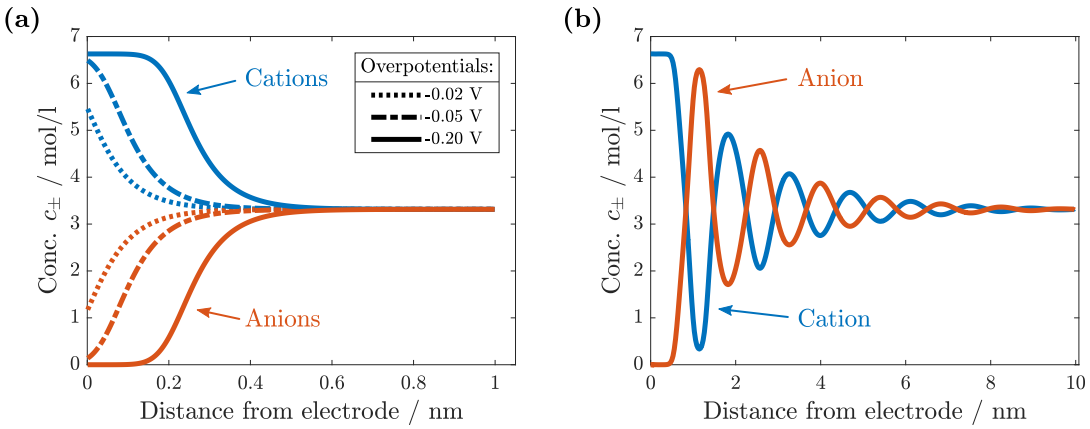

Figure 4.4 Multilayer structure of ionic concentrations in the vicinity of a negatively charged electrode surface. (a) Without hardcore interactions, we observe depletion of anions and crowding of cations. (b) With hardcore interactions, a quasi-crystalline structure of alternating layers forms. Reproduced from Hoffmann et al. [9].

Modeling makes separating the effect of different material properties possible. In a first step, we simulate the static electrochemical surface layer of a binary RTIL without hardcore interactions in figure 4.4a. At a negatively charged electrode, cations are attracted by the electric field to the interface and the electrochemical surface layer becomes positively charged. At low overpotentials, the charge density decays exponentially as predicted by Gouy and Chapman for dilute electrolytes. The width of this charged double layer is the Debye length [9, 95]. At larger overpotentials, the volumetric constraint on ions,

$$\sum_{\alpha=1}^{N} \nu_\alpha c_\alpha = 1, \tag{4.4}$$

imposed through equation 2.11 counteracts the electric field and leads to crowding of cations and depletion of anions. In a second step, we include hardcore interactions via equation 2.33 (see figure 4.4b). Because the ionic diameters are incommensurate with the required screening charge, alternating mono-layers of cations and anions form. This phenomenon is denoted overscreening. Our simulations show that the electrochemical double layer can become much larger than the Debye length.

For validation, we compare forces on the AFM tip with our simulation by multiplying the Lorentz with the molecular volume in Hoffmann et al. [9]. We find that both quantities agree within one to two orders of magnitude. This is an

excellent agreement if we take into account the differing set-ups. We simulate elastic perturbations of an equilibrium state. In contrast, ions are pushed away, when the AFM tip penetrates the multilayer structure.

Our model is the first to take into account the impact of neutral and charged additives, e.g., water and ionic silver onto the electrochemical double layer. By assuming small concentrations of the additive, we find

$$\vec{\nabla}\left(\ln\frac{c_{\text{additive}}}{c_0}\right) = -\frac{F z_{\text{additive}}}{RT}\vec{\nabla}\varphi. \tag{4.5}$$

In the case of water, equation 4.5 predicts a constant concentration. Therefore, the multilayer structure can only be disrupted by large water concentrations as shown in experiments [116]. The concentration of charged silver additives ($z_{\text{Ag}} = 1$) in contrast, obeys a Boltzmann distribution. Therefore, the silver ion concentration grows exponentially towards a negatively charged electrode. For the potential difference $\Delta\varphi = -0.2\text{V}$ between bulk electrolyte and electrode, the silver concentration at the electrode is $c_{\text{Ag}} = 2.4 \cdot 10^3\, c_{\text{Ag;bulk}}$ and becomes relevant compared to the RTIL ($c_{\text{Ag}} \sim 1 \cdot \text{mol/l}$) for $c_{\text{Ag;bulk}} \geq 0.4 \cdot 10^{-3}$ mol/l. This agrees excellently with our experiments which show a disruption of the multilayer structure for bulk concentrations $c_{\text{Ag}} \gtrsim 0.5 \cdot 10^{-3}$ mol/l [9]. Our analysis, however, becomes complicated by chemical interactions in the electrolyte. Most importantly, speciation can lead to varying charge numbers [228, 238] as shown for neutral aqueous electrolytes in this habilitation [5].

4.4 Growth of solid electrolyte interphase (SEI)

Above, we discuss reactions on electrode surfaces [7], electrochemical double layers at electrode surfaces [9], and nucleation on electrode surfaces [8]. However, bare electrode surfaces are rare inside batteries. On negative electrodes of lithium-ion batteries, a thin layer of electrolyte reduction products forms as described in section 1.3. Even though this solid electrolyte interphase (SEI) suppresses the further electrolyte reduction, continued SEI grows is the main contributor to lithium-ion loss, capacity fade, and limited battery lifetime [83, 84]. Since 1979 a multitude of experimental research has been performed [80, 239–243], but several key questions about SEI chemistry and mechanisms remain unanswered. Most importantly, the origin of continued SEI growth was

not identified prior to our work [12]. The experimentally observed square-root-of-time dependence of capacity fade suggests a transport limitation, but it does not distinguish between different transport mechanisms. We developed a series of models to predict additional dependencies, i.e., morphology of SEI and potential dependence of SEI growth [10–12]. Dedicated experiments can then identify the long-term growth mechanisms (LTGM), e.g., neutron reflectometry [244] and battery storage at various SoC [83, 84].

Atomistic simulation methods address elementary processes in the SEI. DFT simulations elucidate reaction [245] and transport processes [246, 247]. MD simulations cover the short-term SEI formation during the first battery cycles [93, 248]. Continuum models are used to study possible LTGMs [10–12, 85, 108, 247, 249–256].

a) Diffusion of solvent/salt molecules/anions through nano-sized SEI pores [10–12, 85, 249, 250, 256]
b) Electron tunneling through a dense, inner layer of the SEI [250, 251]
c) Electron conduction through the SEI [10–12, 108, 250, 252, 254]
d) Diffusion of neutral radicals such as lithium interstitials [11, 12, 246, 247]

All mechanisms are in good agreement with the experimentally observed square-root-of-time dependence of capacity fade. Note that Tang et al. use the potential dependence of capacity fade to rule out solvent diffusion as possible LTGM [250].

We developed the one-dimensional growth model shown in figure 1.2 and predict SEI porosity $\varepsilon(t,x)$ and thickness $L(t)$ [10, 11]. This is possible by taking into account two counter-propagating transport processes, i.e., motion of charges from the electrode to the electrolyte and motion of solvent molecules from the electrolyte to the electrode. We volume-average the SEI in planes parallel to the electrode surface and model transport with the porous electrode model introduced in section 2.2. In this way, we simulate the spatially-resolved dynamics of solvent concentrations, electrolyte convection velocity, electric SEI potential, and SEI porosity (see equation 3.2). We derive expressions for the specific surface area of SEI compounds,

$$A_i = \frac{6}{a_0}\varepsilon\left(\tilde{\varepsilon}_i + \frac{a_0^2}{6}\frac{\partial^2\tilde{\varepsilon}_i}{\partial x^2}\right), \tilde{\varepsilon}_i = \varepsilon_i + \varepsilon_{\text{init}}, \tag{4.6}$$

that take into account the enlarged surface area at the SEI front through a second derivative of the SEI volume fractions ε_i. Here, a_0 describes the size of elementary domains inside the SEI. This phase-field-like approach smooths the porosity profile and allows propagation of SEI into the electrolyte. Because we want to elucidate the universal SEI properties, we simplify SEI chemistry and consider up to two reactions at a time, namely the combinations I, I+II and I+III. We model a single reduction reaction for solvent (EC) and co-solvent (DMC) [11]

$$2\mathrm{EC} + 2\mathrm{Li}^+ + 2\mathrm{e}^- \rightarrow \mathrm{LiEDC} + R, \tag{I}$$

$$\mathrm{DMC} + \mathrm{Li}^+ + \mathrm{e}^- \rightarrow \mathrm{LiMC} + R. \tag{II}$$

with gaseous by-products R. As alternative, we implement the conversion reaction,

$$0.1\mathrm{LiEDC} + \mathrm{Li}^+ + \mathrm{e}^- \rightarrow 0.6\mathrm{Li_2O} + 0.4\mathrm{C}. \tag{III}$$

Conversion reactions change the volume of solids. Below a critical volume fraction of solid SEI $\varepsilon_{\mathrm{SEI}} < \varepsilon_{\mathrm{SEI}}^{\mathrm{crit}}$, we assume that the volume change is accommodated locally. Above it $\varepsilon_{\mathrm{SEI}} > \varepsilon_{\mathrm{SEI}}^{\mathrm{crit}}$, a displacement or convection of the solid is modeled [12]. In the following subsections, we present simulations of a single-layer SEI and a dual-layer SEI. Finally, we compare our model predictions with experiments and identify diffusion of neutral radicals as LTGM.

4.4.1 Single-layer SEI

In our first simulations, we assume that the solvent EC is reduced and the co-solvent DMC is inert [10, 11]. Electrons are conducted through the solid SEI and solvent molecules diffuse through the electrolyte-filled SEI pores. A typical evolution of SEI volume fraction $\varepsilon_{\mathrm{LiEDC}}$ is shown in figure 4.5a. We find that the SEI growth rate is limited by electron conduction and that the SEI predominantly grows at its front [10]. Therefore, SEI thickness grows like the square-root of time in agreement with capacity fade experiments [257]. By assuming that SEI growth occurs only at the SEI front, we derive an analytic formula for SEI thickness evolution which is in excellent agreement with simulations and experiments (see figure 4.5b). Besides SEI thickness, our model predicts SEI porosity. We find that the SEI volume fraction is almost constant. It approaches a stable value $\varepsilon_{\mathrm{SEI}}^*$ determined by electrolyte transport

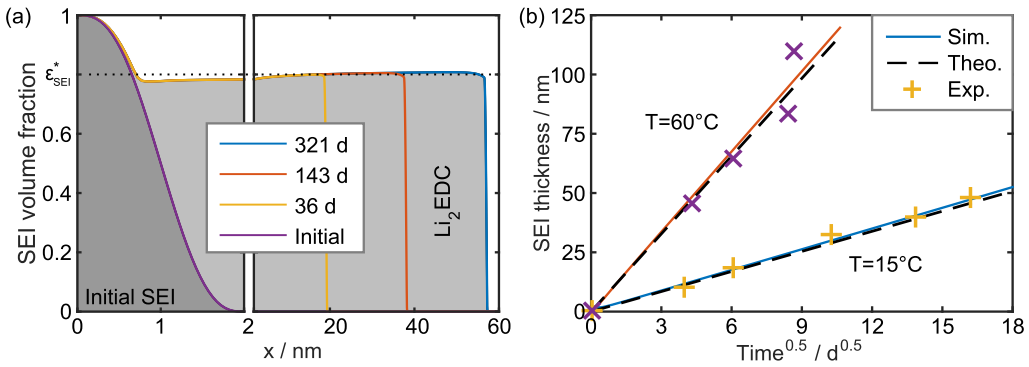

Figure 4.5 Simulation of single-layer SEI. (a) Time evolution of the SEI volume fraction. (b) SEI thickness evolution from experiment [85, 257] (dots), simulation [10] (dashed) and analytic theory [10] (lines). Reproduced from Single et al. [10].

properties, e.g., the Bruggeman coefficient β (see equation 2.19), because the SEI is growing faster than the solvent molecules can diffuse into the SEI. Our analytic estimate for the stable volume fraction $\varepsilon^*_{\text{SEI}}$ agrees nicely with the simulations.

As alternative mechanism for charge transport from the electrode through the SEI into the electrolyte, diffusion of neutral radicals was proposed [11, 12, 246, 247]. In the case of lithium interstitial diffusion, lithium ions take up an electron at the electrode-SEI interface, diffuse as neutral lithium interstitials through the SEI, and release an electron at the SEI-electrolyte interface. SEI profiles simulated with this mechanism share the same features as those described above for electron conduction [11].

4.4.2 Dual-layer SEI

Additional SEI formation reactions lead to a dual-layer SEI with a compact, non-porous, inner layer [11]. In the case of co-solvent reduction with reactions I and II, our model shows an inner dense layer and an outer porous layer (see figure 4.6a). As the primary SEI compound LiEDC is formed by EC reduction, EC concentration in the SEI pores becomes very small. The co-solvent DMC, however, is present in the SEI and can be reduced due to the low electric potential close to the electrode. In the case of a conversion of the primary SEI compound with reactions I and III, the critical volume fraction of solid SEI $\varepsilon^{\text{crit}}_{\text{SEI}}$ determines the porosity of the inner layer (see figures 4.6b and 4.6c).

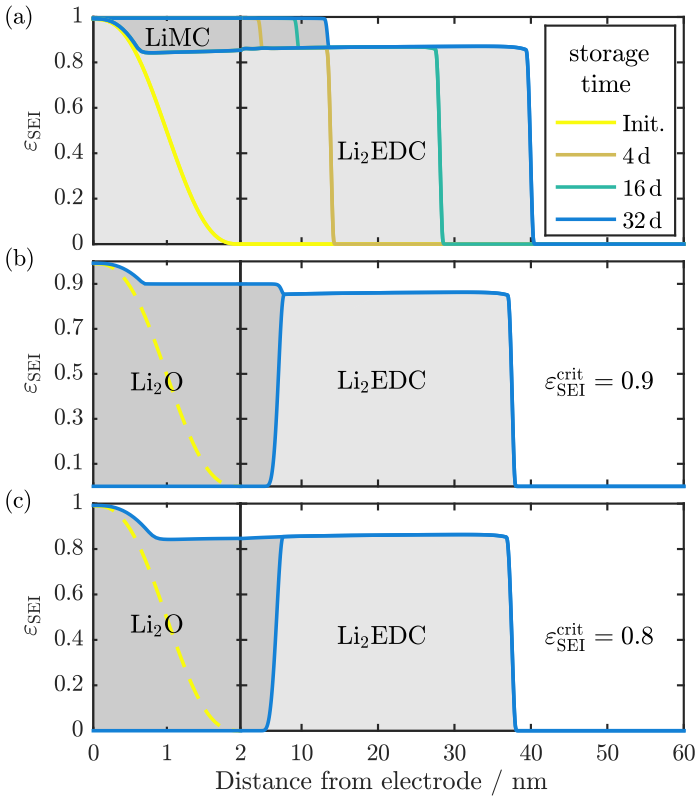

Figure 4.6 (a) SEI volume fraction evolution with active co-solvent. (b) and (c) show the SEI volume fraction of a dual layer SEI formed with inert co-solvent and unstable Li_2EDC. These simulations differ in the choice of $\varepsilon_{\mathrm{SEI}}^{\mathrm{crit}}$. Reproduced from Single et al. [11].

We further analyze the growth of a dual-layer SEI analytically [11]. The ratio between the thickness of the inner and the outer layer is determined by electrode potential and material parameters. Simulations illustrate that this stationary thickness ratio is quickly re-attained after the SEI is disturbed. Most importantly, SEI thickness and capacity fade grow with the square-root of time for dual-layer morphologies, too.

4.4.3 Identifying the long-term growth mechanism

We study the transition from electron conduction to solvent diffusion as limiting growth mechanism by taking into account solid convection in a single-layer SEI, [11]. Imposing low critical SEI volume fractions $\varepsilon_{\mathrm{SEI}}^{\mathrm{crit}}$, solvent diffusion becomes rate limiting. This moves the reaction zone to the electrode-SEI interface. Our stability analysis shows that SEI growth rate is very susceptible to porosity

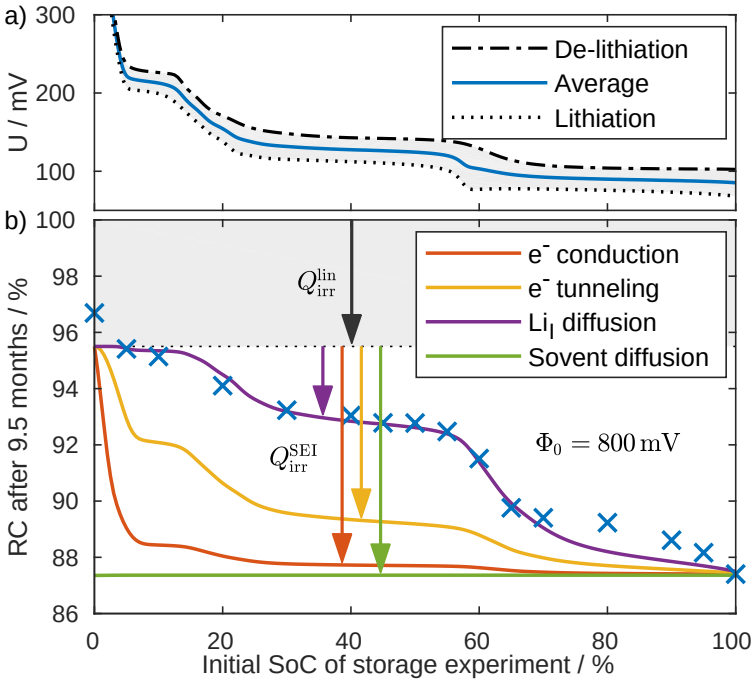

Figure 4.7 (a) Open circuit voltage of the negative electrode gained by averaging the lithiation and delithiation voltages (half cell, cycled at C/20). (b) Experimentally obtained relative capacity after 9.5 months of storage (crosses) compared to that predicted by four different long-term growth mechanisms (lines) . Reproduced from Single et al. [12].

fluctuations if solvent diffusion is rate-limiting. Therefore, an inhomogeneous SEI thickness distribution would be observable if solvent diffusion was the LTGM.

As final highlight of this habilitation, we compare the predictions of different LTGMs with dedicated experiments [12]. Jossen et al. show that the SEI growth rate strongly depends on graphite potential and state-of-charge (SoC) [84]. We create simple theories based on the four LTGMs enlisted above: electrolyte diffusion, electron tunneling, electron conduction, and lithium interstitial diffusion. As shown in figure 4.7, solvent diffusion does not reproduce a SoC dependence. The SoC dependence of electron conduction and electron tunneling does not agree with the experiment for any reasonable choice of parameters. Only a mechanism such as lithium interstitial diffusion results in a promising agreement with the experiment and remains as candidate for the LTGM.

Chapter 5

Summary and Outlook

In this habilitation, we contribute to the development of electrochemical systems (see chapter 1) by improving consistent theory-based models derived from non-equilibrium thermodynamics (see chapter 2). Electrochemical devices rely on processes on a multitude of length scales. Our continuum models explain effects from the meso-scale to the macro-scale. By combining several sub-models into one multi-scale model, we predict the performance and steady degradation of batteries. In some cases, our theoretic proposals for materials and structures are successfully realized experimentally.

On the macro-scale, this habilitation focuses on next-generation batteries based on air electrodes (see chapter 3). Metal-air batteries promise overwhelmingly high energy densities. We develop 1D models explaining experimental results and proposing new research directions. These 1D models on the macro-scale are coupled to sub-models on the micro-scale representing the main performance limitations. Lithium-air batteries with aprotic electrolytes receive most attention [1], but we demonstrate the unique benefits of using aqueous electrolytes [2, 3]. We refine our approach in the case of zinc-air batteries which are the most advanced type of metal-air batteries [4]. Neutral aqueous electrolytes based on ammonia buffer are tolerable to atmospheric carbon dioxide. We present a novel modeling concept that makes possible the dynamic simulation of such buffered electrolytes. As a consequence, we were the first to simulate these cells and proposed novel electrolyte compositions for further experimental research [5].

Meso-scale processes determine battery performance and safety (see chapter 4). The rate of oxygen reduction, for example, is quite low and limits the efficiency of metal-air batteries. We analyze the oxygen reaction in a

mean-field approach and discuss the adoption of density functional theory for parameter determination [7]. In aprotic lithium-air batteries, the morphology of crystallized lithium oxide determines charge capacity. We use a phase-field like approach for modeling the electrochemically-driven surface growth and explain its current dependence [8]. The quest for battery chemistries with higher cell voltages motivates research on novel electrolytes, e.g., ionic liquids. We develop a rigorous physics-based model that captures both bulk and surface properties. Our validated simulations interpret the impact of additives on the multilayer electrochemical surface layers of ionic liquids [9].

Commercialized lithium-ion batteries stand out among energy storage devices because they offer good energy and high power densities. We develop a novel model for growth of the meso-scale solid electrolyte interphase (SEI) determining the safety of lithium-ion batteries [10–12]. Going beyond the standard SEI models, we predict the morphology of SEI. From the potential dependence of SEI growth rate, our model predicts the mechanism behind continued SEI growth. We present the first indirect experimental evidence that neutral radicals carry a negative charge and diffuse through the SEI [12].

The work in this habilitation suggests further research in several directions. We show that metal-air batteries are in a promising state of research and that experimental progress is accelerated by theory-based rational design [6]. Models in 2D and 3D will successively become expedient, when research and development converges to a few cell setups, e.g., for zinc-air batteries. Alternative next-generation batteries, including metal-ion batteries, keep equally good prospects. Our consistent modeling based on non-equilibrium thermodynamics is especially fruitful for advancing progress on novel electrolytes, e.g., buffered aqueous solutions and ionic liquids. We will contribute to research on bulk and surface properties by studying speciation in the bulk and structuring at surfaces. The development of lithium-ion batteries will be addressed by phase-field like models of metal deposition and SEI growth as lithium metal and silicon electrodes try to outperform carbon-based negative electrodes.

Finally, we highlight that stochastic processes and structures are prevalent in batteries. For example, the internal structure of an individual battery and the external condition it is exposed to are unknown. Furthermore, modeling is based on complexity reduction and produces intrinsically uncertain output. Therefore, one should not over-interpret the accuracy of local and deterministic simulation results. Instead, battery lifetime and safety should be described

with statistics. However, this notion is hardly mentioned in the field of battery modeling. Therefore, future models on all length scales will benefit from a stochastic perspective.

Bibliography

[1] J. P. Neidhardt, D. N. Fronczek, T. Jahnke, T. Danner, B. Horstmann and W. G. Bessler. A Flexible Framework for Modeling Multiple Solid, Liquid and Gaseous Phases in Batteries and Fuel Cells. *Journal of The Electrochemical Society* **159**, A1528–A1542 (2012).

[2] B. Horstmann, T. Danner and W. G. Bessler. Precipitation in aqueous lithium–oxygen batteries: a model-based analysis. *Energy & Environmental Science* **6**, 1299 (2013).

[3] T. Danner, B. Horstmann, D. Wittmaier, N. Wagner and W. G. Bessler. Reaction and transport in Ag/Ag2O gas diffusion electrodes of aqueous Li-O2 batteries: Experiments and modeling. *Journal of Power Sources* **264**, 320–332 (2014).

[4] J. Stamm, A. Varzi, A. Latz and B. Horstmann. Modeling nucleation and growth of zinc oxide during discharge of primary zinc-air batteries. *Journal of Power Sources* **360**, 136–149 (2017).

[5] S. Clark, A. Latz and B. Horstmann. Rational Development of Neutral Aqueous Electrolytes for Zinc-Air Batteries. *ChemSusChem* **10**, 4735–4747 (2017).

[6] S. Clark, A. Latz and B. Horstmann. A Review of Model-Based Design Tools for Metal-Air Batteries. *Batteries* **4**, 5 (2018).

[7] D. Eberle and B. Horstmann. Oxygen Reduction on Pt(111) in Aqueous Electrolyte: Elementary Kinetic Modeling. *Electrochimica Acta* **137**, 714–720 (2014).

[8] B. Horstmann, B. Gallant, R. Mitchell, W. G. Bessler, Y. Shao-Horn and M. Z. Bazant. Rate-Dependent Morphology of Li2O2 Growth in Li-O2 Batteries. *The Journal of Physical Chemistry Letters* **4**, 4217–4222 (2013).

[9] V. Hoffmann, G. Pulletikurthi, T. Carstens, A. Lahiri, A. Borodin, M. Schammer, B. Horstmann, A. Latz and F. Endres. Influence of a Silver Salt on the Nanostructure of an Au(111) Ionic Liquid Interface: an Atomic Force Microscopy Study and Theoretical Concepts. *Physical Chemistry Chemical Physics* **20**, 4760–4771 (2018).

[10] F. Single, B. Horstmann and A. Latz. Dynamics and morphology of solid electrolyte interphase (SEI). *Physical Chemistry Chemical Physics* **18**, 17810–17814 (2016).

[11] F. Single, B. Horstmann and A. Latz. Revealing SEI Morphology: In-Depth Analysis of a Modeling Approach. *Journal of The Electrochemical Society* **164**, E3132–E3145 (2017).

[12] F. Single, A. Latz and B. Horstmann. Identifying the Mechanism of Continued Growth of the Solid-Electrolyte Interphase. *ChemSusChem* **11**, 1950–1955 (2018).

[13] S. Clark, A. Latz and B. Horstmann. Cover: Rational Development of Neutral Aqueous Electrolytes for Zinc-Air Batteries. *ChemSusChem* **10**, 4666 (2017).

[14] H. Schlesinger. *The Battery: How Portable Power Sparked a Technological Revolution* (Collins, Harper, New York, 2011), 2010 edn.

[15] B. Scrosati. History of lithium batteries. *Journal of Solid State Electrochemistry* **15**, 1623–1630 (2011).

[16] J.-F. Drillet, F. Endres and H.-U. Reichardt. Das Batteriesystem Zink / Luft. In *Handbuch Elektromobilität*, 145–156 (EW Medien und Kongresse, 2013).

[17] Y. Li and H. Dai. Recent advances in zinc air batteries. *Chem. Soc. Rev.* **43**, 5257–5275 (2014).

[18] B. Dunn, H. Kamath and J.-M. Tarascon. Electrical Energy Storage for the Grid: A Battery of Choices. *Science* **334**, 928–935 (2011).

[19] O. Gröger, H. A. Gasteiger and J.-P. Suchsland. Review Electromobility: Batteries or Fuel Cells? *Journal of The Electrochemical Society* **162**, A2605–A2622 (2015).

[20] P. Bai, J. Li, F. R. Brushett and M. Z. Bazant. Transition of lithium growth mechanisms in liquid electrolytes. *Energy & Environmental Science* **9**, 3221–3229 (2016).

[21] R. V. Noorden. The rechargeable revolution: A better battery. *Nature* **507**, 26–28 (2014).

[22] A. Latz and J. Zausch. Multiscale modeling of lithium ion batteries: thermal aspects. *Beilstein Journal of Nanotechnology* **6**, 987–1007 (2015).

[23] J.-S. Lee, S. Tai Kim, R. Cao, N.-S. N.-S. Choi, M. Liu, K. T. Lee and J. Cho. Metal-Air Batteries with High Energy Density: Li-Air versus Zn-Air. *Advanced Energy Materials* **1**, 34–50 (2011).

[24] T. Zhang, Z. Tao and J. Chen. Magnesium–air batteries: from principle to application. *Materials Horizons* **1**, 196–206 (2014).

[25] L. D. Chen, J. K. Norskov and A. C. Luntz. Theoretical Limits to the Anode Potential in Aqueous Mg-Air Batteries. *The Journal of Physical Chemistry C* **119**, 19660–19667 (2015).

[26] P. Fischer, R. M. Schwarz, M. Marinaro, M. Wachtler and L. Jörissen. Investigation of the Electrochemical Oxygen Reduction Reaction in Non-Aqueous, Magnesium-Ion-Containing Electrolytes for Magnesium Air Batteries. *ECS Transactions* **75**, 3–12 (2017).

[27] G. Vardar, A. E. S. Sleightholme, J. Naruse, H. Hiramatsu, D. J. Siegel and C. W. Monroe. Electrochemistry of magnesium electrolytes in ionic liquids for secondary batteries. *ACS Applied Materials and Interfaces* **6**, 18033–18039 (2014).

[28] D. R. Egan, C. Ponce De León, R. J. Wood, R. L. Jones, K. R. Stokes and F. C. Walsh. Developments in electrode materials and electrolytes for aluminium-air batteries. *Journal of Power Sources* **236**, 293–310 (2013).

[29] P. Adelhelm, P. Hartmann, C. L. Bender, M. Busche, C. Eufinger and J. Janek. From lithium to sodium: Cell chemistry of room temperature sodium-air and sodium-sulfur batteries. *Beilstein Journal of Nanotechnology* **6**, 1016–1055 (2015).

[30] P. Hartmann, C. L. Bender, M. Vračar, A. K. Dürr, A. Garsuch, J. Janek and P. Adelhelm. A rechargeable room-temperature sodium superoxide (NaO2) battery. *Nature Materials* **12**, 228–232 (2012).

[31] J. Kim, H. Park, B. Lee, W. M. Seong, H.-D. Lim, Y. Bae, H. Kim, W. K. Kim, K. H. Ryu and K. Kang. Dissolution and ionization of sodium superoxide in sodium oxygen batteries. *Nature Communications* **7**, 10670 (2016).

[32] Y. E. Durmus. *Modeling of silicon air-batteries*. Ph.D. thesis, University of Ulm (2013).

[33] P. Jakes, G. Cohn, Y. Ein-Eli, F. Scheiba, H. Ehrenberg and R.-A. Eichel. Limitation of discharge capacity and mechanisms of air-electrode deactivation in silicon-air batteries. *ChemSusChem* **5**, 2278 (2012).

[34] Y. E. Durmus, Ö. Aslanbas, S. Kayser, H. Tempel, F. Hausen, L. G. de Haart, J. Granwehr, Y. Ein-Eli, R. A. Eichel and H. Kungl. Long run discharge, performance and efficiency of primary Silicon–air cells with alkaline electrolyte. *Electrochimica Acta* **225**, 215–224 (2017).

[35] G. Girishkumar, B. McCloskey, A. C. Luntz, S. Swanson and W. Wilcke. Lithium-Air Battery: Promise and Challenges. *The Journal of Physical Chemistry Letters* **1**, 2193 (2010).

[36] K. M. Abraham and Z. Jiang. A Polymer Electrolyte-Based Rechargeable Lithium / Oxygen Battery. *Electrochemical Science and Technology* **143**, 1 (1996).

[37] P. Albertus, G. Girishkumar, B. McCloskey, R. S. Sanchez-Carrera, B. Kozinsky, J. Christensen and A. C. Luntz. Identifying Capacity Limitations in the Li/Oxygen Battery Using Experiments and Modeling. *Journal of The Electrochemical Society* **158**, A343–A351 (2011).

[38] B. D. McCloskey, D. S. Bethune, R. M. Shelby, G. Girishkumar and A. C. Luntz. Solvents ' Critical Role in Nonaqueous Lithium-Oxygen Battery Electrochemistry. *The Journal of Physical Chemistry Letters* **2**, 1161–1166 (2011).

[39] S. A. Freunberger, Y. Chen, Z. Peng, J. M. Griffin, L. J. Hardwick, F. Bardé, P. Novák and P. G. Bruce. Reactions in the rechargeable

lithium-O2 battery with alkyl carbonate electrolytes. *Journal of the American Chemical Society* **133**, 8040–8047 (2011).

[40] B. D. McCloskey, A. Speidel, R. Scheffler, D. C. Miller, V. Viswanathan, J. S. Hummelshøj, J. K. Nørskov, A. C. Luntz, D. S. Bethune, R. M. Shelby, T. Mori, R. Scheffler, A. Speidel, M. Sherwood and A. C. Luntz. Twin Problems of Interfacial Carbonate Formation in Nonaqueous Li-O2 Batteries. *The Journal of Physical Chemistry Letters* **3**, 997–1001 (2012).

[41] S. A. Freunberger, Y. Chen, N. E. Drewett, L. J. Hardwick, F. Bardé and P. G. Bruce. The lithium-oxygen battery with ether-based electrolytes. *Angewandte Chemie (International ed. in English)* **50**, 8609–13 (2011).

[42] Z. Peng, S. A. Freunberger, Y. Chen and P. G. Bruce. A Reversible and Higher-Rate Li-O 2 Battery. *Science* **337**, 563 (2012).

[43] V. Viswanathan, K. S. Thygesen, J. S. Hummelshøj, J. K. Nørskov, G. Girishkumar, B. D. McCloskey and A. C. Luntz. Electrical conductivity in Li2O2 and its role in determining capacity limitations in non-aqueous Li-O2 batteries. *The Journal of Chemical Physics* **135**, 214704 (2011).

[44] B. M. Gallant, D. G. Kwabi, R. R. Mitchell, J. Zhou, C. Thompson and Y. Shao-Horn. Influence of Li2O2 morphology on oxygen reduction and evolution kinetics in Li-O2 batteries. *Energy & Environmental Science* **6**, 2518 (2013).

[45] N. B. Aetukuri, B. D. McCloskey, J. M. Garcia, L. E. Krupp, V. Viswanathan and A. C. Luntz. Solvating additives drive solution-mediated electrochemistry and enhance toroid growth in non-aqueous Li-O2 batteries. *Nature Chemistry* **7**, 50–56 (2015).

[46] L. D. Griffith, A. E. S. Sleightholme, J. F. Mansfield, D. J. Siegel and C. W. Monroe. Correlating Li/O2 cell capacity and product morphology with discharge current. *ACS Applied Materials and Interfaces* **7**, 7670–7678 (2015).

[47] P. Andrei, J. P. Zheng, M. Hendrickson and E. J. Plichta. Some Possible Approaches for Improving the Energy Density of Li-Air Batteries. *Journal of The Electrochemical Society* **157**, A1287–A1295 (2010).

[48] A. Manthiram and L. Li. Hybrid and aqueous lithium-air batteries. *Advanced Energy Materials* **5**, 1401302 (2015).

[49] P. Stevens, G. Toussaint, G. Caillon, P. Viaud, P. Vinatier, C. Cantau, O. Fichet, C. Sarrazin and M. Mallouki. Development of a lithium air rechargeable battery. In *ECS Transactions*, vol. 28, 1–12 (2010). URL http://dx.doi.org/10.1149/1.3507922.

[50] Y. Wang and H. Zhou. A lithium-air battery with a potential to continuously reduce O2 from air for delivering energy. *Journal of Power Sources* **195**, 358–361 (2010).

[51] J.-F. Drillet, F. Holzer, T. Kallis, S. Müller and V. M. Schmidt. Influence of CO2 on the stability of bifunctional oxygen electrodes for rechargeable zinc/air batteries and study of different CO2 filter materials. *Physical Chemistry Chemical Physics* **3**, 368–371 (2001).

[52] J. Lu, Y. Jung Lee, X. Luo, K. Chun Lau, M. Asadi, H.-H. Wang, S. Brombosz, J. Wen, D. Zhai, Z. Chen, D. J. Miller, Y. Sub Jeong, J.-B. Park, Z. Zak Fang, B. Kumar, A. Salehi-Khojin, Y.-K. Sun, L. A. Curtiss and K. Amine. A lithium oxygen battery based on lithium superoxide. *Nature* **529**, 1–7 (2016).

[53] L. Johnson, C. Li, Z. Liu, Y. Chen, S. A. Freunberger, P. C. Ashok, B. B. Praveen, K. Dholakia, J.-M. Tarascon and P. G. Bruce. The role of LiO2 solubility in O2 reduction in aprotic solvents and its consequences for Li–O2 batteries. *Nature Chemistry* **6**, 1091–1099 (2014).

[54] X. Gao, Y. Chen, L. Johnson and P. G. Bruce. Promoting solution phase discharge in Li-O2 batteries containing weakly solvating electrolyte solutions. *Nature Materials* **15**, 882–888 (2016).

[55] T. Vegge, J. M. Garcia-Lastra and D. J. Siegel. Lithium–oxygen batteries: At a crossroads? *Current Opinion in Electrochemistry* **6**, 100–107 (2017).

[56] L. Grande, E. Paillard, J. Hassoun, J. B. Park, Y. J. Lee, Y. K. Sun, S. Passerini and B. Scrosati. The lithium/air battery: Still an emerging system or a practical reality? *Advanced Materials* **27**, 784–800 (2015).

[57] J. Lu, K. C. Lau, Y.-K. Sun, L. A. Curtiss and K. Amine. Review—Understanding and Mitigating Some of the Key Factors that Limit Non-Aqueous Lithium-Air Battery Performance. *Journal of The Electrochemical Society* **162**, A2439–A2446 (2015).

[58] T. Liu, M. Leskes, W. Yu, A. J. Moore, L. Zhou, P. M. Bayley, G. Kim, C. P. Grey, Y. Wanjing, A. J. Moore, L. Zhou, P. M. Bayley, G. Kim and C. P. Grey. Cycling Li-O2 batteries via LiOH formation and decomposition. *Science* **350**, 530–533 (2015).

[59] A. R. Suresh Kannan, S. Muralidharan, K. B. Sarangapani, V. Balaramachandran and V. Kapali. Corrosion and anodic behaviour of zinc and its ternary alloys in alkaline battery electrolytes. *Journal of Power Sources* **57**, 93–98 (1995).

[60] M. Yano, S. Fujitani, K. Nishio, Y. Akai and M. Kurimura. Effect of additives in zinc alloy powder on suppressing hydrogen evolution. *Journal of Power Sources* **74**, 129–134 (1998).

[61] Y. Li, F. El Gabaly, T. R. Ferguson, R. B. Smith, N. C. Bartelt, J. D. Sugar, K. R. Fenton, D. A. Cogswell, A. L. D. Kilcoyne, T. Tyliszczak, M. Z. Bazant and W. C. Chueh. Current-induced transition from particle-by-particle to concurrent intercalation in phase-separating battery electrodes. *Nature Materials* **13**, 1149–1156 (2014).

[62] F. R. McLarnon and E. J. Cairns. The Secondary Alkaline Zinc Electrode. *Journal of The Electrochemical Society* **138**, 645–656 (1991).

[63] M.-B. Liu, G. Cook and N. P. Yao. Passivation of Zinc Anodes in KOH Electrolytes. *Journal of The Electrochemical Society* **128**, 1663–1668 (1981).

[64] G. Prentice, Y.-C. Chang and X. Shan. A Model for the Passivation of the Zinc Electrode in Alkaline Electrolyte. *Journal of The Electrochemical Society* **138**, 890–894 (1991).

[65] A. R. Mainar, O. Leonet, M. Bengoechea, I. Boyano, I. de Meatze, A. Kvasha, A. Guerfi and J. A. Blazquez. Alkaline aqueous electrolytes for secondary zinc-air batteries: an overview. *International Journal of Energy Research* **40**, 1032–1049 (2016).

[66] D. Schröder, N. N. Sinai Borker, M. König and U. Krewer. Performance of zinc air batteries with added K2CO3 in the alkaline electrolyte. *Journal of Applied Electrochemistry* **45**, 427–437 (2015).

[67] F. W. Thomas Goh, Z. Liu, T. S. A. Hor, J. Zhang, X. Ge, Y. Zong, A. Yu and W. Khoo. A Near-Neutral Chloride Electrolyte for Electrically Rechargeable Zinc-Air Batteries. *Journal of the Electrochemical Society* **161**, A2080–A2086 (2014).

[68] A. Sumboja, X. Ge, G. Zheng, F. T. Goh, T. A. Hor, Y. Zong and Z. Liu. Durable rechargeable zinc-air batteries with neutral electrolyte and manganese oxide catalyst. *Journal of Power Sources* **332**, 330–336 (2016).

[69] D. R. MacFarlane, M. Forsyth, P. C. Howlett, M. Kar, S. Passerini, J. M. Pringle, H. Ohno, M. Watanabe, F. Yan, W. Zheng, S. Zhang and J. Zhang. Ionic liquids and their solid-state analogues as materials for energy generation and storage. *Nature Reviews Materials* 15005 (2016).

[70] Z. Liu, S. Z. E. Abedin and F. Endres. Electrodeposition of zinc films from ionic liquids and ionic liquid/water mixtures. *Electrochimica Acta* **89**, 635–643 (2013).

[71] Z. Liu, S. Z. El Abedin and F. Endres. Dissolution of zinc oxide in a protic ionic liquid with the 1-methylimidazolium cation and electrodeposition of zinc from ZnO/ionic liquid and ZnO/ionic liquid-water mixtures. *Electrochemistry Communications* **58**, 46–50 (2015).

[72] J. Fu, Z. P. Cano, M. G. Park, A. Yu, M. Fowler and Z. Chen. Electrically Rechargeable Zinc–Air Batteries: Progress, Challenges, and Perspectives. *Advanced Materials* **29**, 1604685 (2017).

[73] S. Amendola, M. Binder, P. J. Black, S. Sharp-Goldman, L. Johnson, M. Kunz, M. Oster, T. Chciuk and R. Johnson. Electrically rechargeable, metal-air battery systems and methods. *International Patent* WO 2012/012558 A2 (2012).

[74] C. Friesen, R. Krishnan and G. Friesen. Rechargeable electrochemical cell system with a charging electrode charge/discharge mode switching in the cells. *United States Patent* US 2011/0070506 A1 (2011).

[75] B. Scrosati and J. Garche. Lithium batteries: Status, prospects and future. *Journal of Power Sources* **195**, 2419–2430 (2010).

[76] M. S. Whittingham. Lithium batteries and cathode materials. *Chemical reviews* **104**, 4271–301 (2004).

[77] K. Mizushima, P. Jones, P. Wiseman and J. B. Goodenough. LiCoO2: A new cathode material for batteries of high energy density. *Solid State Ionics* **3**, 171–174 (1981).

[78] T. Nagaura and K. Tazawa. Lithium Ion Rechargeable Battery. *Progress in Batteries and Solar Cells* **9**, 209 (1990).

[79] B. D. Guyornard and J.-m. Tarascon. Rocking-Chair or Lithium-Ion Rechargeable Lithium Batteries. *Advanced Materials* **6**, 408–412 (1994).

[80] E. Peled. The Electrochemical Behavior of Alkali and Alkaline Earth Metals in Nonaqueous Battery Systems–The Solid Electrolyte Interphase Model. *Journal of The Electrochemical Society* 2047–2051 (1979).

[81] D. Aurbach. Review of selected electrode-solution interactions which determine the performance of Li and Li ion batteries. *Journal of Power Sources* **89**, 206–218 (2000).

[82] A. J. Smith, J. C. Burns, X. Zhao, D. Xiong and J. R. Dahn. A High Precision Coulometry Study of the SEI Growth in Li/Graphite Cells. *Journal of The Electrochemical Society* **158**, A447 (2011).

[83] P. Keil, S. F. Schuster, J. Wilhelm, J. Travi, A. Hauser, R. C. Karl and A. Jossen. Calendar Aging of Lithium-Ion Batteries. *Journal of The Electrochemical Society* **163**, A1872–A1880 (2016).

[84] P. Keil and A. Jossen. Calendar Aging of NCA Lithium-Ion Batteries Investigated by Differential Voltage Analysis and Coulomb Tracking. *Journal of The Electrochemical Society* **164**, A6066–A6074 (2017).

[85] M. B. Pinson and M. Z. Bazant. Theory of SEI Formation in Rechargeable Batteries: Capacity Fade, Accelerated Aging and Lifetime Prediction. *Journal of the Electrochemical Society* **160**, A243–A250 (2012).

[86] M. Petzl, M. Kasper and M. A. Danzer. Lithium plating in a commercial lithium-ion battery - A low-temperature aging study. *Journal of Power Sources* **275**, 799–807 (2015).

[87] J. Steiger, D. Kramer and R. Mönig. Mechanisms of dendritic growth investigated by in situ light microscopy during electrodeposition and dissolution of lithium. *Journal of Power Sources* **261**, 112–119 (2014).

[88] M. Wohlfahrt-Mehrens, C. Vogler and J. Garche. Aging mechanisms of lithium cathode materials. *Journal of Power Sources* **127**, 58–64 (2004).

[89] M. Jäckle and A. Groß. Microscopic properties of lithium, sodium, and magnesium battery anode materials related to possible dendrite growth. *Journal of Chemical Physics* **141** (2014).

[90] J. Nørskov and J. Rossmeisl. Origin of the overpotential for oxygen reduction at a fuel-cell cathode. *The Journal of Physical Chemistry B* **108**, 17886–17892 (2004).

[91] J. A. Keith and T. Jacob. Theoretische Untersuchungen zu potentialabhängigen und konkurrierenden Mechanismen der elektrokatalytischen Sauerstoffreduktion an Pt(111). *Zeitschrift für Angewandte Chemie* **122**, 9711 (2010).

[92] S. Loftager, J. M. Garcia-Lastra and T. Vegge. A Density Functional Theory Study of the Ionic and Electronic Transport Mechanisms in LiFeBO3Battery Electrodes. *Journal of Physical Chemistry C* **120**, 18355–18364 (2016).

[93] D. Bedrov, O. Borodin and J. B. Hooper. Li+ Transport and Mechanical Properties of Model Solid Electrolyte Interphases (SEI): Insight from Atomistic Molecular Dynamics Simulations. *The Journal of Physical Chemistry C* **121**, 16098–16109 (2017).

[94] O. Borodin and D. Bedrov. Interfacial Structure and Dynamics of the Lithium Alkyl Dicarbonate SEI Components in Contact with the Lithium Battery Electrolyte. *The Journal of Physical Chemistry C* **118**, 18362–18371 (2014).

[95] J. S. Newman and K. Thomas-Alyea. *Electrochemical Systems* (John Wiley & Sons, 2004).

[96] A. Latz and J. Zausch. Thermodynamic consistent transport theory of Li-ion batteries. *Journal of Power Sources* **195**, 3296–3302 (2011).

[97] A. Latz and J. Zausch. Thermodynamic derivation of a Butler–Volmer model for intercalation in Li-ion batteries. *Electrochimica Acta* **110**, 358–362 (2013).

[98] M. Z. Bazant. Theory of Chemical Kinetics and Charge Transfer based on Nonequilibrium Thermodynamics. *Accounts of Chemical Research* **46**, 1144–1160 (2013).

[99] P. Bai and M. Z. Bazant. Charge transfer kinetics at the solid-solid interface in porous electrodes. *Nature communications* **5**, 3585 (2014).

[100] D. A. Cogswell and M. Z. Bazant. Theory of Coherent Nucleation in Phase-Separating Nanoparticles. *Nano Letters* **13**, 3036 (2013).

[101] J. E. Guyer, W. J. Boettinger, J. A. Warren and G. B. McFadden. Phase field modeling of electrochemistry. I. Equilibrium. *Physical Review E - Statistical, Nonlinear, and Soft Matter Physics* **69**, 021603 (2004).

[102] W. Dreyer, J. Jamnik, C. Guhlke, R. Huth, J. Moskon and M. Gaberscek. The thermodynamic origin of hysteresis in insertion batteries. *Nature Materials* **9**, 448 (2010).

[103] M. Z. Bazant, B. D. Storey and A. A. Kornyshev. Double Layer in Ionic Liquids: Overscreening versus Crowding. *Physical Review Letters* **106**, 046102 (2011).

[104] N. Gavish and A. Yochelis. Theory of Phase Separation and Polarization for Pure Ionic Liquids. *Journal of Physical Chemistry Letters* **7**, 1121–1126 (2016).

[105] S. Braun, C. Yada and A. Latz. Thermodynamically Consistent Model for Space-Charge-Layer Formation in a Solid Electrolyte. *Journal of Physical Chemistry C* **119**, 22281–22288 (2015).

[106] J. Lück and A. Latz. Theory of reactions at electrified interfaces. *Phys. Chem. Chem. Phys.* **18**, 17799–17804 (2016).

[107] W. Dreyer, C. Guhlke and M. Landstorfer. A mixture theory of electrolytes containing solvation effects. *Electrochemistry Communications* **43**, 75–78 (2014).

[108] J. Christensen and J. Newman. A Mathematical Model for the Lithium-Ion Negative Electrode Solid Electrolyte Interphase. *Journal of The Electrochemical Society* **151**, A1977 (2004).

[109] S. Hein and A. Latz. Influence of local lithium metal deposition in 3D microstructures on local and global behavior of Lithium-ion batteries. *Electrochimica Acta* **201**, 354–365 (2016).

[110] T. Danner, M. Singh, S. Hein, J. Kaiser, H. Hahn and A. Latz. Thick electrodes for Li-ion batteries: A model based analysis. *Journal of Power Sources* **334**, 191–201 (2016).

[111] S. Whitaker. The equations of motion in porous media. *Chemical Engineering Science* **21**, 291 (1966).

[112] T. F. Fuller, M. Doyle and J. Newman. Simulation and Optimization of the Dual Lithium Ion Insertion Cell. *Journal of The Electrochemical Society* **141**, 1 (1994).

[113] X. Lin, H. E. Perez, S. Mohan, J. B. Siegel, A. G. Stefanopoulou, Y. Ding and M. P. Castanier. A lumped-parameter electro-thermal model for cylindrical batteries. *Journal of Power Sources* **257**, 1–11 (2014).

[114] S. Piller, M. Perrin and A. Jossen. Methods for state-of-charge determination and their applications. *Journal of Power Sources* **96**, 113–120 (2001).

[115] A. Eddahech, O. Briat, N. Bertrand, J.-Y. Delétage and J.-M. Vinassa. Behavior and state-of-health monitoring of Li-ion batteries using impedance spectroscopy and recurrent neural networks. *International Journal of Electrical Power & Energy Systems* **42**, 487–494 (2012).

[116] T. Cui, A. Lahiri, T. Carstens, N. Borisenko, G. Pulletikurthi, C. Kuhl and F. Endres. Influence of water on the electrified ionic liquid/solid interface: A direct observation of the transition from a multilayered structure to a double-layer structure. *The Journal of Physical Chemistry C* **120**, 9341–9349 (2016).

[117] I. Müller. *Thermodynamics, Interaction of Mechanics and Mathematics Series* (Pitman, Trowbridge, 1985).

[118] A. Kovetz. *Eletromagnetic Theory* (Oxford University Press, 2000).

[119] C. Guhlke. *Theorie der elektrochemischen Grenzfläche*. Ph.D. thesis, Technische Universität Berlin (2014). URL http://dx.doi.org/10.14279/depositonce-4342.

[120] P. Goyal and C. W. Monroe. New Foundations of Newman's Theory for Solid Electrolytes: Thermodynamics and Transient Balances. *Journal of The Electrochemical Society* **164**, E3647–E3660 (2017).

[121] Y. Zeng, R. B. Smith, P. Bai and M. Z. Bazant. Simple formula for Marcus-Hush-Chidsey kinetics. *Journal of Electroanalytical Chemistry* **735**, 77–83 (2014).

[122] T. Danner, S. Eswara, V. P. Schulz and A. Latz. Characterization of gas diffusion electrodes for metal-air batteries. *Journal of Power Sources* **324**, 646–656 (2016).

[123] S. Hein, J. Feinauer, D. Westhoff, I. Manke, V. Schmidt and A. Latz. Stochastic microstructure modeling and electrochemical simulation of lithium-ion cell anodes in 3D. *Journal of Power Sources* **336**, 161–171 (2016).

[124] J. S. Newman and C. W. Tobias. Theoretical Analysis of Current Distribution in Porous Electrodes. *Journal of The Electrochemical Society* **109**, 1183–1191 (1962).

[125] D. M. Bernardi and M. W. Verbrugge. A Mathematical Model of the Solid-Polymer-Electrolyte Fuel Cell. *Journal of The Electrochemical Society* **139**, 2477 (1992).

[126] T. Jahnke, G. Futter, A. Latz, T. Malkow, G. Papakonstantinou, G. Tsotridis, P. Schott, M. Gerard, M. Quinaud, M. Quiroga, A. A. Franco, K. Malek, F. Calle-Vallejo, R. Ferreira De Morais, T. Kerber, P. Sautet, D. Loffreda, S. Strahl, M. Serra, P. Polverino, C. Pianese, M. Mayur, W. G. Bessler and C. Kompis. Performance and degradation of Proton Exchange Membrane Fuel Cells: State of the art in modeling from

atomistic to system scale. *Journal of Power Sources* **304**, 207–233 (2016).

[127] W. Bessler, S. Gewies and M. Vogler. A new framework for physically based modeling of solid oxide fuel cells. *Electrochimica Acta* **53**, 1782–1800 (2007).

[128] J. A. Keith, G. Jerkiewicz and T. Jacob. Theoretical investigations of the oxygen reduction reaction on Pt(111). *ChemPhysChem* **11**, 2779–2794 (2010).

[129] T. Jacob and W. A. Goddard. Water formation on Pt and Pt-based alloys: a theoretical description of a catalytic reaction. *ChemPhysChem* **7**, 992–1005 (2006).

[130] P. Légaré. Interaction of oxygen with the Pt(111) surface in wide conditions range. A DFT-based thermodynamical simulation. *Surface Science* **580**, 137 (2005).

[131] H. A. Stone and D. Margetis. Continuum Descriptions of Crystal Surface Evolution. In Y. S. (ed.) *Handbook of Materials Modeling. Volume I: Methods and Models*, vol. I, chap. 4.8, 1 (Springer, Netherlands, 2005).

[132] A.-L. Barabasi and H. E. Stanley. *Fractal Concepts in Surface Growth* (Cambridge University Press, 1995).

[133] J. W. Cahn and J. E. Hilliard. Free Energy of a Nonuniform System. I. Interfacial Free Energy. *The Journal of Chemical Physics* **28**, 258 (1958).

[134] M. Z. Bazant. Thermodynamic Stability of Driven Open Systems and Control of Phase Separation by Electroautocatalysis. *Faraday Discussions* **199**, 423–463 (2017).

[135] J. Christensen, P. Albertus, R. S. Sanchez-Carrera, T. Lohmann, B. Kozinsky, R. Liedtke, J. Ahmed and A. Kojic. A Critical Review of Li/Air Batteries. *Journal of The Electrochemical Society* **159**, R1–R30 (2012).

[136] R. Padbury and X. Zhang. Lithium–oxygen batteries—Limiting factors that affect performance. *Journal of Power Sources* **196**, 4436–4444 (2011).

[137] B. M. Gallant, R. R. Mitchell, D. G. Kwabi, J. Zhou, L. Zuin, C. V. Thompson and Y. Shao-Horn. Chemical and Morphologic Changes of Li-O2 Battery Electrodes upon Cycling. *The Journal of Physical Chemistry C* **116**, 20800–20805 (2012).

[138] Z. Peng, S. A. Freunberger, Y. Chen and P. G. Bruce. A reversible and higher-rate Li-O2 battery. *Science (New York, N.Y.)* **337**, 563–6 (2012).

[139] Y.-C. Lu, B. M. Gallant, D. G. Kwabi, J. R. Harding, R. R. Mitchell, M. S. Whittingham and Y. Shao-Horn. Lithium-Oxygen batteries: Bridging Mechanistic Understanding and Battery Performance. *Energy & Environmental Science* **6**, 750 (2013).

[140] K. U. Schwenke, S. Meini, X. Wu, H. A. Gasteiger and M. Piana. Stability of superoxide radicals in glyme solvents for non-aqueous Li-O2 battery electrolytes. *Physical Chemistry Chemical Physics* **15**, 11830–11839 (2013).

[141] S. Meini, N. Tsiouvaras, K. U. Schwenke, M. Piana, H. Beyer, L. Lange and H. A. Gasteiger. Rechargeability of Li-air cathodes pre-filled with discharge products using an ether-based electrolyte solution: implications for cycle-life of Li-air cells. *Physical Chemistry Chemical Physics* **15**, 11478—-11493 (2013).

[142] G. A. Elia, J. Hassoun, W.-J. J. Kwak, Y.-K. K. Sun, B. Scrosati, F. Mueller, D. Bresser, S. Passerini, P. Oberhumer, N. Tsiouvaras and J. Reiter. An advanced lithium-air battery exploiting an ionic liquid-based electrolyte. *Nano Letters* **14**, 6572–6577 (2014).

[143] S. Lau and L. A. Archer. Nucleation and Growth of Lithium Peroxide in the Li–O2 Battery. *Nano Letters* **15**, 5995–6002 (2015).

[144] K. U. Schwenke, M. Metzger, T. Restle, M. Piana and H. A. Gasteiger. The Influence of Water and Protons on Li2O2 Crystal Growth in Aprotic Li-O2 Cells. *Journal of The Electrochemical Society* **162**, A573–A584 (2015).

[145] D. G. Kwabi, M. Tułodziecki, N. Pour, D. M. Itkis, C. V. Thompson and Y. Shao-Horn. Controlling Solution-Mediated Reaction Mechanisms

of Oxygen Reduction Using Potential and Solvent for Aprotic Lithium-Oxygen Batteries. *The Journal of Physical Chemistry Letters* **7**, 1204–1212 (2016).

[146] D. Aurbach, B. D. McCloskey, L. F. Nazar and P. G. Bruce. Advances in understanding mechanisms underpinning lithium–air batteries. *Nature Energy* **1**, 16128 (2016).

[147] K. G. Gallagher, S. Goebel, T. Greszler, M. Mathias, W. Oelerich, D. Eroglu and V. Srinivasan. Quantifying the promise of lithium–air batteries for electric vehicles. *Energy & Environmental Science* **7**, 1555 (2014).

[148] J. Lu, L. Li, J.-B. Park, Y.-K. Sun, F. Wu and K. Amine. Aprotic and Aqueous Li-O2 Batteries. *Chemical Reviews* **114**, 5611–5640 (2014).

[149] P. Andrei, J. P. Zheng, M. Hendrickson and E. J. Plichta. Modeling of Li-Air Batteries with Dual Electrolyte. *Journal of The Electrochemical Society* **159**, A770 (2012).

[150] S. Sandhu, J. Fellner and G. Brutchen. Diffusion-limited model for a lithium/air battery with an organic electrolyte. *Journal of Power Sources* **164**, 365 (2007).

[151] R. Williford and J.-G. Zhang. Air electrode design for sustained high power operation of Li/air batteries. *Journal of Power Sources* **194**, 1164 (2009).

[152] J. Yuan, J.-S. Yu and B. Sundén. Review on mechanisms and continuum models of multi-phase transport phenomena in porous structures of non-aqueous Li-Air batteries. *Journal of Power Sources* **278**, 352–369 (2015).

[153] M. Safari, B. D. Adams and L. F. Nazar. Kinetics of oxygen reduction in aprotic Li-O2 cells: A model-based study. *Journal of Physical Chemistry Letters* **5**, 3486–3491 (2014).

[154] K.-H. Xue, T.-K. Nguyen and A. A. Franco. Impact of the Cathode Microstructure on the Discharge Performance of Lithium Air Batteries: A Multiscale Model. *Journal of the Electrochemical Society* **161**, E3028–E3035 (2014).

[155] K.-H. Xue, E. McTurk, L. Johnson, P. G. Bruce and A. A. Franco. A Comprehensive Model for Non-Aqueous Lithium Air Batteries Involving Different Reaction Mechanisms. *Journal of the Electrochemical Society* **162**, A614–A621 (2015).

[156] M. D. Radin, C. W. Monroe and D. J. Siegel. Impact of Space-Charge Layers on Sudden Death in Li/O2 Batteries. *The Journal of Physical Chemistry Letters* **6**, 3017–3022 (2015).

[157] A. Rinaldi, O. Wijaya and H. E. Hoster. Lithium-Oxygen Cells : An Analytical Model to Explain the Key Features in the Discharge Voltage Profiles. *ChemElectroChem* **3**, 1–8 (2016).

[158] D. Grübl, B. Bergner, D. Schröder, J. Janek and W. G. Bessler. Multi-step Reaction Mechanisms in Nonaqueous Lithium-Oxygen Batteries with Redox Mediator: A Model-Based Study. *The Journal of Physical Chemistry C* **120**, 24623–24636 (2016).

[159] C. W. Monroe. Does Oxygen Transport Affect the Cell Voltages of Metal/Air Batteries? *Journal of The Electrochemical Society* **164**, E3547–E3551 (2017).

[160] S. J. Visco, B. Katz, Y. Nimon and L. De Jonghe. Protected active metal electrode and battery cell structures with non-aqueous interlayer architecture. *U.S. Patent Number* 7,282,295 (2007).

[161] T. Zhang, N. Imanishi, S. Hasegawa, A. Hirano, J. Xie, Y. Takeda, O. Yamamoto and N. Sammes. Water-Stable Lithium Anode with the Three-Layer Construction for Aqueous Lithium–Air Secondary Batteries. *Electrochemical and Solid-State Letters* **12**, A132 (2009).

[162] Y. Shimonishi, T. Zhang, N. Imanishi, D. Im, D. J. Lee, A. Hirano, Y. Takeda, O. Yamamoto and N. Sammes. A study on lithium/air secondary batteries - Stability of the NASICON-type lithium ion conducting solid electrolyte in alkaline aqueous solutions. *Journal of Power Sources* **196**, 5128–5132 (2011).

[163] L. Puech, C. Cantau, P. Vinatier, G. Toussaint and P. Stevens. Elaboration and characterization of a free standing LiSICON membrane for aqueous lithium-air battery. *Journal of Power Sources* **214**, 330–336 (2012).

[164] H. He, W. Niu, N. M. Asl, J. Salim, R. Chen and Y. Kim. Effects of aqueous electrolytes on the voltage behaviors of rechargeable Li-air batteries. *Electrochimica Acta* **67**, 87–94 (2012).

[165] T. Zhang, N. Imanishi, Y. Shimonishi, A. Hirano, Y. Takeda, O. Yamamoto and N. Sammes. A novel high energy density rechargeable lithium/air battery. *Chemical Communications* **46**, 1661–1663 (2010).

[166] T. Zhang, N. Imanishi, Y. Takeda and O. Yamamoto. Aqueous Lithium/Air Rechargeable Batteries. *Chemistry Letters* **40**, 668–673 (2011).

[167] D. Grübl and W. G. Bessler. Cell design concepts for aqueous lithium-oxygen batteries: A model-based assessment. *Journal of Power Sources* **297**, 481–491 (2015).

[168] J. P. Zheng, P. Andrei, M. Hendrickson and E. J. Plichta. The Theoretical Energy Densities of Dual-Electrolytes Rechargeable Li-Air and Li-Air Flow Batteries. *Journal of The Electrochemical Society* **158**, A43 (2011).

[169] F. Bidault, D. Brett, P. Middleton and N. Brandon. Review of gas diffusion cathodes for alkaline fuel cells. *Journal of Power Sources* **187**, 39 (2009).

[170] E. C. Kumbur, K. V. Sharp and M. M. Mench. Validated Leverett Approach for Multiphase Flow in PEFC Diffusion Media. *Journal of The Electrochemical Society* **154**, B1315 (2007).

[171] J. Nyvlt, O. Söhnel, M. Matuchova and M. Broul. *The Kinetics of Industrial Crytsallization* (ACADEMIA, Prague, 1985).

[172] O. Söhnel and J. Garside. *Precipitation : Basic Principles and Industrial Applications* (Butterworth-Heinemann, Oxford, 1992).

[173] J. W. Mullin. *Crystallization* (Butterworth-Heinemann, Oxford, 2001), 4 edn.

[174] D. Kashchiev and G. M. van Rosmalen. Review: Nucleation in solutions revisited. *Crystal Research and Technology* **38**, 555 (2003).

[175] M. Xu, D. Ivey, Z. Xie and W. Qu. Rechargeable Zn-air batteries: Progress in electrolyte development and cell configuration advancement. *Journal of Power Sources* **283**, 358–371 (2015).

[176] K. Harting, U. Kunz and T. Turek. Zinc-air Batteries: Prospects and Challenges for Future Improvement. *Zeitschrift für Physikalische Chemie* **226**, 151–166 (2012).

[177] Y. Li, M. Gong, Y. Liang, J. Feng, J. E. Kim, H. Wang, G. Hong, B. Zhang and H. Dai. Advanced zinc-air batteries based on high-performance hybrid electrocatalysts. *Nature Communications* **4**, 1–7 (2013).

[178] V. Neburchilov, H. Wang, J. J. Martin and W. Qu. A review on air cathodes for zinc-air fuel cells. *Journal of Power Sources* **195**, 1271–1291 (2010).

[179] D. A. Cogswell. Quantitative phase-field modeling of dendritic electrodeposition. *Physical Review E* **92**, 011301 (2015).

[180] T. Arlt, D. Schröder, U. Krewer and I. Manke. In operando monitoring of the state of charge and species distribution in zinc air batteries using X-ray tomography and model-based simulations. *Phys. Chem. Chem. Phys.* **16**, 22273–22280 (2014).

[181] M. Chamoun, B. J. Hertzberg, T. Gupta, D. Davies, S. Bhadra, B. Van Tassell, C. Erdonmez and D. a. Steingart. Hyper-dendritic nanoporous zinc foam anodes. *NPG Asia Materials* **7**, e178 (2015).

[182] J. F. Parker, C. N. Chervin, E. S. Nelson, D. R. Rolison and J. W. Long. Wiring zinc in three dimensions re-writes battery performance—dendrite-free cycling. *Energy & Environmental Science* **7**, 1117–1124 (2014).

[183] D. Schröder and U. Krewer. Model based quantification of air-composition impact on secondary zinc air batteries. *Electrochimica Acta* **117**, 541–553 (2014).

[184] W. G. Sunu and D. N. Bennion. Transient and Failure Analyses of the Porous Zinc Electrode. *Journal of The Electrochemical Society* **127**, 2007–2016 (1980).

[185] M. J. Isaacson, F. R. McLarnon and E. J. Cairns. Current density and ZnO precipitation-dissolution distributions in Zn-ZnO porous electrodes and their effect on material redistribution. A two-dimensional mathematical model. *Journal of the Electrochemical Society* **137**, 2014–2021 (1990).

[186] Z. Mao and R. E. White. Mathematical modeling of a primary zinc/air battery. *Journal of the Electrochemical Society* **139**, 1105–1114 (1992).

[187] E. Deiss, F. Holzer and O. Haas. Modeling of an electrically rechargeable alkaline Zn-air battery. *Electrochimica Acta* **47**, 3995–4010 (2002).

[188] T. P. Dirkse, C. Postmus and R. Vandenbosch. A Study of Alkaline Solutions of Zinc Oxide. *Journal of the American Chemical Society* **76**, 6022–6024 (1954).

[189] Q. C. Horn and Y. Shao-Horn. Morphology and Spatial Distribution of ZnO Formed in Discharged Alkaline Zn/MnO2 AA Cells. *Journal of The Electrochemical Society* **150**, A652–A658 (2003).

[190] A. H. G. Cents. *Mass Transfer and Hydrodynamics in Stirred Gas-Liquid-Liquid Contactors*. Ph.D. thesis, Universiteit Twente (2003). URL http://doc.utwente.nl/41072/.

[191] A. H. G. Cents, D. W. F. Brilman and G. F. Versteeg. CO2 absorption in carbonate/bicarbonate solutions: The Danckwerts-criterion revisited. *Chemical Engineering Science* **60**, 5830–5835 (2005).

[192] P. V. Danckwerts. Absorption by simultaneous diffusion and chemical reaction. *Trans. Faraday Soc.* **46**, 300–304 (1950).

[193] J. Jindra, J. Mrha and M. Musilová. Zinc-air cell with neutral electrolyte. *Journal of Applied Electrochemistry* **3**, 297–301 (1973).

[194] K. Kinoshita. *Electrochemical Oxygen Technology, Electrochemical Society Series* (John Wiley & Sons, 1992).

[195] J. Suntivich, H. A. Gasteiger, N. Yabuuchi, H. Nakanishi, J. B. Goodenough and Y. Shao-Horn. Design principles for oxygen-reduction activity on perovskite oxide catalysts for fuel cells and metal-air batteries. *Nature Chemistry* **3**, 546–550 (2011).

[196] N. M. Markovic, R. Adzic, B. Cahan and E. Yeager. Structural effects in electrocatalysis: oxygen reduction on platinum low index single-crystal surfaces in perchloric acid solutions. *Journal of Electroanalytical Chemistry* **377**, 249–259 (1994).

[197] N. Markovic, H. A. Gasteiger and P. N. Ross. Oxygen reduction on platinum low-index single-crystal surfaces in sulfuric acid solution: rotating ring-Pt(hkl) disk studies. *The Journal of Physical Chemistry* **99**, 3411 (1995).

[198] T. Jacob, R. P. Muller and W. A. Goddard. Chemisorption of Atomic Oxygen on Pt(111) from DFT Studies of Pt-Clusters. *The Journal of Physical Chemistry B* **107**, 9465 (2003).

[199] T. Jacob. The Mechanism of Forming H2O from H2 and O2 over a Pt Catalyst via Direct Oxygen Reduction. *Fuel Cells* **6**, 159 (2006).

[200] V. Stamenkovic, B. S. Mun, K. J. J. Mayrhofer, P. N. Ross, N. M. Markovic, J. Rossmeisl, J. Greeley and J. K. Nørskov. Changing the activity of electrocatalysts for oxygen reduction by tuning the surface electronic structure. *Angewandte Chemie (International ed. in English)* **45**, 2897 (2006).

[201] J. Rossmeisl, V. Tripkovic, G. a. Tritsaris and F. Calle-Vallejo. Electro-Catalysis of Oxygen Reduction Reaction. *ECS Transactions* **33**, 43–50 (2010).

[202] D. C. Ford, A. U. Nilekar, Y. Xu and M. Mavrikakis. Partial and complete reduction of O2 by hydrogen on transition metal surfaces. *Surface Science* **604**, 1565–1575 (2010).

[203] Y. Sha, T. H. Yu, B. V. Merinov and W. A. Goddard. Prediction of the Dependence of the Fuel Cell Oxygen Reduction Reactions on Operating Voltage from DFT Calculations. *The Journal of Physical Chemistry C* **116**, 6166–6173 (2012).

[204] V. Tripkovic, H. A. Hansen, J. Rossmeisl and T. Vegge. First principles investigation of the activity of thin film Pt, Pd and Au surface alloys for oxygen reduction. *Physical Chemistry Chemical Physics* **17**, 11647–11657 (2015).

[205] V. Tripkovic and T. Vegge. Potential- and Rate-Determining Step for Oxygen Reduction on Pt(111). *The Journal of Physical Chemistry C* **121**, 26785–26793 (2017).

[206] H. A. Hansen, V. Viswanathan and J. K. Norskov. Unifying Kinetic and Thermodynamic Analysis of 2e-and 4e-Reduction of Oxygen on Metal Surfaces. *The Journal of Physical Chemistry C* **118**, 6706–6718 (2014).

[207] J. Wang, F. Uribe, T. Springer, J. Zhang and R. Adzic. Intrinsic kinetic equation for oxygen reduction reaction in acidic media: the double Tafel slope and fuel cell applications. *Faraday Discussions* **140**, 347–662 (2008).

[208] B. Temel, H. Meskine, K. Reuter, M. Scheffler and H. Metiu. Does phenomenological kinetics provide an adequate description of heterogeneous catalytic reactions? *The Journal of Chemical Physics* **126**, 204711 (2007).

[209] R. Jinnouchi, K. Kodama, T. Hatanaka and Y. Morimoto. First principles based mean field model for oxygen reduction reaction. *Physical Chemistry Chemical Physics* **13**, 21070–21083 (2011).

[210] J. Carrasco, A. Hodgson and A. Michaelides. A molecular perspective of water at metal interfaces. *Nature Materials* **11**, 667–674 (2012).

[211] J. X. Wang, N. M. Markovic and R. R. Adzic. Kinetic Analysis of Oxygen Reduction on Pt(111) in Acid Solutions: Intrinsic Kinetic Parameters and Anion Adsorption Effects. *The Journal of Physical Chemistry B* **108**, 4127–4133 (2004).

[212] S. Zecevic and J. Wainright. Kinetics of O2 reduction on a Pt electrode covered with a thin film of solid polymer electrolyte. *Journal of The Electrochemical Society* **144**, 2973 (1997).

[213] R. R. Mitchell, B. M. Gallant, C. V. Thompson and Y. Shao-Horn. All-carbon-nanofiber electrodes for high-energy rechargeable Li–O2 batteries. *Energy & Environmental Science* **4**, 2952–2958 (2011).

[214] B. D. Adams, C. Radtke, R. Black, M. L. Trudeau, K. Zaghib and L. F. Nazar. Current density dependence of peroxide formation in the Li–O2 battery and its effect on charge. *Energy & Environmental Science* **6**, 1772–1778 (2013).

[215] G. K. Singh, G. Ceder and M. Z. Bazant. Intercalation dynamics in rechargeable battery materials: General theory and phase-

transformation waves in LiFePO4. *Electrochimica Acta* **53**, 7599–7613 (2008).

[216] P. Bai, D. A. Cogswell and M. Z. Bazant. Suppression of phase separation in LiFePO4 nanoparticles during battery discharge. *Nano Letters* **11**, 4890–4896 (2011).

[217] D. A. Cogswell and M. Z. Bazant. Coherency strain and the kinetics of phase separation in LiFePO4 nanoparticles. *ACS Nano* **6**, 2215–2225 (2012).

[218] T. R. Ferguson and M. Z. Bazant. Nonequilibrium Thermodynamics of Porous Electrodes. *Journal of The Electrochemical Society* **159**, A1967–A1985 (2012).

[219] W. K. Burton, N. Cabrera and F. C. Frank. The Growth of Crystals and the Equilibrium Structure of their Surfaces. *Philosophical Transactions of the Royal Society of London. Series A, Mathematical and Physical Sciences* **243**, 299–358 (1951).

[220] D. Margetis, M. Aziz and H. Stone. Continuum approach to self-similarity and scaling in morphological relaxation of a crystal with a facet. *Physical Review B* **71**, 165432 (2005).

[221] R. R. Mitchell, B. M. Gallant, Y. Shao-Horn and C. V. Thompson. Mechanisms of Morphological Evolution of Li2O2 Particles during Electrochemical Growth. *The Journal of Physical Chemistry Letters* **4**, 1060–1064 (2013).

[222] A. Varzi, R. Raccichini, S. Passerini and B. Scrosati. Challenges and prospects of the role of solid electrolytes in the revitalization of lithium metal batteries. *Journal of Materials Chemistry A* **4**, 17251–17259 (2016).

[223] M. Galiński, A. Lewandowski and I. Stkepniak. Ionic liquids as electrolytes. *Electrochimica Acta* **51**, 5567–5580 (2006).

[224] F. Endres. Ionic liquids: Solvents for the electrodeposition of metals and semiconductors. *ChemPhysChem* **3**, 144–154 (2002).

[225] G. Pulletikurthi, A. Lahiri, T. Carstens, N. Borisenko, S. Zein El Abedin and F. Endres. Electrodeposition of silicon from three different ionic liquids: possible influence of the anion on the deposition process. *Journal of Solid State Electrochemistry* **17**, 2823–2832 (2013).

[226] S. Zein El Abedin, E. M. Moustafa, R. Hempelmann, H. Natter and F. Endres. Electrodeposition of Nano- and Microcrystalline Aluminium in Three Different Air and Water Stable Ionic Liquids. *ChemPhysChem* **7**, 1535–1543 (2006).

[227] Z. Liu, G. Pulletikurthi and F. Endres. A Prussian Blue/Zinc Secondary Battery with a Bio-Ionic Liquid-Water Mixture as Electrolyte. *ACS Applied Materials and Interfaces* **8**, 12158–12164 (2016).

[228] M. A. Gebbie, M. Valtiner, X. Banquy, E. T. Fox, W. A. Henderson and J. N. Israelachvili. Ionic liquids behave as dilute electrolyte solutions. *Proceedings of the National Academy of Sciences* **110**, 9674–9679 (2013).

[229] R. Atkin and G. G. Warr. Structure in confined room-temperature ionic liquids. *The Journal of Physical Chemistry C* **111**, 5162–5168 (2007).

[230] F. Endres, N. Borisenko, S. Z. El Abedin, R. Hayes and R. Atkin. The interface ionic liquid(s)/electrode(s): In situSTM and AFM measurements. *Faraday Discussions* **154**, 221–233 (2012).

[231] R. Hayes, G. G. Warr and R. Atkin. Structure and Nanostructure in Ionic Liquids. *Chemical Reviews* **115**, 6357–6426 (2015).

[232] D. Henderson and J. Wu. Electrochemical properties of the double layer of an ionic liquid using a dimer model electrolyte and density functional theory. *The Journal of Physical Chemistry B* **116**, 2520–2525 (2012).

[233] J. Jiang, D. Cao, D.-E. Jiang and J. Wu. Time-dependent density functional theory for ion diffusion in electrochemical systems. *Journal of Physics: Condensed Matter* **26**, 284102 (2014).

[234] M. H. Ghatee and Y. Ansari. Ab initio molecular dynamics simulation of ionic liquids. *The Journal of Chemical Physics* **126**, 154502 (2007).

[235] J. M. Black, M. Zhu, P. Zhang, R. R. Unocic, D. Guo, M. B. Okatan, S. Dai, P. T. Cummings, S. V. Kalinin, G. Feng and N. Balke. Fundamental aspects of electric double layer force-distance measurements at liquid-solid interfaces using atomic force microscopy. *Scientific Reports* **6**, 32389 (2016).

[236] Z. A. H. Goodwin, G. Feng and A. A. Kornyshev. Mean-Field Theory of Electrical Double Layer In Ionic Liquids with Account of Short-Range Correlations. *Electrochimica Acta* **225**, 190–197 (2017).

[237] N. Gavish, D. Elad and A. Yochelis. From solvent-free to dilute electrolytes: Essential components for a continuum theory. *Journal of Physical Chemistry Letters* **9**, 36–42 (2018).

[238] Z. A. Goodwin and A. A. Kornyshev. Underscreening, overscreening and double-layer capacitance. *Electrochemistry Communications* **82**, 129–133 (2017).

[239] A. Wang, S. Kadam, H. Li, S. Shi and Y. Qi. Review on modeling of the anode solid electrolyte interphase (SEI) for lithium-ion batteries. *npj Computational Materials* **4**, 15 (2018).

[240] P. Verma, P. Maire and P. Novák. A review of the features and analyses of the solid electrolyte interphase in Li-ion batteries. *Electrochimica Acta* **55**, 6332–6341 (2010).

[241] S. H. Kang, D. P. Abraham, A. Xiao and B. L. Lucht. Investigating the solid electrolyte interphase using binder-free graphite electrodes. *Journal of Power Sources* **175**, 526–532 (2008).

[242] A. Xiao, L. Yang, B. L. Lucht, S.-H. Kang and D. P. Abraham. Examining the Solid Electrolyte Interphase on Binder-Free Graphite Electrodes. *Journal of The Electrochemical Society* **156**, A318 (2009).

[243] M. Nie, D. P. Abraham, Y. Chen, A. Bose and B. L. Lucht. Silicon solid electrolyte interphase (SEI) of lithium ion battery characterized by microscopy and spectroscopy. *The Journal of Physical Chemistry C* **117**, 13403–13412 (2013).

[244] M. Steinhauer, M. Stich, M. Kurniawan, B.-K. Seidlhofer, M. Trapp, A. Bund, N. Wagner and K. A. Friedrich. In Situ Studies of Solid Electrolyte Interphase (SEI) Formation on Crystalline Carbon Surfaces by

Neutron Reflectometry and Atomic Force Microscopy. *ACS Applied Materials & Interfaces* **9**, 35794–35801 (2017).

[245] K. Ushirogata, K. Sodeyama, Z. Futera, Y. Tateyama and Y. Okuno. Near-Shore Aggregation Mechanism of Electrolyte Decomposition Products to Explain Solid Electrolyte Interphase Formation. *Journal of The Electrochemical Society* **162**, A2670–A2678 (2015).

[246] S. Shi, P. Lu, Z. Liu, Y. Qi, L. G. Hector, H. Li and S. J. Harris. Direct calculation of Li-ion transport in the solid electrolyte interphase. *Journal of the American Chemical Society* **134**, 15476–87 (2012).

[247] F. A. Soto, Y. Ma, J. M. Martinez De La Hoz, J. M. Seminario and P. B. Balbuena. Formation and Growth Mechanisms of Solid-Electrolyte Interphase Layers in Rechargeable Batteries. *Chemistry of Materials* **27**, 7990–8000 (2015).

[248] O. Borodin, G. R. V. Zhuang, P. N. Ross and K. Xu. Molecular Dynamics Simulations and Experimental Study of Lithium Ion Transport in Dilithium Ethylene Dicarbonate. *The Journal of Physical Chemistry C* **117**, 7433–7444 (2013).

[249] H. J. Ploehn, P. Ramadass and R. E. White. Solvent Diffusion Model for Aging of Lithium-Ion Battery Cells. *Journal of The Electrochemical Society* **151**, A456 (2004).

[250] M. Tang, S. Lu and J. Newman. Experimental and Theoretical Investigation of Solid-Electrolyte-Interphase Formation Mechanisms on Glassy Carbon. *Journal of the Electrochemical Society* **159**, A1775–A1785 (2012).

[251] D. Li, D. Danilov, Z. Zhang, H. Chen, Y. Yang and P. H. L. Notten. Modeling the SEI-Formation on Graphite Electrodes in LiFePO4 Batteries. *Journal of the Electrochemical Society* **162**, A858–A869 (2015).

[252] M. Broussely, S. Herreyre, P. Biensan, P. Kasztejna, K. Nechev and R. Staniewicz. Aging mechanism in Li ion cells and calendar life predictions. *Journal of Power Sources* **97-98**, 13–21 (2001).

[253] F. Röder, R. D. Braatz and U. Krewer. Multi-Scale Modeling of Solid Electrolyte Interface Formation in Lithium-Ion Batteries. *26th European*

Symposium on Computer Aided Process Engineering **38**, 157–162 (2016).

[254] F. Röder, R. D. Braatz and U. Krewer. Multi-Scale Simulation of Heterogeneous Surface Film Growth Mechanisms in Lithium-Ion Batteries. *Journal of The Electrochemical Society* **164**, E3335–E3344 (2017).

[255] A. M. Colclasure, K. A. Smith and R. J. Kee. Modeling detailed chemistry and transport for solid-electrolyte-interface (SEI) films in Li-ion batteries. *Electrochimica Acta* **58**, 33–43 (2011).

[256] F. Hao, Z. Liu, P. B. Balbuena and P. P. Mukherjee. Mesoscale Elucidation of Solid Electrolyte Interphase Layer Formation in Li-Ion Battery Anode. *The Journal of Physical Chemistry C* **121**, 26233–26240 (2017).

[257] P. Liu, J. Wang, J. Hicks-Garner, E. Sherman, S. Soukiazian, M. Verbrugge, H. Tataria, J. Musser and P. Finamore. Aging Mechanisms of LiFePO[sub 4] Batteries Deduced by Electrochemical and Structural Analyses. *Journal of The Electrochemical Society* **157**, A499–A507 (2010).

Appendix A

Curriculum Vitae

From 2001 to 2007, I studied physics at the Friedrich-Schiller University of Jena and mathematics at the University of Cambridge, United Kingdom. Subsequently, I performed research on quantum simulations of out-of-equilibrium phenomena at the Max-Planck-Institute for Quantum Optics in Garching near Munich under the supervision of Prof. J. Ignacio Cirac. In 2011, I received my Ph.D. in physics from the Technical University of Munich.

Since 2011, I am working at the German Aerospace Center and the Helmholtz-Institute Ulm under the supervision of Prof. Wolfgang Bessler and Prof. Arnulf Latz. Here I develop theory-based models for the dynamics of lithium ion and metal-air batteries. My electrochemical theories are derived from non-equilibrium thermodynamics and applied to understand processes from mesoscopic (2 nm) to macroscopic length scales (1 mm).

In 2013, I visited the group of Prof. Martin Bazant at the Massachusetts Institute of Technology, Cambridge, MA, USA, and simulated crystallization morphologies inside lithium-oxygen batteries [8]. In 2016, Prof. Tejs Vegge hosted my visit at the Danish Technical University in Lyngby near Copenhagen, where I developed a novel approach to understand the dynamics of speciation and pH variations in aqueous electrolytes [5].

The curriculum vitae has been removed for privacy reasons.

The curriculum vitae has been removed for privacy reasons.

The curriculum vitae has been removed for privacy reasons.

The curriculum vitae has been removed for privacy reasons.

The curriculum vitae has been removed for privacy reasons.

The curriculum vitae has been removed for privacy reasons.

The curriculum vitae has been removed for privacy reasons.

The curriculum vitae has been removed for privacy reasons.

The curriculum vitae has been removed for privacy reasons.

The curriculum vitae has been removed for privacy reasons.

The curriculum vitae has been removed for privacy reasons.

The curriculum vitae has been removed for privacy reasons.

Appendix B

Publications on electrochemical cells

- J. P. Neidhardt, D. N. Fronczek, T. Jahnke, T. Danner, B. Horstmann and W. G. Bessler. A Flexible Framework for Modeling Multiple Solid, Liquid and Gaseous Phases in Batteries and Fuel Cells. *Journal of The Electrochemical Society* **159**, A1528–A1542 (2012).
- B. Horstmann, T. Danner and W. G. Bessler. Precipitation in aqueous lithium–oxygen batteries: a model-based analysis. *Energy & Environmental Science* **6**, 1299 (2013).
- T. Danner, B. Horstmann, D. Wittmaier, N. Wagner and W. G. Bessler. Reaction and transport in Ag/Ag2O gas diffusion electrodes of aqueous Li-O2 batteries: Experiments and modeling. *Journal of Power Sources* **264**, 320–332 (2014).
- J. Stamm, A. Varzi, A. Latz and B. Horstmann. Modeling nucleation and growth of zinc oxide during discharge of primary zinc-air batteries. *Journal of Power Sources* **360**, 136–149 (2017).
- S. Clark, A. Latz and B. Horstmann. Rational Development of Neutral Aqueous Electrolytes for Zinc-Air Batteries. *ChemSusChem* **10**, 4735–4747 (2017).
- S. Clark, A. Latz and B. Horstmann. A Review of Model-Based Design Tools for Metal-Air Batteries. *Batteries* **4**, 5 (2018).

J. P. Neidhardt, D. N. Fronczek, T. Jahnke, T. Danner, B. Horstmann and W. G. Bessler. A Flexible Framework for Modeling Multiple Solid, Liquid and Gaseous Phases in Batteries and Fuel Cells. *Journal of The Electrochemical Society* **159**, A1528–A1542 (2012).

Journal of The Electrochemical Society, **159** (9) A1528-A1542 (2012)
0013-4651/2012/159(9)/A1528/15/$28.00 © The Electrochemical Society

A Flexible Framework for Modeling Multiple Solid, Liquid and Gaseous Phases in Batteries and Fuel Cells

Jonathan P. Neidhardt,[a,b,*] David N. Fronczek,[a,c] Thomas Jahnke,[a] Timo Danner,[a,b] Birger Horstmann,[a,b] and Wolfgang G. Bessler[a,b,c,,d,z]**

[a] *German Aerospace Center (DLR), Institute of Technical Thermodynamics, 70569 Stuttgart, Germany*
[b] *Institute of Thermodynamics and Thermal Engineering (ITW), Stuttgart University, 70569 Stuttgart, Germany*
[c] *Helmholtz-Institute Ulm for Electrochemical Energy Storage (HIU), 89081 Ulm, Germany*

Multi-phase management is crucial for performance and durability of electrochemical cells such as batteries and fuel cells. In this paper we present a generic framework for describing the two-dimensional spatiotemporal evolution of gaseous, liquid and solid phases, as well as their interdependence with interfacial (electro-)chemistry and microstructure in a continuum description. The modeling domain consists of up to seven layers (current collectors, channels, electrodes, separator/membrane), each of which can consist of an arbitrary number of bulk phases (gas, liquid, solid) and connecting interfaces (two-phase or multi-phase boundaries). Bulk and interfacial chemistry is described using global or elementary kinetic reactions. Multi-phase management is coupled to chemistry and to mass and charge transport within bulk phases. The functionality and flexibility of this framework is demonstrated using four application areas in the context of post-lithium-ion batteries and fuel cells, that is, lithium-sulfur (Li-S) cells, lithium-oxygen (Li-O) cells, solid oxide fuel cells (SOFC) and polymer electrolyte membrane fuel cells (PEFC). The results are compared to models available in literature and properties of the generic framework are discussed.
 [DOI: 10.1149/2.023209jes]

Manuscript submitted March 23, 2012; revised manuscript received June 15, 2012. Published August 14, 2012.

Electrochemical cells for energy storage and conversion, such as batteries and fuel cells, are characterized by the presence of multiple solid, liquid and/or gaseous phases. These phases are essential for cell functionality. Therefore, understanding and optimization of multi-phase management is among the key factors to onward development of electrochemical energy technology:

(1) Bulk solid and gaseous phases store the chemical energy (e.g., H_2 and O_2 in fuel cells; lithium and lithium compounds in batteries).[1,2]
(2) Bulk solid and liquid phases provide electronic and ionic conduction pathways.[3]
(3) Secondary solid phases play a key role in cell durability and cyclability, for example, secondary phase formation in solid oxide fuel cells (SOFC)[4,5] or complex phase formation-dissolution cycles in lithium-sulfur (Li-S)[6] or lithium-oxygen (Li-O) batteries.[7]
(4) Management of the liquid water phase is a crucial issue regarding the performance of polymer electrolyte membrane fuel cells (PEFC).[8]
(5) Electrochemical reactions take place at the boundaries between bulk phases, giving rise to the concepts of two-phase and three-phase boundaries. Spatial or temporal variation of bulk phase volume fractions affects local microstructure and, therefore, electrochemical reactivity.

In this article we present a generic framework for modeling the properties and interconversion of multiple solid, liquid and/or gaseous phases in fuel cells and batteries. High flexibility is achieved through the following approach. The computational domain consists of up to seven layers (electrodes, separator, channels, current collectors). Each layer can have an arbitrary number of bulk phases (gaseous, liquid, solid). Each bulk phase can consist of an arbitrary number of chemical species. Each layer can also host an arbitrary number of phase boundaries. Each phase boundary can host an arbitrary number of surface-adsorbed species. Each phase boundary also accommodates arbitrary (electro)chemical reactions between bulk or surface species. Within a single modeling tool, this framework allows for the description of many different applications. In this article, examples will be presented from the context of Li-S-batteries, Li-O batteries, SOFCs, and PEFCs. In the case of Li-S and Li-O batteries, results will be compared to models available in literature; in the case of SOFCs and PEFCs, original results will be presented.

The body of fuel cell and battery modeling literature is vast (cf. background section below). Model development has been followed along relatively independent lines for SOFCs, PEFCs, and lithium-ion batteries (LIB). The present approach combines those lines into one single tool. This has several advantages: (1) Flexibility in modeling: The framework can host various existing as well as future electrochemical cells with little or no need for additional model development – the main emphasis can be put on parameterization. (2) Flexibility in simulation: Multiple scientists work on one single computational tool, thereby considerably reducing development time. (3) Minimization of modeling and simulation errors: Model extensions can rely on a base of established and validated sub-models; the simulation methodology is established and free from computing errors. (4) Multi-phase detailed-chemistry functionality: We are not aware of commercial modeling tools that allow the treatment of multi-phase management or elementary kinetic electrochemistry. (5) Increased knowledge transfer between different fields, for example, new cells as combination of existing half-cells (fuel cell and Li-O), precipitation (Li-S and aqueous Li-O), gas diffusion electrodes (PEFC and Li-O).

After giving a detailed assessment of background literature, this article presents the modeling and simulation framework. Central parts are the multi-phase management and the approach for handling phase formation and phase transitions as special case of bulk reactions. In the following, background on four different applications and simulation results for these cases will be shown and discussed: (1) Discharge of a Li-S battery, where complex phase formation-dissolution can be reproduced; (2) discharge of a Li-O battery, where four individual phases contribute to the cathode reaction; (3) formation of nickel oxide in the anode of an SOFC; and (4) liquid water formation and pore flooding in PEFCs. Finally, the methodology will be discussed and the results summarized.

Background and motivation

Mathematical modeling and numerical simulation is becoming increasingly important for both understanding the complex processes taking place in electrochemical cells, as well as supporting the optimization of cell and system design. Modeling and simulation are being carried out on all spatial scales – from the atom to the system. This article and the following literature overview focuses on the continuum scale of the basic cell repeat unit, consisting of the two electrodes, the electrolyte/separator, and the two current collectors; this is the

*Electrochemical Society Student Member.
**Electrochemical Society Active Member.
[d] Present address: Offenburg University of Applied Sciences, Badstrasse 24, 77652 Offenburg, Germany.
[z] E-mail: wolfgang.bessler@hs-offenburg.de

smallest possible fully functional electrochemical cell. In technical applications, the thickness of the repeat unit varies approximately between 100 μm (lithium batteries) and 5 mm (fuel cells).

A large body of modeling literature is available for this scale. LIB models have been pioneered by Newman and co-workers as early as in the 1970s[9,10] and are being widely used today.[11–14] Modeled battery chemistries include mostly intercalation systems (e.g., LiC_6, $LiCoO_2$), but also phase-change materials such as $LiFePO_4$. Several review articles are available.[15–18] Only few studies are available for multi-phase systems such as Li-S[19] and Li-O.[20,7,21] These studies serve as basis for assessing the functionality of the present framework.

SOFC models show their own development line. They were initially presented in the 1990s by a number of groups[22–26] and are being widely used today.[27,28] Several review articles are available.[29–34] Models focusing on multi-phase behavior such as secondary-phase formation are scarce.[35]

PEFC models have also been developed since the 1990s,[36–38] including their various types (low-temperature PEFC, direct methanol fuel cells (DMFC), high-temperature PEFC). Different than in LIB and SOFC, the modeling of bulk phase formation is today standard in the low-temperature PEFC and DMFC literature, namely, the formation and transport of liquid water. The approach is referred to as two-phase model (liquid and gas-phase water), sometimes also as three-phase model (referring to water dissolved in Nafion-type membranes). There are a number of reviews.[39–41] Moreover, the formation of ice as solid bulk phase has been modeled in the context of cold-start behavior.[42] In the latter case, the respective systems of PEFC cathodes ($2\ H^+ + \frac{1}{2}O_2 + 2\ e^- \rightarrow H_2O(s)$) and Li-O cathodes ($2\ Li^+ + O_2 + 4\ e^- \rightarrow Li_2O_2(s)$) show considerable similarity.

Based on this literature overview, our development of a generic modeling framework is motivated as follows:

- There are considerable similarities in the modeling methodology used in LIB, PEFC and SOFC. These similarities are exploited within a generic framework, leading to significant synergies and thus increased efficiency in model development.
- Knowledge transfer between different fields is enhanced, for example, by combining half cells (battery and fuel cell to Li-O) or using the same components (gas diffusion electrodes in PEFC and Li-O).
- As many model equations are similar in the various electrochemical cells, a generic framework offers a validated base functionality, strongly reducing modeling and simulation errors.
- In LIB and SOFC, only very few present models are capable of describing the evolution of bulk phases. The development of a generic framework opens up new directions in modeling these systems.
- Finally, a generic framework opens pathways for systems beyond those discussed in this article; this includes aqueous lithium-oxygen cells, redox flow cells, direct methanol fuel cells with CO_2 bubble formation, and other battery and fuel cell types.

A number of generic commercial codes are available and being used for modeling electrochemical cells. Those are usually based on built-in computational fluid dynamics (CFD) functionality, which can be coupled to additional mathematical models either via equation interpreters (e.g., COMSOL Multiphysics) or via coupling to user-defined C/Fortran code (e.g., ANSYS, STAR-CD). Due to their high-level CFD capability, those tools are particularly useful for 2D/3D transport on structurally complex computational domains. However, integrating multi-step electrochemical reaction mechanisms and multi-phase management can be tedious, as systems of rate equations need to be implemented manually. The present modeling framework provides a complementary functionality: While transport is modeled on structurally simple 1D+1D computational domains, complex electrochemistry (thermodynamics, multi-step kinetics with parallel and side reactions, mixed-potential formation) and phase management (solid, liquid, gaseous) functionality is provided based on simple text input files.

Modeling and simulation framework

Computational domain and definition of constituents.— The computational domain for the generic framework is shown in Fig. 1. It represents the basic repeat unit of a battery or a fuel cell. The model is based on the following assumptions and constituents:

(1) The computational domain consists of up to seven layers, as shown in Fig. 1. The base cell functionality requires at least three layers, representing anode, cathode and electrolyte/separator. Additional layers can be added for gas supply (gas channels), for example in Li-O batteries and fuel cells, and for current collection. The layers are characterized by their macroscopic geometry (thickness).

(2) Each layer consists of an arbitrary number of bulk phases. They can either be solid, liquid, or gaseous. The phases are characterized by their respective volume fraction ε and density ρ. For layers consisting of multiple phases, a continuum (homogenization) approach is applied.[27] For the systems studied here, the phases are shown schematically in Fig. 2.

(3) Each bulk phase consists of an arbitrary number of chemical species. This can be a single species making up a bulk phase (e.g., S_8 in bulk sulfur), or a mixture of species in the gas phase or a liquid solvent. The species are characterized by their concentrations c (or mole fractions X).

(4) Each layer can also contain an arbitrary number of phase boundaries. These can be two-phase boundaries (interfaces) or three-phases boundaries (edges). They are characterized in the continuum approach by their volume-specific area A^V and the volume-specific boundary length l^V, respectively. Area and length generally depend on the volume fraction of the adjacent bulk phases; this dependence describes the influence of microstructure on reactivity. Phase boundaries are illustrated in Fig. 2 for the systems studied here.

(5) Optionally, surface-adsorbed species can be defined at each interface. This allows to describe electrochemical reactions based

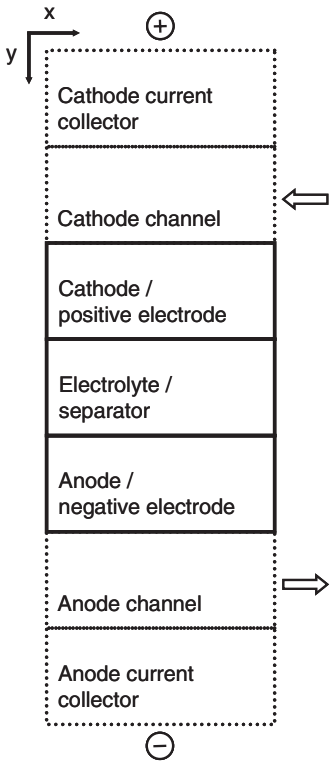

Figure 1. Fundamental repeat unit consisting of up to seven layers representing the modeling domain for batteries and fuel cells. Dotted lines represent optional components.

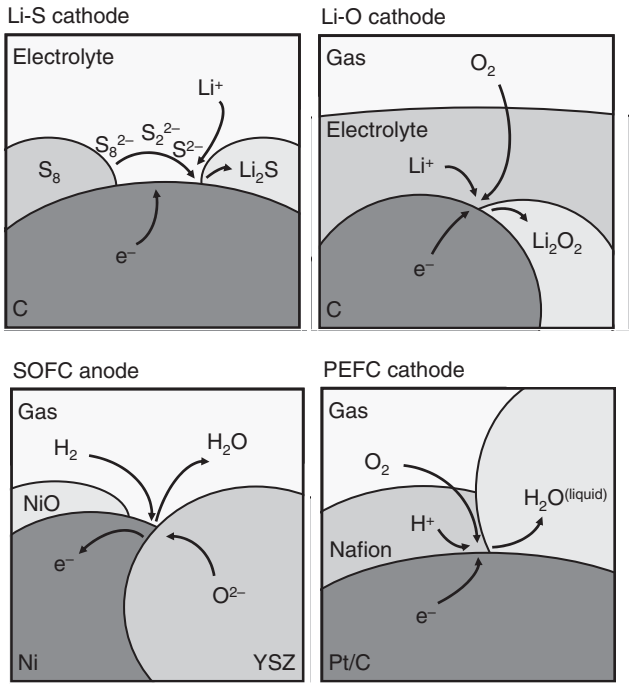

Figure 2. Illustration of multi-phase reactions taking place on the micro-scale during the operation of batteries (top) and fuel cells (bottom).

on elementary kinetics.[29] Surface adsorbates are characterized by their coverage θ.

(6) An arbitrary number of chemical reactions takes place at each phase boundary. Reactions may involve species from one or several adjacent bulk phases and/or surface-adsorbed species.

(7) Mass and charge transport occur within the modeling domain. We model different transport scale regimes in a multi-scale approach, which are separately solved in 1D and coupled through the exchange of boundary conditions: (1) Gas flow along fuel cell channels (x direction), (2) mass and charge transport through the porous composite electrodes and the solid or liquid electrolyte/separator (y direction), (3) surface transport towards three-phase boundaries in fuel cells[43] or bulk transport in active material particles (z direction).[44] This approach allows capturing all relevant physicochemical transport processes while keeping computational cost at a reasonable level. Each scale can be individually enabled, leading to either 1D, 1D+1D, or 1D+1D+1D computational domains.

(8) The model is assumed isothermal.

Within this generic framework, different applications differ only in number and type of constituents (layers, phases, boundaries, species, reactions) as well as their structural, chemical and transport properties. The flexibility described here is achieved via a generalized implementation of the computational domain and model equations (see Section on Simulation Methodology).

Governing transport equations.— Mass and charge transport take place within bulk phases (e.g., molecules in the gas phase, ions in liquid electrolytes, electrons in solid conductors). Depending on the layer and phase type, different transport mechanisms are possible. For clarity, the governing equations are summarized in Table I. The derivation of these equations has been described in detail earlier[45,27,43] and is therefore not included here, except liquid-electrolyte charge transport which will be described below. We model the following transport processes:

(1) Channels/gas-phase: Gas-phase convective and diffusive flow, described with a one-dimensional form of the Navier-Stokes equations (Table I, Eqs. (40)–(43)).

(2) Porous electrodes/gas-phase: Diffusive and convective flow, described by coupled diffusion (Stefan-Maxwell law using Bosanquet diffusion coefficients that account for ordinary and Knudsen diffusion) and pressure-driven flow (Darcy law) (Table I, Eqs. (44)–(46)).

(3) Porous electrodes/liquid-electrolyte phase: Diffusion and migration of ions, described under assumption of electroneutrality using concentrated or dilute solution theory (Table I, Eqs. (47)–(51)).

(4) Porous electrodes and separator/solid phase: Electronic and ionic charge transport, described by Ohm's law (Table I, Eqs. (52) and (53)).

(5) Cell current and voltage are derived from the electric potential distribution and the current due to electrochemical reactions and double layer charge/discharge (Table I, Eqs. (54)–(58)).

In the channels, mass transport is modeled in one dimension x in flow direction. In the electrodes, mass transport is modeled in one dimension y perpendicular to the membrane/separator. This yields an overall 1D+1D model. In the present framework, the model can be extended by surface transport perpendicular to the three-phase boundary[43] or by bulk-phase transport in active materials particles,[44] giving rise to overall 1D+1D+1D models (not used in the applications presented here).

Mass and charge transport in liquid electrolytes.— Transport in liquid electrolytes is commonly described using concentrated solution theory[17] or, alternatively, by diluted solution theory[46,44] which neglects interactions between dissolved species. Here, we cast these two theories into one consistent framework of equations.

Continuity of species i in a liquid electrolyte is given by the Nernst-Planck equation,[47]

$$\frac{\partial(\varepsilon c_i)}{\partial t} = -\mathrm{div}\left(-D_i^{\mathrm{eff}}\,\mathrm{grad}\,c_i - D_i^{\mathrm{migr,eff}}\,\mathrm{grad}\,\phi_{\mathrm{elyt}}\right) + \sum_m A_m^{\mathrm{V}}\dot{s}_{i,m} \quad [1]$$

where transport occurs via diffusion (gradient of concentration c_i) and migration (gradient of the electric potential in the electrolyte ϕ_{elyt}), and chemical source terms occur at all phase boundaries m. The effective transport coefficients D_i^{eff} and $D_i^{\mathrm{migr,eff}}$ account for the microstructure of the medium (see Sec. Mass and charge transport coefficients). We assume electroneutrality to determine the electric potential (cf. Table I, Eq. (49)).

$$0 = -\sum_i z_i F\,\mathrm{div}J_i + \sum_m z_i F\,A_m^{\mathrm{V}}\dot{s}_{i,m} \quad [2]$$

In dilute solutions, the migration coefficients D_i^{migr} are given as a function of the diffusion coefficients D_i according to

$$D_i^{\mathrm{migr}} = \frac{z_i F}{RT} c_i D_i. \quad [3]$$

The theory of concentrated solutions requires more parameters. Here we restrict ourselves to a binary salt ($z_+ = |z_-|$) with a single cation (Li^+) and a single anion (PF_6^-) without convection. Such binary solutions are commonly[17] described by the equations

$$\frac{\partial(\varepsilon c)}{\partial t} = -\mathrm{div}\,(D_{\mathrm{LiPF_6}}\,\mathrm{grad}\,c) + \frac{i t_+}{z_+ F}, \quad [4]$$

and

$$i = -\frac{\sigma_D}{c}\,\mathrm{grad}\,c - \sigma\,\mathrm{grad}\,\phi_{\mathrm{elyte}}, \quad [5]$$

with $\sigma_D = \frac{2}{z_+ F}(t_+ - 1)\,c\,\frac{\partial \mu_+}{\partial c}$ and the chemical potential μ_+ of Li^+. We transform these equations into our framework (Eq. 1) by choosing

$$D_\pm = D_{\mathrm{LiPF_6}} + \frac{t_\pm}{z_\pm F}\frac{\sigma_D}{c_\pm} \quad [6]$$

Table I. Summary of transport models included in the present framework (cf. List of symbols for definitions).

Physicochemical process	Model equation	
Gas-phase transport in channels[45]		
Continuity	$\frac{\partial \rho}{\partial t} = -\frac{\partial(\rho v)}{\partial x} + \frac{P^{\text{cha}}_{\text{chem}}}{A^{\text{cha}}} \sum \dot{s}^{\text{cha}}_i M_i$	[40]
Momentum conservation	$\frac{\partial(\rho v)}{\partial t} = -\frac{\partial(\rho v v)}{\partial x} - \frac{\partial p}{\partial x} - \frac{P^{\text{cha}}_{\text{h}}}{A^{\text{cha}}} \tau_{\text{w}}$	[41]
Species conservation	$\frac{\partial(\rho Y_i)}{\partial t} = -\frac{\partial(\rho v Y_i)}{\partial x} - \frac{\partial j^{\text{diff}}_i}{\partial x} + \frac{P^{\text{cha}}_{\text{chem}}}{A^{\text{cha}}} \dot{s}^{\text{cha}}_i M_i$	[42]
Ideal gas law	$p = \rho R T \sum_i Y_i / M_i$	[43]
Gas-phase transport in porous electrodes[27]		
Species conservation	$\frac{\partial(\varepsilon c^{\text{g}} X_i)}{\partial t} = -\frac{\partial J^{\text{diff}}_i}{\partial y} - \frac{\partial J^{\text{flow}}_i}{\partial y} + \sum_m A^{\text{V}}_m \dot{s}_{i,m}$	([44]
Diffusive fluxes: Stefan-Maxwell law	$\frac{\partial(c^{\text{g}} X_i)}{\partial y} = \sum_{j \in S_{\text{g}}} \frac{X_i J^{\text{diff}}_j - X_j J^{\text{diff}}_i}{D^{\text{eff}}_{ij}}$	[45]
Pressure-driven porous fluxes: Darcy flux	$J^{\text{flow}}_i = X_i c^{\text{g}} \frac{B}{\mu} \frac{\partial p}{\partial y}$	[46]
Charge transport in liquid electrolytes[46,17]		
Sepcies conservation	$\frac{\partial(\varepsilon c_i)}{\partial t} = -\frac{\partial J_i}{\partial y} + \sum_m A^{\text{V}}_m \dot{s}_{i,m}$	[47]
Species fluxes	$J_i = -D^{\text{eff}}_i \frac{\partial c_i}{\partial y} - D^{\text{migr,eff}}_i \frac{\partial \phi_{\text{elyt}}}{\partial y}$	[48]
Charge conservation	$0 = -\sum_i z_i F \frac{\partial J_i}{\partial y} + \sum_m z_i F A^{\text{V}}_m \dot{s}_{i,m}$	[49]
Coefficients: Dilute solution theory[44]	$D^{\text{migr}}_i = \frac{z_i F}{RT} c_i D_i$	[50]
Coefficients: Concentrated solution theory (this work)	$D_{\pm} = D^0 + \frac{t_{\pm}}{z_{\pm} F} \frac{\sigma_D}{c_{\pm}}$ and $D^{\text{migr}}_{\pm} = \frac{t_{\pm}}{z_{\pm} F} \sigma$	[51]
Charge transport in solid ionic and electronic conductors[27]		
Coupled ionic and electronic charge transport (anode and cathode)	$\frac{\partial}{\partial y}\left(\sigma_{\text{elyt}} f_\sigma \frac{\partial(\Delta\phi)}{\partial y}\right) = -\left(i^{\text{V}}_{\text{F}} + i^{\text{V}}_{\text{dl}}\right)$	[52]
Ionic charge transport (solid electrolyte)	$\frac{\partial}{\partial y}\left(\sigma_{\text{elyt}} \frac{\partial \phi_{\text{elyt}}}{\partial y}\right) = 0$	[53]
Cell current and voltage[27]		
Cell voltage	$E = \phi_{\text{elde,ca}} - \phi_{\text{elde,an}}$	[54]
Total current density (anode and cathode)	$i = \int_{y=0}^{L_{\text{electrode}}} (i_{\text{F}} + i_{\text{dl}}) \text{d}y$	[55]
Current density due to electrical double layer (anode and cathode)	$i_{\text{dl}}(t) = A_{\text{dl}} C_{\text{dl}} \frac{\partial(\Delta\phi)}{\partial t}$	[56]
Faradaic current density	$i_{\text{F}} = \sum_m F \dot{s}_{\text{electron},m} A^{\text{V}}_m + \sum_n F \dot{s}_{\text{electron},n} l^{\text{V}}_n$	[57]
Potential step (anode and cathode)	$\Delta\phi = \phi_{\text{elde}} - \phi_{\text{elyt}}$	[58]

and

$$D^{\text{migr}}_{\pm} = \frac{t_{\pm}}{z_{\pm} F} \sigma \qquad [7]$$

with $t_- = 1 - t_+$.

(Electro-)chemistry rate laws.— The species continuity equations in the porous electrode (Table I, Eqs. (44) and (47)) include source terms $\dot{s}_i$ due to interfacial reactions. According to mass-action kinetics,[48] the net production rate of species i due to an (electro-) chemical reaction is given by

$$\dot{s}_i = \nu_i \left(k_f \prod_{j \in R_f} a_j^{\nu'_j} - k_r \prod_{j \in R_r} a_j^{\nu''_j} \right), \qquad [8]$$

where k_f and k_r are the forward and backward rate constants, ν_i denotes the stoichiometric coefficient of species i, a_j the activities, and ν' and ν'' represent the positive stoichiometric coefficients for all reactants of the forward and backward reaction, respectively. The activity depends on the type of each species. For gas-phase and dissolved species it is equal to concentration [mol m^{-3}], for surface adsorbates it equal to surface concentration [mol m^{-2}], and for solid bulk phases it is unity.

The forward rate constant is given by a modified Arrhenius expression,

$$k_{\text{f}} = k^{\text{f}}_0 T^{\beta} \exp\left(-\frac{E^{\text{act}}_{\text{f}}}{RT}\right) \exp\left(-\frac{\alpha z F}{RT} \Delta\phi\right), \qquad [9]$$

where k^{f}_0 is the preexponential factor, T the temperature, $E^{\text{act}}_{\text{f}}$ the activation energy, β a temperature exponent, and R the ideal gas constant. In case of a charge-transfer reaction, the last exponential term represents the influence of the electric potential difference $\Delta\phi$, with a net transfer of z electrons, the Faraday's constant F and a symmetry factor α.[48,49] For thermochemical reactions (no charges involved), $z = 0$, and Eq. 9 reduces to the standard Arrhenius expression.

The reverse rate constant follows from thermodynamic consistency using the thermodynamic data,

$$\frac{k_{\text{f}}}{k_{\text{r}}} = \exp\left(-\frac{\Delta G}{RT}\right), \qquad [10]$$

Table II. Definition of parameters for the lithium-sulfur cell; converted from Kumaresan et al.[19] Values are given for T = 298.15 K and p = 101325 Pa.

Cathode	**Thickness**	41 μm			
	Control volumes	1×4			
	Bulk phases	**Volume fraction (ε_0)**	**Species**	**Density / Inital concentration**	**Diffusion coefficient**
	Sulfur	0.16	$S_8^{(solid)}$	$2.07 \cdot 10^3$ kg · m^{-3}	–
	Carbon	0.062	C	$2.26 \cdot 10^3$ kg · m^{-3}	–
	Electrolyte	0.778	$C_4H_6O_3$	$1.20 \cdot 10^3$ kg · m^{-3} /$1.023 \cdot 10^4$ mol · m^{-3}	–
			Li^+	$1.024 \cdot 10^3$ mol · m^{-3}	$1 \cdot 10^{-10}$ m^2 · s^{-1}
			PF_6^-	$1.023 \cdot 10^3$ mol · m^{-3}	$4 \cdot 10^{-10}$ m^2 · s^{-1}
			S^{2-}	$8.456 \cdot 10^{-10}$ mol · m^{-3}	$1 \cdot 10^{-10}$ m^2 · s^{-1}
			S_2^{2-}	$5.348 \cdot 10^{-7}$ mol · m^{-3}	$1 \cdot 10^{-10}$ m^2 · s^{-1}
			S_4^{2-}	$2.046 \cdot 10^{-2}$ mol · m^{-3}	$1 \cdot 10^{-10}$ m^2 · s^{-1}
			S_6^{2-}	$3.314 \cdot 10^{-1}$ mol · m^{-3}	$6 \cdot 10^{-10}$ m^2 · s^{-1}
			S_8^{2-}	$1.821 \cdot 10^{-1}$ mol · m^{-3}	$6 \cdot 10^{-10}$ m^2 · s^{-1}
			$S_8^{(dissoluted)}$	$1.943 \cdot 10^1$ mol · m^{-3}	$1 \cdot 10^{-9}$ m^2 · s^{-1}
	Lithium sulfide (Li_2S)	$1 \cdot 10^{-4}$	$Li_2S^{(solid)}$	1640 kg · m^{-3}	–
	Interfaces	**Specific area (A_0)**	**Reactions**	**Forward rate**	**Reverse rate**
	Sulfur-Electrolyte	$1.0 \cdot 10^5$ m^2 · m^{-3}	$S_8^{(solid)} \rightleftarrows S_8^{(liquid)}$	$1.900 \cdot 10^{-2}$ m$^{-0.5}$ · mol$^{0.5}$ · s^{-1}	1 s^{-1}
	Carbon-Electrolyte	$1.32 \cdot 10^5$ m^2 · m^{-3}	$^1/_2\ S_8^{(liquid)} + e^- \rightleftarrows {}^1/_2\ S_8^{2-}$	$7.725 \cdot 10^{13}$ m$^{-0.5}$ · mol$^{0.5}$ · s^{-1}	$2.940 \cdot 10^{-27}$ m$^{-0.5}$ · mol$^{0.5}$ · s^{-1}
			$^3/_2\ S_8^{2-} + e^- \rightleftarrows 2\ S_6^{2-}$	$4.331 \cdot 10^{16}$ m · mol$^{-0.5}$ · s^{-1}	$1.190 \cdot 10^{-23}$ m^4 · mol^{-1} · s^{-1}
			$S_6^{2-} + e^- \rightleftarrows {}^3/_2\ S_4^{2-}$	$3.193 \cdot 10^{14}$ s^{-1}	$4.191 \cdot 10^{-24}$ m · mol$^{-0.5}$ · s^{-1}
			$^1/_2\ S_4^{2-} + e^- \rightleftarrows S_2^{2-}$	$2.375 \cdot 10^{11}$ m$^{-0.5}$ · mol$^{0.5}$ · s^{-1}	$7.505 \cdot 10^{-24}$ s^{-1}
			$^1/_2\ S_2^{2-} + e^- \rightleftarrows S^{2-}$	$4.655 \cdot 10^{12}$ m$^{-0.5}$ · mol$^{0.5}$ · s^{-1}	$4.738 \cdot 10^{-22}$ s^{-1}
	Li_2S-Electrolyte	$1.0 \cdot 10^5$ m^2 · m^{-3}	$2\ Li^+ + S^{2-} \rightleftarrows Li_2S^{(solid)}$	$2.750 \cdot 10^{-5}$ m^6 · mol^2 · s^{-1}	$8.250 \cdot 10^{-19}$ s^{-1}
Separator	**Thickness**	9 μm			
	Control volumes	1×5			
	Bulk phases	**Volume fraction (ε_0)**	**Species**		
	Electrolyte	1.0	See cathode		
Anode	**Thickness**	100 μm			
	Control volumes	1×5			
	Bulk phases	**Volume fraction (ε_0)**	**Species**	**Molar Gibbs energy**	**Density / Inital concentration**
	Lithium	0.63	Li	0	$5.34 \cdot 10^2$ kg · m^{-3}
	Electrolyte	0.37	See cathode		
	Interfaces	**Specific area (A_0)**	**Reactions**	**Forward rate**	**Reverse rate**
	Lithium-Electrolyte	$1 \cdot 10^5$ m^2 · m^{-3}	$Li \rightleftarrows Li^+ + e^-$	$4.086 \cdot 10^{-9}$ m^{-5} · mol^2 · s^{-1}	1 m^{-2} · mol · s^{-1}

where ΔG is the molar Gibbs reaction enthalpy. The latter can be calculated by the sum over the species chemical potentials μ_i

$$\Delta G = \sum_{i \in R} \nu_i \mu_i = \sum_{i \in R} \nu_i (h_i - T s_i), \qquad [11]$$

where h is the molar enthalpy of formation and s the molar entropy of formation. We correct Eq. 10 for the units of k_f and k_r with the total concentration of the phases. Values for h and s are taken from literature (either explicitly from thermodynamic tables or implicitly by converting from kinetic data). Note that thermodynamics require the definition of reference states, for example, the pure elements at standard conditions and – for each solution phase – a reference dissolved species. For those reference species, h and/or μ are set to zero (cf. Tables II–V).

The local volumetric faradaic current density i_F is calculated from the source term of electrons, normalized by the electrochemically active surface area

$$i_F = \sum_m F \dot{s}_{\text{electron},m} A_m^V, \qquad [12]$$

with Faraday's constant F, the net production rate of electrons $\dot{s}_{\text{electron},m}$ and the corresponding surface area A_m^V, where the sum m runs over all reactions and surfaces. For reactions including more than two phases, the term of the surface area is replaced by the boundary length l_m^V,

$$i_F = \sum_m F \dot{s}_{\text{electron},m} l_m^V. \qquad [13]$$

Chemistry between species within bulk phases.— Chemistry between species within bulk phases, like gas-phase reactions, is included in our framework and described by Eqs. 8–11. However, it can be necessary to describe reactions for special cases by additional expressions. One example is modeling the solubility of gas in a liquid phase, such as molecular oxygen inside the electrolyte of a Li-O battery,

$$O_2^{(gas)} \rightleftarrows O_2^{(elyt)}. \qquad [14]$$

In this case, thermodynamics for the reaction follows from Henry's law,[48]

$$p_i = c_i K, \qquad [15]$$

which states, that the partial pressure p of species i is proportional to its concentration c_i in the liquid (valid at chemical equilibrium for low solvent concentrations). K is Henry's constant.

Surface and interfacial chemistry.— Electrochemical reactions are interfacial processes taking place at surfaces and phase boundaries. There are different approaches to account for interfacial reactions,

Table III. Definition of parameters for the lithium-oxygen cell; converted from Andrei et al.[7] Values are given for T = 298.15 K and p = 101325 Pa. Reverse reaction coefficients follow from thermodynamic consistency.

Cathode channel	**Length × Width**	–	**Species**	**Initial concentration**		
	Control volumes	1×1	O_2	$0.21\ mol \cdot mol^{-1}$		
			N_2	$0.79\ mol \cdot mol^{-1}$		
Cathode	**Thickness**	750 μm				
	Control volumes	1×35				
	Bulk phases	**Volume fraction (ε_0)**	**Species**	**Molar Gibbs energy**	**Density / Inital concentration**	**Diffusion coefficient**
	Carbon	0.25	C	0	$2.26 \cdot 10^3\ kg \cdot m^{-3}$	–
	Electrolyte	0.75	EC-EMC	–	$1.21 \cdot 10^3\ kg \cdot m^{-3}$ / $1.07 \cdot 10^4\ mol \cdot m^{-3}$	–
			Li^+	0	$1.0 \cdot 10^3\ mol \cdot m^{-3}$	See[66]
			PF_6^-	–	$1.0 \cdot 10^3\ mol \cdot m^{-3}$	See[66]
			$O_2^{(dissolved)}$	−43[63]	$1.62\ mol \cdot m^{-3}$	$7 \cdot 10^{-10}\ m^2 \cdot s^{-1}$[63]
	Lithium peroxide (Li_2O_2)	0.0	Li_2O_2	−644	$2.14 \cdot 10^3\ kg \cdot m^{-3}$	–
	Interfaces	**Specific area (A_0)**	**Reactions**	**Forward rate**		
	Carbon-Li_2O_2-Electrolyte	$8.66 \cdot 10^7\ m^2 \cdot m^{-3}$	$2\ Li^+ + O_2^{(dissolved)} + 2\ e^- \rightleftarrows Li_2O_2$	$9.23 \cdot 10^{31}\ m^7 \cdot mol^{-2} \cdot s^{-1}$		
	Carbon-$Gas^{(cathode\ channel)}$	–	$O_2^{(gas)} \rightleftarrows O_2^{(dissolved)}$	Assumed in equilibrium[63]		
Separator	**Thickness**	250 μm				
	Control volumes	1×5				
	Bulk phases	**Volume fraction (ε_0)**	**Species**			
	Electrolyte	0.9	See cathode			
	Glass separator	0.1	–			
Anode	**Thickness**	0.01 μm				
	Control volumes	1×1				
	Bulk phases	**Volume fraction (ε_0)**	**Species**	**Molar Gibbs energy**	**Density / Inital concentration**	
	Lithium	1.0	Li	0	$5.34 \cdot 10^2\ kg \cdot m^{-3}$	
	Interfaces	**Specific area (A_0)**	**Reactions**	**Forward rate**		
	Lithium-Electrolyte	$1 \cdot 10^8\ m^2 \cdot m^{-3}$	$Li \rightleftarrows Li^+ + e^-$	$1.31 \cdot 10^{-7}\ m \cdot s^{-1}$		

that is, global kinetics and elementary kinetics.[29] In a global kinetic approach, surface-adsorbed intermediates are neglected, either because they are not relevant (e.g., solution/dissolution reactions, electron transfer to species in solution without catalyst), or because their properties are unknown or too time-consuming to model (e.g., when applying half-cell electrochemical reactions such as $O_2 + 4\,H^+ + 4\,e^- \rightleftarrows 2\,H_2O$). In these cases, interfacial reactions are assumed to take place between species of adjacent bulk phases, and reaction rates only depend on the concentration of the reactants in the bulk phases.

In an elementary kinetic approach, reactions involve surface adsorbates. This includes surface-surface-reactions (Langmuir-Hinshelwood type mechanism), charge transfer, adsorption and desorption, as well as bulk/surface reactions (Eley-Rideal type mechanisms).[29,50] Surface chemical kinetics are calculated according to Eqs. 8–11. The absolute production rates of bulk species are obtained by multiplying area-specific (or line-specific) rates of production with the surface area A^V or the boundary length l^V, respectively (cf. Table I, Eqs. (44) and (47)).

Multi-phase management

Multi-phase management is a core component of the present modeling framework. The volume fraction of a bulk phase can change by three different processes, phase formation/dissolution, phase transition, and phase transport:

(1) Phase formation/dissolution is characterized by mass transfer from one phase to another by an (electro-)chemical reaction. For example, considering the oxidation of nickel metal by oxygen creates a new phase of solid nickel oxide (NiO), dissolving the nickel phase,

$$2Ni + O_2^{(gas)} \rightleftarrows 2NiO. \quad [16]$$

Reaction kinetics of the phase formation/dissolution can be described by Eqs. 8–11.

(2) Phase transition describes the change between different states of aggregation. Even though a phase transition is not a chemical reaction in a conventional sense, it obeys the laws of thermodynamics and can be treated as special case of a reaction between two bulk phases. Therefore we apply the formulation above (see Eqs. 8–11) to phase transitions as well. For example, the transition from liquid water to steam is written as reversible reaction,

$$H_2O^{(liquid)} \rightleftarrows H_2O^{(gas)}. \quad [17]$$

(3) Phase transport occurs, for example, in PEFCs where liquid water moves due to a gradient in capillary pressure. Phase transport is not considered in the present models.

Modeling the evolution of phases participating in these processes requires the introduction of a multi-phase management. Its purpose is accounting for the volume fractions ε of all phases within a layer as a function of time and spatial location inside the cell. Mass conservation of each phase i is described in terms of the mass density (ρε) via the continuity equation,

$$\frac{\partial(\rho_i \varepsilon_i)}{\partial t} = R_i M_i, \quad [18]$$

where ρ_i is the density and M_i the mean molar mass of phase i. We assume that phase formation/dissolution reactions occur at interfaces between two or more phases. The rate of formation R_i follows from the chemical source terms $\dot{s}_{i,m}$ of all reactions m involving phase i, including surface reactions, surface/gas phase reactions, surface/bulk

Table IV. Definition of parameters for the solid oxide fuel cell. Values are given for T = 1073 K and p = 101325 Pa. Reverse reaction coefficients follow from thermodynamic consistency.

Cathode channel	**Length × Width**	0.05 × 0.001 m	**Species**	**Initial concentration**		
	Control volumes	10 × 1	O_2	0.21 mol · mol^{-1}		
			N_2	0.79 mol · mol^{-1}		
Cathode	**Thickness**	20 μm				
	Control volumes	10 × 7				
	Bulk phases	**Volume fraction (ε_0)**	**Species**	**Molar enthalpy**	**Molar entropy**	**Density**
	LSM	0.3	–	–	–	–
	YSZ	0.3	YSZ	–	–	6100 kg · m^{-3}
			V_{YSZ}	0 kJ · mol^{-1}[177]	0 J · K^{-1}mol^{-1}[177]	–
			O^{2-}_{YSZ}	−236.4 kJ · mol^{-1}[177]	0 J · K^{-1}mol^{-1}[177]	–
	Gas	0.4 ($\tau = 2$)	See channel			
	Interfaces	**Specific length (l_0)**	**Reactions**	**Forward rate**	**Activation energy**	
	LSM-YSZ-Gas	$3.95 \cdot 10^8$ m · m^{-3}	$O_2 + 2\,V_{YSZ} + 4\,e^- \rightleftarrows 2\,O^{2-}_{YSZ}$	6 m^8 · kmol^{-2} · s^{-1}[173]	125 kJ · mol^{-1}[173]	
Separator	**Thickness**	20 μm				
	Control volumes	10 × 7				
	Bulk phases	**Volume fraction (ε_0)**	**Species**			
	YSZ	1.0	See cathode			
Anode	**Thickness**	500 μm				
	Control volumes	10 × 22				
	Bulk phases	**Volume fraction (ε_0)**	**Species**	**Molar enthalpy**	**Molar entropy**	**Density**
	Nickel	0.33	Ni	24.2 kJ · mol^{-1}[178]	69.2 J · K^{-1}mol^{-1}[178]	8908 kg · m^{-3}
	YSZ	0.34	See cathode			
	Gas	0.33 ($\tau = 8.568$)	See channel			
	Nickel oxide (NiO)	$1 \cdot 10^{-9}$	NiO	−190.1 kJ · mol^{-1}[179]	113.9 J · K^{-1}mol^{-1}[179]	7450 kg · m^{-3}
	Interfaces	**Specific area (A_0)**	**Reactions**	**Forward rate**	**Activation energy**	
	Nickel-YSZ-Gas	$4.55 \cdot 10^8$ m^2 · m^{-3}	$H_2 + O^{2-}_{YSZ} \rightleftarrows H_2O + V_{YSZ} + 2\,e^-$	$7 \cdot 10^6$ m^5 · kmol^{-1} · s^{-1}[173]	235 kJ · mol^{-1}[173]	
	Nickel-NiO-YSZ-Gas	$2.3 \cdot 10^6$ m^2 · m^{-3}	$Ni + H_2O \rightleftarrows NiO + H_2$	$1 \cdot 10^{-4}$ m^4 · kmol^{-1} · s^{-1}	120 kJ · mol^{-1}	
			$Ni + O^{2-}_{YSZ} \rightleftarrows NiO + V_{YSZ} + 2\,e^-$	$1 \cdot 10^{-7}$ m^4 · kmol^{-1} · s^{-1}	120 kJ · mol^{-1}	
Anode channel	**Length × Width**	0.05 × 0.001 m	**Species**	**Initial concentration**		
	Control volumes	10 × 1	H_2	0.1 mol · mol^{-1}		
			H_2O	0.9 mol · mol^{-1}		

reactions, and charge-transfer reactions. It is given by

$$R_i = \sum_m \dot{s}_{i,m} A^{\mathrm{V}}_m, \qquad [19]$$

where A^{V}_m accounts for the volume specific surface area corresponding to reaction m. For reactions including more than two phases, the term of the active surface area is replaced by the active boundary length l^{V}_m inbetween all involved phases,

$$R_i = \sum_m \dot{s}_{i,m} l^{\mathrm{V}}_m. \qquad [20]$$

Phase formation/dissolution reactions, like growth of solid structures out of the electrolyte or gas-phase, can cause changes to the total volume of the solid materials. As a result the pressure and/or volume of the system can vary. This effect is handled by defining compressible phases. If present, the gas phase fulfills this role (e.g., in fuel cells): Upon solid volume fraction increase, gas-phase volume fraction decreases and gas-phase pressure increases, as described by the ideal gas law. If no gas phase is present (e.g., in batteries), we assign the liquid electrolyte the property of a "compressible" phase: Upon solid volume fraction increase, electrolyte volume fraction decreases, and concentrations of electrolyte species increase. This assumption ensures mass conservation. It could also be interpreted as presence of a buffer volume for the liquid phase not included in the computational domain (e.g., by slight expansion of the cell dimensions). A full description of such effects would require the integration of a mechanical model (describing pressure increase and compression effects inside the electrode) as well as convective liquid flux into the buffer volume, which is out of the scope of the present work. For convenience, we solve for the volume fraction of the compressible phase by applying the constraint

$$\sum_i \varepsilon_i = 1. \qquad [21]$$

Eqs. 18–21 are of central importance for modeling multi-phase behavior of electrochemical systems. Firstly, they allow following the dynamic change of bulk phases, which is fundamental for both batteries (where the state of charge is directly related to volume fractions) and fuel cells (where secondary phase formation represents important degradation mechanisms). More importantly, they allow a direct coupling to both chemical kinetics (via modification of interfacial areas) and transport (via modification of transport coefficients and available transport pathways). This will be further described below.

Feedback between multi-phase management and structure/chemistry/transport

Microstructural properties.— The spatial appearance of secondary phases, as well as changes in the volume fractions of primary phases, has multiple effects on structure, chemistry and bulk transport processes. Concerning microstructure, key parameters used in the present model are the volume-specific two-phase interfacial areas $A^{\mathrm{V}}_{m,n}$ between two bulk phases m, n, and the volume-specific three-phase specific lengths $l^{\mathrm{V}}_{m,n,o}$ between three phases m, n, o. We use a general expression to describe their dependence on changes of bulk-phase

Table V. Definition of parameters for the polymer electrolyte fuel cell. Values are given for T = 354 K and p = 101325 Pa. Reverse reaction coefficients follow from thermodynamic consistency.

Cathode channel	**Length × Width**	0.9282 × 0.002 m	**Species**	**Initial concentration**		
	Control volumes	8 × 1	O_2	$0.17\ mol \cdot mol^{-1}$		
			N_2	$0.68\ mol \cdot mol^{-1}$		
			H_2O	$0.15\ mol \cdot mol^{-1}$		
Cathode	**Thickness**	30 μm				
	Control volumes	8 × 9				
	Bulk phases	**Volume fraction (ε_0)**	**Species**	**Molar enthalpy**	**Molar entropy**	**Density**
	Pt/C	0.3	–	–	–	–
	Nafion	0.3	H^+	$-100\ kJ \cdot mol^{-1}$	$0\ J \cdot K^{-1}mol^{-1}$	–
	Gas	0.4	See channel			
	Water$^{(liquid)}$	$1 \cdot 10^{-7}$	$H_2O^{(liquid)}$	$-281.620\ kJ \cdot mol^{-1}$ [78]	$82.8851\ J \cdot K^{-1}mol^{-1}$ [78]	$1000\ kg \cdot m^{-3}$
	Interfaces	**Specific area (A_0)**	**Reactions**	**Forward rate**	**Activation energy**	
	Pt/C-Nafion-Gas	$2.3 \cdot 10^6\ m^2 \cdot m^{-3}$	$4\ H^+ + O_2 + 4\ e^- \rightleftarrows H_2O^{(liquid)}$	$1 \cdot 10^{26}\ m^{13} \cdot mol^{-1} \cdot s^{-1}$	$300\ kJ \cdot mol^{-1}$	
	Water$^{(liquid)}$-Gas	$1\ m^2 \cdot m^3$	$H_2O^{(liquid)} \rightleftarrows H_2O^{(gas)}$	$1.48 \cdot 10^4\ K^{0.5} \cdot m \cdot s^{-1}$	$42\ kJ \cdot mol^{-1}$	
Separator	**Thickness**	50 μm				
	Control volumes	8 × 9				
	Bulk phases	**Volume fraction (ε_0)**	**Species**			
	Nafion	1.0	See cathode			
Anode	**Thickness**	0 μm (flat anode)				
	Control volumes	8 × 1				
	Bulk phases	**Volume fraction (ε_0)**	**Species**			
	Pt/C	0.3	–			
	Nafion	0.4	See cathode			
	Gas	0.3	See channel			
	Interfaces	**Specific area (A_0)**	**Reactions**	**Forward rate**	**Activation energy**	
	Pt/C-Nafion-Gas	$2.3 \cdot 10^6\ m^2 \cdot m^{-3}$	$H_2 \rightleftarrows 2\ H^+ + 2\ e^-$	$1 \cdot 10^{51}\ m \cdot s^{-1}$	$300\ kJ \cdot mol^{-1}$	
Anode channel	**Length × Width**	–	**Species**	**Initial concentration**		
	Control volumes	1 × 1	H_2	$0.85\ mol \cdot mol^{-1}$		
			H_2O	$0.15\ mol \cdot mol^{-1}$		

volume fractions,

$$A^{V}_{m,n} = A^{V}_{0} \cdot f_{m,n}(\varepsilon_m, \varepsilon_n), \quad [22]$$

$$l^{V}_{m,n,o} = l^{V}_{0} \cdot f_{m,n,o}(\varepsilon_m, \varepsilon_n, \varepsilon_o), \quad [23]$$

where A^{V}_{0} is the initial surface area and l^{V}_{0} the initial boundary length. The functions f describe the change of A^{V}_{0} or l^{V}_{0} depending on the volume fractions of adjacent phases. These relationships can be either empirical, or based on geometrical considerations.

In this work, empirical relationships are used for all solid-electrolyte interfaces in the Li-S cathode according to

$$f_{\text{Solid-Electrolyte}} = \left(\frac{\varepsilon_{\text{solid}}}{\varepsilon_{\text{solid},0}} \right)^{1.5}, \quad [24]$$

for the nickel-YSZ-gas three-phase boundary in the SOFC anode according to

$$f_{\text{Nickel-YSZ-Gas}} = \left(\frac{\varepsilon_{\text{nickel}}}{\varepsilon_{\text{nickel},0}} \frac{\varepsilon_{\text{YSZ}}}{\varepsilon_{\text{YSZ},0}} \frac{\varepsilon_{\text{gas}}}{\varepsilon_{\text{gas},0}} \right)^{10}, \quad [25]$$

and for the gas-platinum interface in the PEFC cathode according to

$$f_{\text{Platinum-Gas}} = \frac{\varepsilon_{\text{gas}}}{\varepsilon_{\text{gas},0} + \varepsilon_{\text{liquid},0}}. \quad [26]$$

In the PEFC model, water evaporation/condensation takes place at the vapor/liquid interface. In order to avoid numerical instabilities, which may occur when reaching volume fractions equal to zero, we assume that the boundary vanishes for very low as well as for very high volume fractions $\varepsilon_{\text{liquid}}$, according to

$$f_{\text{Liquid-Gas}} = 1 - \exp(-\xi\varepsilon_{\text{liquid}}) - \exp(\xi(\varepsilon_{\text{liquid}} - \varepsilon_{\text{gas},0} - \varepsilon_{\text{liquid},0})), \quad [27]$$

with $\xi = 100$.

Based on geometrical considerations, other relationships can be derived. For example, assuming the formation of a surface film in a system of cylindrical pores[7] yields an expression used for the carbon-electrolyte interface in the Li-O cathode,

$$f_{\text{Carbon-Electrolyte}} = \sqrt{\varepsilon_{\text{elyt}}}. \quad [28]$$

Fig. 3 shows the dependence of volume-specific surface area or length on volume fraction according to the relationships given in

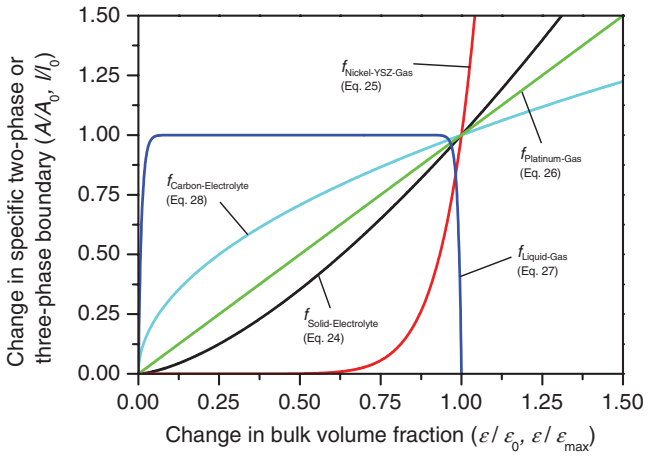

Figure 3. (color online): Effect on volume-specific two-phase or three-phase boundary as function of change in bulk volume fraction for the cases used in this work.

Eqs. 24–28. A large value of the exponent in Eq. 24 and Eq. 25 means a strong microstructural influence on bulk phase volume fraction and phase boundaries. Three-phase boundaries are expected to be more strongly influenced by the three adjacent bulk phases than two-phase boundaries.

Interfacial chemistry.— Chemical source terms in the governing equations are proportional to the volume-specific boundaries (cf. Table I, Eqs. (44) and (47)). Therefore, changes in microstructure directly influence reaction rates. Let us illustrate this at the case of a Li-S cell discharge: If bulk sulfur volume fraction tends to zero due to dissolution reactions (Eq. 18), the sulfur-electrolyte interfacial area also tends to zero (Eq. 24), which in turn reduces the dissolution reaction rate to zero (Eq. 19).

Mass and charge transport coefficients.— In the continuum approach used in this work, mass and charge transport are described through effective coefficients (diffusion coefficients, conductivities). They are assumed to depend on volume fraction ε_i as well as on tortuosity factor τ_i[2] of the bulk phase according to

$$D_i^{\text{eff}} = \frac{\varepsilon_i}{\tau_i^2} D_i \quad \text{and} \quad \sigma_i^{\text{eff}} = \frac{\varepsilon_i}{\tau_i^2} \sigma_i, \qquad [29]$$

where D is a diffusion coefficient (e.g., gas-phase or liquid-phase species diffusion coefficient), σ is a conductivity (solid-phase ionic or electronic conductivity), and τ is a tortuosity. In other cases (e.g., concentrated solution theory in liquid electrolytes) we combine these dependencies in a Bruggemann coefficient β,

$$D_i^{\text{eff}} = \varepsilon^{\beta} D_i \quad \text{and} \quad \sigma_i^{\text{eff}} = \varepsilon^{\beta} \sigma_i. \qquad [30]$$

Transport capacitances.— In the transport equations, the time derivative of the conservation variable includes the volume fraction of the respective phase (cf. Table I, Eqs. (44) and (47)). This can be interpreted as a chemical capacitance. The dynamic behavior of mass and charge transport is thus strongly influenced by multi-phase management.

Simulation methodology

The modeling framework presented in this paper is mathematically represented by a differential-algebraic equation (DAE) system that describes the implicit relationship between cell current density i and cell voltage E (Table I, Eqs. (54) and (55)) under consideration of multi-phase management (Eq. 18 and 21), chemistry (Eqs. 8, 12, 19), and transport processes (Table I, Eqs. (40)–(51)). In our implementation, we can solve either for E when i is specified, or for i when E is specified, or for i and E when the power density $P = i \cdot E$ is specified.

The model framework was implemented into the in-house software package DENIS (detailed electrochemistry and numerical impedance simulation).[27] In order to evaluate the chemical source terms ($\dot{s}_i$ in Eq. 8), we use the software CANTERA developed by Goodwin and co-workers.[51] CANTERA is an open-source software for solving complex chemical reaction systems based on conveniently-structured input files. We connect CANTERA (written in C++) to our in-house software DENIS (written in C/C++), making the full CANTERA functionality available during DENIS runtime. For numerical simulation, the computational domain is spatially discretized using the finite-volume method. The numbers of control volumes for all examples discussed in this work are listed in Tables II–V. Number and distribution of control volumes was chosen such that a further increase did not affect the calculated results within 0.5% and 5% for the discretization in y and x dimension, respectively. The resulting DAE system is solved using LIMEX.[52,53] For determining consistent initial values, LIMEX's built-in Newton solver yields good stability.[54] The code takes advantage of several subroutines from Numerical Recipes.[55] Analytic expressions for specific boundaries (Eqs. 22 and 23) are evaluated using muParser.[56] The full model functionality is controlled via two ASCII input files, a DENIS input file controlling phase management, transport parameters and simulation methodology, and a CANTERA input file controlling thermodynamic and kinetic properties of phases and species.

Lithium-sulfur battery

Background.— The lithium-sulfur (Li-S) battery is a promising system for energy storage. Its energy density (up to 2.6 kWh/kg) is the highest of all "closed-system" batteries known. Even though the system has been known for decades,[57] recently it gained increasing attention due to the demand for lightweight high-capacity batteries for application in electric vehicles.[21]

While the negative electrode of a Li-S cell consists of pure metallic lithium, the positive electrode typically is a compound of finely dispersed sulfur, electronically conducting carbon, and a stabilizing binder.[6] The overall reaction of the Li-S cell can be formulated as

$$S_8 + 16\text{Li} \rightleftarrows 8\text{Li}_2\text{S}. \qquad [31]$$

Unlike in lithium-ion batteries, where Li atoms are intercalated into various lattice materials, all reactants and products are pure solids. The charge and discharge processes involve the dissolution and precipitation as well as the chemical transformation of these materials. The reaction proceeds over a large number of intermediate sulfur species at different oxidation states, which are partially soluble. The large number and different properties of those intermediates represent a major challenge in understanding Li-S electrochemistry. Several proposed mechanisms for the reduction of sulfur in the Li-S cell have been published.[19,58,59,57] The Li-S battery model presented here is based on the work of Kumaresan et al.[19]

Modeling and simulation.— Table II defines the layers, bulk phases, phase boundaries, species and reactions used in the Li-S model. The parameters have been converted from Kumaresan et al.[19] The model assumes a conversion of metallic lithium and solid sulfur to solid Li_2S via the reaction pathway shown in Table II. Even though all reactions take place at liquid/solid surfaces, no explicit surface states (i.e., adsorbates) are resolved. Furthermore, to simplify the model and reduce the number of parameters, side reactions are neglected in this work. Galvanostatic discharge was simulated at a current of $0.34\ \text{A} \cdot \text{m}^{-2}$, corresponding to a discharge rate of C/50.

Results.— Fig. 4 depicts the simulated discharge curve together with the volume fractions of the S_8 and Li_2S phases. From this figure, the two distinct stages of the discharge curve, which are observed in experiment,[60] can be explained: During the first stage, solid sulfur is present in the cell and the voltage remains relatively high. In the second stage, when all solid sulfur is completely dissolved, the voltage drops until it reaches a plateau as soon as solid Li_2S starts to form from

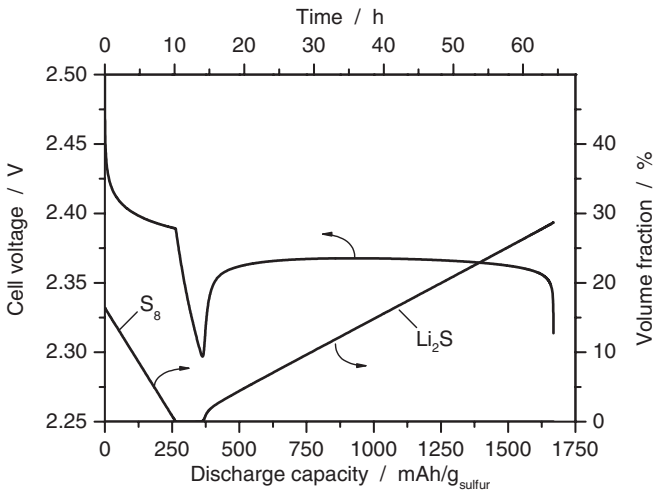

Figure 4. Lithium-sulfur battery: A typical Li-S low current discharge curve alongside with the volume fractions of pure sulfur and Li_2S.

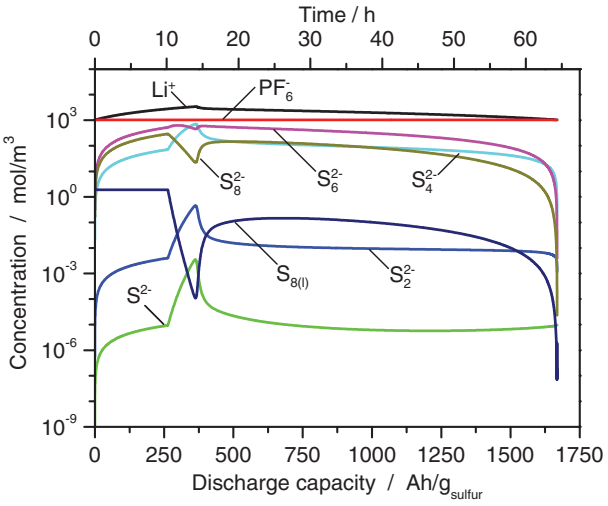

Figure 5. (color online): Lithium-sulfur battery: Concentrations of ions in the electrolyte during the galvanostatic discharge shown in Fig. 4.

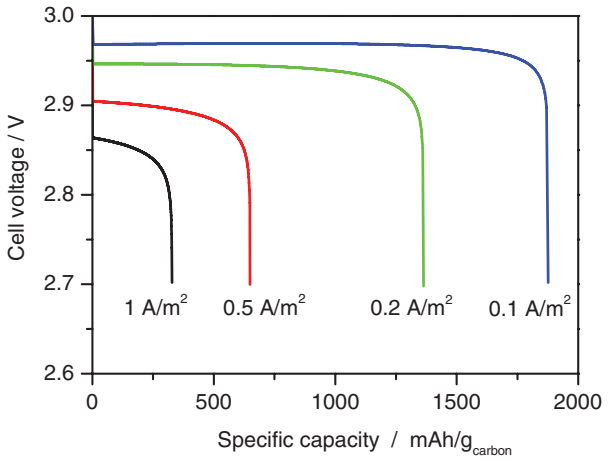

Figure 6. (color online): Lithium-oxygen battery: Discharge curves at various current densities between 0.1 A/m^2 and 1 A/m^2.

dissolved Li^+ and S^{2-} ions. This can be further understood from the concentration variation of the dissolved intermediate species shown in Fig. 5. As long as there is still solid sulfur in the cathode, the concentration of dissolved sulfur $S_8^{(liquid)}$ in the electrolyte remains constant. During this stage, the main reaction taking place is the reduction of $S_8^{(liquid)}$, accompanied by the formation of various polysulfides. Once the reservoir of solid sulfur is used up, the concentrations of $S_8^{(liquid)}$ and subsequently S_8^{2-} and S_6^{2-} start to decrease. The electrical current now results from the reduction of the polysulfides down to S^{2-}, which is removed from the solution by precipitation of Li_2S. Note that, only by including detailed multi-phase management into the model, the typical discharge curve and in particular the minimum between the two stages of the discharge (cf. Fig. 4) can be reproduced.

Lithium-oxygen battery

Background.— Li-O batteries receive great attention in the current literature due to their large theoretical energy density (11.9 kWh/kg without the O_2 mass), which is a factor of ∼5 above that of conventional Li-ion technology.[61] At the cathode, four bulk phases are involved in the reaction according to

$$2Li^{+(electrolyte)} + O_2^{(gas)} + 2\,e^{-(carbon)} \rightleftarrows Li_2O_2^{(solid)}. \qquad [32]$$

Added catalysts such as MnO_2 may represent a fifth bulk phase. Connected to the multi-phase management, a long list of issues needs to be solved for Li-O batteries.[62] The formation of solid lithium oxide as product phase can clog pore space and/or form an insulating film on the carbon support. Oxygen solubility and diffusivity are very low in organic electrolytes.[63] Furthermore, standard carbonate-based electrolytes decompose during discharge of Li-O cells.[64] Aqueous electrolytes are interesting alternatives, but their reactivity toward lithium is a major security risk.

Modeling attempts of Li-O cells are scarce,[20,7,21,65] compared to the large body of experimental work. The modeling literature focuses on problems arising from the deposition of solids in the porous cathode as a result of discharge (e.g., Li_2O_2)[7] or degradation (e.g., Li_2CO_3) reactions.[20] These solids accumulate in the porous structure of the cathode.

Modeling and simulation.— Table III defines the layers, bulk phases, phase boundaries, species, and reactions used in the Li-O model. The model has been converted from Andrei et al.,[7] exchanging the electrolyte. Our modeling framework captures solid-phase deposition conveniently: Eq. 18 describes the creation of solid reaction products, Eq. 21 the consecutive change in porosity, i.e., the volume fraction of the electrolyte. The reduction in porosity triggers two effects: The transport speed in the electrolyte is reduced resulting in pore clogging, described by Bruggemann coefficients (see Eq. 6), and the surface area of the cathodic discharge reaction decreases, described via Eq. 28. Other authors assume that a layer of insulating reaction products passivates the cathode surface,[20] an effect neglected in the present work.

The electrolyte is in equilibrium with air at the cathode surface ($y = 0$ in Fig. 6). The oxygen concentration at the interface is determined by Henry's law (see Eq. 15). The equilibrium concentration of oxygen determines its flux into the electrolyte; all other species obey no-flux conditions at the cell boundaries.

We treat the transport of the salt $LiPF_6$ in the aprotic solvent EC:EMC (3:7) with concentrated solution theory[17] (Eqs. 4, 5). For O_2 diffusion we apply Eq. 1, assuming that the low oxygen concentration does not influence the Li^+-transport. As described above, carbonate-based solvents decompose in a Li-O cell. Nevertheless, we choose this standard solvent because its properties have been completely measured. Transport parameters for the salt (Li^+ diffusion coefficient, transference number, conductivity, activity coefficient) are taken from Nyman et al.,[66] transport and thermodynamic parameters for oxygen (O_2 diffusion coefficient, Henry constant) are taken from Xu et al.[63] We take into account the finite electronic conductivity of the cathodic graphite matrix.[7] The reaction mechanisms and the discharge products in Li-O cells are not fully understood yet, but thermodynamic calculations predict that the formation of Li_2O_2 is favored against the formation of other oxides.

Results.— Fig. 6 shows discharge curves for various current densities between 0.1 $A \cdot m^{-2}$ and 1 $A \cdot m^{-2}$. Those comparatively low values were chosen because the low solubility and diffusivity of oxygen in the organic electrolyte limits the performance of the system (cf. below). After an initial drop due to activation and concentration overpotentials, the voltage remains nearly constant for a long period. The discharge capacity is limited by pore clogging due to Li_2O_2 deposition, as discussed in the following.

Fig. 7 shows spatial profiles along the cathode thickness. Initially (SOC = 100%), oxygen concentration and current production are homogeneously distributed in the cathode (Fig. 7a/7b). Quickly, a steep concentration gradient of oxygen evolves due to its slow transport and low solubility (Fig. 7a). Thus, the reaction mainly proceeds at the front of the cathode (Fig. 7b). In this region, Li_2O_2, which is deposited during discharge, is concentrated (Fig. 7c). Consequently, the volume fraction of the electrolyte-filled pore space decreases in time, especially at the front of the pores. This enhances the problem of slow oxygen transport until the pores are completely blocked (Fig. 7c). In Fig. 7d we show that inhomogeneities and pore clogging are accelerated at high discharge currents.

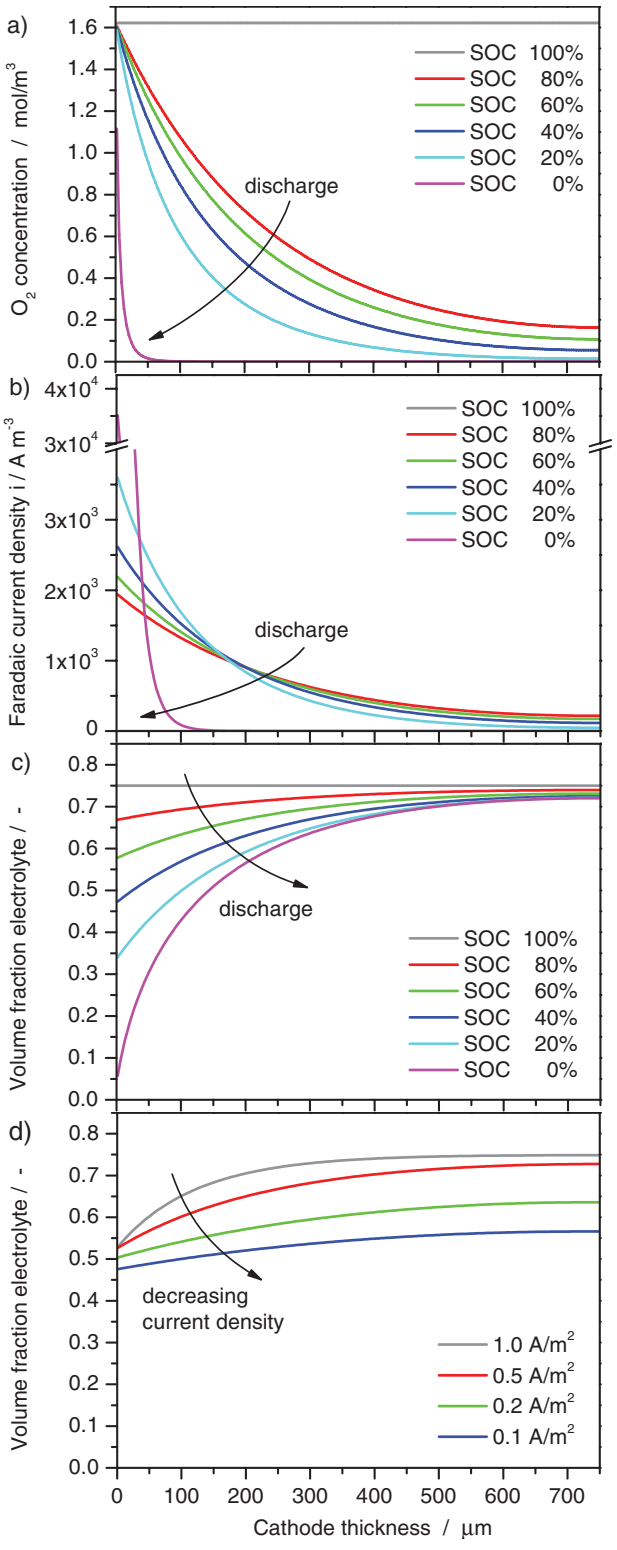

Figure 7. (color online): Lithium-oxygen battery: Spatial profiles inside the porous cathode. a) O_2 concentration, b) faradaic current and c) porosity at various SOC and a current density of 0.5 A/m^2. d) Porosity at various current densities and SOC = 50%.

Solid oxide fuel cell

Background.— As example for secondary phase formation in solid oxide fuel cells (SOFC) a two-dimensional model incorporating nickel (Ni) oxidation is presented. Oxidation of Ni inside the nickel/yttria-stabilized zirconia (Ni/YSZ) composite anode is one of the prominent degradation modes of SOFCs. As an insulating material, nickel oxide (NiO) blocks the electrochemically active areas of the electrodes, reducing the active triple-phase boundary.[67,68] Additionally, NiO formation can cause irreversible structural damages, because its molar volume is about 69.9% higher as it is for metallic nickel.[5]

Two different pathways of the oxidation process can be distinguished. The first possible mechanism is a themochemical reaction, driven by molecular oxygen (O_2) or a high water content of the fuel gas,

$$Ni + {}^1/_2O_2 \rightleftarrows NiO \quad [33]$$

$$Ni + H_2O \rightleftarrows NiO + H_2 \quad [34]$$

These reactions take place at the interface between metallic nickel and gas phase. The thermodynamic equilibrium between Ni, NiO and O_2 depends on temperature and local oxygen partial pressure. Thermodynamics predict a limiting oxygen partial pressure; above this partial pressure, NiO formation is thermodynamically favored, below this partial pressure Ni formation takes place.[69–71] During SOFC operation, high O_2 partial pressures can occur if the fuel utilization is too high, causing a low H_2/H_2O ratio at some parts of the cell.

The second oxidation mechanism is the electrochemical oxidation of Ni,[72] taking place at the interface between YSZ and metallic Ni,

$$Ni + O^{2-} \rightleftarrows NiO + 2\,e^- \quad [35]$$

Here the metal is reduced by oxygen ions from the electrolyte, releasing electrons. This may be the case, for example, upon an interruption of the fuel supply during galvanostatic operation.

Modeling and simulation.— Table IV defines the layers, bulk phases, phase boundaries, species, and reactions used in the SOFC model. The model shown here includes both oxidation pathways (Eqs. 33–35). Electrochemical hydrogen oxidation and oxygen reduction at anode and cathode, respectively, are formulated as global reactions, with kinetics taken from experiments of Bessler et al.[73] Kinetics for the nickel oxidation reactions are assumed, since no applicable experimental data are available to date. The feedback between Ni oxidation and cell performance was taken into account by applying a loss in kinetic performance via reducing three-phase boundary length (Eq. 23).

The model can be used to simulate the spatial and temporal evolution of NiO volume fraction and cell performance for different operating scenarios (e.g., cell voltage cycling or high fuel utilization). Here we show results for NiO formation upon cycling to a low voltage of 0.34 V at $T = 1073$ K in highly humidified fuel gas. The anode gas is composed of 10% H_2 and 90% H_2O with an inflow rate of 5 m/s, and the cathode gas is air with a flow rate of 1 m/s.

Results.— Fig. 8 shows the temporal evolution of cell current and average NiO volume fraction for a voltage variation over 12 h operating time with a fuel gas composition of 10% H_2 and 90% H_2O. Starting at $t = 0$, the voltage is linearly reduced from OCV down to

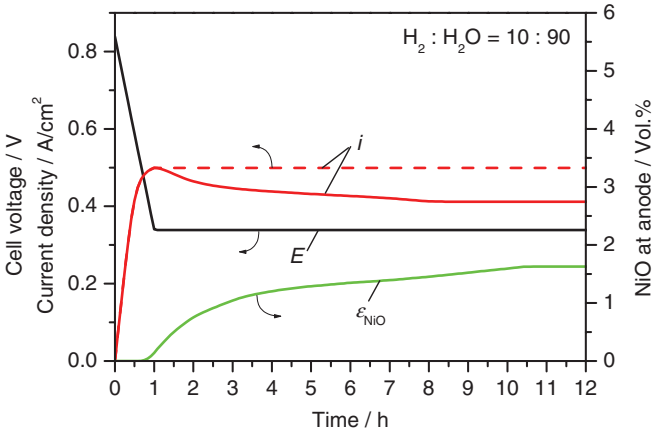

Figure 8. (color online): Solid oxide fuel cell: Formation of nickel oxide during polarization down to low voltages in highly humidified fuel gas.

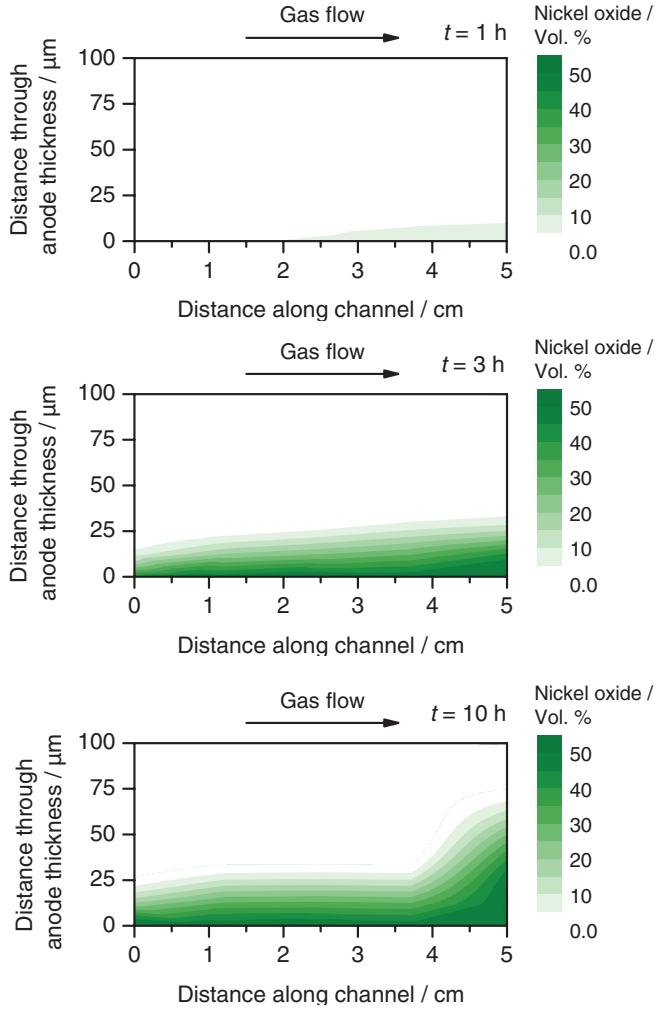

Figure 9. (color online): Solid oxide fuel cell: Spatial evolution of NiO formation inside the porous anode. Shown are the first 100 µm from the solid electrolyte. A volume fraction of 51% corresponds to the totally available pore space.

0.34 V within 1 h (black line). At this level it is held for 11 h. As expected, lowering the voltage leads to an increase of current density (blue line). The blue dotted line, which holds a constant level between 1 and 12 hours, shows the simulated current density without considering Ni oxidation. NiO volume fraction (green line) starts to increase from $t = 0.6$ h until it reaches a maximum value of after about 10.5 h. Ni oxidation is delayed relative to the voltage variation; with the parameters used in the present study, it occurs on a time scale of around 10 hours. Ni oxidation leads to a reduction of current density which is due to the combined effects of three-phase boundary length reduction and porosity decrease. Under the presently assumed operating conditions with low fuel utilization (40%), the nickel oxide volume fraction does not increase above 1.6 Vol.-%.

Fig. 9 shows the spatially resolved evolution of NiO volume fraction inside the porous anode during the voltage variation shown in Fig. 8. Three time points are chosen, which correspond to the beginning ($t = 1$ h), the intermediate region ($t = 3$ h), and the end ($t = 10$ h) of the oxidation process. The simulations show that NiO formation starts close to the solid electrolyte at the gas outlet side. In the following hours it spreads through the anode, increases concentration and finally develops the highest values close to the solid electrolyte at the gas outlet side. Note that a volume fraction of 51% corresponds to the total available pore space. The model allows identifying the regions and time scale of NiO formation and therefore enables the development of optimized operating strategies for avoiding degradation due to Ni oxidation.

Polymer electrolyte membrane fuel cell

Background.— One of the key issues for the functionality of PEFCs is proper water management.[8] On the one hand, sufficiently high water content is required for high proton conductivity of the membrane. Insufficient humidification of the inflow gases leads to a drying-out of the membrane, causing an increase in resistance. On the other hand, oxygen transport may be blocked due to high liquid water content at the cathode side (so-called flooding). In this section we focus on the second aspect, demonstrating the breakdown of fuel cell function caused by flooding.

In PEFCs, liquid water may occur due to two mechanisms: First, it is created by the oxygen reduction reaction at the cathode side,

$$O_2 + 4\,H^+ + 4\,e^- \rightleftarrows 2\,H_2O^{(\text{liquid})} \qquad [36]$$

Second, depending on partial pressure and temperature, gaseous water may condensate to liquid water or liquid water may evaporate into the gas phase, respectively, according to

$$H_2O^{(\text{liquid})} \rightleftarrows H_2O^{(\text{gas})}. \qquad [37]$$

Furthermore, water is dragged from anode to cathode side via electro-osmosis.

Modeling and simulation.— Table V defines the layers, bulk phases, phase boundaries, species, and reactions used in the PEFC model. The model used here is based on the single-phase PEFC model of Eschenbach et al.,[74] which is extended by liquid water formation, as described in the following. The liquid water evaporation rate (Eq. 37) can be described by the Hertz-Knudsen equation[75]

$$R_{H_2O} = \alpha \frac{p_0(T) - p}{\sqrt{2\pi M R T}}, \qquad [38]$$

where α is the so-called evaporation coefficient, which strongly depends on the particular flow situation (cf. 75), p denotes the partial pressure of water, whereas $p_0(T)$ is the temperature dependent saturation pressure, which can be approximated by

$$p_0(T) = p_1 \exp\left(-\frac{\Delta H}{R}\left(\frac{1}{T} - \frac{1}{T_1}\right)\right), \qquad [39]$$

where p_1 is the vapor pressure at temperature T_1 and ΔH the enthalpy of evaporation. Thus, the evaporation rate constant can be brought into the form of an Arrhenius expression (Eq. 9) with $k_0^f = (\alpha p_1)/(\rho_{H_2O,(\text{liquid})}) \cdot (M/(2\pi R))^{0.5} \cdot \exp(\Delta H/(RT_1)))$, $\beta = -0.5$, $E_{act} = \Delta H$ and $z = 0$.

In this model we investigate the flooding in the cathode catalyst layer (CL), which occurs due to the mechanisms described above. The increase of liquid water content in the catalyst layer leads to a reduction of the pore space, i.e., lowers the diffusion of oxygen. This eventually causes a breakdown of the cell function. To demonstrate this, we increase the power density within 50 seconds up to 800 W/m^2 and subsequently keep it constant. We consider inlet air with relative humidity RH = 0.3 at temperature $T = 354$ K and pressure $p = 101325$ Pa. The evaporation coefficient is assumed to be $\alpha = 0.01$. Note that in the present simulations we do not include gas diffusion layers or microporous layers, which would alter the flooding behavior.

Results.— Fig. 10 shows the time evolution of current density and cell voltage. In the first 50 seconds the values change according to the linear increase of the power density. Subsequently the power density is kept constant. However, the volume fraction of liquid water inside the CL increases with time (Fig. 11), which leads to a decrease of the cell voltage. In order to keep the power density constant, this drop of the cell voltage is compensated by an increase of the current density. Eventually, at about $t = 168$ s, the cell function breaks down, since the CL is almost completely flooded. Fig. 11 shows the spatial distribution of liquid water in the CL at three different points in time. Liquid water is mainly created close to the membrane, where the oxygen-reduction reaction takes place. Furthermore, liquid water is created faster at

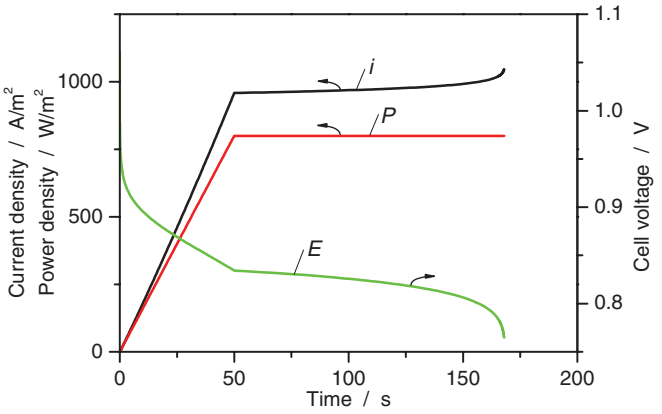

Figure 10. (color online): PEM fuel cell: Temporal evolution of power density, current density and cell voltage.

the inlet of the channel due to the higher oxygen concentration and consequently high local current density. At $t = 150$ s the CL is already highly flooded. Note that a volume fraction of 40% corresponds to the total available pore space.

Discussion

In the previous Sections, results for four different electrochemical systems dominated by multi-phase effects were presented. Two cases are based on published parameters (Li-S[19] and Li-O[7]), and two cases represent original models (SOFC, PEFC).

The Li-S and Li-O simulations can be used to assess the accuracy and performance of our simulations. Both models are based on published models.[20,7,19] Our framework reproduces the literature results qualitatively identical and quantitatively very closely. The difference arises from a different choice of model parameters here (Li-O: Transport coefficients based on experiments;[66] Li-S: additional product phase Li_2S_2 not considered here). For identical parameters, our simulations yield the quantitatively identical results compared to literature. Note that the current modeling framework does not use Butler-Volmer type equations. Instead, an elementary kinetic description based on mass-action kinetics with potential-dependent kinetic coefficients is used (cf. Eqs. 8–11). The coefficients, as given in Tables II, III, IV, V, were converted from the exchange current densities given in literature. Note also that both models yield results that compare qualitatively well with typical published experiments on these systems.[19,76] A quantitative comparison and validation with experimental data is subject of ongoing studies.

The SOFC and PEFC simulations further demonstrate the flexibility of the framework. In the case of SOFC, we could simulate for the first time the phase-change behavior due to nickel oxidation – one of the prominent degradation mechanisms in the SOFC anode – and its influence on cell performance. In the case of PEFC, flooding by liquid water and subsequent performance breakdown was successfully reproduced.

Using a generic framework may increase computational effort, as system-specific code optimization is difficult. The computational times of the four models shown above strongly depend on the number of grid points ($x \times y$) and are 3 min (Li-O, 1×41 grid points), 40 s (Li-S, 1×13 grid points), 15 h (SOFC, 10×38 grid points) and 14 h (PEFC, 8×29 grid points), all on a standard desktop computer. The computing time is naturally longer for the 2D models (SOFC, PEFC) than for the 1D models (Li-S, Li-O). For moderate discretization, the simulations are considerably faster than real time for 1D models, and slower than real time for 2D models. The performance strongly depends on the discretization used. For example, in the case of Li-O, if the discretization is changed to 36 or to 206 grid points, computational time changes nonlinearly to 22 s or to 3.5 h, respectively. Note that the code is not particularly optimized for speed; for example, we estimate that a proper exploitation of the Jacobian structure might decrease

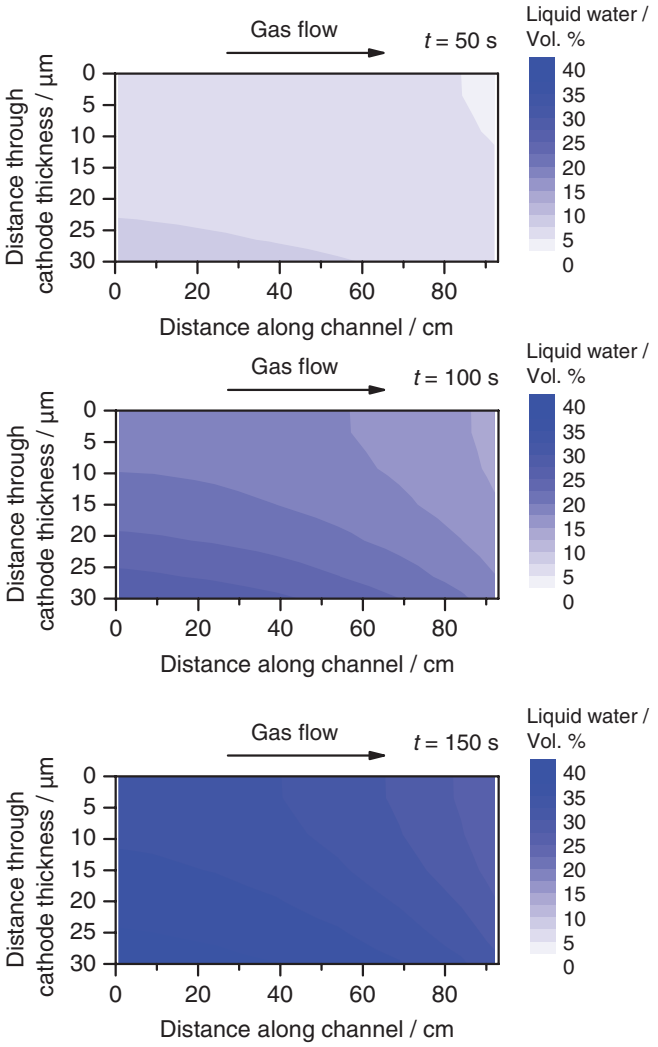

Figure 11. (color online): PEM fuel cell: Spatial evolution of liquid water inside the porous cathode. A volume fraction of 40% corresponds to the totally available pore space.

computing time by a factor of 10 for 2D models. A comparison with literature is difficult. Andrei et al. (Li-O) claim a time of < 1 min, however without stating their discretization; Kumaresan et al. (Li-S) do not comment on computing time.

Summary and Conclusions

Multi-phase management is crucial for both performance and durability of batteries and fuel cells. In this paper we have presented a generic framework for describing the spatiotemporal evolution of gaseous, liquid and solid phases, as well as their interdependence with interfacial (electro-)chemistry and structure in a continuum description. The modeling domain consists of up to seven layers (current collectors, channels, porous electrodes, separator/membrane), each of which can consist of an arbitrary number of bulk phases (gas, liquid, solid) and connecting interfaces (two-phase or multi-phase boundaries). Chemical source terms for global or elementary interfacial reactions are calculated based on mass-action kinetics with potential-dependent kinetic coefficients. Mass and charge transport within bulk phases is described using a 1D+1D approach. The functionality and flexibility of this framework was demonstrated using four application areas in the context of post-lithium-ion batteries and fuel cells.

Lithium-sulfur (Li-S) batteries are characterized by a complex sulfur redox chemistry. Based on eight chemical reactions (including charge transfer and dissolution/precipitation reactions) between four solid phases and eight electrolyte-dissolved species, we were able to

predict the discharge behavior. The discharge curve consists of two distinct plateau regions, one of which corresponds to the dissolution of solid sulfur, the other one to the precipitation of lithium sulfide.

The functionality of lithium-oxygen (Li-O) cells is based on the presence of four phases in three different states of aggregation at the positive electrode (gas-phase O_2, liquid-phase dissolved Li^+, solid-phase Li_2O_2, solid-phase electronic conductor). The performance of the Li-O battery is limited by oxygen transport in the electrolyte. Thus, already at moderate discharge currents the reaction and its product Li_2O_2 are concentrated near the cathode-gas interface and block the pores of the cathode. When the oxygen transport through the electrolyte is completely inhibited, the discharge stops prematurely.

Nickel-based solid oxide fuel cell (SOFC) anodes are sensitive toward formation of nickel oxide upon high fuel utilization (chemical pathway) or low cell voltages (electrochemical pathway). The formation of NiO was shown to occur predominantly in the composite anode close to the solid electrolyte and close to the channel outlet. Although the global current/voltage characteristic is only moderately affected, full Ni oxidation can occur locally.

Water management of polymer electrolyte membrane fuel cells (PEFC) is of high importance for good performance. Water evaporation/condensation is integrated into the present framework as chemical reaction. Spatiotemporal simulation of water saturation in the PEFC cathode shows flooding, which eventually inhibits the cell function.

The present methodology provides a useful tool for understanding and optimizing multi-phase management in electrochemical cells. Due to its flexibility, it allows rapid, efficient and robust modeling and simulation. It furthermore enables knowledge transfer between previously separated development lines for various battery and fuel cell models.

Acknowledgments

JPN and WGB acknowledge funding from the Initiative and Networking fund of the Helmholtz Association. DNF acknowledges financial support of the Foundation of the German Industry (sdw). TJ acknowledges funding from the European Union within the PREMIUM ACT project supported by the FCH-JU (2009 JTI project). TD and BH acknowledge funding from the German Federal Ministry of Education and Research (2011 BMBF 03X3624B). The authors thank Klaus Göckelmann (DLR) for supporting software development.

List of Symbols

Symbol	Unit	Meaning	Introduced in Eq.
A_m^{V}	$\mathrm{m^2 \cdot m^{-3}}$	Volume-specific surface area corresponding to reaction m	1
A_0^{V}	$\mathrm{m^2 \cdot m^{-3}}$	Initial volume-specific surface area	22
$\mathrm{A^{cha}}$	$\mathrm{m^2}$	Channel cross-sectional area	40
B	$\mathrm{m^2}$	Permeability of the porous electrode	46
c_i	$\mathrm{mol \cdot m^{-3}}$	Concentration of species i in a bulk phase	1
c^g	$\mathrm{mol \cdot m^{-3}}$	Total gas-phase concentration	44
C_{dl}	$\mathrm{F \cdot m^2}$	Area-specific double layer capacitance	56
D_i^{eff}, $D_i^{\mathrm{migr,eff}}$	$\mathrm{m^2 \cdot s^{-1}}$, $\mathrm{m^{-1} \cdot s^{-1} \cdot V^{-1}}$	Effective transport coefficients of species i	1
E	V	Cell voltage	54
$E_{\mathrm{f}}^{\mathrm{act}}$	$\mathrm{J \cdot mol^{-1}}$	Activation energy of forward and reverse reactions	9
f_σ		Ratio of ionic conductivity of porous over bulk electrolyte	52
F	$\mathrm{C \cdot mol^{-1}}$	Faraday's constant	2
h_i	$\mathrm{J \cdot mol^{-1}}$	Molar enthalpy of species i	11
i		Index of species and phases	1
i_F	$\mathrm{A \cdot m^{-3}}$	faradaic current density	4
j_i^{diff}	$\mathrm{kg \cdot m^{-2} \cdot s^{-1}}$	Mass diffusion flux of species i	42
J_i	$\mathrm{mol \cdot m^{-2} \cdot s^{-1}}$	Flux of species i	2
J_i^{flow}	$\mathrm{mol \cdot m^{-2} \cdot s^{-1}}$	Darcy flux of species i	46
$\mathrm{k_f}$, $\mathrm{k_r}$		Forward and backward rate constant	8
k_0^{f}		Preexponential factor in Arrhenius equation	9
K	Pa	Henry's constant	15
l_m^{V}	$\mathrm{m \cdot m^{-3}}$	Volume-specific three-phase boundary length corresponding to reaction m	20
l_0^{V}	$\mathrm{m \cdot m^{-3}}$	Initial volume-specific three-phase boundary length	13
m		Index of chemical reactions and interfaces	12
M_i	$\mathrm{kg \cdot mol^{-1}}$	Mean molar mass of phase i	18
p	Pa	Pressure	15
P	$\mathrm{W \cdot m^{-2}}$	Power density	
$P_{\mathrm{chem}}^{\mathrm{cha}}$	m	Electrochemically active channel perimeter	40
$P_{\mathrm{h}}^{\mathrm{cha}}$	m	Hydrodynamic channel perimeter	41
R	$\mathrm{J \cdot K^{-1} \cdot mol^{-1}}$	Ideal gas constant	3
R	Ω	Ohmic resistance	
R_i	$\mathrm{mol \cdot m^{-3} \cdot s^{-1}}$	Net rate of production of phase i	18
s_i	$\mathrm{J \cdot K^{-1} \cdot mol^{-1}}$	Molar entropy of species i	11
$\dot{s}_i^{cha}$	$\mathrm{mol \cdot m^{-2} \cdot s^{-1}}$	Exchange rate of species i between porous electrode and channel	40
$\dot{s}_{i,m}$	$\mathrm{mol \cdot m^{-2} \cdot s^{-1}}$ $\mathrm{mol \cdot m^{-1} \cdot s^{-1}}$	Chemical production rate of species i in reaction m (in units of $\mathrm{m^{-2}}$ for two-phase reactions and $\mathrm{m^{-1}}$ for three-phase reactions)	1
$\dot{s}_{\mathrm{electron},m}$	$\mathrm{mol \cdot m^{-2} \cdot s^{-1}}$ $\mathrm{mol \cdot m^{-1} \cdot s^{-1}}$	Electron production rate in reaction m (in units of $\mathrm{m^{-2}}$ for two-phase reactions and $\mathrm{m^{-1}}$ for three-phase reactions)	12
t	s	Time	1
$t_\pm$		Transference number	4
T	K	Temperature	9
v	$\mathrm{m \cdot s}$	Channel velocity	40
x	m	Spatial position in dimension of channel length	
X_i		Mole fraction of species i	45
x	m	Spatial position in dimension of channel length	
y	m	Spatial position through channel thickness	
Y_i		Mass fraction of species i	42
z		Number of electrons transferred in charge-transfer step	2
$z_\pm$		Number of ions transferred	4
α		Symmetry factor of charge transfer reaction	9
α		Evaporation coefficient	38
β		Temperature exponent in Arrhenius equation	9
β		Bruggemann coefficient	30
$\Delta\phi$	V	Electric potential difference between electrode and electrolyte	9
ΔG	$\mathrm{J \cdot mol^{-1}}$	Molar Gibbs reaction enthalpy	10
ε_{i}		Volume fraction of phase i	1
ε_0		Initial volume fraction	24
ϕ	V	Electric potential	1
η	V	Overpotential	
μ	$\mathrm{kg \cdot m^{-1} \cdot s^{-1}}$	Gas-phase viscosity	46
μ_{i}	$\mathrm{J \cdot mol^{-1}}$	Chemical potential of species i	11
ν_{i}		Stoichiometric coefficient of species i	11
ρ	$\mathrm{kg \cdot m^{-3}}$	Density	18
σ	$\mathrm{S \cdot m}$	Solid-phase ionic or electronic conductivity	5
τ		Tortuosity of a porous phase	29
τ_{w}	$\mathrm{kg \cdot m^{-1} \cdot s^{-2}}$	Shear-stress factor	41
ξ		Fit parameter describing the microstructure of an electrode	27

References

1. D. Linden and T. B. Reddy, *Handbook of batteries*, McGraw-Hill, New York (2001).
2. W. Vielstich, A. Lamm, and H. A. Gasteiger, *Handbook of fuel cells. Fundamentals, technology and applications.*, Wiley, Chichester, England (2003).
3. B. C. H. Steele and A. Heinzel, *Nature*, **414**, 345 (2001).
4. G. J. Offer, J. Mermelstein, E. Brightman, and N. P. Brandon, *Journal of the American Ceramic Society*, **92**, 763 (2009).
5. D. Sarantaridis and A. Atkinson, *Fuel Cells*, **7**, 246 (2007).
6. Ş. Sörgel, R. Hiesgen, I. Wehl, R. Costa, L. D. Carlé, B. Pascucci, and K. A. Friedrich, *J. Power Sources*, submitted (2011).
7. P. Andrei, J. P. Zheng, M. Hendrickson, and E. J. Plichta, *J. Electrochem. Soc.*, **157**, A1287 (2010).
8. H. Wu, X. Li, and P. Berg, *Electrochimica Acta*, **54**, 6913 (2009).
9. J. Newman, K. E. Thomas, H. Hafezi, and D. R. Wheeler, *Journal of Power Sources*, **119**, 838 (2003).
10. J. Newman and W. Tiedemann, *Aiche Journal*, **21**, 25 (1975).
11. A. M. Colclasure and R. J. Kee, *Electrochimica Acta*, **55**, 8960 (2010).
12. A. Latz and J. Zausch, *Journal of Power Sources*, **196**, 3296 (2011).
13. G. Ning, R. E. White, and B. N. Popov, *Electrochimica Acta*, **51**, 2012 (2006).
14. M. Safari and C. Delacourt, *J. Electrochem. Soc.*, **158**, A562 (2011).
15. M. Doyle and J. Newman, *Electrochimica Acta*, **40**, 2191 (1995).
16. P. M. Gomadam, J. W. Weidner, R. A. Dougal, and R. E. White, *Journal of Power Sources*, **110**, 267 (2002).
17. J. S. Newman and K. E. Thomas-Alyea, *Electrochemical systems*, J. Wiley (2004).
18. V. Ramadesigan, P. W. C. Northrop, S. De, S. Santhanagopalan, R. D. Braatz, and V. R. Subramaniana, *J. Electrochem. Soc.*, **159**, R31 (2012).
19. K. Kumaresan, Y. Mikhaylik, and R. E. White, *J. Electrochem. Soc.*, **155**, A576 (2008).
20. P. Albertus, G. Girishkumar, B. McCloskey, R. S. Sanchez-Carrera, B. Kozinsky, J. Christensen, and A. C. Luntz, *J. Electrochem. Soc.*, **158**, 343 (2011).
21. S. S. Sandhu, J. P. Fellner, and G. W. Brutchen, *Journal of Power Sources*, **164**, 365 (2007).
22. S. B. Adler, J. A. Lane, and B. C. H. Steele, *J. Electrochem. Soc.*, **143**, 3554 (1996).
23. N. F. Bessette, W. J. Wepfer, and J. Winnick, *J. Electrochem. Soc.*, **142**, 3792 (1995).
24. P. Costamagna, P. Costa, and V. Antonucci, *Electrochimica Acta*, **43**, 375 (1998).
25. J. R. Ferguson, J. M. Fiard, and R. Herbin, *Journal of Power Sources*, **58**, 109 (1996).
26. A. Hirano, M. Suzuki, and M. Ippommatsu, *J. Electrochem. Soc.*, **139**, 2744 (1992).
27. W. G. Bessler, S. Gewies, and M. Vogler, *Electrochimica Acta*, **53**, 1782 (2007).
28. D. Larrain, F. Marechal, and D. Favrat, *Journal of Power Sources*, **131**, 304 (2004).
29. S. B. Adler and W. G. Bessler, in *Handbook of Fuel Cells—Fundamentals, Technology and Applications*, W. Vielstich, H. Yokokawa, and H. A. Gasteiger Editors, p. 441, John Wiley & Sons, Chichester, UK (2009).
30. M. Andersson, J. Yuan, and B. Sunden, *Applied Energy*, **87**, 1461 (2010).
31. K. N. Grew and W. K. S. Chiu, *Journal of Power Sources*, **199**, 1 (2012).
32. V. M. Janardhanan and O. Deutschmann, *Zeitschrift Fur Physikalische Chemie-International Journal of Research in Physical Chemistry & Chemical Physics*, **221**, 443 (2007).
33. S. Kakac, A. Pramuanjaroenkij, and X. Y. Zhou, *International Journal of Hydrogen Energy*, **32**, 761 (2007).
34. M. A. Khaleel and J. R. Selman, in *High-temperature solid oxide fuel cells: Fundamentals, design and application*, S. C. Singhal and K. Kendall Editors, p. 291, Elsevier Science, Oxford (2003).
35. A. Nakajo, P. Tanasini, S. Diethelm, J. Van Herle, and D. Favrat, *J. Electrochem. Soc.*, **158**, B1102 (2011).
36. D. M. Bernardi and M. W. Verbrugge, *J. Electrochem. Soc.*, **139**, 2477 (1992).
37. T. E. Springer, T. A. Zawodzinski, and S. Gottesfeld, *J. Electrochem. Soc.*, **138**, 2334 (1991).
38. C. Ziegler and D. Gerteisen, *Journal of Power Sources*, **188**, 184 (2009).
39. D. Cheddie and N. Munroe, *Journal of Power Sources*, **147**, 72 (2005).
40. M. A. Khan, B. Sunden, and J. Yuan, *Journal of Power Sources*, **196**, 7899 (2011).
41. H. Li, Y. Tang, Z. Wang, Z. Shi, S. Wu, D. Song, J. Zhang, K. Fatih, J. Zhang, H. Wang, Z. Liu, R. Abouatallah, and A. Mazza, *Journal of Power Sources*, **178**, 103 (2008).
42. H. Meng and B. Ruan, *International Journal of Energy Research*, **35**, 2 (2011).
43. M. Vogler, A. Bieberle-Hutter, L. Gauckler, J. Warnatz, and W. G. Bessler, *J. Electrochem. Soc.*, **156**, B663 (2009).
44. C. Hellwig, S. Sörgel, and W. G. Bessler, *ECS Transactions*, **35**, 215 (2011).
45. W. G. Bessler and S. Gewies, *J. Electrochem. Soc.*, **154**, B548 (2007).
46. D. Danilov and P. H. L. Notten, *Electrochimica Acta*, **53**, 5569 (2008).
47. A. J. Bard and L. R. Faulkner, *Electrochemical Methods, Fundamentals and Applications*, Wiley, N.Y. (1980).
48. P. W. Atkins and J. De Paula, *Atkins' Physical chemistry*, Oxford University Press, Oxford [u.a.] (2006).
49. V. S. Bagockij, *Fundamentals of electrochemistry*, Wiley-Interscience, Hoboken, NJ (2006).
50. K. Christmann, *Surface Physical Chemistry*, Steinkopff, Darmstadt (1991).
51. D. G. Goodwin, Cantera, in (http://code.google.com/p/cantera, 2001-2010).
52. P. Deuflhard, E. Hairer, and J. Zugck, *Num. Math.*, **51**, 501 (1987).
53. R. Ehrig, U. Nowak, L. Oeverdieck, and P. Deuflhard, in *High performance scientific and engineering computing. Lecture notes in computational science and engineering*, H.-J. Bungartz, F. Durst, and C. Zenger Editors, p. 233, Springer (1999).
54. V. Boovaragavan and V. R. Subramanian, *Electrochemistry Communications*, **9**, 1772 (2007).
55. W. H. Press, W. T. Vettering, S. A. Teukolsky, and B. P. Flannery, *Numerical Recipes in C: The art of scientific computing*, Cambridge University Press, New York (1992).
56. I. Berg, muParser, in (http://muparser.sourceforge.net, 2005-2011).
57. H. Yamin, A. Gorenshtein, J. Penciner, Y. Sternberg, and E. Peled, *J. Electrochem. Soc.*, **135**, 1045 (1988).
58. H. S. Ryu, H. J. Ahn, K. W. Kim, J. H. Ahn, J. Y. Lee, and E. J. Cairns, *J. Power Sources*, **140**, 365 (2005).
59. J. Shim, K. A. Striebel, and E. J. Cairns, *J. Electrochem. Soc.*, **149**, A1321 (2002).
60. D. Marmorstein, T. H. Yu, K. A. Striebel, F. R. McLarnon, J. Hou, and E. J. Cairns, *J. Power Sources*, **89**, 219 (2000).
61. G. Girishkumar, B. McCloskey, A. C. Luntz, S. Swanson, and W. Wilcke, *J. Phys. Chem. Lett.*, **1**, 2193.
62. R. Padbury and X. W. Zhang, *Journal of Power Sources*, **196**, 4436 (2011).
63. W. Xu, J. Xiao, J. Zhang, D. Y. Wang, and J. G. Zhang, *Journal of the Electrochemical Society*, **156**, A773 (2009).
64. S. A. Freunberger, Y. H. Chen, Z. Q. Peng, J. M. Griffin, L. J. Hardwick, F. Barde, P. Novak, and P. G. Bruce, *J. Am. Chem. Soc.*, **133**, 8040 (2011).
65. R. E. Williford and J.-G. Zhang, *Journal of Power Sources*, **194**, 1164 (2009).
66. A. Nyman, M. Behm, and G. Lindbergh, *Electrochim. Acta*, **53**, 6356 (2008).
67. A. Faes, A. Hessler-Wyser, D. Presvytes, C. G. Vayenas, and J. Van Herle, *Fuel Cells*, **9**, 841 (2009).
68. H. Sumi, R. Kishida, J.-Y. Kim, H. Muroyama, T. Matsui, and K. Eguchi, *J. Electrochem. Soc.*, **157**, B1747 (2010).
69. M. Henke, J. Kallo, K. A. Friedrich, and W. G. Bessler, *Fuel Cells*, **11**, 581 (2011).
70. D. Larrain, J. Van herle, and D. Favrat, *Journal of Power Sources*, **161**, 392 (2006).
71. J. Neidhardt, M. Henke, and W. G. Bessler, *ECS Transactions*, **35**, 1621 (2011).
72. C.-H. Wang, M.-C. Lee, T.-J. Huang, Y.-C. Chang, W.-X. Kao, and T.-N. Lin, *Electrochemistry Communications*, **11**, 1381 (2009).
73. W. G. Bessler, S. Gewies, C. Willich, G. Schiller, and K. A. Friedrich, *Fuel Cells*, **10**, 411 (2010).
74. M. P. Eschenbach, R. Coulon, A. A. Franco, J. Kallo, and W. G. Bessler, *Solid State Ion.*, **192**, 615 (2011).
75. I. W. Eames, N. J. Marr, and H. Sabir, *International Journal of Heat and Mass Transfer*, **40**, 2963 (1997).
76. J. Read, *Journal of the Electrochemical Society*, **149**, A1190 (2002).
77. W. G. Bessler, J. Warnatz, and D. G. Goodwin, *Solid State Ion.*, **177**, 3371 (2007).
78. B. J. McBride, M. J. Zehe, and S. Gordon, NASA Glenn coefficients for calculating thermodynamic properties of individual species, National Aeronautics and Space Administration, John H. Glenn Research Center at Lewis Field (2002).
79. R. D. Holmes, H. S. C. O'Neill, and R. J. Arculus, *Geochimica et Cosmochimica Acta*, **50**, 2439 (1986).

B. Horstmann, T. Danner and W. G. Bessler. Precipitation in aqueous lithium–oxygen batteries: a model-based analysis. *Energy & Environmental Science* **6**, 1299 (2013).

Energy & Environmental Science

RSC Publishing

PAPER

View Article Online
View Journal | View Issue

Precipitation in aqueous lithium–oxygen batteries: a model-based analysis

Cite this: *Energy Environ. Sci.*, 2013, **6**, 1299

Birger Horstmann,*[abc] Timo Danner[abc] and Wolfgang G. Bessler[abd]

In this paper we present a model of the discharge of a lithium–oxygen battery with aqueous electrolyte. Lithium–oxygen batteries (Li–O_2) have recently received great attention due to their large theoretical specific energy. Advantages of the aqueous design include the stability of the electrolyte, the long experience with gas diffusion electrodes (GDEs), and the solubility of the reaction product lithium hydroxide. However, competitive specific energies can only be obtained if the product is allowed to precipitate. Here we present a dynamic one-dimensional model of a Li–O_2 battery including a GDE and precipitation of lithium hydroxide. The model is parameterized using experimental data from the literature. We demonstrate that GDEs remove power limitations due to slow oxygen transport in solutions and that lithium hydroxide tends to precipitate on the anode side. We discuss the system architecture to engineer where nucleation and growth predominantly occurs and to optimize for discharge capacity.

Received 7th December 2012
Accepted 31st January 2013

DOI: 10.1039/c3ee24299d

www.rsc.org/ees

Broader context

Rechargeable batteries are generally believed to be an important ingredient in future carbon-neutral energy systems, both for stationary and mobile applications. Stationary applications primarily demand low cost per energy stored, while mobile ones demand low mass per energy stored. Because standard lithium intercalation batteries cannot meet all application requirements for, for example, electric vehicles and grid storage, new battery concepts are currently explored relying on conversion chemistries. During operation of conversion batteries, crystalline phases are formed inside the battery cell. Especially lithium–oxygen batteries receive great attention due to their potentially large gravimetric energy density. In lithium–oxygen batteries, lithium ions and oxygen molecules react to form solid reaction products. Most research is focused on batteries with organic electrolytes where lithium peroxide is formed. Here we provide a model-based analysis of lithium–oxygen batteries with aqueous electrolyte and highlight their advantages. Interestingly, the reaction product first dissolves in the electrolyte before it precipitates as solid lithium hydroxide monohydrate. Our model predicts that precipitation occurs outside the electrode explaining earlier experimental observations. This is advantageous as the electronically insulating precipitates do not hinder the electrode reactions as observed for organic electrolytes.

1 Introduction

The lithium–oxygen (Li–O_2) chemical system is a promising candidate for next-generation batteries. Above all, their theoretical energy density is outstanding.[1–6] In this respect, several designs with various electrolytes have been proposed. Most experiments and models focus on liquid aprotic electrolytes, but the ones used in state-of-the-art lithium-ion batteries decompose in the positive electrode during cycling.[7–14] Solid electrolytes grant stability, but their ionic conductivities are low at room temperature.[15,16] In this paper we illustrate that designs based on aqueous electrolytes are viable alternatives:[17–22]

(1) Oxygen reduction and evolution are well studied and reversible (*cf.*, alkaline fuel cells and electrolyzers[23]).

(2) Aqueous electrolytes offer a large ionic conductivity, not requiring thin-film electrodes (*cf.*, Pb battery[17]).

(3) Water is highly abundant and environmentally friendly.

Some challenges with Li–O_2 batteries remain:

(1) Oxygen solubility and diffusivity are low.[24]

(2) The reaction product lithium hydroxide precipitates and blocks transport paths.[25]

(3) The lithium metal anode strongly reacts with water.

(4) In contact with carbon dioxide lithium carbonates are formed.[26]

In the present work, we circumvent the last two challenges with adjusted model assumptions. Our model assumes the availability of a perfect lithium conducting membrane. Lithium ions can pass this infinitely thin layer without any resistance; all other species cannot pass it. We further assume to work with pure oxygen instead of ambient air. In this way, we can model fully functioning cells.

In this article, we address the first two challenges, that is, oxygen transport and precipitation, and show that these do not represent major obstacles in aqueous-electrolyte based Li–O_2 cells. In aqueous electrolytes, gas diffusion electrodes (GDE) are

[a]*German Aerospace Center (DLR), Institute of Technical Thermodynamics, Pfaffenwaldring 38–40, 70569 Stuttgart, Germany. E-mail: birger.horstmann@dlr.de*
[b]*Stuttgart University, Institute of Thermodynamics and Thermal Engineering (ITW), Pfaffenwaldring 6, 70569 Stuttgart, Germany*
[c]*Helmholtz Institute Ulm (HIU) Electrochemical Energy Storage, Albert-Einstein-Allee 11, 89081 Ulm, Germany*
[d]*Offenburg University of Applied Sciences, Badstraße 24, 77652 Offenburg, Germany*

frequently used, for example, for sensors and fuel cells.[27] In GDEs hydrophobic material, *e.g.*, polytetrafluoroethylene (PTFE) or polyvinylidene fluoride (PVDF), enables the coexistence of gaseous and aqueous phases. If oxygen is supplied to the reaction centers through the gas phase of such GDEs, oxygen transport does not limit the cell performance. In this study, we compare the performance of cells with flooded electrodes to ones with GDEs.

During discharge of an aqueous Li–O_2 battery, lithium ions are produced in the anode and hydroxide ions in the cathode until the dissolved LiOH concentration reaches its solubility limit $c_s \approx 5.2$ mol l^{-1} ($T = 298.15$ K). When discharge continues, lithium hydroxide monohydrate ($LiOH \cdot H_2O$) precipitates. The theoretical energy density of this battery with respect to the mass of water when discharged from $c_{OH^-} = 0$ to $c_{OH^-} = c_s$ is

$$E = \frac{F c^s_{LiOH} U_0}{\rho_{H_2O}} = 490 \text{ W h kg}^{-1}, \quad (1)$$

whereas the theoretical energy density of a cell fully discharged to solid $LiOH \cdot H_2O$ is

$$E = \frac{F U_0}{M_{LiOH \cdot H_2O}} = 2200 \text{ W h kg}^{-1}. \quad (2)$$

Thus, the solid form of the final reaction product is indispensable to reach the energy density of current lithium intercalation technologies.[2] However, solid $LiOH \cdot H_2O$ can block transport paths.[28] Our simulations based on the classical theory of nucleation and growth show that $LiOH \cdot H_2O$ particles predominantly nucleate close to the lithium anode, that is, not in the cathode, in agreement with experimental findings.[20] This results from a salt concentration gradient in the cell. We will discuss how cells could be designed to influence precipitation and avoid pore blocking.

Modeling batteries aims at understanding experimental results and evaluating potential cell concepts. Continuum simulations at the cell level were pioneered by Newman,[29] who coupled the ionic transport in porous electrodes with Butler–Volmer kinetics at the active surfaces.[30] Recently, phase transformation kinetics in batteries became an important topic.[31] Major electrode materials, *e.g.*, lithium iron phosphate, undergo phase transformations during battery operation that result in distinct features in cell voltage. Models of such batteries combine transport in porous media with phase transformation kinetics in active particles. On the one hand, inhomogeneities in the reaction rates emerge even on the micro-scale and electrolyte transport is crucial.[30,32–37] On the other hand, the description of phase boundaries inside active particles requires a thermodynamically consistent approach that allows us to include the full variational chemical potential.[38] Under certain conditions this results in suppression of phase separation.[32,39–41] Next-generation battery chemistries such as lithium–air or lithium–sulfur represent a different class of phase-change systems, where phases do not transform inside solid particles or only on active surfaces, but also in the bulk electrolyte.

Despite considerable experimental activities on Li–O_2 batteries, only few modeling studies have been shown so far. Most modeling activities treat Li–O_2 batteries with aprotic electrolytes,[42–47] and focus on the deposition of solid lithium oxides or lithium carbonates in the cathode. On the one hand, these deposits can block pore space and inhibit the transport of oxygen into the cathode.[42–44,46,47] Since most oxygen is available at the oxygen inlet, reaction products tend to deposit there, so that finally oxygen cannot enter the cathode. On the other hand, these isolating deposits can passivate active surfaces.[45] To the best of our knowledge, only one single model for aqueous electrolytes has been published.[28] This model treats the oxygen reduction reaction and the subsequent precipitation of lithium hydroxide monohydrate within a single global reaction in a flooded cathode. Therefore, it predicts that $LiOH \cdot H_2O$ crystallizes in the cathode and blocks pore space. Our model, instead, takes into account the specifics of aqueous electrolytes and presents approaches to influence precipitation.

This paper contains a comprehensive model of the cell due to the lack of data on experimental Li–O_2 batteries with aqueous electrolytes. Our basic principle for model development is to make the simplest realistic assumptions. At the present stage, the model allows us to predict why a cell fails, but not when it fails. Even though experimental validation is still missing, the model allows analyzing potential design and operation scenarios.

Our paper is structured as follows. We present the mathematical and physical description of our model in Section 2. We arrange this presentation into physical topics, that is, electrochemical reactions, oxygen dissolution, transport phenomena, phase coexistence in GDEs, and precipitation. In Section 3 we present the parameterization of the model based on the literature available for aqueous solutions. We find in Section 4.1 that preferential nucleation close to the anode can be the capacity-limiting process in Li–O_2 batteries. In Section 4.2 we address power limitations during battery discharge in flooded electrodes and in GDEs. We discuss in Section 4.3 implications of our findings on potential cell architecture. Finally, we conclude in Section 5.

2 Physical and mathematical model

In this section our model framework is outlined, which is partially relevant for a wider range of electrochemical systems, for example, the dynamic gas diffusion electrode or the precipitation, as occurring in fuel cells and non-aqueous Li–O_2 batteries. We begin by outlining our implementation of classical electrochemical modeling,[30] *i.e.*, electrochemistry (see Section 2.2), oxygen dissolution (see Section 2.3), and convective transport (see Section 2.4). Then we discuss the phase coexistence of gaseous and liquid phases in gas diffusion electrodes (see Section 2.5). Finally, we extract the kinetics of crystallization from the classical theory of nucleation and growth in Section 2.6.

2.1 Computational domain

During discharge of a Li–O_2 battery, oxygen enters the GDE from a gas channel and dissolves in the aqueous electrolyte (see

Fig. 1). At catalytically active surfaces in the cathode, oxygen and water electrochemically react to form hydroxide ions. While these OH^- ions migrate through the cell to the anode, the Li^+ counter-ions migrate in the opposite direction. They are electrochemically formed at a lithium metal foil, pass a lithium-ion-conducting membrane, which prevents direct contact between lithium metal and the aqueous electrolyte, and dissolve in the electrolyte. Lithium hydroxide monohydrate particles will nucleate when the ion concentration increases sufficiently beyond its solubility limit. In the GDE, gaseous oxygen and liquid electrolyte coexist. On the one hand, an overpressure tries to push water into the GDE, on the other hand, the capillary effect of hydrophobic binders, *e.g.*, PTFE or PVDF, tries to keep it out and leave space for the gas phase.

We model these processes along a single direction, associated with the *y*-coordinate, and divide the computational domain into the lithium anode, the separator, the cathode, and the gas channel. The details of our model are outlined below as a combination of transport physics and chemical reactions. Even though our model is intrinsically dynamic, we make sure that it is thermodynamically consistent and describes stationary states correctly. All symbols are defined in the List of symbols.

2.2 Electrochemical reactions

Two electrochemical half-cell reactions enter our model. In the anode, lithium dissolves in the electrolyte

$$\mathrm{Li} \rightleftarrows \mathrm{Li^+} + \mathrm{e^-}. \tag{3}$$

The reaction rate is calculated with global (*i.e.*, single-step) electrochemical kinetics

$$\dot{s}_{\mathrm{an}} = k_{\mathrm{an}}^{\mathrm{f}} \exp\left(-\alpha_{\mathrm{an}} \frac{F\Delta\Phi_{\mathrm{an}}}{RT}\right) - k_{\mathrm{an}}^{\mathrm{r}} c_{\mathrm{Li^+}} \exp\left((1-\alpha_{\mathrm{an}}) \frac{F\Delta\Phi_{\mathrm{an}}}{RT}\right) \tag{4}$$

where $\Delta\Phi_{\mathrm{an}} = \Phi_{\mathrm{an}} - \Phi_{\mathrm{elyte}}$ is the potential step between the lithium anode and the electrolyte. The cathodic oxygen reduction reaction in alkaline water

$$\mathrm{O_2^{aq}} + 2\ \mathrm{H_2O} + 4\ \mathrm{e^-} \rightleftarrows 4\ \mathrm{OH^-} \tag{5}$$

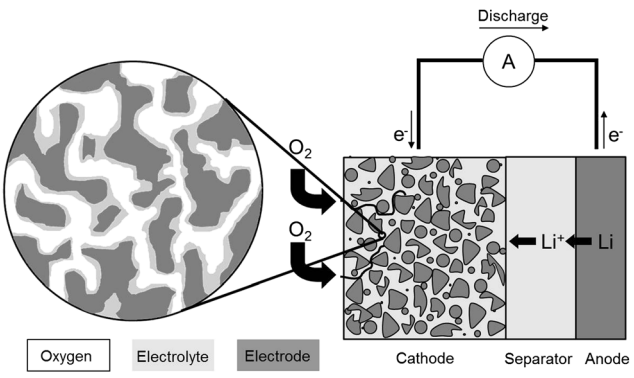

Fig. 1 Schematic representation of a Li–O_2 battery with a gas diffusion electrode.

is also modeled by global kinetics

$$\dot{s}_{\mathrm{ca}} = k_{\mathrm{ca}}^{\mathrm{f}} c_{\mathrm{O_2}} c_{\mathrm{H_2O}}{}^2 \exp\left(-\alpha_{\mathrm{ca}} \frac{F\Delta\Phi_{\mathrm{ca}}}{RT}\right) - k_{\mathrm{ca}}^{\mathrm{r}} c_{\mathrm{OH^-}}{}^4 \exp\left((1-\alpha_{\mathrm{ca}}) \frac{F\Delta\Phi_{\mathrm{ca}}}{RT}\right). \tag{6}$$

Thermodynamics determines the open-circuit voltage under equilibrium conditions ($\dot{s}_{\mathrm{ca}} = \dot{s}_{\mathrm{an}} = 0$). Consequently, the rates of the reverse reactions $k_{\mathrm{an}}^{\mathrm{r}}$, $k_{\mathrm{ca}}^{\mathrm{r}}$ are calculated from the rates of the forward reaction, $k_{\mathrm{an}}^{\mathrm{r}} = k_{\mathrm{an}}^{\mathrm{f}} c_{\mathrm{Li^+}}{}^{-1} \exp(\Delta\mu_{\mathrm{an}}/RT)$ and $k_{\mathrm{ca}}^{\mathrm{r}} = k_{\mathrm{ca}}^{\mathrm{f}} c_{\mathrm{O_2}} c_{\mathrm{H_2O}}{}^2 c_{\mathrm{OH^-}}{}^{-4} \exp(\Delta\mu_{\mathrm{ca}}/RT)$, where $\Delta\mu_{\mathrm{an}}$ and $\Delta\mu_{\mathrm{ca}}$ are the Gibbs reaction enthalpies.[48]

2.3 Oxygen dissolution

Dissolution from gaseous phases is thermodynamically described by Henry's law, $c_{\mathrm{O_2}}^{\mathrm{s}} = H p_{\mathrm{O_2}}$ with the solubility $c_{\mathrm{O_2}}^{\mathrm{s}}$. Henry's law does not include kinetics. Therefore, we model oxygen dissolution within our framework as chemical reaction (see ref. 47)

$$\mathrm{O_2^g} \leftrightarrows \mathrm{O_2^{aq}}. \tag{7}$$

Thus, we can naturally model the oxygen dissolution kinetics with the rate equation

$$\dot{s}_{\mathrm{s}} = k_{\mathrm{s}}^{\mathrm{f}} p_{\mathrm{O_2}} - k_{\mathrm{s}}^{\mathrm{r}} c_{\mathrm{O_2}} \tag{8}$$

The solubility is determined by the equation $\dot{s}_{\mathrm{s}} = 0$, *i.e.*, by the ratio of the reaction rates. We choose to parameterize the solubility *via* thermodynamic data and set

$$\frac{k_{\mathrm{s}}^{\mathrm{r}}}{k_{\mathrm{s}}^{\mathrm{f}}} = \frac{p_{\mathrm{O_2}}}{c_{\mathrm{O_2}}} \exp\left(\frac{\Delta\mu_{\mathrm{s}}}{RT}\right). \tag{9}$$

We determine the forward rate constant $k_{\mathrm{s}}^{\mathrm{f}} = 0.01(2\pi M_{\mathrm{O_2}} RT)^{-0.5}$ from the Hertz–Knudsen equation,[49] assuming that one percent of gas particles hitting the phase boundary enter the liquid.

2.4 Transport

Three transport mechanisms are relevant in this article: diffusion and migration of dissolved species, convection of the liquid solvent, and convection of the gas phase.

Lithium and hydroxide ions as well as oxygen molecules are dissolved in the electrolyte. While oxygen travels from the gas channel to the cathode surface, the lithium hydroxide ions carry charge between the electrodes. First, we describe the transport of this binary salt with concentrated solution theory.[29,50] We reformulate the traditional equations.[47] The concentrations of dissolved particles obey the continuity equations

$$\frac{\partial(\varepsilon_{\mathrm{elyte}} c_i)}{\partial t} = -\mathrm{div}\vec{j}_i^{\mathrm{D}} - \mathrm{div}\vec{j}_i^{\mathrm{M}} - \mathrm{div}\left(c_i \vec{v}_{\mathrm{elyte}}\right) + A^{\mathrm{spez}} \dot{s}_i. \tag{10}$$

The third term in eqn (10) is due to the convective transport of the electrolyte (see eqn (15)), the fourth term is the total production rate due to reactions (see Sections 2.1, 2.2, and 2.5),[47] and the first two terms are the ionic currents due to

diffusion and migration, respectively. For lithium c_+ and hydroxide c_- ions the latter are determined by

$$\vec{j}_{\pm}^{\,\mathrm{D}} = -\varepsilon_{\mathrm{elyte}}^{\beta} D_{\pm} \mathrm{grad} c_{\pm}, \vec{j}_{\pm}^{\,\mathrm{M}} = -\varepsilon_{\mathrm{elyte}}^{\beta} D_{\pm}^{\mathrm{M}} \mathrm{grad} \Phi_{\mathrm{elyte}}. \quad (11)$$

The diffusion and migration coefficients are chosen according to concentrated solution theory

$$D_{\pm} = D_0 + \frac{t_{\pm}}{z_{\pm} F} \frac{\kappa^{\mathrm{D}}}{c_{\pm}} \quad \text{and} \quad D_{\pm}^{\mathrm{M}} = \frac{t_{\pm}}{z_{\pm} F} \kappa \quad (12)$$

with $\kappa^{\mathrm{D}} = 2/z_+ F(t_+ - 1) c_+ \kappa \partial \mu_+ / \partial c_+$. Here t_+ is the transference number of lithium ions, D_0 is the self-diffusion coefficient of lithium hydroxide salt, and κ is its conductivity. The Bruggeman coefficient β takes into account the porosity and tortuosity of the medium. We achieve electro-neutrality by postulating local charge conservation

$$\begin{aligned} 0 &= \sum_i z_i F \frac{\partial \left(\varepsilon_{\mathrm{elyte}} c_i \right)}{\partial t} \\ &= \sum_i z_i F \left[- \mathrm{div} \vec{j}_i^{\,\mathrm{D}} - \mathrm{div} \vec{j}_i^{\,\mathrm{M}} - \mathrm{div} \left(\varepsilon_{\mathrm{elyte}} c_i \vec{v}_{\mathrm{elyte}} \right) + A^{\mathrm{spez}} \dot{s}_i \right] \end{aligned} \quad (13)$$

and choosing electro-neutral initial conditions. Eqn (13) determines the electric potential Φ_{elyte}. We assume here that the transport of dissolved oxygen molecules does not influence the ionic transport.[44,45] In the case of neutral oxygen molecules, the fluxes in eqn (10) are given by

$$\vec{J}_{\mathrm{O_2}}^{\,\mathrm{D}} = -\varepsilon_{\mathrm{elyte}}^{\beta} D_{\mathrm{O_2}} \mathrm{grad} c_{\mathrm{O_2}} \quad \text{and} \quad \vec{J}_{\mathrm{O_2}}^{\,\mathrm{M}} = 0. \quad (14)$$

Eqn (11)–(14) describe the transport of all dissolved species relative to the solvent. The dynamics of the solvent, however, are treated differently. In a closed battery cell, solvent transport is a minor effect and disregarded in typical models.[30] In an open Li–O_2 battery with a GDE, solvent transport is a major issue for two reasons. Firstly, the solvent H_2O is consumed in the cathode during discharge making a constant flux of water into the GDE necessary. Secondly, the phase coexistence of gas and liquid in the GDE requires knowledge of the state of each phase, including pressure (see Section 2.4). A pressure gradient drives water transport and in turn water transport reduces the pressure gradient.

We determine the solvent velocity from Darcy's law, inspired by fuel cell models,[51]

$$\vec{v}_{\mathrm{elyte}} = -\frac{B_{\mathrm{elyte}}}{\eta_{\mathrm{elyte}}} \mathrm{grad} p_{\mathrm{elyte}} \quad (15)$$

with the viscosity η_{elyte} of the liquid phase. The oxygen gas obeys the analogous equation[48]

$$\vec{v}_{\mathrm{gas}} = -\frac{B_{\mathrm{gas}}}{\eta_{\mathrm{gas}}} \mathrm{grad} p_{\mathrm{gas}}, \quad (16)$$

where η_{gas} is the viscosity of gaseous oxygen.

2.5 Gas diffusion electrode

Gas diffusion electrodes (GDEs) contain hydrophobic materials, *e.g.*, PTFE or PVDF. Therefore, the aqueous electrolyte cannot fully flood the electrode. The coexistence of liquid electrolyte and gaseous oxygen in a GDE for a Li–O_2 battery allows for significantly faster oxygen flow towards the electro-active sites *via* the gas phase (see Fig. 1).

As shown below, our description of multi-phase transport in GDEs takes into account the real equation of state of the liquid phase, rarely done in battery modeling. This is crucial here in order to simulate the consumption of solvent at nearly constant salt concentration.

We keep track of the states of the coexisting phases through macroscopic parameters along the computational direction, for example, $\varepsilon_s(y)$, $p_s(y)$, and balance their pressures with an empirical coarse-grained approach.[52–54] In this way, we neglect details of the complex pore network containing hydrophilic/hydrophobic and microscopic/mesoscopic pores. More sophisticated approaches are employed in some steady-state fuel cell models,[27] which are, however, beyond the scope of the present modeling approach.

In the following, we outline our model equations. Phase coexistence is constrained by the total volume at each position y

$$\sum_s \varepsilon_s(p_s) = 1, \quad (17)$$

where the sum extends over all phases s. The volume fractions ε_s depend on the pressures p_s of the phases. In a Li–O_2 battery under regular operating conditions, only liquid and gas are compressible and depend on pressures. Therefore, eqn (17) represents a condition for the pressures of the gas phase p_{gas} and the liquid phase p_{elyte}. In the hydrophobic environment of the GDE, the aqueous phase has a larger pressure than the gaseous phase. This phenomenon is analogous to regular capillary depression. We describe it with the empirical law[52–54]

$$p_{\mathrm{capillary}} = p_{\mathrm{gas}} - p_{\mathrm{elyte}} = -J(s), \quad (18)$$

where $J(s)$ is the Leverett function and $s = \varepsilon_{\mathrm{elyte}} (\varepsilon_{\mathrm{elyte}} + \varepsilon_{\mathrm{gas}})^{-1}$ is the saturation of the liquid phase in the free pore space. The equation of state $\varepsilon_{\mathrm{gas}}(p_{\mathrm{gas}})$ is given by the ideal gas law

$$p_{\mathrm{gas}} V_{\mathrm{gas}} = N_{\mathrm{gas}} RT \quad (19)$$

and the equation of state $\varepsilon_{\mathrm{elyte}}(p_{\mathrm{elyte}})$ by[67]

$$\sum_i \frac{\partial V_{\mathrm{elyte}}}{\partial N_i} c_i = \varepsilon_{\mathrm{elyte}}. \quad (20)$$

Eqn (20) follows from basic thermodynamics valid for any phase. The partial molar volume $\partial V_{\mathrm{elyte}} / \partial N_i$ of species i splits up into two parameters, the partial molar volume $\bar{V}$ at standard pressure p_0 and the partial molar compressibility $\bar{\kappa}$

$$\frac{\partial V_{\mathrm{elyte}}}{\partial N_i} = \bar{V}_i + (p - p_0) \bar{\kappa}_i \quad (21)$$

With these equations of state at hand, we can determine the pressures p_{gas} and p_{elyte} based on eqn (17) and (18). Since the gas phase is absent outside the GDE, eqn (17) (together with eqn (20)) suffices to determine the system dynamics there.

2.6 Nucleation and growth

Because precipitation of lithium hydroxide monohydrate $LiOH \cdot H_2O$

$$Li^{+(aq)} + OH^{-(aq)} + H_2O \rightleftarrows LiOH \cdot H_2O \quad (22)$$

determines the discharge capacity of an aqueous Li–O_2 battery (see Section 4), we develop a detailed model of its kinetics. When the salt concentration $c_{Li^+} = c_{OH^-}$ increases sufficiently beyond the solubility limit $c^s_{Li^+}$, small stable crystal clusters nucleate and start to grow. The process of precipitation involves two main steps, nucleation of seed crystals and subsequent growth of nuclei. It is governed by the quantum behavior of crystals containing ~10 particles and the classical behavior of crystals of size ~1 mm. Consequently, mechanisms of precipitation strongly vary with precipitate and conditions. We choose to model precipitation within the classical theory of nucleation and growth (CNG).[55–58] The theoretical validity of this phenomenological theory has been a subject of discussions,[55] but it has been shown to agree with experiments after adjusting its parameters.[59] In Section 4.3 we analyse the sensitivity of our model to the critical parameters. The CNG assumes that the reaction enthalpy of formation of a single crystal nucleus of size n consists of a bulk and a surface term[55–58]

$$\Delta G = \Delta G_V + \Delta G_A = -n2kT\ln S + A(n)\gamma, \quad (23)$$

where γ is the macroscopic surface energy and the factor of 2 arises for a binary salt. The supersaturation ratio $S = c_{Li^+}/c^s_{Li^+}$ is the driving force for nucleation. For larger nucleus sizes the bulk energy is increasingly negative, whereas the surface energy is increasingly positive. Thus, the former dominates for large crystals and the latter for small crystals. In Fig. 2 we illustrate that the nucleus formation energy ΔG passes a maximum at a critical nucleus size n_{crit}. Crystal clusters must exceed this critical size before they can grow in a stable way. In the case of heterogeneous disc-shaped nucleation[58] the critical formation energy is

$$\Delta G_{crit} = \frac{\gamma^2 a^4}{2kT\ln S}. \quad (24)$$

The rate of nucleation of critical nuclei is then estimated as[55]

$$\dot{N} = D_0 a_D{}^{-2} Z N_0 \exp\left(-\frac{\Delta G_{crit}}{kT}\right). \quad (25)$$

Here the last term represents the activation of a critical complex from thermal fluctuations, N_0 is the number of sites on which nucleation can occur, the Zeldovich factor $Z = (\Delta G_{crit}/3\pi kT)^{0.5}/n_{crit}$ expresses the fact that a critical nucleus can disintegrate again, and the activation frequency for diffusion $D_0 a_D{}^{-2}$ describes a diffusion-limited nucleation process. It is difficult to determine N_0, we will address this issue below.

After this brief discussion of nucleation, we turn to crystal growth. In the simplest case, one can assume linear growth. This is predicted by the excellent bulk diffusion model[55] at large supersaturation ratios $S > 10^{-5}$, which we generally find in our case. Furthermore, linear growth is observed experimentally for quite soluble substances like, for example, potassium chloride.[60,61] The reaction rate for this growth process is

$$\dot{s}_{cryst} = \frac{D_0}{\delta}\left(c_{Li^+} - c^s_{Li^+}\right), \quad (26)$$

where δ is the diffusion layer thickness. We treat the diffusion layer thickness as a parameter (see below).

After summarizing the results of CNG in eqn (25) and (26), we are now describing the application of this theory in the Li–O_2 battery model. In this paper we will distinguish two cases, firstly, nucleation on functional surfaces in the cathode and the separator (see Fig. 3a), and, secondly, nucleation on sedimenting dust particles in a separator of pure electrolyte (see Fig. 3b). These two models differ in the number of nucleation sites N_0 entering eqn (25) and, consecutively, in the specific area for crystal growth A^{spez}_{cryst}.

In the presence of surfaces as in the pore space of a GDE, heterogeneous nucleation on the surfaces (supports) usually dominates homogeneous nucleation. Exact modeling of heterogeneous nucleation requires knowledge of contact angles between crystalline and supporting materials. Battery cells,

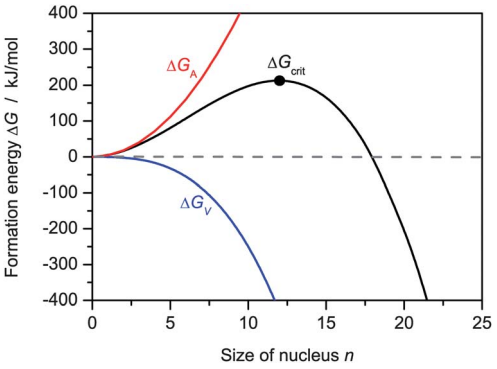

Fig. 2 Formation energy of crystal nucleus consisting of n particles. The bulk contribution ΔG_V is decreasing with size and the surface contribution ΔG_A is increasing with size. The total formation energy goes through a maximum at the critical energy ΔG_{crit}.

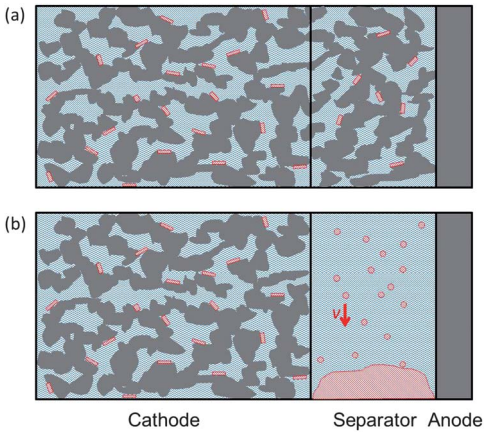

Fig. 3 Schematic depiction of precipitation kinetics: (a) nucleation on surfaces in a porous separator and a cathode, and (b) nucleation on dust particles inside a separating bulk electrolyte with sedimentation due to gravity.

however, contain plenty of different materials and surface morphologies so that an exact approach is not feasible. Thus, we assume disc-shaped heterogeneous nucleation valid for nucleation on crystal material itself (see Fig. 3a). The area supporting the nucleus evolves according to

$$\frac{\partial A_{\text{cryst}}^{\text{spez}}}{\partial t} = \pi {r_{\text{crit}}}^2 \dot{N}(N_0) \quad \text{with} \quad N_0 = A_{\text{cryst}}^{\text{spez},0} a^{-2}. \tag{27}$$

Here $A_{\text{cryst}}^{\text{spez},0}$ is the specific surface area of the pristine cathode/separator surfaces. $LiOH \cdot H_2O$ can subsequently crystallize on top of these discs according to eqn (26), where we assume a constant diffusion layer thickness $\delta = \delta_0$ determined by the pore structure. Crystal growth is described with a single volume fraction

$$\frac{\partial \varepsilon_{\text{cryst}}}{\partial t} = \dot{s}_{\text{cryst}} A_{\text{cryst}}^{\text{spez}} V_{\text{cryst}}^{\text{M}}. \tag{28}$$

As a result, we simulate nucleation and growth of column-shaped crystals on surfaces in the cell.

In state-of-the-art lithium batteries, both the cathode and the separator are porous so that nucleation on surfaces will dominate. In the following we discuss an alternative cell design (see Fig. 3b). Due to the large ionic conductivity of aqueous electrolytes, *e.g.*, lead-acid batteries, a reservoir of pure electrolyte can serve as the separator, as proposed by Stevens *et al.*[20] In such separators, nucleation predominantly occurs on dust particles. These could be small amounts of foreign particles that enter the cell during its assembly, detached carbon particles, or $LiOH \cdot H_2O$ particles from previous battery cycles. In fact, true homogeneous nucleation has been seldom measured. The crystal nuclei sediment due to gravity and form a reservoir of precipitates at the bottom of the cell. Under these conditions, crystal nuclei of different sizes coexist.[62] We evolve the size distribution of spherical crystal nuclei

$$N(r) = f(r)\mathrm{d}r \tag{29}$$

with radii r *via* the equation

$$\frac{\partial f(r)}{\partial t} = \dot{N} {\mathrm{d}r_0}^{-1} \delta_{r_0} - f\tau^{-1} - \frac{\partial}{\partial r}\left(f\frac{\mathrm{d}r}{\mathrm{d}t}\right). \tag{30}$$

The first term in eqn (30) describes nucleation of crystals, where the nucleation rate is $\dot{N}$ with a constant N_0 (see eqn (25)) and the first discretization compartment contains radii from 0 to $\mathrm{d}r_0$. The second term in eqn (30) describes sedimentation due to gravity, modeled as a decay process with typical time

$$\tau(r) = \frac{h\varepsilon_{\text{elyte}}}{v(r)}. \tag{31}$$

Here h is the height of the battery and

$$v(r) = \frac{2}{9} r^2 \frac{g\left(\rho_{\text{LiOH}\cdot\text{H}_2\text{O}} - \rho_{\text{elyte}}\right)}{\eta} \tag{32}$$

the sedimentation velocity from Stoke's law. The last term in eqn (30) represents crystal growth with radial growth rate[60]

$$\frac{\mathrm{d}r}{\mathrm{d}t} = V_{\text{cryst}}^{\text{M}} \dot{s}_{\text{cryst}}(\delta), \tag{33}$$

where the diffusion layer thickness $\delta = r(1 + vr/D_0)^{-0.285}$ is determined by sedimentation.[56] By integrating the crystal size distribution we get the volume fraction $\varepsilon_{\text{cryst}} = V_{\text{cryst}}^{\text{M}} {N_{\text{A}}}^{-1} \int (4/3)\pi r^3 f \mathrm{d}r$ of sedimenting crystals and the volume fraction of the crystal reservoir at the cell bottom

$$\frac{\partial \varepsilon_{\text{res}}}{\partial t} = V_{\text{cryst}}^{\text{M}} {N_{\text{A}}}^{-1} \int \frac{4}{3}\pi r^3 f \tau^{-1} \mathrm{d}r + \dot{s}_{\text{cryst}} A_{\text{res}}^{\text{spez}} V_{\text{cryst}}^{\text{M}}. \tag{34}$$

The second term in eqn (34) denotes direct crystal growth of the reservoir from solution if a film of $LiOH \cdot H_2O$ had already been formed at the cell bottom, *i.e.*, $A_{\text{res}}^{\text{spez}} = h^{-1}$ for $\varepsilon_{\text{res}} \geq r_{\text{crit}}/h$ and $A_{\text{res}}^{\text{spez}} = 0$ for $\varepsilon_{\text{res}} < r_{\text{crit}}/h$. This is the same as heterogenous crystal growth (see eqn (28)).

The latter cell design with nucleation on dust particles contains a separator that can accommodate the precipitate. At the end of discharge, the separator should be completely and homogeneously filled with $LiOH \cdot H_2O$ to increase capacity. This can be achieved, for example, by shaking the cell or stirring the crystal reservoir. We model stirring *via* a diffusion equation

$$\frac{\partial \varepsilon_{\text{res}}}{\partial t} = -C\,\text{div}(-\text{grad}\varepsilon_{\text{res}}). \tag{35}$$

that makes the reservoir homogeneous along the computational direction y.

3 Parameterization and computational details

In Section 2 we presented the general modeling approach. In this section we discuss the parameters for the specific simulation of an aqueous $Li–O_2$ battery. These parameters are based on measurements of lithium hydroxide solutions published in the literature. Our simulations are isothermal at temperature $T_0 = 298.15\ K$. However, we parameterize over a wide temperature range to support future studies on aqueous lithium batteries.

3.1 Geometric structure

We divide the computational domain into the oxygen channel, the cathode, and the separator (see Table 1). A lithium foil terminates the separator. We compare the performance of different cell designs. Thus, we distinguish between a standard cathode (a GDE, *cf.* Fig. 1), and an alternative cathode (a fully flooded cathode). We further distinguish between a standard separator (a porous one with surface nucleation, *cf.* Fig. 3a), and an alternative separator (containing only electrolyte with nucleation on sedimenting dust particles, *cf.* Fig. 3b). Gaseous oxygen can enter the cell from the channel; apart from this, the battery cell is closed.

In this paper, capacities are given with respect to the mass of water. The initial mass of water with respect to the cell area is 0.27 kg m^{-2} (GDE, surface nucleation), 0.29 kg m^{-2} (GDE, nucleation on dust particles), and 0.45 kg m^{-2} (flooded electrode, surface nucleation); the mass of carbon is 0.28 kg m^{-2} ($\rho_{\text{S}} = 2260$ kg m^{-3}); the separator mass is negligible. The mass

Table 1 Structure of porous cell components. If two values are given in the cathode, the first corresponds to a cell with a GDE and the second to a cell with a flooded electrode. In the separator, the first corresponds to a cell with a porous separator and the second to a cell with a bulk separator region

Channel	**Pressure**	101 325 Pa
	Phases (species)	**Volume fraction**
	Gas (O_2^g)	1.0
Cathode	**Thickness**	500 μm
	Phases (species)	**Initial volume fraction**
	Gas (O_2)	0.375/0.0
	Liquid electrolyte (H_2O, Li^+, OH^-, O_2^{aq})	0.375/0.75
	$LiOH \cdot H_2O$	0.0($\rho = 1510$ kg m^{-3})
	Carbon	0.25
Separator/anode	**Thickness**	100 μm
	Phases (species)	**Initial volume fraction**
	Liquid electrolyte (H_2O, Li^+, OH^-, O_2^{aq})	0.8/1.0
	$LiOH \cdot H_2O$	0.0
	Glass separator	0.2/0.0
	Lithium metal (Li^+)	0.0

of oxygen bound in the cell after discharge, 0.3 mg mA^{-1} h^{-1}, depends on capacity.

The height of the battery is $h = 10$ cm (entering the model in the case of sedimentation, see eqn (31)). The typical diffusion layer thickness in the GDE is $\delta_0 = 10$ μm (see eqn (26)). The balance between the volume fractions of gaseous oxygen and liquid electrolyte in GDEs is determined by capillary pressure (see eqn (18)). We describe it based on Kumbur *et al.*[52] with the Leverett function

$$J(s) = 1.5 \times 10^6[-0.000178T + 0.1247]\left(\frac{293\ \mathrm{K}}{T}\right)^6 [0.05(0.0469 - 0.00152 \cdot 0.05 - 0.0406s^2 + 0.1430s^3) + 0.0561\ln(s)] \quad (36)$$

for $s > 0.03$ and $J(s) = 0$ for $s \leq 0.03$. Eqn (36) describes a gas diffusion layer from SGL with five weight percent PTFE loading. We assume an ideal microporous layer that prevents the electrolyte from leaking into the oxygen channel. The stirring coefficient is $C = 10^{-9}$ m^2 s^{-1} (see eqn (35)).

3.2 Thermodynamics

The chemical potentials of species in the electrolyte are a function of the standard potentials μ_i^0, the activities a_i, the partial molar volumes $\bar{V}_i$, and the partial molar compressibilities $\bar{\kappa}_i$

$$\mu_i = \mu_i^0 + \ln a_i + \bar{V}_i(p - p_0) + \bar{\kappa}_i(p - p_0)^2. \quad (37)$$

The standard molar enthalpies h_i^Θ, entropies s_i^Θ, and capacities $c_i^{p,\Theta}$ for the species O_2^g, H_2O, Li^+, and OH^- are taken from Atkins' Physical chemistry.[63] From these values we calculate the temperature-dependent thermodynamic data for the standard states according to

$$H_i^0 = h_i^\Theta + (T - T^0)c_i^{p,\Theta}, \quad (38)$$

$$S_i^0 = s_i^\Theta + Rc_i^{p,\Theta}\ln(T/T^0) \quad (39)$$

$$\mu_i^0 = H_i^0 - TS_i^0. \quad (40)$$

The remaining thermodynamic parameters are found in the context of LiOH and O_2^{aq} solubilities below.

The solubility of oxygen in alkaline water strongly depends on the salt concentration, an effect referred to as salting-out. If lithium hydroxide is added to the solution, the solubility of oxygen is reduced and gaseous molecular oxygen evolves. First, we parameterize the solubility in pure water with the measurements reviewed by Tromans.[64] We deduce as standard thermodynamic properties $h_{O_2}^\Theta = 5.090$ kJ mol^{-1}, $s_{O_2}^\Theta = 166.95$ J mol^{-1} K^{-1}, and $c_{O_2}^{p,\Theta} = 209.35$ J mol^{-1} K^{-1} in the concentration scale. Salting-out is described *via* the empirical Setchenov relation[65]

$$\left(\mu_{O_2} - \mu_{O_2}^0\right)\Big/RT = \ln\left(\frac{c_{O_2}}{\mathrm{mol\ l^{-1}}}\right) + k_{sca}c_{Li^+}. \quad (41)$$

From the measurements of Lang and Zander[65] and Elliot *et al.*[66] we deduce $k_{sca} = 0.01057/(T - 277)$. In Fig. 5 we show that the solubilities obtained in this way agree well with the measurements of Elliot *et al.*,[66] but disagree with the measurements of Lang and Zander[65] However, the trend of the latter agrees with our fit (see Fig. 5).

Measurements of the solubility of lithium hydroxide in water are reviewed in the work of Monnin and Dubois.[25] In this reference, the activities of the solution are taken into account. These are fitted with the Pitzer formalism in the molality scale, which is based on the Debye–Hückel theory.[67] The correct fit for the Pitzer parameter A^Φ is given in ref. 68. The thermodynamic data of $LiOH \cdot H_2O$ are $h_{LiOH \cdot H_2O}^\Theta = -787.07$ kJ mol^{-1}, $s_{LiOH \cdot H_2O}^\Theta = 83.352$ J^{-1} mol^{-1} K^{-1}, and $c_{LiOH \cdot H_2O}^{p,\Theta} = 9.7674$ J mol^{-1} K^{-1}, as determined from the solubility data reviewed in the work of Monnin and Dubois (see Fig. 4).[25]

We further determine the partial molar volumes of H_2O, Li^+, and OH^- from the measurements of Herrington *et al.*[69] and

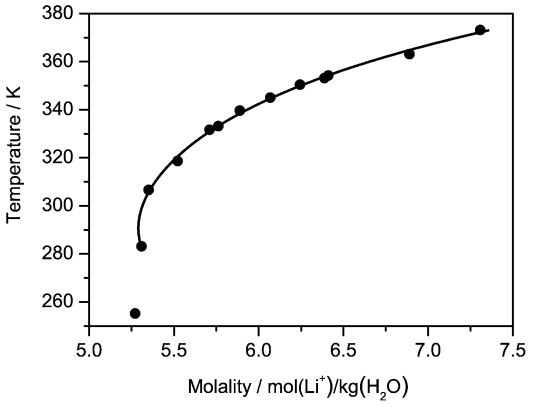

Fig. 4 Solubility of lithium hydroxide in aqueous solution for various temperatures. The symbols represent measurements by Monnin and Dubois[25] The solid line represents the fit with thermodynamic data $h_{LiOH \cdot H_2O}^\Theta$, $s_{LiOH \cdot H_2O}^\Theta$, and $c_{LiOH \cdot H_2O}^{p,\Theta}$ (see text).

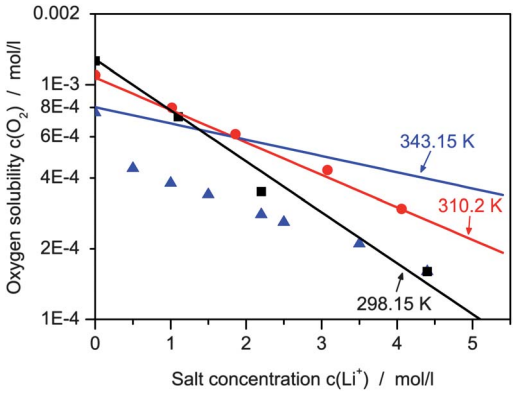

Fig. 5 Oxygen solubility at various salt concentrations and temperatures. The black squares and red circles represent measurements by Elliot *et al.*,[66] the blue triangles represent measurements by Lang and Zander.[65] The solid lines represent fits according to eqn (41).

Roux *et al.*[70] In Fig. 6 we compare our fit with these measurements, which are scarce at high salt concentrations. The partial molar volumes $\bar{V}_i$ are fitted with the Pitzer formalism again (this is possible because $\bar{V}_i = \partial\mu_i/\partial p$ holds), where we include the volumes at infinite dilution as additional parameters.[67,69] The Pitzer parameters are given in Table 2.

We parameterize the partial molar compressibilities according to Millero *et al.*[71] for NaOH, but exchange the partial molar compressibility of Li^+ at infinite dilution with the measurement of Roux *et al.*[70] for LiOH. The partial volumes and compressibilities are important for the liquid equation of state only (see eqn (20) and (21)). Thus, we neglect the partial molar volume of dissolved oxygen due to its low concentration ($\bar{V}_{O_2} = \bar{\kappa}_{O_2} = 0$).

3.3 Transport and kinetics

Electrolyte transport properties strongly depend on viscosity η. The viscosity of lithium hydroxide solutions was measured by Laliberte.[72] With the Einstein–Stokes relationship, we extend the range of measurements of lithium diffusivity at infinite dilution[73]

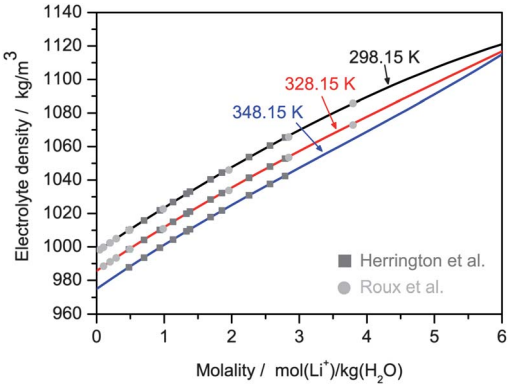

Fig. 6 Density of lithium hydroxide solution at various salt concentrations and temperatures. The squares and circles refer to the measurements of Herrington *et al.*[69] and Roux *et al.*[70] respectively.

$$D_{\pm} = 6.8 \times 10^{-9}\ \mathrm{m^2\ s^{-1}} \frac{\eta_{H_2O}}{\eta}\frac{T}{T_0}\left[8.90466 \times 10^{-4} m_{Li^+}{}^4 - 0.0127732 m_{Li^+}{}^3 + 0.0538298 m_{Li^+}{}^2 - 0.0381098 m_{Li^+} + 0.856882\right] \quad (42)$$

and the oxygen diffusivity in pure water[74]

$$D_{O_2} = 1.693 \times 10^{-6}\ \mathrm{m^2\ s^{-1}} \frac{\eta_{H_2O}}{\eta} \exp\left(-\frac{16\,739\ \mathrm{J\ mol^{-1}}}{RT}\right) \quad (43)$$

to a wider range of salt concentrations and temperatures. The conductivity of a lithium hydroxide solution is[75]

$$\kappa = (-37.72629 + 0.13245\,T/\mathrm{K}) - (27.60862 - 0.14199\,T/\mathrm{K}) m_{Li^+} - 1.39623 m_{Li^+}{}^2 \quad (44)$$

and the transference number is

$$t_+ = 0.1637 \quad (45)$$

We use the standard Bruggeman coefficient $\beta = 1.5$.[29] Convective transport is governed by the permeabilities (see eqn (15) and (16)),[76] in the GDE we use

$$B_{gas} = 5 \times 10^{-12}\ \mathrm{m^2}(1-s)^{3.5},\ B_{elyte} = 5 \times 10^{-12}\ \mathrm{m^2} \times s^{3.5}. \quad (46)$$

In the separator we employ the quasi-infinite permeability

$$B_{elyte} = 10^{-9}\ \mathrm{m^2}.$$

The kinetics of the (electro-)chemical reactions depend on the specific surface areas and the forward reaction rates. In this paper, the former are $A_{ca}^{spez} = 10^6\ \mathrm{m^{-1}}$, $A_{O_2}^{spez} = 10^4\ \mathrm{m^{-1}}$, and $A_{cryst}^{spez,0} = 10^6\ \mathrm{m^{-1}}$; A_{an}^{spez} is chosen to represent a non-porous lithium foil; the latter are $k_{an}^f = 3.84 \times 10^{15}\ \mathrm{mol\ m^{-2}\ s^{-1}}$ ($\beta_{an} = 0.5$) and $k_{ca}^f = 1.1 \times 10^{-17}\ \mathrm{m^4\ mol^{-3}\ s^{-1}}$ ($\beta_{ca} = 0.09$).[77]

The surface energy γ of $LiOH \cdot H_2O$ is taken from the theoretical prediction of Mersmann[78]

$$\gamma = -0.414 \frac{kT}{a^2} \ln\left(c_{Li^+}^s V_{LiOH\cdot H_2O}^M\right) \quad (47)$$

which is in good agreement with the fits of Nielsen *et al.* to experiments.[59]

3.4 Simulation methodology

All simulations are performed with the multi-phase electrochemical simulation tool DENIS.[47,48] The computational domain is divided into 55 compartments with widths between 1 μm and 40 μm, simulations of flooded cathodes utilize a finer discretization at the oxygen inlet. The crystal size distribution is simulated with 29 discretization compartments. We use finite-volume discretization along the computational domain and upwind finite-element discretization for the crystal size distribution. Rate equations are evaluated using the software CANTERA.[79] The discretized equation system is numerically time-integrated with LIMEX.[80,81]

Table 2 Pitzer parameters for electrolyte volume, fitted to polynoms $g = \sum_n g_n \left(\frac{T}{K}\right)^n$

n	$V^0_{Li^+}$	$M_{H_2O}/V^0_{H_2O}$ [83]	$\partial A^\Phi/\partial p$ [84]	$\partial \beta_0^\Phi/\partial p$	$\partial \beta_1^\Phi/\partial p$	$\partial C^\Phi/\partial p$
−1	0	0	-2.437359×10^{-7}	0	0	0
0	7.314575×10^{-5}	-5.585541×10^{3}	3.776468×10^{-9}	$-7.217791 \times 10^{-10}$	-5.443222×10^{-9}	4.335196×10^{-10}
1	-7.532795×10^{-7}	9.323917×10^{1}	-2.333318×10^{-9}	2.833843×10^{-12}	4.358444×10^{-11}	$-1.404855 \times 10^{-12}$
2	2.524541×10^{-9}	-5.295044×10^{-1}	6.308666×10^{-14}	0	$-8.388285 \times 10^{-14}$	0
3	$-2.837367 \times 10^{-12}$	1.513766×10^{-3}	$-6.788572 \times 10^{-17}$	0	0	0
4	0	-2.181633×10^{-6}	0	0	0	0
5	0	1.261439×10^{-9}	0	0	0	0

4 Results and discussion

In this section we discuss the predictions of the model outlined in Sections 2 and 3. We concentrate on understanding and overcoming power and capacity limitations of aqueous Li–O_2 batteries. Above all, this paper highlights that in aqueous Li–O_2 batteries crystallization tends to occur close to the anode. Thus, we begin by explaining this inhomogeneous crystallization effect in Section 4.1. In Section 4.2 we demonstrate how GDEs offer higher power densities than flooded electrodes. By engineering the cell design, crystallization can be altered and cell capacities can be increased as described in Section 4.3.

4.1 Inhomogeneous precipitation

First, we study the galvanostatic discharge of a Li–O_2 battery with a GDE and a porous separator at moderately high currents $i = 10$ A m^{-2} (see Fig. 7). Note that current densities are given with respect to the macroscopic separator area in this one-dimensional model. The cell takes 7.7 h to discharge. For comparison, commercial lithium-ion batteries can be completely discharged in less than 1 h at currents up to $i = 60$ A m^{-2}.[35,82]

The Li–O_2 battery discharges in two stages (see Fig. 7). Initially, up to point B, the salt concentration rises from its initial value to the solubility limit, the voltage decreases slowly, and LiOH·H_2O does not form. After point B, the salt concentration remains constant, slightly above its solubility limit, the voltage is constant, and the LiOH·H_2O volume fraction increases linearly in time. Eventually, at point D, an abrupt drop in cell voltage represents the end of discharge. This happens well before the mean volume fraction of LiOH·H_2O (*ca.* 0.095 at point D) reaches the void pore volume (0.375 for the electrode, 0.8 for the separator, *cf.* Table 1). During discharge, Li^+ forms at the anode and OH^- in the cathode. When the salt concentration increases, oxygen solubility decreases due to salting-out (see eqn (41)). Therefore, the cell voltage slightly decreases during this first stage. LiOH·H_2O crystals nucleate while the salt concentration is slightly overshooting at point B (this will be discussed below, *cf.* Fig. 11). Subsequently, LiOH·H_2O particles grow at a constant rate owing to a small but constant supersaturation and a constant precipitation surface area. During this period the cell voltage is nearly constant. This voltage plateau is typical for conversion reactions under stationary operating conditions, as for example observed in fuel cells. We explain the abrupt end of discharge in the following.

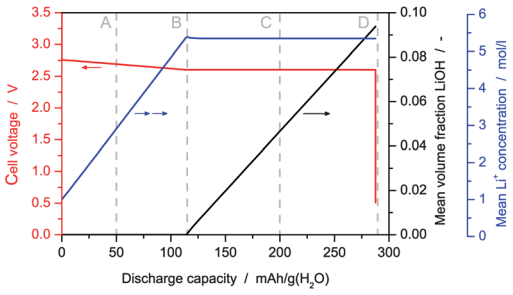

Fig. 7 Discharge of a Li–O_2 battery with a GDE and surface nucleation at $i = 10$ A m^{-2}. Cell voltage (red line), average volume fraction of LiOH·H_2O (black line), and average salt concentration (blue line) are shown. The dashed lines and capital letters refer to data shown in Fig. 8.

Fig. 8 shows spatial profiles of dissolved salt concentration, precipitate volume fraction, and the surface area of precipitation during discharge. At point A, we observe a salt concentration gradient with increasing concentration towards the separator and the anode. We emphasize that this is a fundamental property of aqueous Li–O_2 batteries due to the small transference number of Li^+ (see eqn (45)). Due to this small transference number, the electric potential in the electrolyte induces faster transport of OH^- than of Li^+. The salt concentration gradient must counteract this asymmetry in order to maintain electroneutrality. At point B, just after the nucleation phase, the specific surface area of precipitation shows that most crystal nuclei have formed next to the anode. Consequently, at point C, most LiOH·H_2O is present in this region. The concentration profile has regained a monotonous increase after the turmoil of nucleation, although inhomogeneous precipitation reduces its gradient. At point D, just before end of discharge, the reason for capacity limitation becomes obvious: A film of LiOH·H_2O forms at the separator/anode interface, completely blocking the lithium ion transport. The battery tries to overcome the transport limitations and further increases the salt concentration near the anode. This results in resumed nucleation (see also Fig. 11) and accelerated end of discharge.

In Fig. 9 we illustrate the role of convective flow for the cell performance. The pressure is approximately constant in the separator and drops from the separator towards the oxygen channel in the cathode. The magnitude of the pressure drop increases during cell discharge. It drives the convection of electrolyte from the separator into the GDE, where H_2O is constantly consumed in the oxygen reduction reaction (see eqn (5)). The

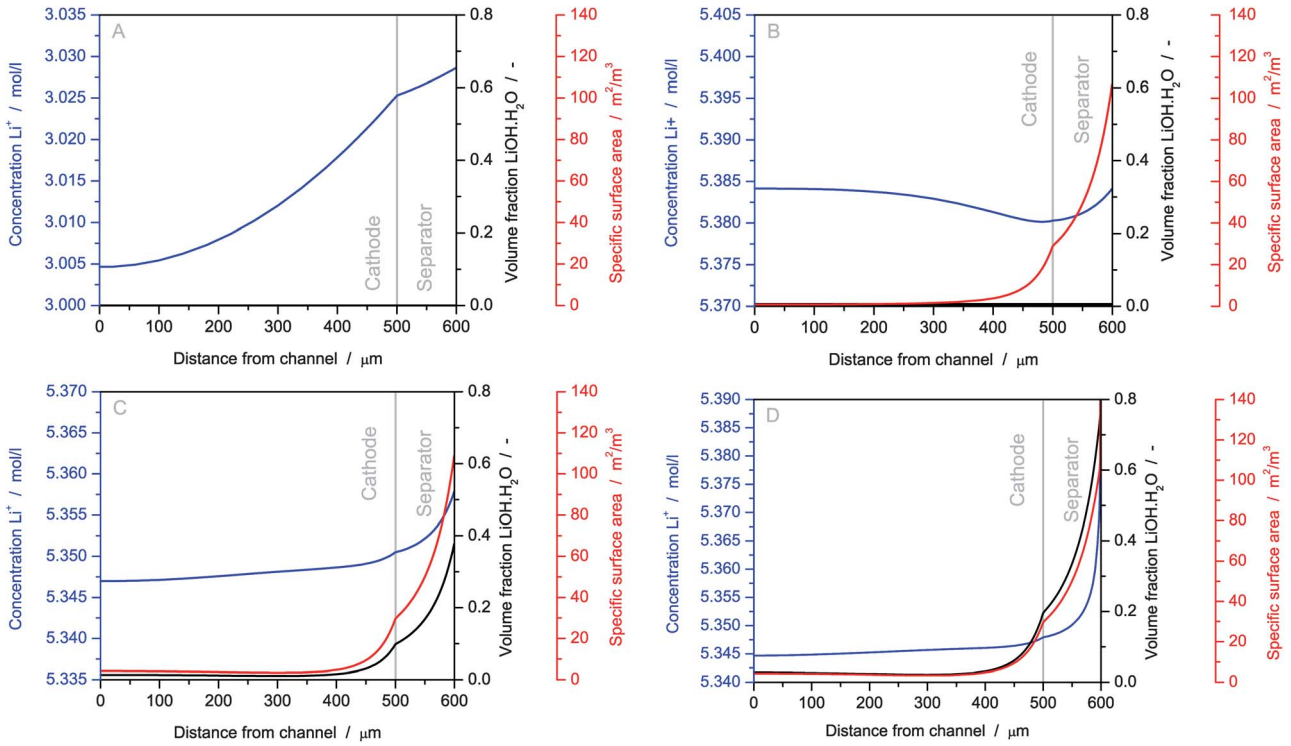

Fig. 8 Spatial profiles of salt concentration, volume fraction of $LiOH \cdot H_2O$ crystals, and the specific surface area of precipitation during galvanostatic cell discharge (i = 10 A m^{-2}) at times A, B, C, D (see Fig. 7). Precipitation occurs mainly close to the anode due to the small transference number of Li^+ (see eqn (45)).

increasing drop reflects the increasingly inhomogeneous liquid phase saturation in the GDE (see eqn (18) and (36)) and leads to slightly inhomogeneous reaction rates in the GDE. The inset of Fig. 9 depicts the decrease in overall electrolyte pressure during cell discharge. The pressure decreases slowly and nonlinearly up to point B, it decreases fast and linearly after point B. The nonlinearity stems from the dependence of the liquid equation of state (see eqn (20)) on the salt concentration. After nucleation, the mean pressure decreases faster because H_2O is now consumed by $LiOH \cdot H_2O$ formation, too (see eqn (22)).

In summary, we have illustrated the main processes inside an aqueous Li–O_2 battery with a GDE during discharge. The cell fails due to inhomogeneous precipitation, particularly due to the formation of a film of $LiOH \cdot H_2O$ at the separator/anode interface. This prediction of our model agrees with experiments and explains the observed film of $LiOH \cdot H_2O$ on the anode-protecting membrane.[20]

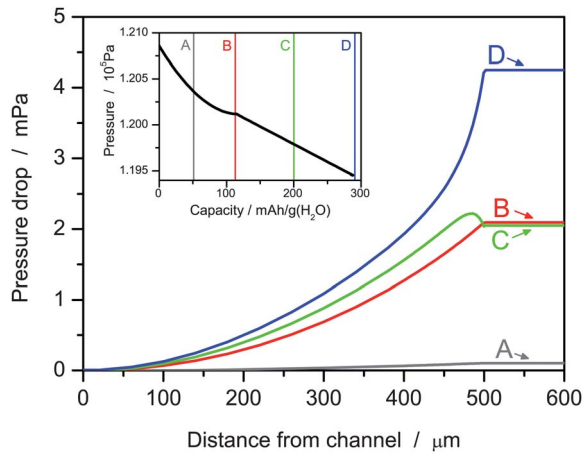

Fig. 9 Pressure drop in electrolyte during discharge of a Li–O_2 battery, normalized to $\Delta p = 0$ at the oxygen channel $y = 0$. The pressure drops inside the GDE from the separator to the oxygen channel, driving convective flow of electrolyte into the GDE. The inset depicts the average electrolyte pressure in the cell that decreases during discharge due to water consumption.

4.2 Rate dependence

Fig. 10 shows the cell behavior during galvanostatic discharge at various currents. The discharge proceeds in the same way as described in Section 4.1 for all currents. An initial voltage drop due to polarization resistances (increasing with current) is followed by a slow linear voltage decrease due to salting-out. A constant voltage plateau occurs after the onset of $LiOH \cdot H_2O$ nucleation. The discharge ends abruptly due to inhomogeneous precipitation. The initial voltage drop is missing at low currents $i \leq 0.1$ A m^{-2} due to negligible overpotentials in the cathode. It is worth noting that the salt concentration reaches its solubility limit and $LiOH \cdot H_2O$ starts to nucleate at approximately the same capacity with respect to the mass of H_2O for any discharge rate; the amount of H_2O determines the amount of salt that can be dissolved in the cell. Most importantly, we observe that the discharge capacity is significantly rate-dependent for high currents $i \geq 10$ A m^{-2}. At higher discharge currents the salt concentration gradient is larger and nucleation is more inhomogeneous. Therefore, precipitation is increasingly

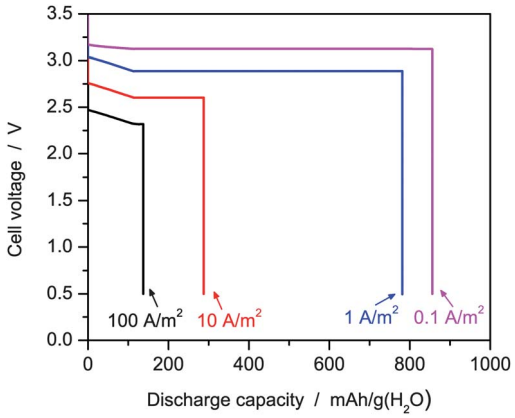

Fig. 10 Cell voltage during galvanostatic discharge of a Li–O_2 battery with a GDE for various discharge currents.

inhomogeneous and the capacity smaller with increasing discharge current.

The overvoltage at the voltage plateau increases with the logarithm of the discharge current in Fig. 10. This indicates that the discharge power is limited by the kinetics of the oxygen reduction reaction (see eqn (5)) in the cathode alone. The ionic transport is fast in aqueous electrolytes, indicated by the small concentration gradients shown in Fig. 8. Thus electrolyte transport and electrode tortuosity do not contribute significantly to the overvoltage at the discharge rates considered.

Analyzing the specific surface area for crystal growth illustrates the crystallization process (see Fig. 11). The surface area sharply increases twice, firstly, when precipitation begins (120 mA h $g_{H_2O}^{-1}$) and, secondly, when discharge ends. Between these events, the surface area is constant during discharge, yet, it depends significantly on current densities. The sharp rises of the surface area correspond to nucleation events. When the salt concentration reaches the critical supersaturation, crystal nucleation sets in. Supersaturation keeps increasing, until the nucleated particles support enough crystal growth. Then, supersaturation is reduced and nucleation stops. At larger discharge currents, more crystal nuclei are required to counteract dissolved salt formation. Therefore, the surface area for crystal growth increases with discharge current. At the end of discharge, transport of ions between the electrodes becomes restricted by precipitates. Consequently, the salt concentration must rise to overcome this and nucleation occurs again.

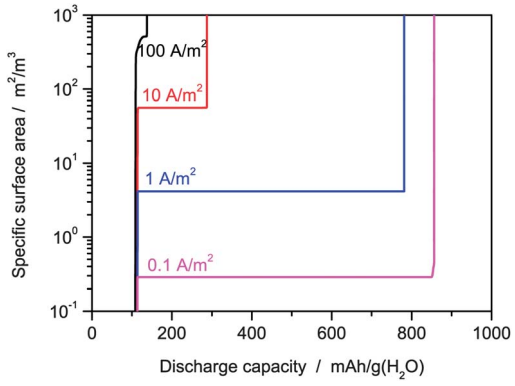

Fig. 11 Specific surface area for crystal growth in the separator region during cell discharge at various currents. After an initial nucleation period, the specific surface stays constant during crystal growth. At end of discharge, nucleation becomes dominant (see text).

In Fig. 12a and c we show the volume fraction of all phases at the end of discharge. Whereas the crystal volume fraction is very inhomogeneous at the moderately high current $i = 10$ A m^{-2} (see Fig. 12a), it is quite homogeneous at the small current $i = 0.1$ A m^{-2} (see Fig. 12). This is why inhomogeneous precipitation limits the discharge capacity at high rates only (see Fig. 10). We observe in Fig. 12c that free volume is still available in the GDE at the end of discharge. The water in the GDE has been consumed nearly completely and the electrolyte pressure cannot deliver additional water into the cathode. This means that inhomogeneous precipitation is not limiting the capacity at low rates.

For comparison, we investigate the discharge of a Li–O_2 battery with a flooded cathode. In this simulation, we neglect the liquid equation of state and electrolyte convection; the density of water is kept constant at $\rho_{H_2O} = 985$ kg m^{-3}; oxygen can only dissolve in the electrolyte from the gas channel. Therefore, oxygen transport is due to electrolyte diffusion only, which limits the cell performance. Resulting discharge behavior is shown in Fig. 13, and spatially resolved oxygen concentration profiles are shown in Fig. 14. Most importantly, battery power is strongly reduced in flooded electrodes, that is, voltages are ~500 mV lower. The flat voltage plateau observed for GDEs (Fig. 10) is absent for flooded cathodes, instead voltages are monotonically decreasing during discharge (Fig. 13). Large currents $i \geq 100$ A m^{-2} cannot even be sustained with flooded electrodes. As shown in Fig. 14, the reason for this behavior is the slow oxygen transport in the liquid phase of a flooded cathode, leading to large concentration gradients and confining electrochemical activity to an electrode volume close to the channel. The rate-dependent capacity (end of discharge) is again due to inhomogeneous precipitation, as discussed above for GDEs (see also Fig. 12b and d). In conclusion, GDEs offer significantly better performance because they strongly reduce oxygen transport limitations as compared to flooded electrodes.

4.3 Design of precipitation

After demonstrating the high performance of aqueous Li–O_2 batteries with GDEs, we further address the rate-dependent discharge capacity due to inhomogeneous precipitation. As pointed out earlier (see Section 2.5), aqueous electrolytes offer high conductivities and allow the use of large non-porous separator regions. In such separator regions, precipitation will probably occur on sedimenting dust particles (see Fig. 3b). In the GDE, however, crystals still nucleate on surfaces. The single unknown parameter in our nucleation model is the density of nucleation sites N_0 (see eqn (25)). One can imagine designing this number by voluntarily adding dust particles. This motivates our approach to optimize the discharge capacity by varying the number of nucleation sites.

We illustrate the effect of varying the number of nucleation sites in the separator region, N_0, with Fig. 15 by discussing the

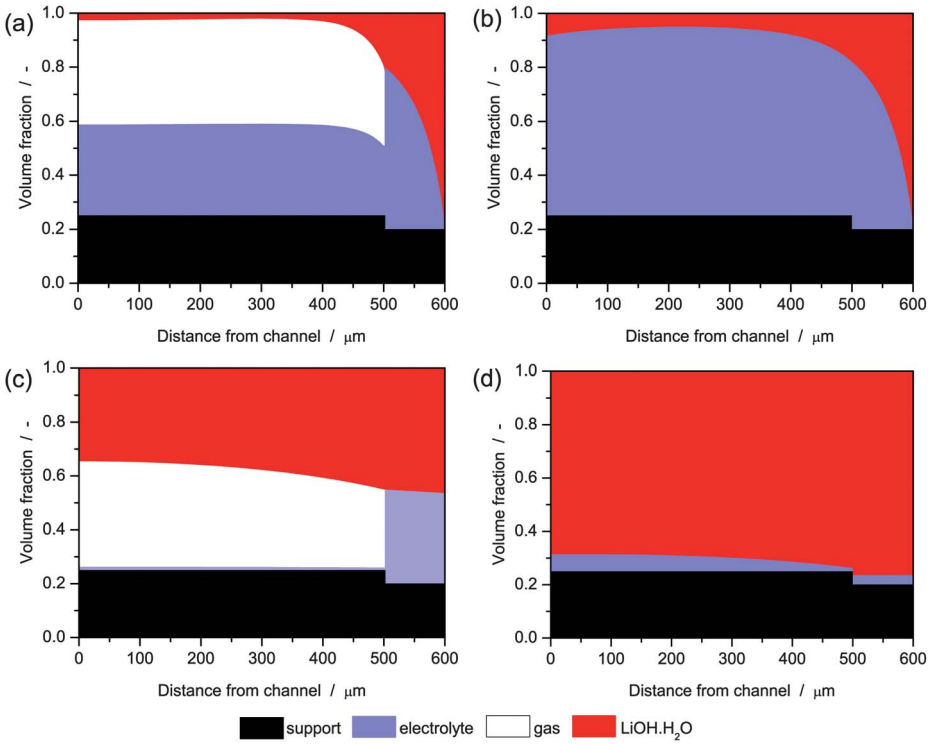

Fig. 12 Volume fraction of phases at end of galvanostatic discharge for a (a) GDE at $i = 10$ A m^{-2}, (b) flooded electrode at $i = 10$ A m^{-2}, (c) GDE at $i = 0.1$ A m^{-2}, and (d) flooded electrode at $i = 0.1$ A m^{-2}.

electrolyte volume at the end of discharge. For small N_0, more crystals nucleate in the cathode than in the separator and consequently discharge ends due to electrolyte depletion at the cathode–separator surface. For large N_0, instead, most crystals nucleate in the separator and discharge ends due to electrolyte depletion in the separator. At intermediate N_0, $LiOH \cdot H_2O$ grows uniformly in the cathode and the separator. Taking into account achievable water purities and surface defect densities, experimental values might be slightly higher than the optimum value $N_0 = 10^{18.5}$ m^{-3} found with this model. However, crystallization outside the cathode is advantageous because it avoids the problem of passivation of active surfaces.

This optimization of the cell capacity is summarized for different N_0 in Fig. 16. The cell capacity is maximum at intermediate N_0, when precipitation occurs in both cathode and separator regions. A bulk separator region has the advantage that external forces (*i.e.*, stirring) can be applied in order to homogenize the sedimented $LiOH \cdot H_2O$, schematically described by eqn (35). This stirring process does not affect the cell performance at low N_0, when precipitation in the cathode dominates. But it is advantageous for large N_0, when precipitation in the separator is critical to cell performance.

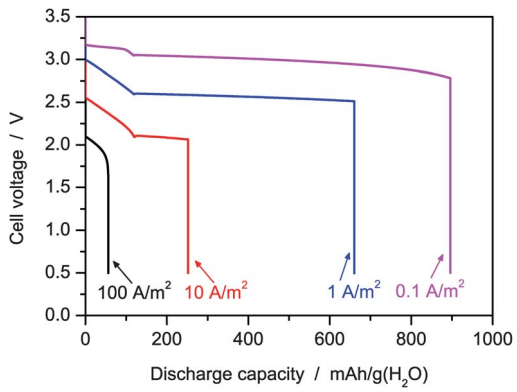

Fig. 13 Cell voltage during galvanostatic discharge of a Li–O_2 battery with a flooded electrode (see text) for various discharge currents.

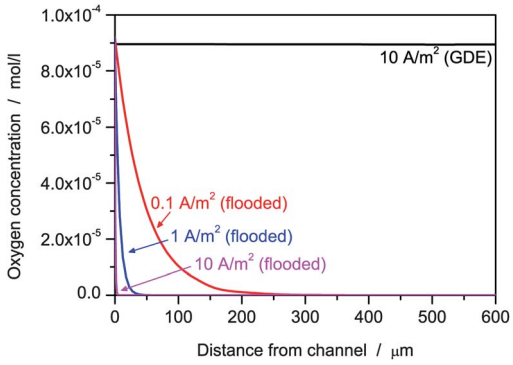

Fig. 14 Dissolved oxygen concentration profile along cell coordinates at 50% SOC for a GDE (see Fig. 7) and a flooded electrode (see Fig. 13). The concentration rapidly drops in the flooded electrode due to the low diffusivity of oxygen in water, even at moderate discharge currents. In the GDE the oxygen concentration is nearly constant.

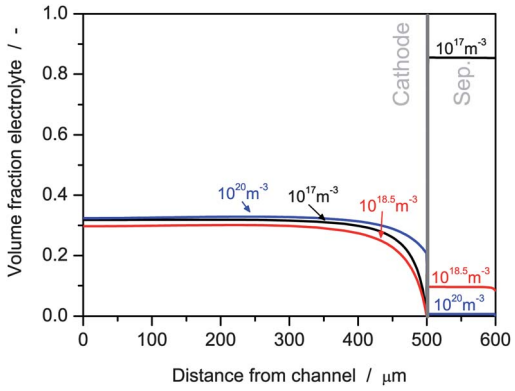

Fig. 15 Volume fraction of a electrolyte at end of discharge with nucleation on dust particles and stirring at various N_0 (see red dots in Fig. 16). At large N_0 precipitation occurs mainly in the cathode, at small N_0 precipitation mainly occurs in the separator. Cell capacity is largest at intermediate N_0 (see Fig. 16).

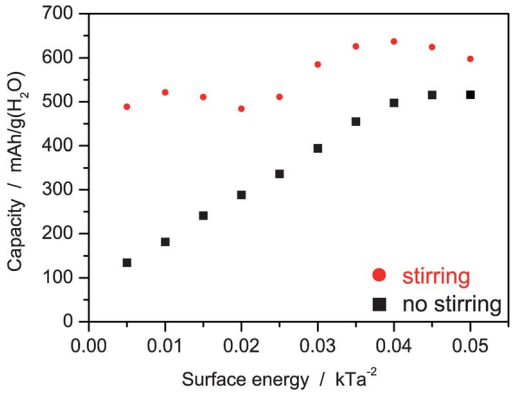

Fig. 17 Discharge capacity of a Li–O_2 battery after galvanostatic discharge at $i = 10$ A m^{-2} with nucleation on dust particles (see Section 2.6) as a function of surface energy γ, that is, the nucleation barrier (see eqn (24)). The number of nucleation centers $N_0 = 10^{18.5}$ is chosen to optimize the capacity (see Fig. 16). In this article we use the surface energy $\gamma = 0.026kT/a^2$ from theoretical predictions,[78] which agree with measurements.[59] Our simulation results strongly depend on the nucleation barrier.

The surface energy γ is another important parameter for adjusting the classical theory of nucleation and growth to experiments.[59] In this paper we choose $\gamma = 0.026kT/a^2$ (see eqn (47)), justified by theory and experiments.[78] A sensitivity analysis of the discharge capacity on γ is presented in Fig. 17. By varying γ over one order of magnitude, we vary the nucleation barrier by two orders of magnitude (see eqn (24)). Without stirring the capacity increases significantly with γ. With stirring the capacity is higher and slightly depends on the surface energy non-monotonically. A greater surface energy generates a greater nucleation barrier and a greater critical supersaturation. Thus, the ratio of salt concentration gradient and critical supersaturation decreases with γ so that precipitation becomes more homogeneous. Without stirring this directly results in an increased capacity. Because stirring creates homogeneous deposits, it enables good capacities even at low critical supersaturations and low γ. The non-monotonic behaviour of the capacity with stirring is due to the complex interplay of inhomogeneous precipitation in cathode and separator regions with different void volumes and nucleation kinetics. To summarize, we find that our model results are sensitive to the exact value of the surface energy γ for precipitation of LiOH·H_2O. However, our general conclusions remain valid and the optimized cell depends on γ only weakly.

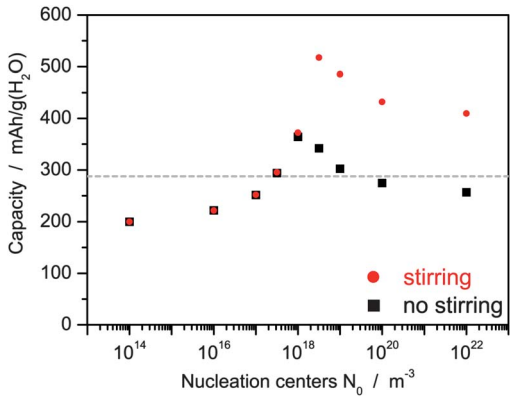

Fig. 16 Discharge capacity of a Li–O_2 battery after galvanostatic discharge at $i = 10$ A m^{-2} with nucleation on dust particles (see Section 2.6) as a function of density of nucleation centers in the separator N_0. The capacity for nucleation on surfaces from Fig. 7 is included as a gray line. The capacity increases at large N_0, when the LiOH·H_2O crystals are actively stirred (red dots) compared to the situation without stirring (black squares).

During the discharge we keep track of the particle size of sedimenting nuclei. A typical distribution is shown in Fig. 18. The particle radius $r \sim 10, \ldots, 100$ μm is determined by the interplay of crystal growth and sedimentation. The size distribution depicted varies along the cell dimension due to inhomogeneous nucleation.

Finally, in Fig. 19 we compare the energy density of galvanostatic discharge of the three designs studied here: First, a GDE with a porous separator, second a flooded cathode with a porous separator, and third a GDE with a bulk separator. In the third case, we use optimized conditions, that is, nucleation on dust particles in the separator, stirring, and $N_0 = 10^{18.5}$ m^{-3}. We observe that flooded electrodes show energy densities comparable with GDEs at low discharge rates. However, they cannot deliver the current densities of modern lithium-ion batteries ($i \geq 10$ A m^{-2}). At high rates, corresponding to discharge in less than one hour ($i = 100$ A m^{-2}), GDEs offer three times larger cell capacities. If we adjust the cell design to the precipitation process, we can reduce capacity fading and further increase the energy density at high rates. A next optimization step would be to enlarge the separator region, which would reduce the relative mass overhead in the cell.

We close this section with a brief outlook on the influence of inhomogeneous precipitation and cell design concepts on charging. On the one hand, a deposit-free cathode offers undisturbed electrochemical surface reactions and transport paths also during charge. On the other hand, inhomogeneously distributed precipitates may limit power densities during charge. While the driving force for dissolution, that is, the difference between salt concentration and solubility, is greater within the porous cathode, the reaction area for dissolution is

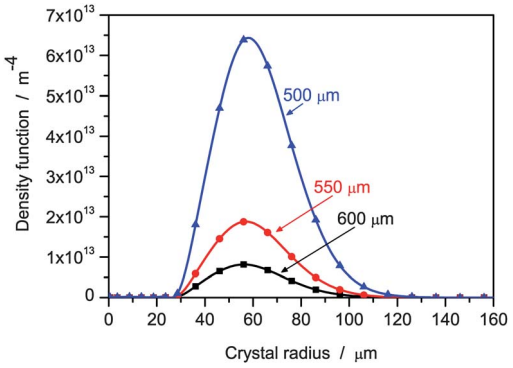

Fig. 18 Particle size distribution density (see eqn (29)) at $y = 600$ μm (blue), $y = 550$ μm (red), $y = 500$ μm (black) at 50% SOC during galvanostatic discharge of a Li–O_2 battery ($i = 10$ A m^{-2}) with nucleation on dust particles and stirring. The lines are interpolations of the simulation results (squares, dots, and triangles). The number of nucleation centers $N_0 = 10^{18.5}$ is chosen to optimize the capacity (see Fig. 16).

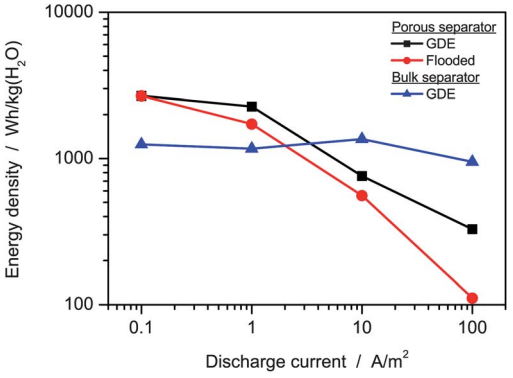

Fig. 19 Energy density of a Li–O_2 battery with different designs: a GDE with surface nucleation, a flooded electrode with surface nucleation, and a bulk separator with nucleation on sedimenting dust particles and stirring. In the latter case, the number of nucleation centers $N_0 = 10^{18.5}$ is chosen to optimize the capacity at $i = 10$ A m^{-2} (see Fig. 16).

greater in the porous separator close to the anode. In a realistic cycling scenario, these effects will not balance each other and cycling efficiency will be reduced. In a bulk separator, however, this issue can be solved by actively distributing the precipitate in the separator, for example by rotating the battery. This would increase the area for dissolution significantly. In summary, a bulk separator region is also advantageous during charging.

5 Conclusions

Lithium–oxygen (Li–O_2) batteries have recently received great attention due to their large theoretical specific energy. Advantages of the aqueous design include the stability of the electrolyte, the existing long-term experience with gas diffusion electrodes (GDEs), and the solubility of the reaction product lithium hydroxide. Not many experimental results on aqueous Li–O_2 batteries have been published, because a number of challenges must be overcome, including the need for a suitable lithium-ion-conducting membrane, a durable lithium metal anode, and strategies to mitigate carbon dioxide poisoning. In this situation, mathematical models have the unique potential to analyze and optimize the fundamental operating principle and therefore support cell development in its initial stages.

In this article we have presented the development and application of a multi-physics continuum model of aqueous Li–O_2 batteries with gas diffusion electrodes. A particular feature of the model is the detailed description of precipitation dynamics based on the classical theory of nucleation and growth. Parameters were taken from the extensive published literature on aqueous solutions. Therefore, the model is completely determined by measured parameters.

Simulations of discharge behavior, including detailed spatiotemporal analysis, were performed for different cell designs and operating conditions. The results showed that batteries with GDEs have high power densities and flat discharge curves. They are superior to cells with flooded electrodes. Inhomogeneous precipitation of solid LiOH·H_2O was predicted to be the capacity-limiting process at high discharge rates relevant for applications. At these rates, precipitation was shown to occur predominantly at the interface between the separator and the anode. This can be interpreted as formation of a solid product film on the anode, explaining earlier experimental findings.[20] Note that this tends to keep solid and insulating reaction products out of the porous cathode, possibly a huge advantage over non-aqueous Li–O_2 batteries. Further simulations showed that the capacity limitation can be reduced by adapting the cell design to the underlying physical processes. Therefore, precipitation of reaction products will not be a key problem for aqueous Li–O_2 batteries. Solid reaction products are in fact necessary to reach competitive energy densities.

To conclude, this paper highlights two major advantages of aqueous Li–O_2 batteries over non-aqueous designs. First, the availability of GDEs reduces limitations due to slow oxygen diffusion. Second, precipitation tends to occur outside of the cathode and to not poison the active surfaces in the cathode. These specific advantages tend to be neglected among the multitude of research on non-aqueous Li–O_2 batteries.

List of symbols

Symbol	Unit	Meaning
α_i	—	Symmetry factor
β	—	Bruggeman coefficient
δ, δ_0	m	Diffusion layer thickness around LiOH·H_2O nucleus
η_j	kg s^{-1} m^{-1}	Viscosity of phase
ε_j	m^3 m^{-3}	Volume fraction of phase
γ	J m^{-2}	Surface energy of LiOH·H_2O
$\bar{\kappa}_k$	m^3 mol^{-1} Pa^{-1}	Partial molar compressibility of species
κ^D	A m^{-1}	Transport parameter of lithium hydroxide solution
κ	A V^{-1} m^{-1}	Conductivity of lithium hydroxide solution
μ_i	J mol^{-1}	Chemical potential of species
μ_i^0	J mol^{-1}	Chemical potential of species in the standard state
$\Delta\mu_i$	J mol^{-1}	Partial molar Gibbs reaction enthalpy

(*Contd.*)

Symbol	Unit	Meaning
Φ_j	V	Electric potential of phase
$\Delta\Phi_i$	V	Electric potential step for reaction
ρ_k	kg m^{-3}	Mass density of species
$A(n)$	m^2	Surface area of $LiOH \cdot H_2O$ nucleus
a	m	Length scale of $LiOH \cdot H_2O$, $a = (V^{M}_{cryst})^{1/3} N_A^{-1}$
a_D	m	Length scale of $LiOH^{aq}$, $a_D = (c_{Li^+})^{-1/3} N_A^{-1}$
a_k	—	Activity of species
A_k^{spez}	m^2 m^{-3}	Specific surface of reaction
B_j	m^2	Permeability of porous material
C	m^{-2} s^{-1}	Coefficient for stirring of $LiOH \cdot H_2O$ reservoir
c_k	mol m^{-3}	Concentration of species
c_k^s	mol m^{-3}	Solubility of species
D_0	m^2 s^{-1}	Self-diffusion coefficient of Li^+
D_k	m^2 s^{-1}	Diffusion coefficient of species
D_k^M	mol m^{-1} s^{-1} V^{-1}	Migration coefficient of species
E	W h kg^{-1}	Gravimetric energy density
$f(r)$, $N(r)$	m^{-1}, —	Size distribution of $LiOH \cdot H_2O$ nucleus
ΔG, ΔG_{crit}, ΔG_V, ΔG_A	J mol^{-1}	Formation energy of crystal nucleus
g	m s^{-2}	Standard gravity
h	M	Height of battery cell
H	mol m^{-3} Pa^{-1}	Henry's constant
H_k^0	J mol^{-1}	Standard partial molar enthalpy of species
h_k^Θ, s_k^Θ, $c_k^{p,\Theta}$		Thermodynamic data of species
$\vec{j}_\pm^D$, $\vec{j}_\pm^M$	mol m^{-2} s^{-1}	Diffusion and migration flux
$J(s)$	Pa	Leverett function
k_i^f, k_i^r		Forward and backward kinetic coefficient of reaction
M_k	kg mol^{-1}	Molar mass of species
n, n_{crit}	—	Number of particles in $LiOH \cdot H_2O$ nucleus
N_0	m^{-3}	Number of nucleation sites
$\dot{N}$	s^{-1} m^{-3}	Nucleation rate of $LiOH \cdot H_2O$
N_j	mol	Number of particle of phase or species
p_k	Pa	Partial pressure of species, pressure of phase
r	m	Radius of $LiOH \cdot H_2O$ nucleus
S	—	Relative supersaturation of LiOH
S_k^0	J mol^{-1}	Standard partial molar entropy of species
$\dot{s}_i$	mol m^{-2} s^{-1}	Rate of reaction
s	—	Saturation of the liquid phase in GDE
t_k	—	Transference number of species
U_0	V	Open-circuit voltage
V_j^M	m^3 mol^{-1}	Molar volume of phase
v^g	m s^{-1}	Velocity of sedimentation
$\bar{V}_k$	m^3 mol^{-1}	Partial molar volume of species
$\vec{v}_j$	m s^{-1}	Convection velocity of phase
V_j	m^3	Volume of phase
y	m	Coordinate along modelling domain
Z	—	Zeldovitch factor
z_k	—	Charge number of species

List of constants

Symbol	Value
F	96 485.256 A s mol^{-1}
k	1.380662×10^{-23} J K^{-1}
N_A	6.0221367×10^{23} mol^{-1}
p_0	101 325 Pa
R	8.3145353 J k^{-1} mol^{-1}
T_0	298.15 K

Notes and references

1 G. Girishkumar, B. McCloskey, A. C. Luntz, S. Swanson and W. Wilcke, *J. Phys. Chem. Lett.*, 2010, **1**, 2193.
2 J. Christensen, P. Albertus, R. S. Sanchez-Carrera, T. Lohmann, B. Kozinsky, R. Liedtke, J. Ahmed and A. Kojic, *J. Electrochem. Soc.*, 2012, **159**, R1.
3 P. G. Bruce, S. A. Freunberger, L. J. Hardwick and J.-M. Tarascon, *Nat. Mater.*, 2012, **11**, 19.
4 Y.-C. Lu, B. M. Gallant, D. G. Kwabi, J. R. Harding, R. R. Mitchell, M. S. Whittingham and Y. Shao-Horn, *Energy Environ. Sci.*, 2013, **6**, 750.
5 B. Scrosati, J. Hassoun and Y.-K. Sun, *Energy Environ. Sci.*, 2011, **4**, 3287.
6 C.-X. Zu and H. Li, *Energy Environ. Sci.*, 2011, **4**, 2614.
7 K. M. Abraham and Z. Jiang, *J. Electrochem. Soc.*, 1996, **143**, 1.
8 S. A. Freunberger, Y. Chen, Z. Peng, J. M. Griffin, L. J. Hardwick, F. Bardé, P. Novák and P. G. Bruce, *J. Am. Chem. Soc.*, 2011, **133**, 8040.
9 F. Mizuno, S. Nakanishi, Y. Kotani, S. Yokoishi and I. Hideki, *Electrochemistry*, 2010, **78**, 403.
10 R. Black, S. H. Oh, J.-H. Lee, T. Yim, B. Adams and L. F. Nazar, *J. Am. Chem. Soc.*, 2012, **134**, 2902.
11 B. D. McCloskey, R. Scheffler, A. Speidel, D. S. Bethune, R. M. Shelby and A. C. Luntz, *J. Am. Chem. Soc.*, 2011, **133**, 18038.
12 B. D. Mccloskey, A. Speidel, R. Scheffler, D. C. Miller, V. Viswanathan, J. S. Hummelshøj, J. K. Nørskov and A. C. Luntz, *J. Phys. Chem. Lett.*, 2012, **3**, 997.
13 Z. Peng, S. A. Freunberger, Y. Chen and P. G. Bruce, *Science*, 2012, **337**, 563.
14 G. Chase, S. Zecevic, W. Walker, J. Uddin, K. Sasaki, V. Giordani, V. Bryantsev, M. Blanco and D. Addison, International Patent application no. 2011033821, 2010.
15 B. Kumar, J. Kumar, R. Leese, J. P. Fellner, S. J. Rodrigues and K. M. Abraham, *J. Electrochem. Soc.*, 2010, **157**(1), A50.
16 H. Kitaura and H. Zhou, *Energy Environ. Sci.*, 2012, **5**, 9077.
17 F. Beck and P. Rüetschi, *Electrochim. Acta*, 2000, **45**, 2467.
18 K. Suto, S. Nakanishi, H. Iba and K. Nishio, An Aqueous Li–Air Battery Based on a Novel Reservoir Concept, in *15th International Meeting on Lithium Batteries*, Montreal, 2010.
19 J. Suntivich, H. A. Gasteiger, N. Yabuuchi, H. Nakanishi, J. B. Goodenough and Y. Shao-Horn, *Nat. Chem.*, 2011, **3**, 546.
20 P. Stevens, G. Toussaint, G. Caillon, P. Viaud, P. Vinatier, C. Cantau, O. Fichet, C. Sarrazin and M. Mallouki, *ECS Trans.*, 2010, **28**, 1.
21 Y. Wang and H. Zhou, *J. Power Sources*, 2010, **195**, 358.

22 H. He, W. Niu, N. M. Asl, J. Salim, R. Chen and Y. Kim, *Electrochim. Acta*, 2012, **67**, 87.
23 F. Bidault, D. J. L. Brett, P. H. Middleton and N. P. Brandon, *J. Power Sources*, 2009, **187**, 39.
24 D. Tromans, *Ind. Eng. Chem. Fundam.*, 2000, **39**, 805.
25 C. Monnin and M. Dubois, *J. Chem. Eng. Data*, 2005, **50**, 1109.
26 S. F. Bender, J. W. Cretzmeyer and T. F. Reise, in *Handbook of Batteries*, ed. D. Linden and T. B. Reddy, McGraw-Hill, New York, 2002.
27 T. Springer and T. Zawodzinski, *J. Electrochem. Soc.*, 1991, **138**, 2334.
28 J. P. Zheng, P. Andrei, M. Hendrickson and E. J. Plichta, *J. Electrochem. Soc.*, 2011, **158**, A43.
29 J. S. Newman and K. E. Thomas-Alyea, *Electrochemical Systems*, J. Wiley, 2004.
30 M. Doyle, T. F. Fuller and J. Newman, *J. Electrochem. Soc.*, 1993, **140**, 1526.
31 V. Ramadesigan, P. W. C. Northrop, S. De, S. Santhanagopalan, R. D. Braatz and V. R. Subramanian, *J. Electrochem. Soc.*, 2012, **159**, R31.
32 T. R. Ferguson and M. Z. Bazant, *J. Electrochem. Soc.*, 2012, **159**, A1967.
33 W. Dreyer, J. Jamnik, C. Guhlke, R. Huth, J. Moskon and M. Gaberscek, *Nat. Mater.*, 2010, **9**, 448.
34 W. Dreyer, C. Guhlke and R. Huth, *Phys. D*, 2011, **240**, 1008.
35 C. Hellwig, S. Sörgel and W. G. Bessler, *ECS Trans.*, 2011, **32**, 215.
36 W. Lai and F. Ciucci, *Electrochim. Acta*, 2011, **56**, 4369.
37 W. Lai and F. Ciucci, *Electrochim. Acta*, 2010, **56**, 531.
38 M. Z. Bazant, 2012, arXiv:1208.1587.
39 P. Bai, D. A. Cogswell and M. Z. Bazant, *Nano Lett.*, 2011, **11**, 4890.
40 R. Malik, F. Zhou and G. Ceder, *Nat. Mater.*, 2011, **10**, 587.
41 D. A. Cogswell and M. Z. Bazant, *ACS Nano*, 2012, **6**, 2215.
42 S. S. Sandhu, J. P. Fellner and G. W. Brutchen, *J. Power Sources*, 2007, **164**, 365.
43 R. E. Williford and J.-G. Zhang, *J. Power Sources*, 2009, **194**, 1164.
44 P. Andrei, J. P. Zheng, M. Hendrickson and E. J. Plichta, *J. Electrochem. Soc.*, 2010, **157**, A1287.
45 P. Albertus, G. Girishkumar, B. McCloskey, R. S. Sánchez-Carrera, B. Kozinsky, J. Christensen and A. C. Luntz, *J. Electrochem. Soc.*, 2011, **158**, A343.
46 Y. Wang, *Electrochim. Acta*, 2012, **75**, 239.
47 J. P. Neidhardt, D. N. Fronczek, T. Jahnke, T. Danner, B. Horstmann and W. G. Bessler, *J. Electrochem. Soc.*, 2012, **159**, A1528.
48 W. Bessler, S. Gewies and M. Vogler, *Electrochim. Acta*, 2007, **53**, 1782.
49 I. W. Eames, N. J. Marr and H. Sabir, *Int. J. Heat Mass Transfer*, 1997, **40**, 2963.
50 A. Latz and J. Zausch, *J. Power Sources*, 2011, **196**, 3296.
51 D. M. Bernardi and M. W. Verbrugge, *J. Electrochem. Soc.*, 1992, **139**, 2477.
52 E. C. Kumbur, K. V. Sharp and M. M. Mench, *J. Electrochem. Soc.*, 2007, **154**, B1315.
53 E. C. Kumbur, K. V. Sharp and M. M. Mench, *J. Electrochem. Soc.*, 2007, **154**, B1305.
54 E. C. Kumbur, K. V. Sharp and M. M. Mench, *J. Electrochem. Soc.*, 2007, **154**, B1295.
55 J. Nyvlt, O. Söhnel, M. Matuchova and M. Broul, *The Kinetics of Industrial Crystallization*, ed. J. Skrivanek, ACADEMIA, Prague, 1985, p. 350.
56 O. Söhnel and J. Garside, *Precipitation: Basic Principles and Industrial Applications*, Butterworth-Heinemann, Oxford, 1992, p. 391.
57 J. W. Mullin, *Crystallization*, Butterworth-Heinemann, Oxford, 4th edn, 2001, p. 594.
58 D. Kashchiev and G. M. van Rosmalen, *Cryst. Res. Technol.*, 2003, **38**, 555.
59 A. E. Nielsen and O. Sohnel, *J. Cryst. Growth*, 1971, **11**, 233.
60 A. E. Nielsen, *J. Cryst. Growth*, 1984, **67**, 289.
61 R. N. Singh and A. C. Chatterji, *J. Phys. Chem.*, 1958, **62**, 1408.
62 S. G. Rinaldo, W. Lee, J. Stumper and M. Eikerling, *Electrochem. Solid-State Lett.*, 2011, **14**, B47.
63 P. W. Atkins and J. De Paula, *Atkins' Physical Chemistry*, Oxford University Press, Oxford, 2006.
64 D. Tromans, *Hydrometallurgy*, 1998, **48**, 327.
65 W. Lang and R. Zander, *Ind. Eng. Chem. Fundam.*, 1986, **25**, 775.
66 A. J. Elliot, M. P. Chenier and D. C. Ouellette, *Fusion Eng. Des.*, 1990, **13**, 29.
67 K. S. Pitzer, in *Activity Coefficients in Electrolyte Solutions*, ed. K. S. Pitzer, CRC Press Inc., Boca Raton, FL, 1991.
68 N. M. Moller, *Geochim. Cosmochim. Acta*, 1988, **52**, 821.
69 T. M. Herrington, A. D. Pethybrldge and M. Roffey, *J. Chem. Eng. Data*, 1986, **31**, 31.
70 A. H. Roux, G. Perron and J. E. Desnoyers, *Can. J. Chem.*, 1984, **62**, 878.
71 F. J. Millero, G. K. Ward and P. V. Chetirkin, *J. Acoust. Soc. Am.*, 1977, **61**, 1492.
72 M. Laliberte, *J. Chem. Eng. Data*, 2007, **52**, 321.
73 E. L. Littauer and K. C. Tsai, *Electrochim. Acta*, 1979, **24**, 351.
74 P. Han and D. M. Bartels, *J. Phys. Chem.*, 1996, **100**, 5597.
75 P. J. Gierszewski, R. C. Prasad and D. W. Kirk, *Fusion Eng. Des.*, 1992, **15**, 279.
76 N. Zamel, X. Li, J. Becker and A. Wiegmann, *Int. J. Hydrogen Energy*, 2011, **36**, 5466.
77 S. Pinnow, N. Chavan and T. Turek, *J. Appl. Electrochem.*, 2011, **41**, 1053.
78 A. Mersmann, *J. Cryst. Growth*, 1990, **102**, 841.
79 D. G. Goodwin, Cantera, http://code.google.com/p/cantera.
80 R. Ehrig, U. Nowak, L. Oeverdieck and P. Deuflhard, in *High performance scientific and engineering computing. Lecture notes in computational science and engineering*, ed. H.-J. Bungartz, F. Durst and C. Zenger, Springer, 1999, p. 233.
81 P. Deuflhard, E. Hairer and J. Zugck, *Numer. Math.*, 1987, **51**, 501.
82 M. Safari and C. Delacourt, *J. Electrochem. Soc.*, 2011, **158**, A562.
83 *CRC Handbook of Chemistry and Physics*, ed. D. R. Lide, CRC Press Inc., Boca Raton, FL, 89th edn, 2008.
84 J. Ananthaswamy and G. Atkinson, *J. Chem. Eng. Data*, 1984, **29**, 81.

T. Danner, B. Horstmann, D. Wittmaier, N. Wagner and W. G. Bessler. Reaction and transport in Ag/Ag2O gas diffusion electrodes of aqueous Li-O2 batteries: Experiments and modeling. *Journal of Power Sources* **264**, 320–332 (2014).

Journal of Power Sources 264 (2014) 320–332

Contents lists available at ScienceDirect

Journal of Power Sources

journal homepage: www.elsevier.com/locate/jpowsour

Reaction and transport in Ag/Ag_2O gas diffusion electrodes of aqueous $Li–O_2$ batteries: Experiments and modeling

Timo Danner [a,b,c,d,*], Birger Horstmann [a,b,c], Dennis Wittmaier [a], Norbert Wagner [a], Wolfgang G. Bessler [b,d]

[a] German Aerospace Center (DLR), Institute of Technical Thermodynamics, Stuttgart, Germany
[b] University of Stuttgart, Institute for Thermodynamics and Thermal Engineering, Stuttgart, Germany
[c] Helmholtz Institute Ulm for Electrochemical Energy Storage (HIU), Ulm, Germany
[d] Institute of Energy System Technology (INES), Offenburg University of Applied Sciences, Offenburg, Germany

HIGHLIGHTS

- We model aqueous lithium–oxygen batteries.
- Multiphase-flow in porous gas diffusion electrodes is important.
- We perform half-cell experiments for validation and parameterization.
- We identify rate-limiting processes via sensitivity analysis.

ARTICLE INFO

Article history:
Received 4 February 2014
Received in revised form
11 February 2014
Accepted 24 March 2014
Available online 26 April 2014

Keywords:
Lithium–oxygen ($Li–O_2$)
Aqueous electrolyte (LiOH)
Half-cell experiments
Modeling and simulation
Electrode design

ABSTRACT

Aqueous lithium–oxygen batteries are promising candidates for electric energy storage. In this paper we present and discuss a multiphase continuum model of an aqueous lithium–oxygen single cell including reactions and transport in a porous gas diffusion electrode (GDE). The model is parameterized using in-house half-cell experiments and available literature data on aqueous electrolytes. We validate our transport model with cyclic voltammetry and electrochemical impedance spectroscopy measurements over a wide range of temperatures (25, 40, 55 °C) and electrolyte concentrations (0.1–2 M). We observe very good agreement between simulations and measurements during oxygen reduction conditions. A sensitivity analysis of the validated model demonstrates the influence of the porous structure on GDE performance and gives directions for the future development of electrodes.

1. Introduction

Recent years showed a strong public interest in the topic of battery-powered electric vehicles. However, the energy density of state-of-the-art lithium-ion technology [1–3] is not sufficient to reach driving ranges comparable to those of cars with conventional combustion engines. Therefore, a focus of research turned to so called post-lithium-ion technologies, including lithium–sulfur (Li–S) and lithium–oxygen ($Li–O_2$) [3]. $Li–O_2$ batteries [4–7] are particularly interesting due to their very high theoretical energy density. Still, there are many challenges in the development of this type of battery [8], including insufficient cycling efficiency and lifetime.

Research on metal–air batteries ($Zn–O_2$, $Li–O_2$, $Al–O_2$, $Mg–O_2$, etc.) using aqueous electrolytes started in the early 1960s [9]. The many practical problems associated with the technology, however, obviated a successful development other than for small primary cells. A renewed interest grew when Abraham et al. [10] demonstrated the use of organic electrolytes in $Li–O_2$ batteries. During discharge the solid reaction product Li_2O_2 is supposed to form in the porous structure of the cathode:

$$2Li^+ + O_2 + 2e^- \rightleftharpoons Li_2O_2. \quad (1)$$

In this case, the capacity of the $Li–O_2$ cell is limited by the low conductivity of Li_2O_2 [11–15] and an insufficient supply of oxygen through the pore space [16–19]. However, the standard electrolytes

* Corresponding author. Helmholtz Institute Ulm, Albert-Einstein-Allee 11, 89069 Ulm, Germany. Tel.: +49 (0)731 50 34306; fax: +49 (0)731 50 34011.
E-mail address: Timo.Danner@DLR.de (T. Danner).

http://dx.doi.org/10.1016/j.jpowsour.2014.03.149
0378-7753/

used in lithium-ion technology were found to be unstable in Li–O_2 batteries [7,20,21]. Thus, the focus of research currently concentrates on finding a suitable and stable organic electrolyte [22–24].

Aqueous electrolyte systems offer an interesting alternative [25]. The lithium salt solutions used in aqueous electrolytes are highly conductive [26] and, most importantly, the alkaline environment offers reversible electrochemistry over a wide potential window. The oxygen reduction reaction (ORR) [27] and oxygen evolution reaction (OER) in alkaline media are given by

$$2H_2O + O_2 + 4e^- \rightleftharpoons 4OH^-. \quad (2)$$

At the anode lithium metal is typically used to attain high energy densities. However, lithium reacts vigorously with water. A challenge for this system is therefore the development of a water-impermeable separator which is stable towards lithium and the alkaline electrolyte [28]. Several groups dedicated their efforts to this topic and demonstrated stable operation over a large number of cycles [29–31].

During discharge, the concentrations of Li^+ and OH^- ions increase until the solubility limit is reached and solid $LiOH \cdot H_2O$ precipitates in the battery according to

$$Li^+ + OH^- + H_2O \rightleftharpoons LiOH \cdot H_2O. \quad (3)$$

This can cause problems similar to the aprotic system, that is, pore clogging and coverage of active surfaces. Yet, solid discharge products are necessary to reach high energy densities. The two-step mechanism of aqueous-electrolyte cells (Eqs. (2) and (3)) offers interesting design options, as charge transfer and precipitation can be spatially separated in contrast to organic-electrolyte cells (Eq. (1)). For example, the problem of pore clogging can be solved by the use of bulk separators as proposed by Stevens et al. and Horstmann et al. [32,33]. Here, the anode protective layer (APL) can be coated with a polymer such that the precipitates accumulate on the bottom of the separator. This way the solid products do not block or passivate the GDE and higher capacities can be reached.

The cathode material and design is of key importance for cell functionality. In the present work, we propose and demonstrate the use of gas diffusion electrodes (GDE) for aqueous Li–O_2 cells. GDEs allow attaining high power densities which are necessary for the propulsion of electric vehicles. A GDE usually consists of a porous catalyst layer (CL) which is placed on a support material such as a metal mesh for mechanical stability. The coexistence of gas and liquid phases in the porous structure ensures a fast transport of oxygen and a large specific surface area.

The saturation management is of utmost importance for the successful operation of the GDE as it determines the transport within the porous network. On the one hand a dry operation will hamper GDE performance due to insufficient transport of the reactants in the liquid phase. On the other hand a flooded electrode limits the transport of oxygen to the active sites. The development of Li–O_2 cathodes benefits from the extensive work done on this topic in fuel cell research [34]. Here, many studies deal with the transport and water management in gas diffusion layers (GDLs) of polymer electrolyte membrane fuel cells (PEMFCs) [35–41].

Mathematical models are very helpful for understanding the interplay of transport and kinetics in these complex systems. Thus, a validated continuum model has to be regarded as an important tool which allows a concerted development of GDE structure and properties in order to optimize its performance. First models on transport in GDEs of alkaline fuel cells were developed on the assumption of thin electrolyte films [42] within the porous electrode. This was later extended to the model of flooded agglomerates [43]. A good agreement with experimental findings was reported [44] for the latter type.

In this work we follow a twofold approach to increase understanding of relevant processes in GDEs of aqueous Li–O_2 batteries. We perform half-cell experiments in a three-electrode setup with commercial Ag_2O electrodes [45]. The extensive parameter field is then used to parameterize and validate a 1D continuum model. The model includes electrochemical reactions, multi-phase transport in the GDE, as well as solid precipitation. This paper is structured as follows: In the first part of this article we explain the measurement setup and give an overview of experimental findings (Section 2). In Section 3 we present a 1D continuum model of a GDE operating in aqueous LiOH solutions. The model is parameterized (Section 4.1) and validated (Section 4.2) based on data from the literature and our own experiments. The validated model is then used in Section 4.3 for the identification and discussion of important parameters, such as porosity, tortuosity or electrode thickness, in order to improve the performance of the GDE.

2. Experiments

2.1. Experimental setup

We used a silver/silver oxide electrode from Bayer Material Science [45] for our measurements. The electrode was made up of a nickel mesh and a catalyst layer consisting of Ag_2O, Ag, and PTFE. The total thickness of the electrode was ~560 μm. An electron micrograph of the cross-section through the electrode is shown in Fig. 1. The inset on the right shows a close-up view of the porous structure in the catalyst layer. The thin connecting fibers stem from the hydrophobic binder and ensure the coexistence of a gas and a liquid phase in the void volume. The electrode was structurally characterized using mercury intrusion porosimetry and krypton adsorption measurements (Porotec). Structural parameters are listed in Table 1. The experimental setup is described in detail in Ref. [46].

Aqueous solutions of LiOH were prepared from $LiOH \cdot H_2O$ (98% Alpha Aesar) and demineralized water at room temperature (0.1, 0.2, 1 and 2 M). The cell was operated under purified oxygen atmosphere at atmospheric pressure. A SGL 35DC gas diffusion layer (Sigracet) was used to prevent leakage of the electrolyte into the gas channel. The temperature of the electrolyte solution was controlled via a water bath. We used the HydroFlex electrode (RHE, Gaskatel) as reference electrode directly in the electrolyte solution. An IM-6 Electrochemical Workstation (Zahner) controlled the electrochemical measurements.

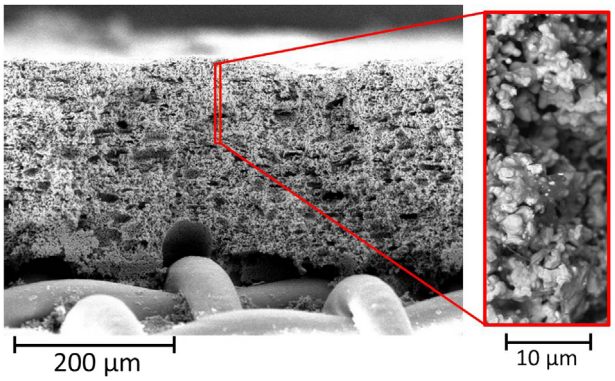

Fig. 1. Electron microscope image of an Ag_2O gas diffusion electrode studied in this work. The inset shows a close-up image of the microstructure of the catalyst layer. Smaller particles are connected by thin filaments forming larger agglomerates. The thin filaments originate from the hydrophobic binder.

Table 1
Summary of geometrical and structural parameters for each modeling domain. Initial values for saturation in the cathode (volume fraction of gas and electrolyte) and electrolyte composition change due to different operating conditions.

Cathode	Thickness (L_{GDE})	560 μm
	Discretization points	30
	Porosity	0.48
	Mean pore diameter	1 μm
	Phases	**Species**
	Conductor	e^-
	Gas	$O_2^{(gas)}$
	Electrolyte	H_2O, OH^-, Li^+, $O_2^{(aq)}$
Electrolyte	Thickness (L_{EB})	10 cm
	Discretization points	10
	Sample holder (L_{SH})	2 cm ($\gamma = 30°$)
	Reference electrode (L_{ref})	5 mm
	Porosity	1
	Phases	**Species**
	Electrolyte	H_2O, OH^-, Li^+, $O_2^{(aq)}$
Anode	Thickness	100 μm
	Discretization points	1
	Porosity	0.99
	Phases	**Species**
	Conductor	e^-
	Electrolyte	H_2O, OH^-, Li^+, $O_2^{(aq)}$
Atmosphere	**Phases**	**Species**
	Gas	$O_2^{(gas)}$

2.2. Electrochemical characterization

Measurements for oxygen reduction and oxygen evolution at a fixed electrolyte concentration were consecutively performed with the same electrode and in the same electrolyte solution. Prior to the measurements we fully reduced the electrode at 500 mV vs. RHE [46]. This ensured a characterization under stable conditions. First we recorded cyclic voltammograms and electrochemical impedance spectra for the ORR at 25, 40, and 55 °C. After these measurements we fully oxidized the electrode at a voltage of 1850 mV vs. RHE and reran the same protocol under oxygen evolution conditions. Finally, we repeated the CV measurements at 55 °C in the ORR regime in order to check the electrode for possible degradation. A fresh electrode of the same batch was used for each concentration. In the following Sections 2.2.1 and 2.2.2 we discuss the typical features of cyclic voltammograms and impedance spectra of the porous Ag GDE. Measurements at different concentrations showed qualitatively similar results. Therefore, we restrict our discussion on the measurements in 1 M LiOH solution. Results at other concentrations are shown in the course of model validation in Section 4.2.

2.2.1. Cyclic voltammetry

As mentioned above, cyclic voltammograms were recorded separately in the ORR and OER regime. The potential range covered was 1100 mV–500 mV (ORR) and 1400 mV–1950 mV (OER), respectively. In order to avoid significant double layer currents, we chose a slow scan rate of 1 mV s^{-1}.

The cyclic voltammograms for the ORR are shown in Fig. 2 at potentials below 1.1 V vs. RHE. After an initial drop, the cathodic current stabilized at a small value. At even lower potential the current linearly increased with overpotential during the forward scan. A rise in temperature led to steeper slopes in the linear region. The maximum current was drawn at the turning point of the potential scan. Below potentials of 1 V the forward and the backward sweep collapsed onto a single line. The initial drop in current can be tentatively attributed to a reduction of remaining small amounts of silver oxides. Surface layers of Ag_2O could have formed at potentials close to the equilibrium potential of silver oxide reduction (1173 mV vs. RHE). At higher overpotentials Ag_2O was fully consumed and the current was produced by the continuous reduction of oxygen alone. The porous structure of the GDE allowed good transport of reactants and caused a linear increase of current towards higher overpotentials. We did not observe a limiting current even at potentials as low as 100 mV. This demonstrates a good supply of oxygen to the active sites of the GDE. Thus, the peak performance of the electrode was not determined by mass or charge transport processes. The negligible contribution of a double layer current to the total current was confirmed by the collapsing lines of the forward and the backward scan. The facile kinetics showed an increase of ORR activity at elevated temperatures. A dashed line in Fig. 2 represents the repetition of the CV measurements after operating the electrode under oxygen evolution conditions. It shows the same features as for the fresh electrode. The lower current, however, is a clear indication for a degradation of the electrode during oxygen evolution. Possible degradation mechanisms are discussed below.

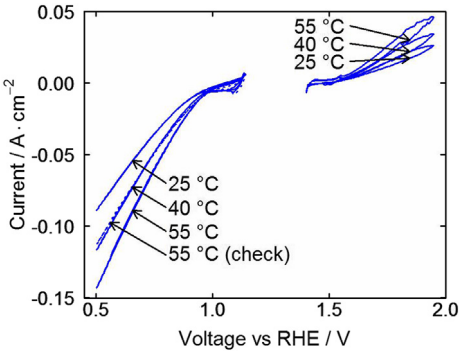

Fig. 2. Experimental cyclic voltammograms under oxygen reduction (0.5–1.1 V) and oxygen evolution (1.4–1.95 V) conditions at 25, 40 and 55 °C. The collapsing lines of forward and backward scan under oxygen reduction demonstrate a negligible influence of the double layer current and a good transport of reactants. The dotted line refers to a repeated measurement of a cathodic cycle at 55 °C after operating the electrode under oxygen evolution conditions. The lower cathodic currents indicate a degradation of the electrode during oxygen evolution.

Cyclic voltammograms of the oxygen evolution are shown above 1.4 V in Fig. 2. At low overpotentials, we measured a small and constant anodic current. After a small dip, the current continuously increased towards higher potentials. A gap of around 0.01 A cm^{-2} existed between the forward and the backward scan. At high currents the measurement signal showed significant noise. This coincided with the observation of gas bubble formation on the GDE surface [47]. These bubbles obstructed the transport of reactants in the porous electrode. The statistical process of bubble nucleation generated noise which could be seen in the current signal. Mechanical damage of the electrode was not observed. In the potential range studied, silver exhibits several oxidation states [48]. The small dips in the forward and backward scan arose from the corresponding changes in oxidation states. Some of these states are reported to dissolve in alkaline electrolytes [49,50]. The resulting changes in the surface morphology in turn led to a degradation of GDE performance. This could also have been an explanation for the gap between forward and backward scan. Another possible reason might have been a depletion of hydroxide ions in the liquid electrolyte due to transport limitations.

2.2.2. Electrochemical impedance spectroscopy

We report electrochemical impedance spectra (EIS) during oxygen reduction only. Under oxygen evolution conditions, the formation of gas bubbles heavily deteriorated the measurement signal. We used EIS to identify relevant physical processes at various polarizations. Impedance spectra were recorded in the frequency range from 100 mHz to 10 kHz. At each working point, the system was polarized for 5 min at a constant voltage before a sinusoidal excitation with an amplitude of 5 mV was imposed.

Fig. 3 shows Nyquist plots of impedance spectra at various polarizations in 1 M LiOH solution and at a temperature of 25 °C. The symbols represent data points from our measurements and the solid lines are the result of a fit to the equivalent circuit depicted in the inset of Fig. 5. The recorded spectra show features typical for porous electrodes [51]. The lowest impedance in the complex plane diagram corresponds to the highest frequency of the sinusoidal excitation. Towards lower frequencies the imaginary part linearly increased at an angle of approximately 45° with the real axis. Attached to this linear region we saw a depressed semi-circle. The radius of the semi-circle and thus the resistance of the electrode decreased at higher polarizations.

The resistance in the limit of infinite frequencies corresponded to the combined ohmic resistance of electrode and liquid electrolyte. The conductivity of silver, however, is very high and the contribution of the electrode to the resistance can be neglected [52]. If the signal of the excitation was not penetrating the whole pore space of the GDE [51], a linear increase of the imaginary part was observed. This feature typically appeared if the penetration depth λ was much smaller than the characteristic length scale of the pore network. In the present case the characteristic length was approximately given by the thickness of the electrode L_{GDE}. The penetration depth follows as [51]

$$\lambda = \sqrt{0.5 r Z_{elode} \sigma_{elyte}}. \quad (4)$$

Here Z_{elode} is the impedance of the electrode, r the mean pore diameter and σ_{elyte} the specific conductivity of the electrolyte solution.

At a frequency of 1 kHz λ is around 3 μm for the measurements shown in Fig. 3. The impedance of the electrode and the penetration depth increase [53] towards lower frequencies. At 1 Hz λ is already around 20 μm and the ac signal is able to penetrate the whole pore space. In this case, the impedance is comparable to one of a flat electrode and is represented by a deformed semi-circle in the complex plane diagram. The diameter of the semi-circle is representative of the charge transfer resistance of the ORR. This is consistent with the observed decrease in kinetic resistance at higher polarizations.

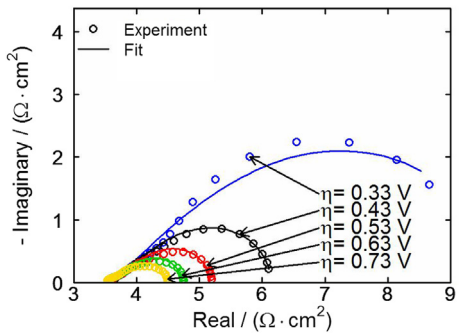

Fig. 3. Nyquist plot (100 mHz–10 kHz) of impedance spectra recorded in aqueous 1 M LiOH solution at a temperature of 25 °C. The corresponding Bode plot can be found in Fig. 7. Symbols represent experimental data and lines show results of the fit to the equivalent circuit model (see Fig. 5).

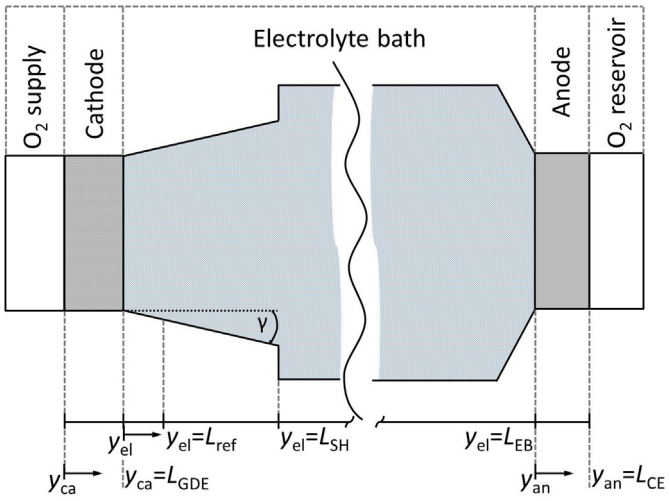

Fig. 4. Schematic depiction of the modeling domain. The geometry represents the experimental half-cell setup introduced in Section 2.1. In our 1D continuum model we consider a transport of reactants in cathode, electrolyte bath and anode. During discharge oxygen is consumed in the cathode (ORR) and released by the reverse reaction (OER) at the anode.

3. Modeling

We use the electrochemical modeling software DENIS [19,54] for our numerical simulations outlined below. Originally developed for the simulation of fuel cells, we recently showed its ability to model Li–O_2 batteries. Our model for aqueous Li–O_2 batteries is described in detail in Ref. [33]. We will summarize it briefly, and discuss some modifications which are due to a different geometry. A list of symbols is given in Table 2, the constitutive equations of the model are provided in Table 3, and the kinetic mechanism is given in Table 4.

3.1. Model description

Fig. 4 schematically depicts the modeling domain describing the experimental setup (Section 2.1). In the 1D continuum model, the

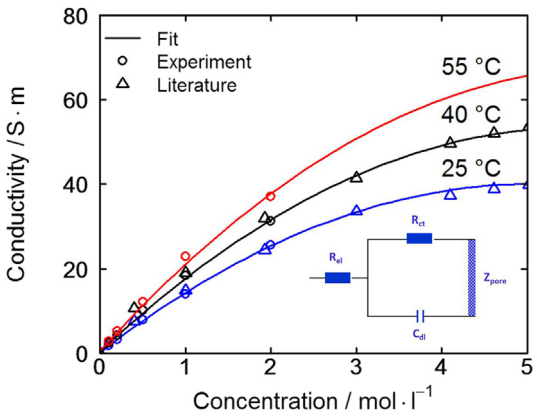

Fig. 5. Conductivity of electrolyte solution at various concentrations and temperatures. Open circles represent our experimental data as a result of the fit to the equivalent circuit (inset). Data from the literature (open triangles) [26] is shown for comparison. The solid line represents the best fit to the combined set of data (see Eq. (7)). Inset: Equivalent circuit model for porous electrodes [46]. The circuit consists of the electrolyte resistance R_{el}, the charge transfer resistance (R_{ct}) and double layer capacitance (c_{dl}). Z_{pore} represents a transmission line element [60].

Table 3
Summary of model equations [54,19] (cf. list of symbols for definition).

Process	Model equation	Nr.
Gas-phase transport in porous electrodes		
Species conservation	$\frac{\partial(\varepsilon_{\text{gas}} c^{\text{gas}} X_i)}{\partial t} = -\frac{\partial J_i^{\text{diff}}}{\partial y} - \frac{\partial J_i^{\text{conv}}}{\partial y} + \sum_m A_m^V \dot{s}_{i,m}$	(12)
Diffusive fluxes	$\frac{\partial(c^{\text{gas}} X_i)}{\partial y} = -\sum_{j \in S_g} \frac{X_i J_j^{\text{diff}} - X_j J_i^{\text{diff}}}{D_{ij}^{\text{eff}}}$	(13)
Convective fluxes	$J_i^{\text{conv}} = \upsilon_{\text{gas}} X_i c^{\text{gas}}$	(14)
Flow velocity	$\upsilon_{\text{gas}} = \frac{B_{\text{gas}}}{\eta_{\text{gas}}} \frac{\partial p_{\text{gas}}}{\partial y}$	(15)
Equation of state	$\rho_{\text{gas}} = \frac{p_{\text{gas}}}{RT} \overline{M}$	(16)
Liquid-phase transport in porous electrodes		
Species conservation	$\frac{\partial(\varepsilon c_i)}{\partial t} = -\frac{\partial\left(J_i^{\text{diff}}\right)}{\partial y} - \frac{\partial\left(J_i^{\text{migr}}\right)}{\partial y} - \frac{\partial(J_i^{\text{conv}})}{\partial y} + \sum_m A_m^V \dot{s}_{i,m}$	(17)
Diffusive fluxes	$J_i^{\text{diff}} = -D_i^{\text{diff,eff}} \frac{\partial c_i}{\partial y}$	(18)
Migrative fluxes	$J_i^{\text{migr}} = -D_i^{\text{migr,eff}} \frac{\partial \phi_{\text{elyte}}}{\partial y}$	(19)
Transport coefficients	$D_{\pm}^{\text{diff}} = D^0 + \frac{t_{\pm}}{z_{\pm} F} \frac{\sigma_D}{c_{\pm}}$ and $D_{\pm}^{\text{migr}} = \frac{t_{\pm}}{z_{\pm} F} \sigma$	(20)
Effective coefficients	$\chi^{\text{eff}} = \varepsilon_{\text{elyte}}^{\beta} \chi^0 = (s\varepsilon_0)^{\beta} \chi^0$	(21)
Convective fluxes	$J_i^{\text{conv}} = \upsilon_{\text{elyte}} c_i$	(22)
Flow velocity	$\upsilon_{\text{elyte}} = \frac{B_{\text{elyte}}}{\eta_{\text{elyte}}} \frac{\partial p_{\text{elyte}}}{\partial y}$	(23)
Equation of state	$\sum_i \left[\overline{V}_i + \left(p_{\text{elyte}} - p_0\right)\overline{\kappa}_i\right] c_i = \varepsilon_{\text{elyte}}$	(24)
Charge conservation	$0 = \sum_i z_i F \left[J_i^{\text{diff}} + J_i^{\text{migr}} + J_i^{\text{conv}} + \sum_m \left(A_m^V \dot{s}_{i,m}\right)\right]$	(25)
Phase management in porous electrodes		
Phase growth	$\frac{\partial \varepsilon_i}{\partial t} = \overline{M}_i \sum_m \left(A_m^V \dot{s}_{i,m}\right)$	(26)
Volume restriction	$\sum_i \varepsilon_i(p_i) = 1$	(27)
Current and voltage		
Half cell voltage	$E = \phi_{\text{elde,ca}} - \phi_{\text{elyte,ref}}$	(28)
Potential step	$\Delta\Phi = \phi_{\text{elde}} - \phi_{\text{elyte}}$	(29)
Current density	$i = \int_{y=0}^{L_{\text{elde}}} (i_{\text{F}} + i_{\text{dl}}) \mathrm{d}y$	(30)
Double layer current	$i_{\text{dl}} = A_{\text{dl}}^V c_{\text{dl}} \frac{\partial(\Delta\Phi)}{\partial t}$	(31)
Double layer capacity	$c_{\text{dl}} = \frac{\varepsilon(c_{\pm}, T)\varepsilon_0}{y_{\text{dl}}}$	(32)
Faraday current	$i_{\text{F}} = \sum_m \left(F A_m^V \dot{s}_{\text{electron},m}\right)$	(33)
Reactions and kinetics		
Species source term	$\dot{s}_i = \nu_i \left(k_{\text{f}} \prod_{j \in R_{\text{f}}} a_j^{\nu_j'} - k_{\text{r}} \prod_{j \in R_{\text{r}}} a_j^{\nu_j''}\right)$	(34)
Forward rate constant	$k_{\text{f}} = k_{\text{f}}^0 \exp\left(-\frac{E_{\text{f}}^{\text{act}}}{RT}\right) \exp\left(-\frac{\beta z F}{RT} \Delta\Phi\right)$	(35)
Thermodynamic consistency	$\frac{k_{\text{f}}}{k_{\text{r}}} = \exp\left(-\frac{\Delta G}{RT}\right)$	(36)

time evolution of concentrations and potentials is determined based on conservation equations for mass and charge, respectively. We simulate CV and EIS measurements at various temperatures. The system is assumed to be isothermal during the measurements. During discharge pure oxygen gas enters the GDE at constant temperature and pressure and dissolves in the liquid electrolyte (Table 4, Eq. (37)). Dissolution is modeled as chemical reaction in our modeling approach (Table 3, Eqs. (34)–(36)). The kinetics of the dissolution reaction follow from the Hertz–Knudsen equation. We assume that 1% of the molecules hitting the gas–liquid interface are absorbed in the electrolyte [33]. Dissolved oxygen reacts with water and electrons forming hydroxide ions (Table 4, Eq. (38)). Transport in the gas phase and in the liquid phase is modeled by the Navier–Stokes equations (Table 3, Eqs. (12)–(15)) and concentrated solution theory (CST) (Table 3, Eqs. (17)–(23)), respectively [54,33]. We assume electroneutrality to determine the potential distribution in the liquid electrolyte (Table 3, Eq. (25)). The electronic resistivity of the GDE can be safely neglected due to the high conductivity of silver [52]. Effective transport coefficients in the liquid electrolyte are calculated via the Bruggeman correlation (Table 3, Eq. (21)).

$$\chi^{\text{eff}} = \varepsilon_{\text{elyte}}^{\beta} \chi^0 = (s\varepsilon_0)^{\beta} \chi^0,$$

where β is the so-called Bruggeman coefficient and $\varepsilon_{\text{elyte}}$ the volume fraction of the electrolyte. $\varepsilon_{\text{elyte}}$ can be calculated from the porosity of the electrode ε_0 and its saturation with liquid electrolyte s. The Bruggeman coefficient is a measure for the tortuosity of transport pathways in the porous structure. We assume that it is independent of the saturation and use the standard value 1.5 in our calculations. In the porous structure of the GDE, gas phase and liquid electrolyte are in mechanical equilibrium. The electrolyte saturation s is determined by the capillary pressure p_{c} which is defined as

$$p_{\text{c}} = \Delta p = p_{\text{gas}} - p_{\text{elyte}} = \sigma_{\text{elyte}} \sqrt{\frac{\varepsilon_0}{B_{\text{elyte}}}} J(s), \tag{5}$$

where p_{gas} and p_{elyte} are the pressures in the gas and liquid phase, respectively, σ_{elyte} is the surface tension of the electrolyte solution with respect to air [55,56], and B_{elyte} the permeability calculated from Kozeny–Carman equation [54,57]. We parameterize the phenomenological Leverett function $J(s)$ according to Hao et al. [41] (see Section 4.1). The pressure level in the liquid phase is determined by the hydrostatic pressure of the electrolyte bath. In our experiment, the liquid pressure is adjusted to meet the pressure of the gas phase ($\Delta p = 0$). The volume fractions of the gas and the liquid phase follow from their respective equations of state (Table 3, Eqs. (16) and (24)) [33]. In Ref. [33] we consider the precipitation of solid $LiOH \cdot H_2O$. In our experiments we keep the concentration of LiOH in the electrolyte bath well below the solubility limit. Thus, the formation of $LiOH \cdot H_2O$ is neglected in this study. At the counter electrode, we model the formation of oxygen via Eq. (40) (OER). The evolved oxygen is dissolved in the electrolyte and assumed to be in equilibrium with a surrounding O_2 atmosphere (Eq. (39)). We do not explicitly model the reference electrode in our approach. The electrolyte potential at the position of the reference electrode ($y_{\text{ref}} = 5$ mm) directly constitutes the potential of a standard hydrogen electrode (SHE).

3.2. Simulation methodology

For the numerical simulation, all transport equations are discretized using a finite-volume (FV) approach in one dimension

Table 4
Summary of reactions in the different layers following Eq. (35).

Reaction	Equation	Nr.	Parameters	Value	Units
Cathode					
O_2 solution			A^V	$1\cdot10^4$	m^{-1}
	$O_2^{(gas)} \rightleftharpoons O_2^{(aq)}$	(37)	k^0	$1.1\cdot10^2$	s^{-1}
			E_a	0	kJ mol^{-1}
O_2 reduction			A^V	$3.3\cdot10^6$	m^{-1}
	$O_2^{(aq)} + 2H_2O + 4e^- \rightleftharpoons 4OH^-$	(38)	k^0	$9.6\cdot10^{-4}$	m^6 $kmol^{-2}$ s^{-1}
			E_a	21.76	kJ mol^{-1}
			β	0.149	–
Anode					
O_2 dissolution			A^V	$1\cdot10^2$	m^{-1}
	$O_2^{(gas)} \rightleftharpoons O_2^{(aq)}$	(39)	k^0	$1.1\cdot10^2$	s^{-1}
			E_a	0	kJ mol^{-1}
O_2 evolution			A^V	$2\cdot10^4$	m^{-1}
	$O_2^{(aq)} + 2H_2O + 4e^- \rightleftharpoons 4OH^-$	(40)	k^0	$9.6\cdot10^{-4}$	m^6 $kmol^{-2}$ s^{-1}
			E_a	21.76	kJ mol^{-1}
			β	0.149	–

(denoted by y). We discretize the GDE with 30 non-uniform compartments. The smallest FV-compartments are located at the boundary to the electrolyte bath. Their width is chosen as 0.56 μm in order to resolve the penetration depth of the ac signal (Eq. (4)). The electrolyte bath itself is discretized with 10 equally-spaced FV-compartments. This coarse discretization is justified by small gradients in concentration and electrolyte potential in the bath. In our model we take into account the changes in the cross-sectional area A of the electrolyte bath (Fig. 4). The resulting equation for the conservation of the mass of species i in the liquid phase is

$$\frac{\partial(\varepsilon c_i)}{\partial t} = -\frac{1}{A}\frac{\partial\left(A\left(J_i^{\text{diff}} + J_i^{\text{migr}} + J_i^{\text{conv}}\right)\right)}{\partial y}. \tag{6}$$

Modeling and simulation methodologies are implemented in the software DENIS [19,54]. We use the software package Cantera [58] for the calculation of (electro-) chemical source terms and the DAE solver LIMEX [59] for time-integration of the set of equations. Electrochemical impedance spectra are calculated by a step excitation of the reference electrode potential and numerical time integration of the current response [53]. The potential and current traces are Fourier transformed to obtain the impedance spectra in the frequency domain.

4. Results and discussion

In this section we discuss the results of measurements and simulations. First, we use the experimental data for the parameterization of the continuum model (Section 4.1). Model parameters, that is, the electrolyte conductivity, the kinetics of the ORR, the double layer capacitance, and the Leverett function, are determined in 1 M solution. We validate our model with CV and EIS measurements at various salt concentrations in Section 4.2. Note that we use a single set of parameters for all calculations.

Finally, in Section 4.3, we perform a sensitivity analysis of our continuum model to identify the most important parameters for electrode design.

4.1. Model parameterization

The model is parameterized based on data from our own experiments and from literature. Thermodynamic and transport parameters are taken from Ref. [33]. A list of geometric parameters of the setup and structural parameters of the GDE can be found in Table 1. Chemical reactions and corresponding kinetic parameters are summarized in Table 4.

We use an equivalent circuit model for the analysis of the electrochemical impedance spectra (see Fig. 5). Equivalent circuit models are a viable and widely-used tool to identify physical processes and to extract physical parameters [60]. The elements of the equivalent circuit are adjusted to match the experimental data. The error in the fit is less than 3% for all measurements. This indicates a reasonable representation of physical processes. The circuit consists of the electrolyte resistance R_{el} in line with an RC element, representing the charge transfer resistance (R_{ct}) and double layer capacitance (c_{dl}) at the electrode-electrolyte interface. The porous electrode element Z_{pore} denotes a transmission line model, which reflects the porous structure of the GDE [60]. The elements of this equivalent circuit are described in detail in Ref. [46]. From the equivalent circuit model we extract the electrolyte conductivity and double layer capacitance. The experimental IV curves in turn are used to determine the kinetic parameters and the saturation of the GDE.

4.1.1. Electrolyte conductivity

The measured electrolyte conductivity is shown as function of temperature and LiOH concentration in Fig. 5. Our data is in good agreement with data from the literature also shown in Fig. 5 [26,61]. The solid line in Fig. 5 represents a fit to the combined set of data according to

$$\sigma_{\text{elyte}} = (-3.83584 + 0.01363T) + (-49.6837 + 0.2193T)c_{\text{LiOH}} + (1.54934 - 0.01038T)c_{\text{LiOH}}^2. \tag{7}$$

The fit agrees well with the experimental data at high concentrations. At low concentrations the conductivity increases strongly with increasing salt concentrations. Therefore, this region is afflicted with small uncertainties (Fig. 12).

4.1.2. Double layer capacitance

Upon characterization under transient conditions (CV, EIS), the electrical double layer at the electrode–electrolyte interface leads to additional capacitive currents. The roughness of the surface or slow adsorption of ions and chemical impurities on the surface can cause a dispersion of the capacitance. A constant phase element (CPE) can capture this dispersive behavior [51]. In our equivalent circuit we use a pure capacitive element and accept a minor decrease in fitting accuracy. Fig. 6 shows the double layer

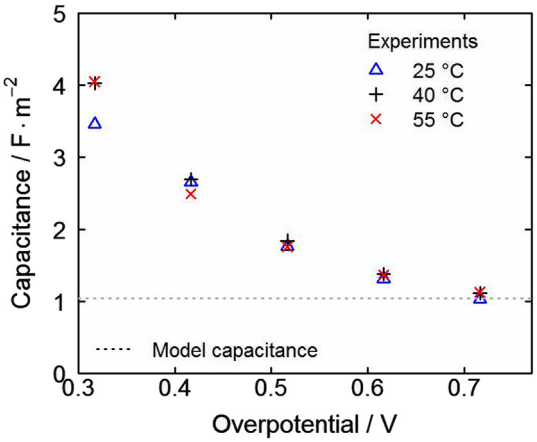

Fig. 6. Double layer capacitance in 1 M LiOH solution. Symbols represent the double layer capacitance from the fit to the equivalent circuit model at various polarizations. The dotted line represents the capacitance of the model and is included as a guide for the eye.

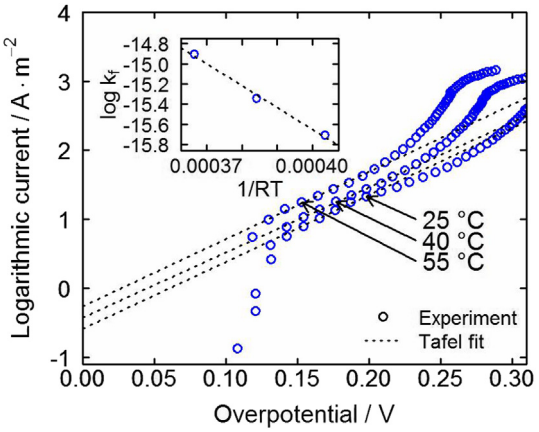

Fig. 8. Tafel analysis for the ORR in 1 M LiOH solution at temperatures of 25, 40 and 55 °C. Open circles show the experimental data of our CV measurements. The data is corrected for effects of mass transport. The dashed lines represent the best Tafel fit at overpotentials between $\eta_{eff} = 150$ mV and 200 mV. The inset shows the Arrhenius plot of the pre-exponential factors which were determined according to our kinetic model from the exchange current densities. All kinetic parameters are summarized in Table 4.

capacitance in 1 M LiOH solution at various polarizations. The capacitance decreases continuously and approaches a constant value at high overpotentials. The influence of temperature is less prominent in our measurements.

We model the electric double layer as an ideal parallel-plate capacitor. The area specific capacitance c_{dl} is given by

$$c_{dl} = \frac{\varepsilon\varepsilon^0}{y_{dl}}, \tag{8}$$

where ε is the dielectric constant of the solution, $\varepsilon^0 = 8.85 \cdot 10^{-12}$ F m^{-1} the permittivity of vacuum and y_{dl} the thickness of the double layer. In lack of experimental data for LiOH we use the dielectric constant for NaOH solution [62,63]. The capacitance at small overpotentials is very high and a polarization dependence of the capacitance alone does not explain the strong decrease of the fitted parameters. Most likely, the equivalent circuit fit includes ad- or desorption processes of ions on the electrode surface. Therefore, we neglect the potential dependence of c_{dl} and adjust y_{dl} to fit our experimental data at high polarization where the capacitance approaches a constant value. The capacitance of our model is shown as dotted line in Fig. 6. We use a double layer thickness y_{dl} of 5.0 Å, which approximately corresponds to two layers of molecular water [64] on the electrode surface. We justify our simplified description of the electrical double layer by comparing the relaxation times $\tau = R_{ct}c_{dl}$ of the charge transfer process. In a Bode plot, τ corresponds to the frequency at the maximum of the imaginary part. The position of the simulated maxima in Fig. 7 agrees fairly well with our experiments. We extrapolate c_{dl} to other salt concentrations by using the correlations for ε given in Refs. [62,63] in Eq. (8).

4.1.3. ORR kinetics

For the calculation of kinetic parameters we utilize the data from CV measurements in 1 M LiOH solution. We eliminate mass transport effects from the porous electrode by correcting the measured potential for corresponding overpotentials. The effective overpotential η_{eff} is

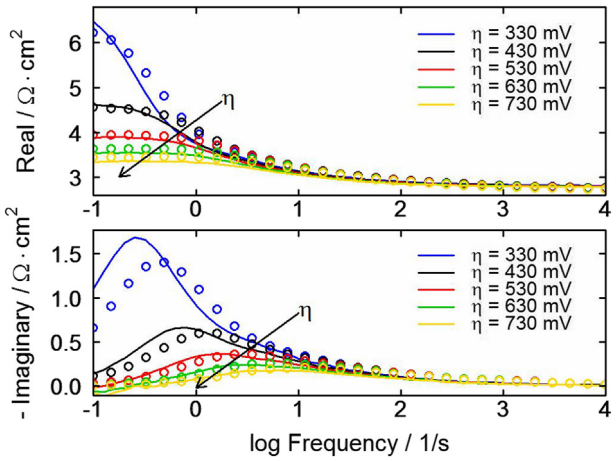

Fig. 7. Bode plots of impedance spectra in 1 M LiOH solution at 40 °C and various polarizations. Symbols represent the experimental data and solid lines show the results of the continuum simulations. The graph demonstrates the good agreement of our simulations with the experiments and validity of our model of the electric double layer.

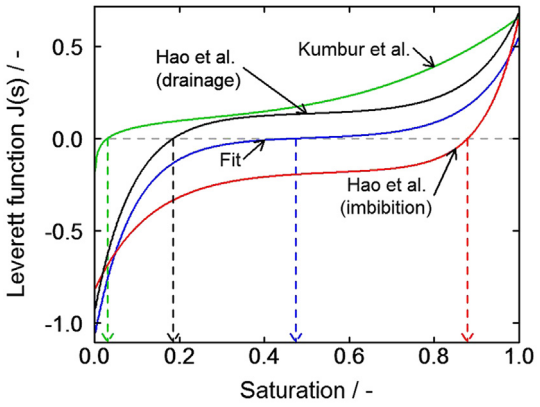

Fig. 9. Leverett function $J(s)$ as proposed by Kumbur et al. [39] (without MPL) and Hao et al. [41]. The correlations describe the relation between capillary pressure and saturation in porous media. Our fit is determined by adjusting an offset to the correlation of Hao et al. [41] to get a good agreement between simulated and measured IV curves (see Fig. 10).

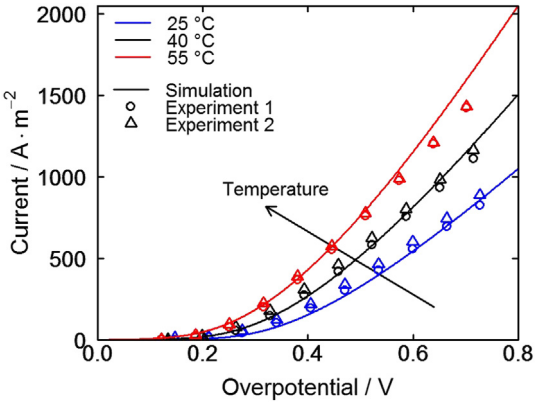

Fig. 10. IV curves in 1 M LiOH solution at various temperatures. The saturation of the GDE was adjusted to obtain a good agreement between experiments (symbols) and simulations (solid lines).

$$\eta_{\text{eff}} = \eta - R_{\text{tot}} i, \tag{9}$$

where $R_{\text{tot}} = R_{\text{el}} + Z_{\text{pore}}$ is the total mass transport resistance. R_{el} and Z_{pore} are determined from the equivalent circuit model. The Tafel plot with corrected overpotentials is shown in Fig. 8. A straight line is fitted to the Tafel regime between $\eta_{\text{eff}} = 150$ mV and 200 mV. The Tafel slope of ~100 mV decade^{-1} gives a symmetry factor β_{Cathode} of ~0.15 [65]. We determine the exchange current densities for three different temperatures as the intercept of the Tafel line with the line of zero overpotential. For the calculation of rate constants, we assume a Butler–Volmer type global kinetic model (see Eq. (34)). The frequency factor and activation energy follow from the Arrhenius plot shown in the inset of Fig. 8. The kinetic parameters are summarized in Table 4. A short derivation of the parameters of the ORR can be found in the appendix.

4.1.4. Saturation of the GDE

In Ref. [33] we use the correlation of Kumbur et al. [39] for the calculation of GDE saturation. It was developed for the saturation of carbon cloth type GDLs in PEMFCs. The predicted saturations at $\Delta p = 0$ are very low. Wang et al. [66] point out that the saturation strongly depends on the structure of the medium. Therefore, we use the simplified expression of Hao et al. [41] (Fig. 9) and adjust the offset of the Leverett function $J(s)$ to fit our experimental IV curves in 1 M LiOH solution, as shown in Fig. 10. The resulting Leverett function is given by

$$J(s) = 1.34 \cdot 10^{-3} + 0.00498 e^{9.404(s-0.5)} - 0.00397 e^{-11.19(s-0.5)}. \tag{10}$$

This function gives a good agreement between simulated and experimental IV-curves over the complete investigated temperature and polarization range. The small deviation at high η is discussed in Section 4.2.1. Our model predicts a saturation of about ~47%. This reflects the wetting behavior of water on Ag surfaces [67] and is slightly below the values previously used in the modeling of alkaline fuel cells [68,69].

4.2. Model validation

The model as outlined above is used to simulate the electrochemical measurements described in Section 2.2. We focus here on the oxygen reduction regime because of electrode degradation and a noisy signal during oxygen evolution. Liquid-phase transport processes during oxygen reduction and oxygen evolution are expected to be similar.

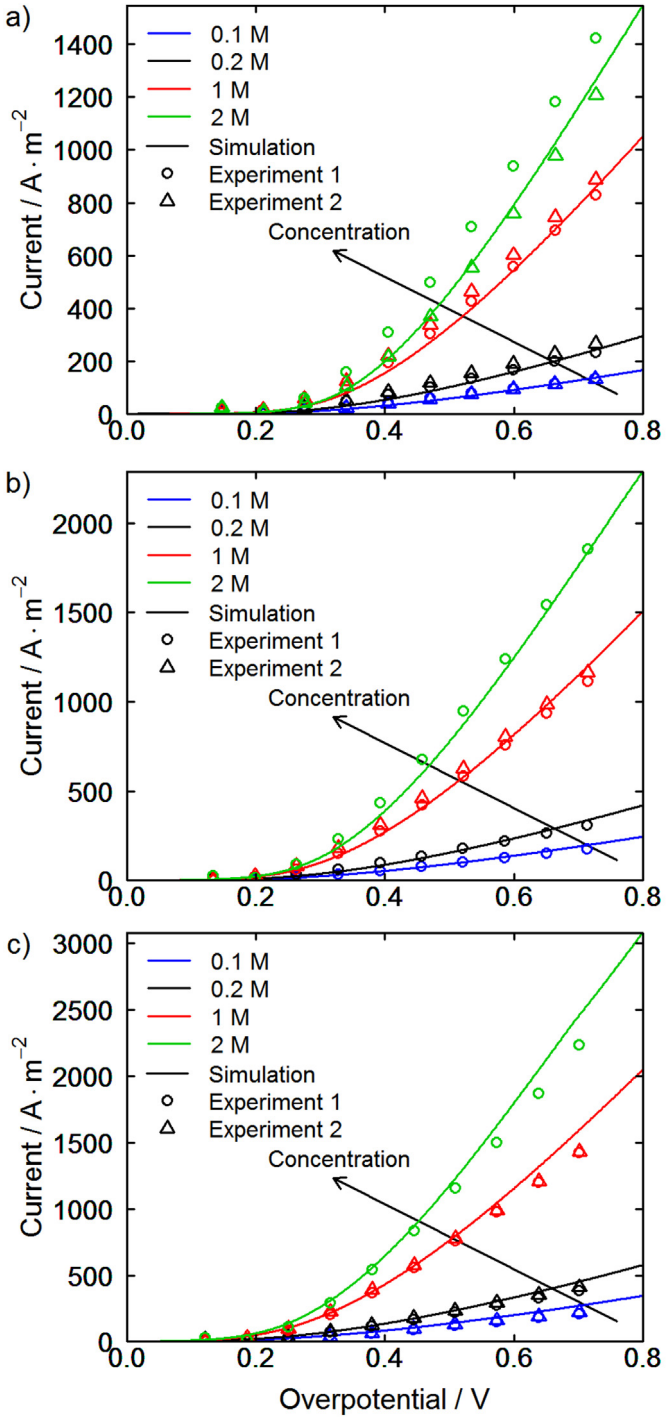

Fig. 11. IV curves in aqueous LiOH solution. The concentration of electrolyte solution was varied between 0.1 and 2 M. Graphs a)–c) show a comparison between simulation (solid lines) and experiment (symbols) at 25, 40 and 55 °C, respectively.

In the following Sections we validate our model separately for IV curves and impedance spectra. For both techniques our simulations agree very well with the experiments over a wide range of concentrations, temperatures and overpotentials.

4.2.1. Cyclic voltammetry

We simulate a potential sweep at a scan rate of 1 mV s^{-1}, like in our experiments. Both experiments and model show a stationary

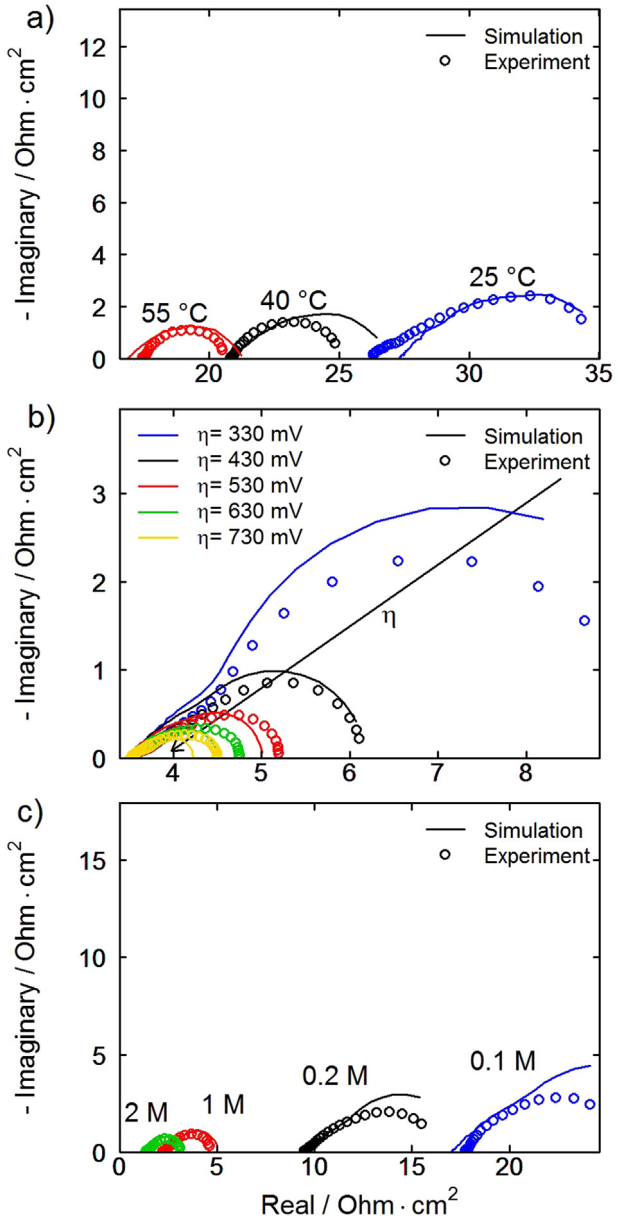

Fig. 12. Impedance spectra of the Ag electrode in the complex plane at various conditions. Symbols represent the experimental data and solid lines are the results of the impedance simulations of our continuum model. a) Spectra in 0.1 M solution and a polarization of 700 mV vs. RHE. b) Series of spectra at various overpotentials in 1 M solution and at a temperature of 25 °C. c) Spectra at 40 °C and a polarization of 900 mV vs. RHE.

behavior at these low scan rates, therefore, results are presented as IV curves. In Fig. 11 we compare IV curves of measurements and simulations for various temperatures. As explained in the previous Section 4.1.4, we adjust the saturation dependence $J(s)$ to give a good fit in 1 M LiOH solution. The good quantitative agreement with the experimental data at other concentrations proves the validity of our model.

The model slightly overpredicts current densities at high overpotentials as already seen in Section 4.1.4. This indicates that relevant rate-limiting processes at high overpotentials and currents are not fully represented in the current model. Pinnow et al. [44] report a change in the apparent Tafel slope of their experiments on silver GDEs in NaOH solution. They explain it with a possible change in the adsorption isotherm of reaction intermediates and use a second Tafel slope at high overpotentials. Similar observations for Pt catalysts in alkaline media [70,71] support this assumption. In the present model we use one single-step charge-transfer reaction to describe the kinetics at all concentrations, temperatures and overpotentials. A more rigorous elementary kinetic description of the ORR could give some additional insights on this topic [27,72,73]. However, such a detailed treatment of kinetics is out of the scope of this work on transport phenomena of porous electrodes. Similar changes in the slope of the IV curve are also reported for PEMFCs [74,75]. This effect is attributed to a limited supply of O_2 through a thin film of ionomer on the electrode surface. The nature of this additional transport resistance is not yet fully understood and subject of ongoing research. Suzuki et al. show that the dissolution of O_2 in the ionomer might be the rate limiting step [75]. However, we could not confirm this observation for our aqueous system (see Section 4.3.1).

In the case of a limiting transport of O_2, we would expect smaller deviations of the IV curves at low concentrations. The solubility and diffusivity of O_2 is high at low salt concentrations in the electrolyte [76,77,33]. Still, we observe the same discrepancy to our experiments. In the literature, flooded agglomerate models are suggested to include the transport of O_2 in the agglomerate and electrolyte film [44,75]. This requires an additional parameterization of the model with unknown structural quantities of the agglomerate. For the sake of simplicity and in order to avoid "over-parameterization" we do not pursue this approach here.

4.2.2. Electrochemical impedance spectroscopy

Impedance spectra from simulation and experiment are shown in Fig. 12 for various conditions. Overall, simulations and experiment are in a good qualitative agreement. We again stress that we use only one set of physical parameters for our simulations for all experimental conditions. This is an important difference to equivalent circuit models, where each spectrum is fitted individually. Our continuum model reproduces the characteristic shape of impedance spectra of porous electrodes in the complex plane. Its features are described in detail in Section 2.2.2. The intersection with the real-axis is in good agreement for experiments and simulations at high concentrations. At lower concentrations we see minor deviations of our simulated data. We attribute this to a lower accuracy of the fit of ionic conductivity in this region (see Section 4.1.1). At lower frequencies we observe a depressed semi-circle closing into a straight line with a slope of 45°, originating from transport and reaction in the porous electrode. The diameter of the semi-circle corresponds to the resistance of the ORR. At low temperatures and η the model overpredicts the experiments, whereas at high temperatures and η experiments are underpredicted. This discrepancy is consistent with the trends observed for IV curves (Section 4.2.1). Deviations at high temperatures and η are probably due to additional transport resistances or changes in the reaction mechanism of the ORR which we do not capture in our simplified 1D model. The increased resistance at low temperatures and η is due to our fitting procedure as we adjust $J(s)$ to get a good agreement at higher currents (see Section 4.1.4).

4.3. Discussion of parameters

We next perform a sensitivity analysis of the validated continuum model in order to identify the most important physicochemical processes. The relative sensitivity s_ζ of the current density i on the change of parameter ζ is given by

$$s_\zeta = \frac{(i - i^0)/i^0}{\left(\zeta - \zeta^0\right)/\zeta^0}. \quad (11)$$

The parameters are varied individually by 5% of their original value (indicated by superscript 0). We perform the sensitivity analysis at 300, 500 and 700 mV overpotential. A sensitivity close to zero indicates parameters with only a small impact, whereas a high sensitivity reveals a limiting influence on the system performance. A sensitivity of unity means direct proportionality between the varied parameter and the current.

Results of the sensitivity analysis in 1 M LiOH at 25 °C are shown in Fig. 13. The parameters are grouped according to their effect on physical processes. The first part shows kinetic parameters, the second part transport parameters and the third part geometrical parameters. In the following discussion we put an emphasis on the structural parameters, which are important design parameters for the future development of GDEs.

4.3.1. Kinetic parameters

The kinetic parameters of the GDE show the highest impact on the system performance. This highlights the need for the development of novel catalysts [47,78–80]. Especially the symmetry factor of the ORR exhibits the highest sensitivity of all parameters. The kinetic parameters of the anode show a negligible sensitivity. This is expected in the simulated three-electrode setup and confirms our model of the counter electrode (Section 3.1). The dynamics of the O_2 dissolution at the cathode are represented by the rate constant of the reaction $k^0_{O_2}$. Even at high overpotentials and currents we do not see a limiting effect of the O_2 dissolution in our model based on the Hertz–Knudsen equation (see Section 4.2.1).

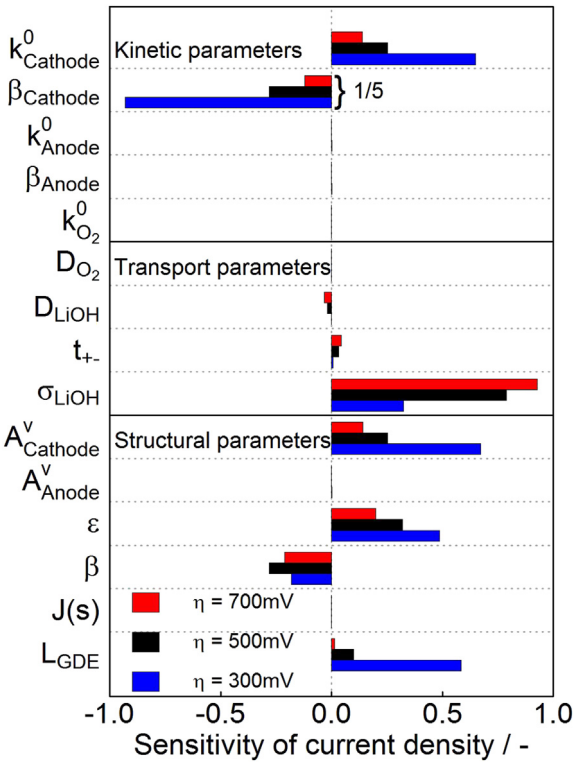

Fig. 13. Sensitivity analysis (Eq. (11)) at 300, 500, and 700 mV overpotential. Upper part: kinetic parameters, middle part: transport parameters, bottom part: geometrical parameters. The sensitivity of $\beta_{Cathode}$ is divided by 5 for convenience.

4.3.2. Transport parameters

The sensitivity of transport parameters is comparatively small. Even at high overpotentials the diffusion coefficients of LiOH and O_2 in the liquid phase show only a small influence on the performance. Particularly, the impact of D_{O_2} is negligible. This is due to the excellent transport of O_2 in the gas phase of the GDE. Additionally, we neglect the transport resistance in the electrolyte film on the electrode surface. Thus, a slightly higher influence can be expected for the 3D system (see Section 4.2.1). Similarly, the sensitivity of the transference number $t_\pm$ and the diffusion coefficient of LiOH D_{LiOH} are quite small. This can be attributed to the high ionic conductivity of the aqueous electrolyte. However, these parameters are very important during deep discharge of the battery as they determine the local precipitation of solid $LiOH \cdot H_2O$. The low sensitivity of these transport parameters is beneficial for the accuracy of our model. They are calculated based on several assumptions from the literature [33]. An exception is the ionic conductivity of the electrolyte σ_{elyte}. Its significance is due to the comparatively large electrolyte region between the GDE and the reference electrode. Here, a large drop in the electrolyte potential occurs. This decreases the potential step $\Delta\Phi$ which drives the electrochemical reaction in the GDE. In a real battery this distance is much smaller. Still the importance of this parameter for the transport of ions will be significant.

4.3.3. Structural parameters

The structure of the GDE shows a high influence on the system performance. Porosity ε_0 and tortuosity τ are important parameters for the transport of reactants (see Eq. (21)). In the present model, the tortuosity is determined by the Bruggeman coefficient β (Eq. (21)). High porosities improve the supply of reactants to the active sites on the electrode surface. In contrast, a high Bruggeman coefficient decreases the effective transport properties and causes the negative sign of the sensitivities. The specific surface areas at the cathode $A^V_{Cathode}$ and anode A^V_{Anode} are multiplicative factors in the rate expression of the electrochemical source term (Eq. (17)). Thus, their sensitivity is the same as $k^0_{Cathode}$ and k^0_{Anode}, respectively.

The thickness of the electrode is an important parameter regarding the power density of the GDE. The sensitivity strongly depends on the applied overpotential. Fig. 14a shows the local Faradaic current along the y direction of the GDE. At low overpotentials the ORR proceeds in the whole GDE at almost the same rate. At high overpotentials the local current shows a considerable gradient, strongly increasing from the gas inlet towards the porous electrode/electrolyte bath interface. The gradient is caused by the ohmic resistance of the electrolyte. It is enhanced by a gradient of dissolved O_2 as shown in Fig. 14b (solid lines, discussed below). If the gradient in the local Faradaic current is small, a change in thickness causes a higher sensitivity compared to sensitivities at higher gradients.

The open symbols in Fig. 14b represent the solubility of O_2 (i.e., the concentration in the limit of thermodynamic equilibrium). The solubility of O_2 depends on the local concentration of LiOH. This effect is known as salting-out [76,77]. During oxygen reduction the local concentration of LiOH in the electrode increases in an inhomogeneous way such that higher concentrations are present close to the porous electrode/electrolyte bath interface. Fig. 14 shows that for all overpotentials, the simulated concentration (which includes transport limitations and salting-out) is very close to the solubility (which includes only salting-out). Thus, the decrease in O_2 concentration towards the electrolyte ($y_{ca} = L_{GDE}$)

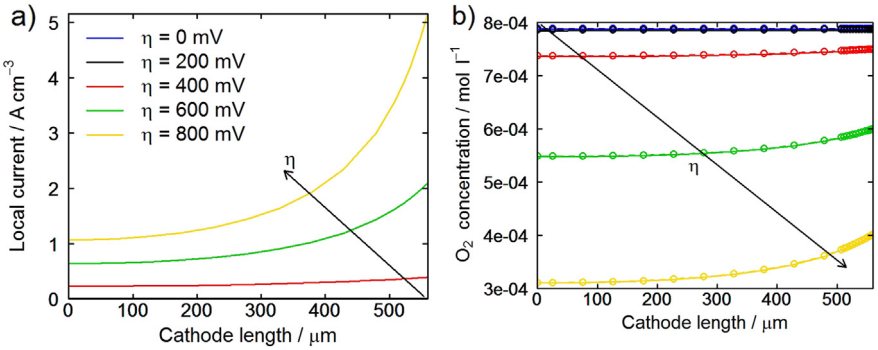

Fig. 14. Spatial profiles of Faradaic current a) and concentration of dissolved O_2 b) in the cathode at various overpotentials. Simulations are run at a temperature of 25 °C and a LiOH concentration of 1 M. Symbols in graph b) indicate the O_2 concentration in thermodynamic equilibrium. The gas inlet is at $y = 0$, the electrolyte bath at $y = 560$ µm.

is only due to salting-out and not due to a mass transport limitation of O_2. This demonstrates the good supply of O_2 even at high overpotentials.

The sensitivity of the saturation is represented in the form of the Leverett function $J(s)$. Although the sensitivity is small in the studied parameter range close to 0.47, the saturation is crucial for the transport of reactants. In Fig. 15 we compare the performance of the system for several Leverett functions from the literature (see Fig. 9). In the correlations of Kumbur et al. [39] we neglect the contribution of the micro-porous layer (MPL). The other correlations are taken from Hao et al. [41] and are the basis for our own fit to the experimental data. Note that the predicted saturations range from 0.05 (Kumbur et al.) to 0.88 (Hao et al. for imbibition).

The Leverett function of Hao et al. for imbibition gives the highest saturation and the simulated electrode shows the best performance in terms of current density. The IV curves of other $J(s)$ are shifted towards higher overpotentials, i.e., the resulting current density is lower. The reason is a slower transport of reactants which is due to smaller effective transport coefficients in the liquid electrolyte (see Eq. (21)). Thus, a large part of the overpotential is needed to sustain the transport of reactants and less can be used to drive the electrochemical reaction. This study clearly shows the importance of the saturation on the system performance. Further investigations, experimentally as well as theoretically, are needed for a better description of two-phase flow in the porous structure of the GDE.

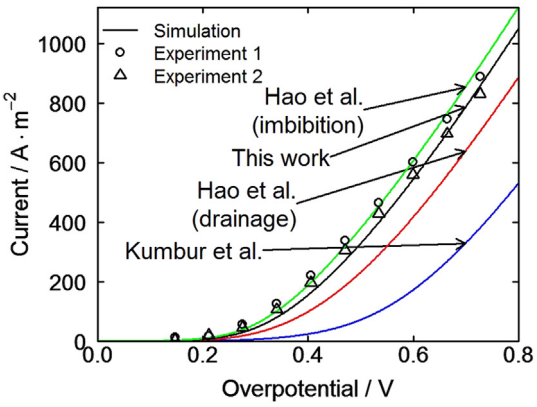

Fig. 15. Simulated IV curves for different correlations of the Leverett function from the literature ([41,39]). Resulting saturations span from 0.05 (Kumbur et al.) up to 0.88 (Hao et al. for imbibition).

5. Conclusions

Aqueous Li–O_2 batteries are interesting candidates for mobile applications due to their high theoretical energy density. We have presented a combined modeling and experimental study of the performance and properties of an Ag/Ag_2O gas diffusion electrode (GDE) in aqueous lithium hydroxide solutions for the use in Li–O_2 batteries.

In the first part of this work, we discussed results of half-cell measurements for ORR and OER. We performed cyclic voltammetry and electrochemical impedance spectroscopy at various LiOH concentrations (0.1–2 mol l^{-1}), temperatures (298.15–328.15 K), and polarizations (500–1100 and 1400–1950 mV vs. RHE). The electrode showed high performance in the ORR regime. The transport of oxygen through the gas phase was found to be fast and not rate limiting. In the OER regime, we observed degradation of the electrode. The measurements provide an excellent basis for subsequent parameterization and validation of a 1D continuum model.

In the second part of this work, we presented a physico-chemical model of the half-cell experiments. The model accounts for the dissolution and reduction of oxygen in the electrolyte, as well as for the two-phase transport of gas-phase oxygen, liquid phase, and dissolved ions in the porous electrode. All parameters stem either from our own experiments or the extensive literature on aqueous electrolytes.

The results of our simulations agree favorably with the experiments over the whole temperature and concentration range studied. Our model reproduces the characteristic shapes of impedance spectra and IV curves. At high overpotentials, however, small deviations in IV curves and impedance spectra were observed, probably due to a change in reaction mechanism or additional transport resistances.

Continuum modeling contributes to gaining a fundamental understanding of relevant physico-chemical processes in the electrode and allows a systematic development of the electrode performance. To this aim, we have identified critical parameters via sensitivity analysis of the validated model. The ORR reaction kinetics were shown to have the biggest impact on the electrode performance. This highlights the need for further development of highly efficient catalysts. Also the electrode micro-structure, which determines the transport of reactants to the active surfaces, influences the battery performance. In this respect, the saturation of the GDE pores with liquid electrolyte is very important. Detailed investigations of this issue have been carried out both experimentally [35–40] and theoretically [41,81,82] in the context of PEM fuel cells. In the present study, the wetting behavior of the Ag-GDE is not known precisely. A closer determination of the electrolyte saturation in the GDE is subject of work in progress.

Table 2
List of symbols.

Symbol	Unit	Meaning	Eq.
A	–	Cross-sectional area perpendicular to y direction	(21)
A_m^{V}	$\mathrm{m^2\ m^{-3}}$	Volume-specific surface area	(12)
B_{j}	$\mathrm{m^2}$	Permeability of the porous electrode	(15) and (23)
c_i	$\mathrm{mol\ m^{-3}}$	Concentration of species i in a bulk phase	(17)
c_{dl}	$\mathrm{F\ m^2}$	Area-specific double layer capacitance	(31)
D_i^{eff}	$\mathrm{m^2\ s^{-1}}$	Effective diffusion coefficient of species i	(21)
D_i^{migr}	$\mathrm{m^2\ s^{-1}}$	Effective migration coefficient of species i	(21)
E	E	Cell/half-cell voltage	(28)
$E_{\mathrm{f}}^{\mathrm{act}}$	$\mathrm{J\ mol^{-1}}$	Activation energy of forward and reverse reactions	(35)
F	$\mathrm{C\ mol^{-1}}$	Faraday constant	(25)
i		Index of species or phases	(12)
i	$\mathrm{A\ m^{-2}}$	Current density	(30)
i_{F}	$\mathrm{A\ m^{-3}}$	Faradaic current density	(33)
i_{dl}	$\mathrm{A\ m^{-3}}$	Current density from electric double layer	(31)
j		Index of species or phases	(18) and (19)
j_i	$\mathrm{mol\ m^{-2}\ s^{-1}}$	Flux of species i	(14)
k_{f}, k_{r}		Forward and backward rate constant	(36)
k^0		Pre-exponential factor in Arrhenius equation	(35)
m		Index of chemical reactions and interfaces	(12)
M_i	$\mathrm{kg\ mol^{-1}}$	Molar mass of species i	(16)
$\overline{M}_j$	$\mathrm{kg\ mol^{-1}}$	Mean molar mass of phase j	(16)
p_j	Pa	Pressure	(15)
r	m	Pore radius	(4)
R	$\mathrm{J\ K^{-1}\ mol^{-1}}$	Ideal gas constant	(16)
R	$\Omega\ \mathrm{cm^2}$	Ohmic resistance	–
s		Saturation of porous electrode	(21)
$\dot{s}_i$	$\mathrm{mol\ m^{-2}\ s^{-1}}$	Chemical production rate of species/phase i	(34)
t	s	Time	(12)
$t_{\pm}$		Transference number	(20)
T	K	Temperature	(16)
$\overline{V}_i$	$\mathrm{m^3\ mol^{-1}}$	Partial molar volume	(24)
X_i		Mole fraction of species i	(13)
y	m	Spatial position through thickness	(12)
z		Number of electrons transferred in charge-transfer step	(35)
z_i		Charge of species i	(20)
Z	$\mathrm{m\Omega\ cm^2}$	Impedance	(4)
β_{m}		Symmetry factor of charge transfer reaction	(35)
β		Bruggeman coefficient	(21)
$\Delta\Phi$	V	Electric potential difference	(29)
ΔG	$\mathrm{J\ mol^{-1}}$	Gibbs free energy of the reaction	(36)
ε		Relative permittivity	(8)
ε^0	$\mathrm{F\ m^{-1}}$	Permittivity of vacuum	(8)
ε_i		Volume fraction of phase i	(12)
ε_0		Porosity	(21)
$\overline{\kappa}_i$	$\mathrm{m^3\ mol^{-1}\ Pa^{-1}}$	Partial molar compressibility	(24)
λ	m	Penetration depth of AC signal	(4)
η	V	Overpotential	(9)
η_j	$\mathrm{kg\ m^{-1}\ s^{-1}}$	Viscosity	(23)
ν_i		Stoichiometric coefficient of species i	(34)
ϕ_j	V	Electric or ionic potential	(19)
ρ_j	$\mathrm{kg\ m^{-3}}$	Density	(16)
σ	S m	Ionic or electronic conductivity	(20)
χ	–	Variable for effective transport properties	(21)
ζ	–	Parameters in the sensitivity analysis	(11)

Acknowledgments

Financial support from the German Ministry of Education and Research (BMBF) in the framework of the LuLi project (03X4624B) is gratefully acknowledged.

Appendix A. Derivation of kinetic parameters

Reaction equations in our framework [54,19,58] follow the law of mass action kinetics according to

$$\dot{s}_i = \nu_i \left(k_f \prod_{j \in R_{\mathrm{f}}} a_j^{\nu_j'} - k_{\mathrm{r}} \prod_{j \in R_{\mathrm{r}}} a_j^{\nu_j''} \right) \tag{A.1}$$

where k_{f} is given in Arrhenius form as function of temperature and the potential step at the electrode–electrolyte interface

$$k_{\mathrm{f}} = \tilde{k}_{\mathrm{f}}(T) \exp\left(-\frac{\beta z F}{RT} \Delta\Phi \right) = k_{\mathrm{f}}^0 \exp\left(-\frac{E_{\mathrm{f}}^{\mathrm{act}}}{RT} \right) \exp\left(-\frac{\beta z F}{RT} \Delta\Phi \right). \tag{A.2}$$

The Faradaic current i_{F} results as the sum of all charge-transfer reactions

$$i_{\mathrm{F}} = \sum_m \left(F A_m^{\mathrm{V}} \dot{s}_{\mathrm{electron},m} \right). \tag{A.3}$$

In the present case the only reaction contributing to the Faradaic current is the oxygen reduction reaction

$$\mathrm{O_2^{(aq)}} + 2\mathrm{H_2O} + 4e^- \rightleftharpoons 4\mathrm{OH^-}. \tag{A.4}$$

The equation for the Faradaic current follows from Eqs. (A.1)–(A.3) as

$$i_F = 4F\left(\tilde{k}_f(T)c_{O_2}c_{H_2O}^2 \exp\left(-\frac{\beta zF}{RT}\Delta\Phi\right) - \tilde{k}_r(T)c_{OH^-}^4 \exp\left(\frac{(1-\beta)zF}{RT}\Delta\Phi\right)\right) \quad (A.5)$$

In the limit of high overpotentials (Tafel analysis) we can neglect the backmost part of Eq. (A.5).

$$i_F = 4F\tilde{k}_f(T)c_{O_2}c_{H_2O}^2 \exp\left(-\frac{\beta zF}{RT}\Delta\Phi\right) \quad (A.6)$$

We define the exchange current density i_0 by

$$i_0 = 4F\tilde{k}_f(T)c_{O_2}c_{H_2O}^2. \quad (A.7)$$

By inserting i_0 in Eq. (A.6) we get the well-known form of the Tafel equation

$$i_F = i_0 \exp\left(-\frac{\beta zF}{RT}\Delta\Phi\right). \quad (A.8)$$

A Tafel analysis yields the parameters i_0 and β at each temperature. We calculate $\tilde{k}_f(T)$ from Eq. (A.7) and determine the pre-exponential factor k_f^0 and the activation energy of the reaction from the Arrhenius plot shown in the inset of Fig. 8. For our simulations we use a temperature average value of β.

References

[1] B. Scrosati, J. Garche, J. Power Sources 195 (2010) 2419–2430.
[2] A. Kraytsberg, Y. Ein-Eli, Adv. Energy Mater. 2 (2012) 922–939.
[3] P.G. Bruce, S.A. Freunberger, L.J. Hardwick, J.-M. Tarascon, Nat. Mater. 11 (2012) 19–29.
[4] G. Girishkumar, B. McCloskey, A.C. Luntz, S. Swanson, W. Wilcke, J. Phys. Chem. Lett. 1 (2010) 2193–2203.
[5] J. Christensen, P. Albertus, R.S. Sanchez-Carrera, T. Lohmann, B. Kozinsky, R. Liedtke, J. Ahmed, A. Kojic, J. Electrochem. Soc. 159 (2012) R1–R30.
[6] A. Kraytsberg, Y. Ein-Eli, J. Power Sources 196 (2010) 886–893.
[7] Y.-C. Lu, B.M. Gallant, D.G. Kwabi, J.R. Harding, R.R. Mitchell, M.S. Whittingham, Y. Shao-Horn, Energy Environ. Sci. 6 (2013) 750–768.
[8] M. Park, H. Sun, H. Lee, J. Lee, J. Cho, Adv. Energy Mater. 2 (2012) 780–800.
[9] K.F. Blurton, A.F. Sammells, J. Power Sources 4 (1979) 263–279.
[10] K.M. Abraham, Z. Jiang, J. Electrochem. Soc. 143 (1996) 1–5.
[11] S.P. Ong, Y. Mo, G. Ceder, Phys. Rev. B 85 (2012) 081105.
[12] J.S. Hummelshoj, J. Blomqvist, S. Datta, T. Vegge, J. Rossmeisl, K.S. Thygesen, A.C. Luntz, K.W. Jacobsen, J.K. Norskov, J. Chem. Phys. 132 (2010) 071101.
[13] V. Viswanathan, K.S. Thygesen, J.S. Hummelshoj, J.K. Norskov, G. Girishkumar, B.D. McCloskey, A.C. Luntz, J. Chem. Phys. 135 (2011) 214704.
[14] P. Albertus, G. Girishkumar, B. McCloskey, R.S. Sanchez-Carrera, B. Kozinsky, J. Christensen, A.C. Luntz, J. Electrochem. Soc. 158 (2011) A343–A351.
[15] B. Horstmann, B. Gallant, R. Mitchell, W.G. Bessler, Y. Shao-Horn, M.Z. Bazant, J. Phys. Chem. Lett. 4 (2013) 4217–4222.
[16] S.S. Sandhu, G.W. Brutchen, J.P. Fellner, J. Power Sources 170 (2007) 196–209.
[17] R.E. Williford, J.-G. Zhang, J. Power Sources 194 (2009) 1164–1170.
[18] P. Andrei, J.P. Zheng, M. Hendrickson, E.J. Plichta, J. Electrochem. Soc. 157 (2010) A1287–A1295.
[19] J.P. Neidhardt, D.N. Fronczek, T. Jahnke, T. Danner, B. Horstmann, W.G. Bessler, J. Electrochem. Soc. 159 (2012) A1528–A1542.
[20] S.A. Freunberger, Y.H. Chen, Z.Q. Peng, J.M. Griffin, L.J. Hardwick, F. Barde, P. Novak, P.G. Bruce, J. Am. Chem. Soc. 133 (2011) 8040–8047.
[21] B.D. McCloskey, D.S. Bethune, R.M. Shelby, G. Girishkumar, A.C. Luntz, J. Phys. Chem. Lett. 2 (2011) 1161–1166.
[22] R. Black, B. Adams, L.F. Nazar, Adv. Energy Mater. 2 (2012) 801–815.
[23] Z. Peng, S.A. Freunberger, Y. Chen, P.G. Bruce, Science 337 (2012) 563–566.
[24] M.J. Trahan, S. Mukerjee, E.J. Plichta, M.A. Hendrickson, K.M. Abraham, J. Electrochem. Soc. 160 (2013) A259–A267.
[25] T. Zhang, N. Imanishi, Y. Takeda, O. Yamamoto, Chem. Lett. 40 (2011) 668–673.
[26] P.J. Gierszewski, P.A. Finn, D.W. Kirk, Fusion Eng. Des. 13 (1990) 59–71.
[27] J.S. Spendelow, A. Wieckowski, Phys. Chem. Chem. Phys. 9 (2007) 2654–2675.
[28] Y. Shimonishi, T. Zhang, N. Imanishi, D. Im, D.J. Lee, A. Hirano, Y. Takeda, O. Yamamoto, N. Sammes, J. Power Sources 196 (2011) 5128–5132.
[29] S. Visco, E. Nimon, B. Katz, Honolulu PRiME, ECS, 2012, p. 1156.
[30] O.Y.N. Imanishi, Y. Takeda, Electrochemistry 80 (2012) 706–715.
[31] J. Wolfenstine, J. Mater. Sci. 45 (2010) 3954–3956.
[32] P. Stevens, G. Toussaint, G. Caillon, P. Viaud, P. Vinatier, C. Cantau, O. Fichet, C. Sarrazin, M. Mallouki, ECS Trans. 28 (2010) 1–12.
[33] B. Horstmann, T. Danner, W.G. Bessler, Energy Environ. Sci. 6 (2013) 1299–1314.
[34] F. Bidault, D.J.L. Brett, P.H. Middleton, N.P. Brandon, J. Power Sources 187 (2009) 39–48.
[35] J.T. Gostick, M.W. Fowler, M.A. Ioannidis, M.D. Pritzker, Y. Volfkovich, A. Sakars, J. Power Sources 156 (2006) 375–387.
[36] T.V. Nguyen, G. Lin, H. Ohn, X. Wang, Electrochem. Solid-State Lett. 11 (2008) B127–B131.
[37] E.C. Kumbur, K.V. Sharp, M.M. Mench, J. Electrochem. Soc. 154 (2007) B1295–B1304.
[38] E.C. Kumbur, K.V. Sharp, M.M. Mench, J. Electrochem. Soc. 154 (2007) B1305–B1314.
[39] E.C. Kumbur, K.V. Sharp, M.M. Mench, J. Electrochem. Soc. 154 (2007) B1315–B1324.
[40] S. Dwenger, G. Eigenberger, U. Nieken, Transp. Porous Med. 91 (2011) 281–294.
[41] L. Hao, P. Cheng, Int. J. Heat Mass Tranfer 55 (2012) 133–139.
[42] S. Srinivasan, H. Hurwitz, Electrochim. Acta 12 (1967) 495–512.
[43] J. Giner, C. Hunter, J. Electrochem. Soc. 116 (1969) 1124.
[44] S. Pinnow, N. Chavan, T. Turek, J. Appl. Electrochem. 1053 (2011) 1–12.
[45] A. Bulan, A Process for Producing Gas Diffusion Electrodes, DE Patent App. DE102005023615A1, 2006.
[46] N. Wagner, M. Schulze, E. . Gülzow, J. Power Sources 127 (2004) 264–272.
[47] D. Wittmaier, T. Danner, N. Wagner, K.A. Friedrich, J. Appl. Electrochem. 44 (2013) 73–85.
[48] S.S. . Abd El Rehim, H.H. Hassan, M.A.M. Ibrahim, M.A. Amin, Monatsh. Chem. 129 (1998) 1103–1117.
[49] V. Maurice, L.H. Klein, H.-H. Strehblow, P. Marcus, J. Phys. Chem. C 111 (2007) 16351–16361.
[50] E.R. Savinova, B. Pettinger, K. Doblhofer, J. Electroanal. Chem. 430 (1997) 47–56.
[51] A. Lasia, in: B.E. Conway, J. Bockris, R. White (Eds.), Modern Aspects of Electrochemistry, vol. 32, Kluwer Academic/Plenum Publishers, New York, 1999, pp. 143–248.
[52] R.A. Matula, J. Phys. Chem. Ref. Data 8 (1979) 1147.
[53] S. Gewies, W.G. Bessler, J. Electrochem. Soc. 155 (2008) B937–B952.
[54] W.G. Bessler, S. Gewies, M. Vogler, Electrochim. Acta 53 (2007) 1782–1800.
[55] N. Vargaftik, B. Volkov, L. Voljak, J. Phys. Chem. Ref. Data 12 (1983) 817–820.
[56] V.S. Markin, A.G. Volkov, J. Phys. Chem. B 106 (2002) 11810–11817.
[57] J. Bear, Dynamics of Fluids in Porous Media, first ed., Elsevier, New York, 1972.
[58] D.G. Goodwin, Cantera, 2012. http://code.google.com/p/cantera.
[59] P. Deuflhard, E. Hairer, J. Zugck, Numer. Math. 51 (1987) 501–516.
[60] N. Wagner, in: E. Barsoukov, J. Macdonald (Eds.), Impedance Spectroscopy: Theory, Experiment, and Applications, second ed., John Wiley&Sons, Inc., 2005, pp. 497–537.
[61] T.S. Light, S. Licht, A.C. Bevilacqua, K.R. Morash, Electrochem. Solid-State Lett. 8 (2005) E16–E19.
[62] R. Buchner, G. Hefter, P.M. May, P. Sipos, J. Phys. Chem. B 103 (1999) 11186–11190.
[63] J. Patek, J. Hruby, J. Klomfar, M. Souckova, A.H. Harvey, J. Phys. Chem. Ref. Data 38 (2009) 21–29.
[64] A.H. Narten, H.A. Levy, J. Chem. Phys. 55 (1971) 2263–2269.
[65] A. Bard, L. Faulkner, Electrochemical Methods: Fundamentals and Applications, second ed., Wiley, 2000.
[66] X. Wang, T.V. Nguyen, J. Electrochem. Soc. 155 (2008) B1085–B1092.
[67] Q. Zhao, Y. Liu, C. Wang, Appl. Surf. Sci. 252 (2005) 1620–1627.
[68] M.C. Kimble, J. Electrochem. Soc. 138 (1991) 3370–3382.
[69] J.-H. Jo, S.-C. Yi, J. Power Sources 84 (1999) 87–106.
[70] R. Faure, R. Durand, L. Genies, Electrochim. Acta 44 (1998) 1317–1327.
[71] D. Sepa, M. Vojnovic, L. Vracar, A. Damjanovic, Electrochim. Acta 31 (1986) 97–101.
[72] D. Eberle, B. Horstmann, submitted for publication, 2014.
[73] V. Yurkiv, A. Utz, A. Weber, E. Ivers-Tiffée, H.-R. Volpp, W.G. Bessler, Electrochim. Acta 59 (2012) 573–580.
[74] T.A. Greszler, D. Caulk, P. Sinha, J. Electrochem. Soc. 159 (2012) F831–F840.
[75] T. Suzuki, K. Kudo, Y. Morimoto, J. Power Sources 222 (2013) 379–389.
[76] W. Lang, R. Zander, Ind. Eng. Chem. Fundam. 25 (1986) 775–782.
[77] A.J. Elliot, M.P. Chenier, D.C. Ouellette, Fusion Eng. Des. 13 (1990) 29–31.
[78] L. Jörissen, J. Power Sources 155 (2006) 23–32.
[79] M.D. Koninck, B. Marsan, Electrochim. Acta 53 (2008) 7012–7021.
[80] F. Cheng, J. Shen, B. Peng, Y. Pan, Z. Tao, J. Chen, Nat. Chem. 3 (2011) 79–84.
[81] J. Park, X. Li, J. Power Sources 178 (2008) 248–257.
[82] X. Niu, T. Munekata, S. Hyodo, K. Suga, J. Power Sources 172 (2007) 542–552.

J. Stamm, A. Varzi, A. Latz and B. Horstmann. Modeling nucleation and growth of zinc oxide during discharge of primary zinc-air batteries. *Journal of Power Sources* **360**, 136–149 (2017).

Journal of Power Sources 360 (2017) 136–149

Contents lists available at ScienceDirect

Journal of Power Sources

journal homepage: www.elsevier.com/locate/jpowsour

Modeling nucleation and growth of zinc oxide during discharge of primary zinc-air batteries

Johannes Stamm [a, b, c], Alberto Varzi [a, d], Arnulf Latz [a, b, e], Birger Horstmann [a, b, *]

[a] Helmholtz Institute Ulm (HIU), Helmholtzstraße 11, 89081 Ulm, Germany
[b] German Aerospace Center (DLR), Institute of Engineering Thermodynamics, Pfaffenwaldring 38-40, 70569 Stuttgart, Germany
[c] Institute for Computational and Applied Mathematics, Universität Münster, Einsteinstraße 62, 48149 Münster, Germany
[d] Karlsruhe Institute of Technology (KIT), PO Box 3640, 76021 Karlsruhe, Germany
[e] Ulm University, Institute of Electrochemistry, Albert-Einstein-Allee 47, 89069 Ulm, Germany

HIGHLIGHTS

- Modeling and simulating of VARTA button cell.
- Validation based on galvanostatic discharge and lifetime analysis.
- Nucleation and growth of ZnO and its impact on discharge curve.
- Degradation due to carbonation of alkaline electrolyte.

GRAPHICAL ABSTRACT

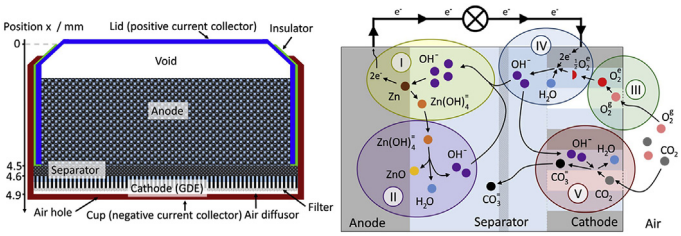

ARTICLE INFO

Article history:
Received 7 February 2017
Received in revised form
12 April 2017
Accepted 22 May 2017
Available online 9 June 2017

Keywords:
Zinc-air battery
Primary button cell
Aqueous alkaline electrolyte
Model and validation
Carbon dioxide absorption
Nucleation and growth

ABSTRACT

Metal-air batteries are among the most promising next-generation energy storage devices. Relying on abundant materials and offering high energy densities, potential applications lie in the fields of electromobility, portable electronics, and stationary grid applications. Now, research on secondary zinc-air batteries is revived, which are commercialized as primary hearing aid batteries. One of the main obstacles for making zinc-air batteries rechargeable is their poor lifetime due to the degradation of alkaline electrolyte in contact with atmospheric carbon dioxide. In this article, we present a continuum theory of a commercial Varta PowerOne button cell. Our model contains dissolution of zinc and nucleation and growth of zinc oxide in the anode, thermodynamically consistent electrolyte transport in porous media, and multi-phase coexistance in the gas diffusion electrode. We perform electrochemical measurements and validate our model. Excellent agreement between theory and experiment is found and novel insights into the role of zinc oxide nucleation and growth and carbon dioxide dissolution for discharge and lifetime is presented. We demonstrate the implications of our work for the development of rechargeable zinc-air batteries.

1. Introduction

Energy production by renewable energies, i.e., wind or solar power, is fluctuating. Therefore, special efforts are required to match energy production and consumption. Traditional power plants are not ideal to compensate for energy fluctuations, especially because renewable energies are strongly decentralized.

* Corresponding author. German Aerospace Center at Helmholtz Institute Ulm, Helmholtzstraße 11, 89081 Ulm, Germany.
E-mail address: birger.horstmann@dlr.de (B. Horstmann).

http://dx.doi.org/10.1016/j.jpowsour.2017.05.073
0378-7753/

Furthermore, portable electronic devices and electro-mobility rely on compact energy storage devices. Metal-air batteries are promising candidates to fulfill this demand, because of their high specific energy density and the use of cheap and abundant materials. These batteries are open at the cathode and use atmospheric oxygen.

Several metals, e.g., lithium, sodium, and zinc, are potential active anode materials in metal-air cells [1]. The high theoretical energy density of lithium-air batteries has stimulated a lot of research [2]. For aprotic electrolytes, the challenge is to influence growth mechanisms in order to maximize capacity, while maintaining sufficient reversibility [3–9]. Aqueous lithium-air batteries require a stable lithium conducting anode protection [10–13]. Non-aqueous sodium-air cells rely on cheap materials having similar challenges as lithium-air batteries [14–16].

Zinc-air batteries stand out as the single commercialized metal-air battery. Primary zinc-air button-cells have a long history in hearing aids. Therefore, also rechargeable zinc-air batteries are in a very mature state [1,17–21]. The discharge product is not passivating and crystallization is reversible. Metallic zinc (Zn) anodes are stable in aqueous electrolytes and can withstand a few hundred cycles. The cells can work with ambient air for a few months. The theoretical specific energy density of zinc-air batteries reaches 1100 Wh kg^{-1} with respect to the mass of Zn [1]. The button cell studied in this work delivers the practical energy density 300 Wh kg^{-1} at 100 Am^{-2}, which is still about three times as high as batteries in modern electric vehicles [22].

Besides its energy density, zinc-air cells offer a couple of additional advantages, e.g., comparatively constant discharge voltage, long storage life, no reaction with water, large abundance of Zn, low costs, and high environmental safety [23]. However, unsolved issues for secondary zinc-air cells remain, particularly with respect to cycle life and lifetime. Major challenges are passivation due to zinc oxide (ZnO) precipitation, shape changes of metallic Zn during cycling, and sluggish kinetics of oxygen reduction [1].

Furthermore, atmospheric carbon dioxide enters the cell and reacts to carbonate in the electrolyte [24,25]. This process entails an irreversible reduction of hydroxide concentration, zincate solubility, and electrolyte conductivity. Therefore, without special precautions, the lifetime of alkaline zinc-air batteries is limited to a few months, which is especially troublesome for secondary cells.

Most research on zinc-air batteries is devoted to improving the alkaline system [17], based on modeling [26], in-situ x-ray measurements [27], and designing nano-materials [19]. Novel research makes use of alternative electrolytes, i.e., aqueous neutral electrolytes [28] to mitigate carbonate formation or ionic liquids [29] to enable reversible Zn deposition.

In order to improve the cycle life of zinc-air batteries, a better understanding of its elementary processes seems necessary. To address this issue, several models on zinc-air cells are discussed in the literature [25,30–32], based on the general, macroscopic, and one-dimensional model for porous electrodes proposed by Newman et al. [33,34].

Sunu and Bennion [30] develop a one dimensional, time dependent model of the Zn anode of zinc-air batteries, based on concentrated ternary electrolyte theory [34]. It is found that electrolyte convection in Zn anodes can lead to a redistribution of Zn inside the anode and into the cathode upon cycling. The redistributed Zn blocks electrolyte pores or electrically shortens the cell. Isaacson et al. [35] discuss a similar, but two dimensional model for Zn electrodes.

Mao and White [31] extend Sunu's model resolving the separator region. It is found that potassium zincate does not precipitate under realistic conditions [36]. Deiss et al. [32] describe a similar model for secondary zinc-air cells based on dilute solution theory, which reaches a fairly good agreement with experimental discharge curves.

Schröder and Krewer [25] develop a model of secondary cells, including a gas diffusion electrode and the effect of atmospheric carbon dioxide. As this model is zero-dimensional, it cannot resolve the nonuniform reaction distribution in the Zn anode [27]. The model demonstrates the reduction in lifetime due to carbonization of the alkaline electrolyte.

In this paper, we develop a one dimensional model for both porous electrodes. Three-phase-coexistence in the gas diffusion electrode [12,13] and inhomogeneous reaction distributions in the Zn anode are modeled at the same time. The electrolyte transport model is based on rational thermodynamics taking into account diffusion, migration, and convection [37,38]. For the first time in zinc-air batteries, we model the nucleation and growth of ZnO and its impact on Zn dissolution. The kinetics of carbon dioxide absorption is described as first order reaction based on a microscopic model [39]. Our model is parametrized and validated with the commercial zinc-air coin cell Varta PowerOne PR44 Type p675 used for hearing aids. We can correlate characteristic features in the discharge curves with specific processes inside the battery, e.g., nucleation of ZnO and diffusion of reactants through ZnO. The limited battery lifetime is explained with carbonation of the electrolyte.

Our paper is structured as follows: First, we give a brief overview of cell design, composition, and the chemical reactions during the discharge process (see Sec. 2). Next, we describe our homogeneous, one-dimensional, continuum cell model (see Sec. 3) and its parameterization (see Sec. 4). Then, we discuss galvanostatic discharge (see Sec. 6) and lifetime (see Sec. 7). In each of these two sections, we compare experiments and simulations. The excellent agreement between theory and experiment allows the discussion of internal battery processes based on simulations. Finally, we summarize our findings in Sec. 8.

2. Zinc-air button cell

In this section, we describe the structure and components of the Varta PowerOne hearing aid battery PR44 Type p675 (see Fig. 1). Anode, separator, cathode, and electrolyte are important for cell performance and described in the subsequent sections.

2.1. Composition and design of zinc-air button cells

The porous *anode* consists of metallic Zn powder connected to the current collector. The pores are flooded with electrolyte. Zn as active material dissolves during discharge at the solid-liquid phase

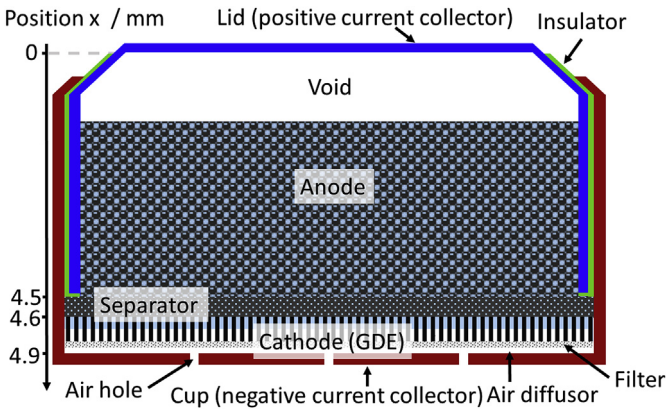

Fig. 1. Components and structure of a zinc-air button cell.

boundary. The fine powder with its large surface area provides a fast and homogeneous Zn dissolution. A void space beneath the cover of the anode accommodates the volume change due to the conversion of active material in the anode. We assume that this void space is filled with gas at standard pressure which does not interact with the cell, but can leave it through the gas diffusion electrode (GDE).

The *electrolyte* in the VARTA cell is an aqueous potassium hydroxide solution at 32wt%. This electrolyte is optimized for conductivity realizing the best combination of ionic strength and viscosity. Additionally, this potassium hydroxide solution offers fast oxygen reduction kinetics.

The *separator* is made of a microporous filtering paper. It prevents electric contact between the two electrodes, but allows the electrolyte to pass through.

As *cathode,* metal-air batteries employ a gas diffusion electrode (GDE) which fulfills two functions. On the one hand, it supplies the cell with atmospheric oxygen, but keeps the electrolyte inside the cell. To this aim, the GDE contains a hydrophobic binder, repelling the aqueous electrolyte and enabling the coexistence of gas and liquid phases. On the other hand, the GDE reduces dissolved oxygen, providing hydroxide to the electrolyte. The cathode is filled with a non-noble catalyst, i.e., manganese oxide, to improve reaction kinetics at low costs. The specific surface area for oxygen reaction is enlarged by using a highly porous structure [20].

2.2. Reactions

The main reactions in a zinc-air battery are shown in Fig. 2. During discharge the anodic Zn is oxidized. However, Zn does not directly transform into ZnO, but dissolves as zincate $Zn(OH)_x^{y-}$ into the electrolyte. The dominant type in the strongly alkaline electrolyte is $Zn(OH)_4^{=}$ [40], and we assume this is the only Zn species in the electrolyte. The chemical equation for the oxidation is

$$Zn + 4OH^- \rightleftharpoons Zn(OH)_4^{=} + 2e^- . \quad (I)$$

The overall reaction can be divided into elementary first order reactions. Several reaction mechanisms are suggested with three [41,42] or four elementary reactions [30,43]

$$Zn + OH^- \rightleftharpoons Zn(OH) + e^- \quad (I.a)$$

$$ZnOH + OH^- \rightleftharpoons Zn(OH)_2^- \quad (I.b)$$

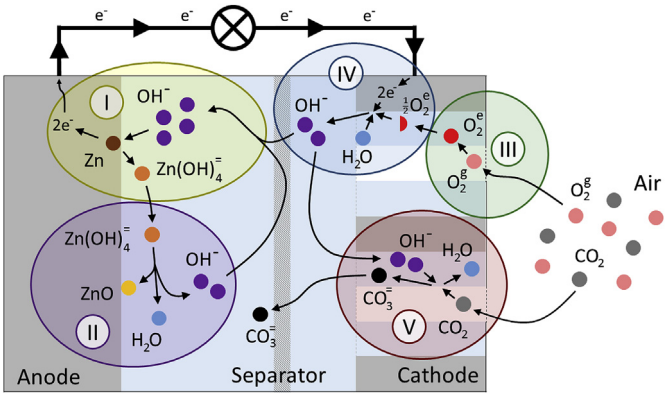

Fig. 2. Reactions in the primary zinc-air cell: I) Zn dissolution, II) ZnO precipitation, III) Oxygen absorption into the electrolyte, IV) Oxygen reduction, V) Dissolution of atmospheric carbon dioxide and carbonate formation.

$$Zn(OH)_2^- + OH^- \rightleftharpoons Zn(OH)_3^- + e^- \quad (I.c)$$

$$Zn(OH)_3^- + OH^- \rightleftharpoons Zn(OH)_4^{=} . \quad (I.d)$$

In both cases oxidation of $Zn(OH)_2^-$ is found to be rate limiting.

If the zincate concentration raises above its solubility limit, precipitation of ZnO becomes possible thermodynamically

$$Zn(OH)_4^{=} \rightleftharpoons ZnO + H_2O + 2OH^- . \quad (II)$$

The reaction takes place on the Zn surface and forms a porous ZnO layer, which retards the hydroxide supply of the anode. Thereby, it reduces the cell voltage and passivates the electrode once the layer is getting to thick [30,44]. If the overvoltage at the Zn surface becomes too large, ZnO type II forms as a compact ZnO layer and completely passivates the Zn. We omit ZnO type II in our model, since the cell voltage in our experiments does not allow its formation in the typical working domain $U > 1.1V$ [42].

In the GDE at the gas-liquid phase boundary, atmospheric oxygen is dissolved [45] in the electrolyte

$$O_2^g \rightleftharpoons O_2^e . \quad (III)$$

Subsequently, dissolved oxygen is reduced to hydroxide at the active cathode surfaces

$$0.5O_2^e + H_2O + 2e^- \rightleftharpoons 2OH^- . \quad (IV)$$

The kinetics of oxygen reduction can be understood based on its elementary reaction steps [46,47] and depends on the employed catalyst [48].

The carbonate reaction is the major degradation process [24]. Atmospheric carbon dioxide dissolves and reacts to carbonate [36]

$$CO_2 + 2OH^- \rightleftharpoons CO_3^{=} + H_2O . \quad (V)$$

In an alkaline medium the rate limiting reaction step is [49]

$$CO_2 + OH^- \xrightarrow{k_{OH^-}} HCO_3^- \quad (V.a)$$

immediately followed by the reaction

$$HCO_3^- + OH^- \rightarrow CO_3^{=} + H_2O . \quad (V.b)$$

The carbonate has various negative effects on the cell performance. The concentration of hydroxide, the main charge carrier, decreases. This leads to a loss of conductivity and enhances the passivation of the anode. Furthermore, carbonate inhibits both of the electrochemical reactions, because the decrease in hydroxide concentration reduces the solubilities of zincate and oxygen.

3. Physical and mathematical model

In this section, we introduce a thermodynamically consistent model for zinc-air cells. Our continuum model represents effects on a single dimension connecting anode, separator, and cathode. We start with a simple diffusion-migration model and successively add convection and reactions to it. First, we state a few central *assumptions* which keep our model simple:

- We model an isothermal system since temperature variations are negligible in small zinc-air button cells.
- The electrolyte is locally charge neutral because we are not interested in capacitive effects.
- The electrolyte is strictly incompressible, i.e., its volume does not respond to pressure.

- The partial pressures in the gas phase are constant because it is connected to the atmosphere and transport of gases is significantly faster than transport in the electrolyte.
- No electrolyte is leaking out off the battery. Consequently, all electrolyte fluxes equal zero on the simulation domain boundaries.

In the following, we denote the solvent H_2O, the three kinds of anions OH^-, $Zn(OH)_4^{\bar{2}}$, $CO_3^{\bar{2}}$, and the cation K^+ with the indices 0, 1, 2, 3, and +, respectively.

3.1. Electrolyte diffusion and migration

We model diffusion and migration based on Latz et al. [37,38]. In this subsection, we discuss transport neglecting volume changes, chemical reactions, and convection. The latter means that we describe transport relative to the center of mass motion of the electrolyte. In the following subsections, we will step by step develop a realistic model with volume changes and chemical reactions, as well as convection. In the first part of this section, we present our model for pure electrolytes.

Dissolved oxygen can diffuse in the electrolyte

$$\partial_t c_{O^2} = \vec{\nabla}\cdot\left(D_{O^2}\vec{\nabla}c_{O^2}\right). \tag{1}$$

For the sake of clarity, we omit the dissolved oxygen below, knowing that it appears only in small amounts and does not influence the transport of the dominant species. According to Latz et al. [38], the entropy production rate in polarizable systems in an external electromagnetic field in the isothermal case is

$$\mathscr{R} = -\vec{j}\cdot\vec{\nabla}\Phi - \sum_{i=1}^{3}\vec{N}_i\cdot\vec{\nabla}\mu_i. \tag{2}$$

Here $\vec{N}_i$ denotes the particle flux density of species i, $\vec{j}$ the current density, $\mu_i := -\tilde{\mu}_0(M_i + z_iM_+)M_0^{-1} + \tilde{\mu}_i + z_i\tilde{\mu}_+$ the effective chemical potential and Φ the electrical potential, which holds $\vec{E} = -\vec{\nabla}\Phi$. The effective chemical potentials μ_i for the anions are valid in the center-of-mass frame assuming local charge neutrality.

The thermodynamical fluxes $\vec{j}$ and $\vec{N}_i$ fulfill the Onsager reciprocal relations, which we write compactly as

$$-\left(\vec{N}_1,\vec{N}_2,\vec{N}_3,\vec{\iota}\right)^T = \mathscr{M}\cdot\left(\vec{\nabla}\mu_1,\vec{\nabla}\mu_2,\vec{\nabla}\mu_3,\vec{\nabla}\phi\right)^T, \tag{3}$$

with the scaling $\vec{\iota} := \vec{j}F^{-1}$ and $\phi := \Phi F$. In this scaling, the Onsager matrix $\mathscr{M}$ is defined as

$$\mathscr{M} := \mathscr{D} + \tilde{\kappa}\vec{\tau}\otimes\vec{\tau}, \tag{4}$$

with $\tilde{\kappa} := \kappa F^{-2}$, $\mathscr{D} := \mathrm{diag}(\tilde{D}_1,\tilde{D}_2,\tilde{D}_3,0)$, and $\vec{\tau} := (-\tau_1,-\tau_2,-\tau_3,1)^T$ with $\tau_i := t_iz_i^{-1}$. Here t_i, κ and F denote the transference numbers, the electrolytic conductivity and the Faraday constant, respectively.

The Onsager matrix has to be positive-semidefinite, since the entropy production rate $\mathscr{R}$ is always non-negative in a physical system. This is obviously fulfilled, if $\tilde{D}_i \geq 0$ and $\tilde{\kappa} \geq 0$, due to the simple calculation

$$\vec{x}^T\mathscr{M}\vec{x} = \sum_{i=1}^{n}\tilde{D}_ix_i^2 + \tilde{\kappa}(\vec{x}\cdot\vec{\tau}). \tag{5}$$

The consequences of the reciprocal relations for the thermodynamical fluxes are more apparent in the standard notation. We express these equations in terms of concentrations, which is more convenient. Assuming that the chemical potential $\mu_i \equiv \mu_i(c_i)$ of any species depends on the corresponding concentration only, we find

$$\vec{N}_i = -D_i\vec{\nabla}c_i - \frac{t_i}{z_iF}\vec{j}, \tag{6}$$

$$\vec{j} = -\kappa\vec{\nabla}\Phi + \frac{\kappa}{F}\sum_{i=1}^{3}\frac{t_i}{z_i}\left(\frac{\partial\mu_i}{\partial c_i}\right)\vec{\nabla}c_i. \tag{7}$$

with $D_i := \tilde{D}_i\left(\frac{\partial\mu_i}{\partial c_i}\right)$ denoting the diffusion coefficients.

In the absence of reactions, concentration and charge density are conserved. Taking the local charge neutrality of the electrolyte into account, they satisfy the continuity equations

$$\partial_t c_i = -\vec{\nabla}\cdot\vec{N}_i \quad \text{and} \quad 0 = -\vec{\nabla}\cdot\vec{j}. \tag{8}$$

Combining these relations with Eqs. (6) and (7), we finally find the transport equations

$$\partial_t c_i = \vec{\nabla}\cdot\left(D_i\vec{\nabla}c_i\right) + \vec{\nabla}\cdot\left(\frac{t_i}{z_iF}\vec{j}\right) \tag{9}$$

$$0 = \vec{\nabla}\cdot\left(\kappa\vec{\nabla}\Phi\right) - \vec{\nabla}\cdot\left(\frac{\kappa}{F}\sum_{i=1}^{3}\frac{t_i}{z_i}\left(\frac{\partial\mu_i}{\partial c_i}\right)\vec{\nabla}c_i\right) \tag{10}$$

In the second part of this section, we consider the electrodes. Therefore, we now allow three coexisting phases: gas, liquid, and solid.

Taking the porous electrode into account changes the model in two ways: fluxes in porous media differ from unhindered fluxes in pure liquids and the transport equations are only applied to the electrolyte volume.

We define the volume fraction of each phase as $\varepsilon_i := \frac{V_i}{V_{\text{total}}}$. This definition obviously yields

$$1 = \varepsilon_s + \varepsilon_e + \varepsilon_g, \tag{11}$$

where the indices s, g, and e denote the solid phase, the gas phase, and the electrolyte, respectively. In agreement with Ref. [34], we model the effects of porosity and tortuosity on the fluxes via the factor ε_e^β, with the Bruggeman coefficient $\beta = 1.5$.

The effective flux density equations are (see eqs. (6) and (7))

$$\vec{N}_i^{\text{eff}} = -\varepsilon_e^\beta D_i\vec{\nabla}c_i - \varepsilon_e^\beta\frac{t_i}{z_iF}\vec{j}, \tag{12}$$

$$\vec{j}^{\text{eff}} = -\varepsilon_e^\beta\kappa\vec{\nabla}\Phi + \frac{\varepsilon_e^\beta\kappa}{F}\sum_{i=1}^{3}\frac{t_i}{z_i}\left(\frac{\partial\mu_i}{\partial c_i}\right)\vec{\nabla}c_i. \tag{13}$$

3.2. Reactions in porous electrodes

In this section, we incorporate the reactions described in Sec. 2.2 into our model. Then particle flux density and current density are not conserved quantities. In our macro-homogeneous approach, reactions appear as species-related source terms S_i (see eq. (18)) in the transport equations. Thus, the continuity Eq. (8) become

$$\partial_t(\varepsilon_e c_i) = -\vec{\nabla}\cdot\vec{N}_i^{\text{eff}} + S_i \tag{14}$$

and

$$0 = -\vec{\nabla}\cdot\vec{j}^{\text{eff}} - \sum_{i=1}^{3} z_i F S_i. \tag{15}$$

We find the macro-homogeneous transport equations with the definition of the effective fluxes 20 and 13

$$\partial_t(\varepsilon_e c_i) = \vec{\nabla}\cdot\left(\varepsilon_e^{\beta} D_i \vec{\nabla} c_i\right) + \vec{\nabla}\cdot\left(\varepsilon_e^{\beta}\frac{t_i}{z_i F}\vec{j}\right) + S_i \tag{16}$$

$$0 = -\sum_{i=1}^{3} z_i F S_i + \vec{\nabla}\cdot\left(\varepsilon_e^{\beta}\kappa\nabla\Phi\right) - \vec{\nabla}\cdot\left(\frac{\varepsilon_e^{\beta}\kappa}{F}\sum_{i=1}^{3}\frac{t_i}{z_i}\left(\frac{\partial\mu_i}{\partial c_i}\right)\vec{\nabla} c_i\right). \tag{17}$$

The species-related source terms depend on the reaction-specific source terms s_j

$$S_i = \sum_{j\in\mathscr{J}} s_j \nu_{ij}, \tag{18}$$

where $\mathscr{J} = \{\text{I}, \ldots, \text{V}\}$ denotes the set of all reaction indices and ν_{ij} the stoichiometric index of species i in reaction j. The reaction-specific source terms s_j are discussed in the following. Generally, the source terms $s_i = A_i \cdot j_i$ are the products of the surface-related reaction rates j_i and the specific surface areas A_i.

3.2.1. Zn oxidation/dissolution

To model the surface-related reaction rate of first order electrochemical reactions, a thermodynamically consistent Butler-Volmer approach is applied [50,51].

$$j = j_0\left[\exp\left(\alpha\frac{zF}{RT}\eta\right) - \exp\left(-(1-\alpha)\frac{zF}{RT}\eta\right)\right], \tag{19}$$

with the exchange current density

$$j_0 := k\left(\frac{c_O}{c_{std}}\right)^{(1-\alpha)}\left(\frac{c_R}{c_{std}}\right)^{\alpha} \tag{20}$$

and the activation overpotential

$$\eta = \eta^0 + \frac{RT}{zF}\ln\left(\frac{c_O}{c_R}\right). \tag{21}$$

Here R, α, z, c_O, and c_R denote the universal gas constant, the symmetry factor, the number of exchanged electrons, and the concentration of the oxidizing and the reducing agents, respectively. The second term on the right hand side takes the chemical potential differences into account, which are caused by the species concentrations in the electrolyte.

Even though the Zn oxidation is not an elementary one-electron reaction (see Reaction I in Sec. 2.2), complex rate expressions based on the rate determining electron transfer exist [30,43]. As, however, diffusion through the ZnO layer is limiting Zn dissolution, we can employ the simpler consistent global rate expression [25,32].

$$j_I = 2k_I\sqrt{\frac{c_{s,OH^-}^4 c_{Zn(OH)_4^=}}{c_{std}^5}}\sinh\left(\frac{F}{RT}\eta_a\right), \tag{22}$$

where we choose the symmetry factor $\alpha = 0.5$. Here k_I denotes the kinetic coefficient and c_{s,OH^-} the hydroxide concentration at the Zn surface, in contrast to the hydroxide bulk concentration $c_{OH^-} = c_{b,OH^-}$. The overpotential yields

$$\eta_a = \Delta\phi_a - \Delta\phi_a^0 + \frac{RT}{zF}\ln\left(\frac{c_{s,OH^-}^4}{c_{Zn(OH)_4^=} c_{std}^3}\right). \tag{23}$$

Thereby, $\Delta\phi_a := \phi_a - \phi_e$ is the potential difference between anode and electrolyte and $\Delta\phi_a^0$ is the open circuit half-cell potential at standard concentrations.

For determining the specific surface area A_I of the anode, we assume that the Zn electrode consists of spherical particles with radius r_{Zn}. Thus, the constant density of spherical Zn particles

$$N_{Zn} = \frac{3\varepsilon_{Zn}^0}{4\pi}\left(r_{Zn}^0\right)^{-3} \tag{24}$$

depends on initial volume fraction ε_{Zn}^0 and radius r_{Zn}^0. At each time step and position, we calculate Zn radius and specific surface area according to

$$r_{Zn} = \left(\frac{3\varepsilon_{Zn}}{4\pi N_{Zn}}\right)^{\frac{1}{3}}, \quad A_I = 4\pi N_{Zn} r_{Zn}^2. \tag{25}$$

The ZnO layer formed around dissolved Zn particles was imaged by Shao-Horn [52,53]. First, ZnO type I forms a porous shell filled with electrolyte and the remaining Zn particle. We assume that the ZnO film forms uniformly with a constant porosity ε_f on each of the Zn particles in a certain control volume. The film thickness is $\delta_{Zn} := r_{ZnO} - r_{Zn}^0$ with the constant inner radius r_{Zn}^0 and the growing outer radius

$$r_{ZnO} = r_{Zn}^0\left(1 + \frac{1}{1-\varepsilon_f}\frac{\varepsilon_{ZnO}}{\varepsilon_{Zn}^0}\right)^{\frac{1}{3}}. \tag{26}$$

The hydroxide concentration c_{s,OH^-} at the Zn surface is limited by diffusion through the porous film and by hydroxide consumption due to Zn oxidation s_I at the surface [43,44]. Hydroxide transport is described by spherical diffusion

$$\frac{4 s_I}{A_I^0} = \varepsilon_f^{3.5} D_{OH^-}\frac{c_{b,OH^-} - c_{s,OH^-}}{\delta_{Zn}}\frac{r_{ZnO}}{r_{Zn}^0}. \tag{27}$$

driven by the concentration gradient between the bulk c_{b,OH^-} and surface c_{s,OH^-} concentration. We increase the Bruggemann coefficient to 3.5 here, in order to simulate the diffusion limitation proven experimentally. This value is realistic for compact materials [54,55].

3.2.2. Oxygen reduction

We model the rate of oxygen reduction (see Reaction IV) via the symmetric Butler-Volmer approach [56].

$$j_{IV} = -2k_{IV}\frac{c_{OH^-}}{c_{std}}\sqrt[4]{\frac{c_{O_2}}{c_{std}^{O_2}}}\sinh\left(\frac{F}{RT}\eta_c\right), \tag{28}$$

with the activation overpotential

$$\eta_c = \Delta\phi_c - \Delta\phi_c^0 + \frac{RT}{zF}\ln\left(\sqrt{\frac{c_{std}^{O_2}}{c_{O_2}}}\frac{c_{OH^-}^2}{c_{std}^2}\right). \tag{29}$$

The oxygen reduction overpotential dominates the cell overpotential, but remains almost constant during discharge. This justifies our approach to make use of simple, but consistent global reaction kinetics. More complex rate expressions are discussed elsewhere [46].

The oxygen reduction does not change the surface of the GDE. Our simulations show that almost no ZnO precipitates in the cathode. Consequently, we assume that the specific surface A_{IV} remains constant during discharge.

3.2.3. ZnO nucleation and growth

Thermodynamics allows ZnO to grow for concentrations above the solubility limit c_{sat} of zincate (see Reaction II). However, nucleation requires greater concentrations [12] and supersaturation ratios up to $s := c_{Zn(OH)_4^=}/c_{sat} \approx 4$ are reported for Zn anodes [44]. Precipitation is typically diffusion limited for reactions with large supersaturation ratios s [12,30], yielding

$$j_{II} = \varepsilon_f^{3.5} D_{Zn(OH)_4^=} \frac{c_{Zn(OH)_4^=} - c_{sat}}{\delta_{ZnO}} \tag{30}$$

with the diffusion layer thickness δ_{ZnO}. Here we apply the same Bruggemann factor as in Eq. (27). The specific surface area for ZnO precipitation A_{II} depends on nucleation and growth of ZnO particles. This process can be described with classical nucleation theory [12]. We apply a more phenomenological approach to keep the model numerically simple. Nucleation occurs abruptly in our model if the concentration exceeds a critical supersaturation c_{crit}, an additional parameter. The specific surface area is

$$A_{II} = \begin{cases} 4\pi N_{Zn} r_{ZnO}^2 & c_{Zn(OH)_4^=} > c_{crit} \vee \varepsilon_{ZnO} > \varepsilon_{ZnO}^0 \\ 0 & \text{else.} \end{cases} \tag{31}$$

To avoid a discontinuity, we linearly ramp up the specific surface area until 100 ZnO monolayers are deposited.

3.2.4. Oxygen dissolution

The solubility of oxygen in water (see Reaction III) depends linearly on the partial oxygen pressure via Henry's Law [12,45]

$$c_{O_2}^* = 10^{-K_{O_2}^s} H_{O_2}^{c,p} p_{O_2}, \tag{32}$$

where $H^{c,p}$ is Henry's constant and p_{O_2} the partial oxygen pressure. The dependence of solubility on salt concentration, denoted salting out, is described with the Sechenov constant K^s [57].

The kinetics of oxygen dissolution is given by the Hertz-Knudsen equation [12,58]

$$j_{III} = \frac{p_{O_2}\xi}{c_{O_2}^* (2\pi M_{O_2} RT)^{0.5}} \left(c_{O_2}^* - c_{O_2}\right). \tag{33}$$

where ξ denotes the ratio of dissolved molecules to molecules hitting the gas-liquid phase boundary. The specific surface area A_{III} corresponds to the gas-liquid phase boundary and is assumed constant during the discharge process.

3.2.5. Carbon dioxide absorption

Upon absorption, carbon dioxide immediately reacts and forms carbonate (see Reaction V). Due to its high rate, this reaction takes place in a small layer at the gas-liquid phase boundary thinner than the resolution of our 1D model. Therefore, we include a simplified macroscopic pseudo first-order reaction rate in our cell model. In the following, we derive it from a microscopic diffusion-reaction model [39,59,60].

We calculate the concentration of dissolved carbon dioxide in one dimension ($y \in [0, \infty)$) perpendicular to the phase boundary at $y = 0$. Diffusion determines its transport since the pressure gradient in the thin surface layer is negligible. Hence, the carbon dioxide concentration fulfills the simple diffusion-reaction equation [60]

$$\partial_t c_{CO_2}(y,t) = D_{CO_2} \partial_y^2 c_{CO_2}(y,t) - s_{CO_3^=}(y,t), \tag{34}$$

with the rate $s_{CO_3^=}$ of Reaction V (see below).

Let us assume that the carbon dioxide concentration remains in equilibrium at the phase boundary. We estimate the solubility $c_{CO_2}^*$ for the dissolution of carbon dioxide with Henry's law and find the boundary condition

$$c_{CO_2}(0,t) = c_{CO_2}^* = 10^{-K_{CO_2}^s} H_{CO_2}^{c,p} p_{CO_2}. \tag{35}$$

The rate of the microscopic Reaction V depends linearly on the deviation of the concentration from equilibrium, according to Danckwerts et al. [49].

$$s_{CO_3^=} = k_{OH^-} c_{OH^-} \left(c_{CO_2} - c_{CO_2}^{eq}\right) c_{std}^{-2}. \tag{36}$$

Here k_{OH^-} denotes the kinetic constant of the rate determining step (see Reaction V.a) for carbon dioxide absorption in alkaline media. The equilibrium concentration $c_{CO_2}^{eq} \approx 0$ is negligibly small. In the thin film, we assume a constant hydroxide concentration. The simplified local reaction rate yields

$$s_{CO_3^=} = k_{OH^-} c_{OH^-} c_{CO_2} c_{std}^{-2}. \tag{37}$$

On macroscopic time scales, reaction and diffusion through the thin surface layer are fast. Thus, the concentration profile is stationary $c_{CO_2}(0,t) = 0$. This simplifies the partial differential equation (34) to the ordinary differential equation

$$D_{CO_3^=} \partial_x^2 c_{CO_2}(y) = k_{OH^-} c_{OH^-} c_{CO_2}(y) c_{std}^{-2}. \tag{38}$$

We solve for the concentration profile

$$c_{CO_2}(y) = c_{CO_2}^* \exp\left(- \sqrt{\frac{k_{OH^-} c_{OH^-}}{D_{CO_2} c_{std}^2}}\, y \right). \tag{39}$$

Next, we evaluate the macroscopic reaction rate by integrating the microscopic, local reaction rate $s_{CO_3^=}(y)$ and get

$$j_V = \int_0^\infty s_{CO_3^=}(y)\, dy \tag{40}$$

$$= c_{CO_2}^* \sqrt{k_{OH^-} c_{OH^-} D_{CO_2}}\, c_{std}^{-1}. \tag{41}$$

The surface area for oxygen and carbon dioxide absorption $A_V = A_{III}$ is the gas-liquid phase boundary surface.

3.3. Electrolyte convection

Reactions can change the volume available for electrolyte (see Sec. 3.4) and the electrolyte composition (see Sec. 3.2). For incompressible electrolytes, such volume changes lead to convection. In this section we add convection to the transport theory described in Sec. 3.1 determining transport relative to the center of mass. The convective velocity $\vec{v}$ is defined via the flux of the center of mass motion $\rho := \sum_i M_i c_i$ [37].

$$\partial_t(\varepsilon_e \rho) = \vec{\nabla} \cdot \left(\varepsilon_e^\beta \rho \vec{v}_e\right) + \sum_i M_i S_i. \tag{42}$$

We employ this transport equation to calculate the concentration of water in our model.

The convective flux density of each species in the electrolyte is

$\vec{N}_i^{\text{conv,eff}} = \varepsilon_e^\beta c_i \vec{v}_e$. Above we discuss diffusion and migration relative to the center of mass. Therefore, the convective flux density is added to the transport Eq. (16).

$$\partial_t(\varepsilon_e c_i) = \vec{\nabla}\cdot\left(\varepsilon_e^\beta D_i \vec{\nabla} c_i\right) + \vec{\nabla}\cdot\left(\varepsilon_e^\beta \frac{t_i}{z_i F}\vec{j}\right) + \vec{\nabla}\cdot\left(\varepsilon_e^\beta c_i \vec{v}_e\right) + S_i. \tag{43}$$

Note that convection has no influence on the current density because the electrolyte is locally charge neutral.

Next, we describe how the convective velocity depends on electrolyte composition. Our Ansatz is that the convective velocity is such that the electrolyte equation of state remains fulfilled [12,13]. The electrolyte equation of state can be expressed in terms of volumes. This is non-trivial because in general $V_{\text{solution}} \neq V_{\text{solute}} + V_{\text{solvent}}$. The volume change of the solution, caused by adding one more particle of species i, is denoted partial molar volume $\overline{V}_i$ of species i. At constant pressure and temperature it still depends on the composition of the solution [61]. Since the volume is an extensive property, the equation of state is

$$1 = \sum_{i=1}^{k} c_i \overline{V}_i(c_1, \ldots, c_k), \tag{44}$$

where we parametrize the partial molar volumes $\overline{V}_i$ as a function of electrolyte composition in this paper. Together with Eq. (43), we find the following equation for the convective velocity

$$\vec{\nabla}\cdot\left(\varepsilon_e^\beta \vec{v}_e\right) = \partial_t \varepsilon_e - \sum_{i=1}^{k} \overline{V}_i\left[S_i + \vec{\nabla}\cdot\left(\varepsilon_e^\beta D_i \vec{\nabla} c_i\right) + \vec{\nabla}\cdot\left(\varepsilon_e^\beta \frac{t_i}{z_i F}\vec{j}\right)\right]. \tag{45}$$

Continuum models of gas diffusion electrodes in fuel cells and metal-air batteries [12,62] use Darcy's law to connect electrolyte velocity $\vec{v}_e$ and pressure p_e in porous media

$$\vec{v}_e = -\frac{B_e}{\eta_e}\vec{\nabla} p_e. \tag{46}$$

Here B_e denotes the permeability of the electrodes with respect to the electrolyte and η_e the dynamic viscosity of the electrolyte.

3.4. Solid and gas phases

In this subsection, we describe volume changes due to transport and reactions. The dynamics of the volume fractions of solid phases is determined by the appropriate source terms [45].

$$\partial_t \varepsilon_{Zn} = \overline{V}_{Zn} S_{Zn} \quad \text{and} \quad \partial_t \varepsilon_{ZnO} = \overline{V}_{ZnO} S_{ZnO} \tag{47}$$

with the constant molar volumes $\overline{V}_i$.

In the real button cell, the gas phase is present in a compact void space under the anode lid (see Sec. 2.1) and in the gas diffusion electrode. In our model, we consider this void space to be evenly distributed throughout the anode and the separator and keep the model numerically simple. Due to its large kinematic viscosity, convection of gas is two orders of magnitude faster than convection of electrolyte at the same pressure gradient. Therefore, we assume that the partial pressures p_{CO_2} and p_{O_2} as well as the overall pressure p_g remain constant throughout the cell.

As frequently done for gas diffusion electrodes [12,13], our model relies on pressure saturation curves which can either be measured or calculated with 3D Lattice-Boltzmann simulations [63]. It is a complex task to lay out the gas diffusion electrode such that it contains an even mixture of electrolyte and gas phase. Commercial button cells, however, are well-designed and the specific form of the Leverett J-function does hardly influence our simulation results. Let the saturation $\tilde{s}$ of the porous media be the ratio of the electrolyte volume to the void space $\tilde{s} := V_e/(V_e^0 + V_g^0) = \varepsilon_e/(\varepsilon_e^0 + \varepsilon_g^0)$. Then the saturation is determined by the electrolyte pressure (see Eq. (46)) via the Leverett J-function [12,13]

$$J(\tilde{s}) = \sqrt{\frac{B_e}{\varepsilon_s \sigma^2}} p_c := \sqrt{\frac{B_e}{\varepsilon_s \sigma^2}}\left(p_e - p_g\right). \tag{48}$$

Here p_e, p_g, p_c denote the pressure in the electrolyte, the gas phase, the capillary pressure, respectively. σ is the surface tension between electrolyte and GDE and B_e is the GDE permeability for electrolyte.

3.5. Galvanostatic condition

The external current density i_{cell} must always match the density of exchanged electrons in the electrochemical reactions in each of the electrodes [38]. For the cathode this yields

$$i_{\text{cell}} = \int_{V_c} z_{IV} F s_{IV} dx. \tag{49}$$

Since the electrolyte is modeled charge neutral, it is sufficient to consider this constraint in a single electrode (see Eq. (17)).

4. Parameterization and computational details

4.1. Parameterization

We model the Varta PowerOne hearing aid coin cell battery PR44 type p675. Therefore, the parameters represent this battery type. Decades ago, thermodynamics [57,64–68] and ionic transport [30,34,39,64,67,69–73,73–76] in the aqueous alkaline electrolyte (32 weight percent KOH) were accurately studied with experiments. We discuss the parameters in the Supplementary Materials A. Our thermodynamic parameters and transport parameters are based on the extensive literature. In contrast, the reaction kinetics are not known with sufficient accuracy. Therefore, we choose to adjust them such that the simulated discharge curves match the measured ones. Nevertheless, we make sure that the reaction parameters are reasonable by comparing to the literature data [12,30,32,44,77–79]. We want to highlight that the qualitative features of our simulation results are robust against variations of the kinetic parameters.

4.2. Computational details

For the simulations, we implement our model in Matlab. The finite volume method is used for space discretization [80]. Time evolution is performed by the implicit, Matlab built-in solver ode15i.

5. Experimental setup and procedure

The electrochemical experiments were carried out with commercial Varta PowerOne hearing aid batteries PR44 Type p675 on a multichannel modular potentiostat/galvanostat VMP3 from Bio-Logic Science Instruments (France). According to the IEC 60086-2 norm, the seal of the cells was removed 10 min before starting each experiment, in order to activate the battery.

Afterwards, two different kinds of test were performed on the

commercial zinc-air cells:

- *Galvanostatic discharge* After recording the open circuit voltage (OCV) for 30 s, the cells were discharged by applying a constant current ranging from 25 to 125 Am^{-2}. The voltage was monitored over time, until it reached the value of 0.9 V, which was selected as the end of discharge cut-off.
- *Lifetime analysis* Firstly, in order to reach the voltage plateau, the cells were subject to a galvanostatic discharge step, whose length and current density was selected to be either 5 h at 100 Am^{-2} or 10 h at 50 Am^{-2}. Afterwards, the cells were left to relax and the OCV recorded for 24 h. After such rest period the cells were partially discharged with a constant current pulse of 100 Am^{-2} or 50 Am^{-2} for 10 min. The cell voltage at the end of each pulse was used to monitor the aging of the cell (see Figure B.1 in the Supplementary Materials). Such OCV-pulse pattern was repeated for several days, until the voltage at the end of the pulse dropped to the cut-off value of 0.9 V.

The tests were performed at room temperature and atmosphere if not stated otherwise. Therefore, small fluctuations in the discharge voltage profiles can be addressed to uncontrollable environmental changes in the laboratory over the experiment time-span.

In order to ensure the reproducibility of the experimental results, each kind of test was repeated at least once. Despite small variation due to uncontrollable factors (e.g., air flow in the laboratory, temperature fluctuation, and eventual differences among the cells coming from the factory), the qualitative features necessary to validate the modeling was always observed. For sake of brevity, we report the most representative measurements only.

6. Galvanostatic discharge

In this section, we discuss the discharge of the zinc-air button cell at various currents. Our simulations allow to study internal variables like ion concentrations and phase distributions which are not directly accessible experimentally. Therefore, we interpret the experimental and theoretical discharge curves by analyzing the simulated internal variables in parallel. The procedure for experiment and simulation is described in detail in Sec. 5.

6.1. Experiment

Discharge profiles at various current densities are plotted in Fig. 3. The voltage generally decreases with increasing discharge current. We observe four characteristic features in each discharge curve:

1. At the beginning of the discharge process, the voltage drops rapidly until a minimum is reached. Then the voltage recovers slightly. This feature occurs at the same discharged capacity regardless of the current.
2. After the initial dip, the cell voltage remains nearly constant for more than half of the discharge time. This plateau is wider at smaller discharge currents.
3. At the end of the voltage plateau, the voltage drops rapidly. This voltage step is larger at higher currents and most pronounced at $i = 125\ Am^{-2}$. At the smallest current density $i = 25\ Am^{-2}$, it is hardly recognizable.
4. After the voltage step, the cell voltage decreases, until it reaches the cut-off voltage.

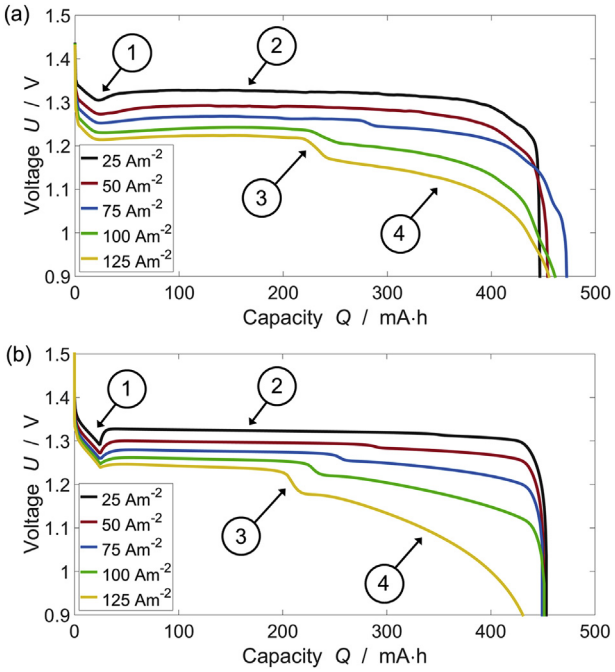

Fig. 3. (a) Experimentally measured and (b) simulated cell voltage profiles during galvanostatic discharge at various current densities. The four key features in the voltage curves are marked with numbers and discussed in the text 1) initial voltage dip, 2) voltage plateau, 3) voltage step, 4) voltage decay.

6.2. Simulation

The simulated discharge curves at various currents are depicted in Fig. 3b. We observe the same four characteristics in the simulated discharge profiles as in the experiments (see Sec. 6.1). After a pronounced dip, the voltage remains constant during most of the discharge. The voltage plateau ends with a deep voltage step. Position and magnitude of the step depend on the applied current. Finally, the voltage drops and approaches the cut-off voltage.

6.2.1. Voltage dip

First, we discuss the initial voltage dip for the discharge current $i = 125\ Am^{-2}$. Activation of the slow oxygen reduction leads to a sharp instantaneous voltage drop from the OCV. The voltage dip is a signature for the nucleation of ZnO. We illustrate this based on the mean ion concentrations in the anode (see Fig. 4a).

Fig. 4a depicts the mean concentrations of hydroxide and zincate ions. Initially, the zincate concentration increases linearly, while the hydroxide concentration decreases linearly. Subsequently, the zincate concentration decreases slightly, while the hydroxide concentration increases. Then the hydroxide concentration at the Zn surface decreases, while the bulk hydroxide concentration increases.

During Zn oxidation, hydroxide is consumed and zincate is formed. This explains the initial linear increase in zincate concentration and the decrease in hydroxide concentration. A lower hydroxide and a higher zincate concentration result in a larger overpotential in the anode. When the critical supersaturation is reached, ZnO starts to nucleate and zincate precipitates as ZnO. With increasing area for precipitation, the zincate concentration decreases and the hydroxide concentration increases. This results in an increase in cell voltage. We will explain the final drop in hydroxide concentration at the Zn surface with the diffusion through ZnO below and correlate it to the cell potential.

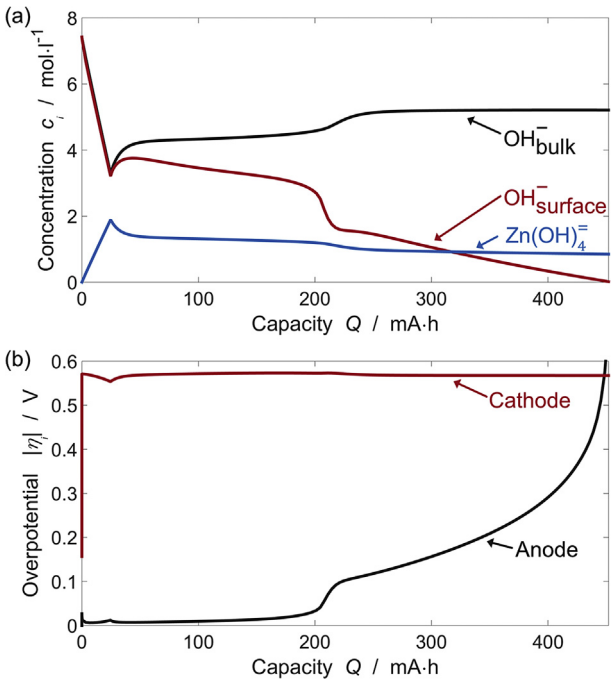

Fig. 4. (a) Mean concentration of hydroxide and zincate in the anode during galvanostatic discharge at 125 Am^{-2}. The zincate concentration rises until the critical supersaturation is reached consuming more hydroxide than replaced by oxygen reduction. Then ZnO nucleates and precipitation starts. In the following, the concentration of zincate decreases slowly due to the growing active surface area of the precipitation reaction. Accordingly, the bulk hydroxide concentration increases again. The hydroxide concentration at the Zn surface is dropping at the end of discharge due to the diffusion through the ZnO shell. (b) Overpotentials during galvanostatic discharge at 125 Am^{-2}. The high cathodic overpotential remains nearly constant during the discharge process. It is the origin of the initial activation overpotential in the voltage profile (see Fig. 3b) and thereby the plateau voltage. The final growth of the anodic overpotential originates from the loss of hydroxide concentration at the Zn surface (see Fig. 4a) and determines the drop in the cell voltage profile.

6.2.2. Voltage plateau

After the nucleation of ZnO, the battery discharges in a quasi-stationary regime as expected for conversion reactions. Only the amounts of Zn and ZnO change and affect the surface areas in the anode. This stationary regime is clearly demonstrated by the cathodic and anodic overpotentials during discharge shown in Fig. 4b. The instant reaction activation overpotentials are very pronounced. The cathodic overpotential dominates and remains constant throughout the full discharge. In the plateau region, the anodic overpotential increases slightly before it rapidly increases after the voltage step. This final increase is due to the diffusion limitation through ZnO (see below).

6.2.3. Voltage step and decay

At the end of the plateau region, a step in cell voltage occurs. Such behavior is typically interpreted with a change in reaction mechanism. The insights from our simulation show, however, that the voltage step originates from the inhomogeneous nucleation of ZnO.

To explain this mechanism, we plot the volume fractions of all phases in the button cell in Fig. 5. We observe that ZnO does not nucleate next to the separator, but precipitates next to the current collector. There a ZnO film passivates the Zn and limits its dissolution. Thus, during the voltage plateau the uncovered Zn close to the separator is preferentially dissolved. When the voltage step is reached, this uncovered Zn is completely gone (see Fig. 5c). The remaining Zn is already covered with a thick ZnO film. After the voltage drop, the Zn beneath this thick film takes over and its oxidation becomes responsible for the cell current. These observations explain the voltage step. It results from the sudden change from the oxidation of uncovered to covered Zn that requires a jump in the driving force for oxidation.

We highlight the importance of electrolyte management based on Fig. 5. Initially, a huge void space filled with gas is present throughout the anode. This is a model representation of the gas space on top of the anode in the real button cell. During discharge the solid volume fraction increases as Zn is converted into ZnO. The void space ensures that the electrolyte is not leaking out of the gas diffusion electrode. This void space just stays open at the end-of-discharge demonstrating that this VARTA button cell is well optimized. In conclusion, we find that the electrolytic parameters remain stable during battery discharge and charge. Furthermore, a well optimized gas diffusion electrode guarantees stable oxygen concentrations throughout the cell at these relatively low current densities, as shown previously [12].

Next, we want to understand the origin of this inhomogeneous precipitation from the concentration profiles depicted in Fig. 6. It shows hydroxide concentration at the electrode surface and in the bulk together with zincate concentration. Note that the potassium concentration is the sum over these anionic concentrations. We observe that the hydroxide concentration is increasing towards the cathode whereas the zincate concentration is maximal in the anode close to the separator. At the voltage dip, the rising zincate concentration surpasses the supercritical concentration next to the current collector where potassium concentration and zincate solubility are lowest (see Supplementary Materials A1.2). Next to the separator, potassium concentration and solubility are higher and do not allow ZnO nucleation.

During further discharge, the concentration of hydroxide at the Zn surface is decreasing in the presence of the ZnO film (see Fig. 6d and Fig. 4a). This causes the final cell voltage loss and increase in anode overpotential at 125 Am^{-2}. The ZnO film is growing during discharge and acts as a diffusion barrier for hydroxide (see Eq. (27)).

6.2.4. Discharge currents

In this section, we compare the simulated discharge curves for various current densities (see Fig. 3b). It is clear that reaction rates, transport rates, and thus the overpotential depend on the discharge current. Higher currents generally result in higher overpotentials. In Fig. 3b, on closer examination it is found that only the discharge curve at 125 Am^{-2} shows the typical shape for diffusion limitations. We find in our simulations that the discharge at lower currents is limited by the total Zn amount in the anode.

The voltage step is an important finding of this paper. The discharged capacity at which this step occurs decreases with increasing discharge current. This can be explained by comparing the profiles of the specific active surface areas for ZnO precipitation in Fig. 7a. The active surface areas increase from current collector to separator in the anode. Next to the separator, no surface area is available. This region increases with increasing discharge current.

The increase in surface area from the current collector to the separator shows that ZnO growth is preferred close to the separator and leads to larger ZnO shells. The absence of surface area next to the separator is explained above via inhomogeneous nucleation. A faster discharge leads to a larger overshoot of the zincate concentration above the supercritical limit, which increases the nucleated surface. Thus, the region without ZnO is smaller and the voltage step is observed at a lower discharged capacity.

6.2.5. Battery cycling

The implications of our analysis for the development of rechargeable zinc-air batteries are demonstrated by simulating one

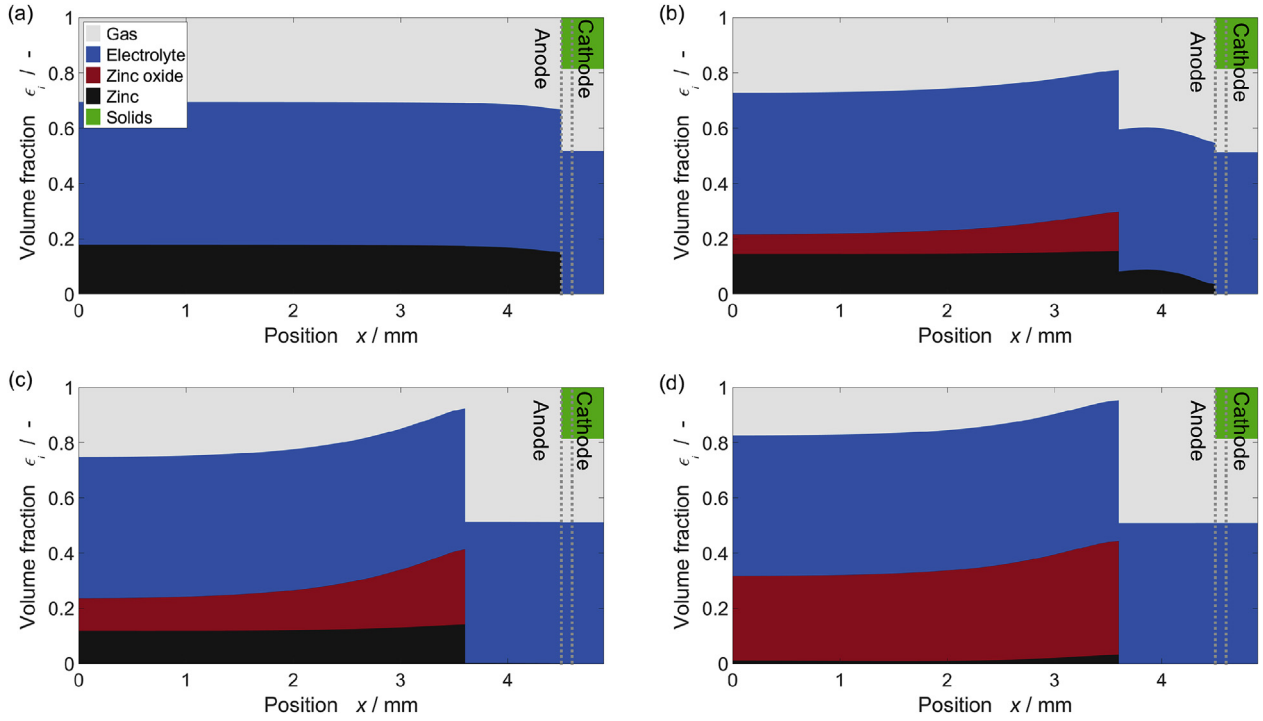

Fig. 5. Volume fractions during galvanostatic discharge at 125 Am^{-2} at characteristic times (see Fig. 3): (a) Dip: No ZnO is precipitating. Zn dissolves slightly faster next to the separator. (b) Plateau: ZnO nucleated and precipitating in the part of the anode close to the current collector (see Fig. 6). Zn dissolution is slowed down in the presence of ZnO. (c) Step: Zn is completely dissolved in the part of the anode in which no ZnO is nucleated. (d) Drop: A thick ZnO film slows down the dissolution of the remaining Zn.

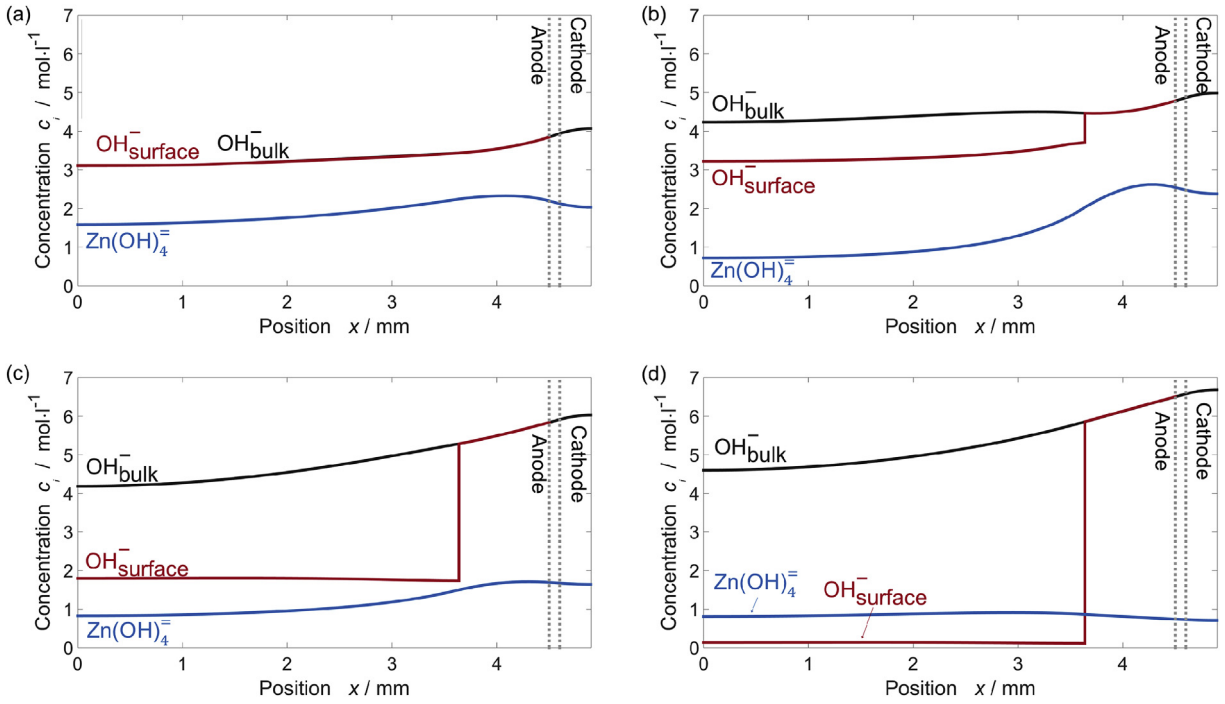

Fig. 6. Various concentration profiles during galvanostatic discharge at 125 Am^{-2} at characteristic times (see Fig. 3): (a) Dip: Zincate concentration is maximum. Critical supersaturation is reached next to the current collector, where zincate solubility is low due to low potassium concentration. (b) Plateau, and (c) Step: Hydroxide bulk concentration and zincate concentration remain nearly constant. Hydroxide surface concentration decreases in parts of the anode due to growing ZnO film. (d) Drop: Hydroxide concentration at the Zn surface is small and limits Zn dissolution.

recharge after a full discharge to the fixed capacity $Q = 407$ mAh or the voltage cut-off $U = 1.1$ V (see Supplementary Materials D). We consider two scenarios: First, we prepare a pure Zn anode; second, we admix 2 volume percent ZnO. In the latter case the voltage dip during discharge disappears. This is because the admixture of ZnO makes its nucleation needless and guarantees more homogeneous

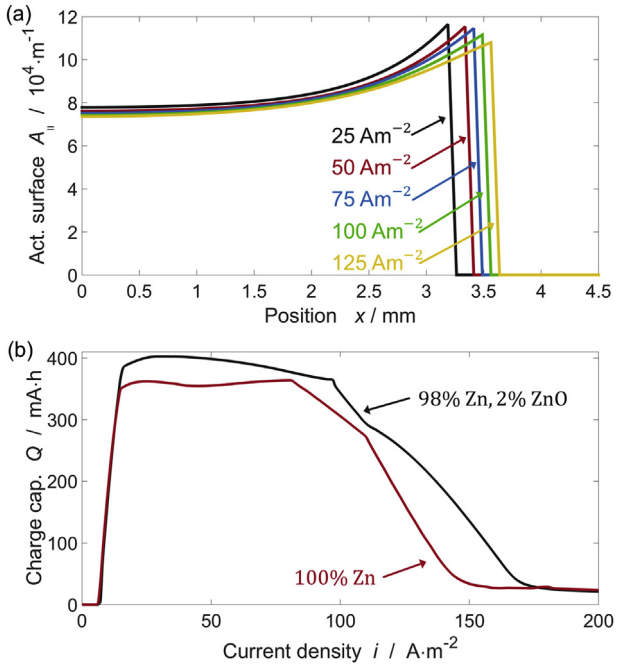

Fig. 7. (a) Active surface for ZnO precipitation during galvanostatic discharge at various current densities. For higher current densities the region where no ZnO precipitates is smaller. Therefore, the capacity at which all Zn is dissolved in this region is smaller for higher currents and the voltage step occurs at lower capacities. (b) Rechargeable capacity after discharge to $Q = 407$ mAh (90% capacity) or $U = 1.1$V. By mixing ZnO into the Zn anode, the rechargeable capacity increases.

deposition of ZnO. As a consequence, Zn dissolves more homogeneously.

We compare the corresponding rechargeable capacities in Fig. 7b. Let us explain the different regimes for the example of a pure Zn anode. At very low current densities $i \lesssim 15$ Am^{-2}, CO_2 absorption limits the capacity. At intermediate current densities 15 Am$^{-2} \lesssim i \lesssim 80$ Am^{-2}, the rechargeable capacity remains almost constant because it is limited by the amount of accessible ZnO. At 80 Am$^{-2} \lesssim i \lesssim 110$ Am^{-2}, dissolution of ZnO is capacity limiting even though ZnO remains available in the anode. Above $i \gtrsim 110$ Am^{-2}, discharge capacity is limiting. We observe that the admixture of ZnO increases the rechargeable capacity because ZnO and Zn remain evenly distributed. This effect is most pronounced at relatively low currents where the surface area for ZnO dissolution is capacity limiting. To conclude, admixture of ZnO leads to more homogeneous precipitation/dissolution and increases the rechargeable capacity of zinc-air batteries.

6.3. Validation and discussion

Finally, we compare measured (see Fig. 3a) and simulated discharge (see Fig. 3b). Note that this paper highlights the qualitative agreement of our theory-based continuum modeling with electrochemical measurements and gives novel insight based on simulations. Excellent quantitative agreement, which is not the aim of this paper, could be gained by adding more parameters and performing extensive parameter adjustments. Nevertheless, we discuss potential model refinements in the following. The four characteristic features, i.e., voltage dip, voltage plateau, voltage step, and voltage drop, are found in both, theory and experiment.

Around the voltage dip, the cell potentials do not exactly agree. Activity coefficients are not included in our modeling, but would affect the cell potential when the zincate concentrations is supercritical at the voltage dip. The increase of the voltage after the dip is very sharp in our simulations. This might be a result of our mean-field description of the nucleation process assuming that nucleation happens in one burst. In reality, small islands might nucleate, grow, and merge to form closed ZnO shells. In this case of agglomeration, the specific surface area for ZnO precipitation would approach full coverage more continuously. This effect would lead to a slower increase in cell voltage.

Magnitude and position of the voltage step agrees very well between model and measurement. At small current densities the voltage step is barely visible in the measured discharge curves, whereas it can still be observed in the simulation. This is a consequence of the lower noise level in the simulations. This excellent agreement supports our interpretation that the voltage dip signals inhomogeneous nucleation. In secondary zinc-air cells it would be advantageous to precipitate ZnO and dissolve Zn homogeneously. This can be achieved by preparing the anode as a mix of ZnO and Zn. The added ZnO will act as nucleation seed for precipitation. This method will reduce the initial discharge capacity, but improve the cycle life of the Zn anode.

The final diffusion limited voltage drop represents a significant shortcoming of our model. In simulations, the diffusion limited regime is only found at 125 Am^{-2}, whereas in experiments, it seems to occur at smaller currents, too. It is interesting that the measurements show a non-monotonous dependence of total discharge capacity on cell current. Furthermore, this behavior at the end of discharge is not exactly reproducible in our experiments. This indicates that the end of discharge is influenced by degradation. Degradation strongly depends on lab conditions, e.g., moisture, temperature. Examples of degradation mechanisms are hydrogen evolution, corrosion of the current collectors, and formation of type II Zn. Type II Zn is not contained in our model but would create an additional diffusion barrier at low enough voltages $U \lesssim 1.1$V at the end of discharge [52]. Also, taking into account a Zn radius distribution would result in a smoother decay of Zn surface area at the end of discharge and a smoother decay in cell voltage as observed in our measurements [12,81]. We capture diffusion limitations at the end of discharge by the simplified rate Eqs. (27) and (30) for Zn dissolution and ZnO precipitation and propose microscopic modeling of electrolyte transport around individual Zn particles.

7. Lifetime analysis

We study the lifetime of the zinc-air button cell (see Sec. 5 for measurement sequence) in this section. To this aim, we perform experiments and simulations giving insights into the underlying degradation process. Our measurement procedure is described in detail in Sec. 6.1. First, we prepare the cell through a continuous discharge and let ZnO nucleate. Every following day we measure the steady-state voltage for the current densities 100 Am^{-2} or 50 Am^{-2}. When the cut-off voltage of 0.9 V is reached, we finish our measurement. The measured voltage as a function of time is shown in the Supplemental Materials in Fig. B1.

Various aging profiles are plotted in Fig. 8a. During the daily measurements, the voltages increase slightly for around 10 days before starting to decrease slowly. Accelerated voltage decay and cell failure occur after one to two months. The voltage profiles are not reproducible and contain a significant amount of noise. In contrast, during short galvanostatic discharge, the voltages are well reproducible. We attribute this noise to the fluctuating environmental conditions in our lab, e.g., temperature, pressure, and air composition. A reference measurement in a climate chamber yields smoother results, even though the air composition is not controlled.

Lifetime simulations are depicted in Fig. 8a. The voltage is

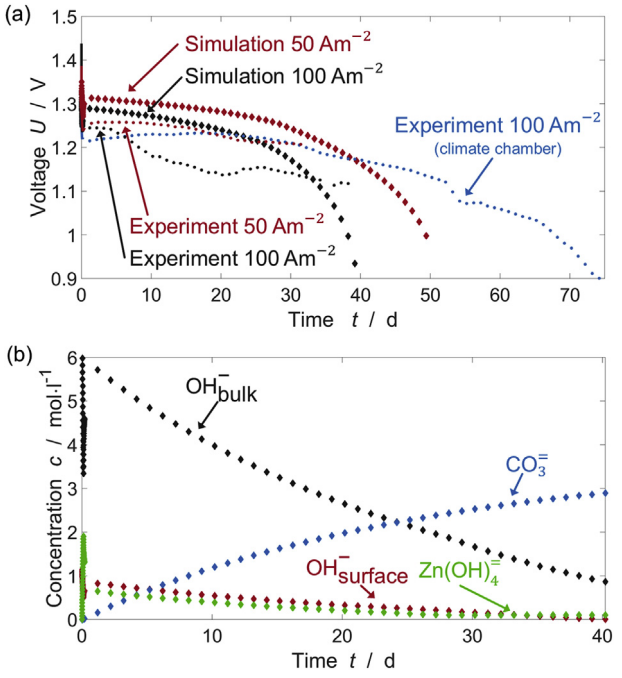

Fig. 8. Lifetime analysis at 50 Am^{-2} (red) and 100 Am^{-2} (black) (a) Cell voltage profile in lifetime experiment (diamonds) and simulation (dots). One experiment (blue) is carried out in the climate chamber at 20 °C, while the other experiments are performed at room temperature and at lab atmosphere. The initial voltage drop is caused by the 5 h galvanostatic discharge. Thereafter, the cell voltage decreases linearly over time. The decrease is independent from the current density. At the end of battery lifetime, faster voltage decay occurs. (b) Mean concentrations of various ions during lifetime experiment at 100 Am^{-2}. The hydroxide concentration c_{OH^-} is decreasing due to carbonate $c_{CO_3^=}$ absorption. This reduces the zincate solubility/concentration $c_{Zn(OH)_4^=}$. The reduction of hydroxide concentration slows down further Zn dissolution and limits the cell lifetime. (For interpretation of the references to colour in this figure legend, the reader is referred to the web version of this article.)

decreasing within a day in our simulations before decreasing logarithmically. The lifetime is limited to 40 days. We study the origin of cell failure by plotting mean ion concentrations in Fig. 8b. The absorption of carbon dioxide and formation of carbonate leads to an almost linear increase in carbonate concentration (see Reaction V). Because this carbonate formation consumes hydroxide, the hydroxide concentration in the electrolyte is reduced significantly. A low hydroxide concentration results in low zincate solubility. The battery cell finally fails due to this decrease in hydroxide concentration and zincate solubility which slow down the further dissolution of Zn. Note that this mechanism does not involve the precipitation of solid carbonates as shown for alkaline electrolytes before [36]. Instead, the reduction in pH is the major consequence of carbon dioxide absorption and the cause for cell failure.

A strategy for mitigating carbon dioxide absorption is illustrated in the Supplementary Materials C. We simulate how a decrease in carbon dioxide content in the feed gas extends the lifetime. Drillet et al. analyze the use of carbon dioxide filters to this aim [24].

We now compare the simulated voltage profile with the measured one (see Fig. 8a). Generally, the simulated voltages are 50 mV too large. This deviation is less distinct during galvanostatic discharge (see Sec. 6). It stems from the relaxation in zincate and hydroxide concentration during battery storage. Agreement would be improved by substituting the global electrochemical kinetics (see Eqs. (22) and (28)) with adjusted expressions [30,43,56] that weaken the dependence of reaction kinetics on ionic concentrations. The good agreement in the voltage slope and the lifetime shows that our simulations qualitatively capture the lifetime limitation. This level of agreement is reached by using a relatively small surface area for carbonate formation, which is two orders of magnitude smaller than expected. Previous studies show a shorter battery lifetime [24,25] of around 10 days. Therefore, we hypothesize that the measured VARTA button cell is optimized to reduce carbon dioxide absorption.

8. Conclusion

Zinc-air batteries were proposed as promising candidates for stationary energy storage due to the use of abundant materials. In this article, we model the discharge of a commercial zinc-air button cell and validate it with experiments. Our simulations describe electrolyte convection and take into account nucleation and growth of the discharge product. We find that the primary zinc-air battery exhibits inhomogeneous deposition and dissolution of ZnO and Zn. Adding ZnO to the zinc anode is shown to improve the rechargeable capacity even though it reduces the initial discharge capacity. Additionally, we show that battery lifetime is limited by carbon dioxide absorption into the aqueous alkaline electrolyte. This effect can be mitigated by using carbon dioxide filters or employing neutral electrolytes.

Acknowledgement

The authors thank Martin Krebs (VARTA Microbattery) and Simon Clark for fruitful discussions. We acknowledge financial support by the EU commission through the project ZAS! Zinc-Air Secondary (Grant Agreement 646186). Further support was provided, by the bwHPC initiative and the bwHPCC5 project through associated compute services of the JUSTUS HPC facility at the University of Ulm.

Appendix A. Supplementary data

Supplementary data related to this article can be found at http://dx.doi.org/10.1016/j.jpowsour.2017.05.073.

References

[1] Y. Li, H. Dai, Recent advances in zinc air batteries, Chem. Soc. Rev. 43 (15) (2014) 5257–5275, http://dx.doi.org/10.1039/C4CS00015C.
[2] L. Grande, E. Paillard, J. Hassoun, J.B. Park, Y.J. Lee, Y.K. Sun, S. Passerini, B. Scrosati, The lithium/air battery: still an emerging system or a practical reality? Adv. Mater. 27 (2015) 784–800, http://dx.doi.org/10.1002/adma.201403064.
[3] N.B. Aetukuri, B.D. McCloskey, J.M. García, L.E. Krupp, V. Viswanathan, A.C. Luntz, Solvating additives drive solution-mediated electrochemistry and enhance toroid growth in non-aqueous LiO2 batteries, Nat. Chem. 7 (January 2015) 50–56, http://dx.doi.org/10.1038/nchem.2132.
[4] L. Johnson, C. Li, Z. Liu, Y. Chen, S.A. Freunberger, P.C. Ashok, B.B. Praveen, K. Dholakia, J.-M. Tarascon, P.G. Bruce, The role of LiO2 solubility in O2 reduction in aprotic solvents and its consequences for LiO2 batteries, Nat. Chem. 6 (12) (2014) 1091–1099, http://dx.doi.org/10.1038/nchem.2101.
[5] T. Liu, M. Leskes, W. Yu, A.J. Moore, L. Zhou, P.M. Bayley, G. Kim, C.P. Grey, Y. Wanjing, A.J. Moore, L. Zhou, P.M. Bayley, G. Kim, C.P. Grey, Cycling Li-O2 batteries via LiOH formation and decomposition, Science 350 (6260) (2015) 530–533, http://dx.doi.org/10.1126/science.aac7730.
[6] J. Lu, Y. Jung Lee, X. Luo, K. Chun Lau, M. Asadi, H.-H. Wang, S. Brombosz, J. Wen, D. Zhai, Z. Chen, D.J. Miller, Y. Sub Jeong, J.-B. Park, Z. Zak Fang, B. Kumar, A. Salehi-Khojin, Y.-K. Sun, L.A. Curtiss, K. Amine, A lithium oxygen battery based on lithium superoxide, Nature 529 (7586) (2016) 1–7, http://dx.doi.org/10.1038/nature16484.
[7] X. Gao, Y. Chen, L. Johnson, P.G. Bruce, Promoting solution phase discharge in LiO2 batteries containing weakly solvating electrolyte solutions, Nat. Mater. 15 (2016) 882–888, http://dx.doi.org/10.1038/nmat4629.
[8] K.U. Schwenke, M. Metzger, T. Restle, M. Piana, H.A. Gasteiger, The influence of water and protons on Li2O2 crystal growth in aprotic Li-O2 cells, J. Electrochem. Soc. 162 (4) (2015) A573–A584, http://dx.doi.org/10.1149/2.0201504jes.
[9] B. Horstmann, B. Gallant, R. Mitchell, W.G. Bessler, Y. Shao-Horn, M.Z. Bazant, Rate-dependent morphology of Li2O2 growth in Li-O2 batteries, J. Phys. Chem.

Lett. 4 (24) (2013) 4217–4222, http://dx.doi.org/10.1021/jz401973c.
[10] P. Stevens, G. Toussaint, G. Caillon, P. Viaud, P. Vinatier, C. Cantau, O. Fichet, C. Sarrazin, M. Mallouki, Development of a lithium air rechargeable battery, ECS Trans. 28 (2010) 1–12, http://dx.doi.org/10.1149/1.3507922.
[11] T. Zhang, N. Imanishi, Y. Takeda, O. Yamamoto, Aqueous lithium/air rechargeable batteries, Chem. Lett. 40 (7) (2011) 668–673, http://dx.doi.org/10.1246/cl.2011.668.
[12] B. Horstmann, T. Danner, W.G. Bessler, Precipitation in aqueous lithium-oxygen batteries: a model-based analysis, Energy & Environ. Sci. 6 (4) (2013) 1299, http://dx.doi.org/10.1039/c3ee24299d.
[13] T. Danner, B. Horstmann, D. Wittmaier, N. Wagner, W.G. Bessler, Reaction and transport in Ag/Ag2O gas diffusion electrodes of aqueous Li-O2 batteries: experiments and modeling, J. Power Sources 264 (2014) 320–332, http://dx.doi.org/10.1016/j.jpowsour.2014.03.149.
[14] P. Adelhelm, P. Hartmann, C.L. Bender, M. Busche, C. Eufinger, J. Janek, From lithium to sodium: cell chemistry of room temperature sodium-air and sodium-sulfur batteries, Beilstein J. Nanotechnol. 6 (1) (2015) 1016–1055, http://dx.doi.org/10.3762/bjnano.6.105.
[15] P. Hartmann, C.L. Bender, M. Vračar, A.K. Dürr, A. Garsuch, J. Janek, P. Adelhelm, A rechargeable room-temperature sodium superoxide (NaO2) battery, Nat. Mater. 12 (3) (2012) 228–232, http://dx.doi.org/10.1038/nmat3486.
[16] J. Kim, H. Park, B. Lee, W.M. Seong, H.-D. Lim, Y. Bae, H. Kim, W.K. Kim, K.H. Ryu, K. Kang, Dissolution and ionization of sodium superoxide in sodium oxygen batteries, Nat. Commun. 7 (2016) 10670, http://dx.doi.org/10.1038/ncomms10670.
[17] M. Xu, D. Ivey, Z. Xie, W. Qu, Rechargeable Zn-air batteries: progress in electrolyte development and cell configuration advancement, J. Power Sources 283 (2015) 358–371, http://dx.doi.org/10.1016/j.jpowsour.2015.02.114.
[18] K. Harting, U. Kunz, T. Turek, Zinc-air batteries: prospects and challenges for future improvement, Z. für Phys. Chem. 226 (2) (2012) 151–166.
[19] Y. Li, M. Gong, Y. Liang, J. Feng, J.E. Kim, H. Wang, G. Hong, B. Zhang, H. Dai, Advanced zinc-air batteries based on high-performance hybrid electrocatalysts, Nat. Commun. 4 (1805) (2013) 1–7, http://dx.doi.org/10.1038/ncomms2812.
[20] V. Neburchilov, H. Wang, J.J. Martin, W. Qu, A review on air cathodes for zinc-air fuel cells, J. Power Sources 195 (5) (2010) 1271–1291, http://dx.doi.org/10.1016/j.jpowsour.2009.08.100.
[21] F.R. McLarnon, E.J. Cairns, The secondary alkaline zinc electrode, J. Electrochem. Soc. 138 (2) (1991) 645, http://dx.doi.org/10.1149/1.2085653.
[22] O. Gröger, H.A. Gasteiger, J.-P. Suchsland, Review electromobility: batteries or fuel cells? J. Electrochem. Soc. 162 (14) (2015) A2605–A2622, http://dx.doi.org/10.1149/2.0211514jes.
[23] J.-S.J.-S. Lee, S. Tai Kim, R. Cao, N.-S.N.-S. Choi, M. Liu, K.T. Lee, J. Cho, Metal-air batteries with high energy density: Li-Air versus Zn-Air, Adv. Energy Mater. 1 (1) (2011) 34–50, http://dx.doi.org/10.1002/aenm.201000010.
[24] J.-F. Drillet, F. Holzer, T. Kallis, S. Müller, V.M. Schmidt, Influence of CO2 on the stability of bifunctional oxygen electrodes for rechargeable zinc/air batteries and study of different CO2 filter materials, Phys. Chem. Chem. Phys. 3 (3) (2001) 368–371, http://dx.doi.org/10.1039/b005523i.
[25] D. Schröder, U. Krewer, Model based quantification of air-composition impact on secondary zinc air batteries, Electrochimica Acta 117 (2014) 541–553, http://dx.doi.org/10.1016/j.electacta.2013.11.116.
[26] D.A. Cogswell, Quantitative phase-field modeling of dendritic electrodeposition, Phys. Rev. E 92 (1) (2015) 011301, http://dx.doi.org/10.1103/PhysRevE.83.061602.
[27] T. Arlt, D. Schröder, U. Krewer, I. Manke, In operando monitoring of the state of charge and species distribution in zinc air batteries using X-ray tomography and model-based simulations, Phys. Chem. Chem. Phys. 16 (40) (2014) 22273–22280, http://dx.doi.org/10.1039/C4CP02878C.
[28] F.W. Thomas Goh, Z. Liu, T.S.A. Hor, J. Zhang, X. Ge, Y. Zong, A. Yu, W. Khoo, A near-neutral chloride electrolyte for electrically rechargeable zinc-air batteries, J. Electrochem. Soc. 161 (14) (2014) A2080–A2086, http://dx.doi.org/10.1149/2.0311414jes.
[29] Z. Liu, S.Z.E. Abedin, F. Endres, Electrodeposition of zinc films from ionic liquids and ionic liquid/water mixtures, Electrochimica Acta 89 (2013) 635–643, http://dx.doi.org/10.1016/j.electacta.2012.11.077.
[30] W.G. Sunu, D.N. Bennion, Transient and failure analyses of the porous zinc electrode, J. Electrochem. Soc. 127 (9) (1980) 2007–2016, http://dx.doi.org/10.1149/1.2130054.
[31] Z. Mao, R.E. White, Mathematical modeling of a primary zinc/air battery, J. Electrochem. Soc. 139 (4) (1992) 1105–1114, http://dx.doi.org/10.1149/1.2069348.
[32] E. Deiss, F. Holzer, O. Haas, Modeling of an electrically rechargeable alkaline Zn-air battery, Electrochimica Acta 47 (25) (2002) 3995–4010, http://dx.doi.org/10.1016/S0013-4686(02)00316-X.
[33] J.S. Newman, C.W. Tobias, Theoretical analysis of current distribution in porous electrodes, J. Electrochem. Soc. 109 (12) (1962) 1183–1191, http://dx.doi.org/10.1149/1.2425269.
[34] J.S. Newman, K. Thomas-Alyea, Electrochemical Systems, John Wiley & Sons, 2004.
[35] M.J. Isaacson, F.R. McLarnon, E.J. Cairns, Current density and ZnO precipitation-dissolution distributions in Zn-ZnO porous electrodes and their effect on material redistribution. A two-dimensional mathematical model, J. Electrochem. Soc. 137 (7) (1990) 2014–2021, http://dx.doi.org/10.1149/1.2086856.
[36] H. Ko, H. Juang, Absorption of CO2 by alkaline electrolyte and its effect on electrical discharge, J. Appl. Electrochem. 13 (6) (1983) 725–730, http://dx.doi.org/10.1007/BF00615821.
[37] A. Latz, J. Zausch, Multiscale modeling of lithium ion batteries: thermal aspects, Beilstein J. Nanotechnol. 6 (2015) 987–1007, http://dx.doi.org/10.3762/bjnano.6.102.
[38] A. Latz, J. Zausch, Thermodynamic consistent transport theory of Li-ion batteries, J. Power Sources 195 (6) (2010) 3296–3302, http://dx.doi.org/10.1016/j.jpowsour.2010.11.088.
[39] A. Cents, Mass Transfer and Hydrodynamics in Stirred Gas-liquid-liquid Contactors, Ph.D. thesis, Universiteit Twente, 2003.
[40] T.P. Dirkse, C. Postmus, R. Vandenbosch, A study of alkaline solutions of zinc oxide, J. Am. Chem. Soc. 76 (23) (1954) 6022–6024, http://dx.doi.org/10.1021/ja01652a041.
[41] Y.-C. Chang, G. Prentice, A model for the anodic dissolution of zinc in alkaline electrolyte kinetics of initial dissolution, J. Electrochem. Soc. 131 (7) (1984) 1463–1468, http://dx.doi.org/10.1149/1.2115875.
[42] G. Prentice, Y.-C. Chang, X. Shan, A model for the passivation of the zinc electrode in alkaline electrolyte, J. Electrochem. Soc. 138 (4) (1991) 890–894, http://dx.doi.org/10.1149/1.2085742.
[43] J.O. Bockris, Z. Nagy, A. Damjanovic, On the deposition and dissolution of zinc in alkaline solutions, J. Electrochem. Soc. 119 (3) (1972) 285–295, http://dx.doi.org/10.1149/1.2404188.
[44] M.-B. Liu, G. Cook, N.P. Yao, Passivation of zinc anodes in KOH electrolytes, J. Electrochem. Soc. 128 (8) (1981) 1663–1668, http://dx.doi.org/10.1149/1.2127707.
[45] J.P. Neidhardt, D.N. Fronczek, T. Jahnke, T. Danner, B. Horstmann, W.G. Bessler, A flexible framework for modeling multiple solid, liquid and gaseous phases in batteries and fuel cells, J. Electrochem. Soc. 159 (9) (2012) A1528–A1542, http://dx.doi.org/10.1149/2.023209jes.
[46] D. Eberle, B. Horstmann, Oxygen reduction on Pt(111) in aqueous electrolyte: elementary kinetic modeling, Electrochimica Acta 137 (2014) 714–720, http://dx.doi.org/10.1016/j.electacta.2014.05.144.
[47] J.A. Keith, G. Jerkiewicz, T. Jacob, Theoretical investigations of the oxygen reduction reaction on Pt(111), ChemPhysChem 11 (13) (2010) 2779, http://dx.doi.org/10.1002/cphc.201000286.
[48] H.A. Hansen, V. Viswanathan, J.K. Nørskov, Unifying Kinetic and Thermodynamic Analysis of 2e-and 4e-Reduction of Oxygen on Metal Surfaces, J. Phys. Chem. C 118 (2014) 67066718, http://dx.doi.org/10.1021/jp4100608.
[49] P.V. Danckwerts, M.M. Sharma, The Absorption of Carbon Dioxide into Solutions of Alkalis and Amines (With Some Notes on Hydrogen Sulphide and Carbonyl Sulphide), Institution of Chemical Engineers, 1966.
[50] A. Latz, J. Zausch, Thermodynamic derivation of a ButlerVolmer model for intercalation in Li-ion batteries, Electrochimica Acta 110 (2013) 358–362, http://dx.doi.org/10.1016/j.electacta.2013.06.043.
[51] M.Z. Bazant, Theory of chemical kinetics and charge transfer based on nonequilibrium thermodynamics, Accounts Chem. Res. 46 (5) (2013) 1144–1160, http://dx.doi.org/10.1021/ar300145c.
[52] Q.C. Horn, Y. Shao-Horn, Morphology and spatial distribution of ZnO formed in discharged alkaline Zn/MnO2 AA cells, J. Electrochem. Soc. 150 (5) (2003) A652–A658, http://dx.doi.org/10.1149/1.1566014.
[53] S. Szpak, C. Gabriel, The Zn-KOH system: the solution-precipitation path for anodic ZnO formation, J. Electrochem. Soc. 126 (11) (1979) 1914–1923, http://dx.doi.org/10.1149/1.2128826.
[54] A. Nyman, M. Behm, G. Lindbergh, Electrochemical characterisation and modelling of the mass transport phenomena in LiPF6-EC-EMC electrolyte, Electrochimica Acta 53 (22) (2008) 6356–6365, http://dx.doi.org/10.1016/j.electacta.2008.04.023.
[55] F. Single, B. Horstmann, A. Latz, Dynamics and morphology of solid electrolyte interphase (SEI), Phys. Chem. Chem. Phys. 18 (2016) 17810–17814, http://dx.doi.org/10.1039/C6CP02816K.
[56] Y.L. Cao, H.X. Yang, X.P. Ai, L.F. Xiao, The mechanism of oxygen reduction on MnO2-catalyzed air cathode in alkaline solution, J. Electroanal. Chem. 557 (2003) 127–134, http://dx.doi.org/10.1016/S0022-0728(03)00355-3.
[57] S. Weisenberger, A. Schumpe, Estimation of gas solubilities in salt solutions at temperatures from 273 K to 363 K, AIChE J. 42 (1) (1996) 298–300, http://dx.doi.org/10.1002/aic.690420130.
[58] I.W. Eames, N.J. Marr, H. Sabir, The evaporation coefficient of water: a review, Int. J. Heat Mass Transf. 40 (12) (1997) 2963–2973, http://dx.doi.org/10.1016/S0017-9310(96)00339-0.
[59] A.H.G. Cents, D.W.F. Brilman, G.F. Versteeg, CO2 absorption in carbonate/bicarbonate solutions: the Danckwerts-criterion revisited, Chem. Eng. Sci. 60 (21) (2005) 5830–5835, http://dx.doi.org/10.1016/j.ces.2005.05.020.
[60] P.V. Danckwerts, Absorption by simultaneous diffusion and chemical reaction, Trans. Faraday Soc. 46 (1950) 300–304, http://dx.doi.org/10.1039/TF9504600300.
[61] S. De Groot, P. Mazur, Non-equilibrium Thermodynamics, Dover Publications, Inc, New York, 1984.
[62] T. Jahnke, G. Futter, A. Latz, T. Malkow, G. Papakonstantinou, G. Tsotridis, P. Schott, M. Gerard, M. Quinaud, M. Quiroga, A.A. Franco, K. Malek, F. Calle-Vallejo, R. Ferreira De Morais, T. Kerber, P. Sautet, D. Loffreda, S. Strahl, M. Serra, P. Polverino, C. Pianese, M. Mayur, W.G. Bessler, C. Kompis, Performance and degradation of proton exchange membrane fuel cells: state of the art in modeling from atomistic to system scale, J. Power Sources 304 (2016)

207–233, http://dx.doi.org/10.1016/j.jpowsour.2015.11.041.
[63] T. Danner, S. Eswara, V.P. Schulz, A. Latz, Characterization of gas diffusion electrodes for metal-air batteries, J. Power Sources 324 (2016) 646–656, http://dx.doi.org/10.1016/j.jpowsour.2016.05.108.
[64] J.A. Dean, N.A. Lange, Lange's Handbook of Chemistry, McGraw-Hill, 1999. http//dx.doi.org/10.1080/10426919008953291.
[65] R. Sander, Compilation of Henry's law constants (version 4.0) for water as solvent, Atmos. Chem. Phys. Discuss. 15 (2015) 4399–4981, http://dx.doi.org/10.5194/acp-15-4399-2015.
[66] W.G. Sunu, Transient and Failure Analyses of Porous Zinc Electrodes, Phd thesis, University of California, Los Angeles, 1978.
[67] S. Siu, J.W. Evans, Density and viscosity measurements of zincate/KOH solutions, J. Electrochem. Soc. 144 (4) (1997) 1278–1280, http://dx.doi.org/10.1149/1.1837583.
[68] D. Möller, Luft: Chemie, Physik, Biologie, Reinhaltung, Recht, Walter de Gruyter, 2003.
[69] R.E. Davis, G.L. Horvath, C.W. Tobias, The solubility and diffusion coefficient of oxygen in potassium hydroxide solutions, Electrochimica Acta 12 (3) (1967) 287–297, http://dx.doi.org/10.1016/0013-4686(67)80007-0.
[70] C.E. May, H.C. Kautz, Determination of the Zincate Diffusion Coefficient and its Application to Alkaline Battery Problems, TM-73879, Nasa Technical Memorandum, NASA, 1978, pp. 1–16.
[71] R.N. Bhatia, K.E. Gubbins, R.D. Walker, Mutual diffusion in concentrated aqueous potassium hydroxide solutions, Trans. Faraday Soc. 64 (1968) 2091–2099, http://dx.doi.org/10.1039/TF9686402091.
[72] R.E. Zeebe, On the molecular diffusion coefficients of dissolved CO2, HCO3-, and CO32- and their dependence on isotopic mass, Geochimica Cosmochimica Acta 75 (9) (2011) 2483–2498, http://dx.doi.org/10.1016/j.gca.2011.02.010.
[73] M.-B. Liu, B. Fauls, G. Cook, N.P. Yao, Conductivity of KOH electrolyte supersaturated with zincate, J. Electrochem. Soc. 128 (10) (1981) 2049–2052, http://dx.doi.org/10.1149/1.2127187.
[74] D.M. See, R.E. White, Temperature and concentration dependence of the specific conductivity of concentrated solutions of potassium hydroxide, J. Chem. Eng. Data 42 (6) (1997) 1266–1268, http://dx.doi.org/10.1021/je970140x.
[75] T. Danner, Modeling and Experimental Investigation of Transport Processes in the Porous Cathode of Aqueous Li-air Batteries, Ph.D. thesis, Universität Stuttgart, 2015.
[76] P.M. Dunlap, S.R. Faris, Surface tension of aqueous solutions of potassium hydroxide, Nature 196 (1962) 1312–1313, http://dx.doi.org/10.1038/1961312a0.
[77] I. Manke, J. Banhart, A. Haibel, A. Rack, S. Zabler, N. Kardjilov, A. Hilger, A. Melzer, H. Riesemeier, In situ investigation of the discharge of alkaline ZnMnO2 batteries with synchrotron x-ray and neutron tomographies, Appl. Phys. Lett. 90 (21) (2007) 214102, http://dx.doi.org/10.1063/1.2742283.
[78] E.L. Gyenge, J.-F. Drillet, The electrochemical behavior and catalytic activity for oxygen reduction of MnO2C toray gas diffusion electrodes, J. Electrochem. Soc. 159 (2) (2012) F23–F34, http://dx.doi.org/10.1149/2.061202jes.
[79] R. Pohorecki, W. Moniuk, Kinetics of reaction between carbon dioxide and hydroxyl ions in aqueous electrolyte solutions, Chem. Eng. Sci. 43 (7) (1988) 1677–1684, http://dx.doi.org/10.1016/0009-2509(88)85159-5.
[80] P. Popov, Y. Vutov, S. Margenov, O. Iliev, Finite volume discretization of equations describing nonlinear diffusion in Li-Ion batteries, in: Numerical Methods and Applications, Volume 6046 of the Series Lecture Notes in Computer Science, Springer, Kaiserslautern, Germany, 2011, pp. 338–346. http//dx.doi.org.10.1007/978-3-642-18466-6_40.
[81] A. Rinaldi, O. Wijaya, H.E. Hoster, Lithium-oxygen cells : an analytical model to explain the key features in the discharge voltage profiles, Chem. Electro. Chem. 3 (June 2016) 1–8, http://dx.doi.org/10.1002/celc.201600184.

Supplementary Information
Nucleation and Growth of Zinc Oxide in Zinc-Air Button Cells

Johannes Stamm[a,b,c], Alberto Varzi[a,d], Arnulf Latz[a,b,e], Birger Horstmann[a,b]

[a] *Helmholtz Institute Ulm (HIU), Helmholtzstraße 11, 89081 Ulm, Germany*
[b] *German Aerospace Center (DLR), Institute of Engineering Thermodynamics, Pfaffenwaldring 38-40, 70569 Stuttgart, Germany*
[c] *Institute for Computational and Applied Mathematics, Universität Münster, Einsteinstraße 62, 48149 Münster, Germany*
[d] *Karlsruhe Institute of Technology (KIT), PO Box 3640, 76021 Karlsruhe, Germany*
[e] *Ulm University, Institute of Electrochemistry, Albert-Einstein-Allee 47, 89069 Ulm, Germany*

Appendix A. Parameterization

We model the Varta PowerOne hearing aid coin cell battery PR44 type p675. Therefore, the parameters represent this battery type. Decades ago, thermodynamics and ionic transport in the aqueous alkaline electrolyte (32 weight percent KOH) were accurately studied with experiments. Thus, in Appendix A.1 we describe thermodynamic parameters and in Appendix A.2 we discuss transport parameters based on the extensive literature. In contrast, the reaction kinetics are not known with sufficient accuracy. Therefore, we choose to adjust them such that the simulated discharge curves match the measured ones (see Appendix A.3). Nevertheless, we make sure that the reaction parameters are reasonable by comparing to the literature data. We want to highlight that the qualitative features of our simulation results are robust against variations of the kinetic parameters.

Basic material parameters and physical constants are given in Tab. A.4. Experiments and Simulations are performed under standard conditions (see Tab. A.3).

In our model, the void space beneath the anode lid, which compensates the volume expansion of the active material, is distributed homogeneously along the anode (see 3.4). We adjust the volume fraction of zinc to get the observed cell capacity of 460 mAh. The (initial) volume fractions and cell dimensions are stated in Tab. A.5.

Appendix A.1. Thermodynamics

Appendix A.1.1. Half-Cell Potentials

The standard half-cell potential for zinc oxidation is $\Delta\phi_{\mathrm{a}}^{0} = -1.285\mathrm{V}$ and for oxygen reduction is $\Delta\phi_{\mathrm{c}}^{0} = 0.401\mathrm{V}$ at standard conditions relative to the standard hydrogen electrode [64].

Appendix A.1.2. Solubilities

The solubility in pure water depends on the partial gas pressure by Henry's law (see Eq. 32) with Henry's constants $H_{\mathrm{O_2}}^{\mathrm{p,c}} = 7.7942 \cdot 10^4\ \mathrm{m^3 Pa\ mol_{gas}^{-1}}$ and $H_{\mathrm{CO_2}}^{\mathrm{p,c}} = 2.98 \cdot 10^4\ \mathrm{m^3 Pa\ mol_{gas}^{-1}}$ for oxygen and carbon dioxide, respectively [65]. At large salt concentrations (32 wt% KOH), the solubility is reduced and we must take into account salting out (see Eq. 32). The Sechenov constant is approximated as [57]

$$K^{\mathrm{s}} = \sum_i h_i c_i, \tag{A.1}$$

Email address: birger.horstmann@dlr.de (Birger Horstmann)

Ion	h_i / $\mathrm{m^3 mol^{-1}}$
Potassium	$0.922 \cdot 10^{-4}$
Hydroxide	$0.839 \cdot 10^{-4}$
Zincate	$1.423 \cdot 10^{-4}$
Carbonate	$1.423 \cdot 10^{-4}$

Table A.1. Coefficients for Sechenov constant [57] (see Eq. A.1). The value for $ZnOH_4^=$ is chosen to be equal to the one for $CO_3^=$.

where the coefficients h_i are given in Tab. A.1. At initial electrolyte concentrations, we find the solubilities $c^*_{O_2} = 13.4\ \mathrm{mol\,m^{-3}}$ and $c^*_{CO_2} = 1.1\ \mathrm{mol\,m^{-3}}$.

We calculate the solubility c_{sat} of zincate depending on the potassium concentration c_{K} [66]

$$c_{\mathrm{sat}} = \begin{cases} -0.21 c_{\mathrm{std}} + 0.975 \cdot 10^{-1} c_{\mathrm{K}} + 0.125 \cdot 10^{-2} \frac{c_{\mathrm{K}}^2}{c_{\mathrm{std}}} & \text{if } c_{\mathrm{K}} > 2.1 c_{\mathrm{std}} \\ 0 & \text{else}\,. \end{cases} \tag{A.2}$$

Note that zinc dissolution is possible even for $c_{\mathrm{sat}} = 0$ due to supersaturation.

Appendix A.1.3. Molar Volumes

The electrolyte density ρ is [67]

$$\rho = \left(1024.1 + 846.6 w_1 + 307.1 w_1^2 + 1039 w_2\right) \mathrm{kg\,m^{-3}}. \tag{A.3}$$

Here, the weight percentage w_1 of potassium hydroxide is defined with respect to the solution H_2O-KOH, while that of zinc oxide w_2 is defined with respect to the whole electrolyte H_2O-KOH-ZnO.

We calculate the partial molar volumes $\bar{V}_i$ from the density in the following [61]. For this purpose, we introduce the molality $b_j := N_j m_0^{-1}$, where m_0 denotes the mass of H_2O. The density is $\rho = m V_{\mathrm{e}}^{-1}$ with the electrolyte mass $m = m_0(1 + \sum_{j=1}^{3} M_j b_j)$ and the molar masses of the salts M_j. Then the partial molar volume is

$$\begin{aligned} \bar{V}_j := \frac{\partial V_{\mathrm{e}}}{\partial n_j} &= \frac{\partial}{\partial n_j}\left(\frac{m}{\rho}\right) = \frac{\partial}{\partial b_j}\left(\frac{1 + \sum_j M_j b_j}{\rho}\right) \\ &= -\frac{1}{\rho^2}\left(\frac{\partial \rho}{\partial b_j}\right)\left(1 + \sum_{i=0}^{3} b_i M_i\right) + \frac{1}{\rho} M_j\,. \end{aligned} \tag{A.4}$$

Molalities b_j and weight percents w_j are related through $w_j = w_0 b_j M_j$. By summing over all species, we find $w_0 = 1/(1 + \sum_{j=1}^{2,3} M_j b_j)$ and

$$w_j = \frac{b_j M_j}{1 + \sum_{j=1}^{2,3} M_j b_j}. \tag{A.5}$$

The sum includes ZnO for w_2, but not for w_1 here because Siu et al. define weight percent in two different ways [67].

The partial molar volume of the solvent is then determined from Eq. 44

$$\bar{V}_0 = M_0 \left(\frac{1 + \sum_{j=1}^{3} M_j b_j}{\rho} - \sum_{j=1}^{3} \bar{V}_j b_j \right). \tag{A.6}$$

Ion	Notation	Value / S m^{2}mol^{-1}	Source
Potassium	λ_{K^+}	$7.35 \cdot 10^{-3}$	[64]
Hydroxide	λ_{OH^-}	$19.8 \cdot 10^{-3}$	[64]
Zincate	$\lambda_{Zn(OH)_4^=}$	$9.035 \cdot 10^{-3}$	[30]
Carbonate	$\lambda_{CO_3^=}$	$6.98 \cdot 10^{-3}$	[64]

Table A.2. Ionic conductivity at infinite dilution

Carbonate is not included in the measurement stated in Eq. A.3. We choose to treat one K_2CO_3 molecules as two KOH molecules in the density calculations. Consequently, we determine its partial molar volume from that of KOH, such that the density is consistent

$$\bar{V}_{K_2CO_3} = \frac{M_{K_2CO_3}}{2M_{KOH}} \bar{V}_{KOH} \tag{A.7}$$

Note that Eq. A.3 uses the salt ZnO, but our model uses $K_2Zn(OH)_4$. The stoichiometry (see Reaction II) gives

$$\bar{V}_{K_2Zn(OH)_4^=} = 2\bar{V}_{KOH} + \bar{V}_{ZnO} + \bar{V}_{H_2O} \tag{A.8}$$

Appendix A.2. Transport

Appendix A.2.1. Diffusion

Davis et al. [69] measure and show the diffusion coefficient of oxygen in potassium hydroxide solution

$$D_{O_2} = \left[1.5 \cdot 10^{-9} \exp(-0.2878 \frac{c_{OH^-}}{c_{std}}) + 0.4 \cdot 10^{-9}\right] \frac{m^2}{s}. \tag{A.9}$$

According to May et al. [70] the diffusion coefficient of zincate depends linearly on potassium ion concentration and is independent from zincate concentration

$$D_{ZnOH_4} = \left[-9.33 \cdot 10^{-11} \frac{c_K}{c_{std}} + 1.2 \cdot 10^{-9}\right] \frac{m^2}{s}. \tag{A.10}$$

The remaining diffusion coefficients stay approximately constant in the relevant electrolyte concentration range. From literature, we find the diffusion coefficient of hydroxide [71], carbonate [72], and carbon dioxide [39] to be

$$D_{OH^-} = 3.5 \cdot 10^{-9}\, m^2 s^{-1}\,, \tag{A.11}$$

$$D_{CO_3^=} = 0.82 \cdot 10^{-9}\, m^2 s^{-1}\,, \tag{A.12}$$

$$D_{CO_2} = 1.5 \cdot 10^{-9}\, m^2 s^{-1}\,. \tag{A.13}$$

Appendix A.2.2. Migration

Liu et al. [73] show that a linear mixture rule is applicable for the determination of the conductivity κ in concentrated KOH based systems

$$\kappa = \Lambda_{KOH} c_{OH^-} + 2\Lambda_{Zn(OH)_4^=} c_{Zn(OH)_4^=} + 2\Lambda_{K2CO3} c_{CO_3^=}\,, \tag{A.14}$$

where the conductivity of binary potassium hydroxide solutions $\kappa_{KOH} = \Lambda_{KOH} c_{K^+}$ is fitted by See et al. [74] as a function of potassium concentration. The equivalent conductivities of zincate is $\Lambda_{Zn(OH)_4^=} = 7 \cdot 10^{-4}$ Sm^{2}mol^{-1} [73] and of carbonate are $\Lambda_{Zn(OH)_4^=} = (-7.14 c_{K^+}/c_{std} + 78.18) \cdot 10^{-4}$ Sm^{2}mol^{-1} [64, 73].

A definition of transference numbers for binary electrolytes is discussed in [34]. Generalizing the definition by applying the above mentioned mixture rule, the transference number of the ion species i in the electrolyte with the three salts becomes

$$t_i := \frac{c_i|z_i|\lambda_i}{c_{\mathrm{K}^+}\lambda_{\mathrm{K}^+} + \sum_{j=1}^{3} c_j|z_j|\lambda_j}. \tag{A.15}$$

We calculate the transference numbers from the mobility at infinite dilution which are known. Values for the ionic conductivities λ_i are given in table A.2.

We model the chemical potentials as dilute solutions and get its derivative with respect to the concentration

$$\frac{\partial \mu_i}{\partial c_i} = \frac{RT}{c_i}\,. \tag{A.16}$$

Appendix A.2.3. Multi-Phase Transport

The dynamic viscosity η_e of aqueous potassium hydroxide solutions is given by Siu et al. [67] the permeability of the gas diffusion electrode at the initial saturation $\tilde{s}^0 = 0.63$ is $B_\mathrm{e} = 1 \cdot 10^{-14}\,\mathrm{m}^2$ [75]. Linear interpolating of the data in [76] yields the surface tension

$$\sigma = \left[7.2252 \cdot 10^{-5}\,\frac{\mathrm{m}^3}{\mathrm{kg}}\,\rho_\mathrm{e} - 6.1263 \cdot 10^{-4}\right]\frac{\mathrm{kg}}{\mathrm{s}^2}. \tag{A.17}$$

We shift the Leverett J-function [75], such that the pressure of both, gas and liquid phase, is the standard pressure at the initial saturation $\tilde{s}^0$

$$\begin{aligned} J = 1.34 \cdot 10^{-3} &+ 4.98 \cdot 10^{-3} \exp(9.404(\tilde{s} - \tilde{s}^0)) \\ &- 3.97 \cdot 10^{-3} \exp(-11.19(\tilde{s} - \tilde{s}^0))\,. \end{aligned}$$

Appendix A.3. Reactions

The reaction kinetics are not as accurately known as transport parameters for zinc-air batteries. Therefore, we adjust the kinetics of the two electrochemical reactions to reach quantitative agreement for the discharge curves in simulation and measurement. Nevertheless, we discuss that their orders of magnitude agree with the available literature.

Appendix A.3.1. Zinc Morphology and Surface Areas

We assume that spherical zinc particles are covered by a porous zinc oxide shell (see Sec. 3). This determines the specific surface areas A_I for the zinc dissolution (see Eq. 25) and A_II for the zinc oxide precipitation (see Eq. 31). The initial radius of the zinc particles is $r^0_\mathrm{Zn} = 35\ \mu\mathrm{m}$ as shown in Ref. [77]. We choose the porosity of the zinc oxide film to be $\epsilon_\mathrm{f} = 0.05$ which is quite low, but still in agreement with Ref. [44]. We adjust the critical supersaturation to be $c_\mathrm{crit} = 3.5\,c_\mathrm{sat}$ according to Ref. [44].

Appendix A.3.2. Cathode Structure and Specific Surface Areas

The reaction surface of the oxygen and carbon dioxide absorption is the gas-liquid phase boundary in the GDE. From the lifetime experiment, we find the specific surface area $A_\mathrm{III} = A_\mathrm{V} = 3 \cdot 10^2\ \mathrm{m}^{-1}$, which is quite low. In the cathode, zinc oxide precipitates on the active surface $A_\mathrm{II} = A_\mathrm{IV}$, which we keep constant during discharge. We assume that this surface coincides with the gas-liquid phase boundary $A_\mathrm{IV} = 3 \cdot 10^2\ \mathrm{m}^{-1}$.

Name	Notation	Value	Unit
Temperature	T	298.15	K
Current density	i_{cell}	100	A m^{-1}
Standard pressure	p_{std}	101 325	Pa
Standard concentration	c_{std}	1 000	mol m^{-3}
Partial pressure oxygen	$p_{\text{O}_2^{\text{g}}}$	21 219	Pa
Partial pressure carbon dioxide	$p_{\text{CO}_2^{\text{g}}}$	39	Pa
Standard oxygen concentration	$c_{\text{O}_2,\text{std}}$	0.867	mol m^{-3}

Table A.3. Conditions for experiment and simulation. The partial gas pressures represent ambient air and are taken from Ref. [68]. The standard oxygen concentration corresponds to equilibrium with oxygen gas at standard pressure.

Appendix A.3.3. Kinetic Coefficients

We adjust the kinetic constant $k_{\text{I}} = 1.8 \cdot 10^{-6}\ \text{mol m}^{-2}\text{s}^{-1}$ (cf. [32]) for zinc dissolution. At typical concentrations, this value corresponds to the exchange current density $i_0 \approx 1\ \text{Am}^{-2}$. This value is two orders of magnitude lower than measured on pure zinc [30]. Modern zinc anodes, however, contain additives in order to suppress hydrogen evolution. These additives can also slow down zinc dissolution.

Our adjusted kinetic coefficient for oxygen reduction $k_{\text{IV}} = 3 \cdot 10^{-10}\ \text{mol m}^{-2}\text{s}^{-1}$ corresponds to the exchange current $i_0 \approx 10^{-4}\ \text{Am}^{-2}$. This results in the exchange current density $i_0^{\text{GDE}} \approx 10^{-5}\ \text{Am}^{-2}$ with respect to the cross-section of the whole GDE in approximate agreement with the measurements of Drillet et al. for carbon based gas diffusion electrodes coated with MnO_2 [78].

The kinetic constant k_{III} of oxygen dissolution follows from the Hertz-Knudsen equation 33. We assume that one percent $\xi := 0.01$ of the gas molecules hitting the gas-liquid phase boundary enter the electrolyte [12]. The kinetics of ZnO growths is determined by the diffusion layer thickness $\delta_{\text{ZnO}} = 1\,\mu\text{m}$ resulting in kinetics similar to previous models [32, 25].

The kinetic coefficient of the carbonate reaction $k_V := k_{\text{OH}^-} c_{\text{OH}^-}$ (see Eq. 37) follows from the kinetic constant k_{OH^-} of the rate determining step (see Reaction V.a) [79]

$$k_{\text{OH}^-} = 8.38 \frac{\text{mol}}{\text{m}^3\text{s}} \cdot 10^{(0.11 c_{\text{K}^+} + 0.11 c_{\text{OH}^-} + 0.17 c_{\text{CO}_3^=})/c_{\text{std}}}. \tag{A.18}$$

Appendix A.4. Initial Conditions

The initial conditions are given in Tab. A.6. Varta PowerOne hearing aid batteries PR44 type p675 contain 32 wt% potassium hydroxide electrolyte. Accordingly, we choose the concentrations of water and potassium. For numerical reasons we set small initial concentrations for carbonate and zincate. Then we calculate the hydroxide concentration, such that charge neutrality is granted.

In our model the void space on top of the anode is homogeneously distributed throughout the cell. The volume fraction of zinc is adjusted to give the observed cell capacity of 460 mAh (see Tab. A.5). The initial zinc particle radius is $r_{\text{Zn}}^0 = 35\,\mu\text{m}$ [77].

Name	Notation	Value	Unit
Ideal gas constant	R	8.3144	$\mathrm{J\,mol^{-1}K^{-1}}$
Faraday constant	F	96485	$\mathrm{C\,mol^{-1}}$
Boltzmann constant	k_B	$1.3806488 \cdot 10^{-23}$	$\mathrm{m^2kg\,s^{-2}K^{-1}}$
Molar mass			
Water	$M_{\mathrm{H_2O}}$	$18.015 \cdot 10^{-3}$	$\mathrm{kg\,mol^{-1}}$
Potassium	M_K	$39.0983 \cdot 10^{-3}$	$\mathrm{kg\,mol^{-1}}$
Oxygen	$M_{\mathrm{O_2}}$	$31.9988 \cdot 10^{-3}$	$\mathrm{kg\,mol^{-1}}$
Hydroxide	$M_{\mathrm{OH^-}}$	$17.00734 \cdot 10^{-3}$	$\mathrm{kg\,mol^{-1}}$
Zincate	$M_{\mathrm{ZnOH_4^=}}$	$133.4094 \cdot 10^{-3}$	$\mathrm{kg\,mol^{-1}}$
Carbon dioxide	$M_{\mathrm{CO_2}}$	$44.0095 \cdot 10^{-3}$	$\mathrm{kg\,mol^{-1}}$
Density Water	$\rho_{\mathrm{H_2O}}$	997.048	$\mathrm{kg\,m^{-3}}$
Molar volume zinc	V_Zn	$9.16 \cdot 10^{-6}$	$\mathrm{m^3mol^{-1}}$
Molar volume zinc oxide	V_ZnO	$14.5 \cdot 10^{-6}$	$\mathrm{m^3mol^{-1}}$

Table A.4. Basic material parameters and physical constants [64].

Name	Notation	Ano.	Sep.	Cat.	Unit
Cell diameter			$11 \cdot 10^{-3}$		m
Length	L_a,L_s,L_c	$4.5 \cdot 10^{-3}$	$0.1 \cdot 10^{-3}$	$0.3 \cdot 10^{-3}$	m
Volume fraction					
Zinc	ϵ^0_Zn	0.185	-	-	-
Zinc oxide	ϵ^0_ZnO	$1{\cdot}10^{-7}$	$1{\cdot}10^{-7}$	$1{\cdot}10^{-7}$	-
Inactive material	$\epsilon^0_\mathrm{inact}$	-	0.185	0.185	-
Electrolyte	ϵ^0_e	0.515	0.515	0.515	-
Gas phase	ϵ^0_g	0.3	0.3	0.3	-
Initial zinc particle diameter	r^0_Zn	75			μm

Table A.5. Geometry for simulating the VARTA PowerOne button cell PR44 type p675.

Name	Notation	Value	Unit
Density electrolyte	ρ^0_e	1301	$\mathrm{kg\,m^{-3}}$
Concentration			
Water	$c^0_{\mathrm{H_2O}}$	49105	$\mathrm{mol\,m^{-3}}$
Potassium	$c^0_{\mathrm{K^+}}$	7419.9	$\mathrm{mol\,m^{-3}}$
Oxygen	$c^0_{\mathrm{O_2}}$	0.0134	$\mathrm{mol\,m^{-3}}$
Hydroxide	$c^0_{\mathrm{OH^-}}$	7417.9	$\mathrm{mol\,m^{-3}}$
Zincate	$c^0_{\mathrm{ZnOH_4^=}}$	1	$\mathrm{mol\,m^{-3}}$
Carbonate	$c^0_{\mathrm{CO_3^=}}$	10^{-8}	$\mathrm{mol\,m^{-3}}$

Table A.6. Initial conditions for electrolyte composition at 32wt% KOH.

Appendix B. Experimental Sequence

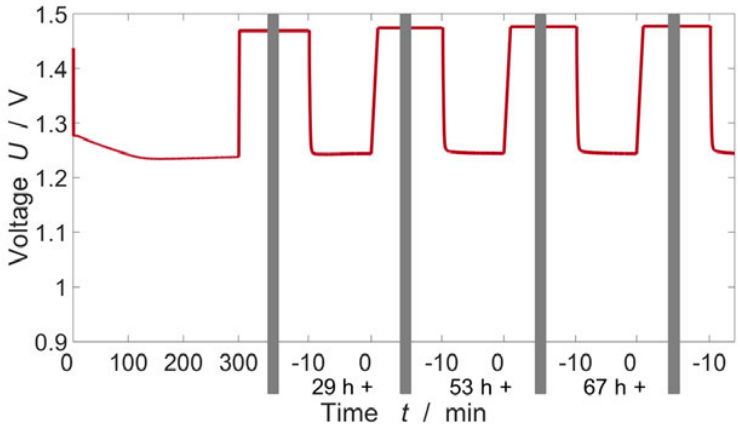

Figure B.1. Lifetime analysis at 100 Am^{-2}. The voltage is shown as a function of measurement time. After an initial discharge for 5 h, the cell is discharged for ten minutes every day. The figure depicts the measurement in the first four days, the gray arrays separate the measurements on different days.

Appendix C. Carbon Dioxide Filter

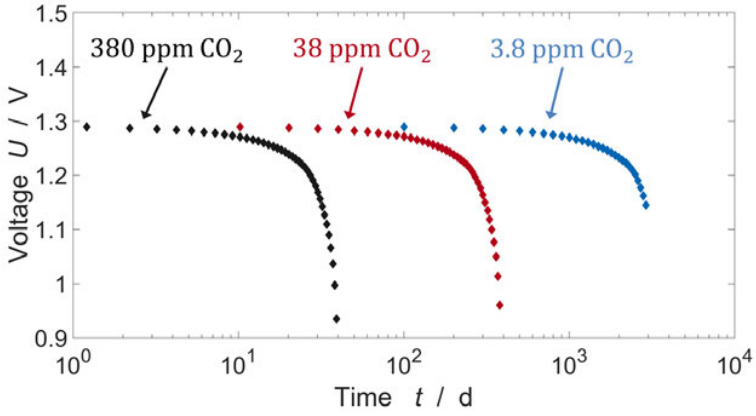

Figure C.2. Simulated lifetime analysis at 100 Am^{-2}. The voltage is shown as a function of measurement time. The discharge proceeds with varying carbon dioxide content in the feed gas. The voltage is measured every 24h, 240h, 2400h for 380ppm CO_2, 38ppm CO_2, 3.8ppm CO_2, respectively. We find that the lifetime is approximately inversely proportional to the carbon dioxide content.

Appendix D. Battery Cycling

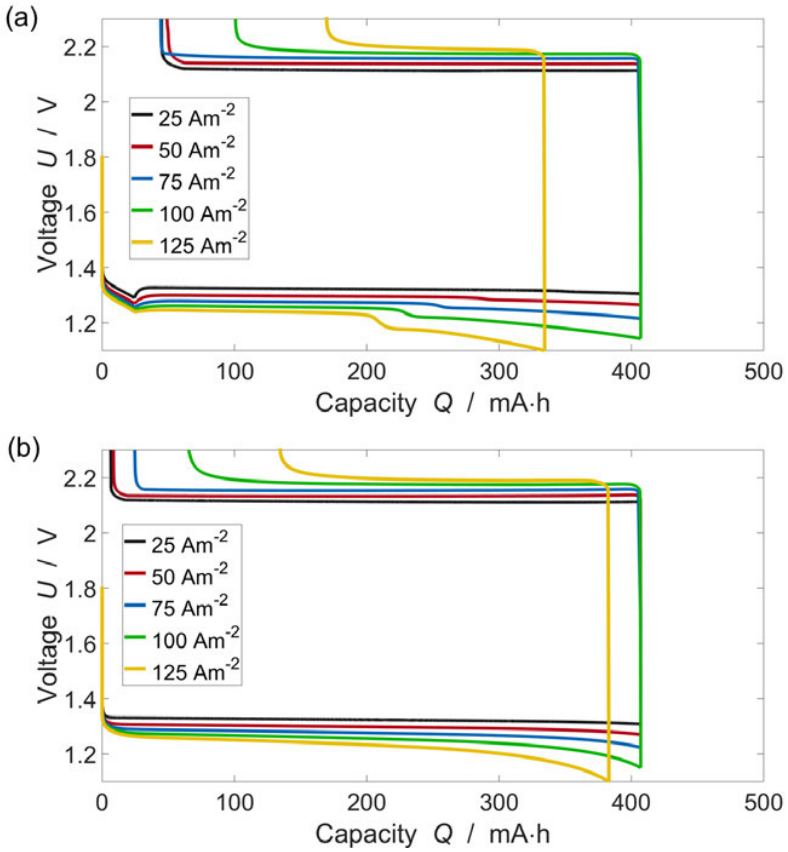

Figure D.3. Simulated voltage curves during discharge and charge as a function of discharged capacity at various current densities. The discharge proceeds to 90% capacity $Q = 407$ mAh or to the voltage cut-off at $U = 1.1$ V. The initial anode consists of (a) pure Zn and (b) a mixture of 2 volume percent ZnO and 98 volume percent Zn.

S. Clark, A. Latz and B. Horstmann. Cover: Rational Development of Neutral Aqueous Electrolytes for Zinc-Air Batteries. *ChemSusChem* **10**, 4666 (2017).

S. Clark, A. Latz and B. Horstmann. Rational Development of Neutral Aqueous Electrolytes for Zinc-Air Batteries. *ChemSusChem* **10**, 4735–4747 (2017)

CHEMISTRY & SUSTAINABILITY

CHEMSUSCHEM

ENERGY & MATERIALS

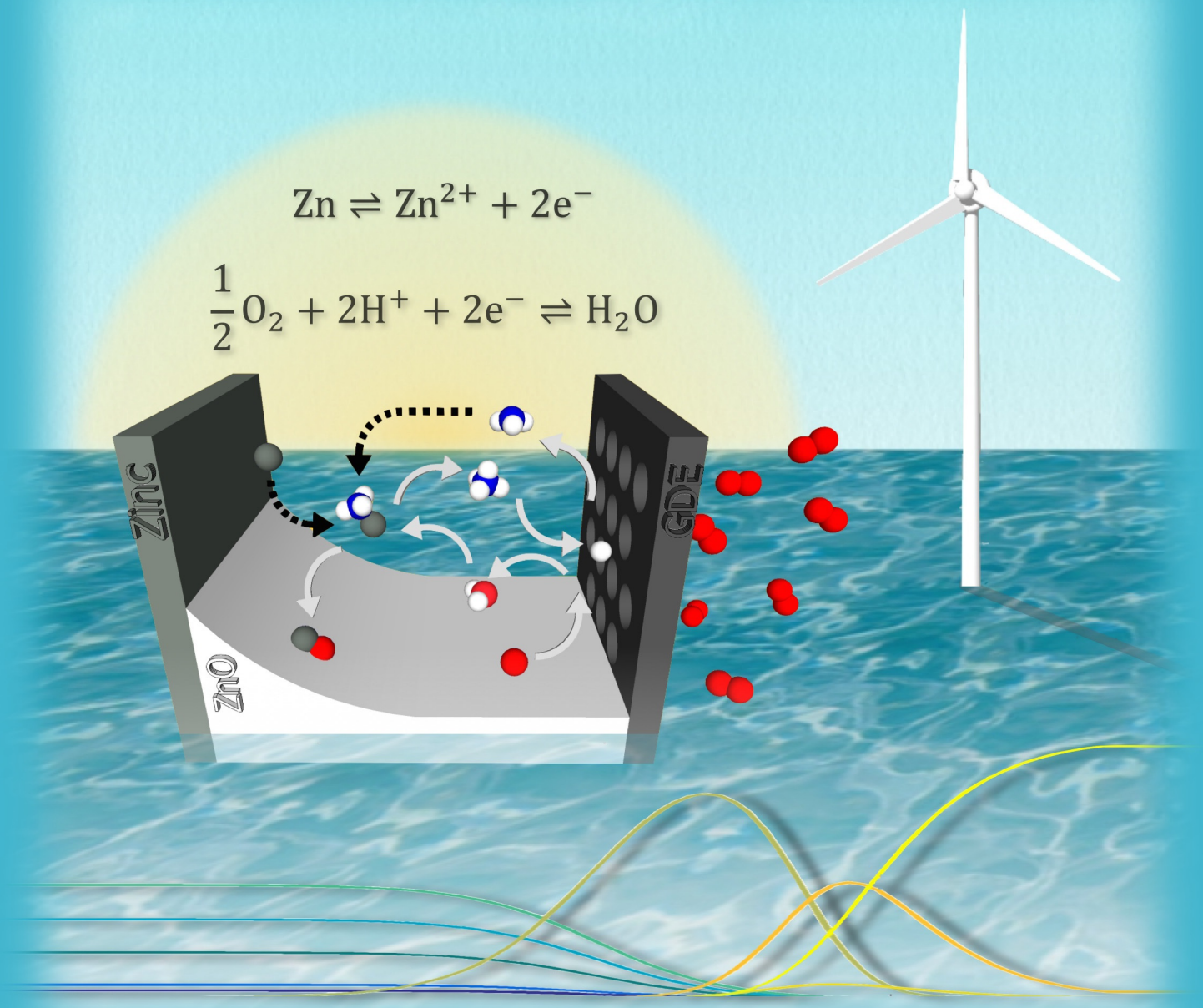

23/2017

Cover Feature:
Clark et al.
Rational Development of Neutral Aqueous Electrolytes for Zinc–Air Batteries

A Journal of
ChemPubSoc Europe

WILEY-VCH

www.chemsuschem.org

ChemPubSoc Europe

DOI: 10.1002/cssc.201701468

CHEMSUSCHEM Full Papers

VIP *Very Important Paper*

Rational Development of Neutral Aqueous Electrolytes for Zinc–Air Batteries

Simon Clark,[a, b] Arnulf Latz,[a, b, c] and Birger Horstmann*[a, b]

Neutral aqueous electrolytes have been shown to extend both the calendar life and cycling stability of secondary zinc–air batteries (ZABs). Despite this promise, there are currently no modeling studies investigating the performance of neutral ZABs. Traditional continuum models are numerically insufficient to simulate the dynamic behavior of these complex systems because of the rapid, orders-of-magnitude concentration shifts that occur. In this work, we present a novel framework for modeling the cell-level performance of pH-buffered aqueous electrolytes. We apply our model to conduct the first continuum-scale simulation of secondary ZABs using aqueous $ZnCl_2$–NH_4Cl as electrolyte. We first use our model to interpret the results of two recent experimental studies of neutral ZABs, showing that the stability of the pH value is a significant factor in cell performance. We then optimize the composition of the electrolyte and the design of the cell considering factors including pH stability, final discharge product, and overall energy density. Our simulations predict that the effectiveness of the pH buffer is limited by slow mass transport and that chlorine-containing solids may precipitate in addition to ZnO.

Introduction

Zinc–air batteries (ZABs) are promising candidates for next-generation energy storage. They offer a high theoretical specific energy (1086 $Wh\,kg_{ZnO}^{-1}$) and energy density (6093 $Wh\,L_{ZnO}^{-1}$), use abundant and non-hazardous materials, and have superior operational safety characteristics. In fact, primary ZABs using alkaline aqueous KOH electrolytes are already widely utilized for low-current commercial applications such as hearing aids. Unfortunately, the electrical rechargeability and calendar life of these cells are limited. When operated in air, dissolved CO_2 reacts with OH^- to produce CO_3^{2-}. This reaction reduces the ionic conductivity of the electrolyte and slows down the cell reactions.[1] Furthermore, inhomogeneous zinc dissolution and dendritic deposition cause the Zn electrode to change shape and severely limit the cycle life of the cell.[2] Improving the cycling stability of zinc batteries is currently a widely researched topic.[3–11] Aqueous electrolytes with near-neutral pH values were proposed[12–14] as a possible solution to this challenge, and the first steps towards commercialization have been taken.

Aqueous $ZnSO_4$ and $ZnCl_2$ electrolytes are commonly used in industrial zinc electroplating processes. As weakly acidic solutions, the coulombic efficiency of Zn electrodeposition in these electrolytes is nearly 100%.[15] Considering in addition their high electrical conductivity, sulfate- and chloride-based electrolytes are favorable for secondary-zinc-battery applications. Experimental studies show that zinc batteries based on these electrolytes can be reliably operated over hundreds or even thousands of cycles.[13,14,16–18] However, to keep the pH value of the electrolyte in the near-neutral regime, a buffer solution is required to counteract the effects of the oxygen-reduction and oxygen-evolution reactions. In the case of $ZnCl_2$, this is accomplished by the addition of NH_4Cl and NH_4OH. The state of the aqueous zinc ion in buffered electrolytes and the solubility of solid precipitates in the near-neutral pH regime is very complex.[15,19–21] A thorough understanding of the composition of the electrolyte and its behavior during cell operation is necessary to develop a feasible battery. In this paper, we develop a framework for modeling the performance of buffered aqueous electrolytes in zinc batteries and apply it to the $ZnCl_2$–NH_4Cl system.

$ZnCl_2$–NH_4Cl has a long history in commercial electrochemical systems, dating back to the 19th century as the standard electrolyte for zinc–carbon (or so-called Leclanché) batteries.[19,22] These batteries consist of a zinc metal anode and a MnO_2/carbon-paste cathode. Because of their low cost and reliability, non-alkaline zinc–carbon batteries held a significant market share well into the 20th century. A major topic of research in the development of Leclanché batteries is the impact of electrolyte composition on performance and capacity. It is commonly noted in the literature that for low NH_4Cl concentrations (e.g., less than 10 wt%) the discharge product is amorphous zinc chloride hydroxide monohydrate (simonkolleite, $ZnCl_2{\cdot}4\,Zn(OH)_2{\cdot}H_2O$) whereas for higher NH_4Cl concentrations the solid product is crystalline zinc diammine chloride

[a] S. Clark, Prof. Dr. A. Latz, Dr. B. Horstmann
German Aerospace Center (DLR)
Pfaffenwaldring 38–40, 70569 Stuttgart (Germany)
E-mail: birger.horstmann@dlr.de

[b] S. Clark, Prof. Dr. A. Latz, Dr. B. Horstmann
Helmholtz Institute Ulm (HIU)
Helmholtzstr. 11, 89081 Ulm (Germany)

[c] Prof. Dr. A. Latz
Ulm University (UUlm)
Albert-Einstein-Allee 47, 89081 Ulm (Germany)

Supporting Information and the ORCID identification number(s) for the author(s) of this article can be found under https://doi.org/10.1002/cssc.201701468.

($ZnCl_2 \cdot 2\,NH_3$).[23–25] Furthermore, it is suggested that because of its crystallization morphology, $ZnCl_2 \cdot 2\,NH_3$ poses a higher risk of passivation than $ZnCl_2 \cdot 4\,Zn(OH)_2 \cdot H_2O$.[26] Unlike alkaline zinc batteries, there is not a standard formulation for the Leclanché electrolyte. The $ZnCl_2/NH_4Cl$ ratio of the electrolyte is adjusted based on the application of the battery.[26] In today's zinc–carbon batteries, $ZnCl_2$–NH_4Cl has mostly been abandoned in favor of KOH because of its high conductivity.

The ongoing search for post-lithium electrochemical energy storage technologies has revived interest in neutral zinc–air batteries. The cheap and non-hazardous materials on which this battery is based, combined with the possibility to achieve a high energy density, make this system a promising contender for sustainable stationary energy storage. The first application of $ZnCl_2$–NH_4Cl in zinc–air batteries was published by Jindra et al. in 1973.[12] They found that a low OH^- concentration in the electrolyte eliminates the formation of carbonates, potentially extending the calendar life of the cell. Nonetheless, the cycling stability was poor. In 2014, Goh, et al.[13] investigated the use of additives such as polyethylene glycol (PEG) and thiourea to improve the homogeneity of zinc electrodeposition. Their cell could be operated continuously for over 1000 h and achieved around 100 cycles. A neutral ZAB developed by Sumboja et al. in 2016 was operated continuously for over 2000 h and achieved around 500 cycles.[14] Although each of these groups has highlighted the importance of the electrolyte composition for optimizing cell performance, there is currently no theoretical analysis of zinc–air batteries using buffered aqueous electrolytes.

Figure 1 shows an operational schematic of a ZAB with $ZnCl_2$–NH_4Cl electrolyte. The battery consists of a metallic Zn electrode and a porous gas-diffusion electrode (GDE) loaded with a bifunctional air catalyst. MnO_2 is the most commonly used non-precious metal catalyst.[17,27] The liquid electrolyte separates the electrodes and conducts ions across the cell. Depending on the distance between the electrodes, this region may or may not contain a porous separator to prevent an internal short circuit.

When the cell is discharged, the metallic Zn electrode dissolves and forms aqueous Zn^{2+} ions, which can then form complexes with other species in solution [Eq. (1)],

$$Zn \rightleftharpoons Zn^{2+} + 2\,e^-, \quad E^0 = -0.762\,V \tag{1}$$

The exact composition of these zinc complexes is highly sensitive to the conditions in the electrolyte and will be discussed in detail in the following sections. When the solubility limit of zinc is reached, various solid products including ZnO, $Zn(OH)_2$, $ZnCl_2 \cdot 4\,Zn(OH)_2 \cdot H_2O$, and $ZnCl_2 \cdot 2\,NH_3$ can precipitate. At the GDE, the oxygen reduction reaction (ORR) consumes dissolved O_2 and H^+ and produces H_2O [Eq. (2)],

$$0.5\,O_2{}^{aq} + 2\,H^+ + 2\,e^- \rightleftharpoons H_2O, \quad E^0 = 1.229\,V \tag{2}$$

There is a tendency for the electrolyte to become alkaline because of the loss of H^+. However, the weakly acidic nature of the electrolyte acts as a pH buffer [Eqs. (3) and (4)],

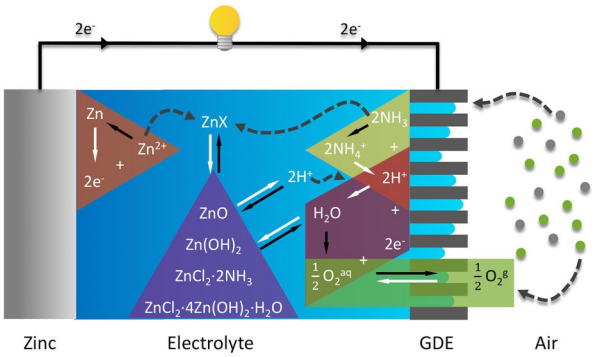

Figure 1. Operational diagram of a zinc–air battery with $ZnCl_2$–NH_4Cl electrolyte. The colors show the various (electro)chemical reactions in the cell; the shapes have no special meaning. The white arrows indicate the direction of these reactions during discharging; the black arrows indicate the direction during charging. The dashed arrows show important transport pathways. Gaseous oxygen molecules enter the cell through the GDE and dissolve in the electrolyte (green). Dissolved oxygen molecules in the GDE are reduced with the help of a bifunctional catalyst and react with H^+ to form H_2O (red). The loss of H^+ disturbs the equilibrium of the $NH_4{}^+/NH_3$ species, and the buffer reaction stabilizes the pH value in the GDE (yellow). The metallic Zn electrode dissolves to form aqueous zinc ions, which can then form complexes with NH_3 and Cl^- (orange). Based on the local pH value and concentrations of Zn^{2+}, NH_3, and Cl^-, a variety of solid discharge products may precipitate (purple). ZnO is the most desirable product, and chlorine-containing solids are least desirable.

$$NH_4{}^+ \rightleftharpoons NH_3 + H^+, \text{ and} \tag{3}$$

$$Zn^{2+} + n\,NH_3 \rightleftharpoons Zn(NH_3)_n{}^{2+}, \tag{4}$$

which stabilizes the pH value in the neutral regime.

It is important to note that the ability of the electrolyte to stabilize the pH value in the neutral range is attributable to the interactions between $ZnCl_2$ and NH_4Cl. The equivalence point of the $NH_4{}^+/NH_3$ buffer[28] is at pH 9.8. A solution containing only NH_4Cl would stabilize the pH value for a short time, but the electrolyte would quickly become alkaline as the concentration of NH_3 increases. When NH_4Cl is mixed with $ZnCl_2$, Zn^{2+} ions form complexes with the NH_3 in solution, which are stable in the in pH range of roughly 6–10. By providing a means to take up free NH_3, the presence of these zinc–ammine complexes increases the capacity of the buffer solution in the neutral range.

When the cell is charged, the oxygen evolution reaction (OER) consumes H_2O and produces $O_2{}^{aq}$ and H^+ at the GDE. Zn^{2+} is deposited from its aqueous forms at the Zn electrode. Again, the buffer reactions stabilize the pH value in the near-neutral domain. As zinc is redeposited from its aqueous state, the concentration decreases to a point below its saturation concentration and the solid precipitates dissolve.

Previous studies simulated ZABs with alkaline KOH electrolytes.[1,29–32] Although much of the same methodology may be applied to ZABs with neutral electrolytes, there is one significant gap. The strongly alkaline composition of standard roughly 30 wt% KOH electrolytes helps maintain a constant pH value during operation. As a result, the thermodynamic stabili-

ty of the dominant aqueous zinc species ($Zn(OH)_4^{2-}$) also remains constant. Other investigations[20,21] of the thermodynamic stability of zinc–ligand complexes in $ZnCl_2$–NH_3Cl show that within the near-neutral pH domain even slight changes in the pH value can induce significant shifts in the dominant zinc complex. This, in turn, influences both the physicochemical properties and the buffering capacity of the electrolyte. Therefore, a dynamic cell-level model of a ZAB with a near-neutral electrolyte should also consider the coupled effects of pH value and aqueous zinc concentration. Our quasiparticle approach makes this possible.

In this work, we present the first mathematical model of zinc–air batteries with aqueous $ZnCl_2$–NH_4Cl electrolytes. In the following sections, we discuss the thermodynamic basis for our model (electrolyte equilibrium thermodynamics) and present a new method for modeling buffered aqueous electrolytes (quasiparticle model). We provide an overview of the parameters and conditions implemented in the model (computational details) and discuss the predictions of the resulting simulations (results and discussion). We compare the results of our simulations with existing experimental measurements, perform an initial optimization of the ZAB cell, and suggest topics for further research.

Model Development and Application

Electrolyte equilibrium thermodynamics

In this section, the equilibrium thermodynamics of aqueous $ZnCl_2$–NH_4Cl solution is discussed. A framework for the thermodynamic model of this system was already laid out in existing works.[20,21]

The first step in modeling the dynamic behavior of $ZnCl_2$–NH_4Cl was to understand its equilibrium composition. In the electrolyte, zinc may exist as either free Zn^{2+} ions or zinc–ligand complexes. Within the near-neutral pH range, the stability of the aqueous zinc–ligand complexes is very sensitive to changes in the electrolyte environment.[19–21,33] Understanding the coupled effects between the formation of these complexes and electrolyte pH value is essential to interpret the performance of the ZAB. To predict this behavior, we developed a thermodynamic model of aqueous $ZnCl_2$–NH_4Cl in the near-neutral pH domain.

Our model considered a total of 16 aqueous species. These included elementary species (H^+, OH^-, Zn^{2+}, Cl^-, NH_4^+, and NH_3), zinc–chloride complexes ($ZnCl^+$, $ZnCl_2$, $ZnCl_3^-$, and $ZnCl_4^{2-}$), zinc–ammine complexes ($Zn(NH_3)^{2+}$, $Zn(NH_3)_2^{2+}$, $Zn(NH_3)_3^{2+}$, and $Zn(NH_3)_4^{2+}$), and ternary zinc complexes ($ZnCl_3(NH_3)^-$ and $ZnCl(NH_3)_3^+$). Additionally, four solid discharge products were possible in the model: ZnO, $Zn(OH)_2$, $ZnCl_2{\cdot}4\,Zn(OH)_2{\cdot}H_2O$, and $ZnCl_2{\cdot}2\,NH_3$.

The homogeneous electrolyte reactions and their corresponding thermodynamic equilibrium constants[20,21,28] are summarized in Table 1. According to the law of mass action, for a system at constant temperature the value of the equilibrium quotient is constant. For example, the equilibrium quotient of the $ZnCl_4^{2-}$ reaction is expressed as $\frac{[ZnCl_4^{2-}]}{[Zn^{2+}][Cl^-]^4} = \beta$, where $\beta = 10^{0.30}$. In this notation, square brackets are used to denote concentrations ($[X] = c_X$) in mol L^{-1}. Using these equilibrium expressions, the concentration of any aqueous species can be expressed in terms of its stability constant and a combination of Zn^{2+}, Cl^-, and NH_3.

Table 1. Homogeneous reactions in the electrolyte and the corresponding thermodynamic stability constants[20,21,28] for ionic strengths 2–8.

Reaction	$\log_{10}\beta$
$Zn^{2+} + Cl^- \rightleftarrows ZnCl^+$	0.10
$Zn^{2+} + 2\,Cl^- \rightleftarrows ZnCl_2$	0.06
$Zn^{2+} + 3\,Cl^- \rightleftarrows ZnCl_3^-$	0.10
$Zn^{2+} + 4\,Cl^- \rightleftarrows ZnCl_4^{2-}$	0.30
$Zn^{2+} + NH_3 \rightleftarrows Zn(NH_3)^{2+}$	2.38
$Zn^{2+} + 2\,NH_3 \rightleftarrows Zn(NH_3)_2^{2+}$	4.88
$Zn^{2+} + 3\,NH_3 \rightleftarrows Zn(NH_3)_3^{2+}$	7.43
$Zn^{2+} + 4\,NH_3 \rightleftarrows Zn(NH_3)_4^{2+}$	9.65
$Zn^{2+} + 3\,Cl^- + NH_3 \rightleftarrows ZnCl_3(NH_3)^-$	3.15
$Zn^{2+} + Cl^- + 3\,NH_3 \rightleftarrows ZnCl(NH_3)_3^+$	7.90
$NH_3 + H^+ \rightleftarrows NH_4^+$	9.80
$OH^- + H^+ \rightleftarrows H_2O$	13.96

The electrolyte was prepared by adding NH_4OH to an aqueous solution of $ZnCl_2$–NH_4Cl until the desired pH value was achieved. As such, the total amount of chloride, zinc, and nitrogen in the system were known and conserved quantities. They were determined from the weighted sums of the concentrations of the component species. The total (T) chloride and zinc concentrations are expressed as Equations (5) and (6):

$$[Cl]_T = [Cl^-] + \sum_{m=1}^{4} m\,[ZnCl_m^{2-m}] + 3\,[ZnCl_3(NH_3)^-] + [ZnCl(NH_3)_3^+] \quad (5)$$

$$[Zn]_T = [Zn^{2+}] + \sum_{n=1}^{4} [Zn(NH_3)_n^{2+}] + \sum_{m=1}^{4} [ZnCl_m^{2-m}] + [ZnCl_3(NH_3)^-] + [ZnCl(NH_3)_3^+] \quad (6)$$

where m and n describe the stoichiometry of the zinc–chloride and zinc–ammine complexes, respectively. The nitrogen atoms in the system are distributed between ammonium and ammonia. The total amount of ammonia is given by Equation (7):

$$[NH_3]_T = [NH_3] + \sum_{n=1}^{4} n\,[Zn(NH_3)_n^{2+}] + [ZnCl_3(NH_3)^-] + 3\,[ZnCl(NH_3)_3^+] \quad (7)$$

and the total nitrogen content is expressed as Equation (8)

$$[N]_T = [NH_3]_T + [NH_4^+] \quad (8)$$

Finally, the local electroneutrality condition in the system must hold, which gives the following relation [Eq. (9)]:

$$2\,[Zn]_T + [NH_4^+] + [H^+] - [Cl]_T - [OH^-] = 0 \quad (9)$$

Considering the twelve equilibrium expressions in Table 1, the conserved quantities in Equations (5), (6), and (8), and the electroneutrality condition in Equation (9), we had sixteen equations and could solve for the sixteen unknown concentrations in the electrolyte.

When the solubility of zinc in the electrolyte is exceeded, solid products precipitate. These reactions reduce the total zinc, chloride, and nitrogen concentrations in the liquid phase, and the formation of solid products plays a decisive role in the performance of the ZAB. Table 2 lists the various solid discharge products considered in our model, their thermodynamic solubility products and

Table 2. Solid discharge products with the corresponding thermodynamic solubility products[20,21,34] and theoretical energy densities of a cell with pH 7.

Precipitate	$\log_{10}K_{sp}$	ρ^E [Wh L_{precip}^{-1}]
$ZnCl_2{\cdot}2\,NH_3$	−6.42	303
$ZnCl_2{\cdot}4\,Zn(OH)_2{\cdot}H_2O$	−14.2	948
$Zn(OH)_2$	−17	1782
ZnO	−16.7	6093

theoretical energy densities as the final discharge products of a neutral ZAB. To incorporate the effects of precipitation into our model, we expressed the solubility, for example of $ZnCl_2{\cdot}2\,NH_3$, as $[Zn^{2+}][Cl^-]^2[NH_3]^2 = K_{sp}$, where the solubility product constant $K_{sp} = 10^{-6.42}$ (mol L^{-1})^5 and the concentrations are in mol L^{-1}.

The final discharge product in ZABs should be ZnO. It is well documented that the product of zinc batteries with $ZnCl_2$–NH_4Cl electrolyte is either $ZnCl_2{\cdot}2\,NH_3$ or $ZnCl_2{\cdot}4\,Zn(OH)_2{\cdot}H_2O$, depending on the pH value and $ZnCl_2/NH_4Cl$ ratio.[23–26,33,35,36] The precipitation of these products presents two main challenges for cell design: they consume chloride from the electrolyte and they have molar volumes that are significantly larger than zinc metal.

The molar volume of the precipitates has two effects on cell performance: it reduces the overall energy density of the battery and it can contribute to the flooding of the GDE. The theoretical energy density of a ZAB based on each of the final discharge products was calculated as Equation (10):

$$\rho_p^E = 2F\frac{U_{OC}}{V} \tag{10}$$

where U_{OC} is the open-circuit voltage of the cell [V], F is the Faraday constant [Ah mol^{-1}], and V is the molar volume of the solid product and consumed electrolyte [L mol^{-1}]. The ZAB was assumed to be rigid with a fixed volume. Volume expansion caused by the precipitation of these solids forces electrolyte into the GDE and degrades the performance of the cell. The loss of chloride causes the ionic conductivity of the electrolyte to decrease.

Using the model described above, we determined the equilibrium composition of the electrolyte and the zinc solubility given the initial formulation.

Quasiparticle model

We present a method for modeling the dynamic behavior of buffered aqueous electrolytes. The following derivation is geared towards readers active in modeling and simulation. Experimentally inclined readers may wish to continue to the section on computational details.

A method of modeling electrolyte transport on the continuum scale was already derived and validated.[1,37–45] An overview of this method applied to ZABs is provided in the Supporting Information. The transport of solutes in the electrolyte was derived from non-equilibrium thermodynamics[1] and can be expressed in generic terms by the mass-continuity equation [Eq. (11)],

$$\frac{\partial(c_i\varepsilon_e)}{\partial t} = -\vec{\nabla}\cdot\left(\vec{N}_i^{DM}\right) - \vec{\nabla}\cdot\left(\vec{N}_i^{C}\right) + \dot{s}_i \tag{11}$$

(where t is time, ε_e is the volume fraction of the electrolyte, $\vec{N}_i^{DM}$ is the diffusion–migration flux, $\vec{N}_i^{C}$ is the convection flux and $\dot{s}_i$ is the source term) and the charge-continuity equation [Eq. (12)],

$$0 = -\vec{\nabla}\cdot\vec{j} + \sum_i z_i\dot{s}_i \tag{12}$$

(where $\vec{j}$ is the electrolyte current density and z_i is the charge number of the solute).

Transport in strongly acidic or basic electrolytes is driven only by heterogeneous chemical reactions, such as those shown in Tables 3 and 4; thus, the continuity equations described above can be easily solved. However, in buffered neutral electrolytes, homogeneous electrolyte reactions can cause the concentrations of individual solutes to shift by orders of magnitude, as shown in the previous section. The enormous changes in concentration make a numerical solution for the continuity equations infeasible. Our quasiparticle framework addressed this challenge. By defining a set of quasiparticles that described the conserved quantities of the homogeneous reactions, we were able to easily solve the continuity equations and determine the state of the electrolyte under dynamic conditions.

Table 3. Fundamental reactions of the zinc–air cell.

Reaction	E^0 [V]
$Zn \leftrightarrows Zn^{2+} + 2\,e^-$	−0.762
$0.5\,O_2(aq) + 2\,H^+ + 2\,e^- \leftrightarrows H_2O$	1.229
$O_2(g) \leftrightarrows O_2(aq)$	–

Table 4. Precipitation reactions in $ZnCl_2$–NH_4Cl.

Reaction
$Zn^{2+} + 2\,Cl^- + 2\,NH_3 \rightleftarrows ZnCl_2{\cdot}2\,NH_3(s)$
$5\,Zn^{2+} + 2\,Cl^- + 9\,H_2O \rightleftarrows ZnCl_2{\cdot}4\,Zn(OH)_2{\cdot}H_2O(s) + 8\,H^+$
$Zn^{2+} + 2\,H_2O \rightleftarrows Zn(OH)_2(s) + 2\,H^+$
$Zn^{2+} + H_2O \rightleftarrows ZnO(s) + 2\,H^+$

Generic form

Please note that the quasiparticles represent quantities that are conserved in the homogeneous reactions. The concentration of the quasiparticles (c_q) can be defined in terms of the concentrations of its constituent components [Eq. (13)]

$$c_q = \sum_i \tau_{i,q}c_i \tag{13}$$

where $\tau_{i,q}$ describes the stoichiometry of the solute i in the quasiparticle q and may take on values $\tau_{i,q} \in Z$.

The homogeneous electrolyte reactions are listed in Table 1. The solute source term attributable to these reactions ($\dot{s}_i^h$) was defined as Equation (14)

$$\dot{s}_i^h = \sum_r \tilde{k}_r^h \nu_{i,r} \tag{14}$$

where $\tilde{k}_r^h$ is the rate of the homogeneous reaction r and $\nu_{i,r}$ is the stoichiometric coefficient of the solute i in the reaction r. Using the stoichiometric coefficient for the quasiparticle ($\tau_{i,q}$), the solute source term was converted into a source term for the quasiparticles [Eq. (15)]:

$$\dot{s}_q^h = \sum_{i,r} \tilde{k}_r^h \nu_{i,r} \tau_{i,q} \tag{15}$$

We demanded that the relation $\sum_i \nu_{i,r}\tau_{i,q} = 0$ holds, such that for any $\tilde{k}_r^h$ Equation (16) was valid:

$$\dot{s}_q^h = 0 \tag{16}$$

Thus, the homogeneous reactions do not contribute to the quasiparticle source term.

Mathematically speaking, the quasiparticles were defined such that the vectors $\vec{\tau}_i = \sum_q \tau_{i,q}\vec{e}_q$ spanned the kernel of the matrix ν^T. Considering that the electrolyte is locally charge neutral, the number of quasiparticles needed to describe the system (n_q) is given by the difference of the number of solutes (n_s) and the number of homogeneous reactions (n_{hr}), $n_q = n_s - n_{hr} - 1$.

By assuming that the kinetics of the homogenous electrolyte reactions are fast, we calculated all individual solute concentrations from a few quasiparticle concentrations. The transport of the quasiparticles is determined by the transport of their individual constituents, assuming that the homogeneous reactions occur very quickly. Therefore, the diffusion–migration flux for quasiparticle q becomes Equation (17):

$$\vec{N}_q^{DM} = \sum_i \tau_{i,q}\vec{N}_i^{DM} = \varepsilon_e^\beta \sum_i \left(\tau_{i,q} D_i \vec{\nabla} c_i\right) + \sum_i \left(\tau_{i,q}\frac{t_i}{z_i F}\right)\vec{j} \tag{17}$$

where β is the Bruggeman coefficient, D_i is the diffusion coefficient, z_i is the charge number, and t_i is the transference number of the solute. The convective flux of quasiparticle q is defined by Equation (18):

$$\vec{N}_q^C = \varepsilon_e^\beta c_q \vec{v}_e \tag{18}$$

where $\vec{v}_e$ is the center-of-mass velocity of the electrolyte. How the electrolyte equation of state and current-density equation are derived can be found in the Supporting Information. Now the transport equations for the quasiparticles can be expressed as

$$\frac{\partial(c_q\varepsilon_e)}{\partial t} = -\vec{\nabla}\cdot\left[\varepsilon_e^\beta \sum_i \left(\tau_{i,q} D_i \vec{\nabla} c_i\right) + \sum_i \left(\tau_{i,q}\frac{t_i}{z_i F}\right)\vec{j}\right] - \vec{\nabla}\cdot\left(\varepsilon_e^\beta c_q \vec{v}_e\right) + \dot{s}_q^{e,p} \tag{19}$$

$$0 = -\vec{\nabla}\cdot\vec{j} + \sum z_i \dot{s}_i^e \tag{20}$$

where $\dot{s}_q^{e,p}$ is the source term due to the combined electrochemical and precipitation reactions, and $\dot{s}_i^e$ is the source term due to the electrochemical reactions.

Because charge is conserved in the homogeneous reactions, they do not contribute to the electroneutrality equation. Our quasiparticle formulation provides a simple method for modeling a series of coupled chemical reactions taking advantage of the conservation of atom numbers and charge. In the next section, we applied this model to the $ZnCl_2$–NH_4Cl system.

Quasiparticle framework in the $ZnCl_2$–NH_4Cl system

The $ZnCl_2$–NH_4Cl system consists of 16 solutes spanning 12 homogeneous reactions. Therefore, three quasiparticles were needed. To describe the quantities conserved in the homogeneous electrolyte reactions, we defined the following quasiparticles: ammonia ($\widetilde{NH_3}$), ammonium ($\widetilde{NH_4}$), and zinc ($\widetilde{Zn}$). According to the definition in Equation (13), the concentrations of the ammonia and zinc quasiparticles are expressed as Equation (21)

$$\left[\widetilde{NH_3}\right] = [NH_3] + \sum_{n=1}^{4} n[Zn(NH_3)_n^{2+}] + [ZnCl_3(NH_3)^-] + 3[ZnCl(NH_3)_3^+] - [H^+] + [OH^-] \tag{21}$$

and Equation (22)

$$[\widetilde{Zn}] = [Zn^{2+}] + \sum_{n=1}^{4} [Zn(NH_3)_n^{2+}] + \sum_{m=1}^{4} [ZnCl_m^{2-m}] + [ZnCl_3(NH_3)^-] + [ZnCl(NH_3)_3^+] \tag{22}$$

The concentration of the ammonium quasiparticle is expressed as Equation (23):

$$\left[\widetilde{NH_4}\right] = \left[NH_4^+\right] + [H^+] - [OH^-] \tag{23}$$

The sum of $\widetilde{NH_4}$ and $\widetilde{NH_3}$ gives the total concentration of nitrogen [Eq. (24)] whereas the total chloride concentration [Eq. (26)] is expressed by a combination of $\widetilde{NH_4}$ and $\widetilde{Zn}$, assuming local electroneutrality. The total zinc concentration is given by $\widetilde{Zn}$ [Eq. (25)].

$$[N]_T = \left[\widetilde{NH_3}\right] + \left[\widetilde{NH_4}\right] \tag{24}$$

$$[Zn]_T = [\widetilde{Zn}] \tag{25}$$

$$[Cl]_T = 2\left[\widetilde{Zn}\right] + \left[\widetilde{NH_4}\right] \tag{26}$$

We defined quasiparticles such that the homogeneous reactions do not contribute to the quasiparticle source term [as shown in Eq. (16)]. The source term is instead governed by the electrochemical and precipitation reactions listed in Tables 3 and 4. We rewrote the stoichiometric equations for these reactions to reflect the quasiparticle definitions, as shown in Table 5.

Table 5. Reactions that contribute to the quasiparticle source terms.

Reaction
$Zn \rightleftharpoons \widetilde{Zn} + 2e^-$
$\frac{1}{2}O_2(aq) + 2\widetilde{NH_4} + 2e^- \rightleftharpoons 2\widetilde{NH_3} + H_2O$
$5\widetilde{Zn} + 8\widetilde{NH_3} + 9H_2O \rightleftharpoons 8\widetilde{NH_4} + ZnCl_2{\cdot}4Zn(OH)_2{\cdot}H_2O(s)$
$\widetilde{Zn} + 2\widetilde{NH_3} \rightleftharpoons ZnCl_2{\cdot}2NH_3(s)$
$\widetilde{Zn} + 2\widetilde{NH_3} + 2H_2O \rightleftharpoons 2\widetilde{NH_4} + Zn(OH)_2(s)$
$\widetilde{Zn} + 2\widetilde{NH_3} + H_2O \rightleftharpoons 2\widetilde{NH_4} + ZnO(s)$

To solve the system, we defined the initial pH value and the total chloride and total zinc concentrations of the system. The concentration of the quasiparticles are given by the mass and charge-continuity equations [Eqs. (19) and (20)], and we used Equations (24), (25), and (26) to solve for $[Zn^{2+}]$, $[Cl^-]$, and $[NH_3]$. With these quantities, the concentrations of all 16 aqueous solutes and the volume fractions of the four solids could be determined.

Computational details

In this section, we discuss the computational details of our model, including the initial conditions and loads used for the simulations. More information on this topic, as well as a complete list of the

physical, chemical, and numerical parameters[13,14,20,21,27,28,42,43,46–61] implemented in the model, is presented in greater detail in the Supporting Information.

Model implementation

Our ZAB model consisted of a system of 13 equations: 5 solid-volume-conservation equations, 4 mass-continuity equations, 1 charge-continuity expression, 1 electrolyte-mass-continuity equation, 1 electrolyte-pressure equation of state, and 1 galvanostatic expression. A complete list of the equations is available in the Supporting Information. A 1D finite volume model was developed in MATLAB to implement the theory described above. The mesh was generated with fixed compartment sizes in the Zn electrode and GDE and a variable cell size in the separator. The system of equations was solved using the ode15i solver, a fully implicit solver for differential and algebraic equations.

The computational domain of the ZAB model consisted of the Zn electrode, separator, and GDE. The domain began at the Zn electrode current collector ($x=0$) and ended at the GDE current collector ($x=L_{cell}$), where L_{cell} is the total thickness of the cell.

Simulation conditions

Our first full-cell simulation was based on the ZAB developed by Goh et al.[13] The electrolyte was 0.51 M $ZnCl_2$–2.34 M NH_4Cl with the pH value adjusted to 6 through the addition of NH_4OH. For simplicity, this electrolyte is referred to in the text as Electrolyte A. The anode was a polished zinc foil with a thickness of 0.5 mm, and the cathode was a carbon GDE loaded with 4.5 mg cm^{-2} MnO_2 as catalyst. The Zn electrode and the GDE were 30 mm apart and separated by an electrolyte bath. The cell was discharged at 5 mA cm^{-2} for 4 h and charged at 2.5 mA cm^{-2} for 8 h. This cell is referred to in the text as Cell A.

Our second full-cell simulation was based on the work of Sumboja et al.[14] The electrolyte was 0.26 M $ZnCl_2$–5 M NH_4Cl with the pH value adjusted to 7. This electrolyte is referred to in the text as Electrolyte B. The anode was a polished zinc foil with a thickness of 0.5 mm, and the cathode was a carbon GDE loaded with 4.5 mg cm^{-2} MnO_2. The electrodes were 24 mm apart and separated by an electrolyte bath. The cell was discharged at 1 mA cm^{-2} for 2 h and charged at 1 mA cm^{-2} for 2 h. This cell is referred to in the text as Cell B.

Finally, we performed a series of simulations in which the electrolyte composition and cell architecture were adjusted to represent a feasible battery. Simulations were carried out to optimize the separator thickness, electrolyte composition, and the architecture of the Zn electrode. The performance of these cells was rated according to pH stability, composition of the discharge product, and the overall energy density of the battery. The optimization simulations were performed under galvanostatic conditions with a charge–discharge current density of 1 mA cm^{-2}.

Results and Discussion

In this section, we present the results of our simulations and discuss the significant findings. We begin by considering the equilibrium composition of the electrolyte and its dependence on the pH value and zinc and chloride concentration. We continue by analyzing the galvanostatic cycling performance of Cell A and compare it with the modifications introduced in Cell B. Finally, we present an optimization of cell performance based on cell design and electrolyte composition and discuss important aspects for future development.

Electrolyte composition

The composition of aqueous $ZnCl_2$–NH_4Cl strongly depends on the total zinc and chloride concentrations as well as on the pH value of the solution.

Figure 2 shows the distribution of zinc–ligand complexes for a system of constant total zinc and chloride concentrations with variations in the pH value. At low pH values, the concentration of NH_3 in solution is very low. As a result, Zn^{2+} tends to form complexes with Cl^- ions. As the pH value of the system increases, NH_4^+ begins to dissociate and more NH_3 becomes available. In the neutral pH range, ternary zinc–chloride–ammonia complexes dominate. Finally, NH_3 is available in significant quantities and zinc–ammine complexes ($Zn(NH_3)_4^{2+}$) dominate.

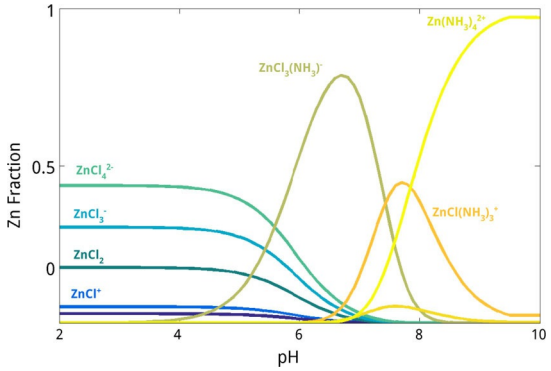

Figure 2. Aqueous zinc complex distribution vs. pH value for 0.51 M $ZnCl_2$–2.34 M NH_4Cl electrolyte. At acidic pH values, low NH_3 concentrations cause the solution to be dominated by zinc–chloride complexes. As the pH increases, more NH_3 becomes available, leading first to mixed complexes in the near-neutral domain and finally to the dominance of zinc–ammine complexes.

The buffering effect in the near-neutral pH range is determined by the formation of zinc–ammine complexes. As a weak acid, NH_4Cl acts as a pH buffer on its own, $NH_4^+ \rightleftarrows NH_3 + H^+$. But as the concentration of NH_3 in the solution increases, the reaction approaches its equivalence point and the pH becomes alkaline. By taking up excess NH_3, the zinc–ammine complexes allow the $NH_4^+ \rightleftarrows NH_3 + H^+$ reaction to act as a proton source while keeping the concentration of free NH_3 relatively low. As shown in Figure 2, the zinc–ammine complexes stabilize the pH value in the range between circa 6 (where $ZnCl_3(NH_3)^-$ begins to dominate) and circa 9.8 (where the NH_4^+/NH_3 reaction reaches its equivalence point). This is one of the main reasons why the electrolyte should be a mix of $ZnCl_2$ and NH_4Cl and not a pure solution of one or the other. Figure 3 presents the thermodynamic stability diagrams of both the zinc–ligand complexes and the solid precipitates for a fixed total chloride concentration while varying the pH value and total zinc concentration. The colored regions correspond to dominant zinc–ligand complexes, the colored lines show the solubilities of the

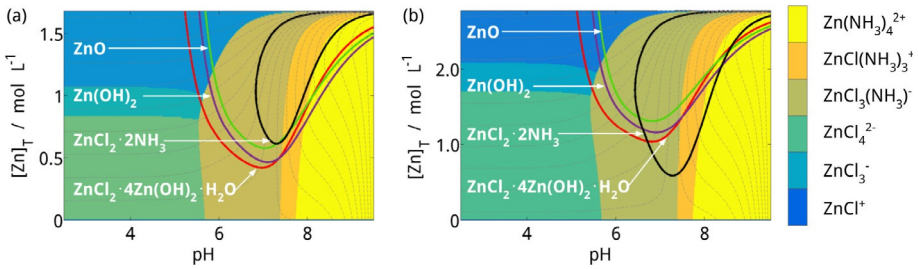

Figure 3. Dominant aqueous zinc complexes and discharge product solubilities for a total chloride concentration of (a) 3.36 mol L^{-1} (Cell A) and (b) 5.54 mol L^{-1} (Cell B). Each colored region of the charts corresponds to the composition of the dominant zinc complex (unit less). The solid lines correspond to the solubility of the various precipitates. The dashed lines show paths of constant nitrogen concentration in the electrolyte.

precipitates, and the dashed lines represent paths of constant total nitrogen concentration. Because the total nitrogen concentration is constant (in the absence of precipitation and evaporation), the electrolyte composition will follow the dashed lines as the cell is discharged or charged. For pH values between 6 and 10, zinc can be dissolved without significantly altering the pH value. This represents the buffer effect caused by the uptake of NH_3 by the zinc–ligand complexes.

The precipitates considered in the model are insoluble in the near-neutral pH domain. Consider the system shown in Figure 3a. By locating the initial condition of pH 6 and $[Zn]_T = 0.51$ mol L^{-1} (Electrolyte A) and following the dashed path of constant nitrogen concentration, $ZnCl_2{\cdot}4\,Zn(OH)_2{\cdot}H_2O$ is the first solid to precipitate, followed by $Zn(OH)_2$ and ZnO. The thermodynamically favored solid discharge product can change according to the pH value and the amount of chloride in the electrolyte, as shown in Figure 3b. Starting at the initial conditions pH 7 and $[Zn]_T = 0.26$ mol L^{-1} (Electrolyte B), the path of constant nitrogen concentration leads directly into the region of $ZnCl_2{\cdot}2\,NH_3$ insolubility. Therefore, it is possible to tune the initial composition of the electrolyte to favor the desired discharge product. This shift in the solid product was also noted in experimental investigations of zinc–carbon batteries.[26,36]

Cell operation and experimental validation

Our simulations elucidate the physicochemical processes that occur in the cell during galvanostatic operation. We begin by simulating the performance of neutral ZABs reported in literature. The experimental evaluation of Cell A[13] shows that under the operating conditions considered in the simulation it can be operated for up to 26 full charge–discharge cycles over about 13 days. We investigate the changes in the electrolyte during cycling, compare the simulated cell voltage with the experimental voltage profiles, and predict possible causes of failure. The development of Cell B builds on the progress of Cell A. The experimental investigation[14] shows that the cell can be stable operated for 540 cycles over 90 days. We simulate the design changes introduced in Cell B and consider what effects could be responsible for the gain in lifetime.

First, the basic processes occurring in the ZAB during galvanostatic cycling are investigated. Figure 4a, c, and e show the concentration profiles of zinc, NH_3, and pH value as the cell is discharged. When the discharge of Cell A begins, the metallic Zn electrode is dissolved to form aqueous species, which may exist as either zinc–ligand complexes or solvated Zn^{2+} ions. At the GDE, the ORR consumes H^+, and the $NH_4^+ \rightleftarrows NH_3 + H^+$ reaction (combined with the uptake of NH_3 by the zinc–ligand complexes) stabilizes the electrolyte pH value. Figure 4a shows that at the end of discharge zinc in the GDE exists mostly as complexes with NH_3. Once zinc exists exclusively as $Zn(NH_3)_4^{2+}$, then its capacity to take up excess NH_3 is exhausted and the concentration of NH_3 increases as shown in Figure 4c. When the concentration of NH_3 approaches its equivalence point with NH_4^+, the pH value becomes steadily more alkaline in the GDE, as shown in Figure 4e. At the Zn electrode, the small amount of NH_3 present is taken up by the excess Zn^{2+} ions and the pH value becomes slightly more acidic.

Figure 4b, d, and f show the concentration profiles in the cell during charging. When the cell is charged, aqueous zinc is redeposited at the Zn electrode. At the GDE, the OER produces H^+ and the equilibrium of the $NH_4^+ \rightleftarrows NH_3 + H^+$ reaction moves towards NH_4^+. The NH_3 that had formed complexes with Zn^{2+} during discharge is now released back into the solution to stabilize the equilibrium with NH_4^+. Figure 4b shows that at the end of charging, zinc in the GDE has released all of the available NH_3 and exists exclusively as zinc chloride complexes. Figure 4d shows that during the OER, the concentration of NH_3 in the GDE steadily decreases as it is converted into NH_4^+. Once the NH_3 released from the locally available zinc complexes is exhausted, additional NH_3 must diffuse into the GDE from the separator. However, some of the zinc–ammine complexes produced during discharge diffuse into the bulk electrolyte and they cannot be quickly transported to the GDE. These effects have significant consequences for the pH value in the cell. Because the amount of NH_3 in the GDE is no longer sufficient to convert the H^+ produced by the OER into NH_4^+, the pH value becomes acidic at the end of charging. This effect is shown in Figure 4f. Conversely, the increase in the concentration of NH_3 at the Zn electrode causes the pH value in that region to become slightly more alkaline.

MnO_2 is often used as an OER catalyst in alkaline and neutral solutions, but it is known to be unstable under acidic conditions due to the dissolution of Mn.[62–64] If the pH value in the GDE drops to a value of 1 or below, as occurs during the charging of Cell A (Figure 4f), the risk of accelerated catalyst degradation is increased.

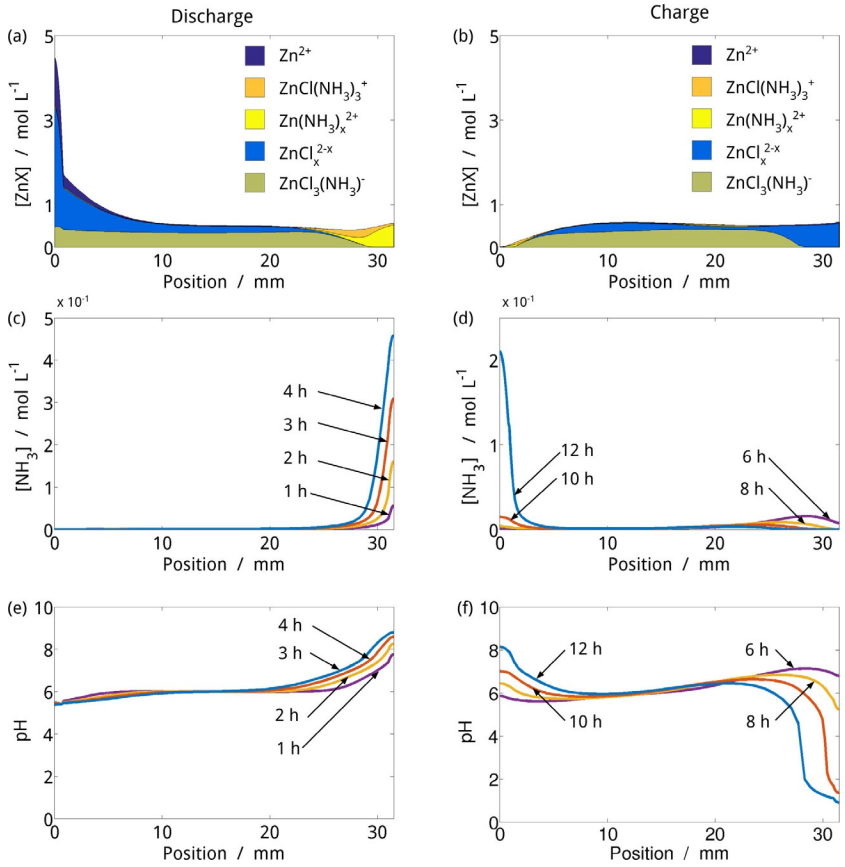

Figure 4. Electrolyte composition in Cell A during discharging and charging. At the end of discharging (a), zinc in the GDE exists as $Zn(NH_3)_4^{2+}$. Once the capacity of zinc to take up NH_3 is completely utilized, NH_3 accumulates in the GDE (c). As the NH_4^+/NH_3 solution approaches its equivalence point, the pH value in the GDE becomes steadily more alkaline (e). At the Zn electrode, the small amount of NH_3 present is taken up by excess Zn^{2+} and the pH value becomes slightly more acidic. When the cell is charged, the production of H^+ in the GDE pushes the equilibrium of the ammonium buffer back towards NH_4^+. The zinc–ammine complexes release NH_3 back to the solution as charging progresses, and at the end of charging, zinc in the GDE exists exclusively as zinc–chloride complexes (b). To stabilize the pH value in the GDE, there must be NH_3 available for the conversion into NH_4^+. However, a considerable amount of the NH_3 produced during discharging diffuses into the bulk electrolyte and cannot be quickly recovered. This leads to a depletion of NH_3 in the GDE (d). At the Zn electrode, the concentration of NH_3 increases because of the redeposition of zinc. Without NH_3 to stabilize the pH value, the electrolyte in the GDE becomes acidic (f). At the Zn electrode, the loss of aqueous Zn^{2+} and the relative excess of NH_3 cause the pH value to increase.

Figure 5 compares the simulated cell voltage over three cycles with experimental data. During discharge, there is a slight negative slope in the cell potential, which can be attributed to the pH shift in the GDE. Between the first and second discharges there is a positive shift in cell potential. In our model it is circa 100 mV, in the experimental data it is circa 250 mV. This shift in discharge voltage is due partly to the increase in the active surface area of the Zn electrode.

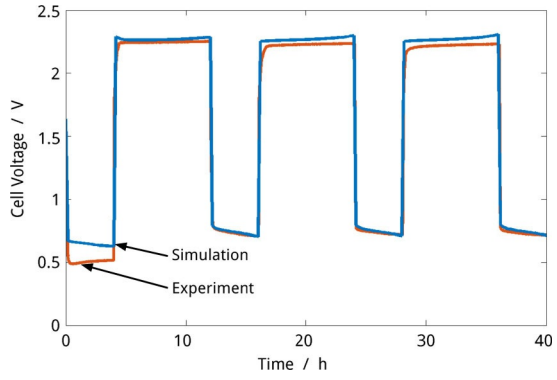

Figure 5. Simulated voltage profile of Cell A over three charge–discharge cycles, compared with experimental results;[13] $j_d = 5$ mA cm^{-2}, $t_d = 4$ h, $j_c = 2.5$ mA cm^{-2}, $t_c = 8$ h.

Initially, the Zn electrode is a polished sheet, but when zinc is electrodeposited, it takes on a porous morphology. This leads to an increase in the active surface area of the Zn electrode and a decrease in the overpotential of the electrochemical reaction. Our model considers this effect by altering the pore size of the deposited zinc. More information on this topic is available in the Supporting Information. However, the overpotential of the zinc reaction cannot be solely responsible for a 250 mV voltage shift. There may be other mechanisms (such as activation of the MnO_2 catalyst) occurring simultaneously, which could increase the magnitude of the voltage shift between the first and second discharge. Further experimental data is required to accurately characterize this effect.

As noted in the previous sections, the final product has a significant effect on cell performance. In the case of Cell A, however, the discharge capacity is rather small and the cell is

operated with an excess of electrolyte. Few solids precipitate, and they have little effect on the cell performance.

In summary, Cell A shows that a zinc–air battery can be reliably cycled in the $ZnCl_2$–NH_4Cl electrolyte. However, the shift towards acidic pH values in the GDE can limit the material stability and cell lifetime. Cell B addresses one of these challenges. The results of our simulation are very similar to those in Cell A, with one notable exception: the pH value in Cell B remains in the near-neutral regime when cycled. By avoiding the drop to acidic pH values, the stability of the catalyst and GDE is maintained, and the cell lifetime is improved. The pH profile of the cell at the end of discharge and end of charge are shown in Figure 6.

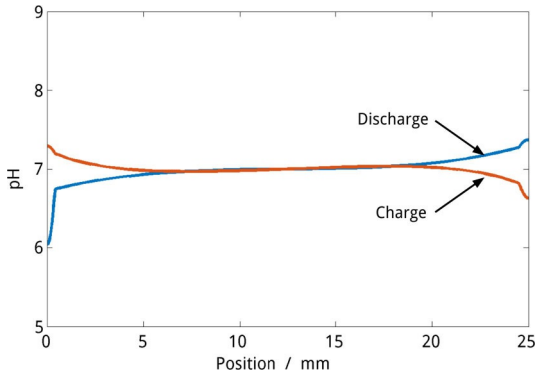

Figure 6. pH profiles of Cell B at the end of the first discharge cycle and end of the first charge cycle.

There are a few factors that contribute to the gain in pH stability. First, Cell B is charged at a lower current density, which reduces the NH_3 concentration gradient and allows more of the capacity of the buffer solution to be utilized. Second, the initial pH value of the electrolyte is 7 instead of 6. That means that initially there is more NH_3 in solution. More importantly, the state of the aqueous zinc ion is dominated by zinc–ammine complexes. As the pH drops to more acidic values, these complexes can release NH_3 to the electrolyte. Third, the separator length is shorter, which reduces the magnitude of the NH_3 concentration gradient and limits the distance NH_3 can diffuse away from the GDE. More information is available in the Supporting Information.

Although Cell B does show a dramatic gain in lifetime and pH stability over Cell A, it is operated at a lower current density and to a shallower depth of discharge (DoD). Our simulations show that the zinc solubility in the electrolyte is barely breached, and few solids precipitate.

Cell B represents another important step towards designing a practical neutral zinc–air cell, but questions remain. In the following simulations we show what happens when the cell is discharged to states at which significant amounts of solids precipitate, and investigate how the electrolyte composition and cell design may be optimized.

Cell-design optimization

The experimental studies modeled in the previous section show the general viability of the neutral electrolyte for secondary zinc–air battery applications. However, these cells are operated at relatively shallow DoDs, thereby avoiding complications that could arise due to the precipitation of chlorine-containing solids.

The precipitation of solids in the zinc–air cell induces a volume expansion, which has the potential to flood the GDE. A means of moderating the electrolyte level is necessary to avoid this effect. In commercial ZAB button cells, a gas void is included in the Zn electrode,[1] which provides room for the electrode to expand during discharge without forcing electrolyte into the GDE. We introduce this mechanism in our model by considering the entire domain of the ZAB to be a porous structure, the saturation of which is calculated using the Leverett approach described in the Supporting Information. The porous structures are initially 40% saturated.

The Zn electrode used in the experimental studies is a polished foil. While this is beneficial for studying the kinetics of the electrochemical reaction, it is impractical for use in a real battery. Commercial ZABs use zinc powder with particles on the order of 100 μm in diameter.[65] This powder may then be mixed with binder and electrolyte to form a paste. We consider a Zn paste electrode for our optimizations. Cells A and B feature a bath of excess electrolyte. This ensures that the cell always has sufficient amounts of electrolyte available, but it can lead to strong concentration gradients, increase the internal resistance of the cell, and lower the overall energy density. It is beneficial to design the cell using a thinner separator.

Figure 7 shows the pH profile across the cell for various separator thicknesses at the end of charging. Reducing the thickness of the separator improves the performance of the battery in three notable ways. First, it reduces the length of the transport paths in the battery, allowing more efficient utilization of NH_3. Second, the reduced volume of the electrolyte accelerates the precipitation of solids, which stabilizes the buffer solution. Third, the reduction of excess volume increases the energy density of the cell. The simulations show that for low current densities (1 mA cm^{-2}), separator lengths less than 2 mm are

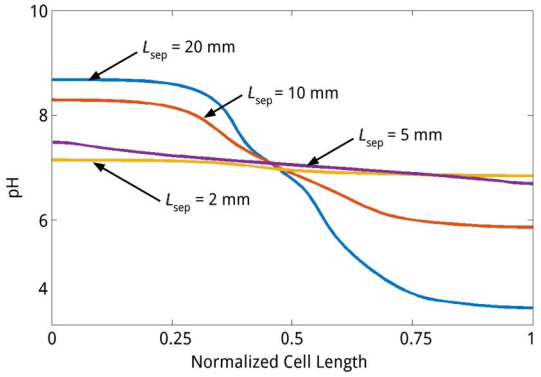

Figure 7. Gradients of the pH value at the end of charging for different separator distances versus the normalized length of the cell.

sufficient to maintain a stable pH value. As the energy density is inversely proportional to the separator length, we choose a 0.5 mm separator for the remainder of the optimizations.

With the optimum size of the separator defined, we turn our attention to the electrolyte composition. We define a standard test architecture to evaluate the effects of different electrolytes on battery performance. Our standard cell consists of a Zn electrode 5 mm in length, a 0.5 mm separator, and a 0.5 mm GDE. The cell is operated at 1 mA cm^{-2}. We first search for electrolyte compositions that thermodynamically favor the desired discharge product. Then we evaluate the stability of the electrolytes during cell operation.

According to existing studies on zinc–carbon batteries and the thermodynamic analysis presented previously, the thermodynamically favored discharge product in most cases is either $ZnCl_2{\cdot}2NH_3$ or $ZnCl_2{\cdot}4Zn(OH)_2{\cdot}H_2O$. As these solids precipitate, the aqueous chloride concentration decreases, altering the properties of the electrolyte. For the system to function as a zinc–air battery, the discharge product should be ZnO or alternatively $Zn(OH)_2$.

To predict an electrolyte composition that features a stable chloride concentration in the near-neutral pH regime and precipitates as either ZnO or $Zn(OH)_2$, we revisit the thermodynamic analysis from the section on electrolyte composition. The risk of precipitating chlorine-containing solids increases with increasing the total chloride concentration. For a total chloride concentrations of circa 3 mol L^{-1} and pH values above 7.5, $Zn(OH)_2$ is the thermodynamically favored product. The initial electrolyte composition should be formulated such that it is at the solubility limit of $Zn(OH)_2$ to facilitate precipitation. We therefore propose an electrolyte composition of 0.5 M $ZnCl_2$–1.6 M NH_4Cl with the pH adjusted to 8 (referred to in the text as Electrolyte C). Evaporation of NH_3 through the GDE is not considered in this analysis and should be a topic for further research. More information on this topic is available in the Supporting Information.

We evaluate the performance of Electrolytes A, B, and C by simulating the complete discharge of the test cell architecture to a cut-off voltage of 0.6 V. Figure 8a shows the total volume fractions of solid precipitates in the cell and the total chloride concentration versus discharged capacity, and Figure 8d shows the cell voltage and average pH value in the GDE for Electrolyte A. The discharge occurs in three stages. In the first stage, the total chlorine concentration decreases as $ZnCl_2{\cdot}4Zn(OH)_2{\cdot}H_2O$ precipitates. The pH value in the GDE becomes steadily more alkaline. This is because the precipitation of $ZnCl_2{\cdot}4Zn(OH)_2{\cdot}H_2O$ only removes 1.6 OH^- for every Zn^{2+} precipitated. In stage 2, the chloride concentration decreases to the lower solubility limit of $ZnCl_2{\cdot}4Zn(OH)_2{\cdot}H_2O$ and the dominant discharge product shifts to $Zn(OH)_2$. The pH value in the GDE begins to stabilize, because the precipitation of $Zn(OH)_2$ removes 2 OH^- for every Zn^{2+} precipitated. In the final stage, the capacity of the buffer solution is exhausted and the pH value in the GDE becomes alkaline. Small amounts of ZnO precipitate.

Figure 8b and e shows the discharge characteristics of a test cell with Electrolyte B. Again, the discharge occurs in three stages. In the first stage, the total chloride concentration de-

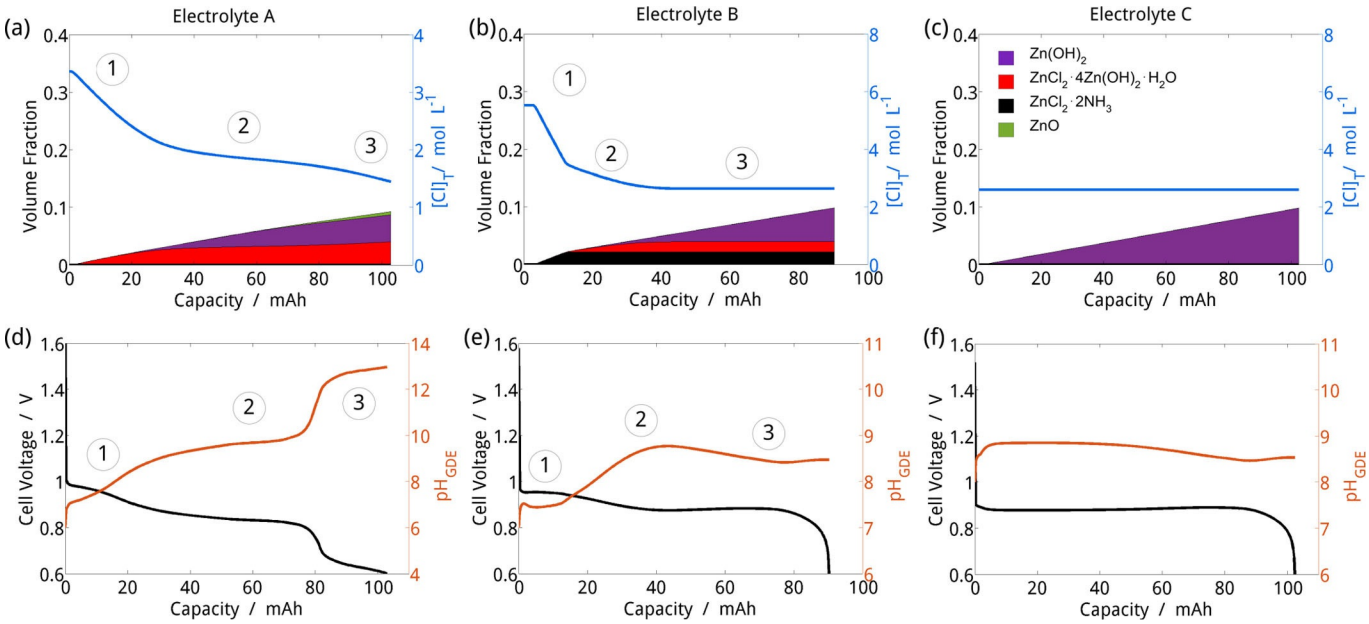

Figure 8. Stability of the total chloride concentration and pH value in ZAB standard test architecture (L_{Zn} = 5 mm) during discharge for various electrolyte compositions. For electrolytes with high initial chloride concentrations (a) and (b), the precipitation of chlorine-containing solids reduces the total chloride concentration until $Zn(OH)_2$ begins to precipitate. By reducing the total chloride concentration and moving to slightly alkaline pH values (c), the discharge product becomes exclusively $Zn(OH)_2$ and the chloride content of the electrolyte is stabilized. The pH stability of the electrolyte is also affected by the discharge product. For electrolytes in which $ZnCl_2{\cdot}4Zn/OH)_2{\cdot}H_2O$ precipitation dominates, the buffer solution is not effectively replenished and the pH is unstable (d). The effects of the pH variations can be seen in the cell potential. The precipitation of $ZnCl_2{\cdot}2NH_3$ and $Zn(OH)_2$ adequately stabilizes the pH value [(e) and (f)]. For these reasons, ZnO or $Zn(OH)_2$ are the desired discharge products.

creases rapidly as $ZnCl_2{\cdot}2\,NH_3$ precipitates and the pH value remains stable. The second stage begins when the total chloride concentration is reduced to a level at which $ZnCl_2{\cdot}4\,Zn(OH)_2{\cdot}H_2O$ precipitation is favored. The pH value becomes steadily more alkaline because of insufficient removal of OH^-. In the final stage, the discharge product shifts to $Zn(OH)_2$ and the total chloride concentration and pH value stabilize.

Figure 8c and f shows the discharge characteristics of a test cell using Electrolyte C. The composition of this electrolyte is tuned to favor only $Zn(OH)_2$ precipitation. The results show that both total chloride concentration and pH value remain stable throughout the discharge of the cell. The end of discharge occurs when the Zn electrode is passivated by $Zn(OH)_2$.

The shift in the solid discharge product observed in these simulations can be clarified by re-examining the thermodynamic stability plots in Figure 3. For high chloride concentrations, neutral pH values, and total zinc concentrations less than 1 mol L^{-1}, the battery discharge follows a path that takes it directly into the region of $ZnCl_2{\cdot}2\,NH_3$ insolubility (Figure 3b). When the total chloride concentration in the electrolyte is reduced, as shown in Figure 3a, the dominant discharge product becomes $ZnCl_2{\cdot}4\,Zn(OH)_2{\cdot}H_2O$ for slightly acidic-neutral pH values and $Zn(OH)_2$ for slightly alkaline pH values.

This analysis yields a few significant insights for zinc–air battery design. First, $ZnCl_2{\cdot}2\,NH_3$ and $ZnCl_2{\cdot}4\,Zn(OH)_2{\cdot}H_2O$ are not desirable discharge products. The precipitation of these solids consumes chloride from the electrolyte and reduces the effectiveness of the pH buffer. Second, electrolytes featuring a high initial chloride concentration will eventually converge to a steady-state chloride concentration at or near the solubility limit of $ZnCl_2{\cdot}2\,NH_3$ and $ZnCl_2{\cdot}4\,Zn(OH)_2{\cdot}H_2O$. Therefore, it should be noted that any advantages of high chloride concentration (e.g., improved conductivity) are only valid for shallow discharges. Third, it is possible to tune the initial concentration of the electrolyte to exclusively precipitate $Zn(OH)_2$, as demonstrated by our proposed Electrolyte C composition. Favoring the precipitation of $Zn(OH)_2$ over chlorine-containing solids is a modest improvement for cell operation. However, a means to thermodynamically or kinetically favor ZnO precipitation should be a topic for ongoing research.

Finally, we consider the design of the Zn electrode, which strongly influences the capacity and energy density of the battery. It is well known that passivation caused by the precipitation of solid products on the electrode surface is perhaps the biggest challenge limiting the full utilization of zinc in batteries. In alkaline zinc batteries, a shell of ZnO or $Zn(OH)_2$ forms around the zinc particles.[65] This shell isolates the surface of the zinc particle from the electrolyte and limits the transport of aqueous species to and from the electrode surface. When the thickness of the ZnO shell surpasses a critical value, the resistance to mass transport becomes so great that the concentrations of aqueous species at the zinc surface are depleted and the reaction cannot proceed. When this occurs, the electrode is said to be passivated.

Although this effect has been extensively studied in alkaline electrolytes, there is little research dedicated to the passivation process in the $ZnCl_2$–NH_4Cl system. It is thought that $ZnCl_2{\cdot}2\,NH_3$ is crystalline and dense and therefore presents a high resistance to the transport of solutes between the electrolyte and electrode. On the other hand, $ZnCl_2{\cdot}4\,Zn(OH)_2{\cdot}H_2O$ is amorphous and porous and presents a lower resistance to mass transport.[26] Therefore, it is likely that $ZnCl_2{\cdot}4\,Zn(OH)_2{\cdot}H_2O$ is less passivating than $ZnCl_2{\cdot}2\,NH_3$ and could help achieving a higher zinc utilization in the battery. This should be the subject of a more in-depth study. For the purpose of this optimization, we assume that the zinc particles are spheres with an initial diameter of 100 μm. When the thickness of solid precipitates around the particle exceeds 5 μm, the particle is considered to be passivated.

Figure 9 shows the energy density of zinc–air batteries considering the electrolyte compositions A, B, and C discussed previously. An electrolyte composition that favors ZnO precipitation is not immediately apparent. However, it is commonly noted that $Zn(OH)_2$ can undergo a decomposition to ZnO. Therefore, we evaluate what the performance of a theoretical ideal electrolyte would be, if the precipitation of ZnO were achieved. We set the composition for this idealized electrolyte at 0.5 M $ZnCl_2$–2 M NH_4Cl pH 7 (referred to in the text as Electrolyte D). For this analysis the Zn electrode thicknesses are varied from 0.5 to 20 mm. A cutoff voltage of 0.6 V is used as a reference.

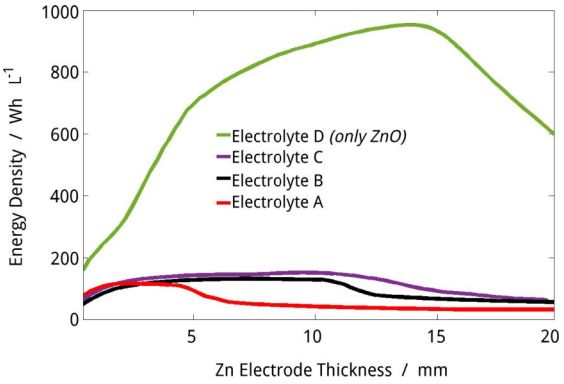

Figure 9. Energy density of the zinc–air cell with various electrolyte compositions versus Zn electrode thickness considering a cutoff voltage of 0.6 V. For thin Zn electrodes, the energy density is limited by the passivation of zinc. For thick Zn electrodes, the pH instability causes a drop in cell voltage.

For small Zn electrodes, solid precipitates accumulate and passivate the electrode quickly. As the size of the electrode increases, the passivation risk becomes less severe and a higher fraction of the zinc is utilized, leading to a higher energy density. For thick Zn electrodes, the long transport path for the aqueous species destabilizes the pH value in the GDE and reduces the energy density and lifetime of the cell. This is strongly the case in Electrolyte A. As shown in Figure 8a, the precipitation of $ZnCl_2{\cdot}4\,Zn(OH)_2{\cdot}H_2O$ cannot stabilize the buffer solution and the pH value becomes steadily more alkaline. This effect is exacerbated by the longer transport paths of thick Zn electrodes. The energy density of a cell with Electrolyte A peaks at 116 Wh L^{-1}. Electrolyte B shows increased pH stability, resulting in improved energy density up to Zn electrode thick-

nesses of about 10 mm. The energy density of a cell with Electrolyte B peaks at 132 Wh L^{-1}. Electrolyte C shows a modest improvement in energy density over Electrolytes A and B, peaking at 151 Wh L^{-1}. Our simulations show that a theoretical ideal electrolyte in which only ZnO is precipitated could give rise to an energy density of 952 Wh L^{-1}, which is comparable to commercial alkaline zinc–air button cells.[1] This improvement is attributable to the lower molar volume and more favorable passivation characteristics of ZnO, as outlined in Tables 2 and 4.

Conclusions

We have developed the first continuum model to simulate the performance of zinc–air batteries (ZABs) with $ZnCl_2$–NH_4Cl electrolytes. The model is based on a quasiparticle approach to describe the dynamic behavior of buffered aqueous electrolytes. Our simulations can determine the transient and concentration-dependent behavior of the electrolyte during cell operation. The results of these simulations are in accord with existing experimental investigations from the literature and suggest topics for future research.

The thermodynamic analysis presented in this work shows that the composition of the electrolyte is complex and highly sensitive to changes in pH value, total zinc concentration, and total chloride concentration. Even small shifts in these quantities can change the state of the aqueous Zn^{2+} ion and alter the thermodynamically favored precipitate.

Cell-level simulations show that concentration and pH gradients develop in the ZAB during operation and have a significant impact on both performance and lifetime. Although $ZnCl_2$–NH_4Cl is able to buffer the pH value of the electrolyte, the practically achievable capacity of the buffer is limited by the transport of NH_3 between the gas-diffusion electrode (GDE) and the separator. For cell architectures featuring a large separator, NH_3 produced during discharge cannot be readily recovered when the cell is charged, causing the pH value in the GDE to become acidic. This effect can be mitigated by decreasing the thickness of the separator and increasing the initial pH value of the electrolyte. We propose that this effect is partially responsible for the experimentally documented gain in lifetime in the cell observed by Sumboja et al.[14] in comparison to that reported by Goh et al.[13]

We present an initial optimization of electrolyte composition and cell architecture. Electrolytes with a high initial chloride concentration will eventually converge to a lower chloride concentration near the solubility limit of $ZnCl_2{\cdot}2\,NH_3$ and $ZnCl_2{\cdot}4\,Zn(OH)_2{\cdot}H_2O$ as these solids precipitate. By altering the initial composition of the electrolyte to reflect this inevitable shift and increasing the pH value to slightly alkaline values, the system can be tuned to exclusively precipitate $Zn(OH)_2$.

The thickness of the Zn electrode should be adjusted according to the needs of the system and the composition of the electrolyte. The capacity of cells with thin Zn electrodes is limited by the passivation of zinc by the solid discharge products. Cells with thick Zn electrodes are limited by the large pH value and concentration gradients that lower the equilibrium potential of the oxygen-reduction reaction. Although tuning the cell to precipitate $Zn(OH)_2$ instead of chlorine-containing solids marginally improves the energy density of the cell, this improvement is small compared to the energy densities achievable with ZnO as the discharge product. Further research should be directed at ways to favor ZnO precipitation in the near-neutral pH regime.

Acknowledgements

*This work is supported by the European Union (EU)through the Horizon 2020 project ZAS!: Zinc Air Secondary innovative nanotech based batteries for efficient energy storage (Grant Agreement 646186). The authors wish to thank Yun Zong at the Institute of Materials Research and Engineering (IMRE) at A*STAR in Singapore for the fruitful discussion. We also acknowledge the support of the bwHPC initiative through the use of the JUSTUS HPC facility at Ulm University.*

Conflict of interest

The authors declare no conflict of interest.

Keywords: batteries · computational chemistry · electrochemistry · thermodynamics · zinc

[1] J. Stamm, A. Varzi, A. Latz, B. Horstmann, *J. Power Sources* **2017**, *360*, 136 – 149.
[2] Y. Li, H. Dai, *Chem. Soc. Rev.* **2014**, *43*, 5257 – 5275.
[3] B. Li, J. Quan, A. Loh, J. Chai, Y. Chen, C. Tan, X. Ge, T. S. A. Hor, Z. Liu, H. Zhang, Y. Zong, *Nano Lett.* **2017**, *17*, 156 – 163.
[4] P. Gu, M. B. Zheng, Q. X. Zhao, X. Xiao, H. G. Xue, H. Pang, *J. Mater. Chem. A* **2017**, *5*, 7651 – 7666.
[5] K. Wang, P. Pei, Z. Ma, H. Chen, H. Xu, D. Chen, X. Wang, *J. Mater. Chem. A* **2015**, *3*, 22648 – 22655.
[6] M. Schmid, M. Willert-Porada, *J. Power Sources* **2017**, *351*, 115 – 122.
[7] D. Kundu, B. D. Adams, V. Duffort, S. H. Vajargah, L. F. Nazar, *Nat. Energy* **2016**, *1*, 16119.
[8] J.-I. Jung, M. Risch, S. Park, M. G. Kim, G. Nam, H.-Y. Jeong, Y. Shao-Horn, J. Cho, *Energy Environ. Sci.* **2016**, *9*, 176 – 183.
[9] K. E. K. Sun, T. K. A. Hoang, T. N. L. Doan, Y. Yu, X. Zhu, Y. Tian, P. Chen, *ACS Appl. Mater. Interfaces* **2017**, *9*, 9681 – 9687.
[10] J. Fu, Z. P. Cano, M. G. Park, A. Yu, M. Fowler, Z. Chen, *Adv. Mater.* **2017**, *29*, 1604685.
[11] T. Arlt, D. Schröder, U. Krewer, I. Manke, *Phys. Chem. Chem. Phys.* **2014**, *16*, 22273 – 22280.
[12] J. Jindra, J. Mrha, M. Musilová, *J. Appl. Electrochem.* **1973**, *3*, 297 – 301.
[13] F. W. T. Goh, Z. Liu, T. S. A. Hor, J. Zhang, X. Ge, Y. Zong, A. Yu, W. Khoo, *J. Electrochem. Soc.* **2014**, *161*, A2080 – A2086.
[14] A. Sumboja, X. Ge, G. Zheng, F. W. T. Goh, T. S. A. Hor, Y. Zong, Z. Liu, *J. Power Sources* **2016**, *332*, 330 – 336.
[15] R. Winand, *Modern Electroplating*, Wiley, Hoboken, New Jersey, **2011**.
[16] H. Pan, Y. Shao, P. Yan, Y. Cheng, K. S. Han, Z. Nie, C. Wang, J. Yang, X. Li, P. Bhattacharya, K. T. Mueller, J. Liu, *Nat. Energy* **2016**, *1*, 16039.
[17] D. U. Lee, P. Xu, Z. P. Cano, A. G. Kashkooli, M. G. Park, Z. Chen, *J. Mater. Chem. A* **2016**, *4*, 7107 – 7134.
[18] B. Lee, H. R. Seo, H. R. Lee, C. S. Yoon, J. H. Kim, K. Y. Chung, B. W. Cho, S. H. Oh, *ChemSusChem* **2016**, *9*, 2948 – 25956.
[19] X. G. Zhang, *Corrosion and Electrochemistry of Zinc*, Plenum Press, New York, NY, **1996**.
[20] J. L. Limpo, A. Luis, M. C. Cristina, *Hydrometallurgy* **1995**, *38*, 235 – 243.
[21] J. L. Limpo, A. Luis, *Hydrometallurgy* **1993**, *32*, 247 – 260.
[22] M. Winter, R. J. Brodd, *Chem. Rev.* **2004**, *104*, 4245 – 4269.
[23] A. M. Bredland, M. N. Hull, *J. Electrochem. Soc.* **1976**, *123*, 311 – 315.

[24] H. F. McMurdie, D. N. Craig, G. W. Vinal, *J. Electrochem. Soc.* **1946**, *90*, 509 – 528.
[25] R. Friess, *J. Am. Chem. Soc.* **1930**, *52*, 3083 – 3087.
[26] S. Zhao, H. An, S. Chen, *J. Power Sources* **1998**, *76*, 218 – 220.
[27] A. R. Mainar, L. C. Colmenares, O. Leonet, F. Alcaide, J. J. Iruin, S. Weinberger, V. Hacker, E. Iruin, I. Urdanpilleta, J. A. Blazquez, *Electrochim. Acta* **2016**, *217*, 80 – 91.
[28] R. Smith, A. Martell, *Critical Stability Constants Volume 4: Inorganic Complexes*, Plenum Press, New York, NY, **1976**.
[29] E. Deiss, F. Holzer, O. Haas, *Electrochim. Acta* **2002**, *47*, 3995 – 4010.
[30] D. Schröder, U. Krewer, *Electrochim. Acta* **2014**, *117*, 541 – 553.
[31] W. G. Sunu, D. N. Bennion, *J. Electrochem. Soc.* **1980**, *127*, 2007 – 2016.
[32] Z. Mao, R. E. White, *J. Electrochem. Soc.* **1992**, *139*, 1105 – 1114.
[33] J. Vazquez-Arenas, F. Sosa-Rodriguez, I. Lazaro, R. Cruz, *Electrochim. Acta* **2012**, *79*, 109 – 116.
[34] T. P. Dirkse, *J. Electrochem. Soc.* **1986**, *133*, 1656 – 1657.
[35] N. C. Cahoon, *J. Electrochem. Soc.* **1947**, *92*, 159 – 172.
[36] J. Larcin, W. C. Maskell, F. L. Tye, *Electrochim. Acta* **1997**, *42*, 2649 – 2658.
[37] B. Horstmann, T. Danner, W. G. Bessler, *Energy Environ. Sci.* **2013**, *6*, 1299.
[38] J. P. Neidhardt, D. N. Fronczek, T. Jahnke, T. Danner, B. Horstmann, W. G. Bessler, *J. Electrochem. Soc.* **2012**, *159*, A1528 – A1542.
[39] A. Latz, J. Zausch, *Electrochim. Acta* **2013**, *110*, 358 – 362.
[40] M. Z. Bazant, *Acc. Chem. Res.* **2013**, *46*, 1144 – 1160.
[41] D. Eberle, B. Horstmann, *Electrochim. Acta* **2014**, *137*, 714 – 720.
[42] F. Single, B. Horstmann, A. Latz, *Phys. Chem. Chem. Phys.* **2016**, *18*, 17810 – 17814.
[43] T. Danner, S. Eswara, V. P. Schulz, A. Latz, *J. Power Sources* **2016**, *324*, 646 – 656.
[44] M. D. Radin, C. W. Monroe, D. J. Siegel, *Chem. Mater.* **2015**, *27*, 839 – 847.
[45] T. Danner, B. Horstmann, D. Wittmaier, N. Wagner, W. G. Bessler, *J. Power Sources* **2014**, *264*, 320 – 332.
[46] D. G. Miller, A. W. Ting, J. A. Rard, *J. Electrochem. Soc.* **1988**, *135*, 896 – 903.
[47] J. A. Rard, D. G. Miller, *J. Solution Chem.* **1990**, *19*, 129 – 148.
[48] J. Newman, K. E. Thmoas-Alyea, *Electrochemical Systems*, Wiley, Hoboken, NJ, **2004**.
[49] M. Qaiser Fatmi, T. S. Hofer, B. M. Rode, *Phys. Chem. Chem. Phys.* **2010**, *12*, 9713 – 9718.
[50] K. Sasaki, T. Takahashi, *Electrochim. Acta* **1959**, *1*, 261 – 271.
[51] P. Atkins, J. De Paula, *Atkins' Physical Chemistry*, W. H. Freeman And Company, New York **2006**.
[52] E. L. Shock, H. C. Helgeson, *Geochim. Cosmochim. Acta* **1988**, *52*, 2009 – 2036.
[53] E. L. Shock, H. C. Helgeson, D. A. Sverjensky, *Geochim. Cosmochim. Acta* **1989**, *53*, 2157 – 2183.
[54] E. L. Shock, D. C. Sassani, M. Willis, D. A. Sverjensky, *Geochim. Cosmochim. Acta* **1997**, *61*, 907 – 950.
[55] D. A. Sverjensky, E. L. Shock, H. C. Helgeson, *Geochim. Cosmochim. Acta* **1997**, *61*, 1359 – 1412.
[56] A. Roux, G. M. Musbally, G. Perron, J. E. Desnoyers, *Can. J. Chem.* **1978**, *56*, 24 – 28.
[57] M. J. W. Frank, J. A. M. Kuipers, W. P. M. Van Swaaij, *J. Chem. Eng. Data* **1996**, *41*, 297 – 302.
[58] Z. Huajun, G. Zhenghai, Z. Jinhuan, *Hydrometallurgy* **2007**, *89*, 369 – 373.
[59] I. Roche, K. Scott, *J. Appl. Electrochem.* **2009**, *39*, 197 – 204.
[60] T. Takashima, K. Hashimoto, R. Nakamura, *J. Am. Chem. Soc.* **2012**, *134*, 1519 – 1527.
[61] F. Single, B. Horstmann, A. Latz, *J. Electrochem. Soc.* **2017**, *164*, E3132 – E3145.
[62] M. Huynh, D. K. Bediako, D. G. Nocera, *J. Am. Chem. Soc.* **2014**, *136*, 6002 – 6010.
[63] T. Takashima, K. Hashimoto, R. Nakamura, *J. Am. Chem. Soc.* **2012**, *134*, 18153 – 18156.
[64] R. Pokhrel, M. K. Goetz, S. E. Shaner, X. Wu, S. S. Stahl, *J. Am. Chem. Soc.* **2015**, *137*, 8384 – 8387.
[65] Q. C. Horn, Y. Shao-Horn, *J. Electrochem. Soc.* **2003**, *150*, A652 – A658.

Manuscript received: August 7, 2017
Accepted manuscript online: September 12, 2017
Version of record online: November 16, 2017

Electronic Supplementary Information: Rational Development of Neutral Aqueous Electrolytes for Zinc-Air Batteries

Simon Clark[1,2], Arnulf Latz[1,2,3], and Birger Horstmann[1,2]
[1]German Aerospace Center (DLR), Institute of Engineering Thermodynamics,
Pfaffenwaldring 38-40, 70569 Stuttgart, Germany
[2]Helmholtz Institute Ulm (HIU) Electrochemical Energy Storage,
Helmholtzstr. 11 89081 Ulm, Germany
[3]Ulm University (UUlm), Institute of Electrochemistry,
Albert-Einstein-Allee 47 89081 Ulm, Germany

A Modeling Electrolyte Transport

As stated in the main text, the general framework for modeling electrolytes in electrochemical systems is derived and validated in existing works.[1–4]

The transport of solutes in the electrolyte is derived from non-equilibrium thermodynamics[1] and can be expressed in generic terms by the mass continuity equation

$$\frac{\partial(c_i\varepsilon_\mathrm{e})}{\partial t} = -\vec{\nabla}\cdot\left(\vec{N}_i^{\mathrm{DM}}\right) - \vec{\nabla}\cdot\left(\vec{N}_i^{\mathrm{C}}\right) + \dot{s}_i, \tag{1}$$

where $\vec{N}_i^{\mathrm{DM}}$ is the diffusion-migration flux, $\vec{N}_i^{\mathrm{C}}$ is the convection flux, and $\dot{s}_i$ is the source term, and the local electroneutrality equations

$$0 = -\vec{\nabla}\cdot\vec{j} + \sum_i z_i\dot{s}_i, \tag{2}$$

where $\vec{j}$ is the electrolyte current density and z_i is the charge number of the solute.

A.1 Diffusion-Migration Flux

The first term in the mass continuity equation describes the concentration change due to the diffusion-migration flux. The diffusion-migration flux,

$$\vec{N}_i^{\mathrm{DM}} = \varepsilon_\mathrm{e}^\beta D_i\vec{\nabla}c_i + \frac{t_i}{z_iF}\vec{j}, \tag{3}$$

features two coupled components: a diffusion term which is driven by the concentration gradient of the species and a migration term which describes the fraction of the electrolyte current density, $\vec{j}$, the flux of the species comprises. The transport coefficients are multiplied with a pre-factor, $\varepsilon_\mathrm{e}^\beta$, to account for the effects of the porous structure. In this factor, ε_e is the volume fraction of the electrolyte and β is the Bruggeman coefficient.

Table 1: Fundamental reactions of the zinc-air cell.

Reaction	$\mathbf{E^0}$ **/ V**
$Zn \rightleftharpoons Zn^{2+} + 2e^-$	-0.762
$\frac{1}{2}O_2(aq) + 2H^+ + 2e^- \rightleftharpoons H_2O$	1.229
$O_2(g) \rightleftharpoons O_2(aq)$	-

The electrolyte current density is driven by both the potential gradient in the electrolyte and the gradient in the chemical potential of the charged species. It is defined as

$$\vec{j} = \varepsilon_e^\beta \Big(- \kappa_e \vec{\nabla}\phi_e - \sum \frac{\kappa t_i}{z_i F} \frac{\partial \mu_i}{\partial c_i} \vec{\nabla} c_i \Big), \tag{4}$$

where κ_e is the ionic conductivity of the electrolyte, ϕ_e is the electric potential of the electrolyte, t_i is the transference number of the ion, and z_i is the ion charge number. The chemical potential is defined as $\mu_i = RT \ln\big(\frac{c_i}{c_0}\big)$.

For uncharged solutes, like oxygen, the diffusion-migration flux simplifies to Fick's law. Recently, it has been discussed that Fick's law might be too inaccurate to model oxygen transport.[5] But in the GDE, the oxygen transport occurs mainly through the gas phase.[2]

A.2 Chemical Reactions

The concentrations in the electrolyte are also affected by the chemical reactions in the cell. For a neutral ZAB, these reactions can be placed into two categories: heterogeneous reactions (occurring at an interface between two phases) and homogeneous reactions (occurring in the bulk of a single phase). The heterogeneous reactions in the ZAB include electrochemical, precipitation, and gas dissolution reactions listed in Tables 1 and 2. In this section, we discuss only the heterogeneous reactions. The effects of the homogeneous reactions are discussed in the main text.

Three quantities are needed to characterize the heterogeneous reactions and their effect on the system: the reaction rate, k_r, the specific active surface area, A_r^{sp}, and the stoichiometric coefficient, $\nu_{i,r}$. The product of these quantities yields a particle source term of species i from reaction r,

$$\dot{s}_i = \sum_r \nu_{i,r} k_r A_r^{\mathrm{sp}}, \tag{5}$$

which is included in the electrolyte transport equations.

The stoichiometric equations and standard potentials of the electrochemical reactions are listed in Table 1. The reaction rates of the electrochemical reactions are calculated using the Butler-Volmer approximation,[6,7] assuming a single-step reaction mechanism

$$\begin{aligned} k_r = k_{0,r} \Big[& \exp\Big(\frac{\alpha_{a,r} n_r F}{RT} \eta_r \Big) - \\ & \exp\Big(- \frac{\alpha_{c,r} n_r F}{RT} \eta_r \Big) \Big]. \end{aligned} \tag{6}$$

Table 2: Precipitation reactions in $ZnCl_2$−NH_4Cl.

Reaction
$Zn^{2+} + 2\,Cl^- + 2\,NH_3 \rightleftharpoons ZnCl_2 \cdot 2\,NH_3(s)$
$5\,Zn^{2+} + 2\,Cl^- + 9\,H_2O \rightleftharpoons ZnCl_2 \cdot 4\,Zn(OH)_2 \cdot H_2O(s) + 8\,H^+$
$Zn^{2+} + 2\,H_2O \rightleftharpoons Zn(OH)_2(s) + 2\,H^+$
$Zn^{2+} + H_2O \rightleftharpoons ZnO(s) + 2\,H^+$

This simplification[8] is justified as the electrochemical reactions remain at a stable working point. The reaction rate constant, $k_{0,r}$, corresponds to the exchange current density. The surface overpotential, η_r, is the driving force for the reaction and is defined from thermodynamics. Under equilibrium conditions, the rate of the forward and backward reactions are equal, causing no net reaction to occur. Using the Nernst equation, the equilibrium voltages for the electrochemical reactions listed in Table 1 are calculated as:

$$U_{\mathrm{Zn}} = -0.762\mathrm{V} + \frac{RT}{2F}\ln\frac{c_{\mathrm{Zn}}}{c^0_{\mathrm{Zn}}}, \tag{7}$$

$$U_{\mathrm{GDE}} = 1.229\mathrm{V} + \frac{2.303RT}{F}\left(- \mathrm{pH} + \log\sqrt{\frac{c_{\mathrm{O_2}^{\mathrm{aq}}}}{c^0_{\mathrm{O_2}}}}\right), \tag{8}$$

for the Zn electrode and the GDE, respectively. The potential jump at the surface of the electrode is $V = \phi_{\mathrm{d}} - \phi_{\mathrm{e}}$. The surface overpotential is defined as the difference between the potential drop at the electrode surface and the equilibrium half-cell voltage, $\eta_r = V_r - U_r$.

The ORR/OER occurs at the so-called three-phase boundary in the GDE, and we assume that this specific surface area is constant. The zinc dissolution/deposition reaction occurs at the interface between the zinc metal and the electrolyte. The Zn electrode may change shape during the charge and discharge processes, affecting the active surface area available for the electrochemical reaction. The specific active surface area is defined as a function of zinc volume fraction,[9] and is expressed as

$$A^{\mathrm{sp}}_{\mathrm{Zn}} = \frac{6}{a_{\mathrm{Zn}}}\varepsilon_{\mathrm{Zn}}(1 - \varepsilon_{\mathrm{Zn}}), \tag{9}$$

where $\varepsilon_{\mathrm{Zn}}$ is the volume fraction of the zinc and a_{Zn} is the pore diameter of the metallic zinc phase.

The dissolution of oxygen into the electrolyte from the gas phase is modeled as described in existing works.[1,2] The solubility of oxygen in the electrolyte is determined by Henry's law, $[{\mathrm{O_2}}^{\mathrm{aq}}] = Hp_{\mathrm{O_2}}$. The kinetics of the reaction are defined as $k_{\mathrm{O_2}} = k^{\mathrm{f}}_s p_{\mathrm{O_2}} - k^{\mathrm{b}}_s[\mathrm{O_2}]$. For cell operation at low current density, we assume that the pressure of oxygen in the GDE remains constant,[2] indicating a state of equilibrium, and the kinetics of the forward reaction are defined using the Hertz-Knudsen equation.

Finally, the precipitation reactions occur when the concentration of aqueous zinc species exceeds the solubility limit. The rate of these reactions is assumed to be diffusion limited. It is described by the diffusion of the limiting species and the degree to which the solubility has been exceeded,

$$k_r = \frac{D_{\mathrm{Zn}}}{\delta}\frac{(c_{\mathrm{Zn}} - c^{\mathrm{sat}}_r)}{c^0_{\mathrm{Zn}}}, \tag{10}$$

where D_{Zn} is the zinc diffusion coefficient, δ is the diffusion length, c_{Zn} is the aqueous zinc concentration, and c_r^{sat} is the zinc saturation concentration of the solid. We define the specific surface area for the precipitation reactions as

$$A_p^{\mathrm{sp}} = \frac{6}{a_{\mathrm{s}}}\varepsilon_{\mathrm{s}}(1-\varepsilon_{\mathrm{s}}), \tag{11}$$

where a_{s} is the pore size of the solid phase and ε_{s} is the total solid volume fraction.

A.3 Convection Flux

Solid, liquid, and gas phases coexist in the ZAB, and the saturation of the porous structures may change due to the chemical reactions. To model this effect,[1–4] we first note that the equation of state for the electrolyte allows to solve for the liquid volume fraction.

$$\sum \bar{V}_i c_i = 1, \tag{12}$$

where the partial molar volume of the solute, $\bar{V}_i$, is a material parameter. With the volume fraction of the electrolyte known, the saturation of the GDE is calculated as

$$\tilde{s} = \frac{\varepsilon_{\mathrm{e}}}{1-\varepsilon_{\mathrm{s}}}, \tag{13}$$

while noting that the sum of the volume fractions of the solid, liquid, and gas phases must be equal to 1.

$$\varepsilon_{\mathrm{e}} + \varepsilon_{\mathrm{s}} + \varepsilon_{\mathrm{g}} = 1. \tag{14}$$

Based on a predetermined pressure-saturation curve, $J(\tilde{s})$, obtained either experimentally or via numerical methods such as Lattice-Boltzmann,[10] the pressure in the electrolyte is determined with the following expression,

$$p_{\mathrm{cap}} = p_{\mathrm{g}} - p_{\mathrm{e}} = -J(\tilde{s}), \tag{15}$$

assuming that the pressure of the gas, p_{g}, is constant.

The electrolyte pressure drives a convective flux in the cell. The flow is assumed to be incompressible, isothermal and laminar. A Darcy approach[3] is therefore sufficient. The center of mass velocity of the electrolyte is defined as

$$\vec{v_{\mathrm{e}}} = -\frac{B_{\mathrm{e}}}{\mu_{\mathrm{e}}}\vec{\nabla} p_{\mathrm{e}}, \tag{16}$$

where B_{e} is the permeability of the porous medium and μ_{e} is the viscosity of the electrolyte. The convective flux is then expressed as

$$\vec{N}_i^{\mathrm{C}} = \varepsilon_{\mathrm{e}}^{\beta} c_i \vec{v_{\mathrm{e}}}. \tag{17}$$

With the definitions for mass flux and chemical reactions presented above, we can now revisit the transport equations for the electrolyte.

A.4 Transport Equations

Considering the expressions for mass continuity and local electroneutrality shown in equations 1 and 2, and the definitions provided in equations 3, 17, and 5 we can define the set of transport equations for the solutes in the electrolyte as

$$\begin{aligned}\frac{\partial(c_i\varepsilon_\mathrm{e})}{\partial t} =& -\vec{\nabla}\cdot\left(\varepsilon_\mathrm{e}^\beta D_i\vec{\nabla}c_i + \frac{t_i}{z_iF}\vec{j}\right) - \\ & \vec{\nabla}\cdot\left(\varepsilon_\mathrm{e}^\beta c_i\vec{v_\mathrm{e}}\right) + \sum_r \nu_{i,r}k_rA_r^\mathrm{sp},\end{aligned} \tag{18}$$

$$0 = -\vec{\nabla}\cdot\vec{j} + \sum_{i,r} z_i\nu_{i,r}k_rA_r^\mathrm{sp}. \tag{19}$$

To determine the concentration of the solvent, we add an additional transport equation to describe the center of mass continuity of the bulk electrolyte, based on the velocity in equation 16

$$\frac{\partial(\rho\varepsilon_\mathrm{e})}{\partial t} = \vec{\nabla}\cdot\left(\varepsilon_\mathrm{e}^\beta\rho\vec{v_\mathrm{e}}\right) + \sum_i M_i\dot{s}_i. \tag{20}$$

These transport equations are sufficient to model most electrochemical systems. But in the case of neutral ZABs, the large quantity of possible solutes and the potential for orders-of-magnitude shifts in concentration make it numerically unfeasible to solve the transport equations for each individual species. To address this challenge, we develop a new quasi-particle framework for modeling electrolyte transport, as outlined in the main text.

B Parameterization and Computational Details

In this section we present an overview of the parameters and computational details implemented in the model.

B.1 Electrolyte Transport

To describe the transport of the electrolyte, 5 solute parameters are required: molar mass, M_i, charge number, z_i, diffusion coefficient, D_i, conductance, λ_i, and partial molar volume, $\bar{V}_i$. Values for these parameters are either obtained from literature or estimated. A complete list is shown in Table 3.

There are currently only a few experimental studies investigating the transport parameters of the $ZnCl_2$−NH_4Cl electrolyte. The diffusion coefficients and ionic transport parameters for the $ZnCl_2 - KCl - H_2O$ system are well documented.[11,12] This data is used to parameterize the transport properties of the zinc-chloride species. We model the diffusion coefficients of the $ZnCl_x$ species as equal. No satisfactory experimental data characterizing the transport of zinc-ammine species could be found in the literature. Therefore, estimates for these parameters were obtained through the Stokes-Einstein and Nernst-Einstein relations[13] using experimental viscosity data and theoretically calculated solvated radii.[14]

$$D_i = \frac{k_bT}{6\pi\mu_\mathrm{e}r_i}, \tag{21}$$

$$\lambda_i = \frac{D_i |z_i| F^2}{RT}. \tag{22}$$

Sasaki, *et al.*[15] investigate the density and viscosity of the $ZnCl_2$−NH_4Cl electrolyte at various mixed concentrations. Their work shows that when the concentration of $ZnCl_2$ is low, the density of the electrolyte increases with increasing NH_4Cl concentration. But for high concentrations of $ZnCl_2$, the density of the electrolyte decreases with increasing NH_4Cl concentration. This indicates a shift in the state of the Zn^{2+} ion due to changes in the solution pH and total chlorine concentration, confirming the prediction of our thermodynamic model. Because of the shifting state of the zinc ion and the quantity of aqueous species which are present, this experimental data is insufficient to determine the partial molar volumes of the solutes.[16] Therefore, the model considers the partial molar volumes of the electrolyte component species at standard conditions.[17–21]

The equilibrium concentrations of the solutes are calculated using the thermodynamic stability constants available in existing works.[22–24]

With the parameters of the individual solutes known, the transport properties of the bulk electrolyte can be calculated. The ionic conductivity of the electrolyte is defined according to its equivalent conductance and the total chlorine concentration

$$\kappa_\mathrm{e} = \frac{\Lambda_\mathrm{e}}{c_\mathrm{Cl}}. \tag{23}$$

The equivalent conductance of the electrolyte is the weighted sum of the conductance of the individual ions:

$$\Lambda_\mathrm{e} = \sum_i X_i \lambda_i, \tag{24}$$

$$X_i = \frac{c_i z_i}{\sum_j c_j z_j}. \tag{25}$$

The concentration of the solvent is calculated using the equation of state for the electrolyte (derived from the Gibbs-Duhem equation),

$$1 = \sum \bar{V}_i c_i, \tag{26}$$

where i refers to the unified set of solutes and solvent. The density of the electrolyte is then calculated as

$$\rho_\mathrm{e} = \sum M_i c_i. \tag{27}$$

Using this approach and the parameters listed in Table 3, we calculate the ionic conductivity and density of the electrolytes, shown in Table 4.

A dimensionless Leverett function is used to model the pressure saturation characteristics of the GDE. This function takes the form

$$J(\tilde{s}) = A + Be^{C(s-0.5)} - De^{-E(s-0.5)} = \frac{p_c}{\sigma}\sqrt{\frac{B_0}{\varepsilon_0}}, \tag{28}$$

where p_c is the capillary pressure, σ is the surface tension of the electrolyte, B_0 is the permeability, and ε_0 is the porosity of the GDE. The coefficients of the Leverett function were determined using a Lattice Boltzmann simulation of a reconstructed GDE structure.[10]

Table 3: Transport parameters of aqueous species.

Species	M_i / $g \cdot mol^{-1}$	z_i / $-$	$D_i \times 10^9$ / $m^2 \cdot s^{-1}$	$\lambda_i^0 \times 10^4$ / $S \cdot m^2 \cdot equiv^{-1}$	$\bar{V}_i \times 10^6$ / $m^3 \cdot mol^{-1}$
$ZnCl^+$	100.8	+1	1.10[12]	35*	-1.28[20]
$ZnCl_2$	136.3	0	1.10[12]	-	24.82[20]
$ZnCl_3^-$	171.7	-1	1.10[12]	35[12]	53.9[20]
$ZnCl_4^{2-}$	207.2	-2	1.10[12]	55[12]	81*
$Zn(NH_3)^{2+}$	82.4	+2	1.12*	84.2*	7.5*
$Zn(NH_3)_2^{2+}$	99.4	+2	1.14*	85.7*	39.2*
$Zn(NH_3)_3^{2+}$	116.5	+2	1.09*	81.5*	70.9*
$Zn(NH_3)_4^{2+}$	133.5	+2	0.83*	62.7*	102.6*
$ZnCl_3(NH_3)^-$	188.8	-1	1.10*	41.3*	86.4*
$ZnCl(NH_3)_3^+$	151.9	+1	1.10*	41.3*	97.2*
H^+	1.0	+1	9.31[13]	349.8[13]	0
OH^-	17.0	-1	5.26[13]	197.6[13]	-4.18[18]
NH_4^+	18	+1	1.95[13]	73.4[13]	18.13[19]
NH_3	17	0	1.94[25]	-	24.43[19]
Cl^-	35.5	-1	2.03[13]	76.34[13]	17.79[19]
Zn^{2+}	65.4	+2	0.71[13]	53[13]	-24.3[18]
O_2^{aq}	32	0	1.5*	-	30.38[17]
H_2O	18	0	-	-	18[16]

*Estimated

Table 4: Calculated physical properties of the electrolytes.

Property	Unit	Electrolyte A	Electrolyte B	Electrolyte C	Electrolyte D
κ_e	$\mathrm{S \cdot m^{-1}}$	31.1	44.7	26.1	28.6
ρ_e	$\mathrm{kg \cdot m^{-3}}$	1117.1	1134.7	1091.2	1104.6

Table 5: Leverett function parameters.

Coefficient	Value
A	0.1872
B	0.02523
C	8.707
D	0.09515
E	5.622

B.2 Reaction Kinetics

The reaction rates of the electrochemical reactions are modeled using a Butler-Volmer approach, assuming a single-step reaction mechanism. In the Zn electrode, the rate constant of the electrochemical reaction is defined according to an experimental Tafel analysis in $NH_3{-}NH_4Cl$ electrolyte.[26]

It is well known that the shape of the Zn electrode changes as zinc metal is stripped and redeposited. This change in the morphology of the electrode affects the active surface area available for the reaction. We calculate the specific active surface area as a function of the zinc volume fraction with the equation

$$A_{\mathrm{Zn}}^{\mathrm{sp}} = \frac{6}{a_{\mathrm{Zn}}} \varepsilon_{\mathrm{Zn}} (1 - \varepsilon_{\mathrm{Zn}}), \tag{29}$$

where $\varepsilon_{\mathrm{Zn}}$ is the volume fraction of the zinc and a_{Zn} is the pore diameter of the metallic zinc phase.[9,27] The experimental cells we simulate use a polished zinc foil as the electrode. When the zinc is redeposited during charging, it does not return to its original dense and smooth state; rather, it takes on a mossy character. To model this effect, we consider a Zn electrode in which the zinc volume fraction is very high in the bulk (*e.g.* 0.95) and decreases to 0 at the interface to the separator. We define the initial pore size such that the specific active surface area of the electrode fulfills the condition,

$$\int_0^{L_{\mathrm{Zn}}} A_{sp}(x) dx = 1. \tag{30}$$

The zinc which is deposited during charging is assigned a pore size of 10 μm.

The kinetics of the ORR/OER on MnO_2 in neutral solution are shown to be sluggish and complex.[28–30] It is experimentally noted that the onset potential of the OER is independent of pH in the slightly acidic to neutral pH range.[29] Given an estimated specific active surface area of the of 4500 $\mathrm{m^2 \cdot m^{-3}}$, the kinetic rate constant is chosen to fit the experimental data available.[29,31]

Table 6: Kinetic parameters for the electrochemical reactions.

Parameter	Value	Unit
k_0^{Zn}	8×10^{-6}	$\mathrm{mol} \cdot \mathrm{m}^{-2} \cdot \mathrm{s}^{-1}$ [26]
α_a^{Zn}	0.5	-
α_c^{Zn}	0.5	-
$A_{\mathrm{sp}}^{\mathrm{Zn}}$	$f(\varepsilon_{\mathrm{Zn}})$	$\mathrm{m}^{-2} \cdot \mathrm{m}^{-3}$
k_0^{GDE}	4×10^{-17}	$\mathrm{mol} \cdot \mathrm{m}^{-2} \cdot \mathrm{s}^{-1}$
α_a^{GDE}	0.5	-
α_c^{GDE}	0.5	-
$A_{\mathrm{sp}}^{\mathrm{GDE}}$	4.5×10^{3}	$\mathrm{m}^{-2} \cdot \mathrm{m}^{-3}$

B.3 Numerical Solution

The ZAB model consists of a system of 13 equations, listed in Table 7. The system is implemented in MATLAB 2014a and solved using the implicit differential equation solver ode15i.

Table 7: System of equations for the ZAB model.

Description, Solver Variable, Equation
Solid Phase Volume Conservation, ε_p, $\frac{\partial \varepsilon_p}{\partial t} = V_p \dot{s}_p$
Solute Mass Continuity, $c_i \varepsilon_\mathrm{e}$, $\frac{\partial (c_i \varepsilon_\mathrm{e})}{\partial t} = -\vec{\nabla} \cdot \left(\vec{N}_i^{\mathrm{DM}}\right) - \vec{\nabla} \cdot \left(\vec{N}_i^{\mathrm{C}}\right) + \dot{s}_i$
Electrolyte Mass Continuity, ρ_e, $\frac{\partial (\rho_\mathrm{e} \varepsilon_\mathrm{e})}{\partial t} = -\vec{\nabla} \cdot \left(\vec{N}_\mathrm{e}^{\mathrm{C}}\right) + \sum \mathrm{M}_i \dot{s}_i$
Electrolyte Pressure Equation of State, ε_e, $\varepsilon_\mathrm{e} = \sum \bar{V}_i (c_i \varepsilon_\mathrm{e})$
Electrolyte Charge Continuity, ϕ_e, $0 = -\nabla \cdot \vec{j} + \sum z_i F \dot{s}_i$
Galvanostatic Condition, U_{GDE}, $\mathrm{j}_{\mathrm{cell}} = \int 2F k_{\mathrm{GDE}} A_{\mathrm{GDE}}^{\mathrm{sp}} dx$

The local concentrations of the quasi-particles are sufficient to determine the total concentration of Zn, Cl, and N which can then be used to solve for the local concentrations of the various solvents, as described in Section 3 of the main text.

C Simulation Results

C.1 Thermodynamics

To better understand the buffering capacity of the electrolyte, we examine the distribution of ammonium and ammonia species as a function of pH. Figure 1 shows the concentrations of NH_4^+, NH_3, and NH_3 containing Zn complexes for 0.51 M $ZnCl_2$ - 2.34 M NH_4Cl on a linear scale (a) and a logarithmic scale (b). For acidic pH values, the concentration of NH_3 is practically zero. Electrolytes in this region would be unable to buffer acidic pH shifts, as there is no NH_3 available to convert into NH_4^+. At pH 6, there are a small amount of zinc-amine complexes in solution, which could act as NH_3 donors to buffer acidic pH shifts, however the capacity would be very limited. Likewise, for pH values ≥ 9.8, the concentrations to NH_3 and NH_4^+ are roughly equal. Electrolytes in this range would be able to buffer acidic pH shifts, but unable to buffer alkaline pH shifts. For ideal buffering performance, the electrolyte should contain an initial total NH_3 concentration about halfway between its lower and upper limit. For this electrolyte composition, that would correspond

to ca. pH 8.

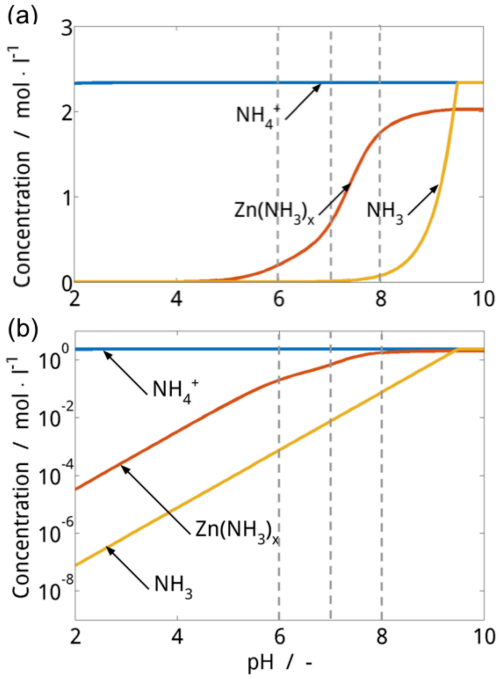

Figure 1: Concentrations of $NH_4{}^+$, NH_3, and NH_3 containing Zn complexes for 0.51 M $ZnCl_2$ - 2.34 M NH_4Cl on a linear scale (a) and a logarithmic scale (b).

A thermodynamic stability analysis is performed to determine an electrolyte composition that favors $Zn(OH)_2$ precipitation. The results are shown in Figure 2. For a fixed total zinc concentration of 0.5 M, $Zn(OH)_2$ precipitation is favored for low total chlorine concentrations (less than 3.5 M) and slightly alkaline pH values (greater than 7.5). As shown in Figure 1, the optimum pH for buffering performance is also ca. 8. Therefore, we propose an electrolyte composition of 0.5 M $ZnCl_2$ - 1.6 M NH_4Cl, pH 8 for further investigation.

C.2 Cell A

The Zn electrode utilized in the experimental cells[31,32] is a polished foil. Initially, the sheet is non-porous and has a low active surface area. We propose that when the cell is cycled, the morphology of the re-deposited zinc takes on a more porous morphology (mossy or dendritic) than the original foil. This effect is partially responsible for the experimentally observed gain in cell potential after the first cycle. To model this behavior, we follow the method outlined in Section B.2.

Figure 3 compares the Zn volume fractions (a) and specific surface areas (b) initially and after the first charge. When the cell is discharged, the bulk of the foil becomes more porous due to the dissolution of zinc. The transport of aqueous zinc ions into/out of this porous structure is limited.

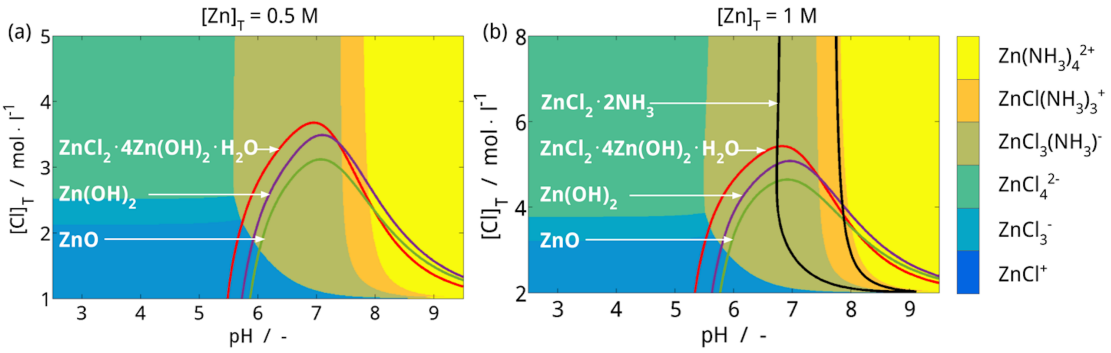

Figure 2: Thermodynamic stability diagram for a fixed total zinc concentration of (a) 0.5 M and (b) 1 M. For slightly alkaline pH values (e.g. 8), $Zn(OH)_2$ is the thermodynamically favored precipitant.

Therefore when the cell is charged, zinc tends to redeposit from the electrolyte on the surfaces which are easiest to reach. This is responsible for the hump in the zinc volume fraction at the foil surface after charging. The morphology of this re-deposited zinc is much more porous than the original foil. This increases the specific surface area available for the reaction and further favors the development of mossy or dendritic structures on the surface.

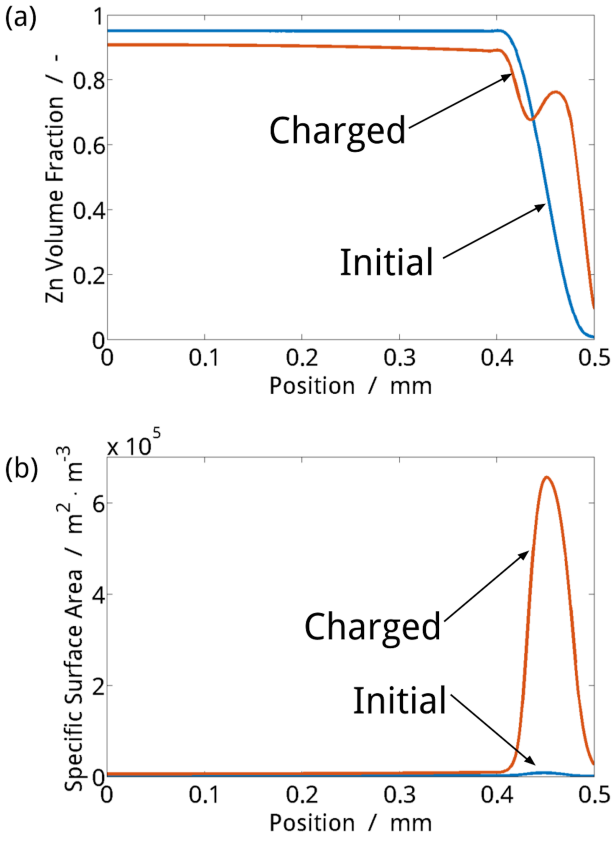

Figure 3: Volume fraction (a) and specific surface area (b) of the Zn electrode in Cell A initially and after the first charge.

C.3 Cell B

Cell B is operated at a lower current density (1 $\mathrm{mA \cdot cm^{-2}}$) and for a shorter period (2 hours discharge, 2 hours charge) than Cell A. Figure 4 shows the distribution of zinc species in Cell B during (a) discharge and (b) charge. The initial pH of the electrolyte is 7. As a result, ternary zinc-chlorine-ammonia complexes tend to dominate the electrolyte composition. Figure 4a shows that at the end of discharge, only about a third of the zinc in the GDE exists as $\mathrm{Zn(NH_3)_x}$ complexes. Furthermore, Figure 4b shows that at the end of charging there is still a significant amount of zinc-amine complexes present in the electrolyte. These results indicate that even with the concentration gradients in the cell, the electrolyte in Cell B is able to successfully buffer the pH during operation.

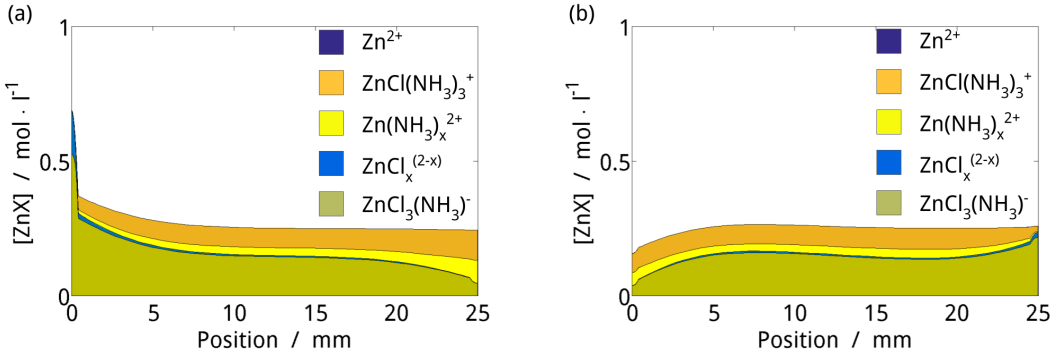

Figure 4: Concentrations of zinc ions in Cell B at (a) the end of the first discharge and (b) the end of the first charge.

References

[1] Stamm, J.; Varzi, A.; Latz, A.; Horstmann, B. *Journal of Power Sources* **2017**, *360*, 136–149.

[2] Horstmann, B.; Danner, T.; Bessler, W. G. *Energy & Environmental Science* **2013**, *6*, 1299.

[3] Neidhardt, J. P.; Fronczek, D. N.; Jahnke, T.; Danner, T.; Horstmann, B.; Bessler, W. G. *Journal of the Electrochemical Society* **2012**, *159*, A1528–A1542.

[4] Danner, T.; Horstmann, B.; Wittmaier, D.; Wagner, N.; Bessler, W. G. *Journal of Power Sources* **2014**, *264*, 320–332.

[5] Radin, M. D.; Monroe, C. W.; Siegel, D. J. *Chemistry of Materials* **2015**, *27*, 839–847.

[6] Latz, A.; Zausch, J. *Electrochimica Acta* **2013**, *110*, 358–362.

[7] Bazant, M. Z. *Accounts of Chemical Research* **2013**, *46*, 1144–1160.

[8] Eberle, D.; Horstmann, B. *Electrochimica Acta* **2014**, *137*, 714–720.

[9] Single, F.; Horstmann, B.; Latz, A. *Phys. Chem. Chem. Phys.* **2016**, *18*, 17810–17814.

[10] Danner, T.; Eswara, S.; Schulz, V. P.; Latz, A. *Journal of Power Sources* **2016**, *324*, 646–656.

[11] Miller, D. G.; Ting, A. W.; Rard, J. A. *Journal of The Electrochemical Society* **1988**, *135*, 896 – 903.

[12] Rard, J. A.; Miller, D. G. *Journal of Solution Chemistry* **1990**, *19*, 129 – 148.

[13] Newman, J.; Thmoas-Alyea, K. E. *Electrochemical Systems*, 3rd ed.; John Wiley & Sons: Hoboken, New Jersey.

[14] Qaiser Fatmi, M.; Hofer, T. S.; Rode, B. M. *Physi. Chem. Chem. Phys.* **2010**, *12*, 9713–9718.

[15] Sasaki, K.; Takahashi, T. *Electrochimica Acta* **1959**, *1*, 261 – 271.

[16] Atkins, P.; De Paula, J. *The Elements of Physical Chemistry*, 8th ed.; W.H. Freeman and Company: New York, 2006; pp 791–820.

[17] Shock, E. L.; Helgeson, H. C.; Sverjensky, D. a. *Geochimica et Cosmochimica Acta* **1989**, *53*, 2157–2183.

[18] Shock, E.; Sassani, D.; Willis, M.; Sverjensky, D. *Geochimica et Cosmochimica Acta* **1997**, *61*, 907–950.

[19] Shock, E. L.; Helgeson, H. C. *Geochimica et Cosmochimica Acta* **1988**, *88*, 803–826.

[20] Sverjensky, D.; Shock, E.; Helgeson, H. *Geochimica et Cosmochimica Acta* **1997**, *61*, 1359–1412.

[21] Roux, A.; Musbally, G. M.; Perron, G.; Desnoyers, J. E. *Canadian Journal of Chemistry* **1978**, *56*, 24 – 28.

[22] Limpo, J.; Luis, A. *Hydrometallurgy* **1993**, *32*, 247–260.

[23] Limpo, J.; Luis, A.; Cristina, M. *Hydrometallurgy* **1995**, *38*, 235–243.

[24] Smith, R.; Martell, A. *Critical Stability Constants Volume 4: Inorganic Complexes*; 1976; Vol. 4.

[25] Frank, M. J. W.; Kuipers, J. a. M.; Swaaij, W. P. M. V. *Journal of Chemical & Engineering Data* **1996**, *41*, 297–302.

[26] Huajun, Z.; Zhenghai, G.; Jinhuan, Z. *Hydrometallurgy* **2007**, *89*, 369–373.

[27] Single, F.; Horstmann, B.; Latz, A. *Journal of The Electrochemical Society* **2017**, *164*, E3132–E3145.

[28] Mainar, A. R.; Colmenares, L. C.; Leonet, O.; Alcaide, F.; Iruin, J. J.; Weinberger, S.; Hacker, V.; Iruin, E.; Urdanpilleta, I.; Blazquez, J. A. *Electrochimica Acta* **2016**, *217*, 80–91.

[29] Takashima, T.; Hashimoto, K.; Nakamura, R. *Journal of the American Chemical Society* **2012**, *134*, 1519–27.

[30] Roche, I.; Scott, K. *Journal of Applied Electrochemistry* **2009**, *39*, 197–204.

[31] Thomas Goh, F. W.; Liu, Z.; Hor, T. S. A.; Zhang, J.; Ge, X.; Zong, Y.; Yu, A.; Khoo, W. *Journal of the Electrochemical Society* **2014**, *161*, A2080–A2086.

[32] Sumboja, A.; Ge, X.; Zheng, G.; Goh, F. T.; Hor, T. A.; Zong, Y.; Liu, Z. *Journal of Power Sources* **2016**, *332*, 330–336.

S. Clark, A. Latz and B. Horstmann. A Review of Model-Based Design Tools for Metal-Air Batteries. *Batteries* **4**, 5 (2018).

.

batteries

MDPI

Review

A Review of Model-Based Design Tools for Metal-Air Batteries

Simon Clark [1,2], Arnulf Latz [1,2,3] and Birger Horstmann [1,2,*]

1 German Aerospace Center (DLR), Pfaffenwaldring 38-40, 70569 Stuttgart, Germany; simon.clark@dlr.de (S.C.); arnulf.latz@dlr.de (A.L.)
2 Helmholtz Institute, Ulm University (UUlm), Helmholtzstr 11, 89081 Ulm, Germany
3 Institute for Electrochemistry, Ulm University (UUlm), Albert-Einstein-Allee 47, 89081 Ulm, Germany
* Correspondence: birger.horstmann@dlr.de; Tel.: +49-(0)731-50-34311

Received: 8 December 2017; Accepted: 19 January 2018; Published: 29 January 2018

Abstract: The advent of large-scale renewable energy generation and electric mobility is driving a growing need for new electrochemical energy storage systems. Metal-air batteries, particularly zinc-air, are a promising technology that could help address this need. While experimental research is essential, it can also be expensive and time consuming. The utilization of well-developed theory-based models can improve researchers' understanding of complex electrochemical systems, guide development, and more efficiently utilize experimental resources. In this paper, we review the current state of metal-air batteries and the modeling methods that can be implemented to advance their development. Microscopic and macroscopic modeling methods are discussed with a focus on continuum modeling derived from non-equilibrium thermodynamics. An applied example of zinc-air battery engineering is presented.

Keywords: metal-air; zinc-air; modeling; simulation; computational chemistry

1. Introduction

In the ever-growing search for safe and high-performance energy storage technology, development of metal-air batteries is taking on new importance [1]. The promise of these systems is clear: a significant increase in energy density over Li-ion batteries, utilization of abundant materials, and improved safety [2]. While great progress has been made in their development, challenges remain before secondary metal-air batteries can become widely commercially viable.

Metal-air batteries comprise a metal electrode (e.g., Zn, Li, Mg, Al, etc.), electrolyte (aqueous or non-aqueous), and a bi-functional air electrode (BAE). The basic operating principle is to electrochemically reduce O_2 from air and oxidize the metal electrode to reversibly form solid metal-oxides. In this way, both the volume and the weight of the battery can be significantly reduced compared to Li-ion systems. Figure 1 compares the theoretical energy density and specific energy of metal-air systems. In some non-ideal cases the precipitation of the solid discharge product can consume active electrolyte components, reducing the achievable energy density [3]. Research into a variety of metal-air chemistries is ongoing. The homogeneous deposition of Mg metal makes Mg-air systems appealing [4–6], but aqueous Mg-air batteries are severely limited by the corrosion of the Mg electrode. Ionic liquid electrolytes have been proposed for Mg-air systems, but they also suffer from electrochemical instability, particularly during charging, and the reversibility of the cell is limited [7]. Another interesting contender is Al-air. Al is an abundant and safe material, and Al-air batteries have high theoretical energy density and specific energy values [8–10]. However theses systems are susceptible to corrosion and have not demonstrated adequate cycling stability. The natural abundance and safety of sodium combined with its comparable properties with lithium have driven research into Na-air [11–13]. These systems are still in a very early stage of research. Si-air batteries have

also attracted attention [14]. They have a high theoretical energy density and are stable in aqueous electrolytes. Experimental studies of Si-air systems have been performed in both ionic liquid [15] and alkaline electrolytes [16], but they currently face challenges with the reversibility of the solid discharge product, precipitation, and pore blockage. Among the metal-air systems under development, Li-air and Zn-air are the most promising [17–19].

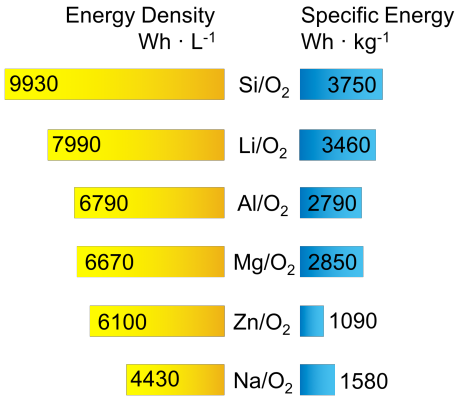

Figure 1. Overview of the theoretical energy density and specific energy (including oxygen) of commonly researched metal-air batteries. Values are calculated considering the specific mass and volume of the discharge product with the OCV and charge transfered in the cell reaction.

Li-air batteries (LABs) have been researched for decades [20], but have only become a widely-pursued topic since the early 2000s. The electrolyte has proved to be a limiting factor in LAB development. The most common electrolyte configurations of Li-air systems are aprotic (non-aqueous) and aqueous. Mixed electrolyte systems have also been proposed. The beginning of the LAB research wave focused on aprotic electrolytes. The first work on the aprotic Li-air system ($LiPF_6$ in ethylene carbonate (EC)) was performed in 1996 by Abraham, et al. [21], who proposed an overall reaction forming Li_2O_2 or Li_2O. Early aprotic Li-air cells were based on a carbonate solvent, but it has since been shown that carbonate solvents are unstable, producing lithium-carbonates during discharging and evolving CO_2 during charing [22–25]. These days, carbonate electrolytes have been abandoned in favor of ether and ester solvents with lithium salts. A second challenge for LABs in aprotic electrolytes relates to the precipitation of Li_2O_2. When this solid precipitates in the cathode, it can form a dense layer over the carbon surface and inhibit the transfer of electrons. As precipitation continues, entire pores in the cathode may become blocked, passivating the electrode and limiting the cell capacity. Finally, it has been noted that oxygen transport in aprotic eletrolytes can be a challenging factor in LAB performance, especially at higher current densities [26,27]. This has motivated researches to learn from the success of the gas diffusion electrode in fuel cells and pursue investigations of LABs with aqueous electrolytes.

It is well known that Li metal reacts violently with water, which had previously limited the use of aqueous electrolytes for Li-air systems. Then in 2004, a glass ceramic layer over the Li electrode was successfully proposed to protect the metal electrode while still allowing the electrochemical reaction to proceed [28,29]. In alkaline aqueous electrolytes, the discharge product is $LiOH \cdot H_2O$ instead of Li_2O_2. In these systems, $LiOH \cdot H_2O$ tends to precipitate at the separator-anode interface [30], which reduces the risk of pore clogging in the cathode as observed in aprotic LABs. However, when aqueous alkaline electrolytes are exposed to air, dissolved CO_2 reacts with OH^- to form carbonates, which slowly reduces the conductivity of the electrolyte and limits the lifetime of the cell.

In the recent wave of interest in the development of Li-air batteries, many theoretical studies have highlighted the impressive possibilities of these systems [30–36] and the company International

Business Machines Corporation (IBM) pursued Li-air systems for commercial applications [17]. Although significant challenges remain [37–41], the future of Li-air batteries is promising.

Zn-air batteries (ZABs) stand alone as the only fully mature metal-air system and have been successfully commercialized as primary cells for many years. They are particularly suitable for low-current applications like hearing aids. However, their calendar life and electrical rechargeability is limited [42]. One major advantage of Zn as an electrode material is that, unlike Li, it is stable in water. In an effort to improve the rechargeability of ZABs, alternative near-neutral aqueous [43,44] and ionic liquid electrolytes [45–47] have been proposed. Current research continues to focus on material development to address the lifetime limitations and cell engineering to improve the performance of these systems [48]. Although some hurdles remain, the development of secondary ZABs has progressed to the point that they could become feasible for stationary storage applications and some Start-Ups like Eos Energy Storage [49] and Fluidic Energy [50] have begun to commercialize the technology. Zn-air systems offer perhaps the most immediate and reliable pathway to a viable secondary metal-air battery.

In this review, we examine model-based design tools that can be applied to advance development of metal-air systems. The majority of existing models were developed for Zn-air cells, as they are the oldest and most mature system. Therefore our review shall focus mainly on the application of models to ZABs and highlight some important advances unique to LABs. Note that these methods are easily translatable to other metal-air systems.

2. Zinc-Air Batteries

In this section, we present a summary of the working principle of ZABs and discuss the main challenges hindering the development of electrically-rechargeable Zn-air systems.

2.1. Working Principle

In their most common configuration, Zn-air batteries contain a metallic Zn electrode, porous separator, circa 30 wt % aqueous KOH electrolyte, and a bi-functional air electrode (BAE). The BAE consists of a porous substrate and a bi-functional air catalyst (e.g., MnO_2) to facilitate the oxygen-reduction and oxygen-evolution reactions (ORR, OER) [51–53]. The design of the BAE is similar to gas diffusion layers (GDL) from fuel cell applications. The porous BAE substrate contains carbon fibers and binder with mixed hydrophilic and hydrophobic properties to promote the formation of the so-called three phase boundary, while hindering the electrolyte from flooding out. The Zn electrode is often a paste consisting of zinc metal powder, electrolyte, and binder [54]. The capacity of the cell is determined by the Zn electrode, which is designed in such a way as to include as much active material as possible while minimizing the effects of shape-change and electrolyte concentration gradients. Aqueous KOH is the most common electrolyte for Zn-air batteries due to its high conductivity (circa 600 $mS \cdot cm^{-1}$).

An operational schematic of a ZAB in alkaline electrolyte is shown in Figure 2. When the cell is discharged, the Zn electrode is electrochemically oxidized to form $Zn(OH)_4^{2-}$ (zincate) complexes,

$$Zn + 4OH^- \rightleftharpoons Zn(OH)_4^{2-} + 2\,e^-, \qquad E^0 = -1.199 \text{ V v. RHE.} \tag{1}$$

Oxygen gas enters the cell through the BAE and dissolves into the electrolyte, where it is reduced to form OH^- ions,

$$0.5\,O_2(aq) + H_2O + 2\,e^- \rightleftharpoons 2\,OH^-, \qquad E^0 = 0.401 \text{ V v. RHE.} \tag{2}$$

When the saturation limit of zinc in the electrolyte is exceeded, solid ZnO precipitates mainly in the anode and the battery achieves a stable working point,

$$Zn(OH)_4^{2-} \rightleftharpoons ZnO(s) + H_2O + 2OH^-. \tag{3}$$

When the cell is charged, ZnO dissolves, zinc is redeposited at the Zn electrode and oxygen gas is evolved in the BAE. The overall cell reaction is given by

$$\mathrm{Zn} + 0.5\,\mathrm{O_2(aq)} \rightleftharpoons \mathrm{ZnO(s)}. \quad (4)$$

The open-circuit voltage of a ZAB in 30 wt % KOH is 1.65 V. The high conductivity of the electrolyte, high mobility of OH^-, and reasonable kinetics of the ORR give the cell a nominal discharge voltage of 1.2 V at current densities of circa 10 $mA \cdot cm^{-2}$ [55]. The molar volume of ZnO is 60% larger than metallic Zn, which causes the cell to expand during discharge. Even so, ZAB button cells demonstrate a practical energy density on the order of 1000 $Wh \cdot L^{-1}$ [55].

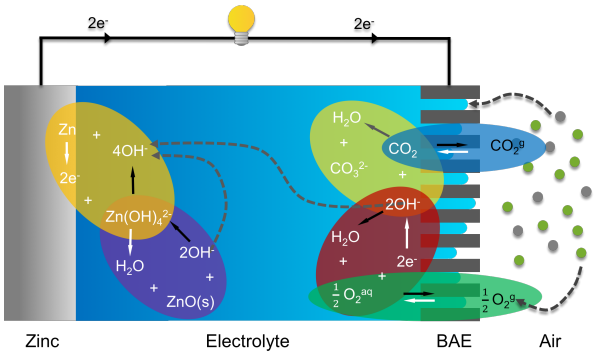

Figure 2. Operational schematic of an alkaline zinc-air battery. The various (electro)chemical reactions are indicated by the colored ovals; white arrows indicated discharging and black arrows indicate charging. Dashed lines show important transport paths.

2.2. Challenges, Progress, and Opportunities

While ZABs have been quite successful as primary cells, there are a number of hurdles that limit their electrical rechargeability and provide opportunities for further research.

The most well-known challenges relate to the aqueous KOH electrolyte. When the ZAB is operated in air, CO_2 can dissolve in the electrolyte and react with OH^- to form CO_3^{2-} [56]. This parasitic reaction reduces the conductivity of the electrolyte, slows down the cell reactions, and eventually kills the cell [55]. As such, the lifetime of alkaline ZABs is limited from the moment they are exposed to air. A CO_2 filter could be applied to scrub the air [57], but this adds cost and complexity to the system. A second challenge for the electrolyte is the evolution of hydrogen gas. The potential of the Zn electrode reaction is below the potential for hydrogen evolution, which causes the electrolyte to be thermodynamically unstable [58]. However, H_2 evolution on the Zn surface can be kinetically suppressed with dopants, such as Hg, In, or Bi [19,59–61].

To address these challenges, current research is focused on the development of alternative electrolytes. An ideal electrolyte for Zn-air batteries should be stable in the electrochemical window of the cell, stable in air, conductive, non-corrosive, and thermodynamically favor the reversible precipitation of the desired final discharge product. Alternatives include aqueous alkaline with additives [62], which were recently evaluated by Schröder et al. [63] and Mainar, et al. [64,65]. Near-neutral chloride-based electrolytes have been experimentally evaluated by Zong and co-workers [43,44] with promising initial results. Chloride-based electrolytes address the carbonation issue and could improve the quality of Zn deposition, but they struggle with the precipitation of zinc-chlorides and the strongly oxidative nature of chlorine. Non-aqueous ionic liquid electrolytes [45,46,66–68] have been proposed with promising results [69], but the rate of these systems is limited and much work remains to be done.

Metal electrodes offer the possibility of achieving very high energy density. However, the formation of mossy or dendritic metal structures during charging can cause the electrode to change shape [70] and lead to an internal short-circuit [71], killing the cell. With its low surface

diffusion characteristics and fast deposition kinetics [72], Zn is specifically vulnerable to electrode shape change. Achieving homogeneous Zn deposition is essential to the development of a secondary ZAB. Electrolyte additives and alternative electrode designs have been proposed to address this challenge [43,73–77], with mixed results.

A further challenge in Zn electrode design is the passivation of the electrode surface due to ZnO precipitation [78]. To achieve a high energy density, the precipitation of ZnO is required. However, when ZnO precipitates on the active surface of the Zn metal, it limits the transport of species to/from the electrolyte. When this ZnO barrier becomes too large, the electrochemical reaction can no longer proceed and the electrode is passivated [62,79]. ZnO passivation can take on two forms [54,80]. Type I ZnO has a porous white morphology. It precipitates near the surface of the Zn particle, but does not block it completely. The formation of type I ZnO is reversible. Type II ZnO forms a black dense layer directly on the surface of the the Zn particle. It is thought that type II ZnO forms on the active sites of the Zn metal, permanently blocking them and creating a passivating avalanche effect [81].

Finally, the development of an active, stable, and cheap bi-functional air catalyst is a hotly pursued topic in material science [44,51,82–84]. It is difficult to find a catalyst that is suitable for both the ORR and the OER. The alternating oxidative and reductive environments present in the BAE during cycling further complicates this challenge, and tends to accelerate the degradation of both the BAE carbon substrate and the catalyst. This difficultly is compounded for near-neutral electrolytes, in which the pH of the electrolyte may vary within the buffering range. From a material science perspective, research into new catalyst combinations and non-carbon BAE substrates is on-going. Alternative 3-electrode cell designs have also been proposed [19].

On a system level, the challenges described above have led to creative engineering solutions including mechanically rechargeable Zn-air fuel cells with some niche applications [69]. However, the logistical challenges of these designs prevented them from being adopted on a wide scale. The goal is to develop a high-performance electrically rechargeable Zn-air battery. To achieve this, new ideas and novel designs are needed on every level from material science up through system engineering. In the following section we discuss how numerical modeling and simulation can help in this pursuit and give an overview of recent progress.

3. Numerical Modeling and Simulation

Experimentally-based research can be expensive and time consuming. The development of theory-based models can help guide researchers down the most promising paths, provide a framework for interpreting experimental results, and lead to new breakthroughs in battery design.

Numerical modeling and simulation serve many purposes in metal-air battery research and can span a wide range of space and time-scales [30,85,86]. In the following sections, we review modeling methods commonly used in development of metal-air batteries. We begin on the material level, highlighting methods for studying the electronic properties of catalysts and metal electrodes as well as electrolyte thermodynamics and composition. We then move up to the electrode level, and discuss numerical studies of electrode architecture and what considerations are important in the design process. Finally, we give an overview of cell-level continuum modeling and discuss recent contributions to the literature.

3.1. Material Development

The first step in designing a feasible battery must be the selection of appropriate materials. Anode, cathode, and electrolytes all have their own, sometimes conflicting, requirements for activity and stability. Applied modeling methods can help screen potential materials, identify promising paths for development, and reduce the reliance on trial-and-error approaches.

3.1.1. Electrode Materials

Catalyst development is one of the most expensive and time consuming aspects of material research in metal-air systems. Bi-functional air catalysts can take on a wide range of compositions, often include expensive or toxic metals (e.g., Pt, Ag, Co, etc.), and are labor intensive to produce and test. Atomic-scale modeling methods can be applied early in the design process to screen potential catalysts.

Density functional theory (DFT) uses quantum mechanical calculations to make predictions about the electronic structure of multi-atom systems [87]. This method allows researchers to investigate the properties of materials considering the influence of things like surface structures and local coordination of atoms. The basic approach of DFT is to analyze a multi-atom system as the movement of electrons through a fixed array of atomic nuclei. Using the Born-Oppenheimer approximation, the state of the nuclei and the electrons can be split into separate mathematical expressions [88]. In this way the adiabatic potential energy surface of the atoms can be calculated and used to investigate the characteristics of the material [87]. Due to the complexity of the calculations involved, the method is confined to considering a limited number of atoms. Nonetheless it has been shown to be effective at screening the properties of metal alloys for a variety of applications [89].

Beginning with the work of Norskov, et al. [90], there have been a wealth of DFT studies investigating the reaction pathway, activity, and stability of materials in metal-air systems. Viswanathan et al. have utilized DFT to predict the activity of different pure and alloyed metals [91,92]. This group has also applied DFT calculations to investigate a range of phenomena in Li-air batteries [93,94]. In 2010, Keith and Jacob clarified a multi-pathway electrochemical mechanism for the ORR, which showed good agreement with experimental data. Eberle and Horstmann correlated the change in reaction pathway to an observed change in the Tafel slope [95]. In 2017, Tripkovic and Vegge elucidated the mechanism of the ORR on Pt (111), and used their results to investigate the high activity of Pt-alloys [96]. Non-metallic catalysts, such as nitrogen-doped graphene, are desirable due to their safety and low cost. A multi-scale model featuring DFT of such systems was recently presented by Vazquez-Arenas, et al. [97], and used to investigate the rate-determining step for the ORR in KOH electrolyte

DFT simulations can also be applied to investigate metal electrode materials and solid precipitants. Siahrostami, et al., modeled the effect of surface structure on zinc dissolution [98]. They applied their model to simulate the dissolution of a Zn kink atom, highlighting the potential steps of the dissolution process and predicting the overpotential of the reaction. For electro-deposition, Jäckle and Groß propose that surface diffusion processes are key to understanding the formation of metallic surface structures [99]. They utilized a DFT model to evaluate a range of metal anode materials for their tendency to form dendrites. In the case of non-aqueous Li-air batteries, the precipitation of Li_2O_2 can electrically isolate the cathode. DFT simulations have been applied to investigate the growth and electronic structure of Li_2O_2 [31,100–103], in an attempt to mitigate the risk of passivation.

3.1.2. Electrolytes

The behavior of liquid electrolytes in electrochemical systems can be quite complex and have a deciding influence on overall cell performance. The first step in determining the suitability of an electrolyte for a given system is to examine its equilibrium thermodynamics.

The speciation of ions, solubility of solids, and equilibrium potential of electrodes in an electrolyte is strongly dependent on pH and solute concentration [80,104,105]. For some systems, such as KOH−ZnO, this behavior is rather straightforward and well-documented [80,106], while for others, such as $ZnCl_2-NH_4Cl$, it is very complex and sensitive [3,107]. Figure 3a shows the speciation of the Zn^{2+} ion in $ZnCl_2-NH_4Cl$. Understanding this behavior can be helpful in interpreting battery performance and optimizing system design.

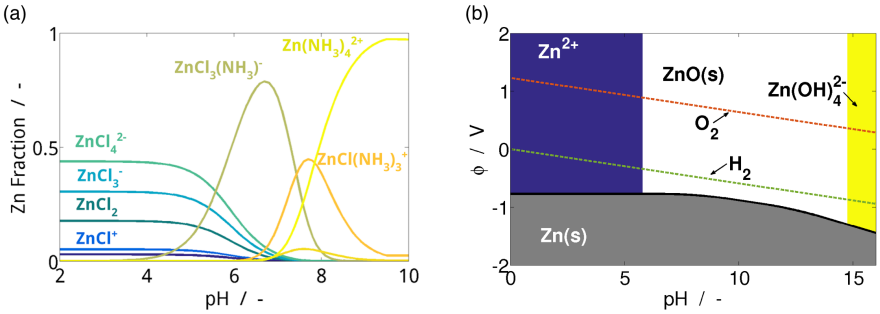

Figure 3. (**a**) Zn speciation plot for 0.51 M $ZnCl_2$−2.34MNH_4Cl with pH adjusted by NH_4OH reproduced from Clark, et al. [3] with permission from Wiley-VCH and (**b**) simplified Pourbaix diagram for $[Zn]_T = 0.5$ M.

According to the law of mass action, for a system at equilibrium with a constant temperature, the value of the reaction quotient is constant. For a generic reaction, this concept is expressed as,

$$aA + bB \rightleftharpoons cC + dD, \qquad \frac{[A]^a[B]^b}{[C]^c[D]^d} = \beta. \tag{5}$$

The value of the constant, β, is referred to as the thermodynamic stability constant (sometimes also called the formation or equilibrium constant). In the 1970s, Smith and co-workers assembled an exhaustive compilation of thermodynamic stability constants of metal-ligand complexes, pKa values of acids, and solubility products of solids for a myriad of both inorganic and organic molecules [108–111]. By incorporating these equilibrium expressions for every electrolyte reaction into simple equations for the conservation of mass and charge, the equilibrium composition of the electrolyte and the solubility of solids can be predicted as a function of pH and solute concentration. A framework for such a model [112,113] was presented by Limpo, et al., in the 1990s, and was expanded upon in more recent research [106,114]. Clark, et al., recently presented a framework for predicting the discharge characteristics of a Zn-air cell with an aqueous near-neutral electrolyte based on equilibrium thermodynamic considerations [3], and showed how they can be incorporated into a dynamic model.

Models of equilibrium thermodynamics can also be used to generate potential-pH, or Pourbaix, diagrams [115]. Figure 3b shows a simplified example for the aqueous Zn system. The Nernst equation describes the connection between solute concentration and the equilibrium electrode potential [116]. The equilibrium potentials for the electrochemical reactions in Zn-air systems [80] can be expressed as:

$$E_{Zn/Zn^{2+}} = -0.762 + \frac{RT}{2F}\ln([Zn^{2+}]), \tag{6}$$

$$E_{H_2/H_2O} = 0 - 2.303\frac{RT}{F}\,\mathrm{pH}, \tag{7}$$

$$E_{O_2/H_2O} = 1.229 - 2.303\frac{RT}{F}\,\mathrm{pH}. \tag{8}$$

Taking this into consideration, researchers can predict the influence of shifts in pH or solute concentration on electrode potential. Aside from describing the voltage of the cell, this is also useful for identifying possible parasitic reactions, such as H_2 evolution or redox shuttles.

In addition to thermodynamic models, DFT can be used to screen properties of electrolytes and their suitability for metal-air applications. One of the major challenges in aprotic LABs is the development of a solvent that is stable and facilitates oxygen solubility and transport. In 2015, Husch and Korth presented a study of non-aqueous LAB electrolytes [117]. In a wide-ranging work requiring about 2 million hours of process time, they integrated DFT calculations into a larger framework to screen 927,000 potential electrolyte solvents for high Li^+ and O_2 solubilities and low

viscosity. An illustration of their work is shown in Figure 4. By strategically applying modeling methods, Husch, et al., were able to by pass the trial-and-error approach and directly highlight electrolyte solvents with the highest chances of success.

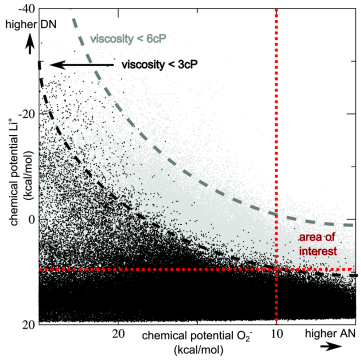

Figure 4. Chemical potentials for Li^+ vs. chemical potentials for O_2 in the bulk candidate compound are plotted for all 927,000 compounds. Black dots indicate compounds with a viscosity below 3 cP, grey dots indicate compounds with a viscosity below 6 cP. Reproduced from Husch, et al. [117]—Published by the Physical Chemistry Chemical Physics (PCCP) Owner Societies.

3.2. Electrode Design

The development of active and stable materials is essential to battery design. However, care must be taken to appropriately scale-up materials to the electrode level. In this section, we discuss modeling tools which can help fashion suitable materials into high-performance electrodes.

3.2.1. Bi-Functional Air Electrode (BAE)

The BAE in Zn-air batteries is comprised of a porous structure (usually carbon fibers and binder) with mixed hydrophilic and hydrophobic properties. The idea is to encourage the formation of the so-called three-phase boundary without either over-saturating (flooding) or under-saturating (drying out) the pores. When the cell is cycled, pressure gradients are induced in the battery due to the precipitation and dissolution of solid products, which can change the saturation of the BAE. To simulate this behavior, a method of predicting the pressure-saturation characteristics of the BAE structure is needed.

The Lattice Boltzmann Method (LBM) is useful for simulating multi-phase flow in porous media. This approach uses the Boltzmann equation to simulate the flow of fluids as a combination of collision and streaming events of particles on a discrete lattice [118,119]. Particle positions are confined to the nodes of the lattice and it is assumed that they can move between their current position and adjacent nodes in discrete lattice directions. The probability to find particles at a lattice node with a velocity component in any of the discrete directions is described by a distribution function [120]. If solid boundaries are present in the system, no-slip boundary conditions can be introduced by a simple bounce back scheme. Implementation of the basic LBM equations is straightforward, and there are a variety of open-source codes available [121].

In electrochemical research [122], Lattice Boltzmann models have been applied to investigate the transport of water in the GDL of PEM fuel cells [123–126]. One significant benefit of LBM is the ability to simulate flow in complex geometries. Using X-ray tomography [127] or focus ion beam scanning electron microscope (FIB-SEM) images [128], real electrode structures can be modeled in 3D and their transport properties evaluated. Recently, Danner, et al., presented a LBM model to predict the pressure-saturation parameters of BAEs in metal-air batteries [128]. Figure 5 shows pressure-saturation curves calculated with LBM for both 2D and 3D simulations of real BAE structures. Their simulations show that the pressure-saturation characteristics of air electrode substrates vary according to whether the electrolyte is draining from the structure (configuration I) or imbibing the structure (configuration

II). They proposed this is because the structure contains some pores that can be filled with electrolyte, but are not easily emptied.

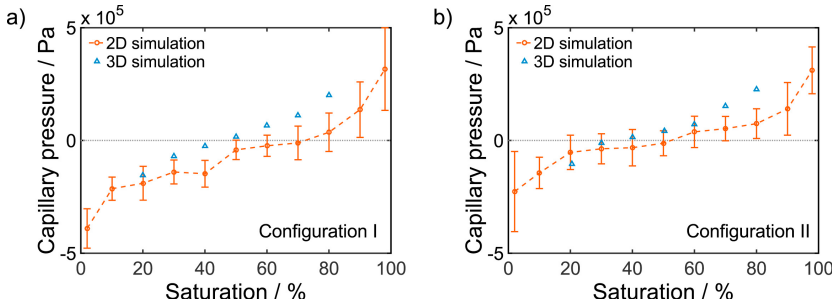

Figure 5. Pressure-saturation curves for real air electrode structures simulated with 2D and 3D Lattice-Boltzmann models for (**a**) draining (configuration I) and (**b**) imbibition (configuration II). Reproduced from Journal of Power Sources, 324, T. Danner, S. Eswara, V.P. Schulz, A. Latz, Characterization of gas diffusion electrodes for metal-air batteries, 646–656, Copyright 2016, with permission from Elsevier [128].

3.2.2. Metal Electrode

The design of the metal electrode is determined mostly by effects linked to passivation and shape change. For Zn-air batteries, the precipitation of ZnO on the electrode surface can isolate it from the electrolyte and slow down the reaction kinetics, eventually killing the electrode. It has been shown that ZnO can take on a porous white morphology (type I) that is reversible, or a dense black morphology (type II) that is irreversible. To model the effects of these precipitants on electrode performance, various models have been developed.

As discussed in Section 2.2, type I ZnO is formed when the dissolved zinc concentration in the electrolyte exceeds the saturation limit, and it precipitates near the electrode surface. This layer of porous ZnO is generally modeled as an additional mass transport barrier [55], slowing diffusion and migration of OH^- to the electrode surface. Early models determined the passivation characteristics using the so-called Sand equation, an empirical expression linking current density, i, and passivation time, t, with constants, k and i_e:

$$i = kt^{0.5} + i_e. \tag{9}$$

In 1981, Liu, et al., expanded this concept taking into account the mechanism for type I ZnO precipitation. They proposed that the passivation due to type I ZnO occurs via a dissolution-saturation-precipitation mechanism. Put simply, the Zn electrode dissolves until the concentration of $Zn(OH)_4^{2-}$ exceeds the saturation limit for nucleation, and the ZnO phase grows as the precipitation reaction proceeds. In their model, they calculate the time required to saturate the electrolyte with $Zn(OH)_4^{2-}$ (t_a), the time to precipitate type I ZnO (t_b), and the time to precipitate type II ZnO (t_c), and define the passivation time as $t = t_a + t_b + t_c$ [78]. The resulting 0D model is a helpful predictor of Zn electrode performance, but is not suitable for use in continuum modeling.

In the continuum model of Zn electrodes developed by Sunu and Bennion in 1980 [129], they considered passivation by assuming that the precipitation of ZnO reduced the active surface area available for the Zn dissolution reaction. More recently in 2017, Stamm, et al., implemented the effect of type I ZnO passivation in a continuum model by calculating the thickness of the ZnO shell and numerically solving for the species concentration at the surface [55], assuming Nernst-Planck transport across the barrier. These values were then used to calculate the Nernst potential and exchange current density of the Zn dissolution reaction.

While models for passivation due to type I ZnO are rather well developed, there are fewer models for type II ZnO passivation. In 1991, Prentice, et al. [81] proposed that type II ZnO forms directly on the surface of the Zn electrode, and does not follow the dissolution-saturation-precipitation

mechanism of type I. By calculating the fractional surface coverage of various zinc-hydroxides as a function of concentration and electrode potential, they were able to simulate rotating disk experiments. Their simulations agreed well with experimental measurements. The model was recreated and the results are shown in Figure 6.

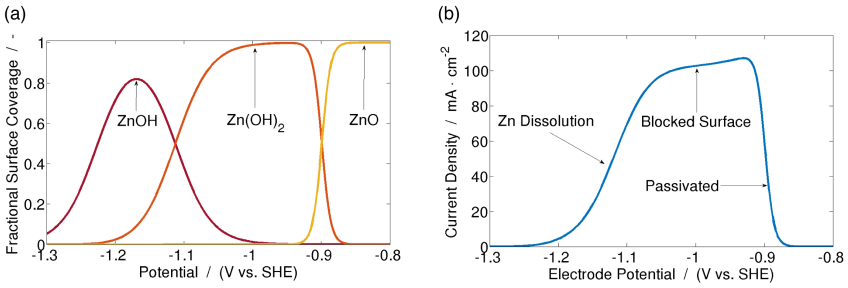

Figure 6. (**a**) Fractional surface coverage of species on the Zn electrode surface, and (**b**) simulated LSV measurement of type II ZnO passivation. Recreated from the model described by Prentice, et al. [81].

While much progress has been made in understanding the mechanisms of Zn passivation, work remains to be done. A more unified theory of type I and type II passivation, along with implementation in a continuum model, could be an area for future research. A dedicated review of experimental and modeling studies of Zn electrode passivation was presented by Bockelman, et al., in 2017 [130].

3.3. Cell Modeling

The modeling methods described above are very useful for evaluating the properties of individual materials or components, but researchers often need to know how these components will interact with each other in a real electrochemical cell.

Continuum models are among the most useful and widely-applied methods for studying the cell-level performance of metal-air batteries. This approach applies the mass and charge continuity equations to describe the transient characteristics of spatially discretized systems [85,131]. A list of important continuum models for metal-air systems from the literature is presented in Table 1. For most applications, a 1D model is sufficient to describe the system. However, 2D and 3D [132,133] finite volume models of batteries can give more in-depth information for detailed analysis. The mass and charge continuity equations can be expressed in generic terms as,

$$\text{Mass Continuity:} \qquad \frac{\partial(c_i \varepsilon_e)}{\partial t} = \underbrace{-\vec{\nabla} \cdot \vec{N}_i^{D,M} - \vec{\nabla} \cdot \vec{N}_i^{C}}_{\text{transport}} + \overbrace{\dot{s}_i}^{\text{source}}, \tag{10}$$

$$\text{Charge Continuity:} \qquad 0 = \underbrace{-\vec{\nabla} \cdot \vec{j}}_{\text{transport}} + \overbrace{\sum_i z_i \dot{s}_i}^{\text{source}}, \tag{11}$$

where c_i is the concentration of solute i, ε_e is the electrolyte volume fraction, $\vec{N}_i^{D,M}$ is the diffusion-migration flux, $\vec{N}_i^{C}$ is the convective flux, $\dot{s}_i$ is the reaction source term, $\vec{j}$ is the electrolyte current density and z_i is the solute charge number. A detailed derivation of these terms based on non-equilibrium thermodynamics and their applicability to metal-air systems can be found in existing works [3,30,55,134]. In their most general form, the continuity equations describe the local conservation of mass and charge due to transport across the boundaries of a control volume and the presence of a source/sink within the bulk of the control volume. To successfully implement these equations physical models for electrolyte transport and (electro)chemical reactions are needed.

Table 1. Comparison of continuum models for metal-air systems. Transport models listed are concentrated solution theory (CST) or dilute solution theory (DST).

Year	Authors	System	Dimension	Transport Model	Notes	Source
1980	Sunu, et al.	Zn-Air	1D	CST	Zn & ZnO shape change	[129]
1991	Mao, et al.	Zn-Air	1D	CST	Precipitation of $K_2Zn(OH)_4$	[135]
2002	Deiss, et al.	Zn-Air	1D	DST	Concentration profiles and cell voltage	[136]
2010	Andrei, et al.	Li-Air	1D	CST	LAB modeling framework	[137]
2011	Albertus, et al.	Li-Air	1D	CST	O_2 transport and Li_2O_2 precipitation	[26]
2012	Neidhardt, et al.	Multiple	1D	CST + Multi-Phase	Flexible framework, convective transport	[131]
2013	Horstmann, et al.	Li-Air	1D	CST + Multi-Phase	Inhomogeneous Li_2O_2 precipitation, aqueous electrolyte	[35]
2014	Danner, et al.	Li-Air	1D	CST + Multi-Phase	Air electrode model with pressure-saturation	[36]
2014	Schröder, et al.	Zn-Air	0D	CST	Effect of air composition on cell performance	[138]
2014	Arlt, et al.	Zn-Air	0D	CST	State-of-charge monitoring with x-ray CT	[139]
2014	Xue, et al.	Li-Air	1D	CST	Li_2O_2 pore clogging with pore size distribution	[140]
2015	Grübl, et al.	Li-Air	1D	CST + Multi-Phase	Engineering evaluation of system design	[141]
2016	Yin, et al.	Li-Air	1D	DST	Affect of Li_2O_2 particle size on charging profile	[142]
2017	Stamm, et al.	Zn-Air	1D	CST + Multi-Phase	Affect of ZnO nucleation and growth on cell discharge profile	[55]
2017	Clark, et al.	Zn-Air	1D	CST + Multi-Phase	Framework for buffered near-neutral electrolytes	[3]

Chemical reaction models feature a term describing the thermodynamic driving force and an expression of the kinetics [143]. In the case of electrochemical reactions, the most widely-used model is the Butler-Volmer approximation [144],

$$k = k_0\left(\exp\left[\frac{\alpha RT}{nF}\eta\right] - \exp\left[-\frac{(1-\alpha)RT}{nF}\eta\right]\right), \tag{12}$$

where k_0 is the rate constant (linked to the exchange current density), α is the symmetry factor, η is the surface overpotential, and the other variables take on their usual meaning. While this approximation is sufficient to describe simple electrodes, the precipitation of solid metal-oxides on the surface of the metal electrode forms an insulating layer and can cause the kinetics of the electrode to deviate from idealized models [62,79,145]. Special models of metal-electrode kinetics considering the effects of passivation have been developed [78,81,130] and implemented [55] in continuum simulations.

The Marcus theory of charge transfer reaction kinetics is a more accurate alternative to the Butler-Volmer approximation [146–148]. The Marcus model builds on an Arrhenius approach, in that the pre-exponential factor is described by the electronic coupling element, H_{ab}, and the reorganization free energy, λ, and the exponential term containing the activation energy. In its quantum mechanical form, the Marcus theory is expressed as

$$k_{ct} = \frac{2\pi}{\hbar}\frac{\mid H_{ab} \mid^2}{\sqrt{4\pi k_B T\lambda}}\exp\left[-\frac{(\lambda + \Delta G^0)^2}{4k_B T\lambda}\right]. \tag{13}$$

Marcus theory results naturally from quantum mechanics, and can be more easily linked to simulations like DFT [149]. While this approach has been applied in some continuum models, it is difficult to parameterize.

Electrolyte transport is modeled using a combination of expressions for diffusion, migration and convective mass flux [116], as well as a source term stemming from the chemical reactions described above [150,151]. While the fundamental components of electrolyte transport models are universal, their exact form can vary based on the ionic strength [116] and pH [3] of the electrolyte. For low ionic strength electrolytes, a simplified dilute solution theory (DST) approach can be applied to model the diffusion and migration transport of solutes [116].

$$\text{Dilute Solution Theory:} \qquad \vec{N}_i^D = -D_i\vec{\nabla}c_i, \qquad \vec{N}_i^M = \frac{D_i c_i z_i F}{RT}\vec{\nabla}\phi_e, \tag{14}$$

$$\text{Concentrated Solution Theory:} \qquad \vec{N}_i^{D,M} = -D_i\vec{\nabla}c_i - \frac{t_i}{z_i F}\vec{j}, \qquad \vec{j} = -\kappa\vec{\nabla}\phi_e + \frac{\kappa}{F}\sum_i \frac{t_i}{z_i}\frac{\partial\mu_i}{\partial c_i}\vec{\nabla}c_i. \tag{15}$$

For high ionic strength electrolytes, a more complete concentrated solution theory (CST) is needed. In this case, a coupled expression for diffusion-migration flux can be derived from non-equilibrium thermodynamics [134,152,153]. For strongly acidic or alkaline electrolytes, the concentrations of H^+ or OH^- are usually so high that concentration gradients do not affect the thermodynamic stability of the solutes. However, for electrolytes in the weakly acidic to weakly alkaline range, the concentrations of solutes in electrolytes can swing by orders of magnitude as pH gradients develop in the cell [80,112,113] and can affect the performance of the cell [3]. A new method for modeling electrolyte transport in near-neutral systems was recently proposed by Clark, et al. [3].

When metal-air batteries are operated, the precipitation and dissolution of solids and the conversion of H_2O by the ORR/OER can induce a convective flux of electrolyte in the cell [30]. In general terms, the convective flux can be expressed as

$$\vec{N}_i^{\,C} = c_i\vec{v}_e, \tag{16}$$

where $\vec{v}_e$ is the center-of-mass velocity of the electrolyte. This adds an additional level of complexity to metal-air battery models over closed systems, such as Li-ion, which often apply a simpler Nernst-Planck

model. A method for considering multi-phase convective flow in continuum models was presented by Horstmann, et al. [30] and is discussed in detail later in the text.

Continuum models of ZABs have been developed intermittently since the 1980s. The first 1D continuum model of a Zn electrode in an alkaline ZAB was developed in 1980 by Sunu and Bennion [129]. It was based on the general 1D model for concentrated transport in porous electrodes outlined by Newman [116]. Their simulations showed the inhomogeneous precipitation of ZnO and investigated the shape change of the Zn electrode during cycling. In 1992, Mao and White [135] developed an extended model that also resolved the separator and air electrode. They found that $K_2Zn(OH)_4$ does not precipitate and compared simulated cell voltages with experimental measurements. Ten years later, Deiss, et al. [136] performed ZAB cycling simulations with a 1D model of the Zn electrode and separator based on dilute solution theory. They studied the redistribution of Zn and the development of concentration gradients in the cell.

In recent years, there has been a boom in continuum modeling frameworks for both Zn-air and Li-air systems, with some areas of overlap. In 2012, Neidhardt, et al., presented a flexible continuum modeling framework for multi-phase management, with direct application to a variety of electrochemical systems [131]. In their work, they applied this framework to simulate a range of fuel cells and batteries to demonstrate the versatility of the approach. In their simulations of non-aqueous $Li-O_2$ batteries, they noted that the system is limited by a combination of slow oxygen transport and blockage of cathode pores with Li_2O_2.

To address the oxygen transport and passivation challenges associated with aprotic LABs, Horstmann, et al., were motivated to examine precipitation in alkaline aqueous LABs [30]. Their model featured two important developments. The first was the introduction of pressure-saturation expression to simulate the electrolyte flooding and drying-out of the BAE. The saturation of porous structures was described with a so-called Leverett approach, which had previously been applied in models of fuel cells. The Leverett function, $J(s)$, uses empirical constants to approximate the saturation of a porous structure as a function of the capillary pressure, $(p_e - p_g)$:

$$J(s) = \sqrt{\frac{B_e}{\varepsilon_0 \sigma^2}}(p_e - p_g) = A + Be^{C(s-0.5)} - De^{-E(s-0.5)}. \quad (17)$$

In this expression, B_e is the electrolyte permeability, ε_0 is the porosity of the electrode, σ is the surface tension, and p_e and p_g are the pressure in the electrolyte and gas phases, respectively. In the expression for the Leverett function, s is the electrode saturation and the remaining variables are constants. These constants can be determined experimentally or predicted numerically by combining 3D structure characterization with LBM simulations [128]. With the pressure of the electrolyte and the saturation of the BAE known, the convective velocity of the electrolyte can be solved using a Darcy model:

$$\vec{v}_e = -\frac{B_e}{\eta_e}\vec{\nabla} p_e, \quad (18)$$

where η_e is the viscosity of the electrolyte. Their simulations found that the availability of gas diffusion electrodes for aqueous systems reduces the oxygen transport limitations seen in non-aqueous LAB systems.

The second development was the implementation of a model for $LiOH \cdot H_2O$ precipitation based on the classical theory of nucleation and growth. By defining terms for the reaction enthalpy of formation for both the bulk and surface of the nucleus, they identified the critical formation energy and nucleus size. Considering a diffusion limited precipitation mechanism and the supersaturation of Li^+ as the driving force for nucleation and growth, they were able to simulate the spatially resolved precipitation of $LiOH \cdot H_2O$. The results, shown in Figure 7, indicate that $LiOH \cdot H_2O$ does not block the cathode pores. Rather it precipitates mostly near the separator-anode interface, thereby addressing the passivation challenge in aprotic LABs.

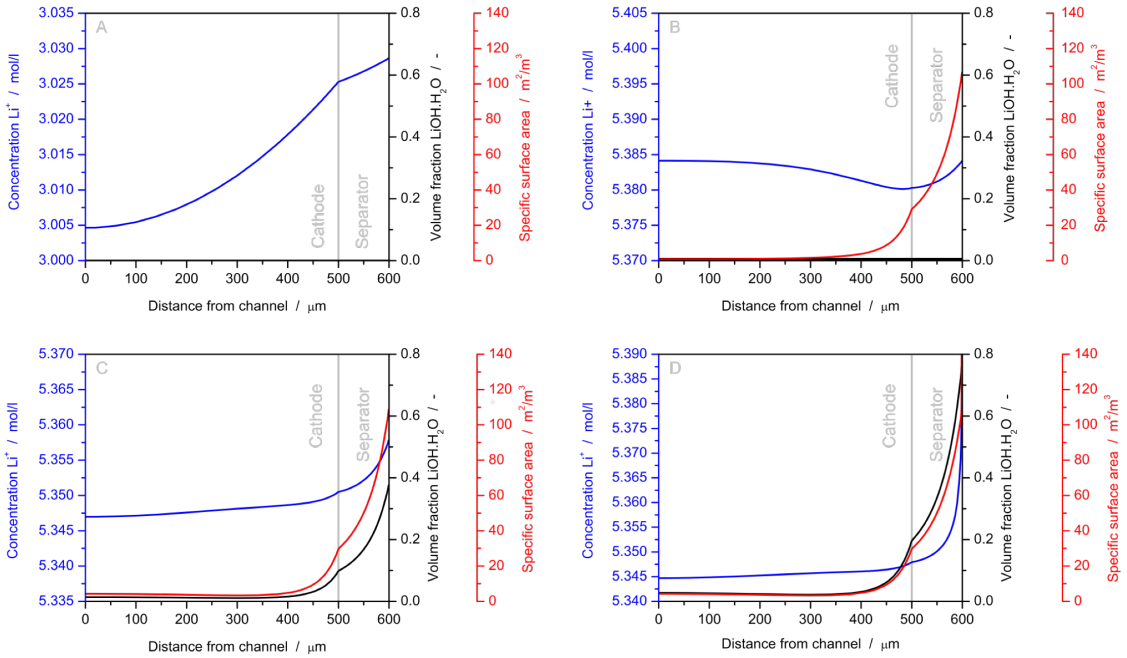

Figure 7. Spatial profiles of salt concentration, volume fraction of $LiOH \cdot H_2O$, and the specific surface are of precipitation during galvanostatic cell discharge (i = 10 $mA \cdot cm^{-2}$). Li^+ concentration increases before $LiOH \cdot H_2O$ nucleates (**A**) As the discharge progresses, $LiOH \cdot H_2O$ nucleates (**B**) and precipitates (**C**) until the cell fails due to a solid film forming at the separator-anode interface (**D**). Precipitation occurs mainly close to the anode due to the small transference number of Li^+. Reprinted from Horstmann, et al. [30]—Reproduced by permission of The Royal Society of Chemistry.

In 2015, the model of Horstmann, et al., was extended by Grübl and Bessler to engineer seven variants of aqueous alkaline LAB systems [141]. They identified improvements to the glass separator and the development of lighter electrode materials as areas for further research. While the potential advantages of aqueous LABs are clear, most recent modeling studies have focused on non-aqueous systems.

One of the first continuum models for non-aqueous LABs was presented by Andrei, et al., in 2010 [137]. Their simulations considered the effects of cell architecture and operational conditions on concentration profiles and cell voltage, and provided a solid foundation for further development. Recent multi-scale modeling studies of non-aqueous LABs focus heavily on the nucleation and growth of solids, and their affect on cell performance. A 1D continuum model of a LAB was developed by Albertus, et al., in 2011 [26]. They found that although O_2 transport can be limiting for high current densities, the main limitation in LABs relates to the precipitation of solids. For carbonate solvents, the dominant discharge product is Li_2CO_3, which, along with Li_2O_2, poses a strong passivation risk to the cathode. The model was based on a CST approach for electrolyte transport. It did not consider the effects of electrolyte convection or cathode saturation, which was identified as an area for future development.

With the shift to non-carbonate electrolytes, the morphology of Li_2O_2 precipitated during discharge became the subject of research. Knowing that pore blockage was a challenge in LAB performance, Xue, et al., developed a continuum model to investigate Li_2O_2 precipitation considering the pore size distributions of cathode materials [140]. They later extended their model to determine the effect of both electrolyte solvent and applied current density on Li_2O_2 morphology [154]. A nano-scale continuum model to study the rate-dependent growth of Li_2O_2 was presented by Horstmann, et al. [35]. They found that the morphology of Li_2O_2 shifts from discrete particles at low discharge rates to an

electronically insulating film at high current densities. This line of research was then expanded to consider the effects of Li_2O_2 precipitation on the charging process. Yin, et al., presented a continuum model for non-aqueous LABs that links the size of the Li_2O_2 particles created during discharging to the two-step voltage profile observed during charging [142]. The effect of the Li_2O_2 reaction mechanism on the discharge/charge characteristics was investigated by Grübl, et al. [155]. They found that the reaction mechanism is partially irreversible, and considered the effects of adding a redox mediator to the electrolyte. Finally, some researchers have highlighted not only the effects of Li_2O_2 morphology, but also its electronic properties. Radin, et al. integrated a DFT simulation of Li_2O_2 with charge carrying dopants into a simple Nernst-Planck continuum model to study ways to promote the OER [103]. They found that dopants, such as Co and Ni could enhance the OER and improve the rechargeability of non-aqueous LABs.

Applying continuum modeling methods to both aqueous and non-aqueous LAB development has illuminated the challenges and the opportunities inherent to these systems. Further research is needed into the effects of solid precipitation and oxygen transport in non-aqueous LABs and the long-term electrolyte stability of aqueous LABs. However, the modeling studies highlighted above have shown promising paths for further investigation.

Zn-air continuum modeling studies provide insight into challenges, such as electrolyte carbonation, Zn electrode passivation, and improved cell design. In 2014, Schröder, et al. published a framework for a 0D ZAB continuum model, which they utilized to study the effect of air composition on cell performance [138]. Examining the effects of the relative humidity (RH) and carbon dioxide content of air, they found that controlling the RH can help reduce electrolyte loss and that the presence of CO_2 can dramatically limit the lifetime of the cell. In a separate paper, they combined this model with x-ray tomography measurements of a primary button cell to monitor the state-of-charge during discharge [139].

Experimental tests of ZAB button cells have shown a voltage step in the middle of discharge, particularly at high current densities [55]. In 2017, Stamm, et al., presented a model to clarify the mechanism behind this observation. Concentration profiles from their model are shown in Figure 8. The nucleation of ZnO requires an over-saturation of $Zn(OH)_4^{2-}$ in the electrolyte. For high current densities, the electrolyte concentration gradients that develop in the cell are strong enough that $Zn(OH)_4^{2-}$ does not reach the critical super-saturation for nucleation in the anode-separator interface and ZnO does not nucleate. As a result, the surface concentration of OH^- in this region is much higher than in areas of the electrode covered by a ZnO film, as shown in Figure 8c. When the uninhibited Zn near the separator is completely utilized, the overpotential of the dissolution reaction increases, causing the observed drop in cell voltage. For this reason, they proposed that Zn electrodes should contain a small amount of ZnO powder. In this way, the effects of inhomogeneous ZnO nucleation can be avoided. Stamm, et al., also considered the effects of CO_2 dissolution in the KOH electrolyte. They found that after about 2 months, the carbonation of the electrolyte becomes so severe that the cell can no longer function. To address this issue, they purpose employing either carbon dioxide filters or neutral electrolytes.

ZABs with near-neutral chloride-based electrolytes could address the electrolyte carbonation issue and have been experimentally investigated [43,44]. The initial results are promising, but the composition and behavior of these electrolytes during cell operation is unclear. In 2017, Clark, et al. presented a continuum framework for modeling pH buffered aqueous electrolytes, and applied it to study ZABs with pH adjusted $ZnCl_2-NH_4Cl$ electrolytes [3]. Utilizing a 0D thermodynamic model of the electrolyte, they determined the pH stability and predicted the conditions under which a range of solids would precipitate. Integrating this method into a 1D continuum model, they simulated the performance of experimental near-neutral ZABs from the literature. Figure 9 shows concentration profiles of in the cell proposed by Goh, et al. [43] during cycling. The Zn electrode is on the left and the BAE is on the right of the domain. To maintain a neutral pH in the BAE, the buffer reaction $NH_4^+ \rightleftharpoons NH_3 + H^+$ counteracts the pH shifts inherent in the ORR/OER. As more NH_3 is produced,

it forms dominant complexes with Zn^{2+}, shown in Figure 9a. Because there is an excess of NH_4^+ in the electrolyte, the buffer reaction is uninhibited and the pH during discharging is relatively stable (Figure 9e). During charging, the buffer reaction is reversed and NH_3 is converted to NH_4^+. As NH_3 is depleted, zinc-chloride complexes dominate in the BAE (Figure 9b). Some of the NH_3 that was produced during discharge diffuses into the bulk electrolyte and cannot be quickly recovered. When NH_3 is locally depleted, the buffer reaction becomes limited and the pH in the BAE becomes acidic (Figure 9f). Acidic pH values can accelerate catalyst degradation and limit the lifetime of the cell. In their work, Clark, et al., discuss how cell architecture and electrolyte composition can be optimized to avoid this effect and improve performance.

Continuum models can be invaluable for investigating a range of phenomena in electrochemical cells, from the effects of discharge product precipitation to the electrolyte stability. Through the development of theory-based models, side-by-side with experimental investigation and validation, researchers can identify and pursue the most promising paths towards advanced metal-air batteries.

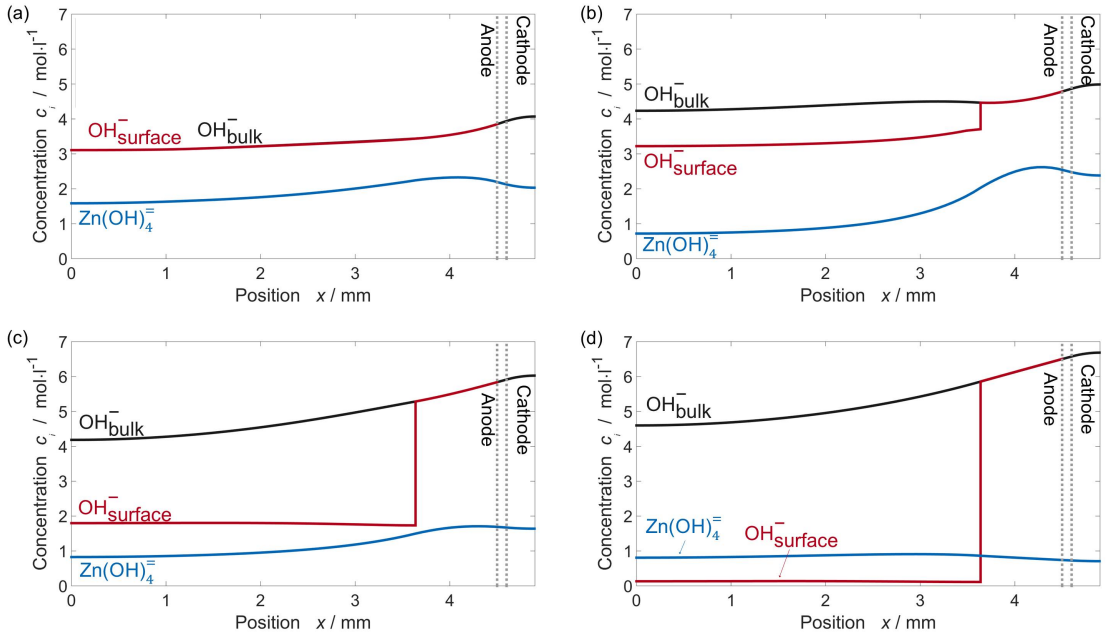

Figure 8. Various concentration profiles in an alkaline ZAB button cell during galvanostatic discharge at 125 Am^{-2} at different times. (**a**) Before ZnO nucleates, the OH^- concentration at the Zn surface and electrolyte bulk are equal and zincate concentration reaches its maximum; (**b**) ZnO precipitates inhomogeneously in the Zn-electrode, causing the OH^- surface concentration to be higher near the separator and fall as the ZnO barrier becomes thicker; (**c**) OH^- concentration continues to fall as ZnO passivation barrier grows; (**d**) OH^- concentration at the Zn-electrode surface is small and limits the further dissolution of Zn. Reproduced from Journal of Power Sources, 360, J. Stamm, A. Varzi, A. Latz, B. Horstmann, Modeling nucleation and growth of zinc oxide during discharge of primary zinc-air batteries, 136–149, Copyright 2017, with permission from Elsevier [55].

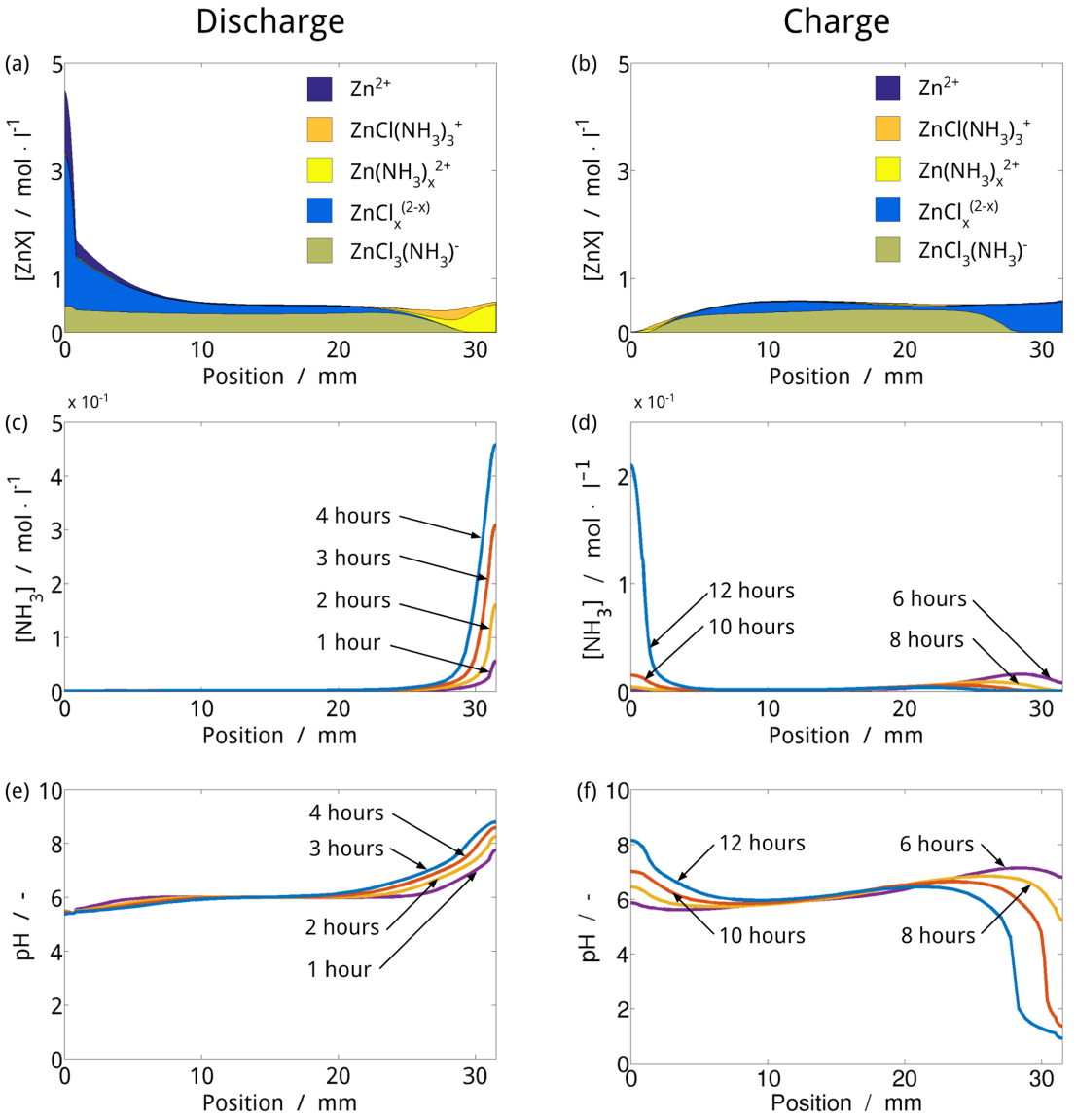

Figure 9. Electrolyte composition of near-neutral ZAB in during discharging and charging. At the end of discharging (**a**), zinc in the gas diffusion electrode (GDE) exists as $Zn(NH_3)_4^{2+}$. Once the capacity of zinc to take up NH_3 is completely utilized, NH_3 accumulates in the GDE (**c**); As the NH_4^+/NH_3 solution approaches its equivalence point, the pH value in the GDE becomes steadily more alkaline (**e**); At the Zn electrode, the small amount of NH_3 present is taken up by excess Zn^{2+} and the pH value becomes slightly more acidic. When the cell is charged, the production of H^+ in the GDE pushes the equilibrium of the ammonium buffer back towards NH_4^+. The zinc–ammine complexes release NH_3 back to the solution as charging progresses, and at the end of charging, zinc in the GDE exists exclusively as zinc–chloride complexes (**b**); To stabilize the pH value in the GDE, there must be NH_3 available for the conversion into NH_4^+. However, a considerable amount of the NH_3 produced during discharging diffuses into the bulk electrolyte and cannot be quickly recovered. This leads to a depletion of NH_3 in the GDE (**d**); At the Zn electrode, the concentration of NH_3 increases because of the redeposition of zinc. Without NH_3 to stabilize the pH value, the electrolyte in the GDE becomes acidic (**f**). At the Zn electrode, the loss of aqueous Zn^{2+} and the relative excess of NH_3 cause the pH value to increase. Reproduced from Clark, et al. [3] with permission from Wiley-VCH.

4. Model-Based Battery Engineering

To provide an example of how modeling and simulation can be applied to advance zinc-air battery development, we performed a series of cell-level continuum simulations using existing ZAB models [3,55]. In this analysis, we optimize the thickness of the zinc electrode to maximize the capacity of the cell while avoiding the unwanted effects of passivation. The initial composition of the electrolyte is 7 M KOH, saturated with ZnO. The BAE and separator are both 0.5 mm in length and the Zn-electrode is varied. The cell is galvanostatically discharged at current densities ranging from 0.1 to 50 mA $\cdot$ cm^{-2}.

Figure 10a shows the magnitude of the KOH concentration drop across the cell at the end of charging. As the thickness of the Zn electrode and the magnitude of the current density increase, the long transport paths and large source terms induce significant concentration gradients in the cell. This is important because KOH gradients can affect the solubility of ZnO and increase the risk of passivation in the Zn electrode.

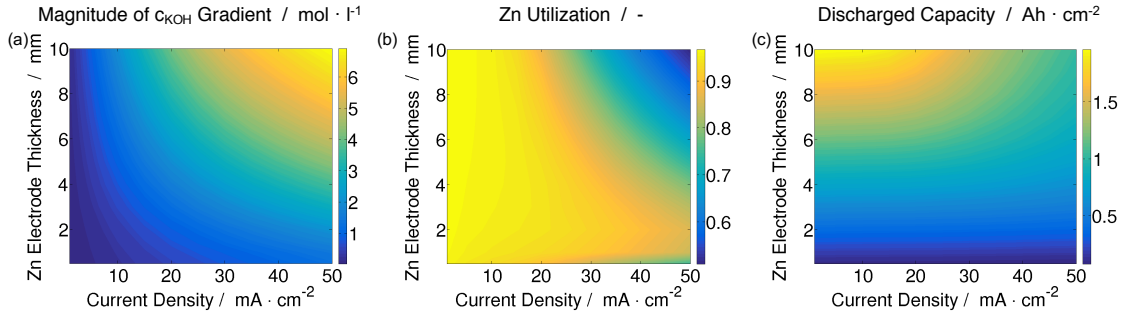

Figure 10. (**a**) Magnitude of the KOH concentration gradient across the cell at the end of discharge; (**b**) Zn utilization; and (**c**) discharged capacity as a function of Zn electrode thickness and current density.

Figure 10b presents the utilization of zinc metal in the battery. The results show that for current densities less than circa 20 mA $\cdot$ cm^{-2}, the active Zn in the electrode is essentially completely utilized (>90%) for all Zn electrode thicknesses. However, for higher current densities, passivation of the electrode occurs due to two competing factors. The ZnO that precipitates in the electrode acts as a barrier to mass transport. For thick Zn electrodes, this barrier to transport is so large that the bulk concentration of KOH in the Zn electrode drops to the point that there is insufficient hydroxide present to form $Zn(OH)_4^{2-}$ complexes, and Zn utilization drops to circa 50%. For thin electrodes, the ZnO transport barrier remains relatively small and the bulk KOH concentration remains in an acceptable range. However, in these electrodes there is less active surface area available for the reaction, which leads to a higher flux term at the surface of the Zn particles. For current densities over 30 mA $\cdot$ cm^{-2} and electrodes less than 2 mm, the magnitude of the flux term is large enough to locally deplete OH^- at the electrode surface and passivate the electrode. The Zn utilization drops to circa 80%.

Figure 10c shows the discharged capacity of the battery. Increasing the thickness of the Zn electrode increases the amount of active material in the cell and the theoretically achievable capacity. However, the passivation of thick electrodes at higher current densities limits the amount of Zn that can be utilized, as shown in the previous figure. The result is that a battery with a 5 mm Zn electrode discharged at 10 mA $\cdot$ cm^{-2} has roughly the same capacity as a battery with a 10 mm Zn electrode discharged at 50 mA $\cdot$ cm^{-2}.

When designing an alkaline ZAB, care should be taken to size the Zn electrode considering the current requirement and the desired capacity. With this information, an informed decision can be taken regarding how much Zn paste should be included in the battery to obtain the optimum performance.

Model-based engineering can also be applied in the testing phase of development to design experiments with the highest chance of success. Because Zn electrodes have a high capacity and can

only be discharged at limited rates, it takes a very long time to study their cycling characteristics. Often, the solution is to perform "accelerated" tests with smaller electrodes or at higher current densities, both of which increase the risk of irreversible passivation.

Consider the case in which a researcher wants to cycle a ZAB 200 times in less than 3 months. One cycle is defined as moving between 70% and 30% state-of-charge (SOC), and the electrode consists of a paste that is 50 vol % Zn and 50 vol % electrolyte. Figure 11a shows the time required to complete 200 cycles under these conditions for different combinations of current density and Zn electrode thickness.

Figure 11b shows the time required to passivate the Zn electrode. By comparing the passivation time with the cycling time and applying an engineering safety factor of 1.3, we can mark the passivation limitations of the system. This region is shaded in black in Figure 11c. Combinations in the red zone of the figure exceed the time limitation, and we assume that electrodes smaller than 100 microns are impractical to manufacture (orange). With these factors in mind, we define a region of combinations (green) which could fit the researcher's needs.

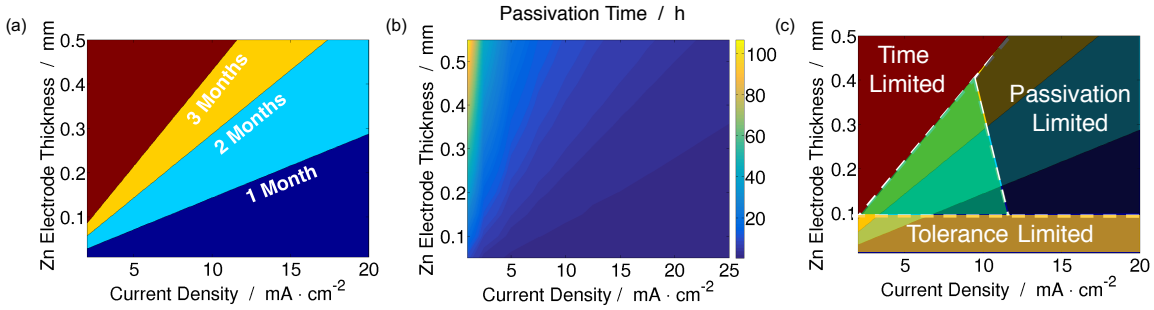

Figure 11. (**a**) Time required to cycle a ZAB 200 times for various Zn electrode thickness and current density combinations; (**b**) passivation time; and (**c**) operational window for a model ZAB.

When appropriately applied, model-based battery design can be of great value to scientists and engineers. The tools we have reviewed and applied in this analysis give insight into every aspect of battery performance, from the atomic structure of materials to the dynamic performance of whole cells. Embracing an integrated approach to modeling and understanding battery performance can help guide researchers towards achieving the goal of viable and high-performance metal-air batteries.

5. Conclusions

A variety of modeling and simulation methods can be applied to aid the development of zinc-air and other metal-air battery systems. While many metal-air systems are currently under development, Li-air batteries (LABs) and Zn-air batteries (ZABs) are the most promising systems.

On the material level, density functional theory (DFT) can be applied to investigate the electronic properties of catalysts and metals. This could help to screen new catalysts for properties like activity, stability, and selectivity and to elucidate the effect of surface structures on metal dissolution and deposition. Furthermore, equilibrium thermodynamic models can be used to predict the speciation of electrolytes and the solubility of precipitants. This can help determine not only the state of the electrolyte for different pH and concentration mixtures, but also its stability within the electrochemical window of the cell.

When it comes to electrode design, one challenge is to develop a bi-functional air electrode (BAE) that maintains an optimum level of saturation (neither flooding nor drying out) during battery operation. Lattice-Boltzmann-Methods (LBM) can be developed to investigate the pressure-saturation characteristics of real BAE structures in 2D or 3D.

Physics-based continuum modeling is the most useful and widely-utilized method for simulating the cell-level performance of metal-air batteries. Models constructed with this method are able to

give researchers insight into a range of phenomena including the coupled effects of electrolyte concentrations, precipitation of solids, electrode kinetics, and cell voltage. The versatility of continuum modeling and the wide array of existing literature on the subject make it a good tool to advance the development of metal-air batteries.

Numerical modeling and simulation studies have shown that the performance LABs with non-aqueous electrolytes is encouraging but limited by slow oxygen transport and pore blockage by Li_2O_2. DFT simulations have been applied to elucidate the electronic structure and reaction mechanisms of Li_2O_2 and investigate possible alternative non-aqueous electrolyte solvents. Continuum models have highlighted the cell-level effects of Li_2O_2 precipitation and O_2 transport. The nucleation and growth of Li_2O_2 particles and films and its effect on the reversibility and performance of non-alkaline LABs is a major topic of research. Aqueous LABs improve oxygen transport in the air electrode and facilitate more favorable precipitation, but the long-term stability of the electrolyte is limited when exposed to CO_2. Continuum models developed for aqueous LABs have provided a framework for integrating the multi-phase flow in the air electrode into models of other metal-air systems.

ZABs stand alone as the only successfully commercialized primary metal-air system so far. Modeling studies of these systems highlight the performance of the alkaline electrolyte in air, passivation and shape change of the Zn electrode, and cell-level engineering. Because of its historical dominance, there is a long history of Zn-air continuum models, going back to the 1980s. Recent studies have been provided a scheme for interpreting and understanding experimental results, and a new framework developed to model ZABs with alternative near-neutral electrolytes could find wide application in other electrochemical systems. Implementing these modeling tools in the design process brings researchers closer to the goal of building high-performance and electrically rechargeable zinc-air batteries.

Acknowledgments: This work has received funding from the European Union's Horizon 2020 research and innovation program under grant agreement No. 646186 (ZAS-project). The support of the bwHPC initiative through the use of the JUSTUS HPC facility at Ulm University is acknowledged. The authors wish to thank Timo Danner for the helpful discussion.

Conflicts of Interest: The authors declare no conflict of interest.

References

1. Gröger, O.; Gasteiger, H.A.; Suchsland, J.P. Review—Electromobility: Batteries or Fuel Cells? *J. Electrochem. Soc.* **2015**, *162*, A2605–A2622.
2. Rahman, M.A.; Wang, X.; Wen, C. High Energy Density Metal-Air Batteries: A Review. *J. Electrochem. Soc.* **2013**, *160*, A1759–A1771.
3. Clark, S.; Latz, A.; Horstmann, B. Rational Development of Neutral Aqueous Electrolytes for Zinc-Air Batteries. *ChemSusChem* **2017**, *10*, 4735–4747.
4. Li, Y.; Zhang, X.; Li, H.B.; Yoo, H.D.; Chi, X.; An, Q.; Liu, J.; Yu, M.; Wang, W.; Yao, Y. Mixed-phase mullite electrocatalyst for pH-neutral oxygen reduction in magnesium-air batteries. *Nano Energy* **2016**, *27*, 8–16.
5. Li, C.S.; Sun, Y.; Gebert, F.; Chou, S.L. Current Progress on Rechargeable Magnesium-Air Battery. *Adv. Energy Mater.* **2017**, *7*, doi:10.1002/aenm.201700869.
6. Chen, L.D.; Norskov, J.K.; Luntz, A.C. Theoretical Limits to the Anode Potential in Aqueous Mg-Air Batteries. *J. Phys. Chem. C* **2015**, *119*, 19660–19667.
7. Vardar, G.; Sleightholme, A.E.S.; Naruse, J.; Hiramatsu, H.; Siegel, D.J.; Monroe, C.W. Electrochemistry of magnesium electrolytes in ionic liquids for secondary batteries. *ACS Appl. Mater. Interfaces* **2014**, *6*, 18033–18039.
8. Mokhtar, M.; Talib, M.Z.M.; Majlan, E.H.; Tasirin, S.M.; Ramli, W.M.F.W.; Daud, W.R.W.; Sahari, J. Recent developments in materials for aluminum-air batteries: A review. *J. Ind. Eng. Chem.* **2015**, *32*, 1–20.
9. Zhang, Z.; Zuo, C.; Liu, Z.; Yu, Y.; Zuo, Y.; Song, Y. All-solid-state Al-air batteries with polymer alkaline gel electrolyte. *J. Power Sources* **2014**, *251*, 470–475.

10. Fu, G.; Chen, Y.; Cui, Z.; Li, Y.; Zhou, W.; Xin, S.; Tang, Y.; Goodenough, J.B. Novel Hydrogel-Derived Bifunctional Oxygen Electrocatalyst for Rechargeable Air Cathodes. *Nano Lett.* **2016**, *16*, 6516–6522.
11. Adelhelm, P.; Hartmann, P.; Bender, C.L.; Busche, M.; Eufinger, C.; Janek, J. From lithium to sodium: Cell chemistry of room temperature sodium-air and sodium-sulfur batteries. *Beilstein J. Nanotechnol.* **2015**, *6*, 1016–1055.
12. Hartmann, P.; Bender, C.L.; Vračar, M.; Dürr, A.K.; Garsuch, A.; Janek, J.; Adelhelm, P. A rechargeable room-temperature sodium superoxide (NaO_2) battery. *Nat. Mater.* **2012**, *12*, 228–232.
13. Kim, J.; Park, H.; Lee, B.; Seong, W.M.; Lim, H.D.; Bae, Y.; Kim, H.; Kim, W.K.; Ryu, K.H.; Kang, K. Dissolution and ionization of sodium superoxide in sodium–oxygen batteries. *Nat. Commun.* **2016**, *7*, 10670, doi:10.1038/ncomms10670.
14. Durmus, Y.E. Modeling of Silicon Air-Batteries. Master's Thesi, Ulm University, Ulm, Germany, 2013, p. 106.
15. Cohn, G.; Ein-Eli, Y. Study and development of non-aqueous silicon-air battery. *J. Power Sources* **2010**, *195*, 4963–4970.
16. Durmus, Y.E.; Aslanbas, O.; Kayser, S.; Tempel, H.; Hausen, F.; de Haart, L.G.; Granwehr, J.; Ein-Eli, Y.; Eichel, R.A.; Kungl, H. Long run discharge, performance and efficiency of primary Silicon–air cells with alkaline electrolyte. *Electrochim. Acta* **2017**, *225*, 215–224.
17. Girishkumar, G.; McCloskey, B.; Luntz, A.C.; Swanson, S.; Wilcke, W. Lithium-air battery: Promise and challenges. *J. Phys. Chem. Lett.* **2010**, *1*, 2193–2203.
18. Lee, J.S.; Kim, S.T.; Cao, R.; Choi, N.S.; Liu, M.; Lee, K.T.; Cho, J. Metal-air batteries with high energy density: Li-air versus Zn-air. *Adv. Energy Mater.* **2011**, *1*, 34–50.
19. Li, Y.; Dai, H. Recent advances in zinc–air batteries. *Chem. Soc. Rev.* **2014**, *43*, 5257–5275.
20. Blurton, K.F.; Sammells, A.F. Metal/air batteries: Their status and potential—A review. *J. Power Sources* **1979**, *4*, 263–279.
21. Abraham, K.M.; Jiang, Z. A Polymer Electrolyte-Based Rechargeable Lithium/Oxygen Battery. *J. Electrochem. Soc.* **1996**, *143*, 1–5.
22. Xu, W.; Xu, K.; Viswanathan, V.V.; Towne, S.A.; Hardy, J.S.; Xiao, J.; Nie, Z.; Hu, D.; Wang, D.; Zhang, J.G. Reaction mechanisms for the limited reversibility of Li-O_2 chemistry in organic carbonate electrolytes. *J. Power Sources* **2011**, *196*, 9631–9639.
23. McCloskey, B.D.; Bethune, D.S.; Shelby, R.M.; Girishkumar, G.; Luntz, A.C. Solvents critical role in nonaqueous Lithium-Oxygen battery electrochemistry. *J. Phys. Chem. Lett.* **2011**, *2*, 1161–1166.
24. Freunberger, S.A.; Chen, Y.; Peng, Z.; Griffin, J.M.; Hardwick, L.J.; Bardé, F.; Novák, P.; Bruce, P.G. Reactions in the rechargeable lithium-O_2 battery with alkyl carbonate electrolytes. *J. Am. Chem. Soc.* **2011**, *133*, 8040–8047.
25. McCloskey, B.D.; Speidel, A.; Scheffler, R.; Miller, D.C.; Viswanathan, V.; Hummelshøj, J.S.; Nørskov, J.K.; Luntz, A.C. Twin problems of interfacial carbonate formation in nonaqueous Li-O_2 batteries. *J. Phys. Chem. Lett.* **2012**, *3*, 997–1001.
26. Albertus, P.; Girishkumar, G.; McCloskey, B.; Sanchez-Carrera, R.S.; Kozinsky, B.; Christensen, J.; Luntz, A.C. Identifying Capacity Limitations in the Li/Oxygen Battery Using Experiments and Modeling. *J. Electrochem. Soc.* **2011**, *158*, A343–A351.
27. Monroe, C.W. Does Oxygen Transport Affect the Cell Voltages of Metal/Air Batteries? *J. Electrochem. Soc.* **2017**, *164*, E3547–E3551.
28. Visco, S.J.; Katz, B.D.; Nimon, Y.S.; De Jonghe, L.C. Protected Active Metal Electrode and Battery Cell Structures with Non-Aqueous Interlayer Architecture. U.S. Patent 7282295 B2, 16 October 2007.
29. Visco, S.J.; Nimon, Y.S. Active Metal/aqueous Electrochemical Cells and Systems. U.S. Patent 7645543 B2, 12 January 2010.
30. Horstmann, B.; Danner, T.; Bessler, W.G. Precipitation in aqueous lithium–oxygen batteries: A model-based analysis. *Energy Environ. Sci.* **2013**, *6*, 1299–1314.
31. Hummelshøj, J.S.; Luntz, A.C.; Norskov, J.K. Theoretical evidence for low kinetic overpotentials in Li-O_2 electrochemistry. *J. Chem. Phys.* **2013**, *138*, 034703, doi:10.1063/1.4773242.
32. Sandhu, S.S.; Brutchen, G.W.; Fellner, J.P. Lithium/air cell: Preliminary mathematical formulation and analysis. *J. Power Sources* **2007**, *170*, 196–209.
33. Zheng, J.P.; Liang, R.Y.; Hendrickson, M.; Plichta, E.J. Theoretical Energy Density of Li–Air Batteries. *J. Electrochem. Soc.* **2008**, *155*, A432–A437.

34. Sahapatsombut, U.; Cheng, H.; Scott, K. Modelling of operation of a lithium-air battery with ambient air and oxygen-selective membrane. *J. Power Sources* **2014**, *249*, 418–430.
35. Horstmann, B.; Gallant, B.; Mitchell, R.; Bessler, W.G.; Shao-Horn, Y.; Bazant, M.Z. Rate-dependent morphology of Li_2O_2 growth in Li-O_2 batteries. *J. Phys. Chem. Lett.* **2013**, *4*, 4217–4222.
36. Danner, T.; Horstmann, B.; Wittmaier, D.; Wagner, N.; Bessler, W.G. Reaction and transport in Ag/Ag_2O gas diffusion electrodes of aqueous Li-O_2 batteries: Experiments and modeling. *J. Power Sources* **2014**, *264*, 320–332.
37. Lu, J.; Jung Lee, Y.; Luo, X.; Chun Lau, K.; Asadi, M.; Wang, H.H.; Brombosz, S.; Wen, J.; Zhai, D.; Chen, Z.; et al. A lithium–oxygen battery based on lithium superoxide. *Nature* **2016**, *529*, 377–382.
38. Johnson, L.; Li, C.; Liu, Z.; Chen, Y.; Freunberger, S.A.; Ashok, P.C.; Praveen, B.B.; Dholakia, K.; Tarascon, J.M.; Bruce, P.G. Erratum: The role of LiO_2 solubility in O_2 reduction in aprotic solvents and its consequences for Li-O_2 batteries. *Nat. Chem.* **2014**, *7*, 87.
39. Gao, X.; Chen, Y.; Johnson, L.; Bruce, P.G. Erratum: Promoting solution phase discharge in Li-O_2 batteries containing weakly solvating electrolyte solutions. *Nat. Mater.* **2016**, *15*, 918.
40. McCloskey, B.D.; Bethune, D.S.; Shelby, R.M.; Mori, T.; Scheffler, R.; Speidel, A.; Sherwood, M.; Luntz, A.C. Limitations in rechargeability of Li-O_2 batteries and possible origins. *J. Phys. Chem. Lett.* **2012**, *3*, 3043–3047.
41. Vegge, T.; Garcia-Lastra, J.M.; Siegel, D.J. Lithium–oxygen batteries: At a crossroads? *Curr. Opin. Electrochem.* **2017**, *6*, 100–107.
42. Pei, P.; Wang, K.; Ma, Z. Technologies for extending zinc-air battery's cyclelife: A review. *Appl. Energy* **2014**, *128*, 315–324.
43. Thomas Goh, F.W.; Liu, Z.; Hor, T.S.A.; Zhang, J.; Ge, X.; Zong, Y.; Yu, A.; Khoo, W. A Near-Neutral Chloride Electrolyte for Electrically Rechargeable Zinc-Air Batteries. *J. Electrochem.Soc.* **2014**, *161*, A2080–A2086.
44. Sumboja, A.; Ge, X.; Zheng, G.; Goh, F.T.; Hor, T.A.; Zong, Y.; Liu, Z. Durable rechargeable zinc-air batteries with neutral electrolyte and manganese oxide catalyst. *J. Power Sources* **2016**, *332*, 330–336.
45. MacFarlane, D.R.; Tachikawa, N.; Forsyth, M.; Pringle, J.M.; Howlett, P.C.; Elliott, G.D.; Davis, J.H.; Watanabe, M.; Simon, P.; Angell, C.A. Energy applications of ionic liquids. *Energy Environ. Sci.* **2014**, *7*, 232–250.
46. Liu, Z.; Abedin, S.Z.E.; Endres, F. Electrodeposition of zinc films from ionic liquids and ionic liquid/water mixtures. *Electrochim. Acta* **2013**, *89*, 635–643.
47. Liu, Z.; El Abedin, S.Z.; Endres, F. Dissolution of zinc oxide in a protic ionic liquid with the 1-methylimidazolium cation and electrodeposition of zinc from ZnO/ionic liquid and ZnO/ionic liquid-water mixtures. *Electrochem. Commun.* **2015**, *58*, 46–50.
48. Fu, J.; Cano, Z.P.; Park, M.G.; Yu, A.; Fowler, M.; Chen, Z. Electrically Rechargeable Zinc–Air Batteries: Progress, Challenges, and Perspectives. *Adv. Mater.* **2017**, *29*, 1604685.
49. Amendola, S.; Binder, M.; Black, P.J.; Sharp-Goldman, S.; Johnson, L.; Kunz, M.; Oster, M.; Chciuk, T.; Johnson, R. Electrically Rechargeable, Metal-Air Battery Systems and Methods. U.S. Patent 2012/0021303 A1, 26 January 2012.
50. Friesen, C.; Krishnan, R.; Friesen, G. Rechargeable Electrochemical Cell System with a Charging Electrode Charge/discharge Mode Switching in the Cells. U.S. Patent US 2011/0070506 A1, 24 March 2011.
51. Lee, D.U.; Xu, P.; Cano, Z.P.; Kashkooli, A.G.; Park, M.G.; Chen, Z. Recent progress and perspectives on bi-functional oxygen electrocatalysts for advanced rechargeable metal–air batteries. *J. Mater. Chem. A* **2016**, *4*, 7107–7134.
52. Neburchilov, V.; Wang, H.; Martin, J.J.; Qu, W. A review on air cathodes for zinc-air fuel cells. *J. Power Sources* **2010**, *195*, 1271–1291.
53. Stoerzinger, K.a.; Risch, M.; Han, B.; Shao-Horn, Y. Recent Insights into Manganese Oxides in Catalyzing Oxygen Reduction Kinetics. *ACS Catal.* **2015**, *5*, 6021–6031.
54. Horn, Q.C.; Shao-Horn, Y. Morphology and Spatial Distribution of ZnO Formed in Discharged Alkaline Zn/MnO_2 AA Cells. *J. Electrochem. Soc.* **2003**, *150*, A652–A658.
55. Stamm, J.; Varzi, A.; Latz, A.; Horstmann, B. Modeling nucleation and growth of zinc oxide during discharge of primary zinc-air batteries. *J. Power Sources* **2017**, *360*, 136–149.
56. Jörissen, L. Bifunctional oxygen/air electrodes. *J. Power Sources* **2006**, *155*, 23–32.
57. Drillet, J.F.; Holzer, F.; Kallis, T.; Müller, S.; Schmidt, V. Influence of CO_2 on the stability of bifunctional oxygen electrodes for rechargeable zinc/air batteries and study of different CO_2 filter materials. *Phys. Chem. Chem. Phys.* **2001**, *3*, 368–371.

58. Hwang, B.; Oh, E.S.; Kim, K. Observation of electrochemical reactions at Zn electrodes in Zn-air secondary batteries. *Electrochim. Acta* **2016**, *216*, 484–489.
59. Suresh Kannan, A.R.; Muralidharan, S.; Sarangapani, K.B.; Balaramachandran, V.; Kapali, V. Corrosion and anodic behaviour of zinc and its ternary alloys in alkaline battery electrolytes. *J. Power Sources* **1995**, *57*, 93–98.
60. Vorkapicc, L.Z.; Drazzicc, D.M.; Despic, A.R. Corrosion of Pure and Amalgamated Zinc in Concentrated Alkali Hydroxide Solutions. *J. Electrochem. Soc.* **1974**, *121*, 1385–1392
61. Baugh, L.M.; Tye, F.L.; White, N.C. Corrosion and polarization characteristics of zinc in battery electrolyte analogues and the effect of amalgamation. *J. Appl. Electrochem.* **1983**, *13*, 623–635.
62. Dirkse, T.; Hampson, N. The anodic behaviour of zinc in aqueous solution—-III. Passivation in mixed KF-KOH solutions. *Electrochim. Acta* **1972**, *17*, 813–818.
63. Schröder, D.; Sinai Borker, N.N.; König, M.; Krewer, U. Performance of zinc air batteries with added K_2CO_3 in the alkaline electrolyte. *J. Appl. Electrochem.* **2015**, *45*, 427–437.
64. Mainar, A.R.; Leonet, O.; Bengoechea, M.; Boyano, I.; de Meatza, I.; Kvasha, A.; Guerfi, A.; Blazquez, J.A. Alkaline aqueous electrolytes for secondary zinc-air batteries: An overview. *Int. J. Energy Res.* **2016**, *40*, 1032–1049.
65. Mainar, A.R.; Iruin, E.; Colmenares, L.C.; Kvasha, A.; de Meatza, I.; Bengoechea, M.; Leonet, O.; Boyano, I.; Zhang, Z.; Blazquez, J.A. An overview of progress in electrolytes for secondary zinc-air batteries and other storage systems based on zinc. *J. Energy Storage* **2018**, *15*, 304–328.
66. Kar, M.; Winther-Jensen, B.; Forsyth, M.; MacFarlane, D.R. Chelating ionic liquids for reversible zinc electrochemistry. *Phys. Chem. Chem. Phys.* **2013**, *15*, 7191–7197.
67. Lee, J.S.; Lee, T.; Song, H.K.; Cho, J.; Kim, B.S. Ionic liquid modified graphene nanosheets anchoring manganese oxide nanoparticles as efficient electrocatalysts for Zn–air batteries. *Energy Environ. Sci.* **2011**, *4*, 4148–4154
68. Endres, F.; Abbott, A.; MacFarlane, D.R. (Eds) *Electrodeposition from Ionic Liquids*, 1st ed.; Wiley-VCH: Weinheim, Germany, 2008; p. 410.
69. Xu, M.; Ivey, D.G.; Xie, Z.; Qu, W. Rechargeable Zn-air batteries: Progress in electrolyte development and cell configuration advancement. *J. Power Sources* **2015**, *283*, 358–371.
70. Mclarnon, F.R.; Cairns, E.J. The Secondary Alkaline Zinc Electrode. *J. Electrochem. Soc.* **1991**, *138*, 645–664.
71. Kim, H.; Jeong, G.; Kim, Y.U.; Kim, J.H.; Park, C.M.; Sohn, H.J. Metallic anodes for next generation secondary batteries. *Chem. Soc. Rev.* **2013**, *42*, 9011–9034.
72. Bockris, J.O.; Nagy, Z.; Damjanovic, A. On the Deposition and Dissolution of Zinc in Alkaline Solutions. *J. Electrochem. Soc.* **1972**, *119*, 285–295.
73. Sun, K.E.; Hoang, T.K.; Doan, T.N.L.; Yu, Y.; Zhu, X.; Tian, Y.; Chen, P. Suppression of Dendrite Formation and Corrosion on Zinc Anode of Secondary Aqueous Batteries. *ACS Appl. Mater. Interfaces* **2017**, *9*, 9681–9687.
74. Banik, S.J.; Akolkar, R. Suppressing Dendritic Growth during Alkaline Zinc Electrodeposition using Polyethylenimine Additive. *Electrochim. Acta* **2015**, *179*, 475–481.
75. Diggle, J.W.; Damjanovic, A. The inhibition of the dendritic electrocrystallization of zinc from doped alkaline zincate solutions. *J. Electrochem. Soc.* **1972**, *119*, 1649–1658.
76. Schmid, M.; Willert-Porada, M. Electrochemical behavior of zinc particles with silica based coatings as anode material for zinc air batteries with improved discharge capacity. *J. Power Sources* **2017**, *351*, 115–122.
77. Zelger, C.; Laumen, J.; Laskos, A.; Gollas, B. Rota-Hull Cell Study on Pulse Current Zinc Electrodeposition from Alkaline Electrolytes. *Electrochim. Acta* **2016**, *213*, 208–216.
78. Liu, M.B. Passivation of Zinc Anodes in KOH Electrolytes. *J. Electrochem. Soc.* **1981**, *128*, 1663–1668.
79. Dirkse, T.; Hampson, N. The anodic behaviour of zinc in aqueous KOH solution—II. passivation experiments using linear sweep voltammetry. *Electrochim. Acta* **1972**, *17*, 387–394.
80. Zhang, X.G. *Corrosion and Electrochemistry of Zinc*, 1st ed.; Plenum Press: New York, NY, USA, 1996.
81. Prentice, G. A Model for the Passivation of the Zinc Electrode in Alkaline Electrolyte. *J. Electrochem. Soc.* **1991**, *138*, 890–894.
82. Jung, J.I.; Risch, M.; Park, S.; Kim, M.G.; Nam, G.; Jeong, H.Y.; Shao-Horn, Y.; Cho, J. Optimizing nanoparticle perovskite for bifunctional oxygen electrocatalysis. *Energy Environ. Sci.* **2016**, *9*, 176–183.
83. Mainar, A.R.; Colmenares, L.C.; Leonet, O.; Alcaide, F.; Iruin, J.J.; Weinberger, S.; Hacker, V.; Iruin, E.; Urdanpilleta, I.; Blazquez, J.A. Manganese oxide catalysts for secondary zinc air batteries: From electrocatalytic activity to bifunctional air electrode performance. *Electrochim. Acta* **2016**, *217*, 80–91.

84. Li, Y.; Gong, M.; Liang, Y.; Feng, J.; Kim, J.E.; Wang, H.; Hong, G.; Zhang, B.; Dai, H. Advanced zinc-air batteries based on high-performance hybrid electrocatalysts. *Nat. Commun.* **2013**, *4*, 1805.
85. Tan, P.; Kong, W.; Shao, Z.; Liu, M.; Ni, M. Advances in modeling and simulation of Li–air batteries. *Prog. Energy Combust. Sci.* **2017**, *62*, 155–189.
86. Grew, K.N.; Chiu, W.K. A review of modeling and simulation techniques across the length scales for the solid oxide fuel cell. *J. Power Sources* **2012**, *199*, 1–13.
87. Sholl, D. S.; Steckel, J.A. *Density Functional Theory: A Practical Introduction*, 1st ed.; John Wiley & Sons: Hoboken, NJ, USA, 2009.
88. Mattsson, A.E.; Schultz, P.A.; Desjarlais, M.P.; Mattsson, T.R.; Leung, K. Designing meaningful density functional theory calculations in materials science—A primer. *Model. Simul. Mater. Sci. Eng.* **2005**, *13*, 1–31.
89. Hörmann, N.G.; Jäckle, M.; Gossenberger, F.; Roman, T.; Forster-Tonigold, K.; Naderian, M.; Sakong, S.; Groß, A. Some challenges in the first-principles modeling of structures and processes in electrochemical energy storage and transfer. *J. Power Sources* **2015**, *275*, 531–538.
90. Nørskov, J.K.; Rossmeisl, J.; Logadottir, A.; Lindqvist, L.; Kitchin, J.R.; Bligaard, T.; Jónsson, H. Origin of the overpotential for oxygen reduction at a fuel-cell cathode. *J. Phys. Chem. B* **2004**, *108*, 17886–17892.
91. Viswanathan, V.; Hansen, H.A.; Rossmeisl, J.; Nørskov, J.K. Universality in oxygen reduction electrocatalysis on metal surfaces. *ACS Catal.* **2012**, *2*, 1654–1660.
92. Hansen, H.A.; Viswanathan, V.; Nørskov, J.K. Unifying kinetic and thermodynamic analysis of 2 e- and 4 e-reduction of oxygen on metal surfaces. *J. Phys. Chem. C* **2014**, *118*, 6706–6718.
93. Viswanathan, V.; Nørskov, J.K.; Speidel, A.; Scheffler, R.; Gowda, S.; Luntz, A.C. Li-O_2 kinetic overpotentials: Tafel plots from experiment and first-principles theory. *J. Phys. Chem. Lett.* **2013**, *4*, 556–560.
94. Aetukuri, N.B.; McCloskey, B.D.; Garcia, J.M.; Krupp, L.E.; Viswanathan, V.; Luntz, A.C. Solvating additives drive solution-mediated electrochemistry and enhance toroid growth in non-aqueous Li-O_2 batteries. *Nat. Chem.* **2015**, *7*, 50–56.
95. Eberle, D.; Horstmann, B. Oxygen Reduction on Pt(111) in Aqueous Electrolyte: Elementary Kinetic Modeling. *Electrochim. Acta* **2014**, *137*, 714–720.
96. Tripkovic, V.; Vegge, T. Potential and Rate Determining Step for Oxygen Reduction on Pt(111). *J. Phys. Chem. C* **2017**, *121*, 26785–26793.
97. Vazquez-Arenas, J.; Ramos-Sanchez, G.; Franco, A.A. A multi-scale model of the oxygen reduction reaction on highly active graphene nanosheets in alkaline conditions. *J. Power Sources* **2016**, *328*, 492–502.
98. Siahrostami, S.; Tripković, V.; Lundgaard, K.T.; Jensen, K.E.; Hansen, H.A.; Hummelshøj, J.S.; Mýrdal, J.S.G.; Vegge, T.; Nørskov, J.K.; Rossmeisl, J. First principles investigation of zinc-anode dissolution in zinc–air batteries. *Phys. Chem. Chem. Phys.* **2013**, *15*, 6416-6421
99. Jäckle, M.; Groß, A. Microscopic properties of lithium, sodium, and magnesium battery anode materials related to possible dendrite growth. *J. Chem. Phys.* **2016**, *141*, doi:10.1063/1.4901055.
100. Hummelshøj, J.S.; Blomqvist, J.; Datta, S.; Vegge, T.; Rossmeisl, J.; Thygesen, K.S.; Luntz, A.C.; Jacobsen, K.W.; Nørskov, J.K. Communications: Elementary oxygen electrode reactions in the aprotic Li-air battery. *J. Chem. Phys.* **2010**, *132*, doi:10.1063/1.3298994.
101. Radin, M.D.; Rodriguez, J.F.; Tian, F.; Siegel, D.J. Lithium peroxide surfaces are metallic, while lithium oxide surfaces are not. *J. Am. Chem. Soc.* **2012**, *134*, 1093–1103.
102. Radin, M.D.; Siegel, D.J. Charge transport in lithium peroxide: relevance for rechargeable metal–air batteries. *Energy Environ. Sci.* **2013**, *6*, 2370.
103. Radin, M.D.; Monroe, C.W.; Siegel, D.J. How dopants can enhance charge transport in Li_2O_2. *Chem. Mater.* **2015**, *27*, 839–847.
104. Dirkse, T.P. The Nature of the Zinc-Containing Ion in Strongly Alkaline Solutions. *J. Electrochem. Soc.* **1954**, *101*, 328.
105. Larcin, J.; Maskell, W.C.; Tye, F.L. Leclanche cell investigations I: $Zn(NH_3)_2Cl_2$ solubility and the formation of $ZnCl_2 \cdot 4\,Zn(OH)_2 \cdot H_2O$. *Electrochim. Acta* **1997**, *42*, 2649–2658.
106. Zhang, Y.; Muhammed, M. Critical evaluation of thermodynamics of complex formation of metal ions in aqueous solutions—VI. Hydrolysis and hydroxo-complexes of Zn2+ at 298.15 K. *Hydrometallurgy* **2001**, *60*, 215–236.
107. Clark, S.; Latz, A.; Horstmann, B. Cover Feature: Rational Development of Neutral Aqueous Electrolytes for Zinc-Air Batteries. *ChemSusChem* **2017**, *10*, 4666.

108. Smith, R.; Martell, A. *Critical Stability Constants*; Springer: New York, NY, USA, 1976; Volume 4.
109. Martell, A.E.; Smith, R.M. *Critical Stability Constants*; Springer: New York, NY, USA, 1977; Volume 5.
110. Martell, A.; Smith, R. *Other Organic Ligands*, 1st ed.; Springer: New York, NY, USA, 1977.
111. Dirkse, T. The Solubility Product Constant of ZnO. *J. Electrochem. Soc.* **1986**, *133*, 1656–1657
112. Limpo, J.; Luis, A. Solubility of zinc chloride in ammoniacal ammonium chloride solutions. *Hydrometallurgy* **1993**, *32*, 247–260.
113. Limpo, J.; Luis, A.; Cristina, M. Hydrolysis of zinc chloride in aqueous ammoniacal ammonium chloride solutions. *Hydrometallurgy* **1995**, *38*, 235–243.
114. Vazquez-Arenas, J.; Sosa-Rodriguez, F.; Lazaro, I.; Cruz, R. Thermodynamic and electrochemistry analysis of the zinc electrodeposition in NH_4Cl-NH_3 electrolytes on Ti, Glassy Carbon and 316L Stainless Steel. *Electrochim. Acta* **2012**, *79*, 109–116.
115. Rojas-Hernández, A.; Ramírez, M.T.; Ibáñez, J.G.; González, I. Construction of multicomponent Pourbaix diagrams using generalized species. *J. Electrochem. Soc.* **1991**, *138*, 365–371.
116. Newman, J.; Thmoas-Alyea, K.E. *Electrochemical Systems*, 3rd ed.; John Wiley & Sons: Hoboken, NJ, USA, 2004.
117. Husch, T.; Korth, M. Charting the known chemical space for non-aqueous lithium–air battery electrolyte solvents. *Phys. Chem. Chem. Phys.* **2015**, *17*, 22596–22603.
118. Chen, S.; Doolen, G.D. Lattice Boltzmann Method for Fluid Flows. *Annu. Rev. Fluid Mech.* **1998**, *30*, 329–364.
119. Trouette, B. Lattice Boltzmann simulations of a time-dependent natural convection problem. *Comput. Math. Appl.* **2013**, *66*, 1360–1371.
120. Aidun, C.K.; Clausen, J.R. Lattice-Boltzmann Method for Complex Flows. *Annu. Rev. Fluid Mech.* **2010**, *42*, 439–472.
121. Sukop, M.C.; Thorne, D.T. *Lattice Boltzmann Modeling*; Springer: Berlin, Germany, 2006; Volume 79, p. 016702.
122. He, X.; Li, N. Lattice Boltzmann simulation of electrochemical systems. *Comput. Phys. Commun.* **2000**, *129*, 158–166.
123. Niu, X.D.; Munekata, T.; Hyodo, S.A.; Suga, K. An investigation of water-gas transport processes in the gas-diffusion-layer of a PEM fuel cell by a multiphase multiple-relaxation-time lattice Boltzmann model. *J. Power Sources* **2007**, *172*, 542–552.
124. Hao, L.; Cheng, P. Lattice Boltzmann simulations of water transport in gas diffusion layer of a polymer electrolyte membrane fuel cell. *J. Power Sources* **2010**, *195*, 3870–3881.
125. Molaeimanesh, G.R.; Akbari, M.H. A three-dimensional pore-scale model of the cathode electrode in polymer-electrolyte membrane fuel cell by lattice Boltzmann method. *J. Power Sources* **2014**, *258*, 89–97.
126. Kim, K.N.; Kang, J.H.; Lee, S.G.; Nam, J.H.; Kim, C.J. Lattice Boltzmann simulation of liquid water transport in microporous and gas diffusion layers of polymer electrolyte membrane fuel cells. *J. Power Sources* **2015**, *278*, 703–717.
127. Ostadi, H.; Rama, P.; Liu, Y.; Chen, R.; Zhang, X.X.; Jiang, K. 3D reconstruction of a gas diffusion layer and a microporous layer. *J. Membr. Sci.* **2010**, *351*, 69–74.
128. Danner, T.; Eswara, S.; Schulz, V.P.; Latz, A. Characterization of gas diffusion electrodes for metal-air batteries. *J. Power Sources* **2016**, *324*, 646–656.
129. Sunu, W.G.; Bennion, D.N. Transient and Failure Analyses of the Porous Zinc Electrode. *J. Electrochem. Soc.* **1980**, *127*, 2007–2016.
130. Bockelmann, M.; Reining, L.; Kunz, U.; Turek, T. Electrochemical characterization and mathematical modeling of zinc passivation in alkaline solutions: A review. *Electrochim. Acta* **2017**, *237*, 276–298.
131. Neidhardt, J.P.; Fronczek, D.N.; Jahnke, T.; Danner, T.; Horstmann, B.; Bessler, W.G. A Flexible Framework for Modeling Multiple Solid, Liquid and Gaseous Phases in Batteries and Fuel Cells. *J. Electrochem. Soc.* **2012**, *159*, A1528–A1542.
132. Hein, S.; Latz, A. Influence of local lithium metal deposition in 3D microstructures on local and global behavior of Lithium-ion batteries. *Electrochim. Acta* **2016**, *201*, 354–365.
133. Hein, S.; Feinauer, J.; Westhoff, D.; Manke, I.; Schmidt, V.; Latz, A. Stochastic microstructure modeling and electrochemical simulation of lithium-ion cell anodes in 3D. *J. Power Sources* **2016**, *336*, 161–171.
134. Latz, A.; Zausch, J. Thermodynamic consistent transport theory of Li-ion batteries. *J. Power Sources* **2011**, *196*, 3296–3302.

135. Mao, Z.; White, R.E. Mathematical modeling of a primary zinc/air battery. *J. Electrochem. Soc.* **1992**, *139*, 1105–1114.
136. Deiss, E.; Holzer, F.; Haas, O. Modeling of an electrically rechargeable alkaline Zn-air battery. *Electrochim. Acta* **2002**, *47*, 3995–4010.
137. Andrei, P.; Zheng, J.P.; Hendrickson, M.; Plichta, E.J. Some Possible Approaches for Improving the Energy Density of Li-Air Batteries. *J. Electrochem. Soc.* **2010**, *157*, A1287–A1295
138. Schröder, D.; Krewer, U. Model based quantification of air-composition impact on secondary zinc air batteries. *Electrochim. Acta* **2014**, *117*, 541–553.
139. Arlt, T.; Schröder, D.; Krewer, U.; Manke, I. In operando monitoring of the state of charge and species distribution in zinc air batteries using X-ray tomography and model-based simulations. *Phys. Chem. Chem. Phys.* **2014**, *16*, 22273–22280.
140. Xue, K.H.; Nguyen, T.K.; Franco, A.A. Impact of the Cathode Microstructure on the Discharge Performance of Lithium Air Batteries: A Multiscale Model. *J. Electrochem. Soc.* **2014**, *161*, E3028–E3035.
141. Grübl, D.; Bessler, W.G. Cell design concepts for aqueous lithium-oxygen batteries: A model-based assessment. *J. Power Sources* **2015**, *297*, 481–491.
142. Yin, Y.; Gaya, C.; Torayev, A.; Thangavel, V.; Franco, A.A. Impact of Li_2O_2 Particle Size on Li-O_2 Battery Charge Process: Insights from a Multiscale Modeling Perspective. *J. Phys. Chem. Lett.* **2016**, *7*, 3897–3902.
143. Bazant, M.Z. Theory of chemical kinetics and charge transfer based on nonequilibrium thermodynamics. *Acc. Chem. Res.* **2013**, *46*, 1144–1160.
144. Latz, A.; Zausch, J. Thermodynamic derivation of a Butler-Volmer model for intercalation in Li-ion batteries. *Electrochim. Acta* **2013**, *110*, 358–362.
145. Breiter, M. Dissolution and passivation of vertical porous zinc electrodes in alkaline solution. *Electrochim. Acta* **1970**, *15*, 1297–1304.
146. Bai, P.; Bazant, M.Z. Charge transfer kinetics at the solid-solid interface in porous electrodes. *Nat. Commun.* **2014**, *5*, 1–13.
147. Zeng, Y.; Smith, R.B.; Bai, P.; Bazant, M.Z. Simple formula for Marcus-Hush-Chidsey kinetics. *J. Electroanal. Chem.* **2014**, *735*, 77–83.
148. Zeng, Y.; Bai, P.; Smith, R.B.; Bazant, M.Z. Simple formula for asymmetric Marcus-Hush kinetics. *J. Electroanal. Chem.* **2015**, *748*, 52–57.
149. Melander, M.; Jónsson, E.O.; Mortensen, J.J.; Vegge, T.; García Lastra, J.M. Implementation of Constrained DFT for Computing Charge Transfer Rates within the Projector Augmented Wave Method. *J. Chem. Theory Comput.* **2016**, *12*, 5367–5378.
150. Yuan, J.; Yu, J.S.; Sunden, B. Review on mechanisms and continuum models of multi-phase transport phenomena in porous structures of non-aqueous Li-Air batteries. *J. Power Sources* **2015**, *278*, 352–369.
151. Andersen, C.P.; Hu, H.; Qiu, G.; Kalra, V.; Sun, Y. Pore-Scale Transport Resolved Model Incorporating Cathode Microstructure and Peroxide Growth in Lithium-Air Batteries. *J. Electrochem. Soc.* **2015**, *162*, A1135–A1145.
152. Monroe, C.W.; Delacourt, C. Continuum transport laws for locally non-neutral concentrated electrolytes. *Electrochim. Acta* **2013**, *114*, 649–657.
153. Latz, A.; Zausch, J. Multiscale modeling of lithium ion batteries: Thermal aspects. *Beilstein J. Nanotechnol.* **2015**, *6*, 987–1007.
154. Xue, K.H.; McTurk, E.; Johnson, L.; Bruce, P.G.; Franco, A.A. A Comprehensive Model for Non-Aqueous Lithium Air Batteries Involving Different Reaction Mechanisms. *J. Electrochem. Soc.* **2015**, *162*, A614–A621.
155. Grübl, D.; Bergner, B.; Schröder, D.; Janek, J.; Bessler, W.G. Multistep Reaction Mechanisms in Nonaqueous Lithium-Oxygen Batteries with Redox Mediator: A Model-Based Study. *J. Phys. Chem. C* **2016**, *120*, 24623–24636.

Appendix C

Publications on electrochemical surfaces

- D. Eberle and B. Horstmann. Oxygen Reduction on Pt(111) in Aqueous Electrolyte: Elementary Kinetic Modeling. *Electrochimica Acta* **137**, 714–720 (2014).
- V. Hoffmann, G. Pulletikurthi, T. Carstens, A. Lahiri, A. Borodin, M. Schammer, B. Horstmann, A. Latz and F. Endres. Influence of a Silver Salt on the Nanostructure of an Au(111) Ionic Liquid Interface: an Atomic Force Microscopy Study and Theoretical Concepts. *Physical Chemistry Chemical Physics* **20**, 4760–4771 (2018).
- B. Horstmann, B. Gallant, R. Mitchell, W. G. Bessler, Y. Shao-Horn and M. Z. Bazant. Rate-Dependent Morphology of Li2O2 Growth in Li-O2 Batteries. *The Journal of Physical Chemistry Letters* **4**, 4217–4222 (2013).
- F. Single, B. Horstmann and A. Latz. Dynamics and morphology of solid electrolyte interphase (SEI). *Physical Chemistry Chemical Physics* **18**, 17810–17814 (2016).
- F. Single, B. Horstmann and A. Latz. Revealing SEI Morphology: In-Depth Analysis of a Modeling Approach. *Journal of The Electrochemical Society* **164**, E3132–E3145 (2017).
- F. Single, A. Latz and B. Horstmann. Identifying the Mechanism of Continued Growth of the Solid-Electrolyte Interphase. *ChemSusChem* **11**, 1950–1955 (2018).

D. Eberle and B. Horstmann. Oxygen Reduction on Pt(111) in Aqueous Electrolyte: Elementary Kinetic Modeling. *Electrochimica Acta* **137**, 714–720 (2014).

Electrochimica Acta 137 (2014) 714–720

Contents lists available at ScienceDirect

Electrochimica Acta

journal homepage: www.elsevier.com/locate/electacta

Oxygen Reduction on Pt(111) in Aqueous Electrolyte: Elementary Kinetic Modeling

Daniel Eberle[a,b], Birger Horstmann[a,b,c,*]

[a] German Aerospace Center (DLR), Institute of Technical Thermodynamics, Pfaffenwaldring 38-40, 70569 Stuttgart, Germany
[b] Institute of Thermodynamics and Thermal Engineering (ITW), Stuttgart University, 70569 Stuttgart, Germany
[c] Helmholtz Institute Ulm (HIU), Albert-Einstein Allee 11, 89069 Ulm, Germany

ARTICLE INFO

Article history:
Received 29 April 2014
Received in revised form 28 May 2014
Accepted 28 May 2014
Available online 5 June 2014

Keywords:
Oxygen reduction reaction
Pt(111) surface
Elementary kinetics model
Tafel slope

ABSTRACT

Oxygen reduction is central to electrochemical energy storage in a carbon-neutral energy system, *e.g.*, in fuel cells or metal-air batteries. In this paper we discuss the kinetics of the oxygen reduction reaction in acidic media via mean-field modeling of surface adsorbents. We put a special focus on the importance of interactions between adsorbents. Our study is based on detailed ab-initio simulations of thermodynamic and kinetic parameters on the Pt(111) surface. The oxygen dissociation and the hydroperoxyl dissociation pathway are found to determine the overall reaction kinetics and to result in the double Tafel slope on Pt(111).

1. Introduction

The oxygen reduction reaction (ORR) is fundamental to many technologies, *e.g.*, oxygen sensors, fuel cells, and metal-oxygen batteries [1]. Various fuel cell designs, *e.g.*, solid-oxide fuel cells, polymer electrolyte fuel cells, and alkaline fuel cells, were driving investigations on the ORR in the last decades [2]. While fuel cells are frequently used in military and aeronautics [3], they have not yet achieved widespread use for energy storage. Today metal-oxygen batteries, especially lithium-oxygen batteries, are attributed an important role for developing a carbon neutral energy system [4–13].

During the ORR

$$O_2 + 4H^+ + 4e^- \rightleftharpoons 2H_2O, \quad (1)$$

the oxygen molecule is reduced to two water molecules via the transfer of four protons and four electrons. The potential of the ORR relative to the reversible hydrogen electrode is 1.23V [1]. Alternatively, the reduction can be incomplete. In this case, two electrons are transferred resulting in production of hydrogen peroxide. Even for complete reduction to H_2O, overpotentials of 0.3V are typically observed [14–16]. We want to develop a detailed understanding of the reaction mechanism here. The development of improved ORR catalysts would benefit from such an understanding.

In this article, we model the coverage of transition metal surfaces during ORR in a mean-field approach, *i.e.*, with continuum equations. Continuum models bridge the gap between microscopic quantum theories and macroscopic electrochemical measurements. They generate understanding of a variety of emergent phenomena in batteries. Lithium-oxygen batteries are limited by transport in the electrolyte [17,18] or by crystallization processes [12,13,19–21], lithium-sulfur batteries suffer from self-discharge [22,23], lithium ion battery performance is determined by a variety of dynamically interacting phases [24–30], and fuel cells require fast supply with reactants [31,17,32].

Mean-field elementary kinetics models rely on binding energies of reactants and intermediates on catalyst surfaces in electrochemical environments. These can be determined by quantum models, *i.e.*, density functional theory (DFT) [33–42]. At low enough rates, the relative position of the free energies of the reactants and reaction intermediates completely determines the catalytic activities [36,38]. At higher rates, however, detailed kinetic modeling is necessary to account for varying surface coverages. Wang et al. [43] performed such elementary kinetics modeling for the ORR via mean-field theory of surface adsorbates. This study adjusts the model parameters to reproduce experimental results. Further insight into reaction mechanisms, however, requires models based on ab-initio simulations [44]. A detailed elementary kinetics study of the ORR based on parameters from density functional theory was

* Corresponding author. Tel.: +07315034007
E-mail address: birger.horstmann@dlr.de (B. Horstmann).

http://dx.doi.org/10.1016/j.electacta.2014.05.144
0013-4686/

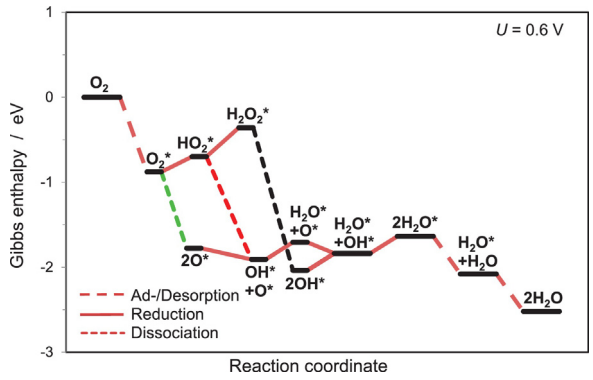

Fig. 1. Three reaction pathways of the ORR (OO (green line), OOH (red line) and HOOH (black line) pathway) at a cell voltage of 0.6 V. The energies include interactions between surface adsorbents.

performed by Jinnouchi et al. [45]. It achieves very good agreement with measurements at large voltages despite some approximations in the reaction mechanism. Beyond mean-field theory, kinetic Monte Carlo was applied to this problem [44,46].

In this paper we discuss a mean-field model of the ORR based on the detailed reaction mechanism proposed by Jacob et al. [36,37]. We highlight that we must take into account interactions among surface adsorbents to yield reasonable predictions. Jacob et al. [36,37] study the ORR in acid aqueous electrolyte on Pt(111), the standard catalyst surface. They conducted detailed computations based on DFT, including three reaction pathways and seven surface species, calculating the corresponding free energies as well as reaction barriers. We illustrate the three reaction pathways [36,37]

1. Oxygen dissociation (OO)
2. Hydroperoxyl dissociation (OOH)
3. Hydrogen peroxide dissociation (HOOH)

in fig. 1. In the OO reaction pathway, adsorbed molecular oxygen O_2^* dissociates into two O*. Then four protons/electrons are transferred, producing two water molecules. In the OOH reaction pathway, adsorbed molecular O_2^* is first reduced to HO_2^*, before dissociating into HO* and O*. Consecutively, HO* and O* are further reduced to two water molecules. In the HOOH reaction pathway, molecular adsorbed oxygen is reduced twice to $H_2O_2^*$. $H_2O_2^*$ can desorb, leading to incomplete reduction of oxygen, or dissociate into two OH*, producing two water molecules via two proton/electron-transfers. For each proton/electron transfer (reduction step) Jacob et al. [36,37] consider Langmuir-Hinshelwood reaction steps (LH), in which protons adsorb on the surface as neutral H* before reducing O*, HO*, HO_2^*, or $H_2O_2^*$, and Eley-Rideal reaction steps (ER), in which dissolved protons reduce O*, HO*, HO_2^*, or $H_2O_2^*$ directly.

In Section 2 we describe our thermodynamically consistent mean-field model and in Section 3 we discuss our choice of parameters. Then we apply it to simulate the activity of the ORR on Pt(111) in Section 4. We describe how we manipulate the thermodynamic and kinetic parameters from Jacob et al. [36,37] and how we add repulsive interactions between surface adsorbents. Our analysis explains the change in the Tafel slope of the ORR via an altered reaction pathway and illustrates the importance of interactions between adsorbents.

2. Model

We determine reaction rates by the mass action law

$$\dot{s}_i = k_i^{\mathrm{f}} \prod_{j\in\text{educts}} a_j^{-\nu_{i,j}} - k_i^{\mathrm{b}} \prod_{j\in\text{products}} a_j^{\nu_{i,j}} \tag{2}$$

Table 1
Activation energies $A_i^{\mathrm{f,act}}$ and symmetry factors α_i for elementary reactions

No.	Reaction	$A_i^{\mathrm{f,act}}$/eV	α_i
1.	$O_2 + 2* \rightleftharpoons O_2^*$	0.00	-
2.	$H^+ + e^- + * \rightleftharpoons H^*$	0.30	0.50
3.	$O_2^* + H^+ + e^- \rightleftharpoons HO_2^*$	0.30	0.69
4.	$HO_2^* + H^+ + e^- \rightleftharpoons H_2O_2^*$	0.30	0.70
5.	$O^* + H^+ + e^- \rightleftharpoons HO^*$	0.30	0.46
6.	$HO^* + H^+ + e^- \rightleftharpoons H_2O^*$	0.30	0.56
7.	$O_2^* + H^* \rightleftharpoons HO_2^* + *$	1.11	-
8.	$HO_2^* + H^* \rightleftharpoons H_2O_2^* + *$	1.48	-
9.	$O^* + H^* \rightleftharpoons HO^* + *$	1.22	-
10.	$HO^* + H^* \rightleftharpoons H_2O^* + *$	1.29	-
11.	$O_2^* \rightleftharpoons 2O^*$	0.68	-
12.	$HO_2^* \rightleftharpoons O^* + HO^*$	0.59	-
13.	$H_2O_2^* \rightleftharpoons 2HO^*$	0.31	-
14.	$H_2O + * \rightleftharpoons H_2O^*$	0.00	-

with the stochiometric coefficients $\nu_{i,j}$ and the activities a_j for the reactions in Table 1. We emphasize that reaction equations based on activities are thermodynamically consistent [24]. Some studies use concentrations instead, which might result in inconsistent physical units [45].

We apply a modified Arrhenius ansatz [31,17] based on transition state theory [47] to calculate the forward reaction rate constants k_i^{f}

$$k_i^{\mathrm{f}} = \frac{k_{\mathrm{B}}T}{h} \exp\left(-\frac{A_i^{\mathrm{f,act}}}{RT}\right) \exp\left(-\frac{\alpha_i z F U}{RT}\right) = k_i^{\mathrm{f},0} \exp\left(-\frac{\alpha_i z F U}{RT}\right). \tag{3}$$

The potential dependent reaction barriers consist of the activation energies $A_i^{\mathrm{f,act}}$ and the electric contribution for charge transfer reactions. The electric contribution is determined by the potential difference between electrode and electrolyte, *i.e.*, the (half-)cell voltage U, the symmetry factors α_i, and the transferred charge z. The attempt frequency $\frac{k_{\mathrm{B}}T}{h}$ is estimated with Boltzmann constant k_{B}, Planck constant h, and temperature $T = 298.15$ K.

The standard backward reaction rate constant $k_i^{\mathrm{b},0}$ follows from thermodynamic consistency, *i.e.*, the de Donder relations,

$$k_i^{\mathrm{b},0} = k_i^{\mathrm{f},0} \exp\left(-\frac{\sum_{j\in\text{products}} \nu_{i,j}\mu_j^{\mathrm{s}} + \sum_{j\in\text{educts}} \nu_{i,j}\mu_j^{\mathrm{s}}}{RT}\right) \tag{4}$$

with the standard chemical potentials μ_j^{s} [31]. The chemical potentials

$$\mu_j = \mu_j^{\mathrm{s}} + RT \ln a_j \tag{5}$$

consist of the standard chemical potentials μ_j^{s} and the Nernst expressions $RT \ln a_j$. We take into account interactions between surface adsorbents, which are essential for a realistic model, and adjust the standard chemical potentials μ_j^{s}

$$\mu_j = \mu_j^0 + \mu_j^{\mathrm{I}} + RT \ln a_j, \tag{6}$$

by introducing the interaction chemical potentials μ_j^{I}.

The interaction energy between adsorbents is a generally highly non-linear function of all activities. In the absence of sufficiently detailed ab-initio studies on the interaction energies, we choose the simplest possible model here. We restrict ourselves to the pairwise interaction of adsorbents on neighbouring surface sites. In this case, the interaction energy density (per surface area) is quadratic in the adsorbent concentration

$$G^{\mathrm{I}} = \frac{n}{2} \sum_{jk} E_{jk}^{\mathrm{I}} \frac{c_{j,\mathrm{surf}} \cdot c_{k,\mathrm{surf}}}{\Gamma_{\mathrm{surf}}}, \tag{7}$$

where E^{I}_{jk} is the interaction energy between surface species j and k, $c_{j,\mathrm{surf}}$ is the surface concentration of species j, and Γ_{surf} is the surface site density. A quadratic interaction could potentially include renormalied higher order interactions. We do not distinguish between fcc and hcc sites. $n=6$ is the coordination number on a hexagonal lattice, *i.e.*, the number of nearest-neighbours. The chemical potential of interactions follows by derivation

$$\mu^{\mathrm{I}}_j = \frac{\partial G^{\mathrm{I}}}{\partial c_{\mathrm{j,surf}}} = n\sum_k E^{\mathrm{I}}_{jk}\frac{c_{k,\,\mathrm{surf}}}{\Gamma_{\mathrm{surf}}} \tag{8}$$

A complete and consistent determination of all interaction energies E^{I}_{jk} is not available. Therefore, we estimate E^{I}_{jk} based on simple assumptions as discussed below. More accurate interaction chemical potentials though desirable are beyond the scope of this paper because they would require exhaustive DFT calculations.

Dynamics of surface coverages $\theta_j = c_{j,\mathrm{surf}}\sigma_j\Gamma_{\mathrm{surf}}$ are governed by

$$\frac{\mathrm{d}\theta_j}{\mathrm{d}t} = \sigma_j \sum_{i\in\mathrm{reaction}} \nu_{i,j}\dot{s}_i, \tag{9}$$

where σ_j is the number of surface sites occupied by species j and Γ_{surf} is the surface site density [31]. In our mean-field treatment, the large molecules O^*_2, HO^*_2 and $H_2O^*_2$ occupy two surface sites, and the small molecules H_2O^*, O^*, HO^* and H^* occupy one surface site.

The electric current density is determined by the charge-transfer reactions (see Table 1).

$$I = F\Gamma_{\mathrm{surf}}(\dot{s}_2 + \dot{s}_3 + \dot{s}_4 + \dot{s}_5 + \dot{s}_6). \tag{10}$$

In this article, we study aqueous solutions with pH=0 and an oxygen gas at atmospheric pressure. In agreement with the standard definitions, we set the corresponding activities to unity $a_{\mathrm{O_2}} = a_{\mathrm{H^+}} = a_{\mathrm{H_2O}} = 1$. For surface species we define activities via surface coverages $a_j = \theta_j$. We emphasize that the choice of activities is somewhat arbitrary and strongly influences the reaction rates of the model. This highlights the necessity to develop detailed ab-initio calculations of the attempt frequency (see Eq. 3) for a specific definition of the activities (see Eq. 2).

We use the software tool Cantera to evaluate the reaction rates (see Eq. 2) [47]. Our in-house software DENIS (Detailed Electrochemistry and Numerical Impedance Simulation) sets up the computation [31]. LIMEX is used to solve for the steady state of the system of algebraic equations in Eq. 9 [48], *i.e.*,

$$\frac{\mathrm{d}\theta_j}{\mathrm{d}t} = 0. \tag{11}$$

3. Parameters

Platinum is an excellent catalyst for the ORR. The low index surfaces of platinum are ideally suited as model system to study the ORR, both experimentally and theoretically [14–16,36,37]. In this section we will discuss the ORR on the Pt(111) surface based on the ab-initio study of Jacob et al. [36,37]. We calculate the thermodynamic and kinetic parameters of our model from these results of DFT.

Jacob et al. [36,37] performed detailed DFT simulations for acidic aqueous electrolyte at $T=298$ K and determined the chemical potentials of the surface species O^*_2, HO^*_2, $H_2O^*_2$, H_2O^*, O^*, HO^*, and H^*. The chemical potentials of gaseous O_2 and H_2 as well as of empty surface sites are zero by definition. Jacob et al. [36,37] calculated the chemical potential of H_2O as −4.57 eV. This number sets the open circuit voltage to $\frac{4.57}{4}\,\mathrm{V} = 1.14\,\mathrm{V}$. In contrast, the experimentally observed open circuit voltage is 1.23 V. This discrepancy is caused by the electron configuration of molecular oxygen which is difficult to capture in DFT calculations. In order to model the experimentally observed open circuit voltage, we shift the binding free energies of all oxygen containing species O^*_2, HO^*_2, $H_2O^*_2$, H_2O^*, O^*, and HO^* accordingly. This results in the chemical potentials −1.69 eV, −2.11 eV, −2.37 eV, −2.83 eV, −1.70 eV, and −2.43 eV, respectively (see Table 2).

Table 2
Chemical potentials of O^*_2, O^*, HO^*, HO^*_2, $H_2O^*_2$, H_2O^*, and H^* on Pt(111).

Species	O^*_2	O^*	HO^*	HO^*_2	$H_2O^*_2$	H_2O^*	H^*
μ/eV	−1.69	−1.70	−2.43	−2.11	−2.37	−2.83	−0.96

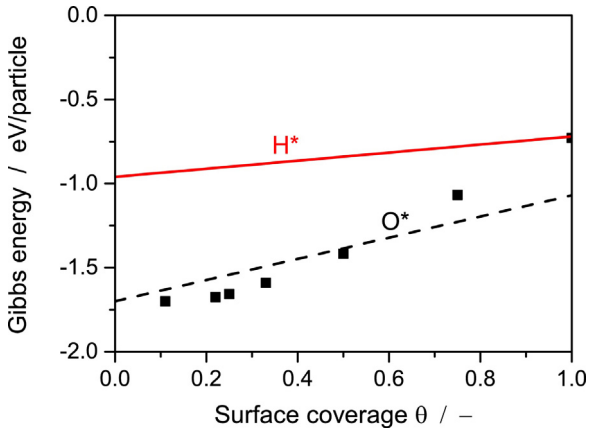

Fig. 2. Coverage dependent Gibbs energies $G_{\mathrm{O^*}} = \mu^0_{\mathrm{O^*}} + \frac{z}{2}E^{\mathrm{I}}_{\mathrm{O^*}}\theta_{\mathrm{O^*}}$ for surfaces containing only O^* (red line) and $G_{\mathrm{H^*}} = \mu^0_{\mathrm{H^*}} + \frac{z}{2}E^{\mathrm{I}}_{\mathrm{H^*}}\theta_{\mathrm{H^*}}$ for surfaces containing only H^* (black dashed line), where $E^{\mathrm{I}}_{\mathrm{O^*}} = 0.21$ eV [49] and $E^{\mathrm{I}}_{\mathrm{O^*}} = 0.08$ eV [50]. The black dots represent the coverage dependent energies calculated by Légaré [49]. Note that these Gibbs energies deviate from the corresponding standard chemical potentials, *e.g.*, $\mu^{\mathrm{s}}_{\mathrm{O^*}} = \mu^0_{\mathrm{O^*}} + zE^{\mathrm{I}}_{\mathrm{O^*}}\theta_{\mathrm{O^*}}$

In this paper, we take into account interactions between surface adsorbents. These contribute significantly to the overall chemical potentials (see Eq. 8). From Jacob et al. [34] and Légaré [49] we estimate $E^{\mathrm{I}}_{\mathrm{O^*}} = 0.21$ eV per interaction between oxygen atoms O^* adsorbed on Pt(111). We use this interaction free energy for the interaction among all surface species except for H^* (see Eq. 6). For interactions containing H^*, we use $E^{\mathrm{I}}_{\mathrm{H^*}} = 0.08$ eV [50]. We discuss the validity of this approximation based on simulations below. Our choice results in corrections to the chemical potentials. If the surface is completely covered with species occupying two surface sites (O^*_2, HO^*_2, and $H_2O^*_2$), $\mu^{\mathrm{I}}_j = 0.63$ eV. If the surface is completely covered with small species (O^*, HO^*, H_2O^*), $\mu^{\mathrm{I}}_j = 1.26$ eV. We illustrate this coverage dependence of free energies in fig. 2.

Reaction kinetics is determined by activation energies (see Eq. 3). The values from Jacob et al. [36,37] are summarized in Table 1. Jacob et al. [36,37] calculate the dependence of the activation energies on the electrolyte potential for ER proton transfer reactions $O^* \to HO^*$, $HO^* \to H_2O^*$, $O^*_2 \to HO^*_2$, and $HO^*_2 \to H_2O^*_2$. We encode this dependence in the symmetry factors α_i (see Eq. 3). LH reactions require adsorbed hydrogen H^*. We assume the activation energy $A^{\mathrm{f,act}} = 0.30$ eV and the symmetry factor $\alpha = 0.50$ for the transfer of protons to the surface $* \to H^*$ [36,37].

4. Results and discussion

In fig. 3 we depict the simulated polarization curve. We observe three regimes. For high cell voltages ($U > 0.7$ V) the Tafel slope 38 mV/decade is low, at intermediate cell voltages ($0.7\,\mathrm{V} > U > 0.2\,\mathrm{V}$) the Tafel slope 131 mV/decade is high, and at low cell voltages $U < 0.2$ V the current decreases again. At high cell voltages, ORR rates clearly follow a Tafel law. The Tafel slope at intermediate

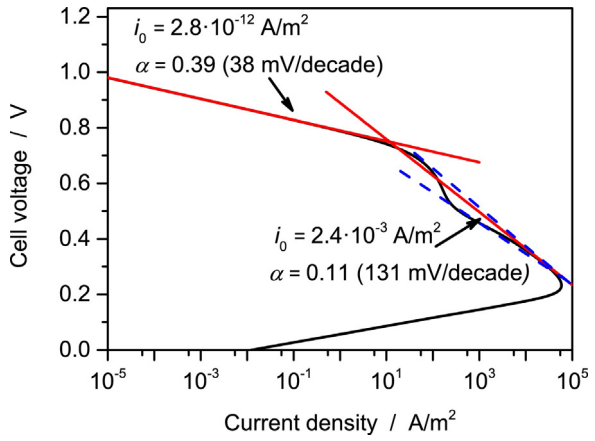

Fig. 3. Polarization curve from elementary kinetic modeling on Pt(111) in acidic electrolyte. We observe a change in Tafel slope at $U = 0.7$ V signalling a change in reaction mechanism. The red lines represent Tafel slopes at high and intermediate cell voltages fitted to the polarization curve. The blue dashed lines demonstrate the measurement uncertainty for the Tafel slope at intermediate cell voltages (see text). Below $U = 0.2$ V, the reaction rate decreases due to surface blocking by H*.

cell voltages, however, is difficult to measure, but lies in the range 110 . . . 140 mV/decade.

The general trend in Tafel slopes agrees with rotating-ring disc experiments on single-crystalline Pt(111) surfaces [14–16], where the Tafel slopes 60 mV/decade and 120 mV/decade were measured at high and low cell voltages, respectively. The absolute values of the overpotentials, however, are approximately 100 mV lower in our model than in experiments. This discrepancy might result from the relatively large activation barriers calculated by Jacob et al. [36,37] and our rough approximation for the attempt frequency $k_i^{f,0}$.

Our modeling explains these trends in reaction activity. First, we analyse the rates of the three dissociation reactions in fig. 4. These rates represent the three reaction mechanisms OO, OOH, and HOOH. They increase exponentially with decreasing cell voltage above $U = 0.2$ V. Below $U = 0.2$ V, the rates collapse, reminiscent of the trends in current density. At high cell voltages the OO pathway is dominating, at low cell voltages the OOH and HOOH pathways [36–38]. Therefore, we attribute the low Tafel slope to the OO mechanism and the large Tafel slope to the OOH/HOOH mechanisms. This transition in reaction mechanism can be rationalized on the basis of the free energies of reaction intermediates (see fig. 1). We

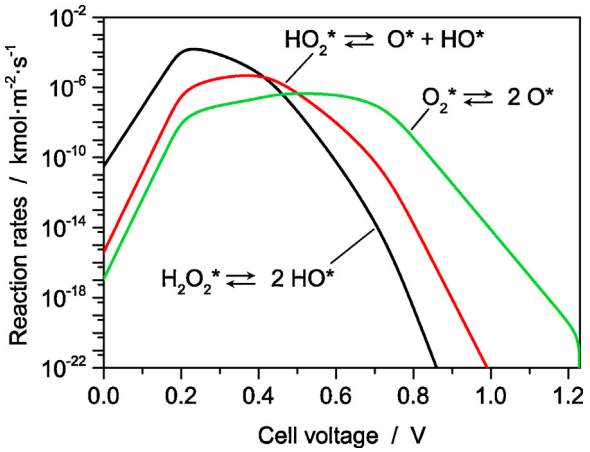

Fig. 4. Dissociation rates of the surface species O_2^*, HO_2^*, and $H_2O_2^*$, representative for the three reaction pathways, over the cell voltage from elementary kinetics simulations. The OO reaction mechanism dominates at large cell voltages, the OOH/HOOH mechanisms at low cell voltages.

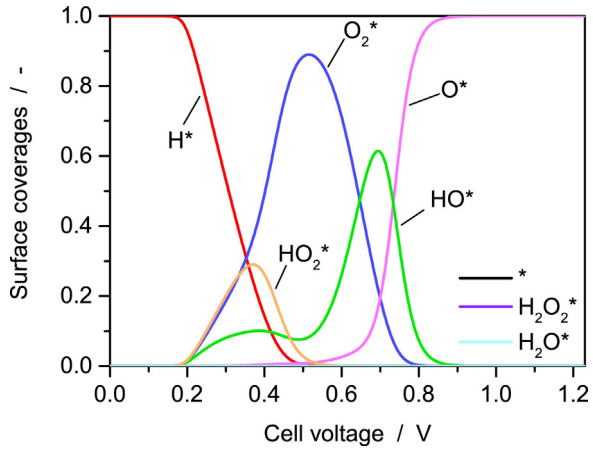

Fig. 5. Coverages of the surface species over the cell voltage from elementary kinetics simulations. The surface is blocked by H* at low cell voltages and by O* at high cell voltages.

observe that at low overpotentials protonization of HO_2^* and $H_2O_2^*$ is thermodynamically unfavoured, in contrast to protonization of O*.

In fig. 5 we show the coverage of surface species. O* completely covers the surface at high cell voltages $U > 0.8$ V, whereas H* covers it at low cell potentials $U < 0.2$ V. We conclude that strongly adsorbed H* inhibits the ORR at low cell voltages. This was suggested by experiments previously [14,16]. The change in reaction mechanism and the surface blocking of H* adsorbents is reflected in the rates of the protonization reactions in fig. 6, too. We note that the ER reaction rates are more than ten orders of magnitude larger than the LH reaction rates. Thus, the ORR mainly proceeds via ER reaction steps which have significantly lower activation barriers than the LH steps [36,37].

The simulated O* surface blocking at high cell voltages demonstrates the limitations of our simple model for adsorbent-adsorbent interactions (see Eq. 6 and 7). Typically, it is believed that HO* covers the surface at these potentials based on two sets of experiments: 1. Crystalline hydrogen bonded networks of HO* and H_2O^* were observed at extremely low temperatures and pressures via microscopy [51]. 2. Improved activity of the ORR was attributed to destabilization of HO* [39,52]. Calculations predict that directed hydrogen bonds mediate attractive adsorbent-adsorbent interactions and improve HO* binding energy [53,54]. The dynamics of HO* on surfaces in aqueous electrolyte at room temperature, however, are not yet fully understood. Furthermore, counting hydrogen

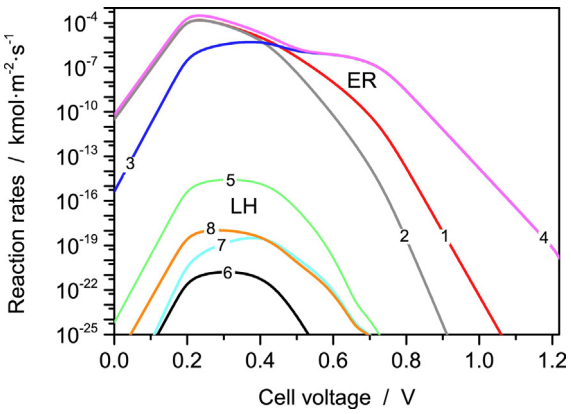

Fig. 6. Reaction rates of proton transfer steps; ER (1, 2, 3, and 4); LH (5, 6, 7 and 8); $O_2^* \rightarrow HO_2^*$ (1 and 5); $HO_2^* \rightarrow H_2O_2^*$ (2 and 6); $O^* \rightarrow HO^*$ (3 and 7); $HO^* \rightarrow H_2O^*$ (4 and 8). The reaction is following the ER steps over the whole potential range.

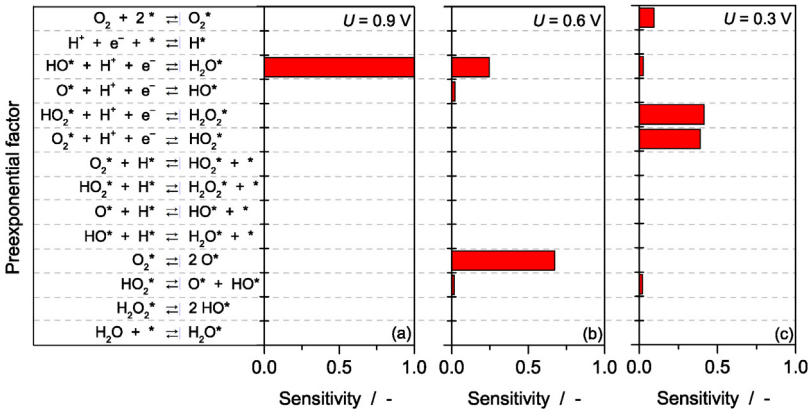

Fig. 7. Sensitivity analysis of current density at different cell voltages ((a) 0.9 V, (b) 0.6 V, (c) 0.3 V). We vary the preexponential factors of all reactions by 10%. The sensitivity of charge transfer reactions confirms our understanding of the reaction mechanisms.

bonds is non-trivial in presence of aqueous solutions and mixtures of adsorbents. Therefore, further research is necessary to improve our understanding of (attractive) hydrogen bonds on surfaces under realistic conditions in competition with other (repulsive) interactions [51].

Rate-limiting steps are determined by sensitivity analysis (see fig. 7). We evaluate the sensitivity

$$\dot{s}_i = \left| (\Delta I/I)/(\Delta k_i^{\mathrm{f},0}/k_i^{\mathrm{f},0}) \right| \tag{12}$$

at various cell voltages by varying the preexponential factors by +10%. This analysis of the reaction mechanism and the determination of rate-limiting steps suffice to predict the change in Tafel slopes observed in simulation (see fig. 3) and experiments [13]. For high cell voltages, the OO reaction pathway is dominant and the reaction $HO^* \rightarrow H_2O^*$ is rate-limiting. Since the remaining reactions are in equilibrium, the coverage of HO^* is in equilibrium

$$a_{\mathrm{HO}^*} \propto a_* \sqrt{a} \exp\left(-\frac{FU}{RT}\right). \tag{13}$$

Assuming that the reaction $O^* \rightarrow HO^*$ is in the Tafel regime, we estimate the current density with reaction 1 (see Table 1)

$$i \propto a_{\mathrm{HO}^*} \exp\left(-\frac{0.56FU}{RT}\right) \propto a_* \sqrt{a} \exp\left(-\frac{0.39zFU}{RT}\right) \tag{14}$$

with the carge number z = 4 and read off the symmetry factor $\alpha = 0.39$. This exactly matches the Tafel slope 38 mV/decade found in our simulation. At low cell voltages, the OOH/HOOH reaction pathway is dominant with the two rate-limiting reactions $O_2^* \rightarrow HO_2^*$ and $HO_2^* \rightarrow H_2O_2^*$. The mixture of reaction pathways and the existence of two rate-limiting steps complicate the analysis. Nevertheless, we present a rough estimate of the Tafel slope. If the coverage of O_2^* is in equilibrium, its coverage will be

$$a_{\mathrm{O}_2^*} \propto a_*^2 a_{\mathrm{O}_2}. \tag{15}$$

With the rough assumption that the reaction $O_2^* \rightarrow HO_2^*$ is in the Tafel regime, we estimate the current density (see Table 1)

$$i \propto a_{\mathrm{O}_2^*} \exp\left(-\frac{0.69FU}{RT}\right) \propto a_*^2 a_{\mathrm{O}_2} \exp\left(-\frac{0.17zFU}{RT}\right) \tag{16}$$

with the charge number z = 4 and read off the symmetry factor $\alpha = 0.17$, *i.e.*, the Tafel slope 87 mV/decade. In summary, we proof how the change in Tafel slope originates from the change in reaction mechanism.

The preceding analysis allows conclusions about the oxygen reaction order. It was measured that the oxygen reaction order of the ORR on Pt(111) is close to unity for all cell voltages [14,55].

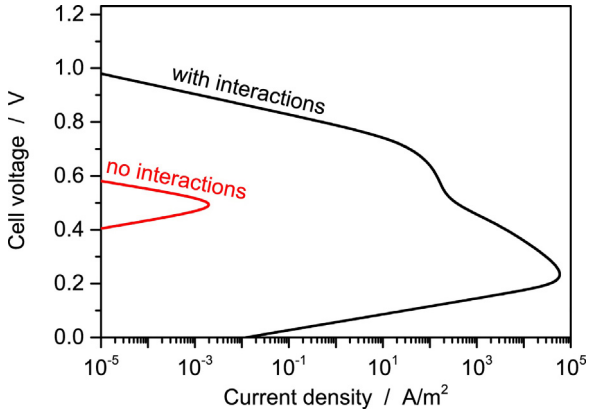

Fig. 8. Polarization curve from elementary kinetic modeling. The red line neglects adsorbent-adsorbent interactions, while the black line includes these interactions (see fig. 3). We conclude that interactions between adsorbents are necessary for an accurate description of the ORR.

At low and intermediate cell voltages, our simulations show rate-limiting O_2 dissociation and the OOH/HOOH mechanisms. In these cases, the oxygen reaction order unity is expected as demonstrated in Eq. 16. At high cell voltages, however, the oxygen reaction order for the OO mechanism expected from Eq. 14 is 0.5. Because the density of free surface sites $\theta_* = a_*$ decreases for increased oxygen partial pressure (see reactions 10-13 in Tabel 1), we find an even smaller oxygen reaction order close to zero. Note that Jinnouchi et al. [45] simulate realistic oxygen partial pressures, but neglect empty sites θ_*, which is thermodynamically inconsistent. We propose that detailed modeling of adsorbent-adsorbent interactions lowers effective binding energies and resolves this issue.

In fig. 8, we compare polarization curves for different interaction strengths between surface adsorbents. In the absence of repulsion, the ORR proceeds in a narrow voltage window around $U = 0.5$ V only. The current density is reduced by eight orders of magnitude, because oxygen atoms at low overpotentials and hydrogen atoms at high overpotentials bind very strongly to the surface and inhibit the ORR. The reaction can only proceed at optimal overpotentials. The strong dependence of ORR reaction kinetics on the adsorbent-adsorbent interactions emphasizes the need for detailed studies of the interactions among all surface adsorbents. These interactions are ignored in most studies, even though their importance is discussed in the literature [56].

5. Conclusion

In this article we discuss elementary kinetics modeling of the ORR on Pt(111). We implemented the detailed reaction mechanism on Pt(111) determined by Jacob et al. [36,37] which includes activation barriers as well as entropic and electrolyte corrections. Despite using mean-field theory, our simulations validate the change in reaction mechanism from OO to OOH/HOOH mechanisms. The associated change in Tafel slope is explained by a change in the rate determining steps. In our simulations, the surface is blocked with O* at low overpotentials and H* at large overpotentials. We emphasize that these properties are strongly affected by the coverage dependence of energies, *i.e.*, the interactions between adsorbents. Our knowledge of these interactions is not sufficient for confident theoretical predictions. Quantitative disagreements between model and experiments are also due to superficial understanding of reaction kinetics.

In summary, we have shown that mean-field theory is able to capture the basics of the ORR in acidic media based on DFT without any fitting parameter. More accurate predictions will require going beyond single particle physics both in static quantum calculations, i.e., DFT, and (semi-)classical dynamic calculations.

Acknowledgements

BH acknowledges funding from the German Federal Ministry of Education and Research (2011 BMBF 03X3624B). The authors thank Wolfgang G. Bessler, Timo Danner, and Arnulf Latz for fruitful discussions.

References

[1] K. Kinoshita, Electrochemical Oxygen Technology, Electrochemical Society Series, John Wiley & Sons, 1992.
[2] W. Vielstich, A. Lamm, H.A. Gasteiger (Eds.), Handbook of Fuel Cells: Fundamentals, Technlogy, Applications - Volume 4, Wiley-VCH, Weinheim, 2003.
[3] A.B. Stambouli, E. Traversa, Solid oxide fuel cells (SOFCs): a review of an environmentally clean and efficient source of energy, Renewable and Sustainable Energy Reviews 6 (5) (2002) 433, http://dx.doi.org/10.1016/S1364-0321(02)00014-X. http://linkinghub.elsevier.com/retrieve/pii/S136403210200014X
[4] G. Girishkumar, B. McCloskey, A.C. Luntz, S. Swanson, W. Wilcke, Lithium-Air Battery: Promise and Challenges, The Journal of Physical Chemistry Letters 1 (14) (2010) 2193, http://dx.doi.org/10.1021/jz1005384. http://pubs.acs.org/doi/abs/10.1021/jz1005384
[5] J. Christensen, P. Albertus, R.S. Sanchez-Carrera, T. Lohmann, B. Kozinsky, R. Liedtke, J. Ahmed, A. Kojic, A Critical Review of Li-Air Batteries, Journal of The Electrochemical Society 159 (2) (2012) R1, http://dx.doi.org/10.1149/2.086202jes. http://link.aip.org/link/JESOAN/v159/i2/pR1/s1&Agg=doi
[6] P.G. Bruce, S.A. Freunberger, L.J. Hardwick, J.-M. Tarascon, Li-O_2 and Li-S batteries with high energy storage, Nature Materials 11 (2012) 172, http://dx.doi.org/10.1038/NMAT3237. http://dx.doi.org/10.1038/nmat3237
[7] Y.-C. Lu, Y. Shao-Horn, Probing the Reaction Kinetics of the Charge Reactions of Nonaqueous Li–O_2 Batteries, The Journal of Physical Chemistry Letters 4 (2013) 93, http://dx.doi.org/10.1021/jz3018368. http://pubs.acs.org/doi/abs/10.1021/jz3018368
[8] P. Hartmann, C.L. Bender, M. Vračar, A.K. Dürr, A. Garsuch, J. Janek, P. Adelhelm, A rechargeable room-temperature sodium superoxide (NaO_2) battery, Nature Materials 12 (2013) 228, http://dx.doi.org/10.1038/nmat3486. http://dx.doi.org/10.1038/nmat3486
[9] P. Jakes, G. Cohn, Y. Ein-Eli, F. Scheiba, H. Ehrenberg, R.-A. Eichel, Limitation of discharge capacity and mechanisms of air-electrode deactivation in silicon-air batteries, ChemSusChem 5 (11) (2012) 2278, http://dx.doi.org/10.1002/cssc.201200199. http://www.ncbi.nlm.nih.gov/pubmed/23033259
[10] R.R. Mitchell, B.M. Gallant, Y. Shao-Horn, C.V. Thompson, Mechanisms of Morphological Evolution of Li_2O_2 Particles During Electrochemical Growth, The Journal of Physical Chemistry Letters 4 (2013) 1060, http://dx.doi.org/10.1021/jz4003586. http://dx.doi.org/10.1021/jz4003586
[11] B.M. Gallant, D.G. Kwabi, R.R. Mitchell, J. Zhou, C. Thompson, Y. Shao-Horn, Influence of Li_2O_2 morphology on oxygen reduction and evolution kinetics in Li-O_2 batteries, Energy & Environmental Science 6 (2013) 2518, http://dx.doi.org/10.1039/c3ee40998h. http://pubs.rsc.org/en/Content/ArticleLanding/2013/EE/c3ee40998h
[12] B. Horstmann, T. Danner, W.G. Bessler, Precipitation in aqueous lithium-oxygen batteries: a model-based analysis, Energy & Environmental Science 6 (4) (2013) 1299, http://dx.doi.org/10.1039/c3ee24299d. http://xlink.rsc.org/?DOI=c3ee24299d
[13] B. Horstmann, B. Gallant, R. Mitchell, W.G. Bessler, Y. Shao-Horn, M.Z. Bazant, Rate-Dependent Morphology of Li_2O_2 Growth in Li-O_2 Batteries, The Journal of Physical Chemistry Letters 4 (2013) 4217, http://dx.doi.org/10.1021/jz401973c. http://pubs.acs.org/doi/abs/10.1021/jz401973c
[14] N.M. Markovic, R. Adzic, B. Cahan, E. Yeager, Structural effects in electrocatalysis: oxygen reduction on platinum low index single-crystal surfaces in perchloric acid solutions, Journal of Electroanalytical Chemistry 377 (1994) 249, http://dx.doi.org/10.1016/0022-0728(94)03467-2. http://dx.doi.org/10.1016/0022-0728(94)03467-2
[15] F.E. Kadiri, R. Faure, R. Durand, Electrochemical reduction of molecular oxygen on platinum single crystals, Journal of Electroanalytical Chemistry 301 (1991) 177, http://dx.doi.org/10.1016/0022-0728(91)85468-5. http://dx.doi.org/10.1016/0022-0728(91)85468-5
[16] N.M. Markovic, H.A. Gasteiger, P.N. Ross, Oxygen Reduction on Platinum Low-Index Single-Crystal Surfaces in Sulfuric Acid Solution: Rotating Ring-Pt(hkl) Disk Studies, The Journal of Physical Chemistry 99 (11) (1995) 3411, http://dx.doi.org/10.1021/j100011a001. http://pubs.acs.org/doi/abs/10.1021/j100011a001
[17] J.P. Neidhardt, D.N. Fronczek, T. Jahnke, T. Danner, B. Horstmann, W.G. Bessler, A Flexible Framework for Modeling Multiple Solid, Liquid and Gaseous Phases in Batteries and Fuel Cells, Journal of The Electrochemical Society 159 (9) (2012) A1528, http://dx.doi.org/10.1149/2.023209jes. http://jes.ecsdl.org/cgi/doi/10.1149/2.023209jes
[18] P. Andrei, J.P. Zheng, M. Hendrickson, E.J. Plichta, Some Possible Approaches for Improving the Energy Density of Li-Air Batteries, Journal of The Electrochemical Society 157 (12) (2010) A1287, http://dx.doi.org/10.1149/1.3486114. http://link.aip.org/link/JESOAN/v157/i12/pA1287/s1&Agg=doi
[19] T. Danner, B. Horstmann, D. Wittmaier, N. Wagner, W.G. Bessler, Reaction and transport in Ag/Ag_2O gas diffusion electrodes of aqueous Li-O_2 batteries: Experiments and modeling, Journal of Power Sources 264 (2014) 320, http://dx.doi.org/10.1016/j.jpowsour.2014.03.149. http://linkinghub.elsevier.com/retrieve/pii/S0378775314005813
[20] P. Albertus, G. Girishkumar, B. McCloskey, R.S. Sanchez-Carrera, B. Kozinsky, J. Christensen, A.C. Luntz, Identifying Capacity Limitations in the Li/Oxygen Battery Using Experiments and Modeling, Journal of The Electrochemical Society 158 (3) (2011) A343, http://dx.doi.org/10.1149/1.3527055. http://link.aip.org/link/JESOAN/v158/i3/pA343/s1&Agg=doi
[21] V. Viswanathan, K.S. Thygesen, J.S. Hummelshøj, J.K. Nørskov, G. Girishkumar, B.D. McCloskey, A.C. Luntz, Electrical conductivity in Li_2O_2 and its role in determining capacity limitations in non-aqueous Li-O_2 batteries, The Journal of Chemical Physics 135 (21) (2011) 214704, http://dx.doi.org/10.1063/1.3663385. http://scitation.aip.org/content/aip/journal/jcp/135/21/10.1063/1.3663385
[22] A.F. Hofmann, D.N. Fronczek, W.G. Bessler, Mechanistic modeling of polysulfide shuttle and capacity loss in lithium-sulfur batteries, Journal of Power Sources 259 (2014) 300, http://dx.doi.org/10.1016/j.jpowsour.2014.02.082. http://dx.doi.org/10.1016/j.jpowsour.2014.02.082
[23] K. Kumaresan, Y. Mikhaylik, R.E. White, A Mathematical Model for a Lithium-Sulfur Cell, Journal of The Electrochemical Society 155 (8) (2008) A576, http://dx.doi.org/10.1149/1.2937304. http://jes.ecsdl.org/cgi/doi/10.1149/1.2937304
[24] M.Z. Bazant, Theory of Chemical Kinetics and Charge Transfer based on Nonequilibrium Thermodynamics, Accounts of Chemical Research 46 (2013) 1144, http://dx.doi.org/10.1021/ar300145c. http://pubs.acs.org/doi/abs/10.1021/ar300145c
[25] P. Bai, D.A. Cogswell, M.Z. Bazant, Suppression of Phase Separation in $LiFePO_4$ Nanoparticles During Battery Discharge, Nano Letters 11 (2011) 4890, http://dx.doi.org/10.1021/nl202764f. http://pubs.acs.org/doi/abs/10.1021/nl202764f
[26] T.R. Ferguson, M.Z. Bazant, Nonequilibrium Thermodynamics of Porous Electrodes, Journal of the Electrochemical Society 159 (12) (2012) A1967, http://dx.doi.org/10.1149/2.048212jes. http://jes.ecsdl.org/cgi/doi/10.1149/2.048212jes
[27] D.A. Cogswell, M.Z. Bazant, Coherency Strain and The Kinetics of Phase Separation in $LiFePO_4$ Nanoparticles, ACS Nano 6 (3) (2012) 2215, http://dx.doi.org/10.1021/nn204177u. http://pubs.acs.org/doi/abs/10.1021/nn204177u
[28] A. Latz, J. Zausch, Thermodynamic consistent transport theory of Li-ion batteries, Journal of Power Sources 196 (6) (2011) 3296, http://dx.doi.org/10.1016/j.jpowsour.2010.11.088. http://linkinghub.elsevier.com/retrieve/pii/S0378775310020793
[29] W. Dreyer, J. Jamnik, C. Guhlke, R. Huth, J. Moskon, M. Gaberscek, The thermodynamic origin of hysteresis in insertion batteries, Nature Materials 9 (5) (2010) 448, http://dx.doi.org/10.1038/nmat2730. http://www.nature.com/nmat/journal/v9/n5/full/nmat2730.html
[30] A. Latz, J. Zausch, Thermodynamic derivation of a Butler-Volmer model for intercalation in Li-ion batteries, Electrochimica Acta 110 (2013) 358, http://dx.doi.org/10.1016/j.electacta.2013.06.043. http://linkinghub.elsevier.com/retrieve/pii/S0013468613011493
[31] W. Bessler, S. Gewies, M. Vogler, A new framework for physically based modeling of solid oxide fuel cells, Electrochimica Acta 53

(4) (2007) 1782, http://dx.doi.org/10.1016/j.electacta.2007.08.030. http://linkinghub.elsevier.com/retrieve/pii/S0013468607010353
[32] V. Yurkiv, A. Gorski, W.G. Bessler, H.-R. Volpp, Density functional theory study of heterogeneous CO oxidation over an oxygen-enriched yttria-stabilized zirconia surface, Chemical Physics Letters 543 (2012) 213, http://dx.doi.org/10.1016/j.cplett.2012.06.057. http://linkinghub.elsevier.com/retrieve/pii/S0009261412007646
[33] T. Jacob, R.P. Muller, W.A. Goddard, Chemisorption of Atomic Oxygen on Pt(111) from DFT Studies of Pt-Clusters, The Journal of Physical Chemistry B 107 (35) (2003) 9465, http://dx.doi.org/10.1021/jp030716r. http://pubs.acs.org/doi/abs/10.1021/jp030716r
[34] T. Jacob, W.A. Goddard, Water Formation on Pt and Pt-Based Alloys: a Theoretical Description of a Catalytic Reaction, ChemPhysChem 7 (5) (2006) 992, http://dx.doi.org/10.1002/cphc.200500613. http://onlinelibrary.wiley.com/doi/10.1002/cphc.200500613/abstract;jsessionid=CA73AA61A4ECD73F506D7E8BA6AF7B8F.f03t04
[35] T. Jacob, The Mechanism of Forming H_2O from H_2 and O_2 over a Pt Catalyst via Direct Oxygen Reduction, Fuel Cells 6 (3-4) (2006) 159, http://dx.doi.org/10.1002/fuce.200500201. http://doi.wiley.com/10.1002/fuce.200500201
[36] J.A. Keith, T. Jacob, Theoretische Untersuchungen zu potentialabhängigen und konkurrierenden Mechanismen der elektrokatalytischen Sauerstoffreduktion an Pt(111), Angewandte Chemie 122 (49) (2010) 9711, http://dx.doi.org/10.1002/ange.201004794. http://doi.wiley.com/10.1002/ange.201004794
[37] J.A. Keith, G. Jerkiewicz, T. Jacob, Theoretical Investigations of the Oxygen Reduction Reaction on Pt(111), ChemPhysChem 11 (13) (2010) 2779, http://dx.doi.org/10.1002/cphc.201000286. http://www.ncbi.nlm.nih.gov/pubmed/20726030
[38] J.K. Nørskov, J. Rossmeisl, A. Logadottir, L. Lindqvist, Origin of the Overpotential for Oxygen Reduction at a Fuel-Cell Cathode, The Journal of Physical Chemistry B 108 (2004) 17886, http://dx.doi.org/10.1021/jp047349j. http://pubs.acs.org/doi/abs/10.1021/jp047349j
[39] V. Stamenkovic, B.S. Mun, K.J.J. Mayrhofer, P.N. Ross, N.M. Markovic, J. Rossmeisl, J. Greeley, J.K. Nørskov, Changing the Activity of Electrocatalysts for Oxygen Reduction by Tuning the Surface Electronic Structure, Angewandte Chemie (International ed. in English) 45 (18) (2006) 2897, http://dx.doi.org/10.1002/anie.200504386. http://onlinelibrary.wiley.com/doi/10.1002/anie.200504386/abstract
[40] Y. Sha, T.H. Yu, B.V. Merinov, W.A. Goddard, Prediction of the Dependence of the Fuel Cell Oxygen Reduction Reactions on Operating Voltage from DFT Calculations, The Journal of Physical Chemistry C 116 (10) (2012) 6166, http://dx.doi.org/10.1021/jp207526u. http://pubs.acs.org/doi/abs/10.1021/jp207526u
[41] J. Rossmeisl, V. Tripkovic, G.A. Tritsaris, F. Calle-Vallejo, Electro-Catalysis of Oxygen Reduction Reaction, ECS Transactions 33 (1) (2010) 43, http://dx.doi.org/10.1149/1.3484500. http://ecst.ecsdl.org/cgi/doi/10.1149/1.3484500
[42] D.C. Ford, A.U. Nilekar, Y. Xu, M. Mavrikakis, Partial and complete reduction of O_2 by hydrogen on transition metal surfaces, Surface Science 604 (19-20) (2010) 1565, http://dx.doi.org/10.1016/j.susc.2010.05.026. http://linkinghub.elsevier.com/retrieve/pii/S0039602810002281
[43] J.X. Wang, F. Uribe, T.E. Springer, J. Zhang, R.R. Adzic, Intrinsic Kinetic Equation for Oxygen Reduction Reaction in Acidic Media: The Double Tafel Slope and Fuel Cell Applications, Faraday Discussions 140 (2008) 347, http://dx.doi.org/10.1039/b814058h. http://xlink.rsc.org/?DOI=b814058h
[44] B. Temel, H. Meskine, K. Reuter, M. Scheffler, H. Metiu, Does phenomenological kinetics provide an adequate description of heterogeneous catalytic reactions? The Journal of Chemical Physics 126 (20) (2007) 204711, http://dx.doi.org/10.1063/1.2741556. http://scitation.aip.org/content/aip/journal/jcp/126/20/10.1063/1.2741556
[45] R. Jinnouchi, K. Kodama, T. Hatanaka, Y. Morimoto, First principles based mean field model for oxygen reduction reaction, Physical Chemistry Chemical Physics 13 (47) (2011) 21070, http://dx.doi.org/10.1039/c1cp21349k. http://pubs.rsc.org/en/Content/ArticleLanding/2011/CP/c1cp21349k#!divAbstract
[46] V. Rai, M. Aryanpour, H. Pitsch, First-Principles Analysis of Oxygen-Containing Adsorbates Formed from the Electrochemical Discharge of Water on Pt(111), Journal of Physical Chemistry C 112 (26) (2008) 9760, http://dx.doi.org/10.1021/jp710811s. http://pubs.acs.org/cgi-bin/doilookup/?10.1021/jp710811s
[47] D. G. Goodwin, Cantera (2010). http://code.google.com/p/cantera
[48] P. Deuflhard, E. Hairer, J. Zugck, One-step and extrapolation methods for differential-algebraic systems, Numerische Mathematik 51 (5) (1987) 501, http://dx.doi.org/10.1007/BF01400352. http://link.springer.com/article/10.1007/BF01400352
[49] P. Légaré, Interaction of oxygen with the Pt(111) surface in wide conditions range. A DFT-based thermodynamical simulation, Surface Science 580 (1-3) (2005) 137–144, http://dx.doi.org/10.1016/j.susc.2005.02.017. http://linkinghub.elsevier.com/retrieve/pii/S0039602805001743
[50] Y.K. Park, P. Aghalayam, D.G. Vlachos, A Generalized Approach for Predicting Coverage-Dependent Reaction Parameters of Complex Surface Reactions: Application to H_2 Oxidation over Platinum, The Journal of Physical Chemistry A 103 (40) (1999) 8101, http://dx.doi.org/10.1021/jp9916485. http://pubs.acs.org/doi/abs/10.1021/jp9916485
[51] J. Carrasco, A. Hodgson, A. Michaelides, A molecular perspective of water at metal interfaces, Nature Materials 11 (8) (2012) 667, http://dx.doi.org/10.1038/nmat3354. http://www.nature.com/nmat/journal/v11/n8/full/nmat3354.html
[52] J.X. Wang, N.M. Markovic, R.R. Adzic, Kinetic Analysis of Oxygen Reduction on Pt(111) in Acid Solutions: Intrinsic Kinetic Parameters and Anion Adsorption Effects, The Journal of Physical Chemistry B 108 (13) (2004) 4127, http://dx.doi.org/10.1021/jp037593v. http://pubs.acs.org/doi/abs/10.1021/jp037593v
[53] G.S. Karlberg, G. Wahnstrom, An interaction model for OH+H_2O-mixed and pure H_2O overlayers adsorbed on Pt(111), The Journal of Chemical Physics 122 (19) (2005) 194705, http://dx.doi.org/10.1063/1.1900088. http://link.aip.org/link/JCPSA6/v122/i19/p194705/s1&Agg=doi
[54] T. Jacob, W.A. Goddard, Agostic Interactions and Dissociation in the First Layer of Water on Pt(111), Journal of the American Chemical Society 126 (30) (2004) 9360, http://dx.doi.org/10.1021/ja049920y. http://pubs.acs.org/doi/abs/10.1021/ja049920y
[55] S.K. Zecevic, J.S. Wainright, M.H. Litt, S.Lj. Gojkovic, R.F. Savinell, Kinetics of O_2 Reduction on a Pt Electrode Covered With a Thin Film of Solid Polymer Electrolyte, Journal of The Electrochemical Society 144 (9) (1997) 2973, http://dx.doi.org/10.1149/1.1837946. http://jes.ecsdl.org/content/144/9/2973.short
[56] A.P.J. Jansen, W.K. Offermans, Lateral Interactions in O/Pt(111): Density-Functional Theory and Kinetic Monte Carlo, in: O. Gervasi, M. Gavrilova, V. Kumar, A. Laganà, H. Lee, Y. Mun, D. Taniar, C. Tan (Eds.), Computational Science and Its Applications - ICCSA 2005 SE - 106, Vol. 3480 of Lecture Notes in Computer Science, Springer, Berlin Heidelberg, 2005, pp. 1020–1029, http://dx.doi.org/10.1007/11424758_106. http://dx.doi.org/10.1007/11424758_106

B. Horstmann, B. Gallant, R. Mitchell, W. G. Bessler, Y. Shao-Horn and M. Z. Bazant. Rate-Dependent Morphology of Li2O2 Growth in Li-O2 Batteries. *The Journal of Physical Chemistry Letters* **4**, 4217–4222 (2013).

THE JOURNAL OF PHYSICAL CHEMISTRY Letters

Letter

pubs.acs.org/JPCL

Rate-Dependent Morphology of Li_2O_2 Growth in Li–O_2 Batteries

Birger Horstmann,*[,†,‡,§,∥] Betar Gallant,[†] Robert Mitchell,[†] Wolfgang G. Bessler,[⊥] Yang Shao-Horn,[†] and Martin Z. Bazant*[,†]

[†]Massachusetts Institute of Technology, 77 Massachusetts Avenue, Cambridge, Massachusetts 02139, United States

[‡]German Aerospace Center, Pfaffenwaldring 38-40, 70569 Stuttgart, Germany

[§]Helmholtz Institute Ulm, Albert-Einstein-Allee 11, 89069 Ulm, Germany

[∥]University of Stuttgart, Pfaffenwaldring 6, 70550 Stuttgart, Germany

[⊥]Offenburg University of Applied Sciences, Badstraße 24, 77652 Offenburg, Germany

Supporting Information

ABSTRACT: Compact solid discharge products enable energy storage devices with high gravimetric and volumetric energy densities, but solid deposits on active surfaces can disturb charge transport and induce mechanical stress. In this Letter, we develop a nanoscale continuum model for the growth of Li_2O_2 crystals in lithium–oxygen batteries with organic electrolytes, based on a theory of electrochemical nonequilibrium thermodynamics originally applied to Li-ion batteries. As in the case of lithium insertion in phase-separating $LiFePO_4$ nanoparticles, the theory predicts a transition from complex to uniform morphologies of Li_2O_2 with increasing current. Discrete particle growth at low discharge rates becomes suppressed at high rates, resulting in a film of electronically insulating Li_2O_2 that limits cell performance. We predict that the transition between these surface growth modes occurs at current densities close to the exchange current density of the cathode reaction, consistent with experimental observations.

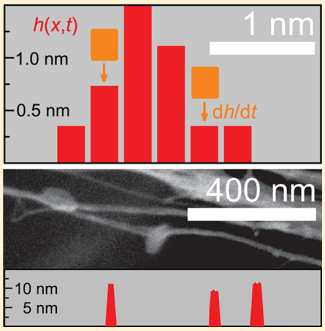

SECTION: Energy Conversion and Storage; Energy and Charge Transport

Crystallization on active surfaces is essential in many battery and electrodeposition processes. Crystalline reaction products offer the potential for compact and lightweight energy storage, but accommodating such deposits is challenging for electrode design. The wide range of conditions during crystallization causes a multitude of growth morphologies in electrochemical systems. In lead–acid batteries, particle sizes of deposited Pb depend on voltage sweeping rates;[1] in alkaline Zn batteries or Zn–O_2 batteries, electrodeposited ZnO undergoes a transition from film-growth to dendritic-growth as a function of cycling depth,[2] influenced by electrolyte additives;[3] in metal electrodeposition, dendritic growth depends sensitively on the electrolyte composition and applied current;[4−6] in rechargeable lithium batteries, morphological changes in Li metal anodes during dissolution, plating, and dendritic growth,[6] are a critical challenge, subject to ongoing modeling efforts.[7,8]

Recent experiments on Li–O_2 batteries with ether-based electrolyte have revealed that the electronically insulating discharge product Li_2O_2 can deposit in complex toroid-like morphologies[11−13] or thin films.[12−14] In contrast, only quad-shaped particles have been observed in sodium–oxygen batteries so far.[15] Li–O_2 batteries are prominent candidates for next-generation batteries that can replace conventional combustion technologies.[16−21] Although the stability of oxygen electrode and electrolyte remains a challenge for practical Li–O_2 batteries, ether-based electrolytes remain relatively stable.[22,23]

The morphology of Li_2O_2 formed upon discharge in ether-based electrolytes has an as-yet unexplained dependence on the applied current. An evolution from single-crystalline disc to complex toroid-like morphologies during discharge was first observed in nanostructured electrodes with large surface areas[9,11] (Figure 1). This has since been confirmed on different carbon substrates at low surface specific rates.[7,9,11,23,24] Although the disc-like particles reach 100 nm sizes, toroid-like particles can grow much larger, and the electron transport path and growth mechanisms are just beginning to be understood.[10] Regardless of this complex behavior at low rates, however, Li_2O_2 forms a crystalline film on the active surfaces of the cathode at high surface specific rates that limits the electrode capacity and achievable power density. When the film thickness approaches 5 nm, the active surfaces become passivated, as electronic resistance increases with thickness.[25]

In this Letter, we model the rate-dependent morphological transition in Li_2O_2 growth, using the recently developed variational theory of electrochemical kinetics[26−31] applied to classical surface-growth models.[32−34] The theory predicts a transition, which starts in the first monolayer, from particle growth to film growth when the current exceeds the exchange current for the oxygen reduction reaction. We validate that this

Received: September 13, 2013
Accepted: November 14, 2013

   dx.doi.org/10.1021/jz401973c | J. Phys. Chem. Lett. 2013, 4, 4217−4222

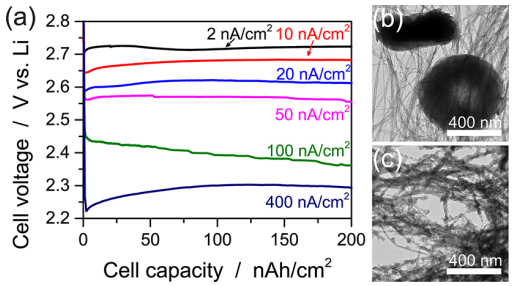

Figure 1. Galvanostatic discharge of Li−O_2 battery with CNT cathode.[9,10] The average Li_2O_2 thickness at 100 nAh/cm^2 is 1 molecular monolayer. (a) Discharge voltage for various discharge currents. (b) TEM micrograph for I = 2 nA/cm^2 at 280 nAh/cm^2 with individual particles. (c) TEM micrograph for I = 50 nA/cm^2 at 840 nAh/cm^2 with coating by small particles. Currents are normalized to true surface area.

is consistent with experimental observations. The mechanism is analogous to the suppression of phase separation in $LiFePO_4$ nanoparticles, first predicted by the same general theory.[28−30]

Theory. Existing models of Li−O_2 batteries are either macroscopic or atomistic. Cell-level models propose pore blocking due to reaction products[35−39] and surface passivation.[25,40] Atomistic models discuss the surface structure of Li_2O_2 crystals,[41−45] the kinetics of the oxygen reduction/evolution in aprotic electrolytes,[41,45,46] and the electron conductivity of Li_2O_2.[25,42,47] Here, we develop a nanoscale continuum model based on these atomistic studies, which bridges the gap to macroscopic models by predicting morphological selection in the early stages of surface growth.

We model the electrodeposition oxygen reduction reaction (ORR),

$$2Li^+ + O_2 + 2e^- \rightleftharpoons Li_2O_2 \tag{1}$$

on a carbon surface in (1 + 1)-dimensional space, i.e., through the height of the crystal $h(x)$ as a function of the projected surface coordinate x (see Figure 2). In this way, Li_2O_2 molecules align in columns growing at the electrochemically controlled rate $\partial h/\partial t$. The continuous evolution of $h(x,t)$ is a standard mathematical description of surface growth.[48]

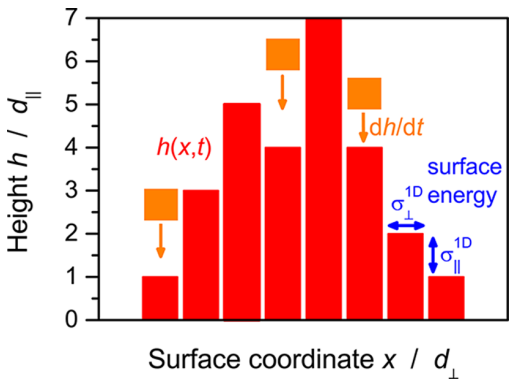

Figure 2. Scheme of the (1 + 1)-D surface model. Individual Li_2O_2 molecules are added on top of a surface crystal of height $h(x,t)$ at the rate $\partial h/\partial t$. The dimensionless variables $\tilde{h} = h/d_\parallel$ and $\tilde{x} = x/d_\perp$ are used for height and surface coordinate, where $d_\parallel$ and $d_\perp$ are the distances between molecules in the horizontal and vertical direction.

We choose the O−rich(0001)-surface for the top-facets and the (1100)-surface for the side-facets.[44] $d_\parallel$ = 0.380 nm and $d_\perp$ = 0.313 nm are the corresponding distances between Li_2O_2 molecules in the bulk crystal.[47] Our choice is motivated by the Wulff shape of the Li_2O_2 crystal, reconstructed from ab initio simulations of the surface energies.[41−44] It agrees with microscopy of the preferred crystal orientation in disc-like and toroid-like particles.[10] Integer values of $\tilde{h} = h/d_\parallel$ correspond to completely deposited monolayers, and noninteger values correspond to intermediate states and partially filled layers.

We extract the surface energies σ from ab initio calculations.[44] Our 1D surface model is based on $\sigma_\perp^{1D} = \sigma_\perp A_\perp/d_\perp$ = 140 meV/$d_\perp$ and $\sigma_\parallel^{1D} = \sigma_\parallel 6A_\parallel/2d_\parallel$ = 540 meV/$d_\parallel$, where $A_\perp = \sqrt{3}d_\perp^2/2$ and $A_\parallel = d_\perp d_\parallel/\sqrt{3}$ are the areas of the top-facets and side-facets of individual molecules, respectively. The predicted Wulff shape varies among different studies,[41−44] but does not affect our main result below; the growth mode goes through a transition close to the exchange current, for any of these Wulff shapes.

We describe the current density profile $I(x,t)$ using generalized Butler−Volmer kinetics based on nonequilibrium thermodynamics, recently developed by Bazant et al.[26] and applied to intercalation dynamics in Li-ion batteries.[27−31,49] Here, we apply the theory for the first time to surface growth, using a different model for the Li_2O_2 chemical potential,

$$\mu = \frac{\delta G[c]}{\delta c} = d_\parallel d_\perp \frac{\delta G[h]}{\delta h} \tag{2}$$

which is the variational derivative of the Gibbs free energy $G = \int_0^L g\,dx$ (defined below), where $c(x,t) = h(x,t)/(d_\parallel d_\perp)$ is the concentration of Li_2O_2 molecules per substrate length. We choose as reference state, where $\mu = \mu^\ominus$, the fully charged state without any Li_2O_2 at room temperature, and atmospheric pressure (h = 0, T = 298.15 K, p = 1 atm). The battery voltage, E, has the open circuit value, E_0 in this reference state. We assume constant activities for lithium ions, oxygen molecules, and electrons, $a_{Li^+} = a_{O_2} = a_{e^-} = 1$, during morphology selection in the early stages of growth, since thin Li_2O_2 deposits (<15 molecular layers) have negligible electronic resistivity[25] and cause negligible electrolyte depletion at typical currents. In equilibrium, the voltage increment, $\Delta\Phi = E - E_0$, is then given by the Nernst equation,

$$\Delta\Phi_{eq} = -\frac{k_B T}{2e} \ln a = \frac{\mu^\ominus - \mu}{2e} \tag{3}$$

where a is the Li_2O_2 activity. The variational activity, a, and the chemical potential, μ, determine the thermodynamics of Li_2O_2 deposits up to a few monolayers and depend sensitively on their profile, $h(x,t)$ (see eq 2).

Out of equilibrium, the two-dimensional current density $I(x,t)$ (per substrate area) is given by the Butler−Volmer equation,

$$I = A \cdot I_0 [e^{-\alpha 2e\eta/k_B T} - e^{(1-\alpha)2e\eta/k_B T}] \tag{4}$$

in terms of the activation overpotential η, the exchange current density I_0,[26] and a geometrical factor converting substrate length to normal surface length A,[48]

$$\eta = \Delta\Phi - \Delta\Phi_{eq} \tag{5}$$

$$I_0 = \frac{2ek_0 a^\alpha}{\gamma_\ddagger} \tag{6}$$

dx.doi.org/10.1021/jz401973c | J. Phys. Chem. Lett. 2013, 4, 4217−4222

$$A = \sqrt{1 + \left(\frac{\partial h}{\partial x}\right)^2} \tag{7}$$

respectively. Note that in our model, I_0 depends on activity, which is a complicated function of the height profile $h(x)$. We assume that the first charge transfer step in the ORR (1) is rate limiting and symmetric ($\alpha^1 = 1/2$), so the overall charge transfer coefficient is $\alpha = 1/4$ (see Supporting Information and also refs 41 and 46), which is consistent with the Tafel slope measured on glassy carbon.[50] The activity coefficient of the transition state $\gamma_{\ddagger}$ is approximately constant and can be estimated by Marcus theory[26] because it is dominated by desolvation. Setting $\gamma_{\ddagger} = 1$, the rate constant k_0 is determined by Tafel analysis below.

The thermodynamics of surface growth are defined by the Li_2O_2 free energy density, $g = g_b + g_s$ per substrate length. We estimate the bulk contribution as

$$g_b = \frac{2e}{d_\perp \pi}[-E_0 \pi \tilde{h} + E_1 \sin^2(\pi \tilde{h})] \tag{8}$$

where $\mu^{\ominus} = -2eE_0$ is determined by the open circuit voltage. Our choice is motivated by the following: With complete molecular layers, i.e., at integer ratios $\tilde{h} = h/d_{\|}$, the system is in equilibrium (Figure 3). The voltage barrier E_1 for homoepitaxial growth of a monolayer between these metastable equilibria accounts for the increased free energy of reaction intermediates (see Figure 3). The parameters E_0 and E_1 are taken from galvanostatic discharge measurements. We find the open circuit voltage $E_0 = 2.96$ V and the typical overpotential $E_1 = 0.2$ V, at which all reaction steps are downhill in energy.[25,46] We add Gaussian noise with standard deviation $0.004\ V = 0.15\ k_BT/e$ to E_1 to model molecular fluctuations. The microscopic surface energy density is $g_s^{micro} = \sigma_\perp^{1D}|\theta(h)| + \sigma_{\|}^{1D}|\partial h/\partial x|$. Our continuous description,

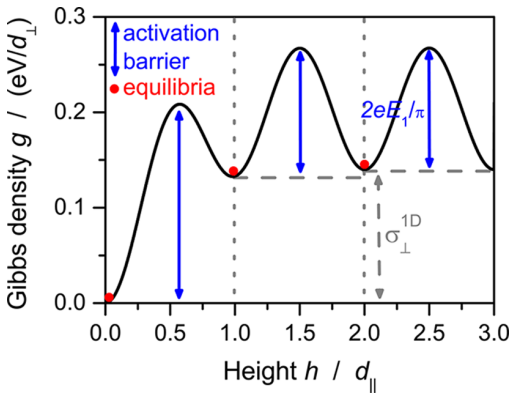

Figure 3. Homogeneous Gibbs free energy density $g_{hom} + 2eE_0\tilde{h}/d_\perp$ (in units of eV/$d_\perp$) of a Li_2O_2 deposit versus dimensionless surface height $\tilde{h} = h/d_{\|}$ with molecule distance $d_{\|}$. The system is in metastable equilibrium at integer $\tilde{h}$. During growth of the first monolayer $\tilde{h} \leq 1$, a nucleation barrier caused by the surface energy $\sigma_\perp$ must be overcome.

$$g_s = \frac{1}{2}[A(\sigma_\perp^{1D} + \sigma_{\|}^{1D}) + \sigma_\perp^{1D} - \sigma_{\|}^{1D}] - \sigma_\perp^{1D} e^{-\beta\tilde{h}^2/2} \tag{9}$$

smoothes the orientation-dependent surface energy (first term)[33] and distributes the nucleation energy $\sigma_\perp^{1D}$ to initiate growth over a few monolayers with $\beta = 6$ (second term).

The chemical potential then takes the dimensionless form

$$\tilde{\mu} = \tilde{\mu}_{hom}(\tilde{h}) - \tilde{\kappa}\frac{\frac{\partial^2 \tilde{h}}{\partial \tilde{x}^2}}{\left[1 + \left(\frac{\partial h}{\partial x}\right)^2\right]^{3/2}} \tag{10}$$

where $\tilde{\mu} = \mu/k_BT$ and $\tilde{x} = x/d_\perp$. The homogeneous term

$$\tilde{\mu}_{hom} = -\tilde{E}_0 + \tilde{E}_1 \sin(2\pi\tilde{h}) + \tilde{E}_2 \tilde{h} e^{-\beta\tilde{h}^2/2} \tag{11}$$

describes a uniform film of $\tilde{h} = h/d_{\|}$ layers, where $E_2 = \beta\sigma_\perp^{1D} d_\perp/2e$ is the nucleation voltage to initiate heteroepitaxial growth and $\tilde{E}_i = 2eE_i/k_BT$. The inhomogeneous term reproduces the Cahn–Hilliard (CH) gradient expansion,[51] $\Delta\tilde{\mu} \sim \tilde{\kappa}\partial^2\tilde{h}/\partial\tilde{x}^2$, for small inclinations $|\partial h/\partial x| \ll 1$ with a dimensionless gradient energy penalty, $\tilde{\kappa} = (\sigma_\perp^{1D} + \sigma_{\|}^{1D})d_{\|}^2/(d_\perp 2k_BT)$. In contrast to the CH model, however, the gradient energy saturates at large inclinations.

The dynamics of surface growth follow from the theory of electrochemical nonequilibrium thermodynamics,[26]

$$\frac{\partial \tilde{c}}{\partial \tilde{t}} - \frac{\partial}{\partial \tilde{x}}\left(\tilde{M}\tilde{c}\frac{\partial \tilde{\mu}}{\partial \tilde{x}}\right) = \tilde{I}(\tilde{\mu}, \Delta\tilde{\Phi}) \tag{12}$$

where $\tilde{M} = Mk_BT/(A_\perp d_\perp^2 k_0)$ is the dimensionless mobility for surface diffusion, and $\tilde{I} = I/(2ek_0)$ is the dimensionless current density scaled to the exchange current density in the standard state ($a = 1$). Since the dynamics is reaction limited, the dimensionless time, $\tilde{t} = tA_\perp k0$, is scaled to the standard exchange time per surface site. This equation generalizes the CH and Allen–Cahn equations for electrochemistry. As in the case of anisotropic $LiFePO_4$ nanoparticles,[27] diffusion can be neglected ($M = 0$) to yield the Butler–Volmer Allen–Cahn reaction (ACR) equation,[26,28] which, using eqs 3-7, takes the dimensionless form

$$\frac{\mathcal{D}\tilde{h}}{\mathcal{D}\tilde{t}} = \frac{\frac{\partial \tilde{h}}{\partial \tilde{t}}}{\sqrt{1 + \left(\frac{\partial h}{\partial x}\right)^2}} = e^{-\alpha\Delta\tilde{\Phi}} - e^{(1-\alpha)\Delta\tilde{\Phi} + \tilde{E}_0 + \tilde{\mu}} \tag{13}$$

where $\Delta\tilde{\Phi} = 2e\Delta\Phi/k_BT$. For galvanostatic discharge, the ACR equation is solved subject to the constraint of constant mean current density,[28]

$$\bar{\tilde{I}} = \frac{1}{L}\int_0^L \tilde{I}\,dx \tag{14}$$

where L is the substrate length. Numerical integration of eq 13 with periodic boundary conditions is performed in MATLAB employing the implicit DAE-solver *ode15s*, and some analytical results are also possible.

Results. The mechanism of rate-dependent morphology can be understood by approximating eq 13 in the linear and the Tafel regimes of small and large dimensionless overpotential, $\tilde{\eta} = 2e\eta/k_BT < 0$, respectively. Since we set $\gamma_{\ddagger} = 1$, the Li_2O_2 chemical potential only influences the backward (dissolution) reaction. At low rates, $\bar{I} \ll I_0$ or $|\tilde{\eta}| \ll 1$, the forward (deposition) and backward reaction both contribute to the overall linear response, so the Li_2O_2 chemical potential drives the growth,

$$\frac{\mathcal{D}\tilde{h}}{\mathcal{D}\tilde{t}} \sim -\tilde{\eta} = -(\Delta\tilde{\Phi} + \tilde{E}_0 + \tilde{\mu}) \tag{15}$$

Aside from the arc-length correction (left side), this is equivalent to the classical Allen-Cahn equation. Analogous to spinodal decompositions, homogeneous growth becomes

dx.doi.org/10.1021/jz401973c | J. Phys. Chem. Lett. 2013, 4, 4217–4222

unstable when $\partial\tilde{\mu}/\partial\tilde{h} = 0$, and particles develop. In the Tafel regime, far above the exchange current, $\bar{I} \gg I_0$ or $|\tilde{\eta}| \gg 1$, the backward reaction is negligible, and the overall rate becomes independent of the chemical potential,

$$\frac{\mathcal{D}\tilde{h}}{\mathcal{D}\tilde{t}} \sim e^{-\alpha\Delta\tilde{\Phi}} \tag{16}$$

enforcing film growth. In summary, the theory predicts a transition from particle to film growth with increasing discharge rate, analogous to the suppression of phase separation in $LiFePO_4$.[28,29]

As with ion intercalation,[28,29] the transition in surface growth can be precisely identified by linear stability analysis. Fluctuations of dimensionless wavenumber $\tilde{k} = kd_\perp = 2\pi/\tilde{\lambda}$ in a uniformly growing, homogeneous film, $\tilde{h}_0 = \tilde{\bar{I}}\tilde{t}$ (the base state), grow with the exponential rate,

$$\tilde{s}(\tilde{k};\tilde{\bar{I}}) = \frac{-\tilde{\bar{I}}}{\exp(-\tilde{\eta}_0) - 1}\left[\frac{\partial\tilde{\mu}_{\text{hom}}}{\partial\tilde{h}} - \tilde{k}^2\frac{\partial\tilde{\mu}}{\partial\frac{\partial^2\tilde{h}}{\partial\tilde{x}^2}}\right]$$

$$= -\frac{\tilde{\bar{I}}[\tilde{E}_1 2\pi\cos(2\pi\tilde{h}) + \tilde{E}_2(1 - \beta\tilde{h}^2)e^{-\beta\tilde{h}^2} + \tilde{\kappa}\tilde{k}^2]}{\exp(-\tilde{\eta}_0) - 1} \tag{17}$$

where $\tilde{\eta}_0$ is the overvoltage required for uniform growth, which solves $\tilde{I}(\tilde{h}_0,\tilde{\eta}_0) = \tilde{\bar{I}}$. We derive this equation in the Suppporting Information (see eq S19). The dynamics are unstable ($\tilde{s} > 0$) for all currents if $\partial\mu/\partial h = \partial^2 g/\partial h^2 < 0$. Indeed, this occurs between the equilibria at full molecular layers (see Figure 3). Development of instabilities into particles requires that they grow faster than the homogeneous film, i.e., $\tilde{s} > \tilde{\bar{I}}$. We evaluate this condition for marginal stability in Figure 4a for the most unstable wavelength $\tilde{\lambda} \to \infty$ and the most stable wavelength $\tilde{\lambda} = 3$ at which particles can still develop. Note that local noise favors small wavelengths. Above a critical current, growth will be homogeneous. This analysis overestimates the critical currents, as it neglects the nonlinearity of the dynamics. The transition from particle growth to film growth is broad because of the strong dependence of the marginal stability on the wavelength of the fluctuation. Growth is most unstable during nucleation of the first monolayer when the nucleation energy $\tilde{E}_2$ must be overcome. Thus, at intermediate currents, nucleation of particles can be followed by homogeneous growth at thicker coatings.

The numerical stability analysis shown in Figure 4b confirms this picture. Far below the exchange current, the growth of distinct particles is signaled by normalized standard deviations of the height profile $h(x)$ larger than unity. Above the exchange current, a tiny surface roughness signals film growth. An intermediate regime of particle coatings separates these extremes.

The exchange current density I_0 is determined via Tafel analysis.[12] We must carefully interpret this measurement because the exchange current density depends on Li_2O_2 activity and height profile in our model (see eq 6). Experimental Tafel analysis adjusts the Tafel slope to match the kinetics of uniform growth at large rates, which is described by eq 16. The current is then extrapolated from the large overpotential regime to zero overpotential $\Delta\Phi = 0$, yielding the value $I_0^\Theta = 2ek_0 = 2$ nA/cm^2. It corresponds to the exchange current density in the thermodynamic standard state, where $a = 1$. The thermodynamic standard state is the fully charged battery without Li_2O_2, i.e., $h(x) = 0$. The instabilities, however, develop close to the spinodal point, $h \approx d_\parallel/4$. Therefore, the critical current for the transition in Li_2O_2 morphology is the exchange current density evaluated at the spinodal point, i.e.,

$$I_c = I_0(h = d_\parallel/4) = I_0^\Theta a_{d_\parallel/4}^\alpha = 500 \text{ nA/cm}^2 \tag{18}$$

This exchange current agrees with the transition current predicted by linear stability analysis as demonstrated in Figure 4. Our Tafel analysis gives the symmetry factor $\alpha = 0.1$ on carbon nanotubes (CNTs)[12] and $\alpha = 0.2$ on glassy carbon.[50] The small apparent symmetry factor observed on CNTs could stem from additional overpotentials, e.g., diffuse double layers in the solid due to low electron conductivity in Li_2O_2.[52,53] Therefore, we evaluate our model for the theoretical value $\alpha = 0.25$ as discussed above.

These parameters allow the quantitative comparison between model and experiment. Electron mircoscopy images of Li_2O_2 on CNT electrodes during galvanostatic discharge are shown in Figure 1b/c.[9−12] The predictions of our surface growth model are summarized in Figure 5a. At very low surface specific discharge rates 2 nA/cm^2 $\ll I_c$, distinct disc-like particles nucleate and evolve into toroid-like ones (compare with Figure

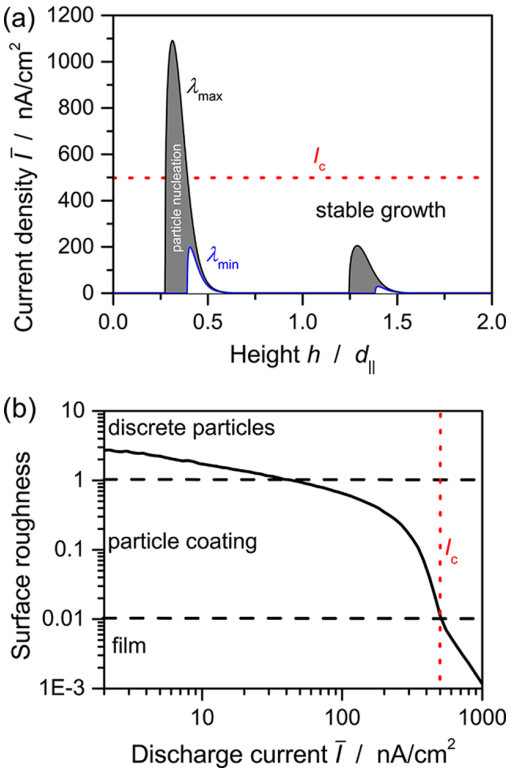

Figure 4. (a) Dependence of spinodal region on the applied current. The curves give the boundary between particle growth and film growth according to linear stability analysis, i.e., $S(\tilde{k};\tilde{\bar{I}}) = \tilde{\bar{I}}$ (see eq 17). The black line corresponds to the most unstable wavelength $\lambda \to \infty$, the blue line to the most stable wavelength $\lambda = 3d_\perp$. Dimensionless height $\tilde{h} = h/d_\parallel$ is shown. (b) Surface roughness after numerical evolution to mean height $\tilde{h} = 2d_\parallel$. The standard deviation $\Delta[h]$ of $h(x)$ normalized by mean height $\bar{h}$ (see eqs S20, S21) is depicted as a function of mean discharge rate $\bar{I}$ (see eq 14). The dashed lines illustrate the transition from growth of discrete particles over particle coating to film growth as a function of discharge current $\bar{I}$.

dx.doi.org/10.1021/jz401973c | J. Phys. Chem. Lett. 2013, 4, 4217−4222

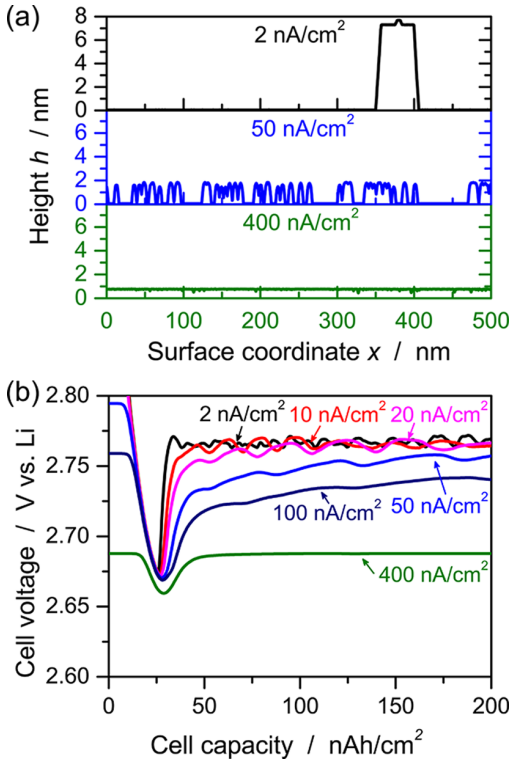

Figure 5. Simulated surface growth for various discharge currents $\bar{I}$. (a) Height profile in during galvanostatic discharge to two molecular monolayers. The Li_2O_2 morphology undergoes a transition from discrete particles (I = 2 nA/cm^2), over particle coatings (I = 50 nA/cm^2) to films (I = 400 nA/cm^2) with increasing rate. (b) Cell potential during galvanostatic discharge. The dip corresponds to the nucleation process.

1b). At intermediate rates 50 nA/cm^2 < I_c, small particles are coating the CNTs (compare with Figure 1c). At very large rates 400 nA/cm^2 $\gtrsim I_c$, a film is coating the CNTs. This prediction is in excellent agreement with the films observed at 1000 nm/cm^2 on glassy carbon in ref 25. We note that the amorphous coatings reported in ref 13 were observed in the regime of intermediate currents.

Next, we validate cell voltages as shown in Figure 1a and Figure 5b. Note that the simulations start at nonzero currents and overvoltages. The cell voltage goes through a minimum when 1/4 molecular monolayers are formed, and the system becomes unstable $\partial\mu/\partial h < 0$ (see eq 17). The dip in cell potential is determined by the nucleation energy at low rates, i.e., $\sigma_\perp^{1D}$. It is a bit smaller in experiment than in theory, possibly due to surface defects, averaging over numerous CNTs and surface capacities. Due to our choice of the symmetry factor, α = 1/4, overvoltages are generally too low, which may also reflect neglected transport and reaction processes in the solid.

Finally, we analyze the predicted particle shape and particle density at very low currents. Our theory explains the presence of disc-shaped particles at low rates and capacities. These were found to be precursors of aggregated toroid-like particles.[10] The aspect ratios $\sigma_\perp^{1D}/\sigma_\parallel^{1D}$ = 0.15 found in our simulation (see Figure 5a) agree with the theoretical Wulff shape and the values observed by microscopy in ref 10. We demonstrate this by continuing our simulations to larger capacities, at which individual discs can be imaged (see Figure 6a). Furthermore, the predicted average particle distance of roughly 500 nm is consistent with experimental imaging (see Figure 6b).

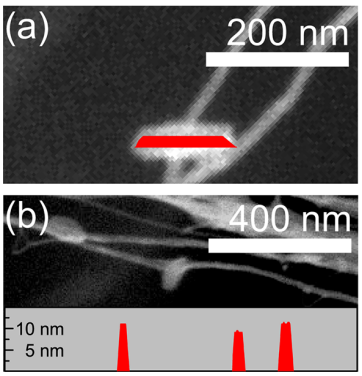

Figure 6. (a) Validation of disc-like particle morphologies realizing the Wulff-shape at I = 2 nA/cm^2.[10] The shaded area shows a modeled disc shape. The aspect ratio in micrograph and model agrees. (b) The average particle distance is in the same order of magnitude, 500 nm, in SEM micrograph and theory.

Conclusion. In this Letter, we have developed a theory of electrodeposition based on nonequilibrium thermodynamics, combining existing models for surface growth and electrochemical reaction rates. The model quantitatively describes the experimentally observed transition from particle growth to film growth of Li_2O_2 during galvanostatic discharge of an Li−O_2 battery with increasing current. The predicted transition takes place around the exchange current I_c of the oxygen reduction reaction evaluated at the nucleation barrier for growth of the first monolayer. This characteristic current is 2 orders of magnitude larger than the exchange current I_0^Θ from Tafel analysis of high-rate film growth observed in experiments.

Our theoretical framework for electrochemically driven surface growth could be applied to other systems, such as Na−O_2 batteries,[15] or extended to further dynamical regimes. After the initial phase of Li_2O_2 particle nucleation analyzed here, the particle morphology evolves from disc-like to toroid-like under certain conditions.[54] This may be describable by our approach, e.g., by including electron transport and elastic strain. Understanding the principles of Li_2O_2 crystallization is important for overcoming cell performance limitations due to the low electronic conductivity of Li_2O_2.

The morphological transition from heterogeneous to homogeneous at a critical rate is a general prediction of the variational theory of chemical kinetics.[26] Using the same theory for reaction-limited dynamics of a concentration variable, $\tilde{c} = \tilde{h}$, such a transition was first predicted for lithium intercalation in Li_XFePO_4 nanoparticles,[28] as the suppression of phase separation into $LiFePO_4$ and $FePO_4$ domains. The only difference lies in the thermodynamics of intercalation, given by a Cahn−Hilliard regular solution model.[27] Li_XFePO_4 intercalation is predicted to be stable and uniform above a critical current $I_c(X)$, somewhat below the typical Tafel exchange current due to coherency strain.[29] In contrast, Li_2O_2 growth is always unstable, but transitions from high to low surface roughness at a critical current far above the Tafel exchange current. In both cases, however, the transition occurs close to the exchange current at the spinodal point due to the exponential (Arrhenius, Butler−Volmer) dependence of the

dx.doi.org/10.1021/jz401973c | J. Phys. Chem. Lett. 2013, 4, 4217−4222

reaction rate on the local overpotential, or free energy of reaction.

■ ASSOCIATED CONTENT

Supporting Information

Numerical details, oxygen reduction reaction, and stability analysis. This material is available free of charge via the Internet at http://pubs.acs.org/.

■ AUTHOR INFORMATION

Corresponding Authors

*E-mail: birger.horstmann@dlr.de.
*E-mail: bazant@mit.edu.

Notes

The authors declare no competing financial interest.

■ ACKNOWLEDGMENTS

This work was supported in part by the MRSEC Program of the National Science Foundation under Award Number DMR-0819762. B.H. acknowledges support from the German Academic Exchange Service (DAAD). B.M.G. acknowledges a National Science Foundation Graduate Research Fellowship. The authors would like to acknowledge Carl V. Thompson for fruitful discussions.

■ REFERENCES

(1) Yamaguchi, Y.; Shiota, M.; Nakayama, Y.; Hirai, N.; Hara, S. *J. Power Sources* **2001**, *93*, 104.
(2) Yuan, Y. F.; Tu, J. P.; Wu, H. M.; Zhang, B.; Huang, X. H.; Zhao, X. B. *J. Electrochem. Soc.* **2006**, *153*, A1719.
(3) Lee, C. W.; Sathiyanarayanan, K.; Eom, S. W.; Kim, H. S.; Yun, M. S. *J. Power Sources* **2006**, *159*, 1474.
(4) Kuhn, A.; Argoul, F. *J. Electroanal. Chem.* **1994**, *371*, 93.
(5) Rosso, M. *Electrochim. Acta* **2007**, *53*, 250.
(6) Nishikawa, K.; Mori, T.; Nishida, T.; Fukunaka, Y.; Rosso, M.; Homma, T. *J. Electrochem. Soc.* **2010**, *157*, A1212.
(7) Monroe, C.; Newman, J. *J. Electrochem. Soc.* **2003**, *150*, A1377.
(8) Ely, D. R.; Garcia, R. E. *J. Electrochem. Soc.* **2013**, *160*, A662.
(9) Gallant, B. M.; Mitchell, R. R.; Kwabi, D. G.; Zhou, J.; Zuin, L.; Thompson, C. V.; Shao-Horn, Y. *J. Phys. Chem. C* **2012**, *116*, 20800.
(10) Mitchell, R. R.; Gallant, B. M.; Shao-Horn, Y.; Thompson, C. V. *J. Phys. Chem. Lett.* **2013**, *4*, 1060.
(11) Mitchell, R. R.; Gallant, B. M.; Thompson, C. V.; Shao-Horn, Y. *Energy Environ. Sci.* **2011**, *4*, 2952.
(12) Gallant, B. M.; Kwabi, D. G.; Mitchell, R. R.; Zhou, J.; Thompson, C.; Shao-Horn, Y. *Energy Environ. Sci.* **2013**, *6*, 2518.
(13) Adams, B. D.; Radtke, C.; Black, R.; Trudeau, M. L.; Zaghib, K.; Nazar, L. F. *Energy Environ. Sci.* **2013**, *6*, 1772.
(14) Mccloskey, B. D.; Speidel, A.; Scheffler, R.; Miller, D. C.; Viswanathan, V.; Hummelshøj, J. S.; Nørskov, J. K.; Luntz, A. C. *J. Phys. Chem. Lett.* **2012**, *3*, 997.
(15) Hartmann, P.; Bender, C. L.; Vračar, M.; Dürr, A. K.; Garsuch, A.; Janek, J.; Adelhelm, P. *Nat. Mater.* **2012**, *12*, 228.
(16) Abraham, K. M.; Jiang, Z. *Electrochem. Sci. Technol.* **1996**, *143*, 1.
(17) Girishkumar, G.; McCloskey, B.; Luntz, A. C.; Swanson, S.; Wilcke, W. *J. Phys. Chem. Lett.* **2010**, *1*, 2193.
(18) Christensen, J.; Albertus, P.; Sanchez-Carrera, R. S.; Lohmann, T.; Kozinsky, B.; Liedtke, R.; Ahmed, J.; Kojic, A. *J. Electrochem. Soc.* **2012**, *159*, R1.
(19) Bruce, P. G.; Freunberger, S. A.; Hardwick, L. J.; Tarascon, J.-M. *Nat. Mater.* **2012**, *11*, 19.
(20) Lu, Y.-C.; Gallant, B. M.; Kwabi, D. G.; Harding, J. R.; Mitchell, R. R.; Whittingham, M. S.; Shao-Horn, Y. *Energy Environ. Sci.* **2013**, *6*, 750.
(21) Scrosati, B.; Garche, J. *J. Power Sources* **2010**, *195*, 2419.
(22) McCloskey, B. D.; Bethune, D. S.; Shelby, R. M.; Girishkumar, G.; Luntz, A. C. *J. Phys. Chem. Lett.* **2011**, *2*, 1161.
(23) Lu, Y.-C.; Kwabi, D. G.; Yao, K. P. C.; Harding, J. R.; Zhou, J.; Zuin, L.; Shao-Horn, Y. *Energy Environ. Sci.* **2011**, *4*, 2999.
(24) Black, R.; Oh, S. H.; Lee, J.-H.; Yim, T.; Adams, B.; Nazar, L. F. *J. Am. Chem. Soc.* **2012**, *134*, 2902.
(25) Viswanathan, V.; Thygesen, K. S.; Hummelshøj, J. S.; Nørskov, J. K.; Girishkumar, G.; McCloskey, B. D.; Luntz, A. C. *J. Chem. Phys.* **2011**, *135*, 214704.
(26) Bazant, M. *Acc. Chem. Res.* **2013**, *46*, 1144.
(27) Singh, G. K.; Ceder, G.; Bazant, M. Z. *Electrochim. Acta* **2008**, *53*, 7599−7613.
(28) Bai, P.; Cogswell, D. A.; Bazant, M. Z. *Nano Lett.* **2011**, *11*, 4890.
(29) Cogswell, D. A.; Bazant, M. Z. *ACS Nano* **2012**, *6*, 2215.
(30) Ferguson, T. R.; Bazant, M. Z. *J. Electrochem. Soc.* **2012**, *159*, A1967.
(31) Cogswell, D. A.; Bazant, M. Z. *Nano Lett.* **2013**, *13*, 3036.
(32) Burton, W. K.; Cabrera, N.; Frank, F. C. *Philos. Trans. R. Soc. London, Ser. A: Math. Phys. Sci.* **1951**, *243*, 299.
(33) Stone, H. A.; Margetis, D. In *Handbook of Materials Modeling. Vol. I: Methods and Models*; Yip, S., Ed.; Springer: The Netherlands, 2005; Vol. *I*; Chapter 4.8, p 1.
(34) Margetis, D.; Aziz, M.; Stone, H. *Phys. Rev. B* **2005**, *71*, 165432.
(35) Sandhu, S.; Fellner, J.; Brutchen, G. *J. Power Sources* **2007**, *164*, 365.
(36) Williford, R.; Zhang, J.-G. *J. Power Sources* **2009**, *194*, 1164.
(37) Andrei, P.; Zheng, J. P.; Hendrickson, M.; Plichta, E. J. *J. Electrochem. Soc.* **2010**, *157*, A1287.
(38) Neidhardt, J. P.; Fronczek, D. N.; Jahnke, T.; Danner, T.; Horstmann, B.; Bessler, W. G. *J. Electrochem. Soc.* **2012**, *159*, A1528.
(39) Horstmann, B.; Danner, T.; Bessler, W. G. *Energy Environ. Sci.* **2013**, *6*, 1299.
(40) Albertus, P.; Girishkumar, G.; McCloskey, B.; Sanchez-Carrera, R. S.; Kozinsky, B.; Christensen, J.; Luntz, A. C. *J. Electrochem. Soc.* **2011**, *158*, A343.
(41) Mo, Y.; Ong, S.; Ceder, G. *Phys. Rev. B* **2011**, *84*, 1.
(42) Radin, M. D.; Rodriguez, J. F.; Tian, F.; Siegel, D. J. *J. Am. Chem. Soc.* **2011**, *134*, 1093.
(43) Radin, M. D.; Tian, F.; Siegel, D. J. *J. Mater. Sci.* **2012**, *47*, 7564.
(44) Hummelshøj, J. S.; Luntz, A. C.; Nørskov, J. K. *J. Chem. Phys.* **2013**, *138*, 034703.
(45) Viswanathan, V.; Speidel, A.; Scheffler, R.; Gowda, S.; Luntz, A. C. *J. Phys. Chem. Lett.* **2013**, *4*, 556.
(46) Hummelshøj, J. S.; Blomqvist, J.; Datta, S.; Vegge, T.; Rossmeisl, J.; Thygesen, K. S.; Luntz, a. C.; Jacobsen, K. W.; Nørskov, J. K. *J. Chem. Phys.* **2010**, *132*, 071101.
(47) Ong, S.; Mo, Y.; Ceder, G. *Phys. Rev. B* **2012**, *85*, 2.
(48) Barabasi, A.-L.; Stanley, H. E. *Fractal Concepts in Surface Growth*; Cambridge University Press: Cambridge, U.K., 1995.
(49) Burch, D.; Bazant, M. Z. *Nano Lett.* **2009**, *9*, 3795.
(50) Lu, Y.-C.; Shao-Horn, Y. *J. Phys. Chem. Lett.* **2013**, *4*, 93.
(51) Cahn, J. W.; Hilliard, J. E. *J. Chem. Phys.* **1958**, *28*, 258.
(52) Bazant, M. Z.; Chu, K. T.; Bayly, B. J. *SIAM J. Appl. Math.* **2005**, *65*, 1463.
(53) Biesheuvel, P.; van Soestbergen, M.; Bazant, M. *Electrochim. Acta* **2009**, *54*, 4857.
(54) Gránásy, L.; Pusztai, T.; Tegze, G.; Warren, J.; Douglas, J. *Phys. Rev. E* **2005**, *72*, 011605.

Rate-dependent morphology of Li_2O_2 growth in Li-O_2 batteries: Supporting Information

Birger Horstmann,[*,†,‡,¶,§] Betar Gallant,[†] Robert Mitchell,[†] Wolfgang G. Bessler,[‖] Yang Shao-Horn,[†] and Martin Z. Bazant[*,†]

Massachusetts Institute of Technology, 77 Massachusetts Avenue, Cambridge, MA 02139, USA, German Aerospace Center, Pfaffenwaldring 38-40, 70569 Stuttgart, Germany, Helmholtz Institute Ulm, Albert-Einstein-Allee 11, 89069 Ulm, Germany, University of Stuttgart, Pfaffenwaldring 6, 70550 Stuttgart, Germany, and Offenburg University of Applied Sciences, Badstraße 24, 77652 Offenburg, Germany

E-mail: birger.horstmann@dlr.de; bazant@mit.edu

1. Numerical details

We numerically integrate the DAE system of Eq. 13 and Eq. 14 in MATLAB employing the DAE-solver *ode15s*. It is an implicit, variable order solver. Periodic boundary conditions are used. Spatial derivatives are calculated with first order central differencing. The spacing of grid points is given by the distance between molecules $d_\perp$. Simulations were performed in systems of length $L = 500$ nm (Figs. 4,5,6a) and $L = 1000$ nm (Fig. 6b).

[*]To whom correspondence should be addressed
[†]Massachusetts Institute of Technology
[‡]German Aerospace Center
[¶]Helmholtz Institute Ulm
[§]Stuttgart University
[‖]Offenburg University of Applied Sciences

2. Oxygen reduction reaction

Here, we explain that the global Butler-Volmer rate in Eq. 4 is based on an elementary kinetics description of the rate of the oxygen reduction reaction. For first charge transfer step of the oxygen reduction reaction (ORR) rate limiting, we predict the symmetry factor $\alpha = \frac{1}{4}$. This is in good agreement with the symmetry factor $\alpha = 0.2$ for the ORR measured on glassy carbon. We take into account the activity of dissolved oxygen $a_{\mathrm{O_2}}$ and the reaction intermediate $a_{\mathrm{LiO_2}}$. Thus, we demonstrate the dependence of the rate of the ORR on the oxygen concentration here. In the main article, however, we work with constant oxygen pressure and assume $a_{\mathrm{O_2}} = 1$. For easy notation, we continue to assume constant activities for lithium ions and electrons, $a_{\mathrm{Li^+}} = a_{\mathrm{e^-}} = 1$.

The ORR reaction involves two single-electron transfer steps with lithium dioxide as the intermediate species

$$\mathrm{Li^+ + e^- + O_2} \longrightarrow \mathrm{LiO_2} \tag{S1}$$

$$\mathrm{Li^+ + e^- + LiO_2} \longrightarrow \mathrm{Li_2O_2}. \tag{S2}$$

If the first charge transfer step is rate limiting, the second one is in equilibrium. The latter allows us to write

$$k_{\mathrm{B}}T \ln a = -\Delta\Phi + k_{\mathrm{B}}T \ln a_{\mathrm{Li_2O}} \tag{S3}$$

or

$$a_{\mathrm{Li_2O}} = a e^{-\frac{e\Delta\Phi}{k_{\mathrm{B}}T}}. \tag{S4}$$

The rate limiting charge transfer should determine the overall rate [Bazant, M. Accounts of Chemical Research 2013, 46, 1144],

$$I^1 = A \cdot I_0^1 \left[e^{-\alpha^1 e\eta^1/k_{\mathrm{B}}T} - e^{\left(1-\alpha^1\right)e\eta^1/k_{\mathrm{B}}T} \right], \tag{S5}$$

where the superscript 1 denotes the first charge transfer step.

In the following, we will show that the global Butler-Volmer rate (see Eq. 4) used in the article is identical to twice the elementary reaction rate (see Eq. S5), i.e., $I = 2I^1$, if we set

$$\alpha = 0.5\alpha^1. \tag{S6}$$

In our case, we describe the ORR symmetric elementary charge transfers, i.e., $\alpha^1 = \frac{1}{2}$, via a global reaction rate with $\alpha = \frac{1}{4}$. We restate the equilibrium potential (see Eq. 3) taking into account a varying oxygen activity a_{O_2}

$$\Delta\Phi_{eq} = -\frac{k_B T}{2e} \ln\left(\frac{a}{a_{O_2}}\right) \tag{S7}$$

and give the equilibrium potential $\Delta\Phi^1_{eq}$ of the first charge transfer

$$\begin{aligned}\Delta\Phi^1_{eq} &= -\frac{k_B T}{e} \ln\left(\frac{a_{O_2}}{a_{Li_2O}}\right) - \Delta\Phi \\ &= 2\Delta\Phi_{eq} - \Delta\Phi\end{aligned} \tag{S8}$$

making use of Eq. S4 and Eq. S7 [Bazant, M. Accounts of Chemical Research 2013, 46, 1144]. This allows us to write the overpotential of the first charge transfer step in the simple form

$$\eta^1 = \Delta\Phi - \Delta\Phi^1_{eq} = 2\eta. \tag{S9}$$

Furthermore, the global exchange current (see Eq. 6) [Bazant, M. Accounts of Chemical Research 2013, 46, 1144]

$$I_0 = \frac{2ek_0 a^\alpha a_{O_2}^{1-\alpha}}{\gamma_\ddagger} \tag{S10}$$

and the one of the first charge transfer step are related by

$$
\begin{aligned}
I_0^1 &= \frac{e k_0^1 a_{\mathrm{Li_2O}}^{\alpha^1} a_{\mathrm{O_2}}^{1-\alpha^1}}{\gamma_{\ddagger}} \\
&= \frac{e k_0 a^{\alpha} a_{\mathrm{O_2}}^{1-\alpha}}{\gamma_{\ddagger}} \frac{a^{\alpha}}{a_{\mathrm{O_2}}^{\alpha}} e^{2\alpha e \Delta\Phi / k_{\mathrm{B}} T} \\
I_0^1 &= \frac{1}{2} I_0 e^{\alpha 2 e \eta / k_{\mathrm{B}} T}.
\end{aligned} \tag{S11}
$$

Finally, we insert the overpotential η^1 (see Eq. S9) and the exchange current I_0^1 (see Eq. S11) into the Butler-Volmer rate of the first charge transfer step (see Eq. S5)

$$
\begin{aligned}
I^1 &= A \cdot I_0^1 \left[e^{-\alpha^1 e \eta^1 / k_{\mathrm{B}} T} - e^{\left(1-\alpha^1\right) e \eta^1 / k_{\mathrm{B}} T} \right] \\
&= \frac{1}{2} A \cdot I_0 \cdot e^{\alpha 2 e \eta / k_{\mathrm{B}} T} \left[e^{-4\alpha e \eta / k_{\mathrm{B}} T} - e^{(2-4\alpha) e \eta / k_{\mathrm{B}} T} \right] \\
&= A \cdot I_0 \left[e^{-\alpha 2 e \eta / k_{\mathrm{B}} T} - e^{(1-\alpha) 2 e \eta / k_{\mathrm{B}} T} \right] \\
I^1 &= \frac{1}{2} I,
\end{aligned} \tag{S12}
$$

to yield half of the global Butler-Volmer rate stated in Eq. 4.

Let us finally rewrite the global Butler-Volmer rate in order to make clear its dependence on oxygen activity

$$
I = A \frac{2 e k_0}{\gamma_{\ddagger}} \left[a_{\mathrm{O_2}} e^{-\alpha 2 e \Delta\Phi / k_{\mathrm{B}} T} - a_{\mathrm{O_2}} e^{(1-\alpha) 2 e \Delta\Phi / k_{\mathrm{B}} T} \right]. \tag{S13}
$$

Thus, the pressure of $\mathrm{O_2}$ drives the forward rate and the activity of $\mathrm{Li_2O_2}$ drives the backward rate.

To summarize, we demonstrated that the global Butler-Volmer rate stated in Eq. 4 is an accurate describtion of the ORR. Its derivation takes into account reaction intermediates as well as the oxygen pressure. The latter is encoded in the overpotential η^1 (see Eq. S9) and the exchange current I_0^1 (see Eq. S11). Because transport of molecular oxygen $\mathrm{O_2}$ is fast in the standard electrolytes for $\mathrm{Li}-\mathrm{O_2}$ batteries and oxygen partial pressure is kept constant during experiments, we do not expect a significant impact of oxygen activity on the electrodeposition of $\mathrm{Li_2O_2}$.

3. Stability analysis

In this section, we provide additional mathematical details on the stability analysis. First, we derive the exponential growth rate for linear instability in Eq. 17. We decompose total surface height $\tilde{h} = \tilde{h}_0 + \delta\tilde{h}_{\tilde{k}}$ into height of the uniform film $\tilde{h}_0$ and of fluctuations $\delta\tilde{h}_{\tilde{k}}$ of wavenumber $\tilde{k}$. Their second derivative is $\frac{\partial^2 \delta\tilde{h}}{\partial \tilde{x}^2} = -\tilde{k}^2 \delta\tilde{h}$. $\delta A = 0$ vanishes because A depends on h through the square of $\frac{\partial h}{\partial x}$ only. In order to determine $\delta(\Delta\tilde{\Phi})_{\tilde{k}}$, we study the effect of fluctuations in surface height on the mean discharge current in Eq. 14

$$\begin{aligned} 0 &= \delta\tilde{\bar{I}} = \frac{1}{L}\int_0^L \delta\tilde{I}\mathrm{d}x \qquad \text{(S14)} \\ &= -\delta(\Delta\tilde{\Phi})_{\tilde{k}}\left[\alpha e^{-\alpha\Delta\tilde{\Phi}_0} + (1-\alpha)a(\tilde{h}_0)e^{(1-\alpha)\Delta\tilde{\Phi}_0}\right] - \frac{(1-\alpha)a(\tilde{h}_0)e^{(1-\alpha)\Delta\tilde{\Phi}_0}}{L}\int_0^L \delta\tilde{\mu}_{\tilde{k}}\mathrm{d}x, \end{aligned}$$

where $\Delta\tilde{\Phi}_0$ is the voltage step required for uniform growth, which solves $\tilde{I}(\tilde{h_0}, \tilde{\eta}_0) = \tilde{\bar{I}}$. The integral

$$\int_0^L \delta\tilde{\mu}_{\tilde{k}}\mathrm{d}x = \left[\frac{\partial\tilde{\mu}}{\partial\tilde{h}} - \tilde{k}^2\frac{\partial\tilde{\mu}}{\partial\frac{\partial^2\tilde{h}}{\partial\tilde{x}^2}}\right]\int_0^L \delta\tilde{h}_{\tilde{k}}\mathrm{d}x = 0 \qquad \text{(S15)}$$

vanishes for all $\tilde{k} > 0$. Therefore, according to Eq. S14, $\delta(\Delta\tilde{\Phi})_{\tilde{k}} = 0$ vanishes, too. We can now calculate the dynamics of the fluctuations $\delta\tilde{h}_{\tilde{k}}$ from Eq. 13

$$\frac{\partial\delta\tilde{h}_{\tilde{k}}}{\partial\tilde{t}} = -\delta\tilde{h}_{\tilde{k}}a(\tilde{h}_0)e^{(1-\alpha)\Delta\tilde{\Phi}_0}\left[\frac{\partial\tilde{\mu}_{\mathrm{hom}}}{\partial\tilde{h}} - \tilde{k}^2\frac{\partial\tilde{\mu}}{\partial\frac{\partial^2\tilde{h}}{\partial\tilde{x}^2}}\right]. \qquad \text{(S16)}$$

We want to substitute $\tilde{\bar{I}}$ and $\tilde{\eta}_0$ for $a(\tilde{h}_0)$ and $\Delta\tilde{\Phi}_0$. To this aim, we write for the homogeneous base state

$$\begin{aligned} \tilde{\bar{I}} &= e^{-\alpha\Delta\tilde{\Phi}_0} - a(\tilde{h}_0)e^{(1-\alpha)\Delta\tilde{\Phi}_0} \\ &= a(\tilde{h}_0)e^{(1-\alpha)\Delta\tilde{\Phi}_0}\left[e^{-\Delta\tilde{\Phi}_0 - \tilde{E}_0 - \tilde{\mu}(\tilde{h}_0)} - 1\right] \\ \tilde{\bar{I}} &= a(\tilde{h}_0)e^{(1-\alpha)\Delta\tilde{\Phi}_0}\left[e^{-\tilde{\eta}_0} - 1\right] \qquad \text{(S17)} \end{aligned}$$

and rewrite Eq. S16

$$\frac{\partial \delta \tilde{h}_{\tilde{k}}}{\partial \tilde{t}} = \frac{-\tilde{\bar{I}} \delta \tilde{h}_{\tilde{k}}}{\exp(-\tilde{\eta}_0) - 1} \left[\frac{\partial \tilde{\mu}_{\mathrm{hom}}}{\partial \tilde{h}} - \tilde{k}^2 \frac{\partial \tilde{\mu}}{\partial \frac{\partial^2 \tilde{h}}{\partial \tilde{x}^2}} \right]. \tag{S18}$$

The exponential growth rate in Eq. 17 is

$$\tilde{s}(\tilde{k}; \tilde{\bar{I}}) = \frac{\frac{\partial \delta \tilde{h}_{\tilde{k}}}{\partial \tilde{t}}}{\delta \tilde{h}_{\tilde{k}}}. \tag{S19}$$

The marginal stability curve in Fig. 4 is determined by solving $\tilde{s} = \tilde{\bar{I}}$ for $\exp(-\tilde{\eta}_0)$ and substituting into Eq. 4.

In Fig. 4, we determine surface roughness $\Delta[h]$ as normalized standard deviation of $h(x)$ according to

$$\Delta[h] = \sqrt{\frac{1}{L} \int_0^L \frac{\left(h(x) - \bar{h}\right)^2}{\bar{h}^2} \mathrm{d}x} \tag{S20}$$

with the mean height

$$\bar{h} = \frac{1}{L} \int_0^L h(x) \mathrm{d}x. \tag{S21}$$

V. Hoffmann, G. Pulletikurthi, T. Carstens, A. Lahiri, A. Borodin, M. Schammer, B. Horstmann, A. Latz and F. Endres. Influence of a Silver Salt on the Nanostructure of an Au(111) Ionic Liquid Interface: an Atomic Force Microscopy Study and Theoretical Concepts. *Physical Chemistry Chemical Physics* **20**, 4760–4771 (2018).

PCCP

PAPER

View Article Online
View Journal | View Issue

Cite this: *Phys. Chem. Chem. Phys.*, 2018, **20**, 4760

Influence of a silver salt on the nanostructure of a Au(111)/ionic liquid interface: an atomic force microscopy study and theoretical concepts†

Viktor Hoffmann,[a] Giridhar Pulletikurthi,[a] Timo Carstens,[a] Abhishek Lahiri,[a] Andriy Borodin,[a] Max Schammer,[bcd] Birger Horstmann,[bc] Arnulf Latz[bcd] and Frank Endres*[a]

Received 8th December 2017,
Accepted 2nd January 2018

DOI: 10.1039/c7cp08243f

rsc.li/pccp

Ionic liquids (ILs) form a multilayered structure at the solid/electrolyte interface, and the addition of solutes can alter it. For this purpose, we have investigated the influence of the silver bis(trifluoromethylsulfonyl)amide (AgTFSA) concentration in 1-butyl-1-methylpyrrolidinium bis(trifluoromethylsulfonyl)amide ([$Py_{1,4}$]TFSA) on the layering using *in situ* atomic force microscopy. AFM investigations revealed that the Au(111)/electrolyte interface indeed depends on the concentration of the salt where a typical "IL" multilayered structure is retained only at quite low concentrations of the silver salt (*e.g.* ≤200 μM). However, at 200 μM AgTFSA/[$Py_{1,4}$]TFSA and above this "IL" multilayered structure is disturbed/varied. A simple double layer structure was observed at 500 μM AgTFSA in [$Py_{1,4}$]TFSA. Furthermore, the widths of the innermost layers have been found to be dependent on the concentration and on the applied electrode potentials. Our AFM results show that the concentration of solutes strongly influences the structure of the electrode/electrolyte interface and can provide new insights into the electrical double layer structure of the electrode/ionic liquid interface. We also introduce a semi-continuum theory to discuss the double layer structure.

1 Introduction

The electrodeposition of silver on Au(111) is a well-investigated example, both from surface science and from the electrochemical perspective due to quite similar lattice constants and the higher surface energy of gold.[1,2] Furthermore, alloying,[1,3] surface reconstruction,[4,5] surface crystallinity,[6] and defects[1] can play a crucial role in the initial stages of metal deposition. Moreover, the neat surfaces of gold minimize their surface energy by reconstruction and an electrode potential dependent lifting of Au has been reported.[7,8] Specific adsorption of anions can also promote such a lifting process[2] and the strong influence of anions on the overlayer structure was observed using atomic force microscopy.[2]

Ionic liquids are interesting solvents for the electrodeposition of reactive metals such as Al and Si, which are not accessible in aqueous media.[9,10] These liquids have wide electrochemical and thermal windows, good ionic conductivities, usually low vapor pressures at room temperature and high solubility for a variety of compounds.[11,12] However, the practical use of these liquids in applied electrochemistry is hindered, as there is still no thorough understanding of the species in the bulk phase and, especially, at the interface.

Several ILs have been employed as electrolytes to deposit silver, such as tetrafluoroborate,[13,14] hexafluorophosphate,[15,16] bis(trifluoromethylsulfonyl)amide,[13,17] dicyanamide,[18] trifluoromethylsulfonate,[19,20] acetate,[21] and nitrate.[21] In most of these studies the focus was on the electrodeposition and the characterization of the deposited films.

In recent years, atomic force microscopy has become a useful tool to explore/probe the electrode/electrolyte interface (EEI) with atomic resolution.[22–34] AFM force–distance curves can provide direct insight into the adsorption structure of ions/species in the double layer (or multilayer) on the electrode/IL interface.[22]

In contrast to aqueous solutions, there are often no simple double layers in ILs, instead the ions adopt a multilayer structure.[28] In brief, the interfacial structure can be divided into the innermost layer, the transition zone, and the bulk liquid phase.[29,30] The innermost layer is composed of the IL layer adsorbed next to the electrode surface. These layers experience large forces when

[a] *Institute of Electrochemistry, Clausthal University of Technology, Arnold-Sommerfeld-Strasse 6, 38678 Clausthal-Zellerfeld, Germany. E-mail: frank.endres@tu-clausthal.de*
[b] *Helmholtz Institute Ulm, Helmholtzstraße 11, 89081 Ulm, Germany*
[c] *German Aerospace Center, Pfaffenwaldring 38-40, 70569 Stuttgart, Germany*
[d] *Universität Ulm, Albert-Einstein-Alle 47, 89081 Ulm, Germany*

† Electronic supplementary information (ESI) available. See DOI: 10.1039/c7cp08243f

the AFM tip pushes through them. At the open circuit potential (OCP) and at more negative electrode potentials the innermost layer is usually enriched with cations. At more positive potentials anions are usually dominant at the interface. The forces for penetrating these layers have been shown to be more than one order of magnitude higher than the ones for molecular liquids.[25,29,31,35–38] Interfacial properties, including the adsorption/co-adsorption of ions at the interface, are determined by the nature of the electrode and the electrolyte. Even a small variation in the electrolyte composition, *e.g.* due to impurities[39] or dissolved solutes,[25,40] can disturb the multilayer arrangement and can also influence electrochemical reactions. The Au(111)/[$Py_{1,4}$]TFSA interface is rather well described in the literature.[35,41] Furthermore, the solvation behaviour of AgTFSA in [EMIm]TFSA has been investigated by spectroscopy and DFT calculations, giving a stable complex like $[Ag(TFSA)_3]^{2-}$.[42] We have reported that water has an influence on the Au(111)/ionic liquid interface.[43] In the case of [EMIm]TfO, a multilayer structure was predominant up to 30 vol% water and above this concentration the multilayer structure was strongly disturbed. In this context the question came up as to what extent the IL layers are influenced by a solute during electrodeposition. For this purpose AgTFSA, from which Ag is easily deposited, has been taken as an example to study the influence of salt concentration on the electrode/ionic liquid interface. In the present paper we report for the first time on the influence of silver salt concentration on the electrode/electrolyte interface using atomic force microscopy.

The experimental work is accompanied by theoretical considerations. Continuum theories allow the dynamic description of macroscopic systems, *e.g.*, electrochemical cells. The nano-sized surface layers, however, are strongly affected by the particle nature of its constituents. The popular modeling approaches on this scale are density functional theory (DFT)[44–47] and molecular dynamics (MD).[48] DFT and MD simulations resolve many of the microscopic complexities of individual molecules and intermolecular interactions, but remain limited to small length and time scales. Bazant *et al.* have proposed a phenomenological continuum theory which captures the multilayer structure of the electrochemical double layer in ionic liquids.[28]

In this paper, we present a novel semi-continuum model which describes ionic liquids as a continuum fluid of hard spheres. It represents a unified theoretical framework for the description of both scales, bulk phase and surface layers. Our approach is derived from fundamental thermodynamical principles and basic physical assumptions, in contrast to phenomenological continuum theory,[28,49,50] Thus, we improve the assignment between material properties and the simulated phenomena. Most importantly, we find that incompressibility leads to crowding and the particle nature of fluids leads to overscreening.

Our consistent continuum model describes both the short-range and long-range behavior of ionic liquids as well as both static and dynamic effects. This generality complements previous modeling efforts. On the one hand, DFT and MD describe electrolytes at smaller length and time scales. Thus, they resolve more detailed ionic properties than our model, *e.g.*, molecular orientation, position, and shape, and make quantitative predictions. The fine resolution, however, comes at the cost of computational complexity. DFT and MD are limited to the nano-scale dimensions of the electrochemical double layer (EDL), whereas our model can calculate properties of ionic liquids from the nano-scale EDL to the micro-scale electrode structure. Most importantly, the simplicity and abstraction of our continuum model brings out the fundamental principles behind the interfacial behavior of ionic liquids clearer than do DFT or MD. Furthermore, our model is time dependent and able to predict the contribution of transport through the EDL structure to the apparent reaction kinetics of ionic liquids.

On the other hand, the phenomenological continuum theory of Bazant *et al.* is numerically simpler than our model, but remains restricted to binary ionic liquids and does not clearly distinguish between different electrolytes. Our model, instead, applies to more complex electrolytes and clearly connects with material properties because we derive it from non-equilibrium thermodynamics and make explicit the hardcore nature of the molecules. In this paper, for example, we can evaluate the effect of water molecules or silver ions onto the EDL structure of ionic liquids and study the effect of molecular size on electrolyte properties.

2 Methods

2.1 Experimental methods

1-Butyl-1-methylpyrrolidinium bis(trifluoromethylsulfonyl)amide ([$Py_{1,4}$]TFSA) was purchased from IOLITEC, Germany, in a purity of 99.5%. Silver bis(trifluoromethylsulfonyl)amide (99.5%) was procured from Solvionics, France. The ionic liquid was dried at 100 °C under vacuum for 3 days to water values below 10 ppm. Several concentrations of AgTFSA in [$Py_{1,4}$]TFSA ranging from 50 μM to 1000 μM were prepared.

The electrochemical measurements were carried out using a PARSTAT 2263 potentiostat/galvanostat controlled by PowerCV and PowerStep software. A three electrode cell was used for all electrochemical experiments. Gold on glass was used as the working electrodes (WE) for cyclic voltammetry experiments. The working electrode for the AFM studies was Au(111) on mica purchased from Agilent Technologies. The electrochemical cell was made of Teflon and clamped over a Teflon-covered Viton O-ring onto the working electrode with a geometric surface area of 0.3 cm^2. Pt wires were used as the counter and quasi reference electrodes, respectively. The deflection–distance curves were obtained using a Molecular Imaging Pico Plus AFM in contact mode inside an argon-filled glove-box at room temperature and transformed to force–distance curves. A silicon SPM-sensor with a spring constant of 6 N m^{-1} from Nano World was employed for all AFM measurements.

2.2 Mathematical model

Our mathematical model of ionic liquids is based on the methodology of rational thermodynamics and describes a thermodynamically consistent transport theory. The modeling methodology has been applied to electrolytes with a dominant

neutral solvent before, as outlined by Latz and Zausch.[51] However, ionic liquids possess unique physical properties which must be captured by fundamental principles and which differ from those of uncharged solvent electrolytes. Therefore, transport theories for such media are not applicable to ionic liquids. This motivates the formulation of a novel transport theory for ionic liquids.

Furthermore, our definition of incompressibility is based on a volumetric constraint[52,53] and differs from the one used in ref. 51. Here we show how to supplement the continuum theory with non-local interactions, modeling the particle nature of the constituents. Therefore, our approach can be used to examine both the bulk behavior, and the quasi-crystalline double-layer behavior of ionic liquids.

Thermodynamics. The equations of motion are derived following the method of Coleman and Noll supplemented by a linear Onsager Ansatz. The central part of this method is the free energy F. First, we assume that the free energy $F(\rho_\alpha,\mathbf{D})$ depends on the mass densities ρ_α and the dielectric displacement $\mathbf{D}$ only. Based on this simple assumption and the fundamental laws of thermodynamics, the transport equations can be systematically derived. Second, by modeling its specific form, we specify all the material properties of the ionic liquid. In this way, the only freedom of modeling is the determination of a suitable free energy, the rest is a rigorous mathematical consequence of this choice.

We divide the free energy

$$F = \int_\Omega \rho\varphi_{\mathrm{H}}\mathrm{d}V + F^{\mathrm{int}} \tag{1}$$

into a standard part described by a single-particle free energy density $\rho\varphi_{\mathrm{H}}$ and a many-particle interaction energy F^{int}. The latter term contains energetic contributions involving more than one particle, *e.g.*, molecular attraction. In this work we restrict F^{int} to hardcore repulsion.

The electrolyte equation of state is formulated as a constraint on the concentrations c_α and the partial molar volumes ν_α, such that $\sum_{\alpha=1}^{N}\nu_\alpha c_\alpha = 1$.[52–54] If the partial molar volumes do not depend on pressure, this describes incompressibility. As consequence, we derive the convective equation of state $\nabla\mathbf{v} = -\sum_{\alpha=1}^{N}\nu_\alpha\nabla\mathbf{N}_\alpha$, where $\mathbf{v}$ is the convective bulk velocity and the ionic fluxes $\mathbf{N}_\alpha$ measure transport in the center-of-mass frame.

The single-particle free energy density is chosen as

$$\rho\varphi_{\mathrm{H}} = \frac{\mathbf{ED}}{2} + \frac{\mathscr{K}}{2}\left(1-\sum_{\alpha=1}^{N}\nu_\alpha c_\alpha\right)^2 + RT\sum_{\alpha=1}^{N}c_\alpha\ln\left(\frac{c_\alpha}{c_0}\right), \tag{2}$$

modeling the electrostatic energy, elastic energy, and entropy. The elastic energy enforces the incompressibility $\sum_{\alpha=1}^{N}\nu_\alpha c_\alpha = 1$ because we let the bulk modulus diverge $\mathscr{K}\to\infty$. The elastic contribution determines the force density *via* the Navier–Stokes equation

$$\rho\dot{\mathbf{v}} = \nabla\left[\frac{\mathscr{K}}{2}\left(1-\left(\sum_{\alpha=1}^{N}\nu_\alpha c_\alpha\right)^2\right) - \rho_{\mathrm{F}}E\right]. \tag{3}$$

We omit the inertial forces $\rho\dot{\mathbf{v}} = 0$ in the highly viscous ionic liquids. Thus, we can express elastic forces in terms of electrostatic forces in our transport equations below. The remnant of the single-particle free energy density is analogous to the one used in ref. 51.

Hardcore particles. We describe ionic liquids as composed of oppositely charged (valency ±1) hard spheres. Although our formalism allows implementing different volumes for particles of different species, we assume an equal volume here. Our approach allows fast simulations of both the interfacial and bulk processes. The particle nature of the electrolyte is modeled *via* an interaction contribution to the free energy. We capture the requirement that the volume of the hard spheres is inaccessible to distinct particles by a repulsive potential between the particles. In particular, we choose

$$F^{\mathrm{int}}[c] = \frac{1}{2}\sum_{\alpha,\beta}\int_\Omega c_\alpha(\mathbf{x})\mathscr{F}_{\alpha\beta}(\mathbf{x}-\mathbf{y})c_\beta(\mathbf{y})\mathrm{d}\mathbf{x}\mathrm{d}\mathbf{y}. \tag{4}$$

This choice of the repulsive interaction $\mathscr{F}_{\alpha\beta}(\mathbf{x}-\mathbf{y})$ models the impenetrable hard spheres, *i.e.*, the repulsive interaction is non-zero in a small volume Ω determined by the particle-radii. The mathematical form of $\mathscr{F}_{\alpha\beta}$ is given in the ESI.† The modification of the chemical potentials due to this inter-particle repulsion is derived with functional derivatives

$$\mu_\alpha^{\mathrm{int}}(\mathbf{x}) = \frac{\delta F^{\mathrm{H}}[c]}{\delta c_\alpha} = \int_\Omega \mathscr{F}_{\alpha\beta}(|\mathbf{x}-\mathbf{y}|)c_\beta(\mathbf{y})\mathrm{d}\mathbf{y}. \tag{5}$$

Transport model. An Onsager Ansatz yields the equations of motion for ionic fluxes and the electric current for the incompressible ionic liquid ([$Py_{1,4}$]TFSA) in the isothermal limit. We restrict the following discussion to the ternary case with the pure ionic liquid and a single additive, *e.g.*, water molecules or silver ions. If we know the charge density ρ_{F} and the additive concentration c_3 we can calculate the concentrations c_i of all the species. This follows from the electrolyte equation of state, $\nu_+c_+ + \nu_-c_- + \nu_3c_3 = 1$, and the expansion of the charge density, $\rho_{\mathrm{F}} = F(c_+ - c_- + z_3c_3)$. We model transport with the following equations

$$\partial_t\rho_{\mathrm{F}} = -\nabla\mathbf{J} - \nabla(\rho_{\mathrm{F}}\mathbf{v}), \tag{6}$$

$$\partial_t c_3 = -\nabla\mathbf{N}_3 - \nabla(c_3\mathbf{v}), \tag{7}$$

$$\rho_{\mathrm{F}} = -\varepsilon_{\mathrm{R}}\varepsilon\Delta\Phi, \tag{8}$$

i.e., the continuity of charge, the continuity of the additive, and the Poisson equation, respectively. The convection velocity is given by

$$\begin{aligned}\nabla\mathbf{v} = {} & \frac{1}{F}\frac{M_-\nu_+ - M_+\nu_-}{M_+z_- - M_-z_+}\cdot\nabla\mathbf{J} - \left(\frac{M_+(z_-\nu_3 - z_3\nu_-)}{M_+z_- - M_-z_+}\right.\\ & \left.+\frac{z_+(M_3\nu_- - M_-\nu_3)}{M_+z_- - M_-z_+} + \frac{\nu_+(M_-z_3 - M_3z_-)}{M_+z_- - M_-z_+}\right)\cdot\nabla\mathbf{N}_3,\end{aligned} \tag{9}$$

where $\mathbf{J}$ denotes the electric current in the center of the mass frame

$$\begin{aligned}\mathbf{J} = {} & -\kappa\cdot\nabla\Phi + \frac{\kappa}{F}\cdot(1-t_3)\cdot\frac{M_-\nabla\mu_+ - M_+\nabla\mu_-}{M_+z_- - M_-z_+}\\ & -\frac{\kappa}{F}\cdot t_3\cdot\frac{M_+\nabla\mu_3 - M_3\nabla\mu_+}{M_+z_3 - M_3z_+}.\end{aligned} \tag{10}$$

Here, the particle flux of the additive

$$\mathbf{N}_3 = D\cdot\frac{M_3z_- - M_-z_3}{M_+z_- - M_-z_+}\cdot\nabla\mu_+ + D\cdot\frac{M_+z_3 - M_3z_+}{M_+z_- - M_-z_+}\cdot\nabla\mu_- - D\cdot\nabla\mu_3 + \frac{t_3}{F}\cdot\frac{M_+}{M_+z_3 - M_3z_+}\cdot\mathbf{J}, \quad (11)$$

depends on the electric current, on the three chemical forces and on the transport parameters of silver in the electrolyte solution, on the diffusion coefficient D, and on the transference number t_3. The chemical forces $\nabla\mu_\alpha$

$$\nabla\mu_\alpha = -\nu_\alpha\rho_F\nabla\Phi + RT\nabla\ln\left(\frac{c_\alpha}{c_0}\right) + \nabla\mu_\alpha^{int} \quad (12)$$

are determined by the Navier–Stokes eqn (3) which couples the elastic and electrostatic forces. The material parameters[55,56] are listed in the ESI.† The above set of equations describes the dynamics and equilibrium of an ionic liquid with additive. In this work, we focus on their stationary solution near an electrified interface. The electrolyte structure is reflected in the electrolyte potential distribution Φ and the charge density ρ_F. In our AFM experiments, we perturb this structure and obtain information on its size and stability. In our simulations, we have access to the elastic reaction of the system when subjected to mechanical excitations. The mechanical forces in the EDL are compensated for by electrostatic forces. As a consequence, the generalized Lorentz force density $\mathbf{f} = \rho_F\nabla\Phi$ appearing in the Navier–Stokes equation resembles these mechanical forces. We obtain a force

$$\mathbf{F} = \frac{(\nu_+ + \nu_-)}{N_A}\mathbf{f} = \frac{(\nu_+ + \nu_-)}{N_A}\rho_F\nabla\Phi \quad (13)$$

by multiplying $\mathbf{f}$ with the molecular volume. This simulated force is compared with the experimental results delivered by AFM measurements testing the stationary multilayer structure of the EDL. While the AFM tip approaches the electrode surface, it penetrates the EDL and pushes ions away. Thus, the AFM measurement is an inelastic probe of the EDL, while our simulations determine an elastic force. Nevertheless, the simulated and measured forces both represent the mechanical reaction to perturbations of the system.

The formalism outlined above can be generalized to electrolytes with a neutral solvent and an arbitrary number of solutes. In future work, we will extend the transport theory in this regard and include viscous media and heat transport. It is the strength of our consistent approach that the contributions of the solvent are not hidden as in standard concentrated solution theory.[57]

3 Results and discussions – electrochemical and interfacial investigations of the electrolytes

3.1 Experimental results

Cyclic voltammetry has been employed to investigate the electrochemical behaviour of the electrolytes at varying concentrations of AgTFSA in $[Py_{1,4}]$TFSA on gold at RT. Multiple-cycles have been recorded for AgTFSA/$[Py_{1,4}]$TFSA electrolytes to investigate changes in the interfacial processes/redox processes. All cyclic voltammograms have been recorded first in the negative direction from the Open Circuit Potential (OCP) to the chosen switching potentials at a scan rate of 10 mV s^{-1}. For the neat liquid, a rise in reduction current has been observed at ~ -0.7 V, which can be due to the adsorption of IL on Au (Fig. 1a).[35] Quite a weak oxidation peak has been observed at -0.9 V in the backward scan of the CV. Upon addition of 50 μM AgTFSA to $[Py_{1,4}]$TFSA, three reduction processes have been noticed in the forward scan of the CV (Fig. 1b). The first two reduction processes C1 and C2 could be due to the adsorption processes of the electrolyte species and to the underpotential deposition of Ag. The reduction process C3 can be clearly correlated with the bulk deposition of silver.

For 50 μM AgTFSA/$[Py_{1,4}]$TFSA, two oxidation processes have been observed in the backward scan of the CV (Fig. 1c). The oxidation process A1′ is related to the reduction process C3 and the oxidation process A1 is associated with the reduction process C2. A broad reduction (C_R) wave has been noticed after the first scan, which can be related to the surface reduction process due to a change in the electrode surface. The third and fifth CVs also exhibit similar features to that of the first scan except for a broad reduction process C_R. For the CV of 100 μM AgTFSA/$[Py_{1,4}]$TFSA, a reduction wave is seen at C1 followed by a reduction step at C2. Here, the reduction step C1 could be due to an adsorption of the electrolyte, and C2 is due to the deposition of silver, respectively. The processes A1′ and A1 are correlated with the desorption of adsorbed layers of the electrolyte from the electrode surface and with the dissolution of the deposited silver films, respectively.

The CV of 200 μM AgTFSA/$[Py_{1,4}]$TFSA (Fig. 1d) consists of a clear reduction peak at C2 along with a broad reduction wave at C1 in the forward scan and three oxidation steps in the backward scan. The reduction process C2 with a peak at -1.6 V is due to the bulk deposition of Ag and the process C1 is likely to be correlated with the underpotential deposition of Ag. The oxidation process A1 can be related to the reduction process C2. Moreover, it has been observed that silver nanoparticles can form chemically under light irradiance. The third and fifth CVs exhibit similar features to those of the first scan. Furthermore, the adsorption process that was observed in the neat IL and at low concentrations of AgTFSA/$[Py_{1,4}]$TFSA (50 and 100 μM) has not been observed for 200 μM AgTFSA/$[Py_{1,4}]$TFSA, obviously an effect of the increase in concentration of AgTFSA. In the case of the zinc ions in ILs, it has been proposed that such interfacial processes can be varied by the arrangement of IL anions and cations adjacent to the electrode in the compact layer (IHP, Inner Helmholtz Plane), which can dictate the kinetics of the redox processes.[58] Based on these electrochemical results the question arises as to how the interfacial processes of ILs vary in the presence of a solute and how are they dependent on its concentration.

In order to describe the electrode/electrolyte interface (or the interfacial structure) of ILs and solutions with a varying concentration of silver salts, we have performed *in situ* Atomic Force Microscopy (AFM) investigations. To the best of the

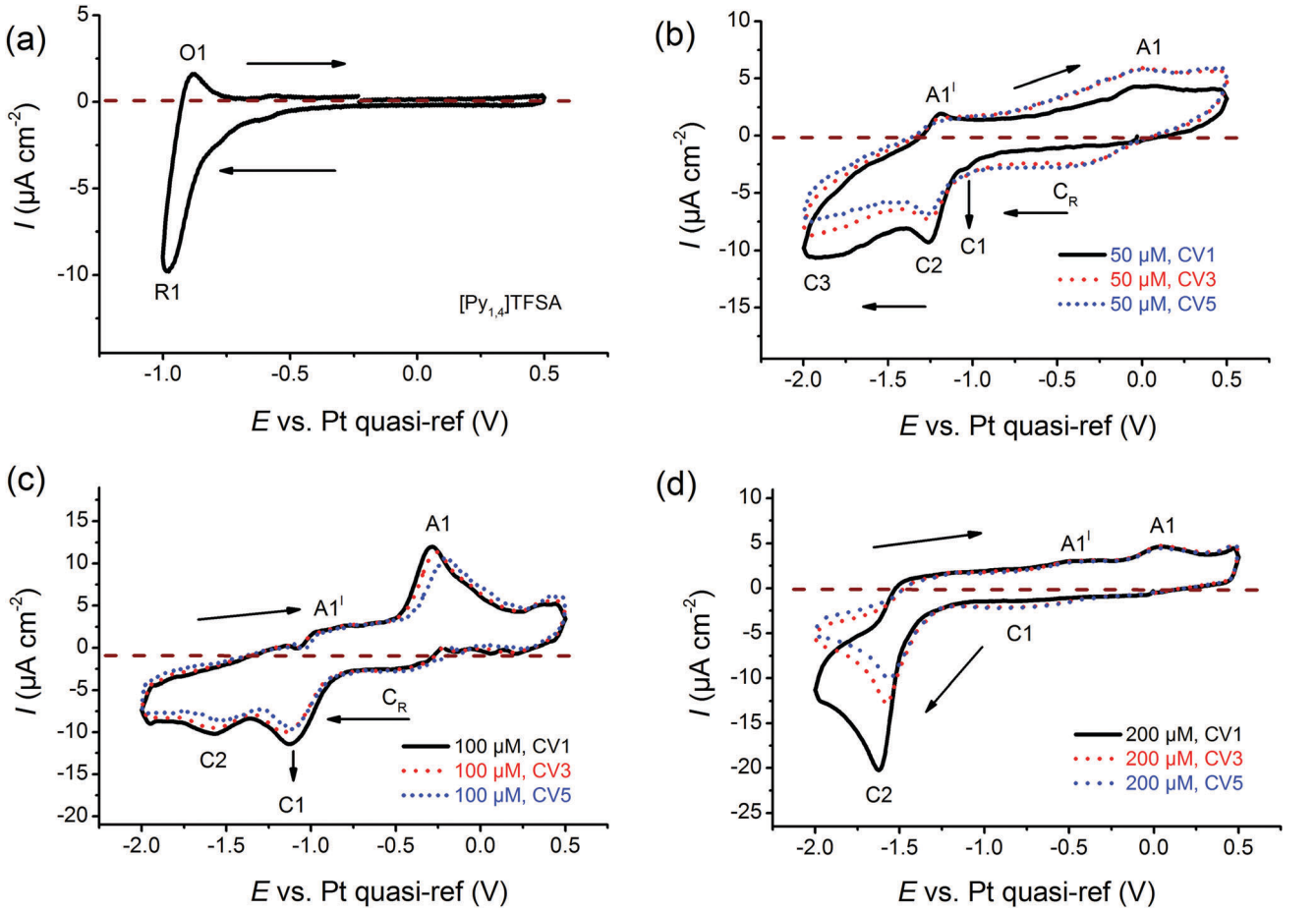

Fig. 1 Comparison of cyclic voltammograms of (a) neat $[Py_{1,4}]TFSA$, (b) 50 μM AgTFSA/$[Py_{1,4}]TFSA$, (c) 100 μM AgTFSA$[Py_{1,4}]TFSA$, and (d) 200 μM AgTFSA/$[Py_{1,4}]TFSA$. Scan rate = 10 mV s^{-1}.

authors' knowledge, such measurements, where a systematic variation of salt concentration has been performed, have not yet been reported so far.

Fig. 2 shows the force *vs.* separation curves for an AFM tip approaching the Au(111) surface in the neat IL and in mixtures with two different concentrations of AgTFSA and at three different electrode potentials (OCP, +0.2 V and −0.2 V). The appearance of the AFM force curves differ with varying concentrations of AgTFSA (addition of solute) from the force curves of the Au(111)/IL interface.[25,40,41] For the neat IL, the interfacial structure consists of at least four discrete steps at the measured electrode potentials, which is in agreement with the literature. This behavior reveals a strong ion–ion interaction between the solvation layers, as in this case by displacing the innermost solvation layers, the AFM tip pulls the other layers as well. For the Au(111) surface the first layer is observed at ∼0.6 nm followed by the 1.5, 2.4, and 3.3 nm steps, which correspond to widths of ∼0.6 and 0.9 nm, respectively. The steps correspond to the rupturing of successive adjacent surface layers as the AFM tip approaches the gold surface. Furthermore, the force required to rupture decreases for the layers farther away from the electrode surface to the bulk, indicating a weaker ordering of the layered structure away from the electrode surface. Upon changing the electrode potentials to either +0.2 V or to −0.2 V, a similar multi-layered structure with a variation in the separation of the layers can be detected (Fig. 2). For the neat IL, the force required to rupture the layer adjacent to the electrode was found to vary with the applied electrode potential. The rupturing forces were found to be 10 nN, 6 nN, and ∼3 nN for the neat IL at −0.2 V, at OCP, and at +0.2 V, respectively, revealing that a relatively strong near surface structure is present at −0.2 V. This indicates an increase in the strength of adsorption at more negative electrode potentials. For the neat IL at −0.2 V, the widths of the innermost and successive layers were found to be 0.5 and ∼0.9 nm, revealing a strong near surface interaction of the ions due to the applied electrode potential. This observation is in agreement with literature data.

For 50 μM AgTFSA/$[Py_{1,4}]TFSA$, a few changes have been recorded in the force–distance curves at all measured electrode potentials. At OCP, the width of the innermost layer is ∼0.8 nm, which can either be due to a rearrangement of the ions or to a change in the composition of the electrolyte (or species like AgTFSA complexes are present). The widths of the subsequent layers have been slightly increased for 50 μM AgTFSA in comparison to the neat IL, with an average width of 1 nm at all electrode potentials. However, the innermost

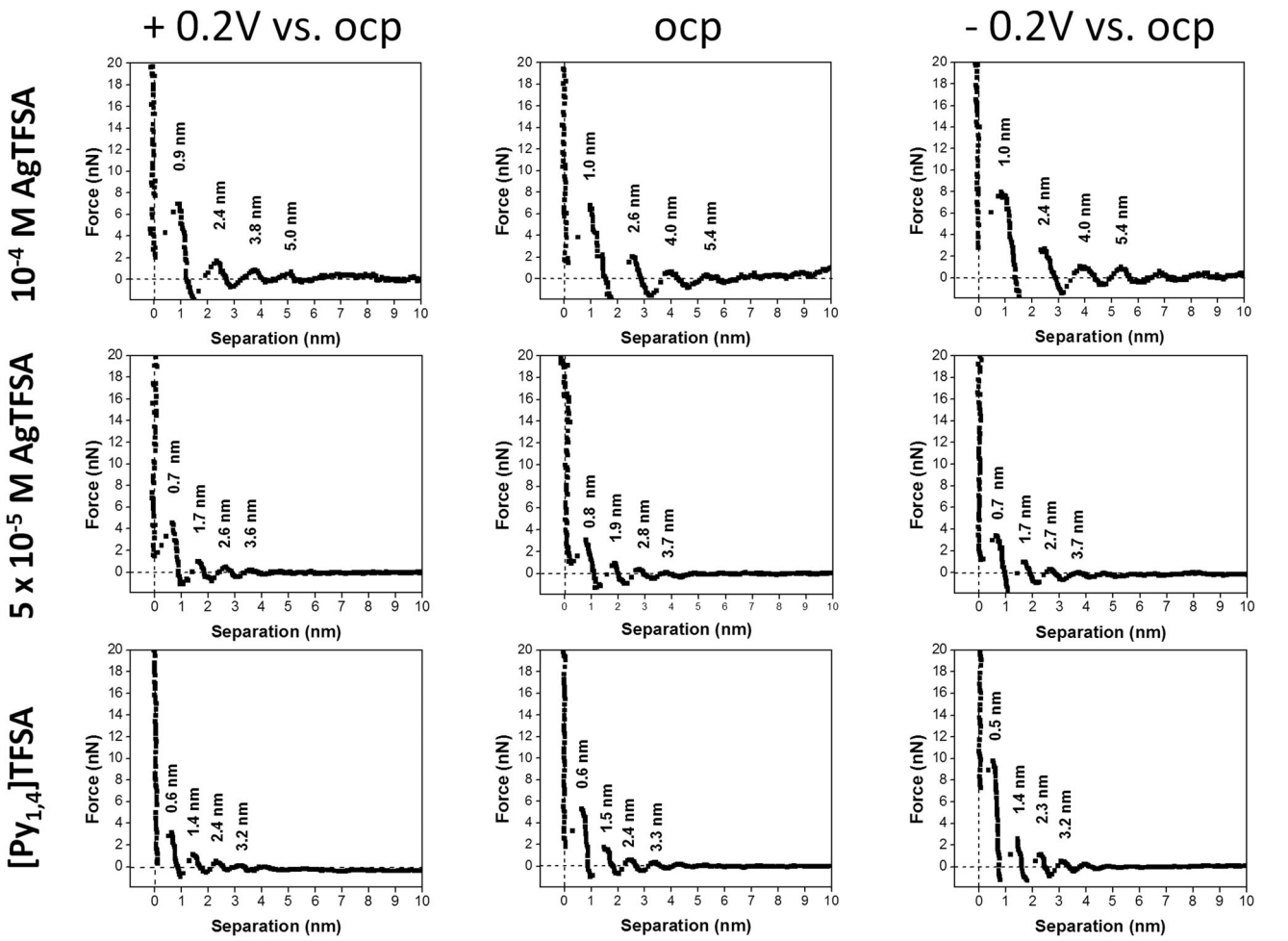

Fig. 2 A comparison of the typical force–separation curves of neat $[Py_{1,4}]$TFSA and of two different concentrations of AgTFSA in $[Py_{1,4}]$TFSA. The curves have been obtained at +0.2 V *vs.* OCP (left column), at OCP (middle column), and at −0.2 V *vs.* OCP (right column). [AgTFSA] = 50 μM and 100 μM.

layer widths were found to be 0.7 nm at −0.2 V and at +0.2 V. The increase in the width of the layers for 50 μM AgTFSA can be attributed either to the presence of AgTFSA complexes or to their changes in orientation (or conformers) of the species. Furthermore, there is a marginal change in the rupturing force in the force–distance curves. The rupturing forces were found to be 3 nN for all electrode potentials, indicating a rather weak near surface interaction of the ions with the electrode.

For 100 μM AgTFSA/$[Py_{1,4}]$TFSA, a further increase in the widths of the layers has been observed at all measured electrode potentials. Typically, the width of the innermost layer was found to be 0.9 ± 0.1 nm at +0.2 V, OCP and at −0.2 V. The average widths of the successive layers were found to be 1.4 nm at OCP and at −0.2 V. The force required to rupture the layers increased to 8 nN at all the measured potentials. However, a clear change was noticed at the 200 μM concentration wherein the number of layers varied upon varying the electrode potential. Four clear and distinct layers with step widths of about 1.0, 1.4, 1.5, and 1.4 nm have been observed at OCP and 0.9, 1.2, 1.4, 1.4 nm have been noticed at −0.2 V. However, only two steps with widths of about 0.9 and 1.5 nm have been recorded at +0.2 V. The force required to rupture the innermost layers is found to be large at OCP (10 nN) and at −0.2 V (14 nN) compared to the one at +0.2 V, which indicates a difference in the strength of the adsorption of the innermost layer with the substrate. Furthermore, the number of steps has been found to be the same at −0.2 V while a decrease in the step width has been noticed (*ca.* 0.9 nm). Quite an interesting result has been obtained at and above the 500 μM AgTFSA concentration, wherein only a single step was noticed at all measured electrode potentials. Furthermore, a change in the widths of the layers by varying the electrode potentials has been found for 500 μM AgTFSA (Fig. 3). Here in this case, one clear step with a layer width of 1 nm has been observed at OCP, whereas the step widths were found to decrease upon varying the electrode potential (*e.g.* 0.9 nm at +0.2 V and 0.8 nm at −0.2 V). Moreover, the forces required to rupture these layers have been nearly the same (*ca.* 2–3 nN). However, no clear and discrete steps have been observed at the OCP and at 0.2 V for 1 mM AgTFSA in the force–distance profiles, rather gradients have been noticed. These gradient widths were found to be ∼0.3 and ∼0.2 nm at the OCP and at +0.2 V, respectively. The forces needed to break the layers were around 6–7 nN in both cases. Furthermore, no clear signal was seen at −0.2 V, which indicates that the applied electrode

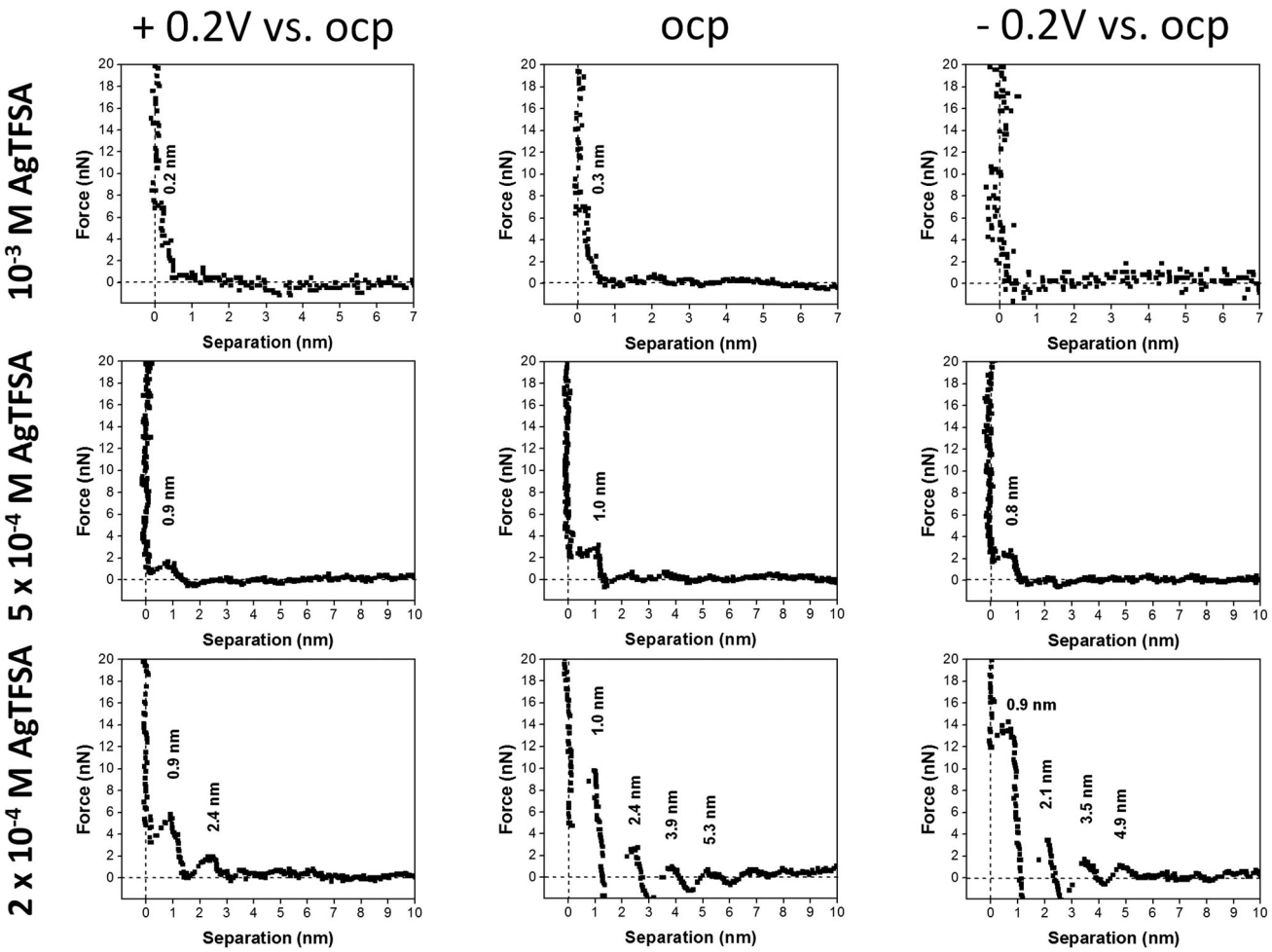

Fig. 3 A comparison of the typical force–separation curves of three different concentrations of AgTFSA in $[Py_{1,4}]$TFSA. The curves have been obtained at +0.2 V *vs.* OCP (left column), at OCP (middle column), and at −0.2 V *vs.* OCP (right column). [AgTFSA] = 200 μM, 500 μM, and 1 mM.

potential affects the interfacial structure. The analysis of force–separation profiles at various concentrations of AgTFSA in $[Py_{1,4}]$TFSA has shown that the number of solvation layers decreases from four layers to a single layer with an increase in concentration from 50 to 200 μM AgTFSA in $[Py_{1,4}]$TFSA. A significant change in the widths of the innermost layers can also be observed at 1 mM AgTFSA.

In order to interpret the present findings of the Au(111)/$[Py_{1,4}]$TFSA interfacial nanostructure at various concentrations of AgTFSA, we compare the results with the reported ones in the literature at varying concentrations of alkali metal salts in ILs[41,59] (*e.g.* LiTFSA/$[Py_{1,4}]$TFSA[41] and NaFSA/$[Py_{1,4}]$TFSA[59]). At OCP, five solvation layers were reported for 0.1 M LiTFSA/$[Py_{1,4}]$TFSA on Au(111). The innermost layer width was found to be 0.16 nm for 0.1 M LiTFSA/$[Py_{1,4}]$TFSA while the innermost layer width was found to be 0.65 nm for $[Py_{1,4}]$TFSA. In the case of the 0.1 M LiTFSA/$[Py_{1,4}]$TFSA, the widths of the successive layers were found to be same ($\sim$0.7 nm) and these steps could be related to the presence of the ion-pairs of $[Py_{1,4}]$TFSA. A similar behaviour was also seen for $[Py_{1,4}]$TFSA, where a multi-layered structure can be observed. The widths of the innermost layers rose by increasing the concentration from 0.1 M to $\geq$0.5 M LiTFSA/$[Py_{1,4}]$TFSA. A decrease in the number of layers can also be observed with an increase in the concentration of LiTFSA. Moreover, the widths of the successive layers (*e.g.* 2nd, 3rd and 4th layers for 0.5 M LiTFSA in $[Py_{1,4}]$TFSA and 2nd and 3rd layers for 1 M LiTFSA/$[Py_{1,4}]$TFSA) were found to be between $\sim$0.85 and $\sim$0.95 nm. This indicates that the presence of $[Py_{1,4}]$TFSA ion-pairs in the successive layers was not influenced by the presence of Li^+ at the interface for varying concentrations of Li^+ between 0.1 M and 0.5 M. However, the interfacial nanostructure was disturbed at 1 M LiTFSA/$[Py_{1,4}]$TFSA upon varying the electrode potential, which was attributed to the formation of upd layers on the electrode. This study clearly showed that the addition of Li^+ can significantly change the interfacial structure where $[Py_{1,4}]^+$ ions are replaced by Li^+, which was observed as a decrease in the innermost layer widths on Au(111). Furthermore, the widths of the innermost layers were increased on increasing the concentration of LiTFSA, which was attributed to the change in configuration between Li^+ and $TFSA^-$.[41]

For NaFSA in $[Py_{1,4}]$FSA, the interfacial nanostructure did not vary upon the addition of 0.05 M NaFSA to $[Py_{1,4}]$FSA[59] in which the innermost layer width was found to be nearly the

same (~0.65 nm) as that of the innermost layer width for $[Py_{1,4}]$TFSA. However, the interfacial nanostructure was changed upon increasing the concentration of NaFSA from 0.05 to ≥0.25 M in $[Py_{1,4}]$FSA, wherein the width of the innermost layer was found to be ~0.35 nm for 0.25 M and 0.5 M NaFSA in $[Py_{1,4}]$FSA. In the case of NaFSA/$[Py_{1,4}]$FSA at OCP, the widths of the innermost layers were found to be invariant upon increasing the concentration of NaFSA. Based on these two studies we can conclude that the structure of the Au(111)/IL interface at a higher concentrations of metal salts (*e.g.* 1 M LiTFSA $[Py_{1,4}]$TFSA or 0.5 M NaFSA/$[Py_{1,4}]$FSA) differed with that of the interfacial structure at lower concentrations (*e.g.* 0.1 M LiTFSA in $[Py_{1,4}]$TFSA or 0.05 M NaFSA in $[Py_{1,4}]$FSA). However, in contrast to the present studies with AgTFSA rather high concentrations of LiTFSA and NaFSA were needed to disturb the interfacial layers.

The following salient features can be drawn from the above discussion. An increase in the width of the innermost layer has been noticed upon increasing the concentration of LiTFSA from 0.1 to 0.5 M in $[Py_{1,4}]$TFSA (0.16 nm for 0.1 M *vs.* 0.25 nm for 0.5 M), which was attributed to changes in the complexation (*i.e.* a change in the coordination number, C.N.) and to configurational changes (*i.e. cis*/*trans* and/or monodentate/bidentate).[41] For the nanostructure of the Au(111)/NaFSA-$[Py_{1,4}]$FSA interface, the authors have observed no significant increase in the push-through forces for 0.05 M NaFSA in $[Py_{1,4}]$FSA at various electrode potentials. These push-through forces were almost comparable with those of $[Py_{1,4}]$FSA under similar conditions. A significant change in the nanostructure of Au(111)/NaFSA-$[Py_{1,4}]$FSA has been observed for 0.25 M NaFSA in $[Py_{1,4}]$FSA, where the innermost layer width significantly decreased (0.37 nm for 0.25 M FSA/$[Py_{1,4}]$FSA *vs.* 0.68 nm for 0.05 M NaFSA/$[Py_{1,4}]$FSA). A stable interfacial structure has been found upon further increasing the concentration from 0.25 M to 0.5 M NaFSA.[59] Here, in the aforementioned two cases, the concentrations of metal salts (LiTFSA/NaFSA) have been varied in the regime of mM to M. However, in the case of AgTFSA reported in the present paper, the interfacial structure was studied at quite low concentrations of the salt from 50 μM to 1 mM of AgTFSA. Moreover, we observe a similar solvation structure for salt concentrations between 50 and 200 μM AgTFSA. The solvation layers formed due to the presence of AgTFSA complexes from 50 to 200 μM should be the same. Therefore, the widths of the innermost layers do not differ largely in this regime of concentration. We indeed observed a similar solvation structure at the interface of the Au(111)/electrolyte in this regime of AgTFSA concentrations, where the innermost layer widths were between 0.8 and 1 nm. However, not only the orientation (*cis*/*trans* configurations) of the solvated species on the electrode surface change but also the solvation layers change upon further increasing the concentration to 500 μM and above. The above *in situ* AFM results reveal that the Au(111)/AgTFSA/$[Py_{1,4}]$TFSA interfacial structure is rather complex and further thorough investigations are needed to comprehensively describe the near surface ionic arrangement at the electrode/electrolyte interface.

In order to investigate the dynamics of the interfacial processes that occur on Au(111), we have recorded the force–distance curves of 50 μM AgTFSA/$[Py_{1,4}]$TFSA by varying the electrode potentials to more negative values like −0.8 V *vs.* OCP and then back to a more positive value, *e.g.* −0.3 V. The corresponding force–distance curves are shown in Fig. 4. Four distinct steps have been observed in the force–distance profiles upon varying the electrode potentials from OCP to −0.8 V. The average widths of the innermost and the

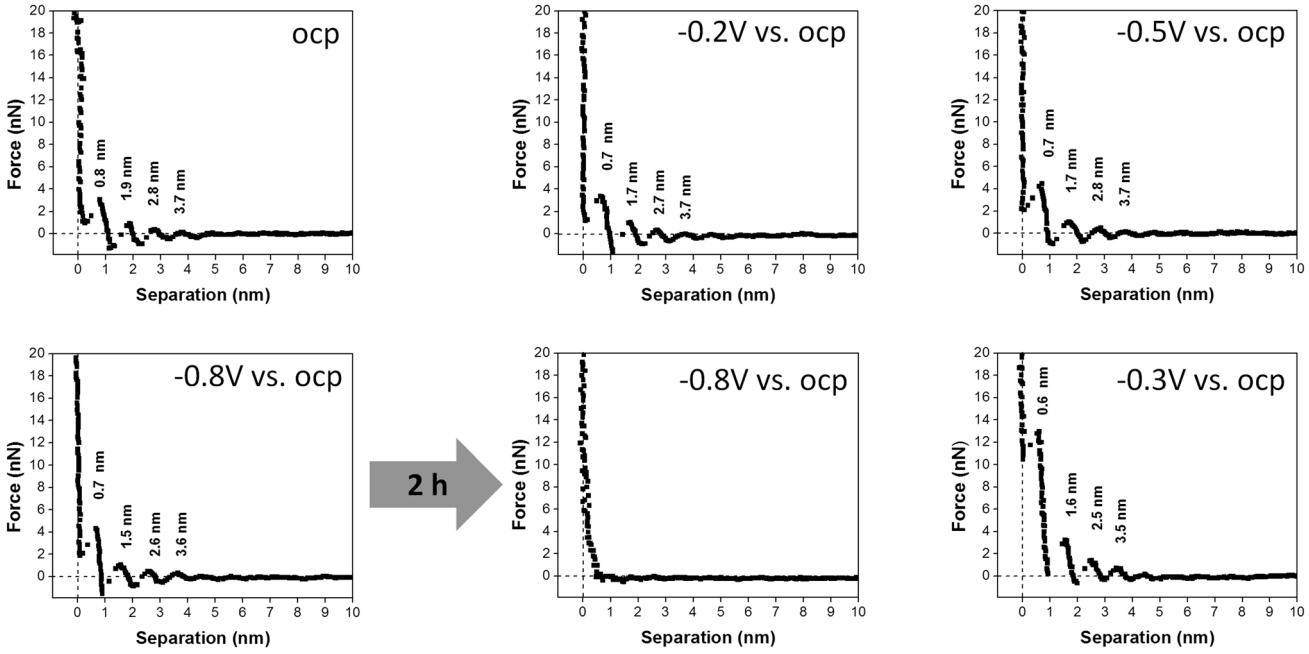

Fig. 4 A comparison of typical force–separation profiles of 50 μM AgTFSA in $[Py_{1,4}]$TFSA. The curves have been obtained at various electrode potentials from OCP to −0.8 V, the potential was held at −1 V for 2 h, and switched back to −0.3 V.

next successive layers were found to be 0.7 and 1 nm, respectively. However, by applying −0.8 V for two hours under the conditions of Ag deposition the force–distance profiles show no steps indicating that the interfacial structure is totally disturbed during the deposition of silver on gold. The deposition process consumes silver ions that are present at the interface resulting in a depletion of silver complexes at the interface. A multilayered structure is resumed after changing the potential back to −0.3 V where the deposited silver is slowly oxidized. The reappearance of this multilayer is typical for quite a low concentration of AgTFSA/[$Py_{1,4}$]TFSA and for the neat IL, which is due to the presence of either AgTFSA complexes or to the ion-pair of the IL at the interface.

In summary, the force–distance profiles obtained for [$Py_{1,4}$]TFSA and for AgTFSA/[$Py_{1,4}$]TFSA are different. The results obtained in this investigation indicate that the multilayered structure is retained in IL solutions with quite low concentrations of the silver salt, and slight changes have been observed for 50 and 100 μM AgTFSA at all measured electrode potentials. The innermost layer thickness for the neat IL varies upon changing the electrode potentials (*e.g.* ±0.2 V *vs.* OCP). There is a slight increase in the width of the innermost layer for AgTFSA/[$Py_{1,4}$]TFSA at the measured potentials, indicating an increase in the dimensions of the ions, which could be due to the presence of the ion-pairs of the IL in a different orientation along with the Ag^+ complexes in the interface. Furthermore, the presence of quite low concentrations of AgTFSA complexes may not influence the interfacial structure strongly and the innermost layer is still dominated by IL ion pairs. A transition in the interfacial structure has been observed at 200 μM AgTFSA in [$Py_{1,4}$]TFSA, wherein the step width is increased with a further increase in the average widths of subsequent layers (*ca.* 1.5 nm). The increase in width of the innermost layer and the layers extending to the bulk (*i.e.* either in the transition zone or in the diffusion zone) could be due to the presence of AgTFSA complexes as these species are large in their sizes compared to the ion-pair sizes of [$Py_{1,4}$]TFSA. A comparably large force is required to rupture the innermost layer at this concentration compared to the one for the neat IL and for lower concentrations of AgTFSA/[$Py_{1,4}$]TFSA, which is due to an increased strength of adsorption of the AgTFSA complexes on the electrode surface.[41] Furthermore, the number of steps has been found to decrease to 2 at +0.2 V. The decrease in the number of layers indicates a change in the ordering of the layers (layers in the diffusion zone/transition zone) away from the electrode surface, which is also dependent on the electrode potential due to changes in the electrostatic attraction.[60,61]

Rather a simple double layer structure is observed at 500 μM AgTFSA, where only a single step is observed in the force–distance profiles at all electrode potentials. Furthermore, the tip experiences quite a low rupturing force of 2 nN indicating that the adsorbed layer can be ruptured easily with minimum force. Such behaviour indicates that the adsorbed layer weakly interacts with the surface. An increase in the concentration of AgTFSA to 1 mM changes the interfacial structure completely as we could not observe any steps in the force–distance measurements. This indicates that the cantilever cannot find any adsorbed layers until it reaches the electrode surface. The AFM results signify that the concentration has a considerable influence on the interfacial structure for Au(111)/AgTFSA in [$Py_{1,4}$]TFSA. This behaviour is rather complex and it is obviously different for aqueous electrolytes, where a classical EDL structure can be observed at very dilute solutions of aqueous electrolytes.

3.2 Simulation results

For comparison with experiments, we simulate the static equilibrium EDL at 200 mV overpotential. First, we simulate the behavior of the binary ionic liquid [$Py_{1,4}$]TFSA at a metallic surface. Second, we discuss the effect of neutral or charged additives. The details of our computational method can be found in the ESI.†

In Fig. 5, we neglect the hardcore constraint to reach a better understanding of the model ($F^{int} = 0$). The simulations show the

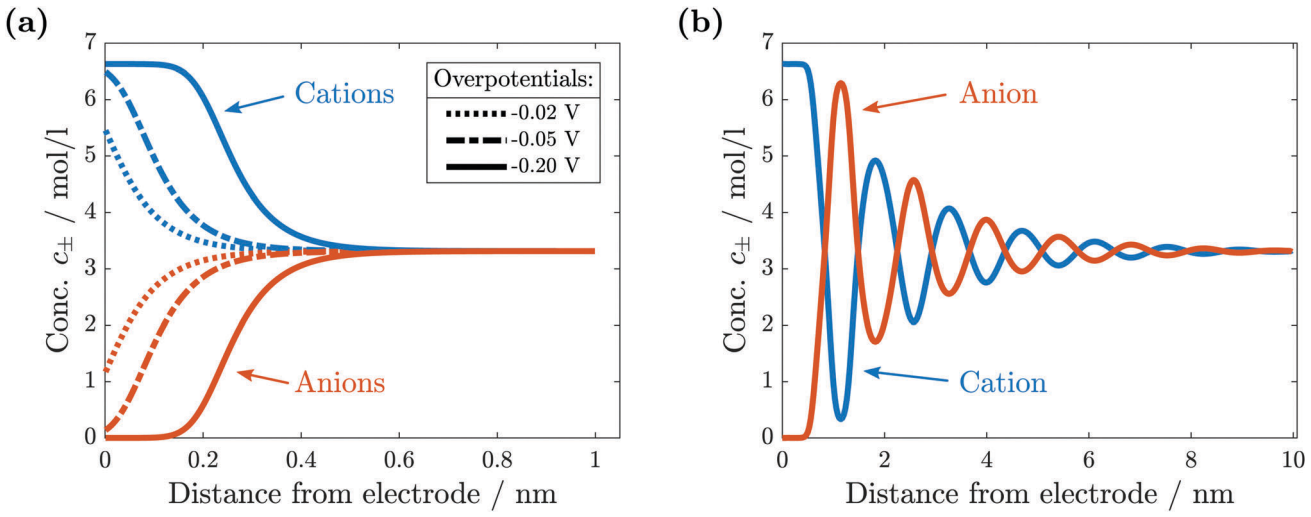

Fig. 5 Comparison of ionic concentrations in the vicinity of a negatively charged electrode surface. (a) Without hardcore interactions we observe the depletions of anions and the crowding of cations. (b) With hardcore interactions a quasi-crystalline structure of alternating layers forms.

crowding of cations at the negative electrode (see Fig. 5(a)). The shape of the ionic layers depends on the applied potential difference. In particular, at small electrode potentials (−0.02 V in Fig. 5(a)), the concentration of cations exhibits a distribution of the Boltzmann-type. The cation concentration at the surface increases with electrode potential until, at sufficiently large polarization (−0.05 V in Fig. 5(a)), it becomes saturated due to incompressibility because limited space is available for the ions. This implies that the concentration of cations at the electrode surface is bound from above. Thereby, the concentration profile changes to the Fermi–Dirac-type. During further increase of electrode polarization (up to −0.2 V in Fig. 5(a)), the cation layer broadens to screen the electric field of the electrode. The decay length of the ionic layers corresponds to the Debye-length expected for a dilute electrolyte, $\lambda_D = \sqrt{2\varepsilon_R \varepsilon RT\nu/F^2} \approx 0.14$ nm.

In conclusion, without the hardcore constraint we observe the standard behavior for electrolytes at electrode interfaces. The electric potential jump is screened by the accumulation of ionic charges.

The simulation results change significantly if the hardcore constraint is taken into account (see Fig. 5(b)). We observe the formation of various alternating layers extending over 5 nm. The first layer adjacent to the negatively charged electrode consists entirely of cations, whereas the anions are depleted completely. The successive layers alternate in the dominating species and decay in amplitude, *i.e.*, the total depletion of the minor species does not appear any more. Finally, the concentrations of the two species converge in the bulk electrolyte. The electrolyte potential is in accordance with the damped oscillations of the ionic concentrations (see Fig. 6). These oscillations show that the ionic diameter is incommensurate with the charge required to screen the electric potential jump.

We calculate the mechanical force as outlined in Section 2.2. The simulated force (see Fig. 7) exhibits the characteristic peaks observed in the AFM experiments. The spacing between the positive peaks agrees with the molecular radius of 0.67 nm (see the ESI†) within numerical accuracy. As shown in Fig. 5(b),

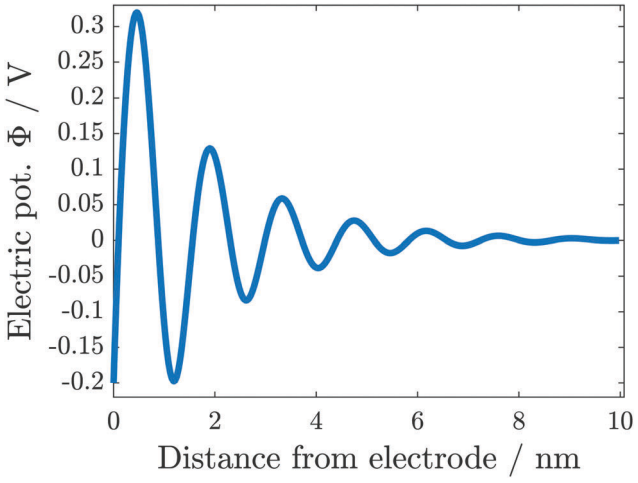

Fig. 6 Electric potential in the electrolyte in the vicinity of a negatively charged electrode surface.

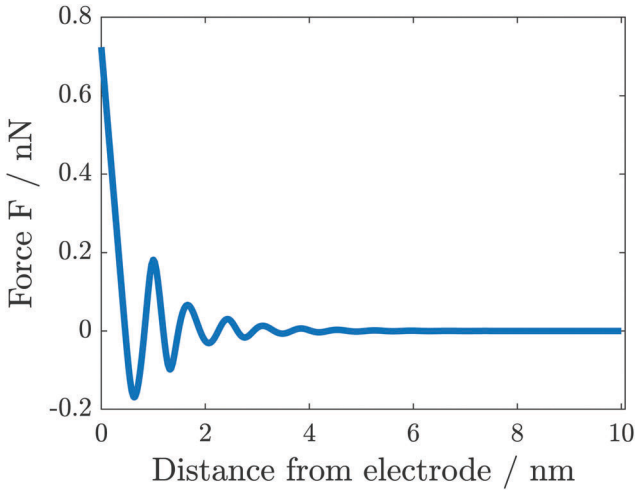

Fig. 7 Simulated force on AFM tip in the vicinity of a negatively charged electrode surface.

the innermost layers are dominated by a single species, in alternating sequence. As these layer widths are qualitatively in good agreement with the experimentally measured layer widths for the pure IL, our model supports the interpretation of AFM measurements to correlate the force peaks with molecular mono-layers. The deviations between the modeled and measured layer widths are not surprising, as our modeling approach neglects microscopic properties, *e.g.*, non-spherical molecular shapes and orientation-dependent interactions.

The deviation between the simulated and experimental forces lies between one to two orders of magnitude. This agreement is very good if we take into account the differing set-ups. The atomic force microscope measures the penetration into a many-particle crystalline structure, including the replacement of particles. In contrast, we simulate elastic perturbations of an equilibrium state.

We discuss the impact of neutral and charged additives, *e.g.*, water H_2O and ionic silver Ag^+ onto the EDL. The dynamics of this third species in the electrolyte is determined by eqn (11). The small concentration of the additive species allows us to neglect the corresponding contributions to convection and to the electric current, setting $M_3 \approx 0$, $\nu_3 \ll \nu_\pm$, and $t_3 \ll 1$ in this principal discussion of the EDL structure. In the stationary case ($\mathbf{J} = 0$ and $\mathbf{N}_3 = 0$) we find from eqn (10) and (11)

$$\nabla\mu_3 = -\frac{Fz_3}{RT}\nabla\Phi. \tag{14}$$

This equation determines the chemical potential and the concentration of the additive from the electric potential. In particular, using eqn (12), we get

$$\nabla\left(\ln\frac{c_3}{c_0}\right) = -\frac{Fz_3}{RT}\nabla\Phi. \tag{15}$$

Note that this relation connects the entropic and electric contributions of the free energy functional.

For the neutral additive water, our theoretical analysis in eqn (15) predicts a uniform distribution throughout the EDL, $c_3 = c_{H_2O} = \text{const}$. This is a consequence of the entropy forcing

neutral additives into the EDL. Therefore, large bulk concentrations of neutral additives are required to reach significant concentrations in the EDL and to affect its multilayer structure. Indeed, previous experiments[43] show that the addition of water perturbs the EDL and destroys the multilayer structure only if it makes up more than half of the solution volume.

Electric forces are to be discussed for charged additives. If we consider silver ($z_{Ag} = 1$) as a third species, eqn (15) shows that its concentration obeys a Boltzmann distribution,

$$c_{Ag}(x) = c_0 \cdot \exp\left(-\frac{F\Delta\Phi(x)}{RT}\right), \quad (16)$$

where $\Delta\Phi(x)$ is the electric potential difference between the bulk electrolyte and point x in the electrolyte. If the electrode is polarized negatively, the Boltzmann distribution describes an exponential growth of silver concentration towards the surface. Even if the electrode is polarized positively, the electric potential in the electrolyte reaches large negative values due to its oscillations shown in Fig. 6. In this case, silver accumulates behind the layer of anions adsorbed at the electrode surface. In the case of the potential difference $\Delta\Phi = -0.2$ V, the silver concentration at the electrode increases to $c_{Ag} = 2.4 \times 10^3 c_{Ag;0}$. We expect that the EDL structure is affected by silver ions once their concentration at the electrode becomes comparable with the bulk concentration of the ionic liquid $c_{Ag} \sim 1$ M. This corresponds to the bulk silver concentration $c_{Ag;0} = 0.4$ mM. Indeed, as shown experimentally in Fig. 3, the EDL structure is changing at these concentrations.

The screening of charges and electric fields cause the electrochemical surface layer. The quasi-crystalline structure emerges because the screening length does not fit the molecular size of the ionic liquids. Metal ions in the surface layer can efficiently shield electric forces and introduce an additional very small molecular length scale. Therefore, we expect that the silver ions very effectively destroy the EDL multi-layer structure.

This argument, however, is complicated by the presence of chemical interactions between the molecules. The chemical interactions could, for example, lead to strong pairing forces. In this case metal ions would mainly be present as a neutral complex and might behave as neutral solutes. Alternatively, neutral solutes could have preferred and strongly polarized bonds with solvent molecules that destroy the quasi-crystalline structure at low concentrations. It remains for further studies to evaluate and classify the effect of the chemical interactions on the EDL.

4 Conclusions

The electrode/electrolyte interface of Au(111)/[$Py_{1,4}$]TFSA and of Au(111)/AgTFSA/[$Py_{1,4}$]TFSA has been investigated using atomic force microscopy. The interfacial structure (or the arrangement of ions) remarkably varies with the concentration of AgTFSA until the layer structure is completely disrupted. Furthermore, changing the electrode potential has some influence on the interfacial structure. The force–separation profiles indicate that a multi-layer structure is found for the neat IL and this multi-layer structure is retained at quite low concentrations of the silver salt (50 to 100 μM AgTFSA/[$Py_{1,4}$]TFSA). However, a clear change in the electrical double layer structure has been noticed at a 200 μM concentration of AgTFSA in [$Py_{1,4}$]TFSA wherein the interfacial layers were found to be different on changing the applied electrode potentials. Furthermore, the widths of the corresponding innermost layers at 200 μM concentration are different from those ones observed at lower concentrations of AgTFSA. A simple double layer structure has been observed for 500 μM AgTFSA, which does not vary with the applied electrode potential. A remarkable difference is observed at this concentration and above, in which no layer structure has been noticed at 1 mM concentration. The observed changes in the widths of the innermost layer from AFM measurements could be attributed to the orientation of the Ag species (or to the conformational changes of the anions that are coordinated to the Ag^+).

Furthermore, we present a model analysis supporting these measurements of the EDL structure. We simulate force profiles that show the multilayer structure and agree with the experimental observations. The distances between force peaks correspond to ionic monolayers. We can show that in contrast to neutral additives ionic additives like AgTFSA are attracted by an electrified interface. Therefore, we predict in good agreement with experiments that roughly 400 μM concentrations are sufficient to reach large concentrations in the EDL and disrupt its structure. By neglecting the microscopic details of chemistry, our model highlights the fundamental relations behind the multilayer EDL structure of ionic liquids.

The AFM results on the dynamics of the interfacial processes reveal that the multilayer structure is disrupted completely during the deposition of silver upon applying −0.8 V for 2 h and the multilayer structure is retained after changing the electrode potential back to −0.3 V. This study signifies that the EDL structure of Au(111)/IL is indeed influenced by the presence of varying concentrations of an added salt to the IL. The general question arises to what extent different solutes alter IL interfacial layers and whether the dynamic processes alter the deposit morphology.

Conflicts of interest

There are no conflicts to declare.

Acknowledgements

Financial support by the German Ministry of Education and Research (BMBF) (project LUZI, BMBF: 03SF0499A, 03SF0499E) and by the German Research Foundation (DFG) (DFG: EN 370/26-1) is gratefully acknowledged.

References

1 V. Rooryck, F. Reniers, C. Buess-Herman, G. Attard and X. Yang, *J. Electroanal. Chem.*, 2000, **482**, 93–101.
2 S. Garcia, D. Salinas, C. Mayer, E. Schmidt, G. Staikov and W. J. Lorenz, *Electrochim. Acta*, 1998, **43**, 3007–3019.
3 A. Morgante, K. Prince, G. Paolucci and E. Tosatti, *Surf. Sci.*, 1987, **189-190**, 620–627.

4 K. Ogaki and K. Itaya, *Electrochim. Acta*, 1995, **40**, 1249–1257.
5 J. Wang, B. M. Ocko, A. J. Davenport and H. S. Isaacs, *Phys. Rev. B: Condens. Matter Mater. Phys.*, 1992, **46**, 10321–10338.
6 G. A. Attard and D. A. King, *Surf. Sci.*, 1987, **188**, 589–598.
7 D. Kolb, G. Lehmpfuhl and M. Zei, *J. Electroanal. Chem. Interfacial Electrochem.*, 1984, **179**, 289–295.
8 D. Kolb and J. Schneider, *Surf. Sci.*, 1985, **162**, 764–775.
9 G. Pulletikurthi, A. Lahiri, T. Carstens, N. Borisenko, S. Zein El Abedin and F. Endres, *J. Solid State Electrochem.*, 2013, **17**, 2823–2832.
10 S. Zein El Abedin, E. M. Moustafa, R. Hempelmann, H. Natter and F. Endres, *ChemPhysChem*, 2006, **7**, 1535–1543.
11 M. Galiński, A. Lewandowski and I. Stepniak, *Electrochim. Acta*, 2006, **51**, 5567–5580.
12 S. Zhang, N. Sun, X. He, X. Lu and X. Zhang, *J. Phys. Chem. Ref. Data*, 2006, **35**, 1475–1517.
13 A. Basile, A. I. Bhatt, A. P. O'Mullane and S. K. Bhargava, *Electrochim. Acta*, 2011, **56**, 2895–2905.
14 Y. Katayama, S. Dan, T. Miura and T. Kishi, *J. Electrochem. Soc.*, 2001, **148**, C102.
15 C. Fu, H. Zhou, W. Peng, J. Chen and Y. Kuang, *Electrochem. Commun.*, 2008, **10**, 806–809.
16 P. He, H. Liu, Z. Li, Y. Liu, X. Xu and J. Li, *Langmuir*, 2004, **20**, 10260–10267.
17 J. M. Reyna-González, J. C. Reyes-López and M. Aguilar-Martínez, *Electrochim. Acta*, 2013, **94**, 344–352.
18 M.-C. Tsai, D.-X. Zhuang and P.-Y. Chen, *Electrochim. Acta*, 2010, **55**, 1019–1027.
19 S. Zein El Abedin and F. Endres, *Electrochim. Acta*, 2009, **54**, 5673–5677.
20 A. Ispas, M. Pölleth, K. H. T. Ba, A. Bund and J. Janek, *Electrochim. Acta*, 2011, **56**, 10332–10339.
21 B. H. R. Suryanto, C. A. Gunawan, X. Lu and C. Zhao, *Electrochim. Acta*, 2012, **81**, 98–105.
22 I. Siretanu, D. Ebeling, M. P. Andersson, S. L. S. Stipp, A. Philipse, M. C. Stuart, D. van den Ende and F. Mugele, *Sci. Rep.*, 2015, **4**, 4956.
23 J. R. MacDonald, *J. Electroanal. Chem. Interfacial Electrochem.*, 1987, **223**, 1–23.
24 J. Wang and A. J. Bard, *J. Phys. Chem. B*, 2001, **105**, 5217–5222.
25 F. Endres, N. Borisenko, S. Z. El Abedin, R. Hayes and R. Atkin, *Faraday Discuss.*, 2012, **154**, 221–233.
26 A. Elbourne, S. McDonald, K. Voichovsky, F. Endres, G. G. Warr and R. Atkin, *ACS Nano*, 2015, **9**, 7608–7620.
27 R. Hayes, G. G. Warr and R. Atkin, *Chem. Rev.*, 2015, **115**, 6357–6426.
28 M. Z. Bazant, B. D. Storey and A. A. Kornyshev, *Phys. Rev. Lett.*, 2011, **106**, 046102.
29 R. Atkin, N. Borisenko, M. Drüschler, S. Z. El Abedin, F. Endres, R. Hayes, B. Huber and B. Roling, *Phys. Chem. Chem. Phys.*, 2011, **13**, 6849.
30 R. Hayes, D. Wakeham and R. Atkin, *Ionic Liq. UnCOILed*, 2012, 51–85.
31 R. Atkin and G. G. Warr, *J. Phys. Chem. C*, 2007, **111**, 5162–5168.
32 R. Hayes, S. Z. El Abedin and R. Atkin, *J. Phys. Chem. B*, 2009, **113**, 7049–7052.
33 R. Hayes, G. G. Warr and R. Atkin, *Phys. Chem. Chem. Phys.*, 2010, **12**, 1709–1723.
34 R. Hayes, N. Borisenko, M. K. Tam, P. C. Howlett, F. Endres and R. Atkin, *J. Phys. Chem. C*, 2011, **115**, 6855–6863.
35 R. Atkin, S. Z. El Abedin, R. Hayes, L. H. Gasparotto, N. Borisenko and F. Endres, *J. Phys. Chem. C*, 2009, **113**, 13266–13272.
36 X. Zhang, Y.-X. Zhong, J.-W. Yan, Y.-Z. Su, M. Zhang and B.-W. Mao, *Chem. Commun.*, 2012, **48**, 582–584.
37 A. Labuda and P. Grütter, *Langmuir*, 2012, **28**, 5319–5322.
38 J. M. Black, D. Walters, A. Labuda, G. Feng, P. C. Hillesheim, S. Dai, P. T. Cummings, S. V. Kalinin, R. Proksch and N. Balke, *Nano Lett.*, 2013, **13**, 5954–5960.
39 F. Endres, E. Abedin, S. Zein and N. Borissenko, *Z. Phys. Chem.*, 2006, **220**, 1377–1394.
40 R. Hayes, N. Borisenko, B. Corr, G. B. Webber, F. Endres and R. Atkin, *Chem. Commun.*, 2012, **48**, 10246–10248.
41 A. Lahiri, T. Carstens, R. Atkin, N. Borisenko and F. Endres, *J. Phys. Chem. C*, 2015, **119**, 16734–16742.
42 T. Liu, Y. Danten, J. Grondin and R. Vilar, *J. Raman Spectrosc.*, 2016, **47**, 449–456.
43 T. Cui, A. Lahiri, T. Carstens, N. Borisenko, G. Pulletikurthi, C. Kuhl and F. Endres, *J. Phys. Chem. C*, 2016, **120**, 9341–9349.
44 J. Wu, T. Jiang, D.-e. Jiang, Z. Jin and D. Henderson, *Soft Matter*, 2011, **7**, 11222.
45 D. Henderson and J. Wu, *J. Phys. Chem. B*, 2012, **116**, 2520–2525.
46 D.-e. Jiang and J. Wu, *J. Phys. Chem. Lett.*, 2013, **4**, 1260–1267.
47 J. Jiang, D. Cao, D.-e. Jiang and J. Wu, *J. Phys.: Condens. Matter*, 2014, **26**, 284102.
48 M. H. Ghatee and Y. Ansari, *J. Chem. Phys.*, 2007, **126**, 154502.
49 Z. A. Goodwin, G. Feng and A. A. Kornyshev, *Electrochim. Acta*, 2017, **225**, 190–197.
50 R. Blossey, A. C. Maggs and R. Podgornik, *Phys. Rev. E*, 2017, **95**, 060602.
51 A. Latz and J. Zausch, *Beilstein J. Nanotechnol.*, 2015, **6**, 987–1007.
52 J. Stamm, A. Varzi, A. Latz and B. Horstmann, *J. Power Sources*, 2017, **360**, 136–149.
53 F. Single, B. Horstmann and A. Latz, *J. Electrochem. Soc.*, 2017, **164**, E3132–E3145.
54 S. Clark, A. Latz and B. Horstmann, *ChemSusChem*, 2017, **10**, 4735–4747.
55 IoLiTec Ionic Liquids Technologies Gmbh, *Technical Data Sheet IL-0035*, 2012.
56 M. Huang, Y. Jiang, P. Sasisanker, G. W. Driver and H. Weingärtner, *J. Chem. Eng.*, 2011, 1494–1499.
57 J. S. Newman and K. E. Thomas-Alyea, *Electrochemical Systems*, John Wiley & Sons, 2004, ISBN: 978-0-471-47756-3.
58 T. J. Simons, P. C. Howlett, A. A. J. Torriero, D. R. MacFarlane and M. Forsyth, *J. Phys. Chem. C*, 2013, **117**, 2662–2669.
59 T. Carstens, A. Lahiri, N. Borisenko and F. Endres, *J. Phys. Chem. C*, 2016, **120**, 14736–14741.
60 S. Millefiorini, A. H. Tkaczyk, R. Sedev, J. Efthimiadis and J. Ralston, *J. Am. Chem. Soc.*, 2006, **128**, 3098–3101.
61 J. Restolho, J. L. Mata and B. Saramago, *J. Phys. Chem. C*, 2009, **113**, 9321–9327.

Supplementary Information:

Influence of a Silver salt on the Nanostructure of a Au(111)/Ionic Liquid Interface: an Atomic Force Microscopy Study and Theoretical Concepts

Viktor Hoffmann,[a] Giridhar Pulletikurthi,[a] Timo Carstens,[a] Abhishek Lahiri,[a] Andriy Borodin,[a] Max Schammer,[b,c,d] Birger Horstmann,[b,c] Arnulf Latz[b,c,d] and Frank Endres*[a]

A Parameters

The parameters for the ionic liquid $[Py_{1,4}]$TFSA are enlisted in Table 1. The parameters for mass density and conductivity of the ionic liquid have been measured by Iolitec.[1] The value for the relative dielectric constant is taken from the literature.[2] The volume-parameters of the theory, common ionic radius and

Parameter	Value	Source
Density ρ / kg/m^3	$1.40{\cdot}10^{3}$	[1]
Electric conductivity κ / S/m	$2.10{\cdot}10^{-1}$	[1]
Dielectric constant ε_R	$1.47{\cdot}10^{1}$	[2]
Particle radius r / nm	$6.70{\cdot}10^{-1}$	calculated
Partial molar volumes ν / m^3/mol	$3.02{\cdot}10^{-4}$	calculated

Table 1 System parameters.

common partial molar volume, are both experimentally hardly accessible. We take a naive approach and define the common partial molar volume as the volume given by $\nu = M/\rho$. The total molar mass of the ionic liquid is given by the sum of the ionic masses, where the silver ions do not contribute in the massless limit . The complex geometry of the constituents leads to non-trivial packing effects. Such volume-defects cannot be resolved within this framework where we model the ions by hard spheres. As an averaged volume effect, we derive the ionic volume from the molar volume by the ratio $\nu\eta/N_A$.[3] Here, the constant packing fraction $\eta = 0.64$ corresponds to random packing of hard spheres.[4] Finally, we define the particle radius in terms of the sphere of volume half the ionic volume,

$$\frac{4}{3}\pi r^3 = \frac{\eta\nu}{2N_A}. \tag{1}$$

The relevant length scale for the interaction potential is then defined by the closest approach of the ions, $\sigma = 2r$.

We model the interaction potential $\mathscr{F}_{\alpha\beta}$ by the product of a dimensionless shape function f_σ

* *frank.endres@tu-clausthal.de*
[a] *Institute of Electrochemistry, Clausthal University of Technology, Arnold-Sommerfeld-Strasse 6, 38678 Clausthal-Zellerfeld, Germany*
[b] *Helmholtz Institute Ulm, Helmholtzstraße 11, 89081 Ulm, Germany.*
[c] *German Aerospace Center, Pfaffenwaldring 38-40, 70569 Stuttgart, Germany.*
[d] *Universität Ulm, Albert-Einstein-Alle 47, 89081 Ulm, Germany*

weighted by a “Coulombic” dimensional prefactor

$$\mathscr{F}_{\alpha\beta} = \frac{F^2}{4\pi\varepsilon_R\varepsilon\sigma} f_\sigma. \tag{2}$$

As shape function, we choose a Lennard-Jones type, $f_\sigma = a\cos(\pi/2\sigma)/(1+bx)^4$, with scaling-coefficients a,b. Beneath repulsion at short distances, this potential also takes account for attractive van-der-Waals interactions at short distances exceeding the particle extension (see Figure 1). Again, the silver ions do not contribute to the interaction term in the indefinitely diluted, massless and dimensionless limit.

B Computational Details

The simulation set up consists of a one-dimensional system composed of the ionic liquid as electrolyte and an ideal planar electrode. The system length L is sufficiently large to contain the electrochemical surface layer. We erect an equidistant spatial grid and implement the system in Matlab. We solve simultaneously for charge density, convection velocity and the electric potential. The system of differential and algebraic equations is solved using the fully implicit Matlab solver ode15s.

We start from the equilibrium state of the system and increase the overpotential up to 200mV. The initial potential of the electrode is set to zero. We set the potential of zero charge to zero, $\Phi_{\text{pzc}} = 0$. In our simulation, we do not consider chemical interactions between electrolyte and electrode and have not incorporated chemical reactions. Furthermore, we neglect specific adsorption of ions at the electrode surface. This is in contrast to the experimental set-up, in which the initial state of the system is the OCP which might not be the potential of zero charge.

C Boundary conditions

We assume that the system is electro-neutral in the bulk electrolyte $\rho_F(x = L) = 0$ and in equilibrium with a reference electrode $\Phi(x = L) = 0$ and set the bulk values for charge density and electric potential to zero. At the electrified interface, no reaction is occurring and all fluxes are vanishing, i.e., $\mathbf{J}(x = 0) = 0$ and $\mathbf{v}(x = 0) = 0$. The electric potential in the electrolyte $\Phi(x = 0)$ is equal to the electrode potential.

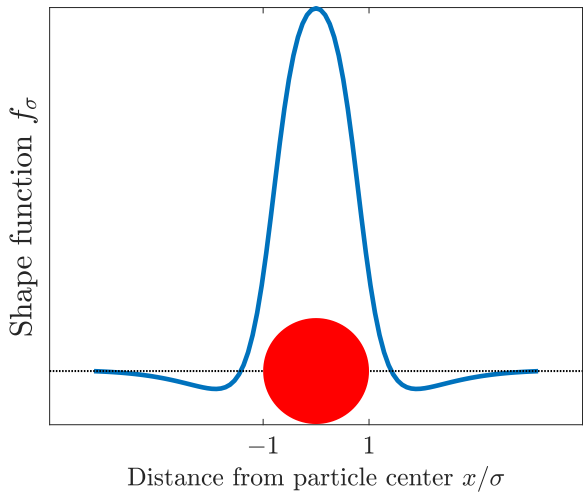

Fig. 1 Dimensionless shape function with indicated particle extension.

References

1 IoLiTec Ionic Liquids Technologies Gmbh, *Technical Data Sheet IL-0035*, 2012.

2 M. Huang, Y. Jiang, P. Sasisanker, G. W. Driver and H. Weingärtner, *Journal of Chemical Engineering*, 2011, 1494–1499.

3 A. A. Lee, D. Vella, S. Perkin and A. Goriely, *The Journal of Physical Chemistry Letters*, 2015, **6**, 159–163.

4 C. Song, P. Wang and H. a. Makse, *Nature*, 2008, **453**, 629–632.

F. Single, B. Horstmann and A. Latz. Dynamics and morphology of solid electrolyte interphase (SEI). *Physical Chemistry Chemical Physics* **18**, 17810–17814 (2016).

PCCP

COMMUNICATION

View Article Online
View Journal | View Issue

Cite this: *Phys. Chem. Chem. Phys.*, 2016, **18**, 17810

Received 27th April 2016,
Accepted 13th June 2016

DOI: 10.1039/c6cp02816k

www.rsc.org/pccp

Dynamics and morphology of solid electrolyte interphase (SEI)†

Fabian Single,‡[ab] Birger Horstmann‡*[ab] and Arnulf Latz[abc]

We develop a novel theory for the continuous electrochemical formation of porous films to study the solid electrolyte interphase (SEI) on lithium ion battery anodes. Existing SEI studies model a homogeneous morphology and a single relevant transport mechanism. Our approach, in contrast, is based on two transport mechanisms and enables us to track SEI porosity in a spatially resolved way. SEI thickness evolution agrees with existing studies and is validated with experiments. This consistent approach is unprecedented in SEI modeling. We predict a non-zero SEI porosity and the dependence of morphology on transport properties. Additionally, we capture dual-layer chemistry and morphology. Analytic expressions which describe the parameter dependence of all key properties are derived and discussed.

The formation of a stable interfacial layer, the so-called solid electrolyte interphase (SEI), on graphite anodes has enabled the success of Li-ion batteries (LIBs).[1] In these batteries, electrolyte solvent is unstable at typical working potentials.[2,3] Solvent reduction products form a thin layer separating anode and electrolyte, the SEI. A well-formed SEI significantly slows down further electrolyte reduction, resulting in the excellent cycling stability of LIBs. However, electrolyte reduction and SEI formation are never fully suppressed and remain the major cause for long-term capacity fade.[4–6]

This critical role has led to numerous experimental and theoretical studies of the SEI. Experimental results are summarized in review articles and systematic studies.[7–14] Recently, isotope tracer experiments demonstrated the potential-dependent dual-layer structure of the SEI.[15–17] It is generally accepted that the SEI consists of a dense inner layer close to the electrode and a porous outer layer. Several long-term measurements find that capacity fade scales with the square root of time,[18–20] a strong indication that SEI formation is a transport limited process. This observation is explored in numerous theoretical studies which use a single rate determining transport mechanism to describe SEI growth. SEI formation controlled by solvent diffusion is assumed by Pinson and Bazant[21] and Ploehn,[4] whereas electron conduction mechanisms are considered by Peled,[22] Christensen,[23] Li[24] and Lin.[25] Most studies describe the evolution of a homogeneous SEI layer with a sharp interface and do not attempt to account for spatial heterogeneity. Only a few models consider a spatially resolved interface with the electrolyte or an inhomogeneous SEI.[26,27]

Despite substantial differences in the chosen rate-limiting transport mechanism, all available models predict SEI thickness evolution in agreement with experiments. Thus, they remain inconclusive with respect to the rate limiting process. Conclusions require further observable predictions with respect to SEI morphology, *e.g.*, porosity and dual-layer structure. For this reason, we develop a theory for the growth of a porous and inhomogeneous layer. Our model studies the dynamics of film porosity in one dimension, perpendicular to the substrate surface. This is possible because the transport of all film precursors within the porous structure is taken into account.

In this work we formulate and parameterize our model specifically to describe SEI evolution, as depicted in Fig. 1. We apply the popular porous electrode theory to the nanoporous SEI. To this aim SEI composition and morphology are averaged in slabs parallel to the anode surface. Thus film growth is modeled along a single coordinate x, see Fig. 1(b). Within the simulation domain we trace the transport of all species involved in SEI formation. Here we assume electron conduction in the SEI material.[23] In the electrolyte, solvent molecules diffuse towards the electrode.[21] The electrochemical potential of lithium ions is assumed to be constant at all times and does not result in inhomogeneous reaction rates. This assumption is justified because lithium ion transport in the SEI[28] is very fast compared to SEI growth, *i.e.*, SEI growth consumes small amounts of lithium and transport quickly

[a] *German Aerospace Center (DLR), Institute of Engineering Thermodynamics, Pfaffenwaldring 38-40, 70569 Stuttgart, Germany. E-mail: birger.horstmann@dlr.de*
[b] *Helmholtz Institute Ulm (HIU), Helmholtzstraße 11, 89081 Ulm, Germany*
[c] *Ulm University, Institute of Electrochemistry, Albert-Einstein-Allee 47, 89069 Ulm, Germany*

† Electronic supplementary information (ESI) available. See DOI: 10.1039/c6cp02816k

‡ These authors contributed equally to this work.

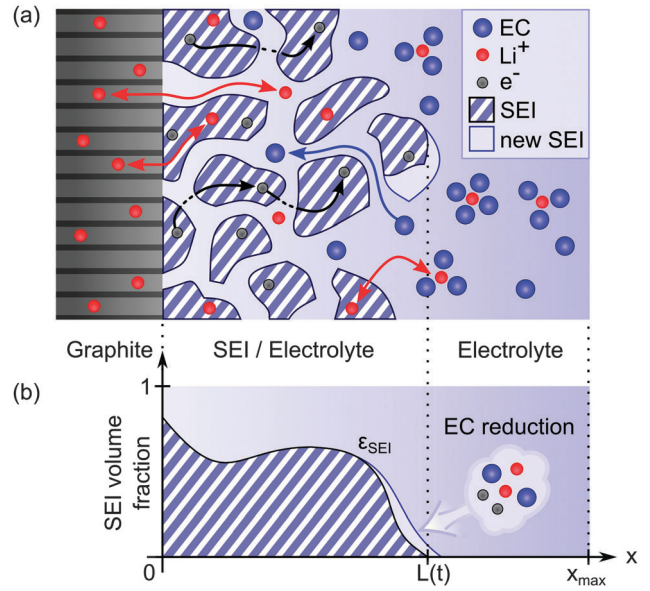

Fig. 1 (a) Cross section through graphite electrode, SEI and electrolyte depicting all relevant species: solvent molecules EC, lithium ions Li^+, and electrons e^-. EC and e^- move in opposite directions (single headed arrows). (b) Profile of the averaged SEI volume fraction along the axis perpendicular to the electrode surface.

restores local equilibrium. SEI is formed when reactions between charge moving away from the electrode and solvent moving towards the electrode occur. In summary, we model diffusion of solvent and conduction of electrons. Therefore, electronic conductivity and solvent diffusivity are key parameters.

The bulk electrolyte phase is a binary mixture of ethylene carbonate (EC) with co-solvent dimethyl carbonate (DMC), *i.e.*, EC:DMC 3:7. As we focus on morphology, SEI chemistry is further simplified by neglecting the salt anion. Because ionic species are neglected, double layer effects[29] cannot be included in our model. Only a single representative reduction reaction per solvent species is considered

$$2\mathrm{EC} + 2\mathrm{Li}^+ + 2\mathrm{e}^- \rightarrow \mathrm{Li_2EDC}\downarrow + R_{\mathrm{EC}}\uparrow, \quad (1a)$$

$$\mathrm{DMC} + \mathrm{Li}^+ + \mathrm{e}^- \rightarrow \mathrm{LiMC}\downarrow + R_{\mathrm{DMC}}\uparrow. \quad (1b)$$

We choose lithium ethylene dicarbonate (Li_2EDC) as a product of EC reduction[30,31] and lithium methyl carbonate (LiMC) from DMC reduction.[32] Gaseous reaction byproducts R_i are neglected. Hereinafter, indices i refer to i = EC, DMC or i = Li_2EDC, LiMC depending on the phase (electrolyte/SEI) of the corresponding variable/parameter.

The production rate $\dot{s}_i$ of each SEI compound drives the evolution of the volume fraction ε_i

$$\frac{\partial \varepsilon_i}{\partial t} = \bar{V}_i^{\mathrm{S}} \dot{s}_i, \quad (2)$$

where $\bar{V}_i^{\mathrm{S}}$ is the molar volume of SEI compound i. This means a solvation/precipitation mechanism[33] is not considered. Solvent molecules move through the electrolyte phase *via* diffusion and convection. The evolution of solvent concentration c_i is coupled to sink terms from SEI formation with mass balance equations

$$\frac{\partial \varepsilon c_i}{\partial t} = -\mathrm{div}\left(j_{\mathrm{D},i} + j_{\mathrm{C},i}\right) - \nu_i \dot{s}_i, \quad (3)$$

where $\varepsilon = 1 - \sum \varepsilon_i$ is the local porosity and $\nu_{\mathrm{EC}} = 2/\nu_{\mathrm{DMC}} = 1$ are stoichiometric coefficients. According to Fick's law, diffusion is driven by concentration gradients $j_{\mathrm{D},i} = -D_i \mathrm{grad} c_i$. Convection is determined by the velocity v of the electrolyte $j_{\mathrm{C},i} = c_i v$. By treating the mixture as an incompressible fluid, we use the volume constraint $\sum \bar{V}_i^{\mathrm{E}} c_i = 1$ to eliminate the co-solvent concentration.[34] Because v is the center-of-mass velocity, we require $D_{\mathrm{DMC}} = D_{\mathrm{EC}} \cdot M_{\mathrm{EC}} V_{\mathrm{DMC}} / (M_{\mathrm{DMC}} V_{\mathrm{EC}})$ with molar masses M_i. Volume constraint and mass balance eqn (3) together determine the convective velocity[35,36]

$$\mathrm{div} v = \sum \left(\bar{V}_i^{\mathrm{S}} - \nu_i \bar{V}_i^{\mathrm{E}}\right) \dot{s}_i + \bar{V}_{\mathrm{EC}}^{\mathrm{E}} \mathrm{div}(D_{\mathrm{EC}} - D_{\mathrm{DMC}}) \mathrm{grad} c_{\mathrm{EC}}. \quad (4)$$

Conservation of "electronic charges" is ensured *via*

$$0 = -\mathrm{div} j_{\mathrm{E}} + F(2\dot{s}_{\mathrm{Li_2EDC}} + \dot{s}_{\mathrm{LiMC}}), \quad (5)$$

where the electron current depends on the electric potential Φ through Ohm's law $j_{\mathrm{E}} = -\kappa \mathrm{grad} \Phi$. We solve eqn (2)–(5) for the spatially-resolved dynamics of $\varepsilon_{\mathrm{Li_2EDC}}$, $\varepsilon_{\mathrm{LiMC}}$, c_{EC}, Φ, and v within the simulation domain $[0, x_{\max}]$.

Volume-averaged transport parameters D_i and κ contain the effects of porosity and tortuosity. The Bruggeman ansatz relates them to their bulk values using the local porosity and SEI volume fraction $\varepsilon_{\mathrm{SEI}} = 1 - \varepsilon$,

$$D_i = \varepsilon^{\beta} D_i^0 \quad \text{and} \quad \kappa = \varepsilon_{\mathrm{SEI}}^{1.5} \kappa^0, \quad (6)$$

where 1.5 is the standard Bruggeman coefficient for conduction[37] in porous media. For simplicity, we choose the same electronic bulk conductivity κ^0 for all SEI compounds. We use large values of $\beta \sim 20$ in our model, representing the difficulty of electrolyte transport in nano-pores.

The compound production rates $\dot{s}_i = A_i \Gamma \dot{r}_i$ depend on specific surface areas A_i, surface site density Γ, and reaction rates $\dot{r}_i$. The latter are given by a symmetric Butler–Volmer expression,[38,39]

$$\dot{r}_i = \frac{1}{2} \frac{k_{\mathrm{B}} T}{h} \left(\frac{c_i}{c_i^0}\right)^{\frac{\nu_i}{2}} \exp\left(\frac{-E_{\mathrm{A}}}{k_{\mathrm{B}} T}\right) \sinh \frac{F \eta_i}{RT}, \quad (7)$$

where solvent reduction is driven by the overpotentials

$$\eta_i = -\left(\Phi - \Phi_i^0\right) + \frac{RT}{F} \ln\left(\frac{c_i}{c_i^0}\right). \quad (8)$$

Reduction reactions are in equilibrium when potential and concentrations are Φ_i^0 and c_i^0, respectively. The activation barrier of the reaction E_{A} is twice the desolvation energy of Li^+ in EC.[40,41] We represent the irreversibility of these reactions by setting $\dot{r}_i = 0$ for negative η, *i.e.*, we disregard the oxidation (SEI components are oxidized at $\Phi \approx 3.25$ V[42]).

A continuous expression is used for the specific surface area. As derived in the ESI,†

$$A_i = \frac{6}{a_0}\varepsilon\left(\tilde{\varepsilon}_i + \frac{a_0^2}{6}\frac{\partial^2\tilde{\varepsilon}_i}{\partial x^2}\right), \quad \tilde{\varepsilon}_i = \varepsilon_i + \varepsilon_{\text{init}}. \tag{9}$$

This smoothes the porosity profile and distributes growth such that the SEI front has finite thickness. Additionally it enables propagation of SEI into the electrolyte as well as numerical convergence.

Simulation details, such as initialization, boundary conditions and parameters are discussed in the ESI.†

Inert co-solvent

We start our discussion with the special case of an inert co-solvent, *i.e.*, we disable co-solvent reduction ($\dot{r}_{\text{DMC}} = 0$) and study the growth of an SEI with homogeneous chemistry. A typical evolution of SEI volume fraction is depicted in Fig. 2(a). We find that growth is concentrated at the SEI front whose spatial width lies in the order of a_0. Thus, electron conduction through the SEI becomes the rate limiting process in our model. The porosity inside the SEI attains a nearly constant value $\varepsilon(x) \approx \varepsilon^* = 1 - \varepsilon^*_{\text{SEI}}$ which we explain below. On closer inspection we find that SEI volume fraction increases slightly with distance from electrode.

In our model the SEI thickness grows with the square root of time in agreement with experiments (see Fig. 2(b)). It has been shown previously that this can be rationalized based on a single rate limiting transport process.[4,21] Therefore, we obtain SEI conductivity by fitting the simulated thickness evolution to experimental data. With capacity fade measurements of Liu *et al.*[19] and an estimate for the electrode surface area by Pinson *et al.*[21] we find $\kappa^0 = 0.3$ pS m^{-1} at $T = 15$ °C and $\kappa^0 = 4.5$ pS m^{-1} at $T = 60$ °C (with $\beta = 25$). These low electron conductivities ensure good passivation and are below the ones for artificial SEIs.[43] The microscopic mechanism underlying this conductivity is still under investigation. Besides conventional conduction, successive electron tunneling[25] or neutral lithium interstitial diffusion[28] are potential mechanisms.

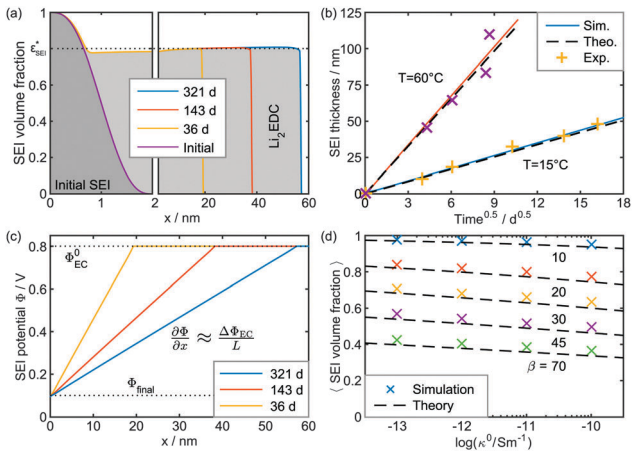

Fig. 2 Results with inert co-solvent. (a) Temporal evolution of the SEI volume fraction $\varepsilon_{\text{Li}_2\text{EDC}} + \varepsilon_{\text{init}}$ ($\kappa^0 = 0.3$ pS m^{-1}, $\beta = 25$, $T = 15$ °C). (b) SEI thickness evolution from experiment[19,21] (dots), simulation (dashed) and eqn (11) (lines). (c) SEI potential distribution at different stages of SEI evolution, corresponding to (a). (d) Influence of β and κ^0 on $\varepsilon^*_{\text{SEI}}$, analytic results from eqn (13) (dashed lines) compared to simulation results (dots). The values were obtained by averaging $\varepsilon_{\text{SEI}}(x)$ between 2 nm and 55 nm after simulating the growth of a 60 nm thick layer.

In Fig. 2(c) we show that the potential increases linearly from the value Φ_{final} at the electrode to Φ^0_{EC} at the SEI front. The linearity demonstrates that crystallization inside the SEI is negligible. A potential drop over the SEI interface is absent because the formation reaction is fast. For a constant porosity ε^* and a linear potential $\Phi(x,t)$ we can approximate the electric current through the bulk SEI phase and calculate the thickness evolution

$$\frac{\partial L}{\partial t} = -\frac{j_{\text{E}}}{2F}\frac{\bar{V}^{\text{S}}_{\text{Li}_2\text{EDC}}}{\varepsilon^*_{\text{SEI}}} \approx \frac{\varepsilon^{*1/2}_{\text{SEI}}\kappa^0\Delta\Phi_{\text{EC}}\bar{V}^{\text{S}}_{\text{Li}_2\text{EDC}}}{2F}\frac{1}{L}, \tag{10}$$

$$\Rightarrow L(t) = \sqrt{\frac{\varepsilon^{*1/2}_{\text{SEI}}\kappa^0\Delta\Phi_{\text{EC}}\bar{V}^{\text{S}}_{\text{Li}_2\text{EDC}}}{F}}\cdot\sqrt{t}. \tag{11}$$

We note that SEI growth is essentially governed by the potential difference $\Delta\Phi_{\text{EC}} = \Phi^0_{\text{EC}} - \Phi_{\text{final}}$. Fig. 2(b) proofs the excellent agreement between experiment, simulation and eqn (11).

We derive an expression for the nearly constant SEI porosity ε^* in this SEI layer. Our approach traces the SEI formation rate in the frame co-moving with the SEI front

$$\frac{\mathrm{d}\varepsilon(L,t)}{\mathrm{d}t} = \frac{\partial\varepsilon}{\partial t} + \frac{\partial\varepsilon}{\partial L}\frac{\partial L}{\partial t}. \tag{12}$$

With few assumptions, *i.e.*, no convection and infinitely fast reactions, we find that $\varepsilon(L,t)$ in eqn (12) has a stationary solution ε^*. This means that in time, the porosity in the co-moving frame tends towards this stable value. An implicit expression for ε^* can be derived from eqn (12)

$$\kappa(\varepsilon^*) = D(\varepsilon^*)\frac{F^2 c^0_{\text{EC}}}{RT}\left(\frac{1}{2} + \beta\frac{1-\varepsilon^*}{\varepsilon^*}\right). \tag{13}$$

Our simulations show that eqn (13) gives an excellent estimate for the dependence of the porosity ε^* on the transport parameters. Very good quantitative agreement is observed for small EC concentrations, see Fig. 2(d). It can be seen that β is the parameter with the highest influence on film porosity. The film porosity is a direct consequence of an interplay between solvent species crossing the moving SEI front and SEI expansion. As the film becomes denser, solvent transport into the film is slowed down. Eventually further growth is distributed such that the film expands and the density no longer increases. As shown in Fig. 2(d), large values of β are needed to see this effect. At $\beta = 10$, film density is nearly one, $\varepsilon^*_{\text{SEI}} \approx 0.98$.

Reactive co-solvent

In the following, we discuss simulations with simultaneous solvent and co-solvent reduction. Fig. 3(a) depicts the corresponding evolution of both SEI volume fractions. Next to the electrode, LiMC grows "on top" of the Li_2EDC phase. This forms a dense inner layer with $\varepsilon_{\text{SEI}}(x) \approx 1$ while the porous

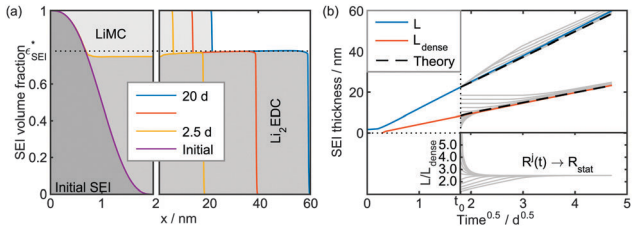

Fig. 3 (a) Temporal evolution of the SEI volume fraction with two reduction reactions (κ^0 = 4.5 pS m^{-1}, β = 25, T = 60 °C). (b) Same simulation, evolution of total and dense SEI layer thickness (lines) compared to numerical solutions of the analytical approximation eqn (14a) (dashed). Additional numerical solutions with different $L^j_{\mathrm{dense}}(t_0)$ (j = 1,...,10) indicate, how SEI growth continues when $R \neq R_{\mathrm{stat}}$ (thin grey lines). The inset in the bottom-right corner shows the corresponding evolution of $R^j = L^j/L^j_{\mathrm{dense}}$.

outer layer with $\varepsilon_{\mathrm{SEI}}(x) \approx \varepsilon^*_{\mathrm{SEI}}$ remains. At Φ^0_{EC} = 0.8 V EC starts to create a SEI layer with pores containing DMC as shown in Fig. 2(a). When the potential drops below Φ^0_{DMC} = 0.3 V, DMC is reduced to form LiMC. Consequently the dense layer appears near the electrode where the potential is lower. This dual-layer structure agrees with experimental observations.[17] Similar to co-solvent reduction, it would emerge from a conversion of the primary SEI compound at low potentials.[44] Because the reduction potential of EC is higher than the one of the co-solvent (see Borodin *et al.*[45,46]), SEI mostly consists of EC reduction products, as recently validated by Grey *et al.*[47]

We compare the evolution of total SEI thickness L and the thickness of the dense layer L_{dense} in Fig. 3(b). Both quickly attain their asymptotic values corresponding to square root like growth. Analogous to eqn (11), SEI growth is driven by potential differences

$$\frac{\partial L}{\partial t} = \frac{\bar{V}^{\mathrm{S}}_{\mathrm{Li_2EDC}}\kappa^0}{2\varepsilon^*_{\mathrm{SEI}}F}\frac{\varepsilon^{*3/2}_{\mathrm{SEI}}\Delta\Phi_{\mathrm{diff}}}{L - L_{\mathrm{dense}}}, \tag{14a}$$

$$\frac{\partial L_{\mathrm{dense}}}{\partial t} = \frac{\bar{V}^{\mathrm{S}}_{\mathrm{LiMC}}\kappa^0}{2\varepsilon^* F}\left(\frac{\Delta\Phi_{\mathrm{DMC}}}{L_{\mathrm{dense}}} - \frac{\varepsilon^{*3/2}_{\mathrm{SEI}}\Delta\Phi_{\mathrm{diff}}}{L - L_{\mathrm{dense}}}\right) \tag{14b}$$

with $\Delta\Phi_{\mathrm{diff}} = \Phi^0_{\mathrm{EC}} - \Phi^0_{\mathrm{DMC}}$. For simple notation, this equation holds for reversible reactions only. Numerical solutions for a slightly modified system, viable for irreversible reactions are shown in Fig. 3(b). Both systems are identical, when $\partial_t L_{\mathrm{dense}}$ as written in eqn (14b) is positive. The inset in Fig. 3(b) shows that independent of initialization, the ratio $R = L/L_{\mathrm{dense}}$ quickly approaches a stationary value R_{stat} stated as quadratic expression

$$\frac{\Delta\Phi_{\mathrm{DMC}}}{\Delta\Phi_{\mathrm{diff}}}{R_{\mathrm{stat}}}^2 - \left(\frac{\Delta\Phi_{\mathrm{DMC}}}{\Delta\Phi_{\mathrm{diff}}} + \varepsilon^{*3/2}_{\mathrm{SEI}}\right)R_{\mathrm{stat}} = \varepsilon^*\sqrt{\varepsilon^*_{\mathrm{SEI}}}\frac{\bar{V}^{\mathrm{S}}_{\mathrm{Li_2EDC}}}{\bar{V}^{\mathrm{S}}_{\mathrm{LiMC}}}. \tag{15}$$

Eqn (15) relates system parameters to the ratio of total SEI thickness over the thickness of the dense layer. We suggest to design the SEI and increase the ratio R_{stat} by adjusting electrolyte composition. This would increase its overall elasticity and allow it to withstand volume changes of electrode particles.[48,49] It allows the validation of our model and/or an estimate of unknown reaction properties from observable SEI properties.

In conclusion, we formulate a novel SEI growth model which extends the common approach of transport limited models. Our theory predicts long-term SEI thickness evolution in agreement with previous models and experiments, *i.e.*, we retain square-root like growth. Additionally, we present the first continuum model which predicts properties of SEI structure. The competition between two counter-moving transport mechanisms, *i.e.*, electron conduction and solvent diffusion, leads to a non-zero SEI porosity. This is a novel insight into porous film growth beyond the standard case of SEI formation on graphite anodes. Two distinct formation reactions result in a dual-layer structure with a dense inner layer and a porous outer layer. Porosity is constant within each layer. We can understand these properties and derive formulas for SEI thickness, SEI porosity, and thickness of the dense layer. Long-term *in situ* experiments, similar to ref. 50 and 51, should allow to test and refine our predictions. We hope that this kind of modeling can be extended to lithium transport through the SEI and the effect of electrochemical double layers. This would allow better understanding of SEI impedance spectra.

This work was supported by the German Federal Ministry of Education and Research (BMBF) in the project Li-EcoSafe (03X4636A). The authors would like to thank Erkmen Karaca for fruitful discussions. Further support was provided, by the bwHPC initiative and the bwHPC-C5 project through associated compute services of the JUSTUS HPC facility at the University of Ulm.

References

1 J. Vetter, P. Novák, M. R. Wagner, C. Veit, K.-C. Möller, J. O. Besenhard, M. Winter, M. Wohlfahrt-Mehrens, C. Vogler and A. Hammouche, *J. Power Sources*, 2005, **147**, 269–281.
2 S. Kang, M. H. Park, H. Lee and Y. K. Han, *Electrochem. Commun.*, 2012, **23**, 83–86.
3 M. Metzger, C. Marino, J. Sicklinger, D. Haering and H. A. Gasteiger, *J. Electrochem. Soc.*, 2015, **162**, A1123–A1134.
4 H. J. Ploehn, P. Ramadass and R. E. White, *J. Electrochem. Soc.*, 2004, **151**, A456.
5 J. Vetter, P. Novák, M. R. Wagner, C. Veit, K. C. Möller, J. O. Besenhard, M. Winter, M. Wohlfahrt-Mehrens, C. Vogler and A. Hammouche, *J. Power Sources*, 2005, **147**, 269–281.
6 M. Broussely, P. Biensan, F. Bonhomme, P. Blanchard, S. Herreyre, K. Nechev and R. J. Staniewicz, *J. Power Sources*, 2005, **146**, 90–96.
7 D. Aurbach, A. Zaban, Y. Ein-Eli, I. Weissman, O. Chusid, B. Markovsky, M. Levi, E. Levi, A. Schechter and E. Granot, *J. Power Sources*, 1997, **68**, 91–98.
8 D. Aurbach, B. Markovsky, I. Weissman, E. Levi and Y. Ein-Eli, *Electrochim. Acta*, 1999, **45**, 67–86.
9 D. Aurbach, *J. Power Sources*, 2000, **89**, 206–218.
10 S. S. Zhang, *J. Power Sources*, 2006, **162**, 1379–1394.
11 P. Verma, P. Maire and P. Novák, *Electrochim. Acta*, 2010, **55**, 6332–6341.
12 A. V. Agubra and J. W. Fergus, *J. Power Sources*, 2014, **268**, 153–162.

13 A. M. Haregewoin, E. G. Leggesse, J.-C. Jiang, F.-M. Wang, B.-J. Hwang and S. D. Lin, *Electrochim. Acta*, 2014, **136**, 274–285.
14 F. A. Soto, Y. Ma, J. M. Martinez De La Hoz, J. M. Seminario and P. B. Balbuena, *Chem. Mater.*, 2015, **27**, 7990–8000.
15 P. Lu and S. J. Harris, *Electrochem. Commun.*, 2011, **13**, 1035–1037.
16 S. J. Harris and P. Lu, *J. Phys. Chem. C*, 2013, **117**, 6481–6492.
17 P. Lu, C. Li, E. W. Schneider and S. J. Harris, *J. Phys. Chem. C*, 2014, **118**, 896–903.
18 M. Broussely, S. Herreyre, P. Biensan, P. Kasztejna, K. Nechev and R. J. Staniewicz, *J. Power Sources*, 2001, **97–98**, 13–21.
19 P. Liu, J. Wang, J. Hicks-Garner, E. Sherman, S. Soukiazian, M. Verbrugge, H. Tataria, J. Musser and P. Finamore, *J. Electrochem. Soc.*, 2010, **157**, A499.
20 A. J. Smith, J. C. Burns, X. Zhao, D. Xiong and J. R. Dahn, *J. Electrochem. Soc.*, 2011, **158**, A447–A452.
21 M. B. Pinson and M. Z. Bazant, *J. Electrochem. Soc.*, 2012, **160**, A243–A250.
22 E. Peled, *J. Electrochem. Soc.*, 1979, **126**, 2047–2051.
23 J. Christensen and J. Newman, *J. Electrochem. Soc.*, 2004, **151**, A1977.
24 D. Li, D. Danilov, Z. Zhang, H. Chen, Y. Yang and P. H. L. Notten, *J. Electrochem. Soc.*, 2015, **162**, A858–A869.
25 Y. X. Lin, Z. Liu, K. Leung, L. Q. Chen, P. Lu and Y. Qi, *J. Power Sources*, 2016, **309**, 221–230.
26 J. Deng, G. J. Wagner and R. P. Muller, *J. Electrochem. Soc.*, 2013, **160**, A487–A496.
27 P. Guan, L. Liu and X. Lin, *J. Electrochem. Soc.*, 2015, **162**, A1798–A1808.
28 S. Shi, P. Lu, Z. Liu, Y. Qi, L. G. Hector, H. Li and S. J. Harris, *J. Am. Chem. Soc.*, 2012, **134**, 15476–15487.
29 Q. Zhang, J. Pan, P. Lu, Z. Liu, M. W. Verbrugge, B. W. Sheldon, Y. T. Cheng, Y. Qi and X. Xiao, *Nano Lett.*, 2016, **16**, 2011–2016.
30 G. V. Zhuang, K. Xu, H. Yang, T. R. Jow and P. N. Ross, *J. Phys. Chem. B*, 2005, **109**, 17567–17573.
31 K. Leung, *Chem. Phys. Lett.*, 2013, **568–569**, 1–8.
32 D. M. Seo, D. Chalasani, B. S. Parimalam, R. Kadam, M. Nie and B. L. Lucht, *ECS Electrochem. Lett.*, 2014, **3**, A91–A93.
33 O. Borodin and D. Bedrov, *J. Phys. Chem. C*, 2014, **118**, 18362–18371.
34 B. Horstmann, T. Danner and W. G. Bessler, *Energy Environ. Sci.*, 2013, **6**, 1299–1314.
35 D. Bothe and W. Dreyer, *Acta Mech.*, 2015, **226**, 1757–1805.
36 S. de Groot and P. Mazur, *Non-equilibrium Thermodynamics*, Dover Publications, 1962.
37 M. Doyle, *J. Electrochem. Soc.*, 1993, **140**, 1526.
38 A. Latz and J. Zausch, *J. Power Sources*, 2011, **196**, 3296–3302.
39 M. Z. Bazant, *Acc. Chem. Res.*, 2013, **46**, 1144–1160.
40 Y. Yamada, Y. Iriyama, T. Abe and Z. Ogumi, *Langmuir*, 2009, **25**, 12766–12770.
41 K. Xu, A. Von Cresce and U. Lee, *Langmuir*, 2010, **26**, 11538–11543.
42 M. Tang and J. Newman, *J. Electrochem. Soc.*, 2012, **159**, A281.
43 J. Li, N. J. Dudney, J. Nanda and C. Liang, *ACS Appl. Mater. Interfaces*, 2014, **6**, 10083–10088.
44 K. Leung, F. A. Soto, K. Hankins, P. B. Balbuena and K. L. Harrison, *J. Phys. Chem. C*, 2016, **120**, 6302–6313.
45 O. Borodin, M. Olguin, C. E. Spear, K. W. Leiter and J. Knap, *Nanotechnology*, 2015, **26**, 354003.
46 O. Borodin, M. Olguin, P. Ganesh, P. R. C. Kent, J. L. Allen and W. A. Henderson, *Phys. Chem. Chem. Phys.*, 2016, **18**, 164–175.
47 A. L. Michan, M. Leskes and C. P. Grey, *Chem. Mater.*, 2015, 385–398.
48 J. Zhang, X. Yang, R. Wang, W. Dong, W. Lu, X. Wu, X. Wang, H. Li and L. Chen, *J. Phys. Chem. C*, 2014, **118**, 20756–20762.
49 V. Kuznetsov, A. H. Zinn, G. Zampardi, S. Borhani-Haghighi, F. La Mantia, A. Ludwig, W. Schuhmann and E. Ventosa, *ACS Appl. Mater. Interfaces*, 2015, **7**, 23554–23563.
50 G. M. Veith, M. Doucet, J. K. Baldwin, R. L. Sacci, T. M. Fears, Y. Wang and J. F. Browning, *J. Phys. Chem. C*, 2015, **119**, 20339–20349.
51 R. L. Sacci, J. M. Black, N. Balke, N. J. Dudney, K. L. More and R. R. Unocic, *Nano Lett.*, 2015, **15**, 2011–2018.

Journal Name

ARTICLE TYPE

Cite this: DOI: 10.1039/xxxxxxxxxx

Electronic Supplementary Information: Dynamics and Morphology of Solid Electrolyte Interphase (SEI)†

Fabian Single,[a,b,‡] Birger Horstmann,*[a,b,‡] and Arnulf Latz [a,b,c]

Received Date
Accepted Date

DOI: 10.1039/xxxxxxxxxx

www.rsc.org/journalname

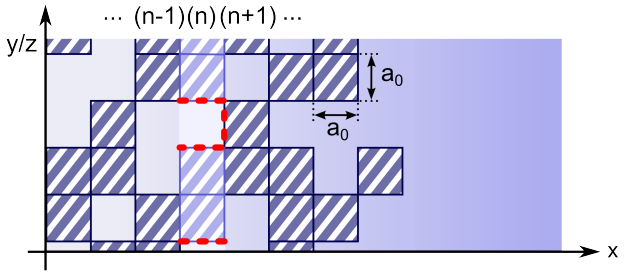

Fig. 1 Scheme for the derivation of eq (9). SEI is assumed to be constructed from cubes with volume a_0^3. The surface area for growth in slice (n) (dashed) is marked red and depends on the occupation probabilities of slice (n) as well as on occupation probability of the neighbouring slices $(n-1)$ and $(n+1)$.

Specific Surface Area

We derive an expression for the local specific surface area from the assumption that SEI consists of cubes with edge length a_0, as shown in Figure 1. All cubes in one slice (n) are occupied with the same probability, the local SEI volume fraction $\varepsilon_{\mathrm{SEI}}^{(n)} = 1 - \varepsilon^{(n)}$. In this way, the surface area in slice (n) also depends on the porosity of the neighbouring slices. This is approximated with the second derivative of ε

$$A_i = \frac{6}{a_0}\varepsilon\left(\tilde{\varepsilon} + \frac{a_0^2}{6}\frac{\partial^2\tilde{\varepsilon}}{\partial x^2}\right),$$

where $\tilde{\varepsilon}$ is the volume fraction of SEI compounds whose surfaces can facilitate SEI formation. We assume that SEI forms only on similar species as well as initial SEI, i.e. $\tilde{\varepsilon} = \varepsilon_i + \varepsilon_{\mathrm{init.}}$. The initial SEI profile is needed to start the simulation, providing a nucleation seed.

Boundary Conditions and Initialization

We initialize the system in equilibrium at $t = 0$. Thus, solvent concentration and electric potential equal the reference and equilibrium values c_{EC}^0 and Φ_{EC}^0 in the whole simulation domain. Both SEI volume fractions and the convective velocity are zero initially. A smooth initial profile $\varepsilon_{\mathrm{init}}$ serves as nucleation seed for SEI growth (see Figure 2(a)). Its thickness of 2 nm is interpreted as the electron tunneling depth through several SEI compounds[1]. Note that $\varepsilon_{\mathrm{init}}$ is zero for $x > 2\,\mathrm{nm}$. The electrode potential $\Phi(0,t)$ is determined by the state of charge (SOC) dependent potential of graphite electrodes[2]. We perform an initial charge at the rate C/20 from Φ_{EC}^0 to Φ_{final} corresponding to a linear ramp of SOC. Then SOC and potential $\Phi(0,t)$ on the left boundary are kept constant. The boundary conditions $j_{\mathrm{E}}(x_{\max}) = 0$, $j_{\mathrm{D,i}}(0) = v(0) = 0$ prevent electrons from leaving the simulation domain and solvent molecules from flowing into the electrode.

Parameters

If not stated elsewhere, parameters used in figures and the results discussed are listed in Table 1. We use the partial molar volumes $\bar{V}_i^{\mathrm{E}}$ of the pure solvents[3]. Γ was calculated from $\bar{V}_{\mathrm{Li_2EDC}}$ by assuming a cubic primitive cell. Initial concentrations c_{EC}^0 are chosen to represent a 3:7 mixture by volume. Equilibrium potentials are chosen to be 0.8 V[4] for EC and 0.3 V for DMC. This value is used because inorganic species are found below this voltage[5]. It is also close to the value of 0.25 V at which Zhang et al. found a transition in SEI properties[6]. The diffusion coefficient is chosen in the same order of magnitude as self-diffusion coefficients measured by Hayamizu et al.[7].

Methods

The system of equations (2)-(5) is solved in MATLAB using the implicit ODE15i function. All equations are discretized with the

* Corresponding Author: *birger.horstmann@dlr.de*
[a] *German Aerospace Center (DLR), Institute of Engineering Thermodynamics, Pfaffenwaldring 38-40, 70569 Stuttgart, Germany*
[b] *Helmholtz Institute Ulm (HIU), Helmholtzstraße 11, 89081 Ulm, Germany*
[c] *Ulm University, Institute of Electrochemistry, Albert-Einstein-Allee 47, 89069 Ulm, Germany*
† Main file available: [Enter DOI].
‡These authors contributed equally to this work'

Table 1 List of simulation parameters, all potentials relative to the Li/Li^+ reduction pair.

Parameter	Description	Value	Unit
Φ^0_{EC}	EC reduction potential	0.8	V[8]
Φ^0_{DMC}	DMC reduction potential	0.3	V[8]
Φ_{final}	electrode potential during simulation	0.1	V
$\bar{V}^E_{EC}$	EC molar volume	66.7	cm^3/mol[3]
$\bar{V}^E_{DMC}$	DMC molar volume	84.2	cm^3/mol[3]
$\bar{V}^S_{Li_2EDC}$	Li_2EDC molar volume	56.8	cm^3/mol[9]
$\bar{V}_{LiMC}$	LiMC molar volume	60.0	cm^3/mol[9]
D^0_{EC}	EC diffusion coefficient	10^{-6}	cm^2/s[7]
c^0_{EC}	EC concentration in bulk electrolyte	4.5	mol/l
a_0	pore-size and size of SEI particles	1.0	nm
Γ	suface site density	4.0	$\mu mol/m^2$[9]
E_A	transition state energy	1.0	eV[10,11]

finite volume method. If κ vanishes ($\varepsilon_{SEI} = 0$), eq (5) cannot be used to solve for the potential. For this reason, we add a small regularization parameter $\Delta\kappa = 0.05 \cdot \kappa^0$ to the effective conductivity in eq (6), mimicking electron jumps into the electrolyte. The spatial resolution used in our simulations is 0.5 Å which realizes the continuum limit.

References

1 Y. X. Lin, Z. Liu, K. Leung, L. Q. Chen, P. Lu and Y. Qi, *Journal of Power Sources*, 2016, **309**, 221–230.
2 M. Safari and C. Delacourt, *Journal of The Electrochemical Society*, 2011, **158**, 562–571.
3 R. Naejus and D. Lemordant, *The Journal of Chemical Thermodynamics*, 1997, **29**, 1503–1515.
4 K. Edström, M. Herstedt and D. P. Abraham, *Journal of Power Sources*, 2006, **153**, 380–384.
5 P. Lu, C. Li, E. W. Schneider and S. J. Harris, *Journal of Physical Chemistry C*, 2014, **118**, 896–903.
6 S. Zhang, M. S. Ding, K. Xu, J. Allen and T. R. Jow, *Electrochemical and Solid-State Letters*, 2001, **4**, A206.
7 K. Hayamizu, *Journal of Chemical and Engineering Data*, 2012, **57**, 2012–2017.
8 S. J. Harris and P. Lu, *Journal of Physical Chemistry C*, 2013, **117**, 6481–6492.
9 O. Borodin, G. D. Smith and P. Fan, *Journal of Physical Chemistry B*, 2006, **110**, 22773–22779.
10 Y. Yamada, Y. Iriyama, T. Abe and Z. Ogumi, *Langmuir*, 2009, **25**, 12766–12770.
11 K. Xu, A. Von Cresce and U. Lee, *Langmuir*, 2010, **26**, 11538–11543.

F. Single, B. Horstmann and A. Latz. Revealing SEI Morphology: In-Depth Analysis of a Modeling Approach. *Journal of The Electrochemical Society* **164**, E3132–E3145 (2017).

JES Focus Issue on Mathematical Modeling of Electrochemical Systems at Multiple Scales in Honor of John Newman

Revealing SEI Morphology: In-Depth Analysis of a Modeling Approach

Fabian Single,[a,b,z] Birger Horstmann,[a,b,z] and Arnulf Latz[a,b,c]

[a] *German Aerospace Center (DLR), Institute of Engineering Thermodynamics, 70569 Stuttgart, Germany*
[b] *Helmholtz Institute Ulm (HIU), 89081 Ulm, Germany*
[c] *Ulm University, Institute of Electrochemistry, 89069 Ulm, Germany*

In this article, we present a novel theory for the long term evolution of the solid electrolyte interphase (SEI) in lithium-ion batteries and propose novel validation measurements. Both SEI thickness and morphology are predicted by our model as we take into account two transport mechanisms, i.e., solvent diffusion in the SEI pores and charge transport in the solid SEI phase. We show that a porous SEI is created due to the interplay of these transport mechanisms. Different dual layer SEIs emerge from different electrolyte decomposition reactions. We reveal the behavior of such dual layer structures and discuss its dependence on system parameters. Model analysis enables us to interpret SEI thickness fluctuations and link them to the rate-limiting transport mechanism. Our results are general and independent of specific modeling choices, e.g., for charge transport and reduction reactions.

Manuscript submitted February 6, 2017; revised manuscript received April 17, 2017. Published May 5, 2017. *This paper is part of the JES Focus Issue on Mathematical Modeling of Electrochemical Systems at Multiple Scales in Honor of John Newman.*

In the near future, automotive and mobile applications demand power storage with large energy and power density. Currently, lithium-ion batteries (LIBs) are the technology of choice for devices with these demands. They operate at high cell potentials and offer high specific capacities while providing long lifetimes. The latter is a consequence of the stable chemistry of modern LIB systems. A significant part of this stability can be attributed to the passivation ability of the solid electrolyte interphase (SEI). This thin layer forms between the negative electrode and the electrolyte. Hence contact between these phases is prevented and the continuous reduction of electrolyte molecules is suppressed. These reduction processes occur because the operating potential of the negative electrode lies well below the stability window of the electrolyte.[1] They are suppressed because reduction products quickly form the SEI during the first charge of a pristine electrode. The self passivating ability is one of the most important distinctions between a well and a badly performing lithium-ion battery chemistry. It is of such importance because the reduction reactions consume lithium-ions, directly reducing battery capacity. However, a real SEI is not perfectly passivating and electrolyte reduction is never completely suppressed. Consequently, the lifetime of a battery is directly related to the long-term passivating ability of the SEI.

Numerous studies on SEI have been conducted since Peled reported on this correlation in 1979.[2] Most of these studies are experimental, investigating cycling stability as well as SEI impedance and composition. Theoretical studies are scarce in comparison, despite established methods such as DFT and DFT/MD derivatives. This can be partially explained with the chemical diversity of SEI, which has been investigated by Aurbach et al. for decades. Results are summarized in Refs. 3, 4 and include the study of SEI formation on graphite electrodes in organic solvent mixtures. The most significant finding of this time is that ethylene carbonate (EC) forms a stable SEI on graphite as opposed to propylene carbonate (PC). Another focus of early studies is the SEI composition, which has been probed by FTIR and XPS and other techniques. Lithium carbonate (Li_2CO_3) and lithium alkyl carbonates have been reported as products from the reduction of organic carbonates.

Studies of simplified systems, i.e., binder-free electrodes have improved our understanding of SEI composition only recently.[5] This advance is also due to the use of novel experimental techniques such as solid state NMR and TEM.[6,7] The focus of these studies are the standard $LiPF_6$/organic carbonate mixtures on graphite and silicon anodes. They find that SEI in EC containing solvents is primarily composed of lithium ethylene dicarbonate ($(CH_2OCO_2Li)_2$, Li_2EDC). Polyethylene oxide is also found as a major product of EC reduction. Linear carbonates like dimethyl carbonate (DMC) are reduced to lithium alkyl carbonates, such as lithium methyl carbonate (CH_3OCO_2Li, LiMC). These compounds play a secondary role when EC is in the solvent mixture. This is linked to the solvation shell of lithium-ions which are preferably coordinated to EC.[6,8] Furthermore, EC has a higher reduction potential.[9] Li_2CO_3 is not present or only found in small quantities in recent studies.[6,7,10] Its presence in several older studies is believed to correlate to water and CO_2 contamination.

The electrolyte salt has a large impact on SEI composition and performance. It can shift the onset potential of SEI formation and influence the total irreversible capacity during the first cycle.[10,11] In $LiPF_6$ solutions, LiF is another major SEI compound while lithium oxyflurophosphates ($Li_xPF_yO_z$) are present in low quantities.[12] The complex $LiPF_6$ decomposition process is investigated by Campion and Lux.[13,14]

Additionally, SEI composition depends on the electrode material. Solvent decomposition reactions proceed differently on graphite and lithium storage alloys.[15] Electrode materials exhibiting large volume change, i.e., silicon, fail to form a stable SEI. SEI needs to be flexible to accommodate volume changes of the underlying substrate without damage by cracking or rupture. It is believed that these properties can be, to some degree, provided by polymeric SEI compounds as found when FEC is used as solvent or additive.[12] Harris and Lu[16,17] show, that SEI consists of a porous outer layer and a dense inner (close the the electrode) layer by using isotope tracer and depth profiling techniques such as TOF-SIMS. Evidence for a dual-layer structure is found in the chemical composition of the film. Solid state NMR studies also suggest that SEI is at least partially porous.[7]

To summarize, there is a general understanding of SEI composition and morphology for few specific systems. Especially SEIs on graphite electrodes in organic solvents are studied and optimized for battery performance in several studies. This vast amount of information creates the elusive conclusion that SEI is well understood. However, several key questions about basic SEI mechanisms have yet to be answered. Most striking is the fact that the mechanism for lithium-ion transport through the SEI is still debated. Shi et al. propose a "knock-of" diffusion mechanism for lithium-ion interstitials in Li_2CO_3.[18] Diffusion of lithium-ions through Li_2EDC is modeled by Borodin et al.[19] At the same time Zhang et al. suggest that lithium-ions diffuse and migrate along boundaries between different SEI species.[20] Another open question is the process of initial SEI formation where

[z] E-mail: fabian.single@dlr.de; birger.horstmann@dlr.de

nucleation and precipitation could play an important role. Ushirogata et al. have recently suggested a "near-shore aggregation" mechanism of electrolyte decomposition products.[21] This is supported by the fact that the occupation of the lithium-ion solvation shell seems to have a large impact on SEI properties,[6,8] which suggests that reduction reactions occur in solution. Alternatively, solvent molecules could be reduced when adsorbed to the electrode. In this case, reduction products could attach to the electrode immediately. Finally, there is an open discussion about the mechanism driving long term SEI growth. The passivation of the SEI is not perfect and irreversible reduction reactions continue throughout the battery life.[22,23] This could be enabled by several different mechanisms, for example electron leakage through the SEI. However, a porous SEI allowing slow solvent diffusion through the film is equally plausible. In this scenario, solvent molecules would reach the electrode if the SEI is porous or ruptured by the "breathing" of the underlying electrode.

The lack of information on these issues can be attributed to several reasons. The results of many common experimental techniques are to some degree ambiguous. Interpretations of FTIR and XPS spectra are difficult because many SEI compounds are similar to each other and to residual electrolyte within the sample.[24] Rinsing the sample of excess electrolyte before the measurement is common, but known to selectively damage SEI. Therefore, SEI is difficult to access experimentally. Furthermore, too many variables influence SEI properties significantly, preventing a systematic investigation. Not only the solvent/salt combination but also the electrode material and its surface treatment influence SEI formation and properties.[25] Formation can take place at different potentials, cycling rates and temperatures. Finally, SEI chemistry is known to be sensitive to air exposure which often occurs during sample transfer. All this makes analyzing and comparing different studies and their results difficult. Especially the identification of universal SEI properties and mechanisms becomes complicated.

Continuum theories describe SEI formation in a simplified way and elucidate such universal properties. In this way, they circumvent specifying the reaction kinetics of the SEI formation reaction. Instead, the formation rate is limited and determined by the throughput of the so called "rate-limiting" transport mechanism. These models assume one such mechanism as the cause for long-term SEI growth, i.e., electron conduction[26,27] and tunneling[28,29] or solvent/salt diffusion.[30,31] However, independent of the assumed mechanism, all of these models predict similar long-term SEI thickness evolution. Therefore, even a successful measurement of this prediction cannot be used to confirm the underlying assumptions.

In conclusion, theoretical models based on transport through the SEI should predict additional measurable properties and dependencies. Tang et al.[32] approach this task by comparing experiments with different models, each based on a single rate-limiting mechanism. Because of the dependence of SEI growth rate on electrode potential, they finally conclude that electron conduction rather than solvent diffusion is rate-limiting.

For this reason, we extend the standard approach, using two potentially rate-limiting transport mechanisms at the same time and modeling a dynamic SEI porosity. This is done in a one dimensional framework. We describe the evolution of SEI thickness and morphology along the axes perpendicular to the electrode surface. The overall objective of this work is to make new observable predictions which allow to test and validate our assumptions. Besides thickness evolution, our model can predict the formation of a porous SEI and explain several dual-layer scenarios. These results are obtained for two different rate-limiting transport mechanisms namely electron conduction and diffusion of neutral lithium interstitials. Additionally, solvent diffusion through the SEI pores can become the rate-limiting transport mechanism. In fact we can smoothly transition the rate-limiting role from the solid phase transport mechanism to solvent diffusion. This reveals an intermediate regime where both transport mechanisms influence the formation rate.

The model and its numerical implementation are discussed in the Model and Model implementation section. We then proceed to study

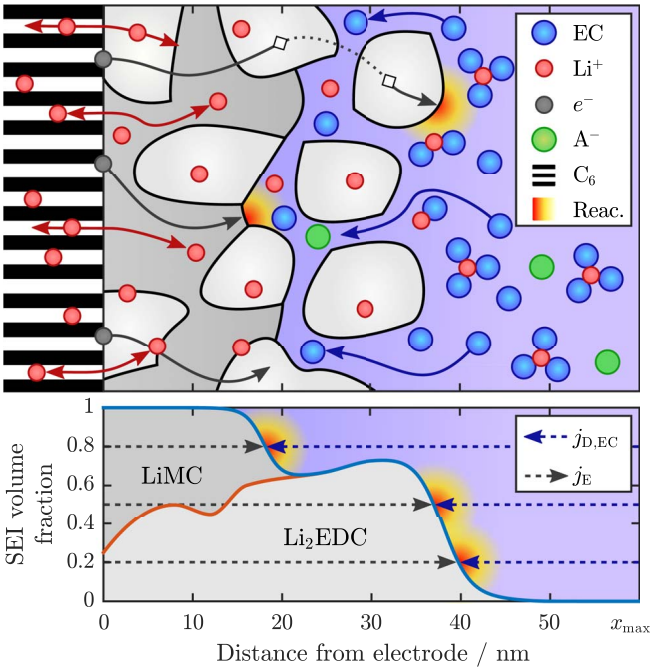

Figure 1. (a) Cross section through the graphite electrode (left, $x < 0$), and a SEI with dual layer structure (right, $x > 0$). Solvent, Li-ions and electrons are mobile species and move as indicated by the corresponding arrows. Reduction reactions (indicated red), consume these species and facilitate SEI growth. (b) SEI volume fraction gained by averaging the structure above in planes parallel to the electrode surface.

different sets of model scenarios, in the Simulation results section. In this way, we show how measurable SEI properties depend on specific assumptions and allow their experimental verification. First, we study our reference scenario, a SEI formed by a single reduction reaction. Then, the impact of an additional SEI formation reaction is studied. This slightly more complex SEI chemistry results in the observed dual-layer structure of the SEI. At the end of the results section we evaluate the effect of material laws dictating a minimum value of the SEI porosity. We find that solvent diffusion can become the rate-limiting transport mechanism under this assumption. We conclude the Simulation results section by illustrating for which parameter set solvent diffusion in the electrolyte or charge transport in the SEI are rate-limiting. We elaborate how these mechanisms can be distinguished by experiments. Finally, we discuss and summarize our results in two dedicated sections.

Model

As mentioned above, experimental studies suggest that the SEI is at least partially porous. We want to capture this property in our model. Therefore, we average the SEI density in planes parallel to the electrode surface. This results in the volume fraction profile of the SEI ε_{SEI}, as depicted in Fig. 1. Our model describes the temporal evolution of this profile within the simulation domain $[0, x_{\text{max}}]$ which reaches from the electrode surface at $x = 0$ into the bulk electrolyte phase. We capture the local formation of each individual SEI compound $i = \text{Li}_2\text{EDC}, \text{LiMC}, \ldots$ which changes the corresponding volume fraction ε_i

$$\frac{\partial \varepsilon_i}{\partial t} = \bar{V}^i_{\text{SEI}} \dot{n}_i, \qquad [1]$$

where $\dot{n}_i$ is the production rate of SEI compound i and $\bar{V}^i_{\text{SEI}}$ is the corresponding partial molar volume. The total SEI volume fraction equals the sum of solid phase volume fractions ε_i. It is directly related

to porosity ε

$$\varepsilon_{\text{SEI}} = \sum_i \varepsilon_i, \qquad \varepsilon_{\text{SEI}} = 1 - \varepsilon.$$

SEI is formed when solvent or salt species are reduced. Reduction processes are driven by local quantities such as the electronic potential and the concentration of active species. These quantities are traced within the simulation domain as they determine the reduction rates. Therefore, mass balance equations are solved for all relevant electrolyte species

$$\frac{\partial \varepsilon c_i}{\partial t} = -\text{div}(j_{\text{M},i} + j_{\text{D},i} + j_{\text{C},i}) + \dot{n}_i, \qquad [2]$$

where div denotes the divergence, $\text{div}\, j = \nabla \cdot j$. Migration of charged species ($j_{\text{M},i}$) and diffusion ($j_{\text{D},i}$) are the microscopic processes which transport particles inside the electrolyte. Together with convection ($j_{\text{C},i}$) they determine the evolution of c_i, the concentration of electrolyte species i = EC, DMC. A source term $\dot{n}_i$ couples the concentrations to consumption by reduction reactions, see Eq. 11. The local porosity ε appears on the left-hand side as we use porous electrode theory to describe the mass balance within the nano-porous SEI.[33]

As mentioned in the introduction, SEI chemistry is complex and highly dependent on the lithium-ion battery chemistry. Our framework is capable of modeling this chemistry in detail for each system individually, however such a realization requires many parameters which are not readily available. Large amounts of parameters for transport and reaction kinetics would make the identification of qualitatively significant results difficult. We simplify SEI chemistry and consider only one or two representative reduction reactions.

Reduction reactions take place at the interface between solid SEI material and the liquid electrolyte. SEI products precipitate immediately. Furthermore, the influence of charged species within the electrolyte is simplified. We assume that the electrochemical potential of lithium-ions is in equilibrium and constant. Lithium consumption due to SEI growth does not perturb the concentration locally because Li^+ mobility inside the SEI is very high compared to the rate of SEI formation. Furthermore the salt anion is neglected as an active species.

To summarize, solvent molecules are the only electrolyte species considered in our simulation. Assuming a binary mixture of solvent and co-solvent, two mass balance equations of type Eq. 2 are solved. Fickian diffusion and convection are the relevant transport processes for these species

$$j_{\text{D},i} = -D_i \nabla c_i, \qquad j_{\text{C},i} = c_i v, \qquad j_{\text{M},i} = 0, \qquad [3]$$

where D_i is the effective diffusion coefficient and v the convection velocity in the center of mass frame. One mass balance equation can be eliminated with the constitutive relation[34]

$$1 = \sum_i \bar{V}^i_{\text{Elyte}} c_i, \quad \text{yielding} \quad 0 = \sum_i \bar{V}^i_{\text{Elyte}} \nabla c_i. \qquad [4]$$

Here, we assume that partial molar volumes $\bar{V}^i_{\text{Elyte}}$ are constant and independent of concentration. By summing all mass balance equations (see Eq. 2) multiplied with $\bar{V}^i_{\text{Elyte}}$, we obtain

$$\text{div}\, v = \text{div} \sum_i \bar{V}^i_{\text{Elyte}} D_i \nabla c_i - \frac{\partial \varepsilon}{\partial t} = \bar{V}^{\text{EC}}_{\text{Elyte}} \text{div}(D_{\text{EC}} - D_{\text{DMC}}) \nabla c_{\text{EC}} - \frac{\partial \varepsilon}{\partial t}. \qquad [5]$$

In the second line, we applied Eq. 4 to a binary solvent mixture of EC and DMC specifically. This definition of the convection velocity ensures that all pores are filled with an incompressible electrolyte.[35,36] Because v is the center of mass velocity, the diffusive mass fluxes in the electrolyte add up to zero

$$\sum_i M_i j_{\text{D},i} = 0, \qquad [6]$$

where M_i is the molar mass of solvent species i. Thus, in the binary mixture, both diffusion coefficients are related, $M_{\text{EC}} D_{\text{EC}} \bar{V}^{\text{DMC}}_{\text{Elyte}} = M_{\text{DMC}} D_{\text{DMC}} \bar{V}^{\text{EC}}_{\text{Elyte}}$.

In the solid SEI phase, we take a second transport mechanism into account. This mechanism needs to transport a reduced species or electrons from the electrode/SEI interface through the SEI. As discussed in the Simulation results section, our results do not depend on the specific transport mechanism chosen. This is important because several different mechanisms seem plausible. For simplicity, we use electron conduction inside the solid SEI phase in our reference case. According to Ohm's law, the electronic current is driven by a potential gradient

$$j_{\text{E}} = -\kappa \nabla \Phi, \qquad [7]$$

where κ is the effective electronic conductivity, assumed equal for all SEI compounds. j_{E} is an electron leakage current through the SEI which fuels SEI formation and is much smaller than the lithium-ion intercalation current. Charge conservation is modeled by coupling the current to the reaction rate of each individual reaction

$$0 = -\text{div}\, j_{\text{E}} + F \sum_j n^j r_j. \qquad [8]$$

Here, $n^j r_j$ is the rate of electron consumption of reduction reaction j.

We consider faradaic surface reactions. Each reaction j is of the general type

$$\sum_i \tilde{s}^j_i \text{S}_i + n^j \left(\text{Li}^+ + e^-\right) \rightarrow \sum_k s^j_k \text{S}_k, \qquad [9]$$

where $\tilde{s}^j_i$ and and s^j_i are the stoichiometric coefficients. The sums include all electrolyte species and SEI compounds. In our simplified SEI chemistry each solvent reacts to a single SEI compound. Therefore, we use the solvent precursor as the reaction index j = EC, DMC. Reaction rates r_j, see Eq. 8, are determined with symmetric Butler-Volmer expressions, see recent works by Latz and Bazant,[37,38] or standard literature, e.g.,[33,39]

$$r_j = \frac{k_{\text{B}} T}{h} \exp\left(\frac{-E_{\text{A}}}{k_{\text{B}} T}\right) \prod_i \left(\frac{c_i}{c^0_i}\right)^{\frac{\tilde{s}_i}{2}} \sinh \frac{n^j F \eta_j}{RT}, \qquad [10]$$

where E_{A} is the energy difference between the initial and the transition state.

The overpotential η_j is the driving force of reaction j and will be discussed below. Oxidation of SEI compounds is only possible at high voltages (>3.25 V, see ref. 40) which are not met in normal battery operation. Generally, anodic reactions do not occur in our simulations because we always polarize the electrode below the onset potential of SEI formation. However, we need to actively prevent anodic reactions if a second SEI compound is considered. This is achieved by using $\tilde{\eta}_j = \max(0, \eta_j)$ for these reactions.

Source terms $\dot{n}_i$ in Eqs. 1 and 2, consist of the sum over all reduction reactions

$$\dot{n}_i = \sum_j \left(s^j_i - \tilde{s}^j_i\right) \rho_j r_j, \qquad [11]$$

where ρ_j is the reaction site density which depends on the type of the reaction j. It equals $\varepsilon_j / \bar{V}^j_{\text{SEI}}$ for bulk reactions in the solid SEI phase. For solvent reduction reactions which occur at the interface between solid SEI material and the liquid electrolyte, ρ_j equals the product ΓA, where A is the specific surface area and Γ is the surface site density. A is a function of porosity, as discussed below, while Γ is assumed constant.

SEI formation reactions.—As mentioned above, every reaction considered in our model introduces additional parameters. Therefore, we simplify SEI chemistry. We study all reactions listed below in different combinations, namely I, I + II and I + III. This means we consider up to two reactions at a time.

We assume a single reduction reaction for solvent and co-solvent

$$2\text{EC} + 2 \cdot (\text{Li}^+ + e^-) \rightarrow \text{Li}_2\text{EDC} + R, \qquad [\text{I}]$$

$$\mathrm{DMC} + \mathrm{Li}^+ + e^- \rightarrow \mathrm{LiMC} + R. \qquad [\mathrm{II}]$$

Gaseous by-products R are neglected in our simulation, as they quickly escape the simulation domain. Given the potential Φ and the concentration of each electrolyte species, we can express the overpotential for these reactions.

$$\eta_{\mathrm{EC}} = \Phi^0_{\mathrm{EC}} - \Phi + \frac{1}{2}\frac{RT}{F}\ln\left(\frac{c_{\mathrm{EC}}}{c^0_{\mathrm{EC}}}\right), \qquad [12a]$$

$$\eta_{\mathrm{DMC}} = \Phi^0_{\mathrm{DMC}} - \Phi + \frac{1}{4}\frac{RT}{F}\ln\left(\frac{c_{\mathrm{DMC}}}{c^0_{\mathrm{DMC}}}\right), \qquad [12b]$$

where Φ^0_i is the reduction onset potential of solvent species i and c^0_i is the corresponding reference concentration.

It is known that SEI species are to some degree unstable, especially at low potentials.[41] Therefore, aside from solvent molecules, SEI compounds can be reduced as well, forming new compounds and by-products. Lithium oxide (Li_2O) has been reported as SEI compound which is mostly found close to the electrode surface.[17,42] Therefore, we assume the formation of Li_2O by successive reduction of Li_2EDC[41]

$$0.1\mathrm{Li_2EDC} + \mathrm{Li}^+ + e^- \rightarrow \quad 0.6\mathrm{Li_2O} + 0.4\mathrm{C}, \qquad [\mathrm{III}]$$

where C denotes carbon. We have normalized this reaction to one lithium-ion, i.e., electron respectively. We calculate the kinetics of this reaction with Eq. 10. The overpotential of conversion reactions has no concentration contribution

$$\eta_{\mathrm{Li_2EDC}} = \Phi^0_{\mathrm{Li_2EDC}} - \Phi. \qquad [13]$$

Solid convection.—Independent of the specific conversion reaction chosen, a volume mismatch between the educts and products is typical. This volume mismatch creates an "excess volume" when the reaction is ongoing. Excess volume can be accommodated by a porosity change or by a displacement of the whole SEI such that porosity remains constant at the location of the reaction. We consider a mixture of both mechanisms by adding solid convection to the model and defining a suitable solid convection velocity $\tilde{v}$. Convective fluxes need to be considered in Eq. 1, which is therefore modified

$$\frac{\partial \varepsilon_i}{\partial t} = \bar{V}^i_{\mathrm{SEI}}\dot{n}_i - \mathrm{div}\,\varepsilon_i\tilde{v}. \qquad [14]$$

In two extreme cases, the solid convection velocity is given as

$$\varepsilon_{\mathrm{SEI}}\mathrm{div}\tilde{v} = 0, \qquad [15a]$$

$$\varepsilon_{\mathrm{SEI}}\mathrm{div}\tilde{v} = \sum_{j=\mathrm{conv}} \Delta\bar{V}^j_{\mathrm{SEI}}\rho_j r_j, \qquad [15b]$$

where the sum includes all conversion reactions. $\Delta\bar{V}^j_{\mathrm{SEI}}$ is the excess molar volume of the reaction. When the porosity is high, volume changes of individual SEI particles do not induce solid convection, as established by Eq. 15a. In Eq. 15b, the convection velocity is defined such that SEI porosity remains unchanged locally. Therefore, the SEI expands in response to SEI formation. Such a behavior can be expected when the porosity is almost zero and SEI cannot become any denser.

We model a smooth transition from local accumulation to SEI expansion as the SEI becomes denser. The solid convection velocity is calculated from

$$\varepsilon_{\mathrm{SEI}}\mathrm{div}\tilde{v} = \alpha(\varepsilon_{\mathrm{SEI}}) \sum_{j=\mathrm{conv}} \Delta\bar{V}^j_{\mathrm{SEI}}\rho_j r_j, \qquad [16]$$

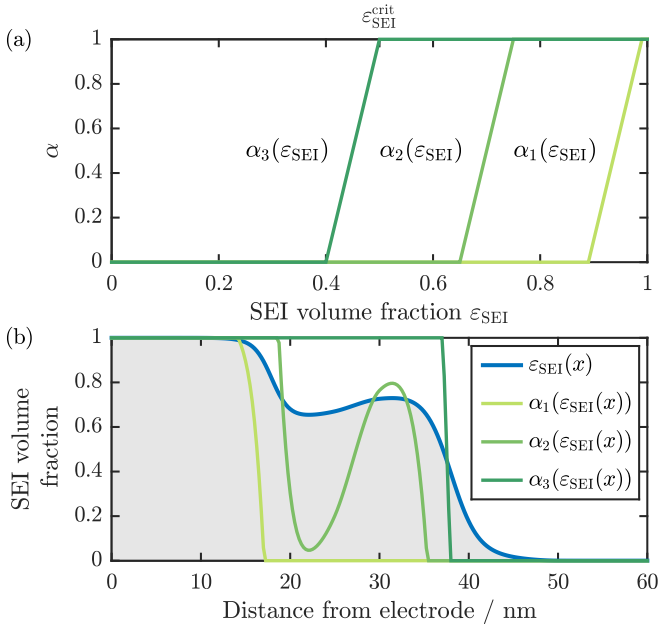

Figure 2. (a) $\alpha(\varepsilon_{\mathrm{SEI}})$ as a function of the SEI volume fraction for $\varepsilon^{\mathrm{crit}}_{\mathrm{SEI}} = 0.99, 0.75$ and 0.5, see Eq. 17. The location of the critical value is indicated for $\alpha_3(\varepsilon_{\mathrm{SEI}})$. (b) Spatial dependence of α for a given SEI volume fraction $\varepsilon_{\mathrm{SEI}}$.

where $\alpha(\varepsilon_{\mathrm{SEI}})$ models a smooth transition between Eqs. 15a and 15b. This transition is performed in a linear way

$$\alpha(\varepsilon_{\mathrm{SEI}}) = \begin{cases} 0 & \varepsilon_{\mathrm{SEI}} \leq \varepsilon^{\mathrm{crit}}_{\mathrm{SEI}} - \Delta\alpha, \\ 1 & \varepsilon_{\mathrm{SEI}} \geq \varepsilon^{\mathrm{crit}}_{\mathrm{SEI}}, \\ 1 + \frac{\varepsilon_{\mathrm{SEI}} - \varepsilon^{\mathrm{crit}}_{\mathrm{SEI}}}{\Delta\alpha} & \text{otherwise.} \end{cases} \qquad [17]$$

Here $\Delta\alpha$ is the width of the transition, chosen to be 0.1. The influence of the empirical parameter $\varepsilon^{\mathrm{crit}}_{\mathrm{SEI}}$ on SEI formation will be studied in the Simulation results section. It is one unless mentioned otherwise. It constitutes the greatest volume fraction that the SEI material can reach. Several versions of $\alpha(\varepsilon_{\mathrm{SEI}})$, differing in the choice of this parameter are shown in Fig. 2a.

Transport in porous media.—The local porosity ε determines the phase distribution in our simulation domain. Pure electrolyte and SEI phase are represented by $\varepsilon = 1$ and $\varepsilon = 0$, respectively. If ε is between zero and one, both electrolyte and SEI phase are present, arranged in a porous structure. As each transport mechanism is restricted to a single phase only, the corresponding transport parameters have to depend on the porosity. They decrease with the volume fraction of the phase they belong to. We use the Bruggeman ansatz to describe this behavior, i.e., we use a power law to relate these parameters at a given porosity to their bulk values. Bruggeman coefficients encode the structural information of the porous structure which is lost when averaging to obtain a one dimensional system. High values of β correspond to large tortuosity. The effective diffusion coefficient depends on the porosity

$$D_i = \varepsilon^{\beta} D_i^{\mathrm{Bulk}}, \qquad [18]$$

where the Bruggeman coefficient β is a parameter in our model whose influence will be part of our study. Analogously, electron conduction scales with the SEI volume fraction

$$\kappa = \varepsilon^{1.5}_{\mathrm{SEI}}\kappa^{\mathrm{Bulk}}. \qquad [19]$$

We have chosen 1.5 as the Bruggeman coefficient for transport in the solid SEI phase because it is the standard value. Percolation effects are not considered by this description. Therefore transport through a phase remains possible until the phase disappears completely, i.e., if $\varepsilon = 0$ or $\varepsilon_{\mathrm{SEI}} = 0$.

Specific surface area.—Solvent reduction and SEI formation take place at the interface between solid SEI material and the liquid electrolyte. Consequently, the source term of solvent reduction reactions is directly proportional to the specific surface area A (see Eq. 11). The specific surface area depends on the local porosity. We derive an approximation for this dependence from the assumption that SEI particles and pores are arranged on a cubic lattice with edge length a_0. This parameter corresponds to the average particle and pore size of the SEI. We consider a large volume $V \gg a_0^3$ in which all sub-cubes are randomly assigned to SEI/pores with uniform probability $\varepsilon_{SEI}/\varepsilon$. The total surface area in V can be approximated as

$$A_{\text{total}} \approx \frac{V}{a_0^3} \cdot 6 \cdot a_0^2 \cdot \varepsilon\varepsilon_{\text{SEI}}, \qquad [20]$$

where $V a_0^{-3}$ is the number of cubes. Every cube has six surfaces, each with an area of a_0^2. The probability of a cube being empty while a neighboring cube is filled equals the product $\varepsilon\varepsilon_{SEI}$. Here, surfaces on the edge of V have been neglected. Then the specific surface area of V reads

$$A = A_{\text{total}}/V = \frac{6}{a_0}\varepsilon\varepsilon_{\text{SEI}}. \qquad [21]$$

We need to adjust this expression because we study porosity profiles, this means porosity changes in one direction. To this aim, we study a slice V with the thickness of a single cube a_0. Now, surfaces on the edge of V can no longer be neglected and have to be taken into account. Therefore, we use the SEI volume fraction of the neighboring slices

$$A = \frac{\varepsilon}{a_0}\Big(4\varepsilon_{\text{SEI}} + \varepsilon_{\text{SEI}}(x - a_0) + \varepsilon_{\text{SEI}}(x + a_0)\Big).$$

Using a second order Taylor expansion for $\varepsilon_{SEI}(x \pm a_0)$ we find

$$A(\varepsilon) \approx \frac{6}{a_0}\varepsilon\left(\varepsilon_{\text{SEI}} + \frac{a_0^2}{6}\frac{\partial^2\varepsilon_{\text{SEI}}}{\partial x^2}\right). \qquad [22]$$

In comparison to Eq. 21, an effective, non-local SEI volume fraction replaces the local value. This modification enables growth into the pure electrolyte phase where ε_{SEI}, and thus A according to Eq. 21, is zero.

This approximation is good, when the porosity changes slowly in space relative to a_0, i.e., $|\partial_x^2\varepsilon| < 2a_0^{-2}$. If $\varepsilon(x)$ has a larger curvature, the Taylor expansion is not valid and Eq. 22 can become negative. However, these situations are averted in our simulations and the small quantitative errors do not influence our main results.

Regularization.—During our simulation SEI is formed and ε_{SEI} increases. When ε_{SEI} reaches unity at a certain location, a pure SEI phase would be formed. Pure phases are numerically difficult because transport equations for the absent phase become ambiguous. To avoid such problems, we implement two regularizations.

We prevent the formation of a dense SEI with vanishing porosity. This is achieved by modifying the specific surface area such that $\varepsilon < 1 - \Delta\varepsilon$ is guaranteed at all times

$$\tilde{A}(\varepsilon, \varepsilon''_{\text{SEI}}) = \frac{6}{a_0}\Big(\varepsilon - \Delta\varepsilon\Big)\left(\varepsilon_{\text{SEI}} + \frac{a_0^2}{6}\frac{\partial^2\varepsilon_{\text{SEI}}}{\partial x^2}\right), \qquad [23]$$

where $\Delta\varepsilon = 0.001$ is small. Mass balance equations, see Eq. 2, are guaranteed to be well defined with this modification.

In a pure electrolyte phase, equation Eq. 8 cannot be used to solve for the potential as $\kappa = \varepsilon_{\text{SEI}}^{1.5}\kappa^{\text{Bulk}}$ is zero. This can be alleviated by using

$$\kappa = \left[\varepsilon_{\text{SEI}}^{1.5} + \Delta\exp(-\varepsilon_{\text{SEI}}^2/\Delta)\right]\kappa^{\text{Bulk}}, \qquad [24]$$

which is equal to the Bruggeman relation at small porosities and attains $\Delta \cdot \kappa^{\text{Bulk}}$ as $\varepsilon \to 1$. This numerical procedure is necessary because our classical continuum theory cannot describe microscopic quantum effects. We describe here the spatial extend of the reaction process as the microscopic cause for SEI expansion. Therefore, the small conductivity in the electrolyte enables SEI growth into the electrolyte phase. We choose $\Delta = 0.05$, quite large compared to $\Delta\varepsilon$. Hence, charge transport into the electrolyte phase is a negligible barrier and does not affect our simulation results. At the same time, we make sure that the electron current does not reach beyond a few Å into the electrolyte.

Model Implementation

Initialization and boundary conditions.—We begin our simulations at $t = 0$. Initially the system is in a stationary state, which means that all reactions are in equilibrium. Consequently, the initial potential and concentration are chosen such that all overpotentials are zero, i.e., $\Phi(x, 0) = \Phi_{\text{EC}}^0$ and $c_{\text{EC}}(x, 0) = c_{\text{EC}}^0$. Thus, both convection velocities vanish, $v = \tilde{v} = 0$. The volume fraction of Li_2EDC is zero apart from a small region next to the electrode $\varepsilon_{\text{Li}_2\text{EDC}}(x > 2\,\text{nm}, 0) = 0$. An initialization profile serves as nucleation seed

$$\frac{\varepsilon_{\text{Li}_2\text{EDC}}(x < 2\,\text{nm}, 0)}{1 - \Delta\varepsilon} = -\frac{3}{16}\left(\frac{x}{\text{nm}}\right)^5 + \frac{15}{16}\left(\frac{x}{\text{nm}}\right)^4 - \frac{5}{4}\left(\frac{x}{\text{nm}}\right)^3 + 1. \qquad [25]$$

where x is the distance from the electrode. The volume fraction changes smoothly from $1 - \Delta\varepsilon \approx 1$ to zero, as shown in Fig. 4a. It represents the roughness of the electrode surface and adsorption layers of SEI formed at voltages above 0.8 V. The thickness correlates to the critical thickness SEI can reach by electron tunneling, as predicted by Lin et al.[29] The volume fraction of the second SEI compound considered is zero initially.

The simulation domain spans from the electrode surface at $x = 0$ into the bulk electrolyte at $x = x_{\text{max}}$. We choose our boundary conditions such that they describe the contact to these phases. While the electrode is a "reservoir" for the electronic current it acts as an impenetrable boundary for the electrolyte. Therefore diffusive and convective fluxes vanish at this interface. Solvent can be drawn from the right-hand side boundary at which electronic currents must vanish.

$$\begin{aligned} \Phi(0, t) &= \Phi_{\text{OCV}}(t), \quad & j_{\text{E}}(x_{\text{max}}, t) &= 0, \\ j_{\text{D,EC}}(0, t) &= 0, \quad & c_{\text{EC}}(x_{\text{max}}, t) &= c_{\text{EC}}^0, \\ v(0, t) &= 0, \quad & \tilde{v}(0, t) &= 0, \end{aligned}$$

where $\Phi_{\text{OCV}}(t)$ is determined from the state of charge (SOC) of a graphite electrode taken from Ref. 43. SOC is ramped linearly such that the electrode potential $\Phi(t)$ decreases from Φ_{EC}^0 at $t = 0$ to the final electrode potential Φ_{E} in 20 hours. Then SOC and potential remain constant, representing storage conditions. We stop the simulations shortly before SEI growth reaches x_{max}. In this way we make sure that the right boundary does not influence the results.

Parameterization.—All parameters used, for example, to create the data for figures and the results discussed, are summarized in Table I. They are listed in four groups according to their type.

- The molar volume of each SEI species determines the evolution rate of the corresponding SEI volume fraction, see Eq. 1. The molar volumes of electrolyte species define the amplitude of convection velocities induced by volume mismatch during reduction reactions in Eq. 5 and Eq. 16.
- Bulk diffusivity and conductivity in solvent and SEI are needed to calculate the electron and solvent flux. The Bruggeman coefficient is used to calculate the effective diffusion coefficient in the nano-porous SEI, see Eq. 18.
- Reaction rates are determined by a couple of parameters, e.g. the transition energy E_{A} and the pore size of the SEI structure a_0. The latter determines the area available for reactions, see Eq. 22.
- The equilibrium of each reaction is characterized by an equilibrium potential and a reference concentration, see Eq. 12.

Table I. List of simulation parameters, all potentials relative to the Li/Li^+ reduction pair.

Parameter	Description	Value Unit
$\bar{V}^{EC}_{Elyte}$	EC molar volume	66.7 cm^3/mol [44]
$\bar{V}^{DMC}_{Elyte}$	DMC molar volume	84.2 cm^3/mol [44]
$\bar{V}^{Li_2EDC}_{SEI}$	Li_2EDC molar volume	96.2 cm^3/mol [45]
$\bar{V}^{LiMC}_{SEI}$	LiMC molar volume	58.1 cm^3/mol [45]
$\bar{V}^{LiEC}_{SEI}$	LiEC molar volume	58.1 cm^3/mol
$\bar{V}^{Li_2O}_{SEI}$	Li_2O molar volume	14.9 cm^3/mol [45]
κ^{Bulk}	Conductivity of all SEI compounds	1 pS/m
D^{Bulk}	EC diffusion coefficient	10^{-10} cm^2/s [46]
β	Bruggeman coefficient for solvent diffusion	20 -
ε_{crit}	Critical (lowest possible) SEI porosity	0.8, 0.9 -
a_0	Pore-size and size of SEI particles	1.0 nm
Γ	Surface site density	4.0 $\mu mol/m^2$ [45]
E_A	Transition state energy	1.0 eV
c^0_{EC}	EC concentration in bulk electrolyte	4.5 mol/l
Φ^0_{EC}	EC reduction potential	0.8 V [16]
Φ^0_{DMC}	DMC reduction potential	0.3 V [16]
$\Phi^0_{Li_2EDC}$	DMC reduction potential	0.3 V [16]
Φ_E	Electrode potential during simulation	0.1 V

We assume that LiEC has the same partial molar volume as LiMC due to the similarity between both molecules. The Bruggeman coefficient $\beta = 20$ is chosen to describe the slow effective mesoscopic transport of solvent within the SEI nano-pores, whose microscopic mechanism is not understood. Furthermore, large values of β lead to larger porosities and allow easier illustration, e.g., in Fig. 4a.

Note that the other relevant symbols are listed and described in Table AI.

Numerical implementation.—*Numerical methods.*—We solve equations 2, 5, 8, 14, and 16 on a static and equidistant grid spanning from 0 to x_{max}. All equations are solved for the primary variables ε_i, c_{EC}, Φ, v, and $\tilde{v}$ in the whole domain at all times. The domain size in this work is 60 nm. All equations are discretized with the finite volume method which ensures continuity of mass and charge. Convective currents, e.g. $j_{C,EC} = c_{EC} v$ are calculated on the boundaries between discretization units. To calculate these currents we use the concentration of the left or right neighbor volume, depending on the sign of the velocity. This is done for solid convection as well. All simulations were performed in MATLAB with the implicit solver ODE15i.

SEI front properties.—In our simulations, we observe no SEI formation reactions inside the pores of the SEI or at the electrode/SEI interface.

Instead, reactions take place at the interphase separating the inner, homogeneous SEI from the pure electrolyte phase. This interphase has a width of roughly 1 nm and is called SEI front below. The porosity increases over the SEI front until it reaches unity, marking the end of the SEI and the beginning of the electrolyte phase, shown in Fig. 3. It is of vital importance that transport and reaction kinetics are solved with the necessary precision at the SEI front. We find that this is only possible, when the discretization is sufficiently fine, i.e., when a high resolution grid is used. The necessary resolution depends on the form of the front, which in turn depends on the small set of parameters and model assumptions

- activation energy E_A, see Eq. 10,
- specific surface area $A(\varepsilon, \varepsilon'')$, see Eq. 22,

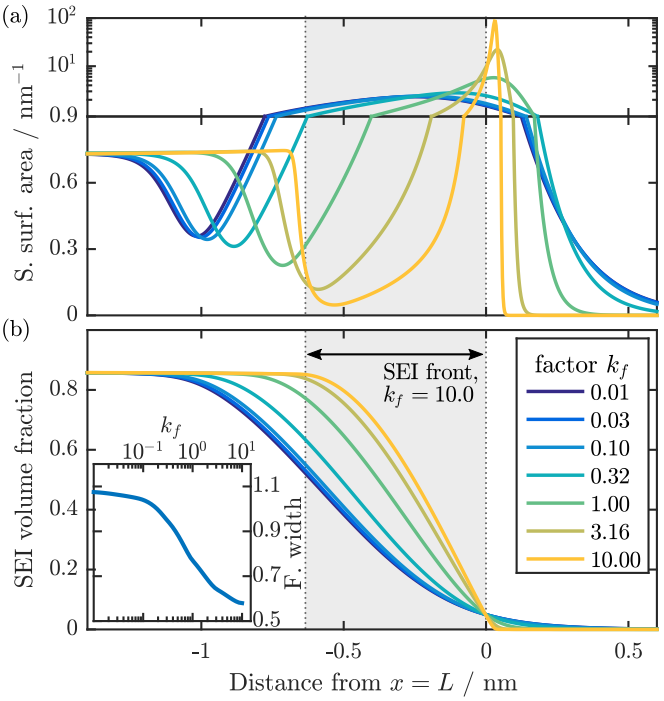

Figure 3. Specific surface area at the SEI front (a), see Eq. 22 (upper part scaled logarithmically) and the corresponding SEI volume fraction (b). Both plots show simulation results which differ only in the kinetic rate scale factor k_f in Eq. 26. The region we refer to as SEI front is marked gray for the simulation with $k_f = 10.0$. The inset shows how the front width depends on k_f.

These parameters influence the shape of the SEI front and the distribution of SEI formation within this region. They impact the thickness evolution and SEI porosity, two important results of our model. We therefore want to dedicate this subsection to discuss how the front shape is affected by these parameters. To do so, we have to go far afield.

Because of the boundary condition $j_E(x_{max}) = 0$, all electronic charge transported through the SEI must be consumed at the front. Consequently, the overpotential η will adjust itself such that electron consumption by SEI formation reactions at the front balances the incoming current $j_E(x = 0)$. In the following, we speak of slow reactions, when this overpotential is large ($\eta > 10\,mV$). Reactions are fast, when the overpotential is small ($\eta < 1\,mV$). Note that the total reaction turnover at the front is almost the same in both cases, only the necessary driving force is different.

To probe the difference between SEI formation in the slow and in the fast regime, we introduce the scale factor k_f. This factor is only used in this section and modifies the reaction rate

$$r_j = k_f \frac{k_B T}{h} \exp\left(\frac{-E_A}{k_B T}\right) \prod_i \left(\frac{c_i}{c_i^0}\right)^{\frac{\tilde{s}_i}{2}} \sinh \frac{n^j F \tilde{\eta}_j}{RT}. \quad [26]$$

When we increase k_f, the overpotentials decrease and reactions become fast. In return overpotentials become larger as we decrease k_f and we enter the slow regime.

As shown in Fig. 3b, the shape of the SEI front changes significantly with k_f. When reactions are slow, the front is wide and smooth. It becomes thinner as the reaction rate increases. At the same time, the specific surface area changes with the front shape, see Fig. 3a. It becomes smaller in the region where the porosity increases. Furthermore, we observe the formation of a singularity which emerges if the front width ΔL is smaller than a_0. As explained in the Model section, our expression for A (see Eq. 22) is derived for a slowly varying porosity. This is not the case when reactions are fast and the front width is below a_0 (see inset of Fig. 3b). To avoid this we adjusted our kinetics such that the width of the SEI front is wide ($\Delta L > a_0$) during

our simulation by choosing E_A accordingly. Therefore the scale factor k_f is not used below ($k_f = 1$).

Whether reactions are fast or slow depends on the overpotential at the front. This overpotential does not remain constant during the evolution of the SEI. It decreases because the electronic current through the SEI decreases as the SEI becomes thicker, see Eq. 27. The reactions become slower due to the decreasing influx of electrons. Therefore, the SEI front becomes wider during SEI formation.

Numeric convergence.—We find that the grid resolution necessary to obtain well converged simulations depends on the shape of the SEI front. Any "kink" in this profile (such as visible in Fig. 3b for $k_f = 10$ at $x \approx 0$), needs to be resolved sufficiently well. If not, the specific surface area will have an almost singular point because it is a function of the second spatial derivative of the porosity profile, see Eq. 22. Not only is this situation costly to solve numerically, it also influences the SEI porosity and growth rate by a few percent. However, we observe a directed and fast convergence of these quantities when the grid parameter becomes small enough. For example, when comparing two porosity profiles of the same simulation, performed with different grid parameters (2 and 0.66 pm), the largest difference inside the SEI is approximately 10^{-5}.

Simulation Results

This section contains four subsections which address potential scenarios of SEI formation. We begin with our reference scenario, the formation of a chemically homogeneous SEI before discussing growth scenarios with higher complexity. Then, we study dual-layer SEIs obtained by adding a second SEI formation reaction. We proceed by taking mechanical properties of the SEI into account so that solvent diffusion can become rate-limiting. Finally, we discuss how the form of the rate limiting transport mechanism affects observable quantities. In this way, we increase the model complexity step-by step and systematically predict SEI properties based on specific sets of assumptions.

Single-layer SEI.—In this section, we study SEI formation assuming an inert co-solvent. This means that SEI formation is represented by a single reduction reaction, i.e., the reduction of EC to Li_2EDC, see Reaction I. We are able to derive analytic expressions for our primary results in this reference scenario. Our simulations start with a nearly uncharged graphite electrode which is charged to $\Phi_E = 0.1$ V in the first 20 hours of the simulation. The electrode potential is then kept constant, simulating long-term storage under open-circuit condition. Fig. 4a shows the temporal evolution of the corresponding SEI volume fraction. We observe the formation of a porous film which gradually becomes thicker in our simulations. SEI formation occurs at the SEI front, shown in Fig. 3, indicating that electron conduction is the rate-limiting transport mechanism. No reactions take place inside the SEI where porosity remains constant in time. Both, the rate of SEI growth and the SEI porosity depend on the simulation parameters. We study this parameter dependence below, where we refer to the average porosity of a specific simulation as $\varepsilon^* = 1 - \varepsilon^*_{SEI}$.

Thickness evolution.—The formation of SEI species is located at the front of the film and thus causes lateral growth. Therefore electron conduction is limiting the rate of SEI growth. This is reflected in the SEI potential which increases linearly from Φ_E to Φ^0_{EC} at any given time, shown in Fig. 4b. The electronic current j_E within the SEI is constant and electrons are transported from the electrode to the SEI front. We use this observation to approximate the electronic current j_E through the SEI

$$j_E(x) = -\kappa(\varepsilon_{SEI}(x))\nabla\Phi(x) \approx -\kappa^* \frac{\Phi(L) - \Phi(0)}{L},$$

$$\approx -\kappa^* \frac{\Phi^0_{EC} - \Phi_E}{L}, \qquad [27]$$

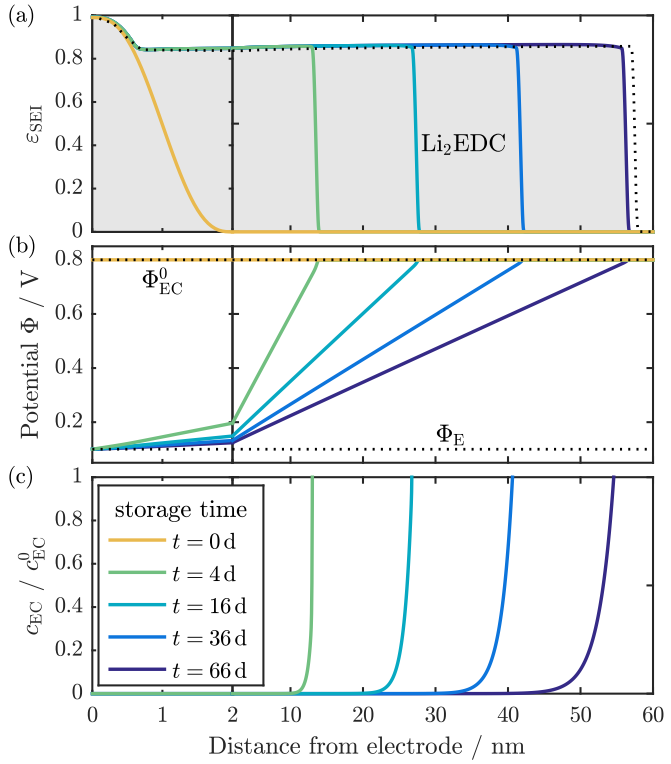

Figure 4. (a) SEI volume fraction $\varepsilon_{SEI}(x, t)$ at various times of the simulation. Note the different scaling of the x-axes to highlight the initial SEI profile. The dashed line is a profile from a simulation where neutral lithium interstitial diffusion has been used as the rate-limiting transport mechanism. (b) Potential $\Phi(x, t)$ and, (c) relative solvent concentration $c_{EC}(x, t)$ ($c^0_{EC} = 4.5$ moll^{-1}).

where $\kappa^* = \varepsilon^{*1.5}_{SEI}\kappa^{Bulk}$. We can couple this current directly to the evolution rate of the SEI thickness L,

$$\frac{\partial L}{\partial t} = \frac{\bar{V}^{Li_2EDC}_{SEI}}{2} \frac{1}{\varepsilon^*_{SEI}} \frac{(-j_E)}{F}, \qquad [28]$$

where the first fraction takes the density of the SEI material and the stoichiometry of the formation reaction into account. The second fraction factors in film porosity. Finally, the Faraday constant F converts the current density into a particle flux density.

Using approximation 27 in Eq. 28 results in a first order differential equation for L. The solution

$$L(t) = \sqrt{\frac{\kappa^* \Delta\Phi_{EC} \bar{V}^{Li_2EDC}_{SEI}}{\varepsilon^*_{SEI} F}}\sqrt{t}, \qquad [29]$$

depends on the mean film porosity ε^*, which is not a parameter but a result of our simulation. The parameter dependence of this value is very complex and will be discussed later. Eq. 29 has the well known $\sqrt{t}$ dependence of transport limited growth. We observe this time dependence of SEI thickness in our simulations, see Fig. 5a. The expression agrees well with simulation results as shown on the right side of this figure. Small derivations can be linked to the offset between $\Phi(L)$ and Φ^0_{EC}. However this error is in the order of few mV and small compared to $\Delta\Phi_{EC} = \Phi(L) - \Phi^0_{EC} \approx 700$ mV.

As seen in Eq. 29, only a few parameters influence the growth rate directly. These are the conductivity κ^{Bulk}, the molar volume of Li_2EDC and the applied potential Φ_E. Other parameters, such as β and D^{Bulk} can influence the average SEI porosity ε^*, which in turn affects the thickness evolution. However, as shown in Fig. 5a, the influence of ε^* on the growth rate is small. Consequently, assuming an inaccurate porosity in Eq. 29 only leads to minor quantitative errors.

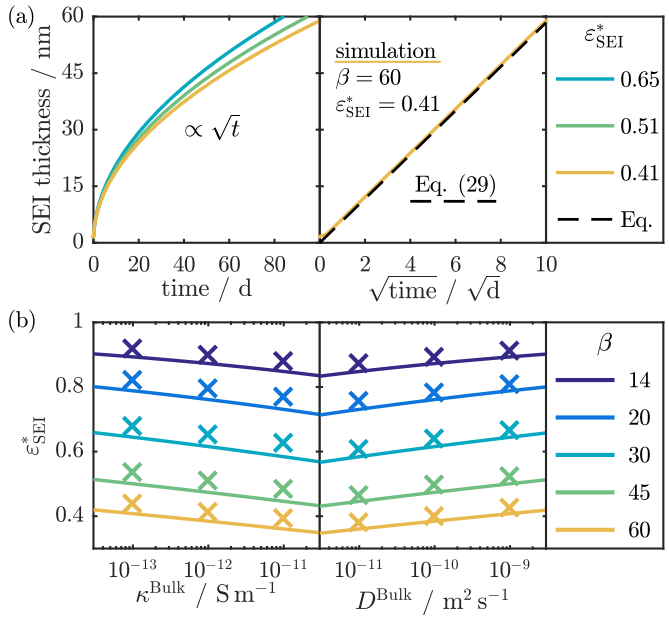

Figure 5. (a) SEI thickness in nm over time t (left) and $\sqrt{t}$ (right) to illustrate the square root of time dependence. The porosity dependence of $L(t)$ is shown on the left side, on the right the simulation is compared to Eq. 29 (dashed line). (b) SEI volume fraction dependence on transport parameters κ (left) and D (right). Crosses mark points measured in simulations, lines show predictions by Eq. 34.

The charge which is irreversibly consumed by SEI formation is equal to

$$Q_{\text{irr.}}(t) = \frac{2\varepsilon^*_{\text{SEI}} F}{\bar{V}_{\text{SEI}}} A^{\text{Elec.}}_{\text{total}} L(t) = 2A^{\text{Elec.}}_{\text{total}} \sqrt{\frac{\varepsilon^*_{\text{SEI}} F \kappa^* \Delta\Phi_{\text{EC}}}{\bar{V}^{\text{Li}_2\text{EDC}}_{\text{SEI}}}}\sqrt{t}, \qquad [30]$$

where $A^{\text{Elec.}}_{\text{total}}$ is the total electrode surface area. We use this expression, to estimate the electron conductivity κ^{Bulk} by comparing it to capacity fade measurements by Broussely et al.[47] For this comparison we use $A^{\text{Elec.}}_{\text{total}} = 173\,\text{m}^2$, taken from[31] and assume $\varepsilon^*_{\text{SEI}} = 0.8$. As shown in Figure 6, we obtain values of $\kappa^{\text{Bulk}} = 0.1\,\text{pSm}^{-1}$ to $\kappa^{\text{Bulk}} = 0.65\,\text{pSm}^{-1}$ for $T = 30°\text{C}$ and $T = 60°\text{C}$ respectively. These values agree with our previous parameterization.[26] The corresponding SEI thicknesses equal 50 and 125 nm after 450 days of storage.

SEI porosity.—As mentioned above, porosity inside the SEI remains constant in time. Further EC reduction stops because the concentration of the active solvent (EC) is too low and pores are filled with inert co-solvent, see Fig. 4c. Diffusion fluxes of active solvent into the pores are suppressed by the small effective diffusion coefficient $D^* = \varepsilon^{*\beta} D^{\text{Bulk}}$. The formation reactions are distributed over the front and cease on its left edge, where porosity equals ε^*. Here solvent cannot be supplied at the same rate at which electrons reach the front, forcing the SEI to expand laterally. Consequently, the porosity observed in our simulations depends on the transport parameters of the electrolyte (D, β, c^0_{EC}). All parameters appearing in Eq. 29 determine the speed of SEI expansion and influence porosity as well.

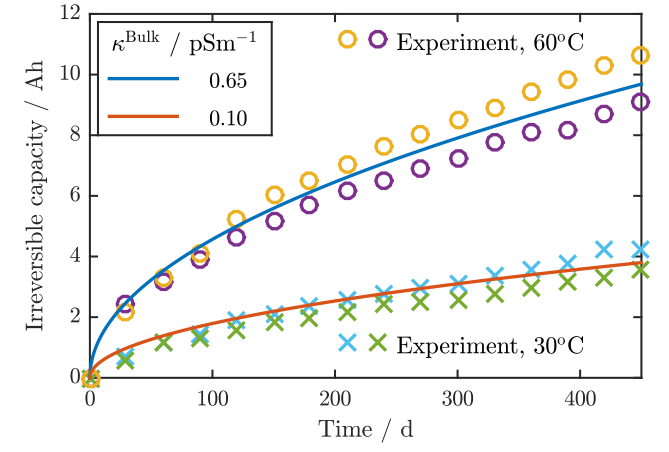

Figure 6. Capacity fade according to Eq. 30 (lines) compared to experimental data (circles and crosses).[47]

We derive an analytic expression to understand the dependence of the mean SEI porosity ε^* on these parameters. This requires to apply some simplifications to the model equations. First and foremost, reaction kinetics are assumed to be infinitely fast. This has almost no influence on our results because SEI growth is limited by transport and not by reaction kinetics. When the reactions are sufficiently fast, the overpotential η is small enough to justify the approximation $\eta_{\text{EC}} = 0$ which implies (see Eq. 12a)

$$c_{\text{EC}} = c^0_{\text{EC}} e^{\frac{F(\Phi-\Phi^0_{\text{EC}})}{2RT}}, \; c'_{\text{EC},x} = \frac{c_{\text{EC}} F}{2RT}\Phi'_x, \qquad [31]$$

where X'_y denotes the partial derivative $\frac{\partial X}{\partial y}$. Secondly, we simplify our principal equations by neglecting convection. This yields

$$\frac{\partial \varepsilon}{\partial t} = -\bar{V}^{\text{Li}_2\text{EDC}}_{\text{SEI}} A\Gamma r_{\text{EC}}, \qquad [32a]$$

$$\frac{\partial \varepsilon c_{\text{EC}}}{\partial t} = \frac{\partial}{\partial x} D c'_{\text{EC},x} - 2A\Gamma r_{\text{EC}}, \qquad [32b]$$

$$0 = \frac{\partial}{\partial x}\frac{\kappa}{F}\Phi'_x + 2A\Gamma r_{\text{EC}}. \qquad [32c]$$

Finally, we analyze Eq. 32b in the stationary regime ($\partial_t \varepsilon c_{\text{EC}} \approx 0$) because porosity and concentration changes in time are small. By summing Equations 32b and 32c while using Eq. 31 to express $c'_{\text{EC},x}$ with Φ'_x, we obtain

$$0 = \frac{\partial}{\partial x}\left(\underbrace{\frac{c_{\text{EC}} F D}{2RT}}_{\tilde{D}} + \underbrace{\frac{\kappa}{F}}_{\tilde{\kappa}}\right)\Phi'_x.$$

Integration yields an expression for Φ'_x, relating it to the local transport parameters

$$\Phi' = \frac{\xi}{\tilde{D}+\tilde{\kappa}}, \text{ resulting in, } \Phi'' = -\frac{\tilde{D}'_\varepsilon + \tilde{\kappa}'_\varepsilon}{\tilde{D}+\tilde{\kappa}}\varepsilon'_x\Phi'_x - \frac{\tilde{D}'_c}{\tilde{D}+\tilde{\kappa}}\frac{c_{\text{EC}}\Phi'^2_x}{2RT},$$

where ξ is an integration constant. When the SEI is sufficiently thick, we can neglect terms scaling with Φ'^2_x because Φ'_x is proportional to L^{-1}. Using this approximation in Equation 32c after inserting 32a yields

$$\begin{aligned}\frac{\partial \varepsilon}{\partial t} &= \frac{\bar{V}^{\text{Li}_2\text{EDC}}_{\text{SEI}}}{2}\frac{\partial}{\partial x}\tilde{\kappa}\Phi'_x \\ &= \frac{\bar{V}^{\text{Li}_2\text{EDC}}_{\text{SEI}}}{2}\left(\tilde{\kappa}'_x\Phi'_x + \tilde{\kappa}\Phi''_{xx}\right) \\ &= \frac{\bar{V}^{\text{Li}_2\text{EDC}}_{\text{SEI}}}{2}\frac{\tilde{D}\tilde{\kappa}'_\varepsilon - \tilde{\kappa}\tilde{D}'_\varepsilon}{\tilde{D}+\tilde{\kappa}}\varepsilon'_x\Phi'_x.\end{aligned}$$

We now trace the porosity at a point co-moving with the left edge of the SEI front, see Fig. 3. Here the porosity changes in time according to

$$\frac{d\varepsilon(L(t),t)}{dt} = \varepsilon'_x\frac{\partial L}{\partial t} + \frac{\partial \varepsilon}{\partial t} \approx \frac{\bar{V}^{\text{Li}_2\text{EDC}}_{\text{SEI}}\varepsilon'_x\Phi'_x}{4}\left(\frac{\tilde{\kappa}}{\varepsilon_{\text{SEI}}} + \frac{\tilde{D}\tilde{\kappa}'_\varepsilon - \tilde{\kappa}\tilde{D}'_\varepsilon}{\tilde{D}+\tilde{\kappa}}\right), \qquad [33]$$

where the approximation for the thickness evolution Eq. 29 is used. The porosity at this location has an attractive point. This means that

ε will converge toward this value in time. This stationary solution equals the mean SEI porosity ε* which satisfies

$$\frac{\tilde{\kappa}^*}{\tilde{D}^*} = \frac{\kappa^*}{D^*}\frac{2RT}{c_{EC}F^2} = \frac{1}{2} + \frac{\beta\varepsilon^*_{SEI}}{\varepsilon^*}. \quad [34]$$

We compare this expression to simulation results in Figure 5b. It describes the dependence of porosity on the transport parameters κ^{Bulk}, D^{Bulk} and β extremely well. There is a small offset between the SEI porosity determined by the simulation and the analytic prediction. We attribute this to the simplifications made in the derivation of Eq. 34. As we neglect electrolyte convection, the porosity predicted is slightly too low. Much better agreement is found, when the active solvent concentration is low and the influence of solvent convection is small.

In summary, we predict a finite SEI porosity which we propose to measure in appropriate in-situ imaging studies. This prediction assumes long-term storage, consequently all samples need to be stored for an appropriate time span before the measurement. Unfortunately, we cannot quantitatively predict ε* because it depends strongly on β, an unknown parameter, see Fig. 5b. Assuming Bruggeman coefficients between β = 5 and β = 20 results in porosities between ε* = 0.002 and ε* = 0.2.

Neutral lithium interstitial diffusion.—In the simulations discussed above, electron conduction is the rate-limiting transport mechanism. Electron conduction is the most prominent among several transport mechanisms in the solid SEI phase suggested in the literature.[18,27,28] The findings for the reference scenario discussed in this section, however, are independent of the specific charge transport mechanism. In the following, we demonstrate this by replacing electron conduction with diffusion of neutral lithium interstitials. The latter mechanism is proposed as a potentially rate-limiting mechanism by Shi et al.[18]

We add a mass balance equation for the neutral lithium interstitial concentration c_{Li}

$$\frac{\partial \varepsilon_{SEI} c_{Li}}{\partial t} = -\mathrm{div}\, j_{D,Li} + \dot{n}_{Li}, \quad [35]$$

where the diffusive flux $j_{D,Li}$ has the same porosity dependence as the migration flux in our standard case, see Eq. 19. This transport equation replaces Eq. 8, which describes electron conduction. In this way, we exchange the rate-limiting transport mechanism.

SEI profiles obtained using this mechanism share the same features as those generated with the conduction type mechanism, see Fig. 4a. Again, we observe the formation of a layer with nearly constant porosity. Similar to above, the thickness evolution follows a $\sqrt{t}$ law. Analytic expressions for the thickness evolution and the porosity can be derived analogously to Eq. 29 and Eq. 34, respectively. In conclusion, SEI thickness evolution and porosity are not sufficient to distinguish between these two charge transport mechanisms in the solid SEI phase. Therefore, we study further SEI quantities in next sections.

Additionally, we find that the interstitial concentrations found by Shi et al.[18] are insufficient to drive SEI formation at a reasonable rate. For the simulation depicted in Fig. 4a we have used the proposed $\approx 10^7$ interstitials/cm^3. To obtain reasonable growth rates we used an the extremely high bulk diffusion coefficient of 0.002 cm^2/s. Alternatively, we obtain reasonable diffusion coefficients for a higher interstitial concentration. Such a concentration would correspond to a smaller interstitial formation energy, approximately 200–300 meV below the value from Shi et al.[18]

Dual-layer SEI.—It is well-known that the SEI is not chemically homogeneous. Therefore, as the next step, we extend the reference scenario by taking a second SEI compound into account. This compound is either produced by co-solvent reduction (II) or by conversion of Li_2EDC (III). The onset potential for these reactions is chosen as $\Phi^0_{DMC} = \Phi^0_{Li_2EDC} = 0.3$ V and is below the reduction potential of EC of 0.8 V. In these scenarios, dual-layer structures emerge, as shown in Fig. 7. Depending on the reaction type, the two layers differ in chemistry, morphology, or both. The total SEI thickness evolves as in the reference scenario. Both layers grow simultaneously and each layer has its own front where the corresponding formation reaction takes place.

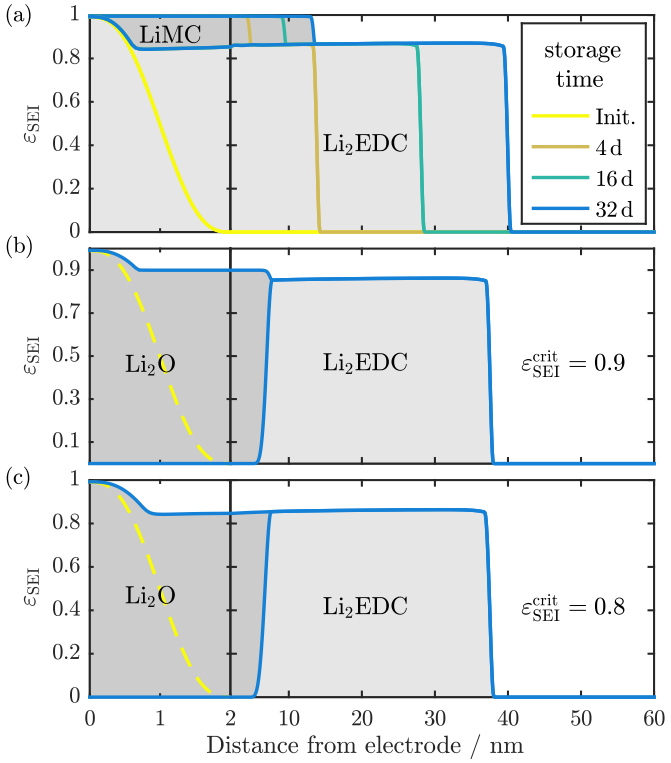

Figure 7. (a) SEI volume fraction evolution with active co-solvent. (b) and (c) show the SEI volume fraction of a dual layer SEI formed with inert co-solvent and unstable Li_2EDC. These simulations differ in the choice of ε^{crit}_{SEI}, see Fig. 2.

Co-solvent reduction.—The volume fraction evolution of a simulation with reacting co-solvent is shown in Fig. 7a. EC reduction proceeds as described in our reference scenario, creating a porous layer of Li_2EDC (see Fig. 4). Additionally, co-solvent is reduced at the front of the inner layer, filling the pores of the outer layer with LiMC. Co-solvent reduction stops when the layer is dense. It is suppressed because the specific surface area vanishes when ε → 0, see Eq. 21. Therefore, a dense layer forms next to the electrode while the outer layer remains porous. Li_2EDC and LiMC are both present in the dense layer.

Volume mismatch between the products and reactants of the second reduction reaction induces a convective flow of the electrolyte. This flow carries additional solvent across the SEI front. In turn, the mean porosity of the outer layer ε* decreases and the SEI becomes denser compared to simulations with inert co-solvent, see Fig. 4a. Therefore, our analytic expression for the porosity Eq. 34 does not predict the porosity of the outer layer as accurately as before.

Conversion Reaction.—The SEI remains to be composed of two layers if co-solvent reduction (II) is replaced with the conversion reaction (III), see Figure 7b and 7c. Again, the outer layer is porous and consists of Li_2EDC. The inner layer is created by the conversion of Li_2EDC and constantly grows at its front. In this case, each layer consists of the products of a single reaction. Compared to simulations with active co-solvent, products of different reduction reactions are no longer mixed in the inner layer.

The porosity of the inner layer depends on the choice of $\alpha(\varepsilon_{SEI})$ (see Eq. 16) or ε^{crit}_{SEI} specifically. As described in the Model section, ε^{crit}_{SEI} determines how dense the SEI can become from accumulation of excess volume by conversion reactions. Here we can distinguish two cases. In Fig. 7b the critical SEI volume fraction ε^{crit}_{SEI} exceeds

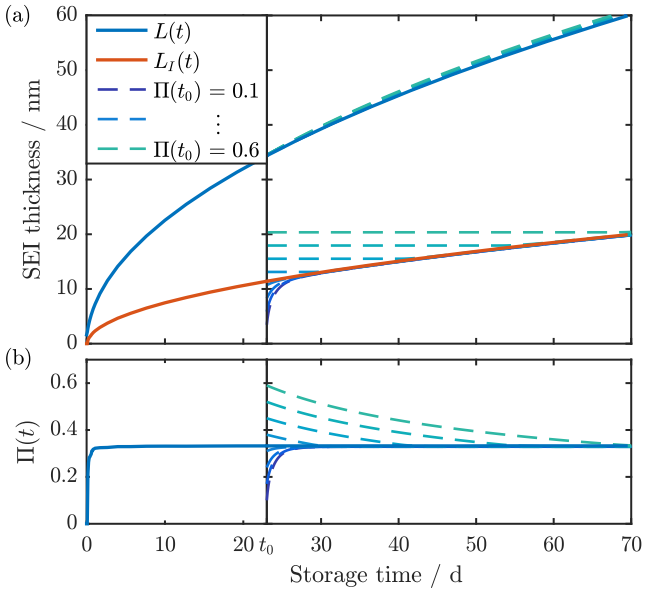

Figure 8. (a) Thickness evolution of the inner and the outer layer in a simulation with active co-solvent (solid lines) compared to numerical solutions of Eqs. 36 (dashed lines). The latter are initialized at $t_0 = 30\,\mathrm{d}$ with different values of $L_I(t_0)$. (b) Evolution of $\Pi(t)$ for both simulation and numerical solutions.

the volume fraction of the outer layer. Therefore, excess volume of the conversion reaction can accumulate locally until the SEI volume fraction has reached this value $\varepsilon_{\mathrm{SEI}}^{\mathrm{crit}}$. Further conversion reactions only induce solid convection, thus increasing the thickness of the inner layer and displacing the outer one. The porosity profile shown in Fig. 7c is created when $\varepsilon_{\mathrm{SEI}}^{\mathrm{crit}}$ is smaller than or equal to the volume fraction of the outer layer. In this case, both layers have the same porosity.

Thickness evolution.—We now discuss the thickness evolution of the dual-layer films. In Fig. 8a, we plot the thickness of the inner layer and the total SEI thickness against the storage time (solid lines). Both layers grow with the square-root of time. In this figure and the subsequent discussion, the inner layer is formed by products of co-solvent reduction (II). For conversion reactions (III), the situation is qualitatively identical.

Analogously to Eq. 29, we derive analytic expressions for the thickness evolution of the dual-layer system. The derivation below is performed for a system with active co-solvent and the index I/O is used for the inner/outer layer respectively, $(L_\mathrm{I} + L_\mathrm{O} = L)$. We couple the electronic current in each layer to its growth rate,

$$\frac{\partial L}{\partial t} = -\frac{\bar{V}_{\mathrm{SEI}}^{\mathrm{Li_2EDC}}}{2\varepsilon_{\mathrm{SEI}}^{*} F}\, j_{\mathrm{E,O}}, \qquad [36a]$$

$$\frac{\partial L_\mathrm{I}}{\partial t} = -\frac{\bar{V}_{\mathrm{SEI}}^{\mathrm{LiMC}}}{\varepsilon^{*} F}\Big(j_{\mathrm{E,I}} - j_{\mathrm{E,O}}\Big). \qquad [36b]$$

We proceed to solve these equations by deriving simple expressions for the current densities in both layers $j_{\mathrm{E},i}$. To this aim, we discuss the shape of the electric potential $\Phi(x)$ in the SEI. As explained above, reactions occur at the layer fronts only and $\Phi(x)$ increases linearly in each layer. Additionally, porosity and conductivity are constant in each layer. We hold the electrode potential constant $\Phi(x{=}0) = \Phi_\mathrm{E}$. At the SEI front, the potential is given by $\Phi(L) \approx \Phi_{\mathrm{EC}}^{0}$.

We use this to approximate $j_{\mathrm{E},i}$, similar to Eq. 27

$$j_{\mathrm{E,O}} = -\kappa^{*}\frac{\Phi_{\mathrm{EC}}^{0} - \Phi(L_\mathrm{I})}{L - L_\mathrm{I}},\; j_{\mathrm{E,I}} = -\kappa^{\mathrm{Bulk}}\frac{\Phi(L_\mathrm{I}) - \Phi_\mathrm{E}}{L_\mathrm{I}}. \qquad [37]$$

If the inner layer grows, it holds

$$\Phi(L_\mathrm{I}) = \Phi_{\mathrm{DMC}}^{0}. \qquad [38]$$

Otherwise, we have to take into account the irreversibility of SEI formation and demand $j_{\mathrm{E,I}} = j_{\mathrm{E,O}}$.

$$\Phi(L_\mathrm{I}) = \Big(\Phi_{\mathrm{EC}} - \Phi_\mathrm{E}\Big)\left(1 + \frac{L_\mathrm{O}}{L_\mathrm{I}}\frac{\kappa^{\mathrm{Bulk}}}{\kappa^{*}}\right)^{-1} + \Phi_\mathrm{E}. \qquad [39]$$

$\Phi(L_\mathrm{I})$ is the maximum of Φ_{DMC}^{0} and this modified expression. To conclude, Eq. 36 together with Eq. 37 is a coupled ODE for L and L_I which describes the thickness evolution of each layer.

According to Eq. 36, the growth rate is determined by the same parameters as in simulations with inert co-solvent. These are the conductivity κ^{Bulk}, the molar volumes of SEI compounds $\bar{V}_{\mathrm{SEI}}^{i}$ and the applied potential Φ_E. Additionally, the porosity of the outer layer $\varepsilon_{\mathrm{SEI}}^{*}$ appears as an indirect parameter which has to be assumed or measured.

Fig. 8a compares the thickness evolution from numerical solutions of Eqs. 36 (dashed) to a simulation of the full model (solid lines). The figure shows several solutions with different initializations i.e. $L_\mathrm{I}(t_0)$ is varied while $L(t_0)$ is fixed. When the initial values match the full simulation, very good agreement is observed and both layers grow with $\sqrt{t}$. The other curves show how the dual layer system reacts to a different initialization. Fig. 8b shows how the ratio of the inner to the total SEI thickness

$$\Pi(t) = L_I(t)/L(t), \qquad \Pi \in [0, 1],$$

evolves in time. This ratio quickly attains the stationary value Π_{stat} and then remains constant for the rest of the simulation. In a real battery, Π can deviate from this stationary value if the electrode potential is varied or if the SEI is physically damaged. As illustrated in Fig. 8b, Π_{stat} is a stationary point of $\Pi(t)$ and satisfies

$$\frac{\partial \Pi}{\partial t} = \frac{\partial_t L_I}{L} - \frac{L_I \partial_t L}{L^2} \overset{!}{=} 0 \rightarrow L\partial_t L_I = L_I \partial_t L.$$

With Eqs. (36) we can rearrange this condition into a quadratic equation in Π_{stat}

$$\frac{\bar{V}_{\mathrm{SEI}}^{\mathrm{Li_2EDC}}}{2\bar{V}_{\mathrm{SEI}}^{\mathrm{LiMC}}}\varepsilon^{*}\Pi_{\mathrm{stat}}^{2} + \left(1 + \frac{\Delta\Phi_{\mathrm{DMC}}}{\varepsilon_{\mathrm{SEI}}^{*1.5}\Delta\Phi_{\mathrm{diff}}}\right)\Pi_{\mathrm{stat}} + \frac{\Delta\Phi_{\mathrm{DMC}}}{\varepsilon_{\mathrm{SEI}}^{*1.5}\Delta\Phi_{\mathrm{diff}}} = 0. \qquad [40]$$

Π_{stat} is the positive solution of this expression. It depends most strongly on the electrode potential Φ_E and the onset potential Φ_i^{0} of each reduction reaction.

The stationary value is attained after long-term storage with constant electrode potential. When the electrode potential is changed, Π will deviate from the new stationary ratio. Then, further SEI growth will be distributed such that this new stationary value Π_{stat} is attained. This process is fast (1–2 days) when $\Pi < \Pi_{\mathrm{stat}}$ as illustrated in Fig. 8b. In this case, the inner layer needs to become thicker. The rate at which Π converges toward Π_{stat} is slow, when $\Pi > \Pi_{\mathrm{stat}}$ because the inner layer cannot decrease its thickness. Instead, the outer layer needs to grow to restore Π_{stat}. This takes longer, in part due to the stoichiometry of both reduction reactions. Furthermore, electrons need to traverse a longer distance to reach the front of the outer layer.

By using the relation $L_I = \Pi_{\mathrm{stat}} L$, we can solve Eq. 36a and obtain an analytical expression for the thickness evolution

$$L(t) = \sqrt{\frac{\kappa^{*}\bar{V}_{\mathrm{SEI}}^{\mathrm{Li_2EDC}}}{\varepsilon_{\mathrm{SEI}}^{*} F}\frac{\Delta\Phi_{\mathrm{diff}}}{1 - \Pi_{\mathrm{stat}}}}\,\sqrt{t}. \qquad [41]$$

Most formulas in this section are not valid if the inner layer is formed by a conversion reaction. For this system, a few changes need to be made in the derivation above. However, these changes do not alter the results in a qualitative way. This means that all results above can be transferred. Eq. 41 remains valid if the correct value of Π_{stat} is used. The only noteworthy quantitative difference is the rate at which $\Pi(t)$ converges toward the stationary value. This process is now slower when $\Pi < \Pi_{\mathrm{stat}}$ because more electrons are needed to expand the inner layer.

We highlight that the SEI dual-layer structure should be observable in long-term storage experiments, e.g., in neutron-scattering imaging.

Charge vs. solvent transport.—In the preceding sections, we discuss scenarios in which charge transport in the solid SEI is the rate-limiting transport mechanism. Even though we model solvent diffusion through the SEI pores, electrolyte transport does not become rate-limiting. This is due to the low porosity of the SEI formed in our simulations which makes solvent diffusion slower than charge transport. Now we discuss how structural properties may prevent the formation of a dense SEI. In this scenario, solvent diffusion inside the SEI becomes faster, potentially making solvent diffusion the rate-limiting transport mechanism. Hence we can study how SEI grows for different rate-limiting transport mechanisms.

Structural properties can emerge from surface tensions in the porous structure which can influence SEI morphology and porosity. In this way, the interplay of surface energy and packing structure results in a minimum porosity. Alternatively, small SEI particles could have a certain tightest packing. In both cases SEI will accumulate locally until this porosity is reached, then reactions will displace existing particles instead of further decreasing the porosity. This effect is reminiscent of the solid convection defined in the Model section. Note that it requires deeper insights into the chemistry and structure of the composite solid SEI material to accurately determine the minimum porosity.

Similar to our reference scenario, we consider the reduction of EC and assume that the co-solvent is inert. This reaction is coupled to the solid convection velocity

$$\varepsilon_{\mathrm{SEI}} \mathrm{div}\tilde{v} = \alpha(\varepsilon_{\mathrm{SEI}}) \cdot \bar{V}_{\mathrm{SEI}}^{\mathrm{Li_2EDC}} \cdot \Gamma A \cdot r_{\mathrm{EC}}. \qquad [42]$$

Here, $\alpha(\varepsilon_{\mathrm{SEI}})$ models a smooth transition from local accumulation to SEI displacement, see Fig. 2a. As elaborated on in the Model section, this transition takes place at the SEI volume fraction $\varepsilon_{\mathrm{SEI}}^{\mathrm{crit}}$, a new parameter of our model. Therefore, Eq. 42 will prevent the SEI volume fraction to exceed $\varepsilon_{\mathrm{SEI}}^{\mathrm{crit}}$.

Now, charge transport and solvent transport compete. The mean solid volume fraction $\varepsilon_{\mathrm{SEI}}^{*}$ inside the SEI determines the rate-limiting transport mechanism. We distinguish two cases by comparing $\varepsilon_{\mathrm{SEI}}^{\mathrm{crit}}$ with the stationary solution $\varepsilon_{\mathrm{SEI}}^{\mathrm{stat}}$ of Eq. 34.

1. For $\varepsilon_{\mathrm{SEI}}^{\mathrm{crit}} > \varepsilon_{\mathrm{SEI}}^{\mathrm{stat}}$, i.e., large SEI volume fractions, SEI formation is not disturbed and proceeds exactly like in our reference scenario. In this case, electron conduction is rate-limiting and the porosity establishes itself through a balance between growth and transport at the SEI front, see Eq. 34. Our model does not allow for a denser structure for a given parameter set.
2. For $\varepsilon_{\mathrm{SEI}}^{\mathrm{crit}} < \varepsilon_{\mathrm{SEI}}^{\mathrm{stat}}$, i.e., small SEI volume fractions, solid convection (42) limits the SEI volume fraction. In this case, the mean SEI volume fraction is decreased $\varepsilon_{\mathrm{SEI}}^{*} = \varepsilon_{\mathrm{SEI}}^{\mathrm{crit}}$ and the SEI porosity is increased. Therefore, solvent diffusion through the SEI pores is accelerated and can become rate-limiting.

In summary, structural properties can only increase the mean porosity ε^{*} and accelerate solvent diffusion.

Our extended model captures the two growth mechanisms studied in the literature. SEI can form at the electrode/SEI interface limited by solvent/salt diffusion through the SEI.[30,31] Additionally, SEI can form at the SEI front limited by charge transport through the SEI.[26–29] Below we will proof this correlation between rate-limiting transport mechanism and reaction interface position. We are the first to find an intermediate regime where the reaction interface is located inside the SEI as depicted in Fig. 9. In this case, both mechanisms contribute to the formation rate and the SEI is divided by the reaction interface (marked red). In the inner region, electrons migrate away from the electrode, whereas solvent molecules diffuse toward the electrode in the outer one.

Now, we calculate the relative location $\tilde{\Pi} = L_{\mathrm{reaction}}/L$ of this interface. Electron and solvent transport to this location are balanced and supply the reaction

$$2j_{\mathrm{E}} = 2Fj_{\mathrm{D,EC}}.$$

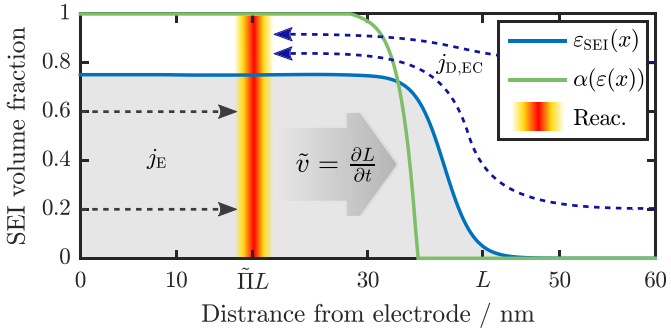

Figure 9. Schematic of self-shaping SEI growth with $\tilde{\Pi} \approx 0.4$. The reaction interface (marked red) is inside the SEI and the reaction is "fueled" by an electronic current j_{E} and a diffusion current of solvent $j_{\mathrm{D,EC}}$. SEI compounds which form at this interface do not decrease the porosity, because $\alpha(\varepsilon_{\mathrm{SEI}}(\tilde{\Pi}L)) = 1$. Instead, they induce the convection velocity $\tilde{v}$ which causes SEI growth.

We can approximate each flux by assuming constant porosity and a linear progression of potential and concentration within the SEI

$$\frac{\kappa^{*}\Delta\Phi_{\mathrm{EC}}}{\tilde{\Pi}L} \approx \frac{FD^{*}c_{\mathrm{EC}}}{(1-\tilde{\Pi})L}, \rightarrow \tilde{\Pi} = \frac{\kappa^{*}\Delta\Phi_{\mathrm{EC}}}{D^{*}Fc_{\mathrm{EC}} + \kappa^{*}\Delta\Phi_{\mathrm{EC}}}. \qquad [43]$$

The ratio $\tilde{\Pi}$ is independent of SEI thickness L. It quantifies the relative share of electron conduction on the rate-limiting role. Fig. 10 shows, how $\tilde{\Pi}$ depends on the effective transport parameters κ^{*} and D^{*}. $\tilde{\Pi} \approx 1$ if electron conduction is the rate-limiting transport mechanism, $\kappa^{*}\Delta\Phi_{\mathrm{EC}} \gg D^{*}Fc_{\mathrm{EC}}$ (top-left). Solvent diffusion is the rate-limiting transport mechanism if $\tilde{\Pi} \approx 0$, $\kappa^{*}\Delta\Phi_{\mathrm{EC}} \ll D^{*}Fc_{\mathrm{EC}}$ (bottom-right). The intermediate regime spans from the bottom-left to the top-right. Here, both transport mechanisms are roughly equally fast, $\kappa^{*}\Delta\Phi_{\mathrm{EC}} \approx D^{*}Fc_{\mathrm{EC}}$.

The transition from electron conduction to solvent diffusion limited growth occurs when $\varepsilon_{\mathrm{SEI}}^{\mathrm{crit}}$ becomes smaller than $\varepsilon_{\mathrm{SEI}}^{\mathrm{stat}}$. Based on the

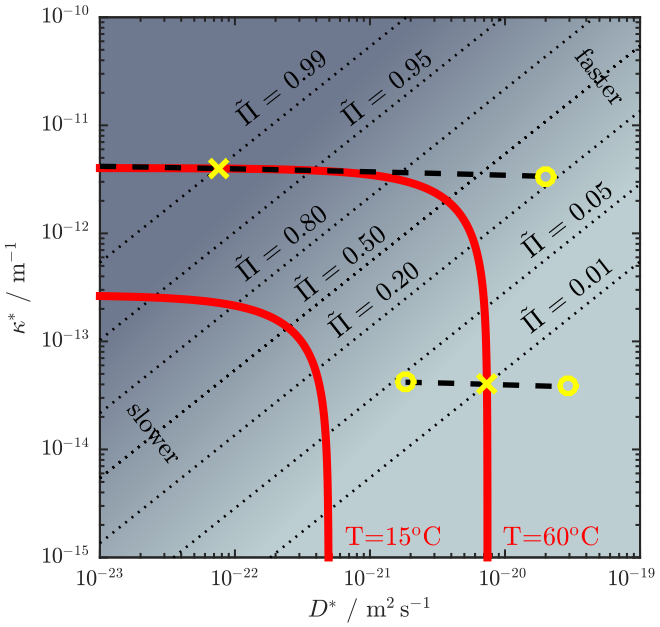

Figure 10. Relative position of the reaction interface $\tilde{\Pi}$ depending on the effective transport parameters D^{*} and κ^{*} according to Eq. 43. The red lines show parameter sets with identical SEI growth rates and satisfy Eq. 45. Dashed black lines show how two parameter sets D^{*}/κ^{*} (marked with yellow crosses) move when porosity is changed but κ^{Bulk} is fixed. The lines end in yellow circles where the formation rate is double (right) or half (left) of the original growth rate.

values discussed earlier, we conclude that $0.8 < \varepsilon_{SEI}^{crit} < 0.998$ would be necessary for solvent diffusion limited growth.

Growth rate analysis.—Let us now evaluate the SEI growth rate for this general, mixed growth scenario (see Fig. 9). Based on the dependence of the growth rate on the material parameters, we discuss how observable SEI properties depend on the underlying rate-limiting mechanism. We obtain an analytical expression for the thickness evolution of these SEIs, by exchanging L with $\tilde{\Pi}L$ in the derivation of Eq. 29

$$L(t) = \sqrt{\frac{\kappa^* \Delta\Phi_{EC} \bar{V}_{SEI}^{Li_2EDC}}{\varepsilon_{SEI}^* F \tilde{\Pi}}}\sqrt{t},$$
$$= \sqrt{\frac{\bar{V}_{SEI}^{Li_2EDC}}{\varepsilon_{SEI}^* F}\left(\kappa^* \Delta\Phi_{EC} + D^* F c_{EC}\right)}\sqrt{t}. \quad [44]$$

Comparison to Eq. 29 reveals that adding solvent diffusion accelerates SEI formation. The $\sqrt{t}$-growth law is still valid as SEI growth is limited by reactant transport.

Naturally, only a subset of the combinations of D^* and κ^* yields reasonable SEI growth rates. A good measure for the growth rate is

$$\frac{\partial L^2}{\partial t} = \dot{L^2} = \frac{\bar{V}_{SEI}^{Li_2EDC}}{F\varepsilon_{SEI}^*}\left(\kappa^* \Delta\Phi_{EC} + D^* F c_{EC}\right) \quad [45]$$

which is constant in time for square-root like growth. In Fig. 10 the red lines correspond to growth rates observed at $T = 15/60\,^{o}C$.[26,30,48] When moving along one of these lines, $\tilde{\Pi}$ increases monotonically from 0 to 1. SEI growth is limited by a single transport mechanism, unless both effective transport parameters, D^* and κ^*, are finely attuned to one another. These cases ($\tilde{\Pi} \approx 1$ and $\tilde{\Pi} \approx 0$) are recovered, when one of the effective transport parameter vanishes. If D^* is small, electron conduction determines the growth rate and κ^* converges toward the values found in.[26] If κ^* is small, solvent diffusion is rate-limiting and D^* converges toward values found in Refs. 30,31

At this point, we want to draw first conclusions with respect to the rate-limiting transport mechanism. As discussed earlier, SEI porosity will attain a small value (0.002 to 0.2) in our reference scenario, where electron conduction is the rate-limiting transport mechanism. Therefore, the SEI volume fraction is approximately one and the growth rate does not depend strongly on the porosity and the Bruggeman coefficient. Instead it is mostly determined by κ^{Bulk}. This is different if solvent diffusion is the rate-limiting. In this case the effective transport parameter scales with ε (to the power of β) which is close to zero. This means that D^* depends strongly on three parameters, namely ε_{SEI}^{crit}, β and D^{Bulk}. SEI formation is a common phenomenon in lithium-ion batteries, occurring in many different systems. The different growth rates of these SEIs lie within two orders of magnitude, even when the SEI chemistry is not comparable. This would imply that ε_{SEI}^{crit} and β are correlated in some way. However, we cannot find any reason why this should be the case. Therefore, it appears unlikely for solvent diffusion to be the rate-limiting transport mechanism.

We now study this difference from another perspective. To this aim, we use the growth rate $\dot{L^2}$ and the relative location of the reaction interface $\tilde{\Pi}$ as parameters to label SEIs (instead of κ^* and D^*). The variation of the SEI growth rate with respect to small porosity fluctuations ε_{SEI}^* is equal to

$$\frac{\partial \dot{L^2}}{\partial \varepsilon_{SEI}^*} = \dot{L^2}\left[\frac{1.5\tilde{\Pi} - 1}{\varepsilon_{SEI}^*} - \frac{\beta(1-\tilde{\Pi})}{1-\varepsilon_{SEI}^*}\right]. \quad [46]$$

We now evaluate and compare the relative variation in the growth rate from a small porosity change $\Delta\varepsilon$

$$\tilde{\Pi} \to 0 \quad \frac{\Delta\dot{L^2}}{\dot{L^2}} \approx \left(1 + \frac{\beta\varepsilon_{SEI}^{\tilde{\Pi}\to 0}}{1-\varepsilon_{SEI}^{\tilde{\Pi}\to 0}}\right)\frac{\Delta\varepsilon}{\varepsilon_{SEI}^{\tilde{\Pi}\to 0}},$$

$$\tilde{\Pi} \to 1 \quad \frac{\Delta\dot{L^2}}{\dot{L^2}} \approx \frac{1}{2}\frac{\Delta\varepsilon}{\varepsilon_{SEI}^{stat}}.$$

This variation is much larger if solvent diffusion is the rate-limiting transport mechanism ($\tilde{\Pi} \to 0$) because either β or $(1-\varepsilon_{SEI}^*)^{-1}$ is large.

We illustrate this in Fig. 10 where two combinations of D^* and κ^* are marked with a yellow cross. Both SEIs have the same growth rate because they are located on the same red line. The difference between these films is the rate-limiting mechanism facilitating the growth. One is solely governed by electron conduction ($\tilde{\Pi} \approx 1$) whereas solvent-diffusion is limiting the other one ($\tilde{\Pi} \approx 0$). We now apply a small perturbation $\Delta\varepsilon$ to the porosity of each film. This changes the effective transport parameters κ^* and D^* according to the Bruggeman relation Eq. 18 and Eq. 19 (κ^{Bulk} is kept constant). The new combination is located on the dashed line in Fig. 10 and has a different growth rate according to Eq. 45. The black lines end in yellow circles where the growth rate is twice or half as large as the original one. It can be seen that the growth rate is hardly influenced by porosity fluctuations if electron conduction is the rate-limiting transport mechanism ($\tilde{\Pi} \approx 1$). Here, the dashed line remains close to the red one for small perturbations. Therefore, large porosity fluctuations are necessary to observe a significant change in the growth rate. If solvent diffusion is the rate-limiting transport mechanism ($\tilde{\Pi} \approx 0$), however, the dashed line is almost orthogonal to the red one. Here, SEI formation is far more susceptible to porosity changes and small fluctuations can alter the growth rate by a factor of two.

Finally, we propose to probe the sensitivity to porosity fluctuations in an experiment and identify the rate-limiting transport mechanism. SEI is deformed during cycling due to volume changes of the electrode particles. These deformations change the porosity which in turn affect the growth rate. This results in systematic variations of SEI thickness when the electrode material deforms anisotropically, e.g., on HOPG. We predict notable thickness differences correlating with the atomistic orientation of the electrode surface.

This could be observed in the imaging experiment proposed earlier in this section. Alternatively, information about the rate-limiting transport mechanism could be obtained in a different experiment. We propose to add additional, marked (e.g. isotopically, see Ref. 7) solvent/electrolyte to a cell with a well-established SEI. The location of newly formed SEI can then be determined with depth profiling techniques after a long storage period.

Discussion

The quality of theoretical studies depends on reliable parameter choices and model assumptions. In this section, we discuss the validity of our choices. To this aim, we justify our assumptions and discuss the dependence of our predictions on them. Our model relies on two important assumptions. Firstly, we assume that the SEI is homogeneous parallel to the electrode surface and develop a one dimensional model. Secondly, we choose a specific dependence of transport parameters on porosity. Besides these assumptions, we make use of physical restrictions such as mass, volume, and charge conservation.

Most obvious, SEI thickness, see Eq. 29, and porosity, see Eq. 34, strongly depend on transport parameters (κ^{Bulk}, D^{Bulk}, β) as discussed above. SEI porosity, for example, is governed by the Bruggeman coefficient β of the electrolyte. Thermodynamic parameters, such as the density of SEI compounds and the onset potential of reduction reactions influence our results as well. However, unlike transport parameters we know these parameters reasonably well. Therefore, an inaccurate choice of these thermodynamic parameters does not influence our results in a significant way. The kinetics of the fast reduction reactions characterized by the activation energy E_A are not critical as well. The only exception is the onset potential of the second reduction reaction. This parameter strongly influences the thickness of the inner layer. Nevertheless, the qualitative observations of the dual-layer systems remain unchanged.

An assailable model assumption is the use of conventional electron conduction in SEI compounds. It is known that several common SEI

compounds have large bandgaps, i.e. Li_2EDC,[21] Li_2CO_3[18] and LiF.[49] Corresponding conductivities are well below the values which are necessary to drive long term SEI formation at realistic rates. Nevertheless, SEI composition is diverse and a conduction like mechanism could emerge. This could be due to defects or band-bending on grain boundaries inside the SEI. Interface effects on such boundaries can promote lithium-ion and potentially electron mobility as shown by Zhang et al.[20] We highlight that the specific transport mechanism used does as demonstrated by replacing conduction with neutral lithium interstitial diffusion. Any mechanism which transports charges though the SEI for the reduction of the solvent at the SEI/electrolyte interface will produce qualitatively similar results. The only requirement is that the mechanism decreases linearly with SEI thickness and that the transport occurs in the solid SEI.

Our assumption of homogeneity parallel to the electrode surface is seemingly contradicted by TEM images of fluctuating SEI thickness.[6] Such measurements, however, typically relate to initial molecular layers of the SEI which our model does not describe. Furthermore, our model offers three explanations for fluctuations in thickness. Fluctuations in the initial SEI composition might locally affect the conductivity. Alternatively, different electrode surfaces, e.g., the basal/edge planes on graphite, can yield different electron injection rates into the SEI. Lastly, SEI thickness fluctuations are expected if solvent diffusion is the rate-limiting process. Our model remains to be applicable locally if these fluctuations occur on a length scale comparable to the SEI thickness. If SEI is exposed to large mechanical stress, e.g., on silicon electrodes,[12] local properties dominate SEI evolution and our model cannot be applied.

Finally, we keep our model simple and clear on purpose and neglect a couple of details. For example, we do not take into account dissolution of SEI species[4] which competes with SEI growth. A nucleation and precipitation process for SEI formation has been proposed by Ushirogata et al.[21] Nucleation and growth of larger SEI particles in solution might be essential during the formation of the initial SEI. Modeling this process would delay the reaction and the precipitation process, which would not influence the long time SEI growth. We neglect this mechanism because we focus on long-term SEI formation. SEI material lost by diffusion into the bulk electrolyte phase could be accounted for by using an effective stoichiometry for the reduction reaction.

Summary

In this work, we discuss a novel one-dimensional model which describes long-term SEI growth.[26] We study several plausible scenarios and predict observable SEI properties depending on the respective assumptions. In all scenarios, SEI thickness evolves with the square root of time because SEI growth is limited by the transport of SEI precursors through the SEI.

In our reference scenario structural properties do not prevent the formation of a dense SEI. Then electron conduction is the rate-limiting transport mechanism. Our model predicts the formation of a porous SEI. SEI porosity is almost constant throughout the film and does not change in time. It is the result of an interplay of two transport processes, electron conduction away from the electrode and solvent diffusion toward the electrode. Therefore, porosity depends solely on the parameters characterizing these processes.

Solvent diffusion is the rate-limiting transport mechanism if structural properties prevent the formation of a dense SEI. We find that the growth rate of the SEI is very susceptible to porosity fluctuations in this case. Therefore, we predict an inhomogeneous thickness distribution of SEI on electrodes with anisotropic volume expansion. If solvent diffusion is the rate-limiting transport mechanism, such fluctuations will be observable in a suitable imaging experiment such as those proposed in the Simulation results section.

Replacing electron conduction with diffusion of neutral lithium interstitials only alters the aforementioned predictions quantitatively. This illustrates that they are universal and independent from the specific transport mechanism in the solid SEI.

In scenarios where two reduction reactions are considered, we observe an additional inner SEI layer close to the electrode. The two layers have different chemical compositions and may also exhibit different morphologies. These properties can be observed and employed to identify the type of the second reduction reaction. We find that the ratio of the inner layer thickness to the total SEI thickness tries to attain a stationary value. This value depends on the electrode potential and will be attained after the electrode potential remained constant for a longer period of time (≈ 60 days). It does not change when the SEI ages and is restored when the SEI is physically damaged. Observing such a connection between the thicknesses of inner and the outer layer would suggest electron conduction to be the rate-limiting transport mechanism.

Conclusions

In this article, we discuss a new model to describe long-term SEI growth on negative electrodes. Our model is the first to capture SEI morphology in a spatially resolved way. Explicitly, we explain the growth of a SEI with finite porosity. We can model different rate-limiting transport mechanisms in the solid SEI phase. Additionally, we can adjust SEI porosity and enable solvent diffusion through the pores to be the rate-limiting transport mechanism. This enables us to predict SEI properties which are unique to each mechanism. These predictions are observable in suitable experiments and should allow to draw conclusions with respect to the rate-limiting transport mechanism for SEI growth. To this aim, we propose in-situ imaging studies of well-established SEI, e.g., with TEM or neutron reflectometry.

Acknowledgments

This work was supported by the German Federal Ministry of Education and Research (BMBF) in the project Li-EcoSafe (03X4636A). Further support was provided, by the bwHPC initiative and the bwHPC-C5 project through associated compute services of the JUSTUS HPC facility at the University of Ulm.

Appendix

Table AI. Nomenclature and description of frequent quantities. Parameters are described and given in Table I.

	Description	Unit
$\varepsilon/\varepsilon_{SEI}$	Porosity/volume fraction of the SEI	-
c	Main solvent (EC) concentration	$mol\,m^{-3}$
c_{Li}	Neutral lithium interstitial concentration	$mol\,m^{-3}$
Φ	Electronic potential (solid SEI)	$V\,m^{-1}$
$v/\tilde{v}$	Electrolyte/solid convective velocity	$m\,s^{-2}$
j_E	Electronic current in the solid SEI phase	$A\,m^{-2}$
r_j	Turnover of reaction "$j \rightarrow k$"	$mol\,s^{-1}\ m^{-3}$
A	Specific surface area of the porous SEI	m^{-1}
L/L_I	Thickness of the SEI / inner SEI layer	nm
Π	Ratio of L_I and L, $\Pi = L_I L^{-1}$	-
$\tilde{\Pi}$	Location of the reaction interface relative to L	-
$\alpha(\varepsilon)$	Transition function between local accumulation and SEI expansion	-
$\varepsilon^*/\varepsilon^*_{SEI}$	Average SEI porosity/volume fraction	-
D^*	Solvent diffusion coefficient at average SEI porosity $D^* = \varepsilon^{*\beta} D^{Bulk}$	$m^2 s^{-1}$
κ^*	SEI conductivity at average SEI volume fraction $\kappa^* = \varepsilon_{SEI}^{1.5}\kappa^{Bulk}$	$S\,m^{-1}$
$\Delta\Phi_{EC}$	$\Phi^0_{EC} - \Phi_E$	V
$\Delta\Phi_{DMC}$	$\Phi^0_{DMC} - \Phi_E$	V
$\Delta\Phi_{diff}$	$\Phi^0_{EC} - \Phi_{DMC}$	V

References

1. S. Kang, M. H. Park, H. Lee, and Y. K. Han, *Electrochemistry Communications*, **23**, 83 (2012).
2. E. Peled, *Journal of The Electrochemical Society*, **126**, 2047 (1979).
3. D. Aurbach, A. Zaban, Y. Ein-Eli, I. Weissman, O. Chusid, B. Markovsky, M. Levi, E. Levi, A. Schechter, and E. Granot, *Journal of Power Sources*, **68**, 91 (1997).
4. D. Aurbach, *Journal of Power Sources*, **89**, 206 (2000).
5. S. H. Kang, D. P. Abraham, A. Xiao, and B. L. Lucht, *Journal of Power Sources*, **175**, 526 (2008).
6. M. Nie, D. P. Abraham, D. M. Seo, Y. Chen, A. Bose, and B. L. Lucht, *The Journal of Physical Chemistry C*, **117**, 25381 (2013).
7. A. L. Michan, M. Leskes, and C. P. Grey, *Chemistry of Materials*, **28**, 385 (2015).
8. K. Xu, Y. Lam, S. S. Zhang, T. R. Jow, and T. B. Curtis, *Journal of Physical Chemistry C*, **111**, 7411 (2007).
9. O. Borodin, M. Olguin, C. E. Spear, K. W. Leiter, and J. Knap, *Nanotechnology*, **26**, 354003 (2015).
10. A. Xiao, L. Yang, B. L. Lucht, S.-H. Kang, and D. P. Abraham, *Journal of The Electrochemical Society*, **156**, A318 (2009).
11. M. Nie and B. L. Lucht, *Journal of The Electrochemical Society*, **161**, 1001 (2014).
12. M. Nie, D. P. Abraham, Y. Chen, A. Bose, and B. L. Lucht, *The Journal of Physical Chemistry C*, **117**, 13403 (2013).
13. C. L. Campion, W. Li, and B. L. Lucht, *Journal of The Electrochemical Society*, **152**, A2327 (2005).
14. S. F. Lux, I. T. Lucas, E. Pollak, S. Passerini, M. Winter, and R. Kostecki, *Electrochemistry Communications*, **14**, 47 (2012).
15. M. Wagner, P. Raimann, A. Trifonova, K.-C. Moeller, J. Besenhard, and M. Winter, *Electrochemical and Solid-State Letters*, **7**, A201 (2004).
16. S. J. Harris and P. Lu, *Journal of Physical Chemistry C*, **117**, 6481 (2013).
17. P. Lu, C. Li, E. W. Schneider, and S. J. Harris, *Journal of Physical Chemistry C*, **118**, 896 (2014).
18. S. Shi, P. Lu, Z. Liu, Y. Qi, L. G. Hector, H. Li, and S. J. Harris, *Journal of the American Chemical Society*, **134**, 15476 (2012).
19. O. Borodin, G. R. V. Zhuang, P. N. Ross, and K. Xu, *Journal of Physical Chemistry C*, **117**, 7433 (2013).
20. Q. Zhang, J. Pan, P. Lu, Z. Liu, M. W. Verbrugge, B. W. Sheldon, Y. T. Cheng, Y. Qi, and X. Xiao, *Nano Letters*, **16**, 2011 (2016).
21. K. Ushirogata, K. Sodeyama, Z. Futera, Y. Tateyama, and Y. Okuno, *Journal of The Electrochemical Society*, **162**, A2670 (2015).
22. A. J. Smith, J. C. Burns, X. Zhao, D. Xiong, and J. R. Dahn, *Journal of The Electrochemical Society*, **158**, A447 (2011).
23. P. Keil, S. F. Schuster, J. Wilhelm, J. Travi, A. Hauser, R. C. Karl, and A. Jossen, *Journal of The Electrochemical Society*, **163**, A1872 (2016).
24. P. Verma, P. Maire, and P. Novák, *Electrochimica Acta*, **55**, 6332 (2010).
25. P. Ganesh, P. R. C. Kent, and D. E. Jiang, *Journal of Physical Chemistry C*, **116**, 24476 (2012).
26. F. Single, B. Horstmann, and A. Latz, *Phys. Chem. Chem. Phys.*, **18**, 17810 (2016).
27. J. Christensen and J. Newman, *Journal of The Electrochemical Society*, **151**, A1977 (2004).
28. D. Li, D. Danilov, Z. Zhang, H. Chen, Y. Yang, and P. H. L. Notten, *Journal of the Electrochemical Society*, **162**, A858 (2015).
29. Y. X. Lin, Z. Liu, K. Leung, L. Q. Chen, P. Lu, and Y. Qi, *Journal of Power Sources*, **309**, 221 (2016).
30. M. B. Pinson and M. Z. Bazant, *Journal of the Electrochemical Society*, **160**, A243 (2012).
31. H. J. Ploehn, P. Ramadass, and R. E. White, *Journal of The Electrochemical Society*, **151**, A456 (2004).
32. M. Tang, S. Lu, and J. Newman, *Journal of The Electrochemical Society*, **159**, A1775 (2012).
33. J. Newman and K. Thomas-Alyea, *Electrochemical Systems*, Electrochemical Society series (John Wiley & Sons, 2004).
34. B. Horstmann, T. Danner, and W. G. Bessler, *Energy & Environmental Science*, **6**, 1299 (2013).
35. D. Bothe and W. Dreyer, *Acta Mechanica*, **226**, 1757 (2015).
36. S. de Groot and P. Mazur, Non-equilibrium Thermodynamics, Dover Books on Physics (Dover Publications, 1962).
37. A. Latz and J. Zausch, *Electrochimica Acta*, **110**, 358 (2013).
38. M. Z. Bazant, *Accounts of Chemical Research*, **46**, 1144 (2013).
39. J. Bockris, A. Reddy, and M. Gamboa-Aldeco, *Modern Electrochemistry 2A: Fundamentals of Electrodics*, Modern electrochemistry (Springer US, 2001).
40. M. Tang and J. Newman, *Journal of The Electrochemical Society*, **159**, A281 (2012).
41. K. Leung, F. A. Soto, K. Hankins, P. B. Balbuena, and K. L. Harrison, *The Journal of Physical Chemistry C*, **120**, 6302 (2016).
42. E. Peled, D. Bar Tow, A. Merson, A. Gladkich, L. Burstein, and D. Golodnitsky, *Journal of Power Sources*, **97-98**, 52 (2001).
43. M. Safari and C. Delacourt, *Journal of The Electrochemical Society*, **158**, 562 (2011).
44. R. Naejus, D. Lemordant, R. Coudert, and P. Willmann, *The Journal of Chemical Thermodynamics*, **29**, 1503 (1997).
45. O. Borodin, G. D. Smith, and P. Fan, *Journal of Physical Chemistry B*, **110**, 22773 (2006).
46. K. Hayamizu, *Journal of Chemical and Engineering Data*, **57**, 2012 (2012).
47. M. Broussely, S. Herreyre, P. Biensan, P. Kasztejna, K. Nechev, and R. J. Staniewicz, *Journal of Power Sources*, **97-98**, 13 (2001) .
48. P. Liu, J. Wang, J. Hicks-Garner, E. Sherman, S. Soukiazian, M. Verbrugge, H. Tataria, J. Musser, and P. Finamore, *Journal of The Electrochemical Society*, **157**, A499 (2010).
49. R. C. Chaney, E. E. Lafon, and C. C. Lin, *Phys. Rev. B*, **4**, 2734 (1971).

F. Single, A. Latz and B. Horstmann. Identifying the Mechanism of Continued Growth of the Solid-Electrolyte Interphase. *ChemSusChem* **11**, 1950–1955 (2018).

CHEMISTRY & SUSTAINABILITY

CHEMSUSCHEM

ENERGY & MATERIALS

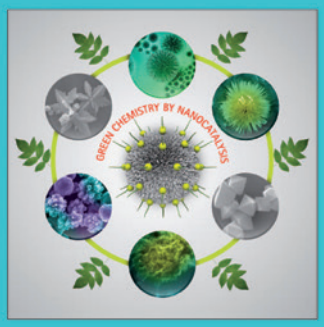

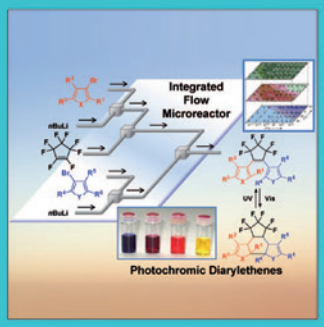

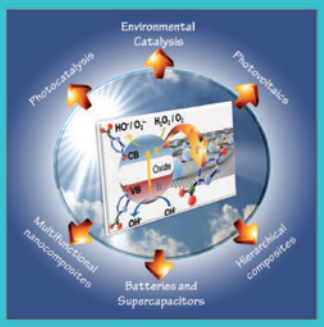

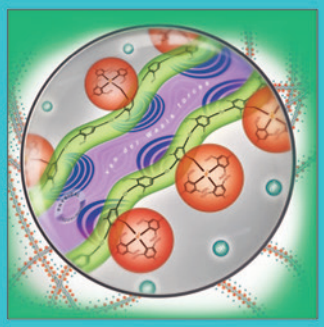

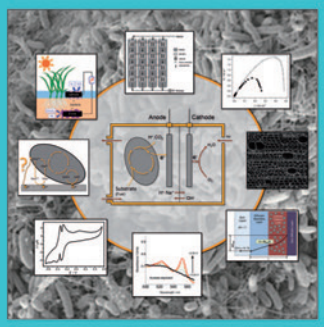

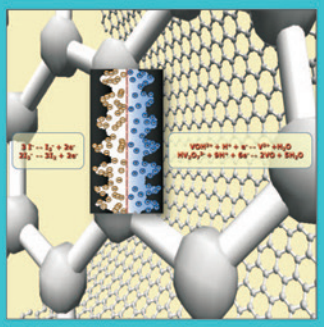

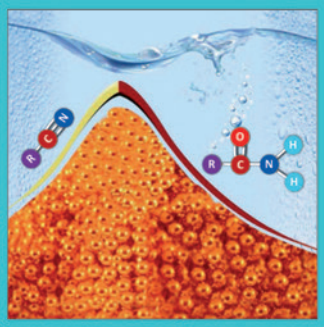

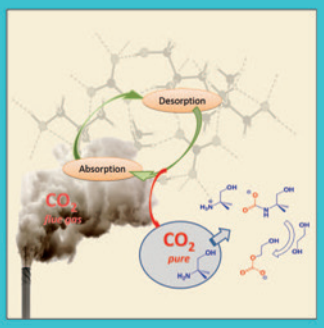

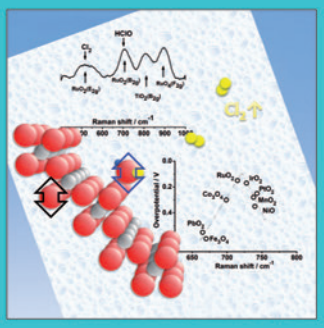

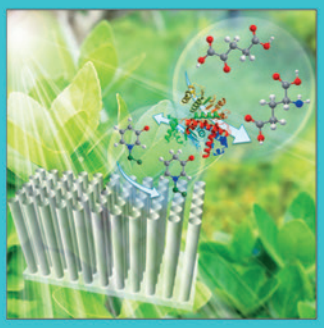

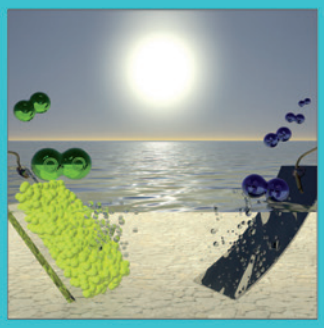

Reprint

A Journal of

ChemPubSoc Europe

WILEY-VCH

www.chemsuschem.org

ChemPubSoc Europe
DOI: 10.1002/cssc.201800077
CHEMSUSCHEM Full Papers

Identifying the Mechanism of Continued Growth of the Solid–Electrolyte Interphase

Fabian Single,[a, b] Arnulf Latz,[a, b, c] and Birger Horstmann*[a, b]

Continued growth of the solid–electrolyte interphase (SEI) is the major reason for capacity fade in modern lithium-ion batteries. This growth is made possible by a yet unidentified transport mechanism that limits the passivating ability of the SEI towards electrolyte reduction. We, for the first time, differentiate the proposed mechanisms by analyzing their dependence on the electrode potential. Our calculations are compared to recent experimental capacity-fade data. We show that the potential dependence of SEI growth facilitated by solvent diffusion, electron conduction, or electron tunneling qualitatively disagrees with the experimental observations. Only diffusion of Li interstitials results in a potential dependence matching the experiments. Therefore, we identify the diffusion of neutral radicals, such as Li interstitials, as the cause of long-term SEI growth.

Introduction

Despite all recent advances, lithium-ion batteries still suffer from continued capacity fade, which ultimately limits battery lifetime. A multitude of processes contribute to the capacity fade. These mechanisms depend on operating conditions as well as on battery chemistry. However, generally, anodic side reactions are found to be the main contributor to capacity fade.[1,2] These reactions reduce electrolyte components, for example, ethylene dicarbonate (EC), while irreversibly consuming cyclable lithium and proceed rapidly on a pristine electrode until they are suppressed by the solid–electrolyte interphase (SEI). SEI is a thin film that covers the electrode surface and consists of insoluble products of anodic reactions.[3–8]

Atomistic simulation methods cover the short-term SEI formation occurring during the first few battery cycles (see Bedrov et al.[9]). After this formation stage, the long-term SEI growth rate is limited by the rate at which SEI precursors cross the SEI. The transport mechanism enabling this flux is referred to as the long-term growth mechanism (LTGM). Even though numerous publications discuss long-term SEI growth,[10–22] the LTGM has not been identified. Several different LTGMs are suggested and studied using continuum models as depicted in Figure 1.

a) Diffusion of solvent/salt molecules/anions through nano-sized SEI pores.[10–12,16,17]
b) Electron tunneling through a dense, inner layer of the SEI.[12,13]
c) Electron conduction through the SEI.[12,14–18]
d) Diffusion of neutral radicals such as lithium interstitials (Li_i).[17,22,23]

Importantly, these four mechanisms predict a similar evolution of long-term capacity fade. Besides electron tunneling, all mechanisms directly result in the experimentally observed $\sqrt{t}$ $\sqrt{t}$ dependence of capacity fade. Electron tunneling predicts a ln$t$ dependence that fits reasonably well with the $\sqrt{t}$ $\sqrt{t}$ behavior if another contribution linear in time is added.[14,24] Such

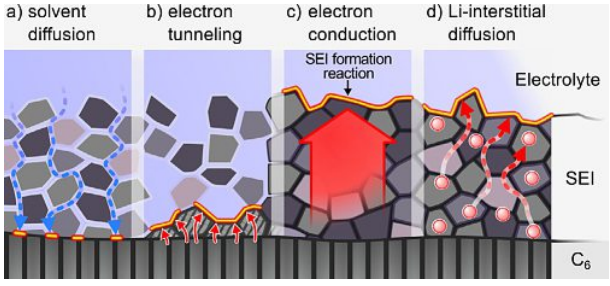

Figure 1. Schematic of four different transport mechanisms suggested to cause long-term SEI growth. a) Solvent diffusion through small SEI pores.[10–12,16,17] b) Electron tunneling through a thin and dense inner SEI layer.[12,13] c) Electron conduction through the SEI.[12,14–18] d) Diffusion of neutral Li_i through the SEI. The SEI formation reaction takes place at different interfaces depending on the mechanism, marked yellow/red.[17,22,23]

[a] F. Single, Prof. Dr. A. Latz, Dr. B. Horstmann
German Aerospace Center (DLR)
Pfaffenwaldring 38–40, 70569 Stuttgart (Germany)
E-mail: birger.horstmann@dlr.de
[b] F. Single, Prof. Dr. A. Latz, Dr. B. Horstmann
Helmholtz Institute Ulm (HIU)
Helmholtzstraße 11, 89081 Ulm (Germany)
[c] Prof. Dr. A. Latz
Ulm University (UUlm)
Albert-Einstein-Allee 47, 89081 Ulm (Germany)
Supporting Information and the ORCID identification number(s) for the author(s) of this article can be found under https://doi.org/10.1002/cssc.201800077.

This publication is part of a Special Issue on Interfacing Theory and Experiment for the Development of Energy Materials.
Please visit the issue at http://doi.org/10.1002/cssc.v11.12.

a term can be attributed to multiple processes, which we will discuss below.

Therefore, additional dependencies must be studied to identify the correct mechanism (or to rule out others). For this reason, we have introduced a SEI model predicting SEI morphology in previous studies.[16,17] If SEI porosity and thickness is measured, for example, with neutron reflectometry,[25] our model offers an alternative feature to compare and validate SEI theory with experiments. Furthermore, we used our models to compare different LTGMs and their response to small porosity fluctuations. Based on this comparison, we concluded that solvent diffusion is unlikely to be the LTGM.[17]

In this paper, we identify the LTGM by comparing the rate of SEI formation at different electrode potentials to experimental capacity-fade data. This dependence has already been used by Tang et al. to rule out solvent diffusion as a possible LTGM.[12] We, however, perform a more comprehensive comparison based on more recent experimental data provided by Keil et al.[1,2] Especially, our comparison includes Li_i diffusion.

The capacity fade of commercial nickel cobalt aluminum oxide (NCA) cells has been measured during long-term open-circuit storage.[1,2] Individual cells were stored at one of 16 different states of charge (SoC), each corresponding to a specific anode potential. These cells were stored for 9.5 months at 50 °C. As capacity fade during open-circuit storage leads to self-discharge, checkup sequences were regularly performed. After these sequences, the SoC referenced to the current cell capacity reached its initial value. The complete measurements are presented in Figure 8 of Ref. [2]. They provide a unique opportunity to compare all plausible LTGMs with respect to the emerging potential dependence.

To this aim, we formulate a model and simulate the evolution of the irreversible capacity (Q_{irr}) and the SoC of a single battery during the experiment. In our previous studies, we considered SEI porosity and dual-layer structure with a novel and extended model.[16,17] Here, we employ a complexity-reduced approach to describe SEI formation. Our method relies on a single effective parameter and allows a consistent comparison of several mechanisms. A sample simulation is presented in Figure 2. During storage, the SEI thickness increases while the relative capacity of the cell decreases, see Figure 2a. In Figure 2b we show the corresponding evolution of the SoC, which decreases smoothly. Note that herein we reference the SoC to the capacity of a fresh cell. With this definition, the SoC increases during the periodically performed checkup sequences but does not reach its initial value. Also shown is the corresponding potential of the negative electrode (U). We determine this potential for a given SoC using the open-circuit potential (OCV) measured by Keil et al. shown in Figure 3a.[1]

Next, we derive the capacity fade model for each LTGM individually. A simplified summary of our models is presented in Equation (8). Detailed model knowledge is not necessary for the subsequent results section in which we compare the potential dependence of each LTGM to an experiment. The interested reader finds additional information in the Supporting Information where we discuss the so-called overhang capacity and elaborate on our parameter choices.

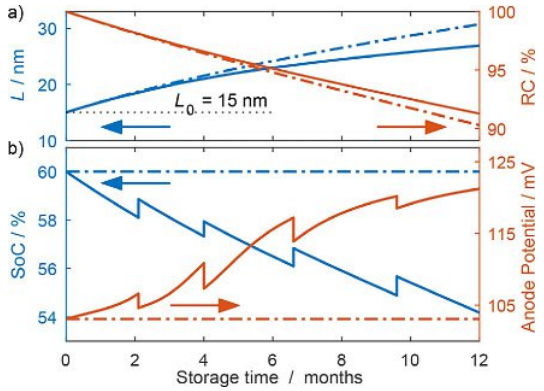

Figure 2. Simulation of a storage experiment with 60% initial SoC and four checkup cycles (Li_i diffusion as the LTGM). a) Evolution of SEI thickness L and the relative capacity of the cell. b) Evolution of the SoC referenced to the original cell capacity and U, the corresponding anode potential vs. Li/Li^+. Jumps in SoC and U correspond to checkup sequences that were part of the experimental procedure. The dash-dotted lines show the evolution of these quantities if the SoC and electrode potential are assumed to be constant.

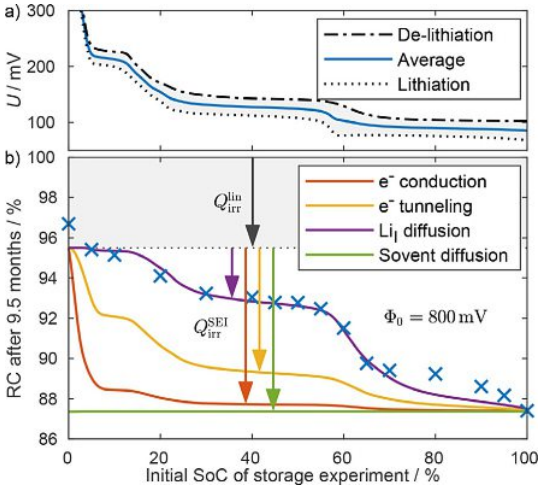

Figure 3. a) OCV of the negative electrode obtained by averaging the lithiation and delithiation voltages (half cell, cycled at C/20). b) Experimentally obtained relative capacity (RC) after 9.5 months of storage (crosses) compared to that predicted by four different LTGMs (lines).

Capacity Fade Model

In our model we assume that the irreversibly lost capacity (Q_{irr}) is the sum of two distinct contributions, $Q_{irr} = Q_{irr}^{SEI} + Q_{irr}^{lin}$. The first part Q_{irr}^{SEI} includes the amount of lithium that is irreversibly consumed by SEI formation during the storage experiment. It is directly coupled to the SEI thickness and its change ($\partial_t Q_{irr}^{SEI}$) can strongly vary with the anode potential, depending on the LTGM assumed. For the second part $Q_{irr}^{lin} = \gamma \cdot t$ we assume no such dependence (γ is a rate constant and t is time). This contribution is assumed to increase at a constant rate with regard to time and factors in various mechanisms, for example, rapid reformation of SEI caused by cracks and delamination of the existing film. Cracks and delamination of the SEI occur during

the periodic checkup sequences. Such physical stress also causes electrode particles to lose contact to the current collector, which causes an irreversible loss of lithium.

SEI formation

We first derive the capacity-fade model, which assumes neutral Li_i diffusing towards the SEI–electrolyte interface as the cause of long-term SEI growth. Li ions take up an electron, forming a neutral radical that diffuses towards the SEI–electrolyte interface and reduces solvent molecules. Note that the following derivation applies to alternative (neutral) radical carriers of negative charge as well. However, it has been suggested that only small radicals such as Li_i are mobile enough in a dense SEI.[22,26] We assume that the SEI is a homogeneous film that spans from $x=0$ (electrode–SEI interface) to $x=L$ (SEI–electrolyte interface). SEI-thickness L is directly related to Q_{irr}^{SEI} through Equation (1),

$$L = \frac{V}{s}\frac{Q_{irr}^{SEI}}{AF} + L_0, \tag{1}$$

where V is the mean partial molar volume of the SEI and s is the mean stoichiometric coefficient of Li_i in the SEI formation reaction. L_0 is the SEI thickness at the start of the experiment, and A is the surface area of the negative electrode.

Continued SEI growth is caused by the LTGM. The corresponding flux density ($j_{SEI}^{(i)}$; [A m^{-2}]) increases the amount of charge lost to SEI formation according to

$$\partial_t Q_{irr}^{SEI} = \pm A \cdot j_{SEI}^{(i)}. \tag{2}$$

Here, the sign has to be set for each mechanism [$(i) = S, e^-, Li_i$ (solvent diffusion, electron conduction, Li_i diffusion)] individually. It is chosen such that the right-hand side of Equation (2) is positive to account for the flux direction and the sign of its charge carriers. $j_{SEI}^{(i)}$ can be approximated as now illustrated for Li_i diffusion. We express the Li_i diffusion flux with Fick's laws as shown in Equation (3),

$$\begin{aligned} j_{SEI}^{Li_i} &= -FD_{Li_i} \cdot \nabla c_{Li_i} \\ &\approx -FD_{Li_i} \cdot \frac{c_{Li_i}|_{x=L} - c_{Li_i}|_{x=0}}{L}. \end{aligned} \tag{3}$$

Here, c_{Li_i} is the Li_i concentration in the SEI and D_{Li_i} is the corresponding diffusion coefficient. F is the Faraday constant. The approximation in the second line is possible because the SEI is homogeneous and reactions take place at the SEI–electrolyte interface only. This is also true if the SEI has nanosized pores, as we have shown in previous studies.[16,17] Note that we do not specify the diffusion pathway. Interstitials could diffuse through the bulk SEI, pass through a selected SEI compound, or move along nanosized SEI pores. The three equations above can be merged into a differential equation for Q_{irr}^{SEI} [Eq. (4)]:

$$\partial_t Q_{irr}^{SEI} = \frac{A^2 s F^2 D}{V} \cdot \frac{c_{Li_i}|_{x=0} - c_{Li_i}|_{x=L}}{Q_{irr}^{SEI} + Q_{irr,0}^{SEI}}, \tag{4}$$

where $Q_{irr,0}^{SEI} = sAL_0F/V$ is the capacity corresponding to L_0.

Next, we determine the Li_i concentration at $x=0$ and $x=L$. At the electrode–SEI interface, interstitials are injected into the SEI. We assume that injection is a fast process and that graphite is in thermodynamic equilibrium with the SEI across the interface. This means that the electrochemical potential of Li in graphite equals the one of Li_i in the SEI

$$\begin{aligned} \mu_{Li_xC_6}^{Li} &= \mu_{SEI}^{Li_i} \\ &= \mu_{SEI,0}^{Li_i} + RT \ln \frac{c_{Li_i}|_{x=0}}{c_{Li_i,max}}. \end{aligned} \tag{5}$$

$c_{Li_i,max}$ is the maximal interstitial concentration and $\mu_{SEI,0}^{Li_i}$ is a (constant) reference value that can be determined using DFT methods. This has been performed by Shi et al. for a Li_2CO_3 host lattice.[23] R is the ideal gas constant and T is the temperature [K]. The electrochemical potential of Li in the electrode is equal to $-FU$.[27,28] Thus, we can express the interstitial concentration at the interface with Equation (6),

$$c_{Li_i}|_{x=0} = c_{Li_i,0} \exp\left(\frac{-FU}{RT}\right), \tag{6}$$

where $c_{Li_i,0}$ is the interstitial concentration at $U=0$ V. $c_{Li_i,0}$ is a model parameter and absorbs all constant contributions in Equation (5). At the SEI–electrolyte interface lithium interstitials do not accumulate. Instead, they are consumed by the fast SEI formation reaction, that is, $c_{Li_i}|_{x=L} = 0$. This is the assumption of transport-limited growth.

Differential equations similar to Equation (4) can be derived for the electron-conduction and solvent-diffusion mechanisms. To this aim, the flux density of the corresponding LTGM is expressed as a function of L and inserted into Equation (2). This is done by applying the same approximations as above to the flux expression. For solvent diffusion we approximate Fick's laws in Equation (7),

$$j_{SEI}^{S} = -FD_{EC} \cdot \nabla c_{EC} \approx -FD_{EC} \cdot \frac{c_{EC,0}}{L}, \tag{7}$$

where c_{EC} is the EC concentration in the SEI pores and D_{EC} is the corresponding diffusion coefficient. c_{EC} is assumed to be zero at the reaction interface ($x=0$). It is assumed to equal the concentration of the active solvent (EC) in the electrolyte, $c_{EC,0}$ at $x=L$. For the electron-conduction model we approximate Ohm's law in Equation (8),

$$j_{SEI}^{e^-} = -\kappa \cdot \nabla \phi \approx -\kappa \cdot \frac{\Phi_0 - U}{L}. \tag{8}$$

Here, ϕ is the electric potential inside the SEI and κ is the (electronic) conductivity. The potential is assumed to equal the onset potential of SEI formation (Φ_0) at the reaction interface and U at the electrode–SEI interface (see Table SI-2).

We use a model developed by Li et al. to describe SEI formation caused by electron tunneling.[13] It assumes a thin inner SEI layer, approximately 2 nm thick, and a much thicker porous outer layer. Electrons tunnel across the inner layer and reduce electrolyte at the interface between these layers. We refer to the original article for a full model description.[13] To simulate this LTGM we replace Equation (2) with Equation (29) in Ref. [13]. It states a differential equation in "Q_{SEI}^{st}", which is equivalent to the variable Q_{irr}^{SEI} in our notation.

Simplified solutions

Equation (4) and the equivalent equations for the other LTGMs can be solved analytically in the simplified case of constant electrode potential (equivalent to constant SoC). We illustrate the accuracy of this assumption in Figure 2. Note that we solve our full model numerically without it. The corresponding solutions in the order solvent diffusion [Eq. (9a)], e^- tunneling [Eq. (9b)], e^- conduction [Eq. (9c)], and Li_i diffusion [Eq. (9d)] are

$$Q_{irr}^{SEI} = A\Gamma\sqrt{FD_{EC}c_{EC}}\sqrt{t+\tau} - Q_{irr,0}^{SEI}, \quad (9a)$$

$$Q_{irr}^{SEI} = A\cdot\alpha(\mathrm{SoC})\cdot\ln[1+\beta(\mathrm{SoC})t], \quad (9b)$$

$$Q_{irr}^{SEI} = A\Gamma\sqrt{\kappa(\Phi_0 - U(\mathrm{SoC}))}\sqrt{t+\tau} - Q_{irr,0}^{SEI}, \quad (9c)$$

$$Q_{irr}^{SEI} = A\Gamma\sqrt{FD_{Li_i}c_{Li_i,0}}e^{-\frac{FU(\mathrm{SoC})}{2RT}}\sqrt{t+\tau} - Q_{irr,0}^{SEI}. \quad (9d)$$

Here, Γ equals $\sqrt{2sF/V}$ and τ is determined by the initial SEI thickness ($L_0(Q_{irr,0}^{SEI})$) through the requirement $Q_{irr}(t=0)=0$. Equation (9b) is the electron-tunneling model derived by Li et al. (see Equation (30) in Ref. [13]). We list all model parameters in Table SI-2 in the Supporting Information.[29–32]

These expressions highlight another way in which electron tunneling differs from the other LTGMs. It is the only mechanism for which time dependence and SoC dependence cannot be separated. This means that Q_{irr}^{SEI} cannot be written in the form $f(\mathrm{SoC})\cdot g(t)$ [see Equation (9a–d)]. Therefore, for electron tunneling, the qualitative shape of the predicted relative capacity in Figure 3b depends on the time it is evaluated at. This behavior is not observed in the experiment.[1]

We emphasize that for most mechanisms, *all* parameters appear as products, forming one effective parameter (after specifying L_0). Specifically, $A\sqrt{D_{EC}c_{EC}s/V}$ for solvent diffusion, $A\sqrt{D_{Li_i}c_{Li_i}s/V}$ for Li_i diffusion, and $A\sqrt{\kappa\Phi_0 s/V}$ (assuming $U \ll \Phi_0$) for electron conduction. Therefore, fitting these theories to the experimental data is a one-dimensional problem. Only a single effective parameter determines the amplitude of capacity fade. This eliminates uncertainties in several parameters. Note that this is not true for the electron-tunneling model.

SoC evolution

Although the SoC of each cell is kept at a relatively constant level during the experiment, we model its evolution for a more accurate description. In this work SoC is referenced to Q_0, the capacity of a fresh cell. During storage, the SoC of each cell decreases due to irreversible reactions

$$\partial_t \mathrm{SoC}(t) = -\partial_t Q_{irr}(t)/Q_0. \quad (9)$$

Equation (9) is used to describe the temporal evolution of the SoC with the initial condition $\mathrm{SoC}(t=0)=\mathrm{SoC}_0$. Open-circuit storage is only interrupted for checkup sequences, which are performed periodically in the experiment. They are used to capture the evolution of the cell capacity $[Q_{actual}(t)=Q_0-Q_{irr}(t)]$. After a checkup sequence, the cells are recharged to their initial SoC (SoC_0). Note that Keil et al. reference their SoC to the current cell capacity $[Q_{actual}(t)]$ for this step.[1] Using Q_0 as the reference, the cells are recharged to

$$\mathrm{SoC}(t_k) = \mathrm{SoC}_0\cdot(1 - Q_{irr}(t_k)/Q_0), \quad (10)$$

at all times t_k at which checkup sequences are performed.

To summarize, during open-circuit storage Equation (9) is used to describe the continuous evolution of the SoC. Equation (10) is used to reset (increase) the SoC after each checkup sequence. Now, both Q_{irr} and the SoC can be integrated simultaneously. Such a simulation is shown in Figure 2. Jumps in the SoC and U correspond to the checkup sequences. It can be seen that the anode potential increases by almost 20 mV during the storage experiment. This affects the rate of SEI formation significantly, depending on the LTGM assumed.

Results and Discussion

We now simulate the storage experiment using different initial SoCs with each of the SEI formation mechanism mentioned above. The capacity fade from these simulations is compared to the experimentally measured one in Figure 3b. The SoC dependence of the relative capacity is evident, and a correlation to the potential of the negative electrode (shown above) can be clearly observed. Capacity fade significantly increases at SoCs larger than 60%, which correlates to the potential step in the OCV. Furthermore, capacity fade remains nearly constant in SoC regions that correspond to the voltage plateaus of graphite.

As elaborated above, we split capacity fade into two contributions. During storage every cell loses the same amount of charge to processes summarized in Q_{irr}^{lin}. This contribution is independent of the SoC and serves as a baseline for the relative capacity in Figure 3b (dotted line). In addition, Q_{irr}^{SEI} is lost to continued SEI formation. This contribution depends on the LTGM assumed and features a SoC dependence.

It is evident that SEI formation facilitated by solvent diffusion does not depend on the potential and cannot reproduce the experimental data. Both, electron conduction and electron tunneling lead to a potential dependence which does not correlate with experimental data. These mechanisms fail to reproduce the pronounced change of the relative capacity at 60% SoC. Instead, they predict a high potential sensitivity at SoCs between 0 and 20%.

Li_i diffusion is the only LTGM that predicts capacity fade in excellent agreement with experimental data. This agreement is attributable to the exponential dependence of capacity fade on electrode potential [see Equation (9d)]. Li_i diffusion correctly describes the capacity fade increase between 10 and 30% SoC as well as the one between 50 and 70% SoC. Small deviations between this model and experimental data are only present at zero SoC and at high SoCs.

We attribute the deviation at zero SoC to the mismatch in electrode areas. Because the coated anode area is larger than the coated cathode area, an overhang area of the anode has no opposed cathode counterpart. The overhang anode acts as a lithium reservoir at small SoCs. We expect a capacity increase of approximately 1% due to the overhang anode at zero SoC as elaborated in the Supporting Information. Taking this into account results in a good agreement with the measured capacity at zero SoC. We attribute the high SoC mismatch to two effects. Because the overhang anode area accumulates lithium during battery storage at low anode potentials, cell capacity is reduced. Most importantly, high SoCs correspond to high cathode potentials that enable electrolyte oxidation reactions. These reactions increase the amount of cyclable lithium in the cell.[33] Modeling these partially counteracting effects is beyond the scope of this work. Therefore, small deviations between our model and the experiment are to be expected at high SoCs.

Now, we evaluate whether alternative parameter choices can improve the agreement between electron conduction/electron tunneling and the experiment shown in Figure 3b. The first option is to assign a potential dependence to one essential model parameter, for instance, the electron conductivity (κ) for electron conduction or the parameter δ for e^- tunneling, see Li et al.[13] However, this seems highly speculative if no physical explanation is given. We can also improve the qualitative agreement of capacity fade resulting from electron tunneling and electron conduction with the experiment by lowering Φ_0. In this way, we reproduce the characteristic decrease of the relative capacity between 50 and 70% SoC (Figure 4). However, in turn, these mechanisms now predict no SEI formation at low SoCs and the required values for Φ_0 are far below any value reported in literature.[6,34] Naturally, SEI formation does not take place at SoCs that correspond to an electrode potential that is larger than the assumed value of Φ_0. One could argue that another process could be responsible for the relative capacity change at low SoC that is observed in the experiment. Theoretically, as calculated in the Supporting Information, full delithiation of the overhang electrode area increases the relative capacity by 1.2%. This increase takes place between zero and 30% initial SoC. However, the measured relative capacity difference between these points equals 3.5%. This means that delithiation of the overhang electrode area alone cannot explain the experimental data. A second process depending on the SoC would be needed to explain this behavior and SEI formation is the only candidate. Thus, SEI formation is present at low SoCs and low values of Φ_0 are unrealistic.

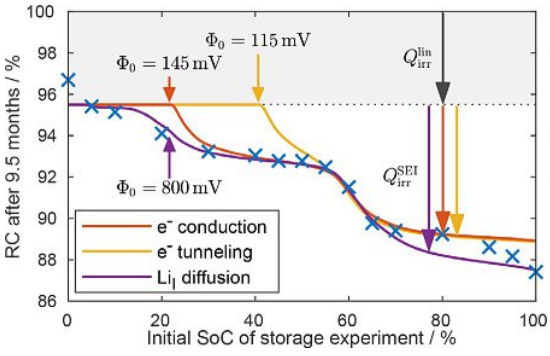

Figure 4. Experimentally obtained relative capacity after 9.5 months of storage (crosses) compared to three different LTGMs (lines). This is the alternative parameterization for which all LTGM-characterizing parameters have been chosen for an optimal fit between 50–80% SoC, see Table SI-1. Note that this choice of parameters is not physically consistent.

Conclusions

To conclude, we compare solid–electrolyte interphase (SEI) growth based on four long-term growth mechanisms (LTGMs) to an experimental study. Only a mechanism such as lithium-interstitial (Li_i) diffusion results in a promising agreement with the experiment, which makes it a very likely candidate for the LTGM. Solvent diffusion does not reproduce a SoC dependence and is very unlikely to be the LTGM. Both, electron conduction and electron tunneling predict a SoC dependence but it does not agree with the experiment for any reasonable choice of parameters. Experimental observation of Li_i within the SEI would provide a further verification of the Li_i diffusion mechanism.

Acknowledgements

We thank Peter Keil for providing us with details and data of his experiments. This work is supported by the German Federal Ministry of Education and Research (BMBF) in the project Li-EcoSafe (03X4636A).

Conflict of interest

The authors declare no conflict of interest.

Keywords: electrochemistry · energy storage · electrolytes · lithium · solid-electrolyte interphase

[1] P. Keil, S. F. Schuster, J. Wilhelm, J. Travi, A. Hauser, R. C. Karl, A. Jossen, *J. Electrochem. Soc.* **2016**, *163*, A1872 – A1880.
[2] P. Keil, A. Jossen, *J. Electrochem. Soc.* **2017**, *164*, A6066 – A6074.
[3] E. Peled, *J. Electrochem. Soc.* **1979**, *126*, 2047 – 2051.
[4] P. Verma, P. Maire, P. Novák, *Electrochim. Acta* **2010**, *55*, 6332 – 6341.
[5] S. H. Kang, D. P. Abraham, A. Xiao, B. L. Lucht, *J. Power Sources* **2008**, *175*, 526 – 532.
[6] A. Xiao, L. Yang, B. L. Lucht, S.H. Kang, D. P. Abraham, *J. Electrochem. Soc.* **2009**, *156*, A318.
[7] M. Nie, D. Chalasani, D. P. Abraham, Y. Chen, A. Bose, B. L. Lucht, *J. Phys. Chem. C* **2013**, *117*, 1257 – 1267.

[8] M. Nie, D. P. Abraham, Y. Chen, A. Bose, B. L. Lucht, *J. Phys. Chem. C* **2013**, *117*, 13403 – 13412.
[9] D. Bedrov, O. Borodin, J. B. Hooper, *J. Phys. Chem. C* **2017**, *121*, 16098 – 16109.
[10] H. J. Ploehn, P. Ramadass, R. E. White, *J. Electrochem. Soc.* **2004**, *151*, A456.
[11] M. B. Pinson, M. Z. Bazant, *J. Electrochem. Soc.* **2012**, *160*, A243 – A250.
[12] M. Tang, S. Lu, J. Newman, *J. Electrochem. Soc.* **2012**, *159*, A1775 – A1785.
[13] D. Li, D. Danilov, Z. Zhang, H. Chen, Y. Yang, P. H. L. Notten, *J. Electrochem. Soc.* **2015**, *162*, A858 – A869.
[14] M. Broussely, S. Herreyre, P. Biensan, P. Kasztejna, K. Nechev, R. J. Staniewicz, *J. Power Sources* **2001**, *97 – 98*, 13 – 21.
[15] J. Christensen, J. Newman, *J. Electrochem. Soc.* **2004**, *151*, A1977.
[16] F. Single, B. Horstmann, A. Latz, *Phys. Chem. Chem. Phys.* **2016**, *18*, 17810 – 17814.
[17] F. Single, B. Horstmann, A. Latz, *J. Electrochem. Soc.* **2017**, *164*, E3132 – E3145.
[18] F. Röder, R. D. Braatz, U. Krewer, *J. Electrochem. Soc.* **2017**, *164*, E3335 – E3344.
[19] A. M. Colclasure, K. A. Smith, R. J. Kee, *Electrochim. Acta* **2011**, *58*, 33 – 43.
[20] F. Röder, R. D. Braatz, U. Krewer in *Computer Aided Chemical Engineering*, Elsevier, Amsterdam, **2016**, pp. 157 – 162.
[21] F. Hao, Z. Liu, P. B. Balbuena, P. P. Mukherjee, *J. Phys. Chem. C* **2017**, *121*, 26233 – 26240.
[22] F. A. Soto, Y. Ma, J. M. Martinez de la Hoz, J. M. Seminario, P. B. Balbuena, *Chem. Mater.* **2015**, *27*, 7990 – 8000.
[23] S. Shi, P. Lu, Z. Liu, Y. Qi, L. G. Hector, H. Li, S. J. Harris, *J. Am. Chem. Soc.* **2012**, *134*, 15476 – 15487.
[24] A. J. Smith, J. C. Burns, X. Zhao, D. Xiong, J. R. Dahn, *J. Electrochem. Soc.* **2011**, *158*, A447.
[25] M. Steinhauer, M. Stich, M. Kurniawan, B.-K. Seidlhofer, M. Trapp, A. Bund, N. Wagner, K. A. Friedrich, *ACS Appl. Mater. Interfaces* **2017**, *9*, 35794 – 35801.
[26] E. Peled, S. Menkin, *J. Electrochem. Soc.* **2017**, *164*, A1703 – A1719.
[27] A. Latz, J. Zausch, *J. Power Sources* **2011**, *196*, 3296 – 3302.
[28] A. Latz, J. Zausch, *Electrochim. Acta* **2013**, *110*, 358 – 362.
[29] O. Borodin, G. D. Smith, P. Fan, *J. Phys. Chem. B* **2006**, *110*, 22773 – 22779.
[30] G. V. Zhuang, K. Xu, H. Yang, T. R. Jow, P. N. Ross, *J. Phys. Chem. B* **2005**, *109*, 17567 – 17573.
[31] K. Edström, M. Herstedt, D. P. Abraham, *J. Power Sources* **2006**, *153*, 380 – 384.
[32] T. L. Kulova, A. M. Skundin, E. A. Nizhnikovskii, A. V. Fesenko, *Russ. J. Electrochem.* **2006**, *42*, 259 – 262.
[33] R. D. Deshpande, P. Ridgway, Y. Fu, W. Zhang, J. Cai, V. Battaglia, *J. Electrochem. Soc.* **2015**, *162*, A330 – A338.
[34] O. Borodin, M. Olguin, C. E. Spear, K. W. Leiter, J. Knap, *Nanotechnology* **2015**, *26*, 354003.

Manuscript received: January 11, 2018
Revised manuscript received: March 8, 2018
Accepted manuscript online: March 12, 2018
Version of record online: April 17, 2018

CHEMISTRY & SUSTAINABILITY
CHEMSUSCHEM
ENERGY & MATERIALS

Supporting Information

Identifying the Mechanism of Continued Growth of the Solid–Electrolyte Interphase

Fabian Single,[a, b] Arnulf Latz,[a, b, c] and Birger Horstmann*[a, b]

cssc_201800077_sm_miscellaneous_information.pdf

1. OVERHANG ANODE AREA

The NCR18650PD cells studied in this experiment are designed such that the coated anode area is larger that the coated cathode area (798 cm^2 vs 767 cm^2).[1] This results in so-called "overhang areas" of the anode. Lithium stored in this part does not participate in regular charge and discharge cycles. However, it can slowly enter/leave the anode during storage and become available for cycling. The driving force for this process is the potential difference between the actual negative electrode and the overhang area. All cells were delivered and stored at approximately 30% SoC before the experiment. We assume this to be the initial SoC of the overhang area. According to the values provided by Keil et al. the overhang area equals 31 cm^2 (note that this is an approximation because the coated area mismatch is reduced slightly when the cell is rolled up). This means that the overhang can store up to 4% of the total cell capacity.

The impact of the overhang area on the lithium balance of the cell depends on the SoC the cell is stored at.

- Cells stored at zero SoC feature a large driving force for overhang delithiation (500 mV). Consequently, we expect full delithiation of the overhang area from its initial SoC of 30%. This corresponds to an increase of the cell capacity by 1.2%.

- The anode potential of cells stored between 20-60% SoC is nearly constant because of the first voltage plateau. This means that the driving force for overhang lithiation is small (1-3 mV). Therefore, we expect little to no impact from this effect for cells stored in this SoC range.

- Cells stored at SoCs larger than 60% feature a driving force of approximately 20 mV which is still relatively small. This causes a capacity decrease because the overlap consumes lithium. Note that this process is slow because of the small driving force. Quantifying the corresponding capacity decrease is beyond the scope of this work.

2. PARAMETERIZATION

We list the model parameters in tables SI-1 and SI-2.

All RLTMs (apart from solvent diffusion) show little to no SEI formation at high electrode potential or low SoC. Therefore, we want to use the experimentally measured capacity fade of the cell stored at zero SoC to calibrate $Q_{\mathrm{irr}}^{\mathrm{lin}}$ (approximately 3.3% capacity fade in 9.5 months). However, the cell stored at this SoC experiences a capacity increase of 1.2% from the overhang anode area, as calculated above. We consider this in our choice of $\gamma = \partial_t Q_{\mathrm{irr}}^{\mathrm{lin}}$ which is chosen such that $Q_{\mathrm{irr}}^{\mathrm{lin}}$ causes 4.5% capacity fade during 9.5 months of storage.

In our simulations, we use an active electrode surface area of $A = 14.34\,\mathrm{m}^2$ which is 187 times the coated geometric electrode area (767 cm^2). Although SEI has a divers chemistry, we use a single SEI formation reaction to parameterize our simulation. Here, we use formation of lithium ethylene dicarbonate (LiEDC) according to ref. 2

$$2\mathrm{EC} + 2\mathrm{Li}^+ + 2e^- \rightarrow (\mathrm{CHOCO_2Li_2})_2 + R\uparrow . \tag{SI-1}$$

The onset potential of SEI formation Φ_0 is chosen as 800 mV vs. $\mathrm{Li}/\mathrm{Li}^+$which is a common value in literature.[3] We have chosen the lithium interstitial diffusion coefficient $D_{\mathrm{Li_I}}$ similar to the lithium diffusion coefficient in graphite.[4] Other parameters which determine the throughput of each transport mechanism are listed in table SI-1 (D_{EC}, A^*, κ and $c_{\mathrm{Li_I},0}$). A^* is the surface area we use for the electron tunneling model exclusively. These parameters are chosen to fit the curves in fig. 3b and fig. 4 to the experimental data. Note that they only scale the amplitude of $Q_{\mathrm{irr}}^{\mathrm{SEI}}(\mathrm{SoC})$ and do not influence the qualitative SoC dependence for all RLTMs except electron tunneling. For the electron tunneling model, most parameters are adopted from the original work, see ref. 5, Table II, 100%. We adjust only two parameters, namely A and U_2. The latter is set to $U_2 = E_{\mathrm{f}}(\mathrm{LiC_6}) - e \cdot \Phi_0$, such that the SEI formation onset potential Φ_0 is equal for all mechanisms.

	Unit	Fig. 3b	Fig. 5
Φ_0	mV vs. Li/Li^+	800/800/800	115/145/800
κ	$S\,m^{-1}$	$8.95{\cdot}10^{-14}$	$8.20{\cdot}10^{-13}$
$c_{Li_I,0}$	$mmol\,m^{-3}$	15.00	15.00
D_{EC}	$m^2\,s^{-1}$	$2.50{\cdot}10^{-22}$	-
A^*	m^2	14.34	57.37

TABLE SI-1: Transport parameters. The three values of the SEI onset potential Φ_0 are given in the following order: electron tunneling/electron conduction/Li_I diffusion. Note that we cannot determine D_{EC},κ and $c_{Li_I,0}$ independently of A because they appear as products only.

	Description	Value	Unit
U	Potential of the negative electrode vs. Li/Li^+		V
Φ_0	Onset potential of SEI formation vs. Li/Li^+[3]	800 / fit	mV
D_{EC}	Diffusion coefficient of EC in SEI pores	fit	$m^2\,s^{-1}$
κ	SEI conductivity	fit	$S\,m^{-1}$
D_{Li_I}	Diffusion coefficient of Li_I in the SEI	$1.0 \cdot 10^{-15}$	$m^2\,s^{-1}$
$c_{Li_I,0}$	Li_I concentration at 0 V vs Li/Li^+	fit	$mol\,m^{-3}$
L	SEI thickness	fit	m
L_0	Initial SEI thickness (at $t = 0$)	15.00	nm
V	Partial molar volume of the SEI (LiEDC)[6]	95.86	$\mu m^3\,mol^{-1}$
s	Stoichiometric coefficient of EC, e^- or Li_I in the SEI formation reaction (SI-1)[2]	2	-
A/A^*	Surface area of the negative electrode	14.34	m^2
Q_0	Nominal cell capacity[7]	10080	C
Q_{actual}	$= Q_0 - Q_{irr}$, cell capacity during storage		C
Q_{irr}	$= Q_{irr}^{lin} + Q_{irr}^{SEI}$, total capacity irreversibly lost during the storage experiment (zero at $t = 0$)		C
Q_{irr}^{lin}	Capacity lost to SEI cracking, delamination and regrowth		C

$Q_{\mathrm{irr}}^{\mathrm{SEI}}$	Capacity lost to SEI formation during the storage experiment (zero at $t = 0$)		C
$Q_{\mathrm{irr},0}^{\mathrm{SEI}}$	Capacity consumed by SEI formation before experiment (corresponds to SEI thickness L_0)		C
$j_{\mathrm{SEI}}^{(i)}$	Flux density of SEI precursor (i) towards the reaction interface		$\mathrm{C\,s^{-1}\,m^{-1}}$
γ	$= \partial_t Q_{\mathrm{irr}}$	18.80	$\mu\mathrm{C\,s^{-1}}$
RC	Relative capacity, relative to Q_0		%
SoC	Full cell state of charge relative to Q_0		%
t	Time measured from the beginning of the storage experiment		s
t_k	Time at which the k-th checkup is performed		s
τ	Constant determined by evaluating eq. (8) at $t = 0$		s
$\mu_{\mathrm{Li}_x\mathrm{C}_6}^{\mathrm{Li}}$	Electrochemical potential of lithium in carbon at x SoC		$\mathrm{J\,mol^{-1}}$
$\mu_{\mathrm{SEI}}^{\mathrm{Li_I}}$	Electrochemical potential of a neutral lithium interstitial in the SEI host lattice		$\mathrm{J\,mol^{-1}}$
$\mu_{\mathrm{SEI},0}^{\mathrm{Li_I}}$	Electrochemical potential of a neutral lithium interstitial in the SEI host lattice at 0 V vs. $\mathrm{Li/Li^+}$		$\mathrm{J\,mol^{-1}}$
F	Faraday constant	96485	$\mathrm{C\,mol^{-1}}$
R	Gas constant	8.314	$\mathrm{J\,mol^{-1}\,K^{-1}}$
T	Temperature (50°C)	323.15	K
e	Elementary charge	$1.602 \cdot 10^{-16}$	C

TABLE SI-2: List of parameters and variables. Note that parameters labeled "fit" are listed in table SI-1.

* Corresponding author: birger.horstmann@dlr.de

[1] Keil, P. Aging of Lithium-Ion Batteries in Electric Vehicles. PhD Thesis, Technische Universität München, München, 2017.

[2] Zhuang, G. V.; Xu, K.; Yang, H.; Jow, T. R.; Ross, P. N. *The Journal of Physical Chemistry B* **2005**, *109*, 17567–17573.

[3] Edström, K.; Herstedt, M.; Abraham, D. P. *Journal of Power Sources* **2006**, *153*, 380–384.

[4] Kulova, T.; Skundin, A.; Nizhnikovskii, E.; Fesenko, A. *Russian Journal of Electrochemistry* **2006**, *42*, 259–262.

[5] Li, D.; Danilov, D.; Zhang, Z.; Chen, H.; Yang, Y.; Notten, P. H. L. *Journal of the Electrochemical Society* **2015**, *162*, A858–A869.

[6] Borodin, O.; Smith, G. D.; Fan, P. *The Journal of Physical Chemistry B* **2006**, *110*, 22773–22779.

[7] Keil, P.; Schuster, S. F.; Wilhelm, J.; Travi, J.; Hauser, A.; Karl, R. C.; Jossen, A. *Journal of The Electrochemical Society* **2016**, *163*, A1872–A1880.

Appendix D

Eidesstattliche Erklärung

Ich erkläre hiermit,

- dass die in der Satzung der Universität Ulm zur Sicherung guter wissenschaftlicher Praxis in der jeweils gültigen Fassung festgelegten Grundsätze eingehalten wurden, insbesondere dass die schriftliche Habilitationsleistung selbstständig verfasst, keine anderen als die angegebenen Quellen und Hilfsmittel benutzt wurden und dass die wörtlich oder inhaltlich übernommenen Stellen als solche kenntlich gemacht sind.
- dass keine weiteren Habilitationsverfahren außerhalb der Fakultät für Naturwissenschaften der Universität Ulm anhängig oder erfolglos beendet wurden.
- dass nie ein Strafverfahren gegen mich eröffnet wurde, und dass auch gegenwärtig kein Strafverfahren gegen mich eröffnet ist.

Ulm, den 15. April 2018